ISINN-25

Neutron Spectroscopy, Nuclear Structure, Related Topics

Dubna 2018

Joint Institute for Nuclear Research

FUNDAMENTAL INTERACTIONS & NEUTRONS, NUCLEAR STRUCTURE, ULTRACOLD NEUTRONS, RELATED TOPICS

XXV International Seminar on Interaction of Neutrons with Nuclei

Dubna, Russia, May 22–26, 2017

Proceedings of the Seminar

Dubna • 2018

УДК 539.125.5(042)
ББК 22.383.2я431+22.383.5я431+22.383.25я431
F97

Fundamental Interactions & Neutrons, Nuclear Structure, Ultracold Neutrons, Related
F97 Topics: Proceedings of the XXV International Seminar on Interaction of Neutrons with Nuclei (Dubna, Russia, May 22–26, 2017). — Dubna: JINR, 2018. — 422 p.
ISBN 978-5-9530-0485-5

This collection of papers reflects the present state of neutron-aided investigations of the properties of the nucleus, including fundamental symmetries, properties of the neutron itself, neutron-excited reactions, and the parameters of the nucleus that determine the reaction cross section, as well as the latest theoretical development of all these problems. The works on experimental investigations in the physics of fission by neutrons of various energies are presented in great detail. The current state of experiments on the physics of ultracold neutrons and facilities to obtain them is described at length. The status achieved by now of the latest (from the viewpoint of technique) experiments and environment studies is covered as well.

Фундаментальные взаимодействия и нейтроны, структура ядра, ультрахолодные нейтроны, связанные темы: Труды XXV Международного семинара по взаимодействию нейтронов с ядрами (Дубна, Россия, 22–26 мая 2017 г.). — Дубна: ОИЯИ, 2018. — 422 с.
ISBN 978-5-9530-0485-5

В сборнике представлено современное состояние исследований свойств ядра с помощью нейтронов: фундаментальных симметрий и свойств самого нейтрона, возбуждаемых им реакций и параметров ядра, определяющих их сечения, а также последние теоретические разработки всех этих вопросов. Очень детально представлены работы по всем аспектам, связанным с экспериментальными исследованиями физики деления ядра нейтронами различных энергий. Достаточно полно описано современное состояние экспериментов по физике ультрахолодных нейтронов и установок для их получения, а также достигнутый к настоящему времени статус методически новейших экспериментов и результаты экологических исследований.

УДК 539.125.5(042)
ББК 22.383.2я431+22.383.5я431+22.383.25я431

ISBN 978-5-9530-0485-5

CONTENTS

Fast Neutron Induced Reactions

Nuclear Structure, Nuclear Data

Preface

On May 23–26, 2017 JINR hosted the 25th International Seminar on Interaction of Neutrons with Nuclei: Fundamental Interactions & Neutrons, Nuclear Structure, Ultracold Neutrons, Related Topics (ISINN-25), dedicated to the 60th anniversary of the Frank Laboratory of Neutron Physics (FLNP). The Seminar is conducted by FLNP annually and attracts experienced and young scientists from JINR laboratories and many countries. About 130 physicists from JINR and the leading neutron centers and universities of Belarus, Belgium, Bulgaria, Canada, China, Estonia, Egypt, France, Germany, Georgia, India, Iran, Poland, Romania, Serbia, Slovakia, South Africa, Turkey, USA, and Russia attended ISINN-25.

The Seminar program traditionally includes reports on new results obtained in the field of fundamental interactions and physics of ultracold neutrons (UCN), nuclear fission, nuclear analytical methods in biology and ecology, nuclear reactions with fast neutrons, the structure and decay of excited nuclei, methodological aspects of experiments with neutrons, subcritical systems controlled by accelerators. This year the program was supplemented by a number of review reports related to the FLNP Jubilee and to the 25th anniversary of the Seminar. In just four days 66 oral and more than 40 poster presentations were presented (for more details, see http://isinn.jinr.ru/past-isinns/isinn-25/program.html).

The first plenary session was opened with a review-report by P. Geltenbort (ILL) on the history of cooperation between ILL (Grenoble) and FLNP JINR, as well as the role of ISINN annual seminars in this cooperation. The reporter participated in these meetings more than 20 times and is the co-author of many joint works carried out by the FLNP and other Russian institutes at ILL. World-class results, such as the extremely precise measurement of the lifetime of a free neutron, the discovery of quantum neutron states in the Earth's gravitational field and the effect of small UCN heating, the measurement of parity violation effects in the interaction of thermal polarized neutrons with light nuclei at a record low (10^{-8}) level of accuracy, are the subject of legitimate pride of cooperating institutes.

A report by A. Frank (FLNP JINR) reviewed the results of many years of research on the quantum optics of UCN performed in the JINR–ILL collaboration. The results of experiments on precision verification of the dispersion law for neutron waves in media, on nonstationary diffraction by moving gratings, and on the propagation of neutron waves in accelerated media were considered. The obtained fundamental results have received the deserved world recognition and, that is especially important, are a basis and stimulus for the further researches. As new experimental results in the field the study of the diffraction of cold neutrons on surface acoustic waves (SAWs) were presented by G. Kulin (FLNP JINR). They showed that with the use of standing SAWs, the applicability of the theory of the effective potential in the case of giant acceleration of the medium can be verified. S. Doege (ILL) reported the results of the first direct studies of the growth of hydrogen and deuterium crystals used in promising sources of UCN. A keen interest was generated by the report given by V. Nesvizhevsky (ILL), on estimations of the inelastic interaction of neutrons with nanostructured media at low energies and temperatures.

New important information on parameters of weak nucleon-nucleon interaction, which was obtained from a very precise study of the P-odd asymmetry of α-particle emission in the reaction $^{10}B(n,\alpha)^{7}Li$ measured with intensive polarized thermal neutron beam of the ILL high flux reactor, was reported by P. Sedyshev (FLNP JINR).

In the session devoted to study of fast-neutron induced reactions, N. Fedorov (FLNP JINR and Lomonosov MSU) and D. Grozdanov (FLNP JINR) presented the first results obtained by TANGRA collaboration with tagged 14 MeV neutrons in inelastic scattering on light nuclei. The results demonstrate an effectiveness of tagged neutrons for study of different nuclear reactions.

The investigation of structure and properties of excited nuclei by slow neutrons is a tradition topic of the Seminar. As usually, new results were reported by Dubna–Hanoi collaboration on study of (n,2γ)-reaction. New measurements of $^{171}Yb(n_{th},2\gamma)$-reaction and respective data analysis were presented. The modified approach to study of the phase transitions

of the superfluidity–Fermi gas in the excitation spectra of heavy nuclei was presented by Vu Du Cong (FLNP JINR). D. Khlyustin (INR RAS) reported on the creation and characteristics of the INES facility on the base of the Moscow meson factory.

The traditional for ISINNs and very popular among the JINR member-states topic – "Nuclear analytical methods in the life and material sciences", was presented by some plenary talks. The coordinator of the United Nations Program on Air Pollution Research in Europe M. Frontasieva (FLNP JINR) reported on the results of an extensive study of atmospheric precipitation by heavy metals and other toxic elements in the last 25 years. A striking impression was made by review talk of I. Zinicovscaia (FLNP JINR) devoted to recent results in bionanotechnology, conducted jointly by biophysicists from Moldova, Georgia and Russia at the IBR-2 reactor. Many interesting reports were done in parallel sessions by young scientists working in the field. Among them the talk by M. Gustova (FLNR JINR) on the study of cosmic dust in the meteor shower of the comet ISON caused a lively discussion.

The methodical aspects of experiment with neutrons were presented in many original talks. Sh. Zeinalov (FLNP JINR) reported on an important improvement in the positional-sensitive method of detecting nuclear fission fragments in combination with the registration of prompt fission neutrons. In a series of reports by colleagues from the Iranian Institute of Nuclear and Technological Studies E. Bavrngin and Z. Gholamzadeh, an overview of the methodological possibilities of applied research at the Tehran Research Reactor was done. D. Wang (XJTU, Xi'an) and J. Zhang (NWINT, Xi'an) presented an original proton imaging systems for the magnetic proton recoil neutron spectrometer.

The last day of the Seminar was entirely devoted to discussing various aspects of nuclear fission. In the reports of I. Guseva (NRC KI PNPI) and A. Göök (JRC, Gel), the experimental study of so-called ROT and TRI effects in binary and ternary fission induced by polarized thermal neutrons were described. Yu. Kopatch (FLNP JINR) told about a first measurement with a hot beam of polarized neutrons provided by the reactor in Munich. The experiment was aimed at investigation of the same effects in the lowest neutron resonance of ^{235}U, which, with increasing experimental statistics, can significantly improve our understanding of the nuclear fission nature. S. Kadmensky (VSU, Voronezh) presented one of the quantum-mechanical approaches to the description of ROT and TRI effects.

A. Vorobiev (NRC KI PNPI) reported on the precise study of angular and energy distributions of the prompt fission neutrons from thermal neutron-induced fission of ^{239}Pu. In A. Gagarsky's (NRC KI PNPI) talk the new measurements of the angular anisotropy of fission fragments from fission of lead and plutonium, caused by neutrons with energies up to 200 MeV, were discussed. The mechanisms of formation of angular distributions and high spins of fission fragments were considered in the second talk of S. Kadmensky (VSU).

D. Gremyachkin and K. Mitrofanov from IPPE, Obninsk presented very interesting results on study of delayed neutrons from fission of ^{241}Am and ^{235}U induced by thermal and fast neutrons.

The Seminar program was concluded by the reports of D. Kamanin (FLNR JINR) and Yu. Pyatkov (MEPhI), devoted to the situation with the study of exotic fission mode, the so-called collinear cluster decay. A comparison was done between the results of recent measurements carried out in ILL, France and the data of previous experiments performed in Dubna. The conclusion was made about the need for new measurements to resolve the inconsistencies between these results.

The success of the Seminar showed that its format is useful not only for presenting the results obtained, but also for discussing the ongoing work and the creation of new working collaborations.

ISINN-25 Co-chairmen

W.I. Furman
V.N. Shvetsov

Neutron Sources, Accelerator Driven Systems

THE PROBLEM OF THE REACTOR ANTINEUTRINO SPECTRUM ERRORS AND PROPOSED SOLUTION IN THE SCHEME WITH REGULATED SPECTRUM

V. I. Lyashuk

Institute for Nuclear Research, Russian Academy of Sciences, Moscow, Russia
National Research Center "Kurchatov Institute", Moscow, Russia

Abstract: The investigation devoted to development and research of performance for novel type of $\bar{\nu}_e$-source which ensures: 1) hard antineutrino flux which significantly larger then reactor $\bar{\nu}_e$-flux; 2) rate of antineutrino detector counts > 10^3 per day.

The proposed scheme is based on ^{7}Li (n,γ)^{8}Li activation near the reactor active zone (AZ) and transport of the fast β$^-$-decaying ^{8}Li ($T_{1/2}$(^{8}Li) = 0.84 s) toward a remote neutrino detector and back in the closed loop to AZ for the next (n,γ)-activation of lithium in the continuous cycle. $\bar{\nu}_e$-spectrum of ^{8}Li is well known and hard: mean energy ~ 6.5 MeV; it's maximum - up to 13 MeV. For the neutrino investigations the source of such combined hard $\bar{\nu}_e$-spectrum (from ^{8}Li and β$^-$-decays of fission products in AZ) has the serious advantages compare to nuclear reactors $\bar{\nu}_e$-spectrum because the neutrino interaction cross section depends on the energy as $\sigma \sim E_\nu^2$. For increasing of hard lithium antineutrinos part in the total spectrum a being pumped reservoir is installed near the $\bar{\nu}_e$-detector. Such an installation will ensure not only harder $\bar{\nu}_e$-spectrum in the detector volume but also an opportunity to register $\bar{\nu}_e$-interaction at different summary spectrum hardness varying smoothly (without stop of the experiment) a rate of ^{8}Li (or it's chemical compound) pumping in the closed loop.

The proposed installation with combined $\bar{\nu}_e$-spectrum can ensure hard antineutrino flux (in the detector position) significantly higher compare to reactor one. The rate of neutrino detector counts in such hard flux can be increased strongly (from times to order and more) compare to counts from reactor $\bar{\nu}_e$-flux part. High count rate allows to use compact detectors with volume about ~ m^3. The calculation confirmed that count errors in such combined $\bar{\nu}_e$-spectrum can be decreased in two times and more compare to errors in reactor $\bar{\nu}_e$-spectrum.

1. INTRODUCTION. ANTINEUTRINO SPECTRUM FROM ^{8}LI AND REACTOR ACTIVE ZONE. GENERALIZED HARDNESS OF THE TOTAL NEUTRINO SPECTRUM (FROM ACTIVE ZONE PLUS FROM ^{8}LI)

The results in registration, accumulation and understanding of neutrino data in many cases are determined by characteristics of the neutrino source, such as neutrino flux and spectrum. First of all the main problems of neutrino detection are associated with extremely small cross sections of these reactions. What is why a high neutrino flux is determining requirement for obtaining of reliable results. Today the maximal intensive neutrino flux is ensured by nuclear reactors - the most widely and traditionally used $\tilde{\nu}_e$-sources.

In spite of the apparent superiority on neutrino flux the nuclear reactors has a disadvantage: too-small hardness of $\tilde{\nu}_e$-spectrum. This character is extremely negative as the probability of registration strongly depends on neutrino energy. For the considered here reactor antineutrino energy the neutrino cross section is proportional to it's energy squared - $\sigma_\nu \sim E_\nu^2$. Antineutrinos $\tilde{\nu}_e$ emitted at β$^-$-decay of fission fragments in a nuclear reactor have

rapidly decreasing spectrum and energy $E_{\bar{\nu}} \leq 10$ MeV (i. e., them spectrum is too-small).

The disadvantage of rapidly dropping spectrum can be filled having realized the idea [1] to use a high-purified isotope ^{7}Li for construction of lithium blanket (also called as converter) around the active zone of a reactor [2]. A short-lived isotope ^{8}Li ($T_{½} = 0.84$ s) is created under flux of reactor neutrons in the reaction ^{7}Li(n,γ)^{8}Li and at β^--decay it emits hard antineutrinos of a well determined spectrum with the maximum energy $E_{\bar{\nu}}^{max} = 13.0$ MeV and mean value $\bar{E}_{\bar{\nu}} = 6.5$ MeV.

The neutrino spectrum from ^{235}U (as the main fuel component) is presented in the Fig. 1 in comparison with ^{8}Li neutrino spectrum [3,4]. The advantages of hard $\bar{\nu}_e$-spectrum of ^{8}Li is clear visible on the example of sharp rise for cross section of inverse beta decay reaction $(\bar{\nu}_e + p \rightarrow n + e^+)$ (see Fig.1).

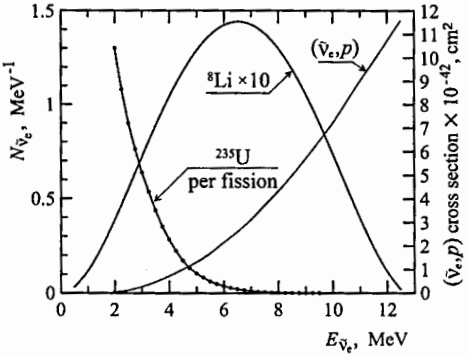

Fig. 1. Spectrum of antineutrinos from β^--decay of ^{8}Li [4] (see left axis) and fission fragments of ^{235}U [3] (left axis). Cross section of $(\bar{\nu}_e, p)$ – reaction is given on the right axis [5].

So, this blanket will act as a converter of reactor neutrons to antineutrinos. In fact the such construction of the blanket around the active zone (as a neutron source) is the most simple scheme of lithium antineutrino source. We can call this type of the $\bar{\nu}_e$ source as steady spectrum source [2, 6–8]. As a result the total $\bar{\nu}_e$-spectrum from the active zone of a reactor and from decays of ^{8}Li isotope becomes considerably harder in comparison with the pure reactor neutrino spectrum. Note that reactor antineutrino spectrum is specified also with another problem as instability in time due to dependence of partial spectra from nuclear fuel composition (^{235}U, ^{239}Pu, ^{238}U, ^{241}Pu) which vary in time in operation period. The distribution of the total reactor $\bar{\nu}_e$–spectrum is known with significant errors which strongly rise at the energy above ~ (5–6) MeV [9,6].

Let us define the productivity factor of the blanket k (or possible to call k as coefficient of blanket efficiency) as number of ^{8}Li nuclei produced in the lithium blanket per one fission in the active zone. It is clear that the hardness of the total spectrum will more larger as productivity factor k will be more higher. An illustration of the resulting total spectrum in case of rising productivity factor is given in the Fig. 2.

For our purpose (creation of the neutrino source of significantly larger hardness than possible to obtain by above mentioned simple scheme) let us introduce the definition of the generalized hardness for total neutrino spectrum [10,11]. Let $F_{Li}(\vec{r})$ and $F_{AZ}(\vec{r})$ - densities of lithium antineutrinos flux from the blanket and antineutrino flux from the active zone, $\bar{n}_\nu = 6.14$ - number of reactor antineutrinos emitted per one fission in the active zone. We admit that the hardness of the summary $\bar{\nu}_e$ - spectrum at the point $\vec{r}$ equals one unit of hardness if the ratio of densities $F_{Li}(\vec{r})/F_{AZ}(\vec{r})$ equals to $1/\bar{n}_\nu$. Then the total spectrum generalized hardness is:

$$H(\vec{r}) = \overline{n}_{\nu} \frac{F_{\mathrm{Li}}(\vec{r})}{F_{\mathrm{AZ}}(\vec{r})} \quad . \tag{1}$$

This definition is very convenient as in so doing the averaged (over the blanket volume) value generalized hardness (for the total $\tilde{\nu}_e$-spectrum) of steady spectrum sources (these models are also considered in [2,6-8]) is estimated by the value of its productivity factor k of the blanket. Taking into account this definition of the hardness the values of productivity factors k on the Fig. 2 coincide with values of the generalized hardness H for total spectra.

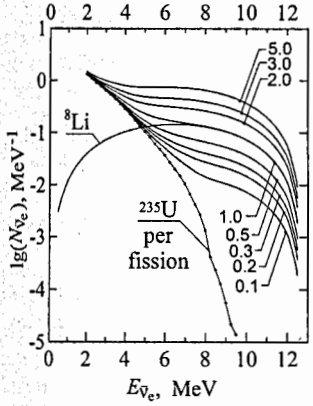

Fig. 2. Neutrino spectrum from: ^{235}U [3], ^8Li [4] and total spectra (from combination of active zone and ^7Li blanket) for different factors k indicated for curves [2,11,12].

2. ANTINEUTRINO SOURCE WITH VARIABLE AND REGULATED SPECTRUM ON THE BASE OF ^{8}LI ISOTOPE

It is possible to supply powerful neutrino fluxes of considerably greater hardness by means a facility with a transport mode of operation: liquid lithium is pumped over in a closed cycle through a blanket and further toward a remote neutrino detector (Fig. 3). For increasing of a part of hard lithium antineutrinos a being pumped reservoir is constructed near the $\tilde{\nu}_e$-detector. Such a facility will ensure not only more hard spectrum in the location of a detector but also an opportunity to investigate $\tilde{\nu}_e$-interaction at different spectrum hardness varying a rate of lithium pumping over in the proposed scheme with the closed loop [10-13].

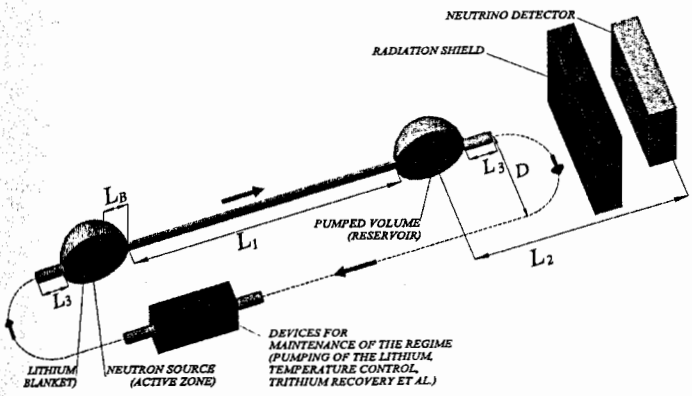

Fig. 3. The principal scheme of the neutrino source with variable (regulated and controlled) spectrum.

Lithium in the blanket (activated by reactor active zone neutrons) is pumped continuously through the delivery channel to the remote volume (reservoir, which is set close to the neutrino detector) and further back to the blanket. The rate of pumping can be smoothly varied by the installation for maintenance of the regime. L_1 - distance between lithium blanket and pumped reservoir. L_2 - distance from the reservoir center and neutrino detector. L_B - the lithium layer in the blanket. L_3 - straight length of the channels before (and after) the channel

turning along the direction of lithium pumping. D - the diameter of channel turning.

Due to the geometrical factor the total $\tilde{\nu}_e$-spectrum in the detector volume (i. e., the resulting $\tilde{\nu}_e$-spectrum formed by $\tilde{\nu}_e$-flux from the reactor active zone plus from β^--decay of ^{8}Li) will be more harder compare to reactor antineutrino spectrum. It is clear that the closer to the reservoir will be detector the total spectrum will be harder. From the other side if the detector will be farther from the reactor then the part of the soft reactor $\tilde{\nu}_e$-spectrum in the total spectrum will be more small. For the fixed distance L_1 between the lithium blanket and the reservoir and fixed L_2 (from the detector to the reservoir) the most harder spectrum is ensured for the position along the direction from the lithium blanket to the pumped reservoir.

3. DEPENDENCE OF $(\tilde{\nu}_e, p)$ – CROSS SECTION AND ERRORS OF THE TOTAL $\tilde{\nu}_e$-SPECTRUM FROM THE GENERALIZED HARDNESS H.

The $\tilde{\nu}_e$-cross section in the total spectrum is the additive value of the cross sections in the $\tilde{\nu}_e$-flux from the active zone and from ^{8}Li antineutrinos [2,11,12,14]. In fact the total number of $\bar{\nu}_e$ (entering to the neutrino detector) is:

$$N_{\tilde{\nu}_e} = N_{AZ} + H(\vec{r})\frac{N_{AZ}}{\bar{n}}, \qquad (2)$$

where N_{AZ} - number of $\bar{\nu}_e$ from the active zone, $\bar{n}_\nu$ - number of $\bar{\nu}_e$ from the active zone per one fission, $H(\vec{r})$ - averaged generalized hardness of the total spectrum in the detector position. The second summand determines the number of lithium antineutrinos.

More strictly for density of the total $\tilde{\nu}_e$-flux in the point $\vec{r}$ we can write:

$$F_{\tilde{\nu}_e}(\vec{r}) = F_{AZ}(\vec{r}) + H(\vec{r})\frac{F_{AZ}(\vec{r})}{\bar{n}}, \qquad (3)$$

where $F_{AZ}(\vec{r})$ - density of the $\tilde{\nu}_e$-flux from the active zone, $H(\vec{r})$ - the exact value of the generalized hardness in the point $\vec{r}$.

As the cross section is the additive value then (similar to (2) and (3)) for the inverse beta decay reaction ($\bar{\nu}_e + p \rightarrow n + e^+$) we can write the cross section for the total $\tilde{\nu}_e$-spectrum:

$$\sigma_{\bar{\nu}_e p}(\vec{r}) = \sigma^{AZ}_{\bar{\nu}_e p} + H(\vec{r}) \times \sigma^{Li}_{\bar{\nu}_e p}. \qquad (4)$$

The threshold of the reaction is 1.8 MeV but often (depending on the background) the used threshold is 3 MeV. Taking into account the data of [5] the cross section (4) was calculated as function of the hardness H for the $E_{threshold}$ = 3 MeV (see Fig. 4).

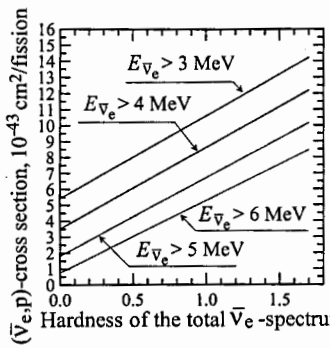

Fig. 4. Cross section of $(\bar{\nu}_e + p \rightarrow n + e^+)$-reaction in the total $\bar{\nu}_e$-spectrum as function of the hardness H. Values of cross sections at H=0 correspond to $\bar{\nu}_e$ – spectrum from pure ^{235}U. The results are given for different thresholds of registration: 3, 4, 5 and 6 MeV.

At increase of H-value the double rise (and more) of the cross section is caused by enlarged part of lithium neutrinos in the total spectrum and energy squared dependence $\sigma_\nu \sim E_\nu^2$.

For lithium spectrum the relative yield to the cross section (4) ensured by more high energy

neutrinos is significantly larger compare to the the reactor spectrum (here in calculation we used $\bar{\nu}_e$-spectrum of ^{235}U [15] as a single fuel isotope). This fact suggest to us to recalculate the cross section for more higher thresholds. The results (for thresholds - $E_{threshold}$ = 4, 5 and 6 MeV) show that for hard total spectrum the lithium yield to the cross section strongly dominates the reactor part [12,14] (see Fig. 4).

For the perspective experiments we need to evaluate the advantages from the combined $\bar{\nu}_e$-flux (from AZ plus from β^--decay of ^8Li) given by well known ^8Li spectrum. Last years the problem of $\bar{\nu}_e$-spectrum errors become very serious as the recent measurements of $\bar{\nu}_e$-spectrum in Daya Bay, Reno and Double Chooz experiments reveal significant excess of neutrinos with energy 5-7 Mev in the spectrum [16]. This bump in experimental spectrum caused active discussion of the used models, nuclear databases and understanding of some results in reactor oscillation experiments.

Here we want to confirm the decrease of count errors in case of such combined $\bar{\nu}_e$-flux. For this purpose we calculated the dependence of errors (in the total $\bar{\nu}_e$-spectrum) on the energy of antineutrinos and then these errors were averaged on their total $\bar{\nu}_e$-spectra for every of thresholds: $E_{threshold}$ = 3, 4, 5, 6 MeV [12,14].

The result dependences of averaged errors on hardness H for the combined spectrum (from AZ with bump in the spectrum plus from ^8Li) for specified thresholds are presented in Fig. 5. In the first evaluation of the count errors (caused by errors of the $\bar{\nu}_e$-spectrum of AZ we had realized the more simple way: the count errors were averaged for whole energy interval from $E_{threshold}$ up to o the maximal energy in the total spectrum of the considered hardness H. After that the obtaned error (specified for the every considered H) were used to calculation of the relative count errors for the every considered hardness H. In spite of the simplicity of the evaluation this rough calculation had allowed to reveal the promising way: to decrease the errors by means of increase of hardness H from one side and increase of the threshold $E_{threshold}$ of registration from the second side.

But the more accurate calculation with detailed energy bins and evaluation of errors for each of bins depending on the hardness H gives more sharp decrease of errors for more harder $\bar{\nu}_e$-spectrum. These results are strongly important as demonstrates the possibility to decrease the count errors in several times compare the significant errors in case of $\bar{\nu}_e$-spectrum of AZ.

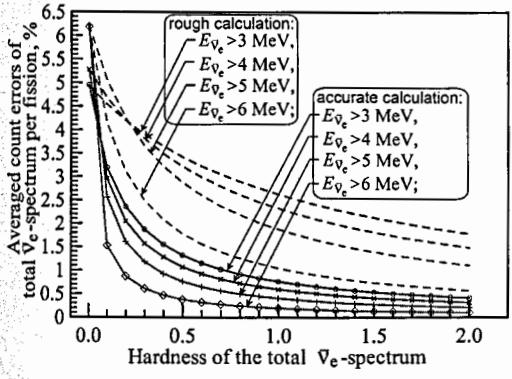

Fig. 5. Dependence of the averaged errors of the total $\bar{\nu}_e$-spectra from value of the hardness H for the indicated $E_{threshold}$ = 3, 4, 5, 6 MeV (the error values for rough and accurate (i.e., detailed) calculations in energy bins) [12,14]. The AZ $\bar{\nu}_e$-spectrum was taken into account with bump as in Daya Bay experiment [16].

The next task of the work is to evaluate the expected $\bar{\nu}_e$ - fluxes at the detector position and number of $(\bar{\nu}_e,p)$- interaction in the scintillator $\bar{\nu}_e$ - detector. The geometry for calculation

is presented in the Fig. 6, where the detector position was shown by dotted lines (detector position along the line from lithium blanket center to the center of the pumped reservoir: S=17.9 m, L_2=3.5 m [11,17]); the detector position appointed by solid lines corresponds the common case. In the calculation the applied proton concentration was typical - about $6.6 \cdot 10^{22}$ cm^{-3} (as in KamLAND liquid scintillator [18]). The considered volume of the detector is small [namely owing to the high density of $\bar{\nu}_e$ - flux and large hardness H of the total antineutrino spectrum (see below)] - 1 m^3. The expected number of interaction in the detector volume is normalized per day (24 hours). The specification of registration efficiency was not take into modelling and was considered conditionally as 100%. The all calculations were normalized on the power of the nuclear reactor power 1000 MW. The density of $\bar{\nu}_e$ - flux from a nuclear reactor is determined by its power P and for distance R is:

$$F\,[\mathrm{cm}^{-2}\cdot\mathrm{s}^{-1}] \cong \bar{n}\,P / 4\pi R^2 \bar{E} = 1.5 \cdot 10^{12} P\,[\mathrm{MW}] / R^2[\mathrm{m}], \qquad (5)$$

where $\bar{n} \cong 6.14$ - mean number of β^--decays for both fission fragments of ^{235}U, $\bar{E} \cong 200$ MeV - mean energy released at ^{235}U-fission.

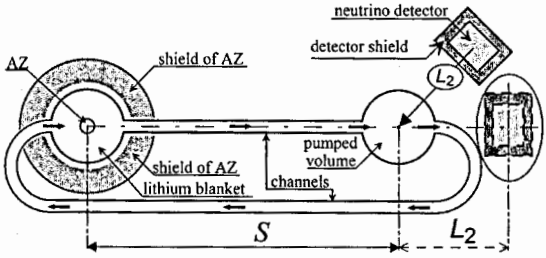

Fig. 6. The installation scheme used for calculation of $\bar{\nu}_e$-fluxes and counts at the detector position. The detector position used for the calculation is shown by dotted lines [it is the position along the line connected the centers of the blanket (around the reactor active zone -AZ) and pumped reservoir].

The obtained $\bar{\nu}_e$ - flux densities at the detector position are shown in the Fig.7. The reactor neutrino fluxes don't depend on the hardness of the total antineutrino flux and are indicated by four levels corresponding to thresholds $E_{\mathrm{threshold}}$ = 3, 4, 5 and 6 MeV. $\bar{\nu}_e$ - fluxes from ^{8}Li rise strongly depending on the hardness H.

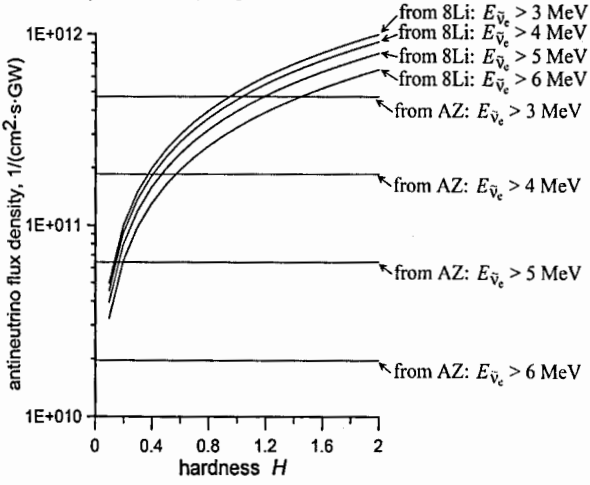

Fig. 7. The $\bar{\nu}_e$-fluxes densities from $\bar{\nu}_e$ of AZ and from whole mass of ^{8}Li in the installation (of the geometry - Fig.6, S=17.9m,L_2=3.5m) depending on the hardness H for different thresholds ($E_{\mathrm{threshold}}$ = 3, 4, 5 and 6 MeV). The all results are normalized on the reactor power 1 GW.

Knowing the antineutrino fluxes we calculated the expected number of interaction in the detector volume 1 m^3: the obtained results are presented in the Fig.8. It is clear that counts ensured by the ^{8}Li antineutrinos are strongly dominates owing to the hardness of $\bar{\nu}_e$-spectrum of ^{8}Li. It is very important to note that the realistic values of the hardness H that can be achievable are about $H \approx 1$ [11,17]. The achievable rate of counts is exclusively high even for the considered small detector volume about 1 m^3 (Fig.8).

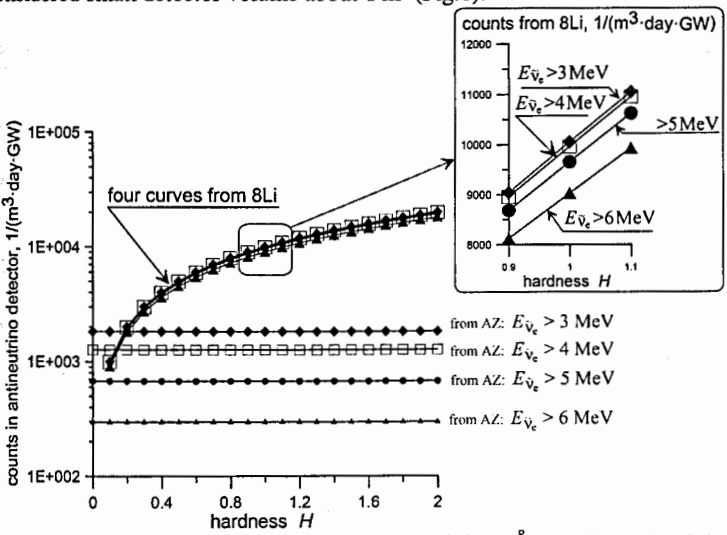

Fig. 8. The expected counts (from AZ $\bar{\nu}_e$-fluxes and from ^{8}Li antineutrinos) in the 1 m^3 detector volume depending on the hardness H for different thresholds $E_{threshold}$ = 3, 4, 5 and 6 MeV. Calculation were realized for the geometry of the Fig.6 (S=17.9 m, L_2=3.5 m) with position of the detector shown by dotted lines. The efficiency of registration was assumed as 100% (by convention). The all results were normalized on the reactor power 1 GW.

4. CONCLUSION

Here we considered the perspective variant of intensive $\tilde{\nu}_e$-source on the base of ^{7}Li isotope in the loop scheme with nuclear reactor (as neutron source).

It was proposed the definition of the generalized hardness H of the total $\tilde{\nu}_e$-spectrum (i.e., the summary $\tilde{\nu}_e$-spectrum from nuclear reactor and from ^{8}Li) at the detector position. Due to the well defined and hard $\tilde{\nu}_e$-spectrum of ^{8}Li (that is very important as the $\tilde{\nu}_e$-cross section is proportional to energy squared - $\sigma_\nu \sim E_\nu^2$) this type of the lithium antineutrino source becomes very perspective to ensure: 1) high $\tilde{\nu}_e$-count rate in the detector and 2) significanly lower errors compare to nuclear reactors as traditional high flux $\tilde{\nu}_e$ - source.

It was obtaned the dependence of the averaged errors of the total $\bar{\nu}_e$-spectra from value of the hardness H for the indicated thresholds ($E_{threshold}$ = 3, 4, 5 and 6 MeV) of neutrino registration. This results reveal the possibility to decrease the errors of the total $\bar{\nu}_e$-spectrum in several times (compare to reactor active zone antineutrinos). That is why this result can be considered as solution of the problem for reactor $\bar{\nu}_e$-spectrum errors.

The obtained spectrum at the detector position becomes hard and namely lithium antineutrinos ensure high count rate (>10^3 per day) in the detector with small (~ 1 m^3) volume that is very exclusively important for sterile neutrino search and another neutrino experiments.

Refererences

[1] Mikaelian L.A., Spivak P.E. and Tsinoev V.G. *A proposal for experiments in low-energy antineutrino physics* // Nucl. Phys. 1965, V.**70**, P. 574-576.

[2] Lyutostansky Yu.S. and Lyashuk V.I. *Powerful Hard-Spectrum Neutrino Source Based on Lithium Converter of Reactor Neutrons to Antineutrino* // Nucl. Sci. Eng., 1994, V.**117**, P. 77-87.

[3] Huber P. *Determination of antineutrino spectra from nuclear reactors* // Phys. Rev. C. 2011, V.**84**, P. 024617.

[4] Aleksankin V.G., Rodichev S.V., Rubtsov P.M., Ruzansky P.A. and Chukreev F.E. 1989 *Beta and antineutrino radiation from radioactive nuclei* (Moscow: Energoatomizdat) ISBN 5-283-03727-4 (in Russian).

[5] Vogel P. and Beacom J.F. *Angular distribution of neutron inverse beta decay* // Phys. Rev. D, 1999, V.**60**. 053003.

[6] Lyashuk V.I. and Lutostansky Yu.S. *Intensive Neutrino Source on the Base of Lithium Converter.* arXiv:1503.01280v2 [physics.ins-det].

[7] Lyutostansky Yu.S. and Lyashuk V.I. *Reactor neutrino-antineutrino converter on the basis of lithium compounds and their solutions* // Sov. J. At. Energ. 1990, V.**69**, P. 696-699.

[8] Lyashuk V.I., Lutostansky Yu.S. *Neutron sources for neutrino factory on the base of lithium converter* // Proc. XXI Int. Seminar of Interaction of Neutrons with Nuclei. Alushta, May 20-25, 2013. Dubna, JINR, 2014, P. 156-164.

[9] Kopeikin V.I. 2012 *Flux and spectrum of reactor antineutrinos* Phys.At. Nucl. **75**, 143-52.

[10] Lyashuk V.I., Lutostansky Yu.S. *Powerful dynamical neutrino source with a hard spectrum* // Phys. Atom. Nucl. 2000, V. **63**, P. 1288-91; [Yad. Fiz. 2000, V.**63**, P.1361].

[11] Lyashuk V.I. *High flux lithium antineutrino source with variable hard spectrum.* arXiv: 1609.02934v2 [physics.ins-det].

[12] Lyashuk V.I. *High flux lithium antineutrino source with variable hard spectrum. How to decrease the errors of the total spectrum?* arXiv: 1612.08096v2 [physics.ins-det].

[13] Lutostansky Yu.S. and Lyashuk V.I. *The concept of a powerful antineutrino source* // Bull. Russ. Acad. Sci. Phys., 2011, V.**75**, P. 468-473.

[14] Lyashuk V.I. *Problem of reactor antineutrino spectrum errors and it's alternative solution in the regulated spectrum scheme* // Results in Physics, 2017, V.**7**, p.1212.

[15] Schreckenbach K., Colvin G., Gelletly W., von Feilitzsch F. *Determination of the antineutrino spectrum from 235U thermal neutron fission products up to 9.5 MeV* // Phys. Lett. B., 1985, V.**160**, P. 325-330.

[16] Hayes A.C., Friar J.L., Garvey G.T., Ibeling Duligur, Jungman Gerard, Kawano T., Mills Robert W. *Possible Origins and Implications of the Shoulder in Reactor Neutrino Spectra.* arXiv:1506.00583v2 [nucl-th].

[17] Lyashuk V.I., Lyutostansky Yu.S. *The conception of the powerful dynamic neutrino source with modifiable hard spectrum.* Preprint ITEP No.38, Moscow, 1997.

[18] Suekane F., Iwamoto T., Ogawa H., Tajima O. and Watanabe H. (for the KamLAND RCNS Group). *An Overview of the KamLAND 1-kiloton Liquid Scintillator.* ArXiv-0404071.

Neutrons Properties and Fundamental Interactions

ESTIMATIONS OF THE INELASTIC INTERACTION OF NEUTRONS WITH NANOSTRUCTURED MEDIA AT LOW ENERGIES AND TEMPERATURES

Artem'ev V.A.[1], Nesvizhevsky V.V.[2], Nezvanov A.Yu.[2,3,4]

[1]Research Institute of Materials Technology, Moscow, 123557, Russia (niitm@inbox.ru)
[2]Institut Max von Laue – Paul Langevin, Grenoble, 38042, France
[3]Moscow Polytechnic University, Moscow, 107023, Russia
[4]Université Grenoble Alpes, Grenoble, 38400, France

Abstract: We consider peculiarities of the inelastic interaction of cold neutrons with nanostructured media (NSM) of two types: 1) powder of spherical nanoparticles, and 2) irregular composition of cylindrical nanowires. Quantitative estimations allow us concluding that cold NSM of these types do not thermalize cold neutrons but reflect them elastically.

Neutron moderators decrease the energy of fast neutrons close to the moderator thermal energy. Much attention is paid to designing moderators with temperatures 20–100 K [1–11]. Neutrons with a temperature of 1–10 K can also find promising applications in neutron research, for designing sources of very cold neutrons (VCNs), or even for designing self-standing neutron sources [12]. Below 10^2 K, medium structure and peculiarities of the inelastic interaction of neutrons have to be taken into account. We will leave other motivation for the following calculations for a detailed publication in the future but simply consider inelastic interaction of slow neutrons with NSM of the two types mentioned above.

Here, we consider the features of the inelastic interaction of cold neutrons with nanostructured media (NSM) at low temperatures. In the following, matter characteristics correspond to diamond. Temperature T is related to energy ε as $\varepsilon = \hbar\omega = k_B T$ for phonons and $E = \hbar^2 k^2 / (2m) = 3k_B T / 2$ for neutrons, where $\hbar$ is the Planck constant, ω is the phonon frequency, k_B is the Boltzmann constant, k is the neutron wave-vector, and m is the neutron mass.

I. A minimum frequency of elastic oscillations for a nanoparticle equals $\omega_{min} = 2\pi c / \lambda_{max}$, where λ_{max} is the maximum wavelength of elastic oscillations in the nanoparticle; c is the sound velocity in the nanoparticle medium. Let c_l and c_t be the velocities of propagation of longitudinal and transverse oscillations respectively. For diamond, $c_l = 17.5 \cdot 10^3$ m/s, and $c_t = 12.8 \cdot 10^3$ m/s.

In a spherical nanoparticle of diameter d, $\lambda_{max}^{(S)} = 2\pi d$ and $\lambda_{max}^{(V)} = 2d$ for surface (S) and volume (V) elastic oscillations. For diamond nanoparticles, $d = 4.5$ nm (a typical size for detonation nanodiamond), and minimum energies of surface and bulk phonons are: $\hbar\omega_{min}^{(S)} = 1.85 \cdot 10^{-3}$ eV = 22 K and $\hbar\omega_{min}^{(V)} = 5.81 \cdot 10^{-3}$ eV = 69 K. Thus, neutrons with an energy of below 20 K cannot slow down to lower temperatures in a nanopowder consisting of such diamond nanoparticles. Therefore, the nanopowder is ineffective for use as a neutron moderator to temperatures of 1–10 K.

II. Consider another model of the nanostructured medium: an irregular composition of diamond nanowires (nanorods) of diameter $d_t \sim 1$–20 nm and length $L_t \sim 1$–100 μm. For the following calculations, we take $d_t = 5$ nm and $L_t = 1$ μm, 5 μm, 10 μm.

We denote $\lambda_{\max}^{(L)} = 2L_t$ the maximum wavelength of the linear (L) elastic waves of the nanowire (L – phonons). Minimum energies of L–phonons are $\hbar\omega_{\min}^{(L)} = 2.65 \cdot 10^{-5}$ eV (0.31 K), $5.30 \cdot 10^{-6}$ eV (0.061 K) and $2.65 \cdot 10^{-6}$ eV (0.031 K) for the lengths $L_t = 1$, 5 and 10 μm, respectively. Minimum energies of surface and bulk phonons in the nanowire are $1.67 \cdot 10^{-3}$ eV (20 K) and $5.23 \cdot 10^{-3}$ eV (62 K), respectively.

Basing on these estimations, we conclude that at temperatures below 20 K, the surface and bulk oscillations in the nanowire are practically absent. Elastic linear oscillations (L–phonons) exist in nanowires down to temperatures of 10^{-2}–10^{-1} K. Therefore, a cold neutron has the theoretical possibility of slowing down to low temperatures via inelastic interaction with L–phonons.

At low temperatures, only the low-frequency part of the phonon spectrum of linear elastic vibrations is excited. In this case, the frequency distribution function $g(\omega)$ of the phonon spectrum of L–phonons has the form [13, 14]: $g(\omega) = L_t/(4\pi c_1)$, where $(c_1)^{-1} = (c_l)^{-1} + 2(c_t)^{-1}$, c_1 is the effective velocity.

The surface of matter can be considered as its separate region, which has physical properties, different from the matter bulk properties. This near-surface region of matter has a characteristic depth h of 3 to 5 atomic layers, can contain defects and structural atomic disorder. Denote by N_h the number of atoms contained in the near-surface layer of the nanowire material of thickness h. Introduce the value $\delta = N_h / N$, where N is the total number of atoms in the nanowire. Denoting the nanowire cross-section radius $R_t = d_t / 2$, we obtain $\delta = [R_t^2 - (R_t - h)^2] / R_t^2$. The atomic density of diamond $n_C = 17.6 \cdot 10^{28}$ m^{-3} [15], the average distance between carbon atoms is $a_C = (n_C)^{-1/3} = 1.78$ Å. Taking $h = (3-5)a_C$, we get an estimation $\delta = 0.38$–0.59.

III. Consider the inelastic scattering of a cold neutron on a nanowire with loss of energy (exciting one L–phonon). We assume the initial energy of the neutron and the temperature T of the nanowire to be below 20 K.

We introduce the notation: E_0 is the initial energy of the neutron (before scattering); E_i and E_f are initial and final energies of the scatterer, respectively; $\varepsilon = E_i - E_f$ is the change in neutron energy during scattering; $\mathbf{k}_0$ and $\mathbf{k}$ are the neutron wave-vectors before and after the collision with the nanowire, respectively; $\boldsymbol{\kappa} = \mathbf{k}_0 - \mathbf{k}$ is the phonon wave-vector.

We direct the z axis of the orthogonal coordinate system $Oxyz$ along the direction of the neutron initial motion $\mathbf{k}_0$ (Fig. 1). The nanowire is located at an angle θ_t to the direction $\mathbf{k}_0$, and the projection of the nanorod on the xOy plane makes an angle φ_t with the x axis. The phonon wave-vector $\boldsymbol{\kappa}$ is directed along the nanowire. The angle θ is the angle of neutron scattering on the nanowire; the direction of the vector $\mathbf{k}$ after the scattering is given by the angles θ and $(\varphi_t + \pi)$.

Double-differential cross-section of incoherent neutron scattering on a nanostructured sample, referred to one nucleus (atom) of matter is:

$$\left(\frac{d^2\sigma}{d\Omega d\varepsilon}\right)_{inc} = \frac{k}{k_0}\frac{1}{2\pi\hbar}\frac{1}{r}\sum_{j=1}^{r}\left[(f_{j,inc})^2+\delta(f_{j,coh})^2\right]e^{-2W_j}\int_{-\infty}^{\infty}dt\; e^{-i\varepsilon t/\hbar}\times$$

$$\exp\{-\frac{1}{N_1}\sum_{\lambda=1}^{3N}\frac{\hbar G(\omega_\lambda)}{2M_j}|\boldsymbol{\kappa}\mathbf{e}_j^\lambda|^2\left(e^{-i\omega_\lambda t}e^{\hbar\omega_\lambda/2k_BT}+e^{i\omega_\lambda t}e^{-\hbar\omega_\lambda/2k_BT}\right)\}.$$

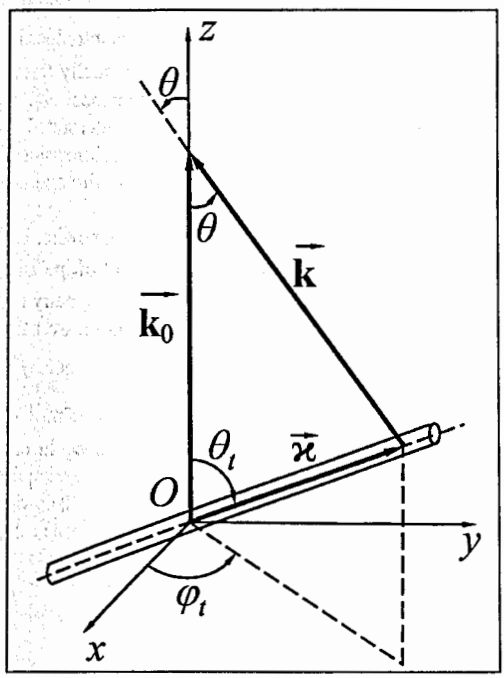

Fig. 1. Scattering of a neutron on a nanowire.

Here, are denoted: $d\Omega$ is the solid angle element into which the neutron with momentum $\hbar\mathbf{k}$ is scattered; $k_0 = |\mathbf{k}_0|$, $k = |\mathbf{k}|$; N_1 is the number of elementary cells in the sample, r is the number of nuclei (atoms of matter) in one unit cell, $N = rN_1$ is the total number of atoms in the sample; the index j serves to designate the nucleus in the unit cell; $f_j = a_j(A_j+1)/A_j$ is the neutron scattering length on the fixed j-th nucleus, a_j is the neutron scattering length on the free j-th nucleus, A_j is the atomic weight of the j–th atom; M_j is the mass of the nucleus of the j–th atom of the unit cell; $f_j = f_{j,coh} + f_{j,inc}$ the coherent and incoherent neutron scattering lengths at the j–th fixed nucleus, respectively; $\exp(-2W_j)$ is the Debye-Waller factor [16], at low temperatures we shall consider it equal to 1; δ is the relative proportion of structurally disordered atoms in the total number of sample atoms; t is an integration variable having the dimension of time; function $G(\omega) = \omega^{-1}\left[1-\exp\left(-\hbar\omega/k_BT\right)\right]^{-1}\exp\left(-\hbar\omega/2k_BT\right)$; ω_λ is the frequency of a phonon with a wave-vector $\boldsymbol{\kappa}$ and a polarization index s, the index λ denotes a pair of indexes s and $\boldsymbol{\kappa}$; $\mathbf{e}_j^\lambda$ is the unit polarization vector for the displacement of the nucleus of the j-th atom of the unit cell.

The nanowire has no physically distinguished directions "top" or "bottom", therefore physically different directions of the orientation of the nanowire in space are limited by the angles $0 \le \theta_t \le \pi/2$ and $0 \le \varphi_t \le \pi$.

At low sample temperatures and neutron energies, the main contribution to inelastic scattering is due to one-phonon scattering. The neutron is inelastically incoherently scattered on individual nuclei. For processes with the excitation of a single phonon, we have $\int_{-\infty}^{\infty}dt\times$

$\exp(-i\varepsilon t/\hbar)\cdot\exp(-i\omega_\lambda t)=2\pi\hbar\cdot\delta(\varepsilon+\omega_\lambda\hbar)$. Therefore, the cross-section for incoherent inelastic scattering of a neutron by a nanowire with excitation of a single phonon, assigned to one nucleus (atom) of matter, is:

$$\left(\frac{d^2\sigma}{d\Omega d\varepsilon}\right)_{inc}^{1ph+}=\frac{k}{k_0}\frac{1}{r}\sum_{j=1}^{r}\left[(f_{j,inc})^2+\delta(f_{j,coh})^2\right]\frac{1}{N_1}\sum_{\lambda=1}^{3N}\frac{\hbar G(\omega_\lambda)}{2M_j}|\kappa\mathbf{e}_j^\lambda|^2 e^{\hbar\omega_\lambda/2k_BT}\times$$
$$\delta(\varepsilon+\omega_\lambda\hbar)\cdot\delta(\varphi-\varphi_t-\pi)\cdot\Theta(-\varepsilon-\varepsilon_{\min}).$$

It is taken into account that the L – phonon energy in a nanowire is limited by the quantity $\varepsilon_{\min}=\hbar\omega_{\min}^{(L)}\cong\pi c_l\hbar/L_t$, thus the function $\Theta(x)=\{1,\text{ for } x\geq 0\mid 0,\text{ for } x<0\}$ is introduced.

It should be noted that the motion of atoms of nanowire material is spatially three-dimensional: each atom oscillates near its equilibrium position as a three-dimensional object. Only the collective vibrational motion of the atoms of the nanowire substance, interpreted as excitation of the quantum of oscillations (L–phonon), has the form of a one-dimensional quasiparticle (plane wave) due to the limited transverse dimensions of the nanowire and the low temperature of the matter and neutron energy.

We make further simplifications. As a scatterer, we consider a separate nanowire. Let us denote by $\varepsilon=(k_0^2-k^2)\hbar^2/(2m)>0$ the energy of a phonon excited as a result of inelastic neutron scattering. We consider a simple chemical substance possessing cubic symmetry for the Bravais lattices. Summation over normal oscillations is replaced by integration over the phonon spectrum $g(\omega)$ [16]: $\sum_{\lambda=1}^{3N}(\kappa\mathbf{e}^\lambda)^2 f(\omega_\lambda)=(\kappa^2/3)\int_{\omega_{\min}}^{\omega_{\max}}d\omega\, g(\omega)f(\omega)$. We denote f_{inc} and f_{coh} are incoherent and coherent neutron scattering lengths at the bound atomic nucleus of the scatterer substance; N is the total number of atomic nuclei of a substance in one nanowire; M is the mass of the nucleus. After the transformations, we obtain an expression for the cross-section of incoherent inelastic neutron scattering by a substance of one nanowire with the excitation of one phonon assigned to one nucleus (atom) of the nanowire substance:

$$\left(\frac{d^2\sigma}{d\Omega d\varepsilon}\right)_{inc}^{1ph+}=\frac{k}{k_0}\left[(f_{inc})^2+\delta(f_{coh})^2\right]\left(\frac{\kappa^2}{6MN}\right)\frac{\exp(\varepsilon/k_BT)}{\left[\exp(\varepsilon/k_BT)-1\right]}\frac{\hbar}{\varepsilon}\cdot g\left(\frac{\varepsilon}{\hbar}\right)\times$$
$$\delta(\varphi-\varphi_t-\pi)\cdot\Theta(\varepsilon-\varepsilon_{\min}).$$

We introduce the notation: $\sigma_1(\theta_t,\varphi_t)=\int\left(\frac{d^2\sigma}{d\Omega d\varepsilon}\right)_{inc}^{1ph+}d\Omega d\varepsilon$ – the total cross-section of incoherent inelastic scattering of a neutron with the excitation of a single phonon, attributed to one nucleus (atom) of a nanowire substance, when the nanowire is oriented in space in the direction of the angles θ_t and φ_t (Fig. 1).

The variation of variables in the integration of the inelastic neutron scattering cross-section will be in the range: $k_0\cos\theta_t-\beta\leq\kappa\leq k_0\cos\theta_t+\beta$, where $\beta=\left[k_0^2\cos^2\theta_t-2m\varepsilon/\hbar^2\right]^{1/2}$; and $\varepsilon_{\min}\leq\varepsilon\leq E_0\cos^2\theta_t=\hbar^2k_0^2\cos^2\theta_t/(2m)$, where $E_0=\hbar^2k_0^2/(2m)$ is the initial neutron energy (before scattering). After the transformations, we get:

$$\sigma_1(\theta_t,\varphi_t)=\iiint d\varepsilon\cdot d\varphi\cdot d\kappa\,\delta(\varphi-\varphi_t-\pi)\left[k_0\kappa/k^2-k_0^2\cos\theta_t/k^2+\cos\theta_t-\kappa^2\cos\theta_t/k^2+\right.$$
$$\left.+k_0\kappa\cos^2\theta_t/k^2\right]\frac{1}{k_0}\left[(f_{inc})^2+\delta(f_{coh})^2\right]\left(\frac{\kappa^2}{6MN}\right)\frac{\exp(\varepsilon/k_BT)}{\left[\exp(\varepsilon/k_BT)-1\right]}\frac{\hbar}{\varepsilon}\frac{L_t}{4\pi c_1}.$$

We introduce a new dimensionless variable $\xi = \varepsilon / E_0$, where $\xi_{\min} \le \xi \le \cos^2\theta_t$, $\xi_{\min} = \varepsilon_{\min} / E_0$, and after the transformations we obtain:

$$\sigma_1(\theta_t,\varphi_t) = A_0 [\, I_1(\theta_t,\varphi_t) + I_2(\theta_t,\varphi_t) + I_3(\theta_t,\varphi_t) + I_4(\theta_t,\varphi_t) + I_5(\theta_t,\varphi_t) \,]. \qquad (1)$$

Here, the notations are: $A_0 = [(f_{inc})^2 + \delta (f_{coh})^2]\, L_t \hbar / (24\pi M N c_1)$;

$$I_1(\theta_t,\varphi_t) = \frac{4mE_0}{\hbar^2}\cos\theta_t \int_{\xi_{\min}}^{\cos^2\theta_t} d\xi \sqrt{\cos^2\theta_t - \xi}\, \frac{(2\cos^2\theta_t - \xi)}{(1-\xi)\xi}\, \frac{\exp(\xi E_0 / k_B T)}{[\exp(\xi E_0 / k_B T) - 1]};$$

$$I_2(\theta_t,\varphi_t) = -\frac{4mE_0}{3\hbar^2}\cos\theta_t \int_{\xi_{\min}}^{\cos^2\theta_t} d\xi \sqrt{\cos^2\theta_t - \xi}\, \frac{(4\cos^2\theta_t - \xi)}{(1-\xi)\xi}\, \frac{\exp(\xi E_0 / k_B T)}{[\exp(\xi E_0 / k_B T) - 1]};$$

$$I_3(\theta_t,\varphi_t) = \frac{4mE_0}{3\hbar^2}\cos\theta_t \int_{\xi_{\min}}^{\cos^2\theta_t} d\xi \sqrt{\cos^2\theta_t - \xi}\, \frac{(4\cos^2\theta_t - \xi)}{\xi}\, \frac{\exp(\xi E_0 / k_B T)}{[\exp(\xi E_0 / k_B T) - 1]};$$

$$I_4(\theta_t,\varphi_t) = -\frac{4mE_0}{5\hbar^2}\cos\theta_t \int_{\xi_{\min}}^{\cos^2\theta_t} d\xi \sqrt{\cos^2\theta_t - \xi}\, \frac{1}{(1-\xi)\xi}\, \frac{\exp(\xi E_0 / k_B T)}{[\exp(\xi E_0 / k_B T) - 1]} \times$$
$$[5\cos^4\theta_t + 10\cos^2\theta_t(\cos^2\theta_t - \xi) + (\cos^2\theta_t - \xi)^2];$$

$$I_5(\theta_t,\varphi_t) = \frac{4mE_0}{\hbar^2}\cos^3\theta_t \int_{\xi_{\min}}^{\cos^2\theta_t} d\xi \sqrt{\cos^2\theta_t - \xi}\, \frac{(2\cos^2\theta_t - \xi)}{(1-\xi)\xi}\, \frac{\exp(\xi E_0 / k_B T)}{[\exp(\xi E_0 / k_B T) - 1]}.$$

We denote by $\langle \sigma_1 \rangle = \int \sigma_1(\theta_t,\varphi_t)\, d\Omega_t \Big/ \int d\Omega_t$ the average value of the total cross section of incoherent inelastic neutron scattering by a substance of one nanowire with the excitation of one phonon assigned to one nucleus (atom); averaging is performed for all spatial orientations (for all angles θ_t, φ_t) of the nanowire (Fig. 1); $\langle \sigma_1 \rangle = \frac{1}{\pi}\int_0^{\pi} d\varphi_t \int_0^{\pi/2} \sigma_1(\theta_t,\varphi_t)\sin\theta_t\, d\theta_t$.

Denote $\varepsilon_\sigma(\theta_t,\varphi_t) = \int \varepsilon \left(d^2\sigma / d\Omega d\varepsilon\right)_{inc}^{1ph+} d\Omega d\varepsilon$. For a nanowire oriented in space in the direction of the angles θ_t and φ_t, the quantity $\langle \varepsilon_1 \rangle_t = \varepsilon_\sigma(\theta_t,\varphi_t) / \sigma_1(\theta_t,\varphi_t)$ is the average value of the phonon energy generated in the incoherent inelastic scattering of a neutron on this nanowire.

We denote by $\langle \varepsilon_1 \rangle = \left[\pi^{-1} \int \langle \varepsilon_1 \rangle_t\, \sigma_1(\theta_t,\varphi_t)\, d\Omega_t\right] \Big/ \left[\pi^{-1} \int \sigma_1(\theta_t,\varphi_t)\, d\Omega_t\right]$ the mean value of the energy of a phonon excited during incoherent inelastic scattering of a neutron on substance of one nanowire; averaging is performed over all spatial orientations of the nanowire; $\langle \varepsilon_1 \rangle = \left[\pi \langle \sigma_1 \rangle\right]^{-1} \int \varepsilon_\sigma(\theta_t,\varphi_t) d\Omega_t$.

After the transformations, we get:

$$\varepsilon_\sigma(\theta_t,\varphi_t) = A_0 [\, B_1(\theta_t,\varphi_t) + B_2(\theta_t,\varphi_t) + B_3(\theta_t,\varphi_t) + B_4(\theta_t,\varphi_t) + B_5(\theta_t,\varphi_t) \,]. \qquad (2)$$

Here, we denote:

$$B_1(\theta_t,\varphi_t) = \frac{4mE_0^2}{\hbar^2}\cos\theta_t \int_{\xi_{\min}}^{\cos^2\theta_t} d\xi \sqrt{\cos^2\theta_t - \xi}\, \frac{(2\cos^2\theta_t - \xi)}{(1-\xi)}\, \frac{\exp(\xi E_0 / k_B T)}{[\exp(\xi E_0 / k_B T) - 1]};$$

$$B_2(\theta_t,\varphi_t)=-\frac{4mE_0^{\,2}}{3\hbar^2}\cos\theta_t\int\limits_{\xi_{\min}}^{\cos^2\theta_t}d\xi\,\sqrt{\cos^2\theta_t-\xi}\,\frac{\left(4\cos^2\theta_t-\xi\right)}{(1-\xi)}\,\frac{\exp\left(\xi E_0/k_BT\right)}{\left[\exp\left(\xi E_0/k_BT\right)-1\right]};$$

$$B_3(\theta_t,\varphi_t)=\frac{4mE_0^{\,2}}{3\hbar^2}\cos\theta_t\int\limits_{\xi_{\min}}^{\cos^2\theta_t}d\xi\,\sqrt{\cos^2\theta_t-\xi}\,\left(4\cos^2\theta_t-\xi\right)\,\frac{\exp\left(\xi E_0/k_BT\right)}{\left[\exp\left(\xi E_0/k_BT\right)-1\right]};$$

$$B_4(\theta_t,\varphi_t)=-\frac{4mE_0^{\,2}}{5\hbar^2}\cos\theta_t\int\limits_{\xi_{\min}}^{\cos^2\theta_t}d\xi\,\sqrt{\cos^2\theta_t-\xi}\,\frac{1}{(1-\xi)}\,\frac{\exp\left(\xi E_0/k_BT\right)}{\left[\exp\left(\xi E_0/k_BT\right)-1\right]}\times$$
$$[5\cos^4\theta_t+10\cos^2\theta_t(\cos^2\theta_t-\xi)+(\cos^2\theta_t-\xi)^2];$$

$$B_5(\theta_t,\varphi_t)=\frac{4mE_0^{\,2}}{\hbar^2}\cos^3\theta_t\int\limits_{\xi_{\min}}^{\cos^2\theta_t}d\xi\,\sqrt{\cos^2\theta_t-\xi}\,\frac{\left(2\cos^2\theta_t-\xi\right)}{(1-\xi)}\,\frac{\exp\left(\xi E_0/k_BT\right)}{\left[\exp\left(\xi E_0/k_BT\right)-1\right]}.$$

Note that the quantities $\sigma_1(\theta_t,\varphi_t)$ and $\varepsilon_\sigma(\theta_t,\varphi_t)$ in (1), (2) do not depend explicitly on the variable φ_t, so we rewrite $\sigma_1(\theta_t)=\sigma_1(\theta_t,\varphi_t)$ and $\varepsilon_\sigma(\theta_t)=\varepsilon_\sigma(\theta_t,\varphi_t)$. The amount of energy transferred from the neutron to the scatterer in an inelastic scattering cannot be smaller than the value $\varepsilon_{\min}=\hbar\omega_{\min}^{(L)}$, i.e. the minimum L–phonon energy. Therefore $\left(d^2\sigma/d\Omega d\varepsilon\right)_{inc}^{1ph+}=0$ when $\varepsilon<\varepsilon_{\min}$; $\sigma_1(\theta_t)=0$ and $\varepsilon_\sigma(\theta_t)=0$ for $\cos^2\theta_t<\xi_{\min}$. To simplify the writing of finite computational formulas, we introduce the notation: $y=\cos^2\theta_t$, $C_0=4A_0mE_0/\hbar^2$. After the transformations, we finally get:

$$\langle\sigma_1\rangle=\frac{1}{2}\int\limits_{\xi_{\min}}^{1}dy\cdot\sigma_1(y),\qquad\qquad \sigma_1(y)=C_0\,I(y),\tag{3}$$

where $I(y)=\int\limits_{\xi_{\min}}^{y}d\xi\,\frac{\exp\left(\xi E_0/k_BT\right)}{\left[\exp\left(\xi E_0/k_BT\right)-1\right]}\,\frac{\sqrt{y-\xi}}{(1-\xi)\xi}\{(2y-\xi)-(4y-\xi)/3+$
$+(4y-\xi)(1-\xi)/3-[5y^2+10y(y-\xi)+(y-\xi)^2]/5+y(2y-\xi)\};$

$$\langle\varepsilon_1\rangle=\frac{1}{2\langle\sigma_1\rangle}\int\limits_{\xi_{\min}}^{1}dy\cdot\varepsilon_\sigma(y)=E_0\left[\int\limits_{\xi_{\min}}^{1}dy\cdot B(y)\right]\left[\int\limits_{\xi_{\min}}^{1}dy\cdot I(y)\right]^{-1},\tag{4}$$

where $\varepsilon_\sigma(y)=C_0\,E_0\,B(y)$, $B(y)=\int\limits_{\xi_{\min}}^{y}d\xi\,\frac{\exp\left(\xi E_0/k_BT\right)}{\left[\exp\left(\xi E_0/k_BT\right)-1\right]}\,\frac{\sqrt{y-\xi}}{(1-\xi)}\{(2y-\xi)-$
$-(4y-\xi)/3+(4y-\xi)(1-\xi)/3-[5y^2+10y(y-\xi)+(y-\xi)^2]/5+y(2y-\xi)\}.$

The total average cross-section $\langle\sigma\rangle$ of inelastic incoherent neutron scattering on a single nanowire of a simple substance containing N atoms (nuclei), averaged all spatial orientations of the nanowire is equal to $\langle\sigma\rangle=N\langle\sigma_1\rangle$.

IV. We have obtained all the necessary analytical formulas for performing numerical calculations. Let us estimate the characteristic values of the quantities for the following parameters. For convenience of comparison and interpretation of the results, we will use the temperature scale of energy measurements. For the minimum energy of L–phonons $\varepsilon_{\min}=k_BT_{\min}$, we select a characteristic value $T_{\min}=0.1$ K. The initial energy of a neutron

(before collision with a nanowire) $E_0 = 3k_B T_0 / 2$; we select a characteristic value $T_0 = 20$ K. The value $\xi_{\min} = \varepsilon_{\min} / E_0 = 2T_{\min} / (3T_0) \cong 3.33 \cdot 10^{-3}$. The characteristic temperature of the nanowire is $T = 1$ K. Substituting the values of the parameters in (4), after the calculations, we obtain $\langle \varepsilon_1 \rangle$, the average value of the energy of the phonon excited in the incoherent inelastic collision of a neutron with the substance of one nanowire; $\langle \varepsilon_1 \rangle \cong 0.04 E_0$, which corresponds to an average phonon energy of 1.2 K. In (4), the integration was carried out numerically using the software package Mathcad11. Thus, for one inelastic collision with a nanowire, the cold neutron reduces its energy on average by ~1 K.

Consider NSM, irregular composition of nanowires. We assume that the substance from which the nanowires are made actually takes 5 % of the total volume of NSM, that is, the NSM has a porosity of $p = 0.95$ and a packing factor of $\gamma = 0.05$, respectively ($p + \gamma = 1$). Nanostructured elements in the NSM are nanowires in the form of straight cylinders $L_t =$ 10 μm in length and $d_t = 5$ nm in diameter, the substance is diamond. For diamond, $M / m =$ 12, $(c_t)^{-1} = 2.134 \cdot 10^{-4}$ s/m. The constants are $\hbar = 1.055 \cdot 10^{-34}$ J·s; $k_B = 1.381 \cdot 10^{-23}$ J·K^{-1}.

For the value $T_0 = 20$ K from (3) after the calculations, we get $\langle \sigma \rangle = N \langle \sigma_1 \rangle = 106.7 \times \left[(f_{inc})^2 + \delta (f_{coh})^2 \right]$. The characteristic value is $\left[(f_{inc})^2 + \delta (f_{coh})^2 \right] = 10^{-28}$ m^2. The volume of a single nanowire is $V_t = \pi d_t^2 L_t / 4 = 1.963 \cdot 10^{-22}$ m^3. The concentration of nanowires n_t in the volume of NSM will be $n_t = \gamma / V_t = 2.55 \cdot 10^{20}$ m^{-3}. The macroscopic cross section of incoherent inelastic scattering of cold neutrons with the excitation of a single phonon in the NSM consisting of nanowires will be $\Sigma^{(1ph+)} = \langle \sigma \rangle n_t = 2.72 \cdot 10^{-6}$ m^{-1}.

The mean free path $l^{(1ph+)}$ of a cold neutron before an inelastic scattering with the excitation of a single phonon in the NSM consisting of nanowires will be $l^{(1ph+)} = 1 / \Sigma^{(1ph+)} = 3.68 \cdot 10^5$ m. The neutron velocity is $v_n = (3k_B T_0 / m)^{1/2} = 704$ m/s. The mean time interval between neutron inelastic collisions is $\Delta t = l^{(1ph+)} / v_n = 523$ s. The neutron lifetime is $\tau_n \cong$ 900 s. Then the mean total number N_{inel} of inelastic collisions of a cold neutron with the NSM does not exceed the value $N_{inel} < \tau_n / \Delta t \cong 1.7$ (even neglecting neutron absorption).

From the estimates obtained, it follows that cold neutrons cannot effectively slow down to lower temperatures in NSM consisting of nanowires. Therefore, the types of NSM considered in this paper are ineffective for use as neutron moderators down to temperatures of 1–10 K but provide excellent properties of the elastic reflection of slow neutrons.

This work was prepared within the framework of the basic part of the State Task to Moscow Polytechnic University, Project No 3.4880.2017/8.9.

REFERENCES

1. Butterworth J., Egelstaff P.A., London H. and Webb, F.J., The production of intense cold neutron beams, *Phil. Mag.*, Vol. **2**, pp. 917–927 (1957).
2. Ageron P., de Beaucourt P., Harig H.D., Lacaze A., *et al.*, Experimental and theoretical study of cold neutron sources of liquid hydrogen and liquid deuterium, *Cryogenics*, Vol. **9**, pp. 42–50 (1969).

3. Altarev I.S., Borovikova N.V., Bulkin A.P., Vesna V.A., *et al.*, Universal liquid hydrogen source of polarized cold and ultracold neutrons at the VVR-M reactor of the Leningrad institute of nuclear physics, *JETP Lett.*, Vol. **44**, pp. 344–348 (1986).
4. Ageron P., Cold neutron sources at ILL, *Nucl. Instr. Meth. A*, Vol. **284**, pp. 197-199 (1989).
5. Gaubatz W., and Gobrecht K., The FRM-II cold neutron source, *Phys. B*, Vol. **104**, pp. 276–278 (2000).
6. Shabalin E. P., Cold Neutron Moderators, *Physics of Elementary Particles and Atomic Nuclei*, Vol. **36**, No. 6, pp. 1425–1444 (2005), [in Russian].
7. Kai T., Harada M., Teshigawara M., Watanabe N., *et al.*, Neutronic performance of rectangular and cylindrical couples hydrogen moderators in wide-angle beam extraction of low energy neutrons, *Nucl. Instr. Meth. A*, Vol. **550**, pp. 329–342 (2005).
8. Kennedy S.J., Construction of the neutron beam facility at Australia's OPAL research reactor, Phys. B, Vol. **385**, pp. 949–954 (2006).
9. Batkov K., Takibayev A., Zanini L., and Mezei F., Unperturbed moderator brightness in pulsed neutron sources, *Nucl. Instr. Meth. A*, Vol. **729**, pp. 500–505 (2013).
10. Anan'ev V.D., Belyakov A.A., Bulavin M.V., Verkhoglyadov A.E., *et al.*, Cold neutron moderator on an upgraded IBR–2 reactor: the first set of results, *Tekh. Phys.*, Vol. **59**, pp. 283–286 (2014).
11. Cook J.C., Barker J.G., Rowe J.M., Williams R.E., *et al.*, Experimental characterization of the advanced liquid hydrogen cold neutron source spectrum of the NBSR reactor at the NIST center, *Nucl. Instr. Meth.* A, Vol. **792**, pp. 15–27 (2015).
12. Artem'ev V. A., Estimate of the Critical Parameters of a Reactor with a Core Consisting of Nanostructural Material, *Atomic Energy*, Vol. **94**, No. 3, pp. 189–192 (2003).
13. Bolt R.H., Frequency Distribution of Eigentones in a Three-Dimensional Continuum, *J. Acoust. Soc. Amer.*, Vol. **10**, No. 3, pp. 228–234 (1939).
14. Maa D.–Y., Distribution of Eigentones in a Rectangular Chamber at Lower Frequency Ranges, *J. Acoust. Soc. Amer.*, Vol. **10**, No. 3, pp. 235–238 (1939).
15. Kittel C., *Introduction to Solid State Physics*. 4th Edition. Published by John Wiley & Sons, Inc., New York, 1971.
16. Gurevich I.I., Tarasov L.V. *Physics of neutrons of low energies*. Moscow, Nauka, 1965, [in Russian].

OPTICAL OBSERVATION OF HYDROGEN AND DEUTERIUM CRYSTAL GROWTH AND IMPLICATIONS FOR ULTRACOLD NEUTRON TRANSMISSION EXPERIMENTS

Stefan Döge (Doege)[1,2,3], Jürgen Hingerl[1,2], Christoph Morkel[1], Bernhard Lauss[4], Nicolas Hild[4,5], Tobias Jenke[2]

[1] Physik Department, Technische Universität München (TUM), Garching, Germany
[2] Institut Laue-Langevin (ILL), Grenoble, France
[3] Université Grenoble Alpes (UGA), Saint-Martin-d'Hères, France
[4] Laboratory for Particle Physics, Paul Scherrer Institut (PSI), Villigen, Switzerland
[5] Institute for Particle Physics, ETH Zürich, Zürich, Switzerland

Abstract

The precise knowledge of UCN cross sections in solid deuterium is pivotal to the design and improvement of new UCN sources, which promise to provide higher UCN densities than the long-time frontrunner – the "turbine" at Institut Laue-Langevin (ILL) in Grenoble, France. However, previous experimental results in this field have been distorted by UCN scattering on rough surfaces and have not been able to describe the size and concentrations of defects present in solid deuterium. In this paper we present a new sample container with highly polished silica windows that eliminate UCN scattering on rough sample surfaces. Preliminary experimental results for UCN scattering cross sections in liquid and solid deuterium are shown. The size and concentration of defects in the deuterium crystals are estimated using the Guinier model.

Key words: cryogenic seal, neutron scattering, optical properties, ultracold neutrons

I. Introduction

Ultracold neutrons (UCNs) are a versatile tool for fundamental physics experiments, such as the exact determination of the free-neutron lifetime [1], the search for a possible non-zero neutron electric dipole moment [2] and other aspects important to cosmology, quantum mechanics and particle physics [3]. It is common to all these experiments that their statistics would be considerably improved, if stronger UCN sources were available.

Superthermal UCN converters [4] based on superfluid helium and solid deuterium (sD_2), see for example [5,6,7], promise higher UCN fluxes than the currently strongest continuously operating converter – the "turbine" at Institut Laue-Langevin (ILL) in Grenoble, France [8]. This promise has, however, only partially been kept. The output of operational UCN converters based on sD_2 in pulse mode is more than an order of magnitude lower than initially predicted [9] and only the best one has a UCN density somewhat higher than that of the turbine [10]. This was the motivation for re-measuring the scattering cross sections of sD_2 in the UCN and lower VCN energy range.

II. Previous Experiments

To our knowledge, the first very cold neutron (VCN) transmission measurements on solid deuterium were done by a group at PNPI, Gatchina [11]. They froze out deuterium from the liquid phase at four different speeds (freezing time 20 min, 1 hour, 2 hours, 3 hours). It was expected to see an unambiguous correlation between freezing speed and VCN transmission. The slower the crystal was frozen, the more transparent for VCNs it should be. The results, however, painted a different, unclear picture, see Fig. 1.

One problem was that the sample container was made from machined (unpolished) titanium. The amount of surface scattering on the container windows could not be quantified. It was equally impossible to optically verify both the fill height of the liquid in the sample container and the uniform freezing of the solid. Instead, the fill level was inferred from the container volume and the pressure difference in the gas reservoir. Therefore, the exact sample thickness was not well known. Also, it is possible that part of the liquid froze out on the walls of the sample container above the liquid level, thereby reducing the sample thickness. The VCN transmission was measured vertically.

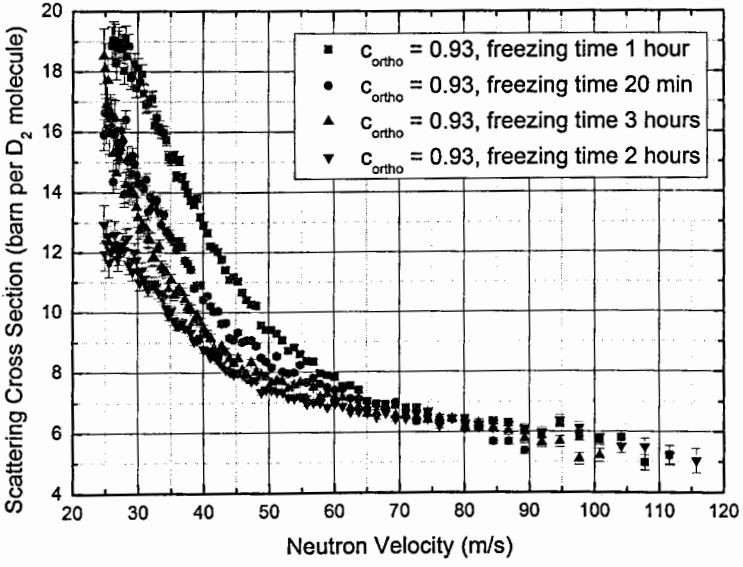

Figure 1. Scattering cross sections for solid deuterium crystals of various freezing speeds as inferred from VCN transmission [11].

The only other direct slow-neutron transmission experiments on deuterium that we are aware of, were carried out by a group from Paul Scherrer Institut in Switzerland [12,13] who used UCNs and VCNs. These experimenters employed an aluminum sample container with neutron windows made from machined aluminum AlMg3. During the experiments these windows bulged due to pressure differentials and introduced an error to the cross sections of about

10%. The final results were modeled using an effective sample thickness. The crystals could be observed laterally through a sapphire window. Photos from [13] suggest cracks being present in the crystals frozen from the liquid phase. The rough surfaces of the aluminum windows, and consequently also the rough surfaces of the deuterium crystals, attenuated the UCN beam by an unquantified magnitude.

III. Experimental Setup

Total UCN cross sections of hydrogen and deuterium were determined in transmission geometry with a time-of-flight (TOF) setup using collimated UCNs, see Fig. 2. The measured transmitted UCN flux through the filled and empty sample containers can be related to the total cross section by Equations 1 and 2:

$$\frac{I_{\text{filled}}}{I_{\text{vacuum}}} = e^{-\Sigma_{\text{tot}} d} = e^{-\sigma_{\text{tot}} N_V d} \qquad (1)$$

$$\sigma_{\text{tot}} = \frac{1}{N_V d} \ln\left(\frac{I_{\text{vacuum}}}{I_{\text{filled}}}\right), \qquad (2)$$

where I is the UCN count rate at the detector (with the subscript *vacuum* for vacuum in the sample cell and *filled* with a sample), d is the sample cell thickness, and N_V the molecular number density of the sample. The condition $\Sigma_{\text{tot}} d < 1$ must be met in order to reduce multiple scattering and not to distort the *single*-scattering cross section, which is measured.

The scattering cross section was obtained by subtracting from the total cross section the absorption cross section of hydrogen and deuterium, respectively, which obeys a $1/v$ behavior from thermal neutron energies down to the UCN range.

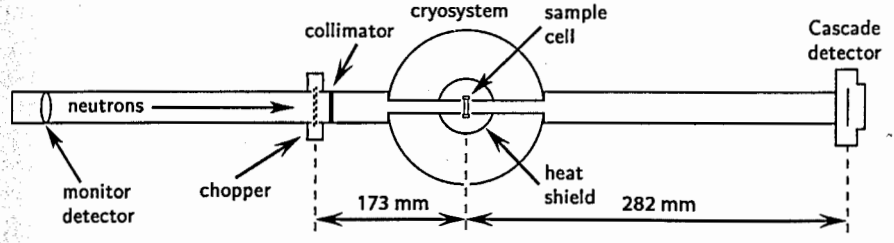

Figure 2. Time-of-flight (TOF) setup used to obtain the experimental results reported in this article.

For the first time, the deuterium crystals and liquids were measured in a sample container with highly polished (R_a < 3 Ångström) and optically transparent windows made from amorphous silica [15], see Fig. 3. This reduced UCN surface scattering [16] to a minimum and allowed for proper online observation of the sample along the beam axis prior to the transmission measurement with UCNs. The sample container was mounted directly onto the cold-head of a closed-cycle helium refrigerator and was used in the same cryostat described in [17].

The key advantages of the new sample container over previous containers using aluminum neutron windows were:

- well defined sample thickness with an uncertainty of ~0.05 mm over the entire sample area
- highly polished ($R_a < 3$ Å) and thin ($d = 1.0$ mm) amorphous silica windows, which do not show any small-angle scattering [18]
- optically transparent windows with a low neutron-optical potential (90 neV for amorphous SiO_2) and of high purity (no scattering length density inhomogeneities in the material)
- vacuum seal that is hydrogen-tight down to 4.5 K

The *para/ortho*-deuterium concentration was monitored before and after each UCN measurement run by Raman spectroscopy. The main results were obtained for $c_{ortho} = 0.982+/-0.002$. Details on the nuclear spin and rotational states (species) of deuterium are given in [17] and a comprehensive review of hydrogen and deuterium properties was published in [19].

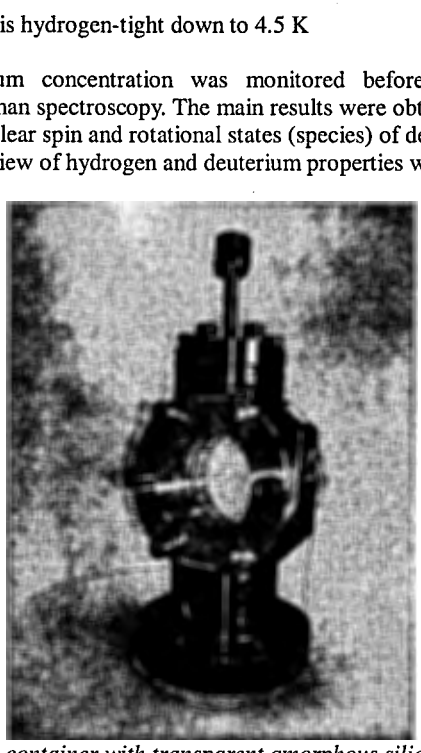

Figure 3. Copper sample container with transparent amorphous silica (SiO_2) windows used to obtain the UCN scattering cross sections presented in Section V.

The new sample container itself is described in detail in [20].

IV. Observations at Cryogenic Temperatures

After the first condensation trials it became clear that it was not possible to freeze a crystal from the gaseous phase in our sample container. Therefore, we focused on producing transparent hydrogen and deuterium crystals from the liquid phase. The liquid was condensed into the sample container by keeping the container's temperature and the gas pressure at the respective substance's triple point (deuterium: 18.7 K, 171.3 mbar [21]). Within a few

minutes, the container was completely filled with liquid while a solid layer had already started forming from the bottom and the side walls of the container. Since the container body was made out of copper, it was well thermalized to the cold-head temperature. Before the entire liquid reservoir became frozen, the gas inlet froze over and no additional liquid could enter the container to fill the space that was vacated during the liquid-to-solid phase transition.

In the case of deuterium, the density increases by 12%, that of hydrogen by 11% upon freezing [21]. This volume shrinkage resulted in the formation of bubbles that rose to the top of the unfrozen liquid reservoir, see Fig. 4 (b). As the freezing progressed radially inward, these bubbles were pushed towards the middle of the sample container. In the end, as almost all the liquid had frozen, the boundaries of the bubbles curled up and formed a phase than can best be called "snow", see Fig. 4 (c).

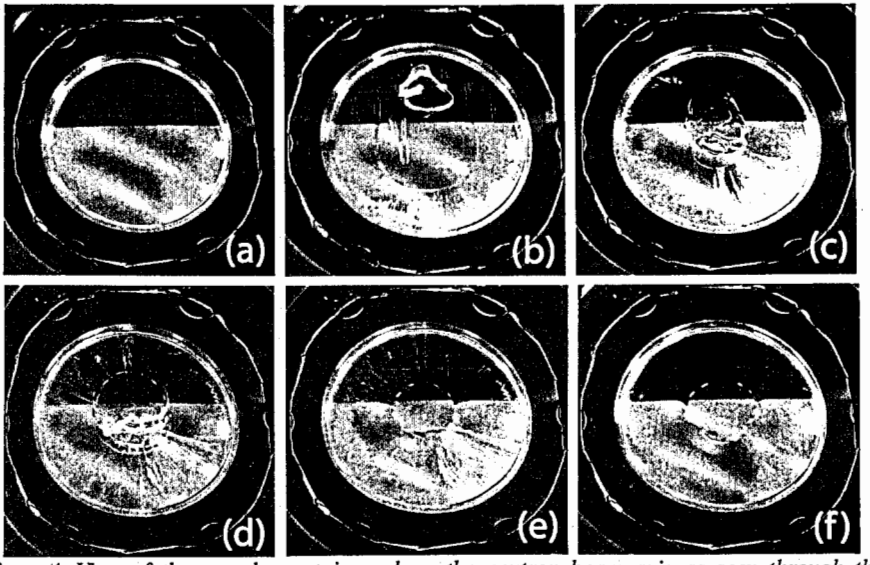

Figure 4. View of the sample container along the neutron beam axis as seen through the viewport and mirror. The upper part of the sample container is blinded out for ultracold neutrons by a 0.5 mm thick cadmium absorber. The marking lines on the absorbers are for reference and are 5 mm apart from each other. Picture (a) shows an empty sample container and (b-f) show liquid and solid para-hydrogen at various stages of freezing, d_{sample} = 4.5 mm. Picture (b) shows a liquid-filled para-hydrogen crystal ring with bubble formation in the liquid phase; (c) freshly frozen solid para-hydrogen, irregular solid–liquid–vacuum phase boundaries ("snow") in the center of the sample container, visible radial streaks; (d) the previous crystal after one melt–refreeze cycle; (e) the previous crystal after about 10 melt–refreeze cycles, where the irregular phase boundaries have disappeared and a void with a smooth surface has formed; (f) the previous crystal after 15 hours at constant temperature (T = 9 K) and one short melt–refreeze cycle, the radial marks have disappeared as they were located not in the crystal bulk, but only on the crystal–window interface.

Since UCNs are very sensitive to surfaces and interfaces, see [14], it was clear that UCN transmission measurements through this snow would not yield any useful data. And that snow always ended up right in the center of the container and hence at the spot of the highest UCN flux. To remedy this problem, the snowy area was melted and refrozen by minimal temperature changes of a few 0.1 K, see Fig. 4 (d). After about ten melt-and-refreeze cycles, the snow had vanished and there remained only one void in the center of the container, see Fig. 4 (e, f).

After observing and learning about the process of bubble formation, we decided to use a flap-shaped 0.5 mm thick cadmium absorber to blind out that area of the UCN window, where the bubble would reliably form. Since that diminished the transmitted UCN flux considerably, the entire sample container was lifted up by placing a 9 mm thick aluminum disk between the cold-head and the sample container. This way, the highest UCN flux passed through the crystal area just below the cadmium absorber. In the end, all measurements on solid samples were done in this configuration, see Fig. 5.

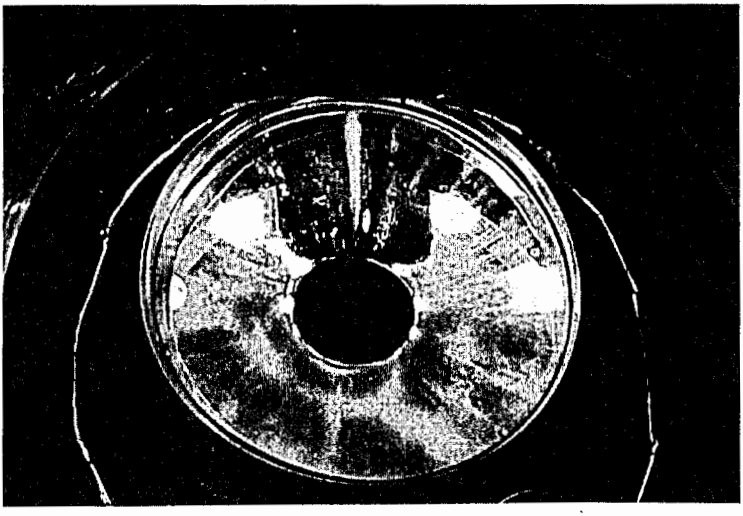

Figure 5. A frozen and temperature-cycled ortho-deuterium crystal (d_{sample} = 6.5 mm) cooled to T = 10K is shown. The central void (filled with deuterium gas at its corresponding vapor pressure) was blinded out by a 0.5 mm thick cadmium absorber for UCNs.

V. Preliminary Experimental Results for Liquid and Solid Deuterium

The preliminary total cross sections (scattering plus absorption, corrected for reflection at the vacuum interface) of liquid *ortho*-deuterium (c_{ortho} = 0.98) for UCNs are shown in Fig. 6. The experimental data for the temperatures 19.0 K, 20.6 K and 23.0 K overlap well with the model published in [17], which was calculated for the respective temperatures using the self-diffusion coefficient of liquid deuterium from O'Reilly et al. [22] and Guarini et al. [23].

The temperature uncertainty for the experimental data was ±0.2 K. The new experimental data on liquid deuterium should be seen as an improvement (and replacement) of the *experimental* data published in [17] and [24].

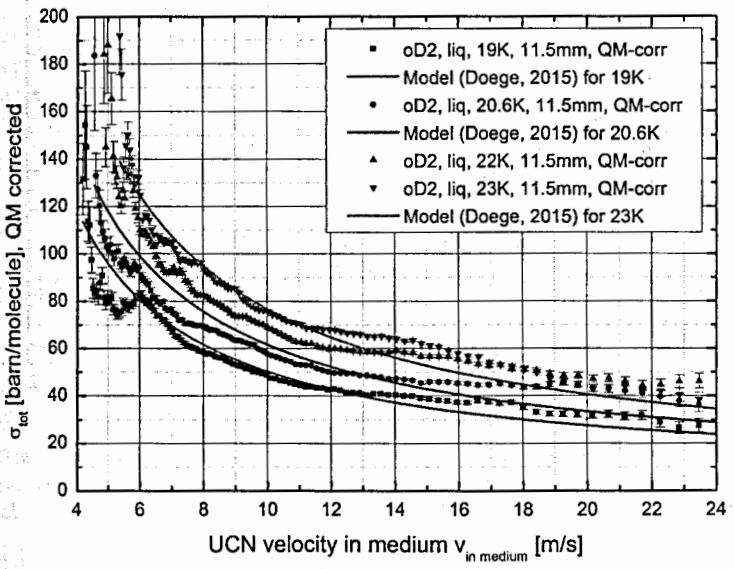

Figure 6. Preliminary experimental data (solid colored symbols) for the total cross section of liquid ortho-deuterium at various temperatures. The theoretical model [17] was calculated for T = 19 K/ 20.6 K/ 23.0 K at c_{ortho} = 0.98 (solid colored lines).

The preliminary total cross sections (scattering plus absorption, corrected for reflection at the vacuum interface) of solid *ortho*-deuterium (c_{ortho} = 0.98) for UCNs are shown in Fig. 7. The black squares represent *normal*-deuterium at 15 K. Below them, the red circles represent solid *ortho*-deuterium at 10 K and the green down triangles stand for the same crystal at 14.5 K. The blue up triangles stand for the same crystal after the temperature cycling 10 K/ 14.5 K/ 10 K. It is clear that temperature cycling does not lower the scattering cross section of a crystal. In the best case, it remains the same. Qualitatively similar findings were published in [12,13]. In the particular case shown here, the cross section increased slightly as a result of temperature cycling. The red dots from Fig. 8 (solid *ortho*-deuterium at 10 K) are plotted again in Fig. 8. There, they are decomposed into their constituents: 1-phonon up-scattering, incoherent elastic nuclear scattering and elastic scattering contributions from defects (R_d = 88 Å, $c = 8.2\times10^{-11}$ per D_2 molecule) as calculated using the Guinier approximation [25]. This is the first time that an estimation of the size and concentration of defects in deuterium crystals was done for the purposes of UCN scattering.

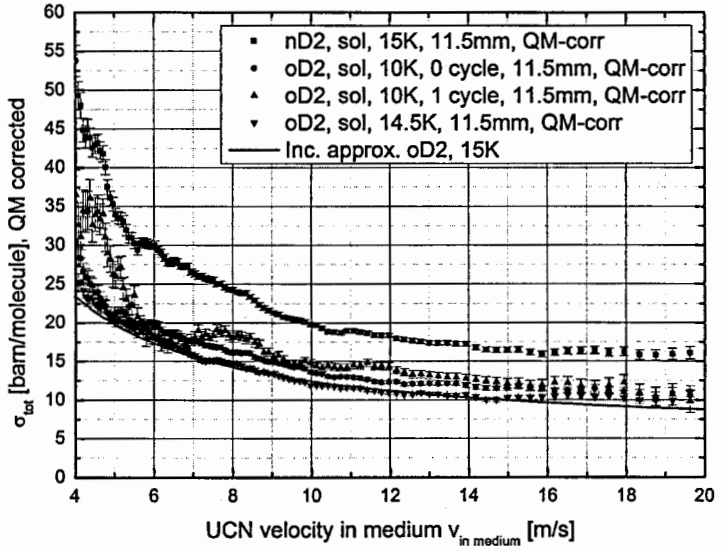

Figure 7. Preliminary experimental data for solid normal- and ortho-deuterium at T = 10 K and 15 K and after no and after one temperature cycling. The theoretical model (incoherent approximation for 1-phonon up-scattering, solid green line) was calculated for T = 15 K.

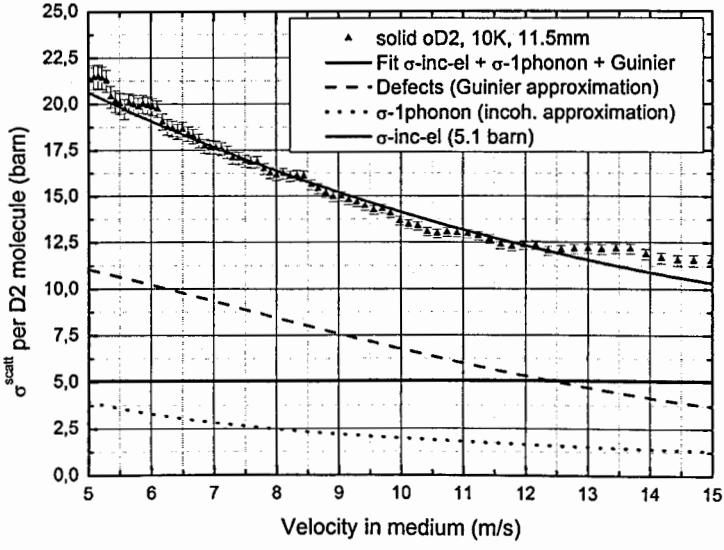

Figure 8. Preliminary total scattering cross section of solid ortho-D_2 (T = 10 K) and its decomposition into 1-phonon up-scattering, incoherent elastic nuclear scattering and the elastic scattering contributions from defects (R_d = 88 Å, $c = 8.2\times10^{-11}$ per D_2 molecule) as calculated using the Guinier approximation [25].

VI. Conclusion

We have conceived, constructed and tested a sample container for cryogenic liquids and solids that produces samples with low surface roughness and allows for optical inspection of the sample preparation process. The highly polished silica windows suppress surface scattering as much as possible and do not bulge under pressure. This sample container design addresses the issues of previous sample containers and permits reliable UCN transmission measurements on cryogenic crystals, such as solid deuterium (sD_2). Measurements of this kind are needed to interpret the performance of operating sD_2-based UCN sources worldwide.

We have used this sample container in recent UCN transmission measurements and were able to determine precise total cross sections of liquid and solid *ortho*-deuterium for UCNs and determine the concentration of defects in an *ortho*-deuterium crystal.

Acknowledgment

The authors are sincerely grateful to ILL and TU Munich technical staff, especially to O. Losserand, E. Bourgeat-Lami, T. Brenner, D. Berruyer and P. Hartung for advice on cryogenics, technical drawings and producing parts of the experimental equipment. A. Frei and T. Lauer of Forschungsneutronenquelle Heinz Maier-Leibniz (FRM-II) and P. Geltenbort of ILL are acknowledged for lending experimental equipment and giving useful advice.

The authors thank Forschungsneutronenquelle Heinz Maier-Leibnitz (FRM-II) at Technische Universität München, Germany, and Leonhard-Lorenz-Stiftung Munich, Germany, who contributed financially to this project.

References

1. C. Patrignani and others (Particle Data Group). 2017 review of particle physics. *Chin. Phys. C* **40**, 100001 (2016 and 2017 update). URL: http://pdg.lbl.gov.
2. P. Schmidt-Wellenburg. The quest for an electric dipole moment of the neutron. *AIP Conference Proceedings* **1753**(1), 060002 (2016).
3. D. Dubbers and M.G. Schmidt. The neutron and its role in cosmology and particle physics. *Rev. Mod. Phys.* **83**, 1111–1171, (2011).
4. R. Golub and J.M. Pendlebury. Super-thermal sources of ultra-cold neutrons. *Physics Letters A* **53**(2), 133–135 (1975).
5. O. Zimmer et al. *Phys. Rev. Lett.* 107, 134801 (2001).
6. B. Lauss, Ultracold neutron production at the second spallation target of the Paul Scherrer Institute, *Physics Procedia* **51**, 98 (2014).
7. A. Saunders et al. *Review of Scientific Instruments* **84**, 013304 (2013).
8. ILL 2017. URL: http://www.ill.eu/instruments-support/instruments-groups/instruments/pf2/
9. F. Atchison et al. Investigation of solid D2, O2 and CD4 for ultracold neutron production. *Nuclear Instruments and Methods* A 611, 252 (2009).
10. D. Ries et al. *Phys. Rev. C* **95**, 045503 (2017).

11. A.P. Serebrov et al. *Pis'ma ZhETF* **74**, 6, 335-338 (2001).
12. F. Atchison et al. *Phys. Rev. Lett.* **95**, 182502 (2005).
13. T. Brys, PhD thesis, ETH Zurich (2008).
14. W.-D. Seiffert, PhD thesis TU Munich (1969) and Euratom Report No. EUR 4455 d (1970).
15. J.S. Laufer, *J. Opt. Soc. Am.* **55**, 458 (1965).
16. Steyerl, A., *Z. Phys.* **254**, 169 (1972).
17. S. Döge (Doege) et al. Scattering cross sections of liquid deuterium for ultracold neutrons: Experimental results and a calculation model. *Phys. Rev. B* **91**, 214309 (2015), also preprint arXiv:1511.07065 [nucl-ex] (2015).
18. M. Roth. *J. Appl. Cryst.*, **10** (3), 172–176 (1977).
19. I.F. Silvera. The solid molecular hydrogens in the condensed phase: Fundamentals and static properties. *Rev. Mod. Phys.* 52, 393–452, (1980).
20. S. Döge (Doege) and J. Hingerl, Rev. Sci. Instrum. 89, 033903 (2018).
21. P.C. Souers. *Hydrogen Properties for Fusion Energy.* Univ. of California Press, Berkeley (1986).
22. D. E. O'Reilly and E. M. Peterson. Selfdiffusion of liquid hydrogen and deuterium. *Journal of Chemical Physics* 66, 934 (1977).
23. E. Guarini et al. Velocity autocorrelation by quantum simulations for direct parameter-free computations of the neutron cross sections. II. Liquid deuterium. *Phys. Rev. B* 93, 224302 (2016) and priv. comm.
24. S. Doege et al. ISINN-23 Conference Proceedings, JINR Dubna (Russia), pp. 119-130 (2016).
25. A. Guinier and G. Fournet, *Small Angle Scattering of X-Rays.* John Wiley, New York (1955).

MEASUREMENT OF P-ODD ASYMMETRY OF α-PARTICLE EMISSION IN THE $^{10}B(n,\alpha)^7Li$ NUCLEAR REACTION

Gledenov Yu.M.[1], Nesvizhevsky V.V.[2], Sedyshev P.V.[1], Shul'gina E.V.[3], Szalanski P.[4], Vesna V.A.[3]

[1]Frank Laboratory of Neutron Physics, Joint Institute for Nuclear Research, Dubna, Russia
[2]Institut Max von Laue – Paul Langevin, Grenoble, France
[3]St. Petersburg Nuclear Physics Institute, National Research Center Kurchatov Institute, Gatchina, Russia
[4]Faculty of Physics and Applied Informatics, University of Lodz, Lodz, Poland

Abstract

We present measurements of P-odd asymmetry of emission of α-particles in the $^{10}B(n,\alpha)^7Li$ nuclear reaction, which are carried out using beams of polarized cold neutrons at Petersburg Nuclear Physics Institute (PNPI, Gatchina, Russia) and Institut Max von Laue – Paul Langevin (ILL, Grenoble, France) nuclear reactors. The α-particle detector is an ionization chamber with insensitive gaseous layer.

We measured the P-odd asymmetry coefficient to be equal $\alpha^{\alpha}_{p\text{-}odd} = -(11.2 \pm 3.4)\cdot 10^{-8}$.

Introduction

Experimental investigations of spatial parity in reactions of polarized neutrons with light nuclei is an important topic in the framework of exploring the fundamental problem of manifestations of weak interaction in nuclear processes as well as evaluating constants of weak nucleon-nucleon (NN) potential. To describe the contribution of weak interaction, the problem is often parameterised in terms of single (π, ρ, ω) and multiple (ππ) meson exchange with one weak and one or more strong vertices (see [1, 2] for reviews). Within this parameterisation, neutral and charged weak currents are described with dimensionless coupling constants f_π and h^0_ρ, respectively. Several models attempt to relate these couplings to more fundamental theory. The quark model by Desplanques, Donoughe and Holstein (DDH) predicts "best values" $f_\pi = 4.6\cdot 10^{-7}$ and $h^0_\rho = -11.4\cdot 10^{-7}$ within "allowed ranges" [3]. The soliton model of nucleon by Kaiser and Meissner (KM) [4, 5] predicts lower values for these couplings. During last years, the weak NN interaction effects have been analyzed actively in the framework of the effective field theory [6–8]. This approach is more general and systematic compared to the one-meson-exchange model. Anyway, one needs new precise relevant experimental data in order to verify theories.

While the observation of parity violation in proton-proton scattering is a manifestation of charged weak currents in accordance with theory [9, 10], no nonzero observation has yet been claimed for neutral weak current contributions in NN-interaction in nuclei. A popular system for the theoretical and experimental investigation of P-odd effects is the radiative neutron capture by protons, $(n,p)\rightarrow(d,\gamma)$. As shown in ref. [2], the coefficient A_γ of the P-odd asymmetry for γ emission depends on the weak neutral current alone, $A_\gamma = -0.11 f_\pi$. The "best value" of the DDH model for f_π corresponds to P-odd asymmetry of the order of $5\cdot 10^{-8}$. The model of KM predicts an even smaller value. Such a tiny observable and the fact that the

cross section for neutron absorption is much smaller than that for scattering, present considerable difficulties to perform a statistically significant measurement.

Until recently, effects of parity violation in reactions with neutron absorption had been observed only in reactions with medium and heavy nuclei, where peculiar enhancement effects may occur [11]. Measurements of P-odd asymmetry coefficients for such nuclei have not provided information on constants of weak interaction in view of the complexity of calculations and corresponding uncertainties [2]. On the other hand, considerable progress has been made in the theoretical description of light nuclear systems involving up to 10 nucleons, starting from phenomenological potential models for NN interactions and including three-body forces. In the absence of parameter-free description of light nuclear systems, we analyse in the following our data using the cluster model.

A set of light nuclei can be described up to the excitation energy of 20–25 MeV as combination of a limited number of clusters; a neutron reaction with such a light nucleus can be considered as reaction in the field of one or a few α-particles. Then the problem can be solved in terms of constants of meson-nucleon interaction. The coefficient of P-odd asymmetry in triton emission in the ^{6}Li(n,α)^{3}H reaction is calculated in ref. [12] in terms of weak couplings; it is equal to $\alpha^t_{p\text{-}odd} \approx -0.45 f_\pi + 0.06 h^0_\rho = -2.8 \cdot 10^{-7}$, where weak constants are "best values" of the DDH model. The measured coefficient is $\alpha^t_{p\text{-}odd}(^6\text{Li}) = -(8.8 \pm 2.1) \cdot 10^{-8}$ [13]. This result constrained the neutral current constant as $0 \le f_\pi \le 1.1 \cdot 10^{-7}$ at the 90% confidence level. This value is smaller than the "best value" in the DDH model. Calculation [14] of P-odd asymmetry coefficient of γ-quantum emission in the reaction ^{10}B(n,α$_1$)^{7}Li* → ^{7}Li(g.s.) + γ, (E_γ =0.478 MeV) provided the following expression: $\alpha^\gamma_{p\text{-}odd} \approx 0.16 f_\pi - 0.028 h^0_\rho = 1.1 \cdot 10^{-7}$ with the DDH "best values". Measured value of this P-odd asymmetry coefficient equals $\alpha^\gamma_{p\text{-}odd}(^{10}\text{B}) = (0.0 \pm 2.6_{stat} \pm 1.1_{sys}) \cdot 10^{-8}$ [15]. Performed experiments would not contradict to calculations if the value of neutral current constant is smaller than the theoretical "best value" and close to zero. That is why a measurement of P-odd asymmetry in the emission of α-particle in the reaction ^{10}B(n,α)^{7}Li, with the predicted effect as high as 10^{-7}–10^{-6} in the α_0-transition [16], is of interest. Observation of a non-zero effect in another nuclear reaction accompanied with theoretical calculations would allow one better evaluating neutral and charged current constants.

Reaction ^{10}B(n,α)^{7}Li

Energy released in this reaction equals 2.79 MeV; it is distributed over reaction products as follows: $E_{\alpha 0}$ = 1.78 MeV, E_{Li0} = 1.01 MeV and, $E_{\alpha 1}$ = 1.47 MeV, E_{Li1} = 0.84 MeV (see Fig. 1).

Unfortunately, in view of complexity of ^{10}B nucleus, theoretical calculations in terms of meson constants have not yet been performed. In accordance with the two level approach [17], S- and P- states with equal spin and opposite parity have to be mixed in order to provide P-odd asymmetry. Here, a single pair of resonances is present in the input channel: P-resonance (E_P = 0.53 MeV, $J^\pi = 5/2^-$) and S-resonance (E_S = 0.17 MeV, $J^\pi = 5/2^+$) [18]. The width of α_1 transition for S-resonance equals zero; thus, P-odd asymmetry for this transition associated with the input channel is absent. A P-odd effect can be associated only with α_0-transition (for the given method of introduction of parity violation). A P-odd effect in the exit reaction channel was evaluated in ref. [19]; it is an order of magnitude smaller than its expectation for the α_0-transition in the input channel. Besides, if P-odd asymmetry exists in α_1-transition, a P-odd effect should exist also in 0.478 MeV γ-transition from 1st excited to

ground state in ^{7}Li. Performed experiments [15] constrained the P-odd asymmetry coefficient of γ-quanta emission $|\alpha^{\gamma}_{p\text{-}odd}(^{10}B)| < 4.3\cdot10^{-8}$ at the 90% confidence level. Thus P-odd effect in α_1-transition in the exit channel is absent in first approximation, and one could consider experiments with mixture of α-transitions, where α_1 is a background transition not contributing to the effect.

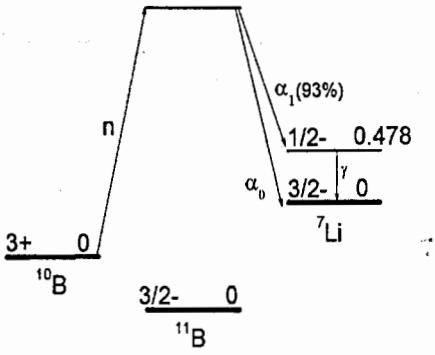

Fig. 1. A scheme of the ^{7}Li nucleus formation following the capture of cold neutron in ^{10}B nucleus.

Unfortunately, in view of complexity of ^{10}B nucleus, theoretical calculations in terms of meson constants have not yet been performed. In accordance with the two-level approach [17], S- and P- states with equal spin and opposite parity have to be mixed in order to provide P-odd asymmetry. Here, a single pair of resonances is present in the input channel: P-resonance (E_P = 0.53 MeV, J^{π} = 5/2$^-$) and S-resonance (E_S = 0.17 MeV, J^{π} = 5/2$^+$) [18]. The width of α_1 transition for S-resonance equals zero; thus, P-odd asymmetry for this transition associated with the input channel is absent. A P-odd effect can be associated only with α_0-transition (for the given method of introduction of parity violation). A P-odd effect in the exit reaction channel was evaluated in ref. [19]; it is an order of magnitude smaller than its expectation for the α_0-transition in the input channel. Besides, if P-odd asymmetry exists in α_1-transition, a P-odd effect should exist also in 0.478 MeV γ-transition from 1st excited to ground state in ^{7}Li. Performed experiments [15] constrained the P-odd asymmetry coefficient of γ-quanta emission $|\alpha^{\gamma}_{p\text{-}odd}(^{10}B)| < 4.3\cdot10^{-8}$ at the 90% confidence level. Thus P-odd effect in α_1-transition in the exit channel is absent in first approximation, and one could consider experiments with mixture of α-transitions, where α_1 is a background transition not contributing to the effect.

In first measurements of P-odd asymmetry, rather significant P-even left-right effect was observed in nearly all neutron reactions with light nuclei accompanied with emission of charged particles. The coefficient of left-right asymmetry for the 1.78 MeV transition in the reaction ^{10}B(n,α)^{7}Li was measured to be equal $\alpha^{\alpha 0}_{lr} = (0.77 \pm 0.06)\cdot10^{-4}$; the coefficient of left-right asymmetry for α_1-transition was estimated as $\alpha^{\alpha 1}_{lr} = -(0.28 \pm 0.14)\cdot10^{-5}$ [20]. As left-right asymmetry has to accompany P-odd asymmetry, the later estimation also indicates that P-odd asymmetry is expected to be present only in α_1-transition.

Ionization chamber

The experimental geometry and the experimental setup were the same as in ref. [13] studying the reaction $^6Li(n,\alpha)^3H$ (see Fig. 2).

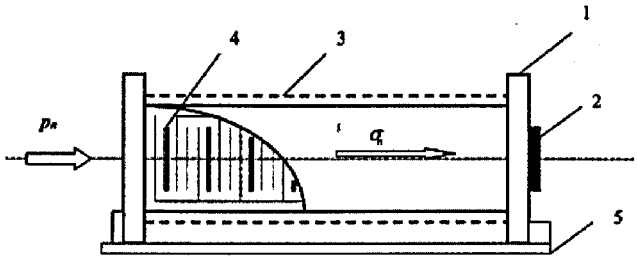

Fig. 2. A sketch of the ionization chamber in the neutron beam: 1 – ionization chamber; 2 – ^6LiF beam-stop for absorption of neutrons at the chamber exit; 3 – solenoid for guiding the magnetic field; 4 – grids and ^{10}B targets; 5 – base plate of the ionization chamber.

Due to large partial ionization losses, passes of α-particles are small, thus solid film absorbers cannot be used for absorbing the heavy component and defining certain mean cosine of α-particle emission. Instead, we created insensitive gas volume with the thickness of 9 mm installed an additional greed between target and signal electrode. Working gas was argon at the pressure of 0.3 bar. Operation of the ionization chamber was simulated using Monte-Carlo method for these parameters and for the actual detector geometry; the target thickness was assumed to be distributed non-uniformly in accordance with the normal statistical law; the mean target thickness was 180 μg/cm^2. The mean cosine of α_0-particle emission angle is calculated to be equal $\langle\cos(\sigma_n p_\alpha)\rangle = 0.77$ (σ_n and p_α are unit vectors of neutron spin and emitted α-particle momentum). Calculated contributions of the reaction products (energies taken into account) into the current measured in the detector are equal: α_0(E = 1.78 MeV) – 11.4%, Li_0(E = 1.01 MeV) – 0.8%, α_1(E = 1.47 MeV) – 82.0 %, Li_1(E = 0.84 MeV) – 5.8%. To shape the neutron beam, we installed three collimators made of ^6LiF ceramics inserted in Al foil envelopes inside the chamber along its total length. The beam is smaller than the target size at both the entrance to and the exit from the chamber. The deviation of the neutron beam along the vertical axis is smaller than 5 mm. The chamber is installed on concrete blocks so that the horizontal misalignment between the neutron beam and the chamber axis is smaller than 5 mm/m. A solenoid wired around the ionization chamber produced the longitudinal magnetic field, which guided the neutron spin. The direction of magnetic field in the chamber is aligned along the chamber axis with the accuracy better than 1°. For this geometry, a contribution of left-right asymmetry into P-odd effect is suppressed by 4-5 orders of magnitude compared to its maximum value.

24 double targets and detection chambers are installed inside the ionization chamber along the longitudinally polarized neutron beam. Targets were produced using sedimentation of amorphous B suspended in acetone to Al foils with the thickness of 20 μm. Each double chamber is equipped with two targets folded back to back so that each B-coated side looks to its own chamber. Target substrates totally absorb reaction products. One half of a double chamber detects α-particles emitted along the neutron momentum ("forward"), another half detects α-particles emitted against the neutron momentum ("backward"). Due to the

correlation ($\sigma_n p_\alpha$), P-odd effects in "forward" and "backward" particle emission are of opposite signs. Signal electrodes of chambers are connected to two common electronic lines: "forward" for chambers detecting α-particles emitted along the neutron momentum and "backward" for chambers detecting α-particles emitted in the opposite direction. Signals of all detector chambers "forward" ("backward") are sent to respective preamplifiers (PA), which transform ionization chamber current into voltage. The voltage at the PA exit is recorded in PC using programmable analog-to-digital converter (ADC).

PA divides signals into variable and constant parts. Variable part is amplified and then recorded. The amplification coefficient is calibrated sending a rectangular-step signal of known amplitude to the PA entrance.

Measuring procedure

To achieve maximum accuracy, we used the scheme of two detectors ("forward" and "backward") and special procedure of measurements. The principle of the scheme is based on the fact that both detector channels measure simultaneously the same process, however the signs of real effects are opposite while the effect of synchronous fluctuations is the same.

P-odd asymmetry in nuclear reactions with polarized neutrons is defined as:

$$\alpha = (N_+ - N_-)/(N_+ + N_-), \tag{1}$$

where N_+ and N_- are detector counts corresponding to the emitted particle momentum parallel and antiparallel to the neutron spin, respectively. For the integral measuring method applied, "number of events" per time interval is equivalent to the sum of variable U and constant U_C parts of the signal integrated over this interval and thus the asymmetry coefficient $\alpha_{p\text{-}odd}$ is written as follows:

$$\alpha_{P-odd} = \frac{\left((U_C^+ + U^+/K) - (U_C^- + U^-/K)\right)}{\left((U_C^+ + U^+/K) + (U_C^- + U^-/K)\right)}. \tag{2}$$

Here U_C^+, U_C^-, U^+, U^- are respectively constant and variable parts of the signal for different neutron spins relative to the detected particle momentum. K is amplification coefficient for variable part. As $U_C >> U$ and $U_C^+ \cong U_C^- = U_C$, thus normalized asymmetry coefficient equals:

$$\alpha_{P-odd} = \left(U^+ - U^-\right)/(K \cdot 2U_C). \tag{3}$$

Time diagram of measurements is shown in Fig. 3. For each detector channel, tetrads $U_1^+, U_2^-, U_3^-, U_4^+$ of variable part of signals from PA averaged over period T are combined in single measurements and calculated as follows: $U^+ = U_1^+ + U_4^+$, $U^- = U_2^- + U_3^-$. Signs "+" and "-" correspond to different neutron spin directions. This combination allows eliminating linear drifts in amplifies. The asymmetry is calculated for single measurement for each detector. N consequent single measurements in both channels are combined in one series; constant signal part is measured ones in each interval T; mean, over the series, values of constant signals are used in the normalized asymmetry coefficient. Results are treated after the series.

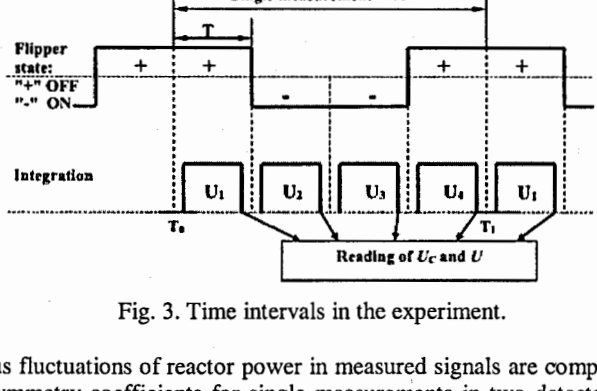

Fig. 3. Time intervals in the experiment.

Synchronous fluctuations of reactor power in measured signals are compensated due to subtraction of asymmetry coefficients for single measurements in two detectors (measuring effects of opposite sign) and summation of these differences at the end of series. Thus, the effect is doubled while reactor power fluctuations are subtracted.

The procedure of data treatment and relevant formulas are described in detail in ref. [13].

In the time diagram in Fig. 3: main time of measurement $T = 0.1$ s, integration time 0.09 s, neutron spin is flipped each 0.2 s, a series consists of $N = 250$ single measurements, i.e. continues for 100 s. Final result is obtained by weighted averaging over many series.

To avoid false asymmetries, the direction of magnetic field in the chamber (guiding the neutron spin) is reversed after each series; the numbers of series with opposite directions of the guiding field are equal. Averaging procedure takes into account that reversion of magnetic field changes the sign of P-odd effect to the opposite one. Thus, combined treatment of data for two detectors and two magnetic field directions eliminates parasitic effects as repeatedly verified in experiments [16], [21], [22]. Earth's magnetic field and external stationary magnetic fields from surrounding are not compensated for; they can increase the contribution of left-right asymmetry into P-odd asymmetry. The sign of corresponding left-right asymmetry does not change when the guiding magnetic field reverses [21]; subtraction of results for opposite directions of guiding field eliminates the contribution of this effect.

Measurements

P-odd asymmetry of α-particle emission in the reaction $^{10}B(n,\alpha)^7Li$ was measured earlier for the sum of α-lines [16]. This experiment was carried out at the vertical polarized neutron beam at the PNPI reactor (Gatchina, Russia). The integral neutron intensity was ~ $(1\text{-}3)\cdot10^{10}$ s^{-1}; the mean neutron polarization was $P = 0.8$. Corrected for the mean cosine of α-particle emission angle and for the neutron polarization, the result was equal

$$\alpha_{P-odd}^{\alpha_0+\alpha_1}(^{10}B, \text{PNPI}) = -(17.4 \pm 12.2)\cdot10^{-8}.$$

Second experiment was carried out at the horizontal polarized neutron beam of PF1B [23] facility at the ILL (Grenoble, France). The mean neutron wavelength is λ =4.7 Å; the integral flux of polarized neutrons is $(4\text{-}5)\cdot10^{10}$ s^{-1}; the neutron polarization is $P = 92 \pm 2\%$.

Neutron polarization is flipped using an adiabatic spin-flipper with the efficiency close to 100%. Fig. 4 shows experimental results; explanations are in the caption.

The experiment at ILL provided the P-odd asymmetry value, corrected for the neutron polarization and the mean cosine of emission of α_0-particle, equal:

$$\alpha_{P-odd}^{\alpha_0+\alpha_1}(^{10}B,\mathrm{ILL}) = -(10.7 \pm 3.5)\cdot 10^{-8}.$$

The two results provide the value of P-odd asymmetry coefficient of α-particle emission in the reaction $^{10}B(n,\alpha)^7Li$ equal

$$\alpha_{P-odd}^{\alpha_0+\alpha_1}(^{10}B) = -(11.2 \pm 3.4)\cdot 10^{-8}.$$

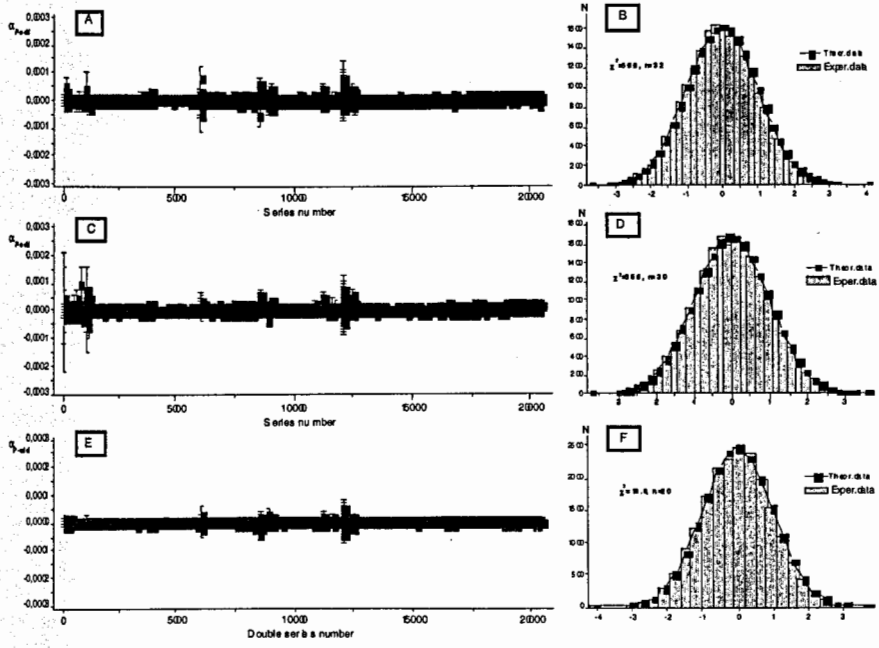

Fig. 4. All results of the presented experiment. A) P-odd asymmetry measured for one direction of the guiding magnetic field (→), C) P-odd asymmetry measured for the opposite direction of the guiding magnetic field (←), E) the resulting P-odd asymmetry. B), D), F) respective distributions, in comparison with Gaussian distributions.

Control experiments

Ref. [13] presents detailed analysis of possible background P-odd effects in different reactions of neutrons with the construction materials of the experimental setup. As reliable calculation of these effects is complicated, we had to verify experimentally the contribution of

possible false asymmetry caused by neutron reactions with other-then-B nuclei. Thus, we measured P-odd asymmetry with all targets covered with foils completely absorbing reaction products. We performed this experiment in studied of P-odd asymmetry of triton emission in the reaction ^{6}Li(n,α)^{3}H [13]. The chamber and all surrounding of the chamber in the two experiments are equivalent. Taking into account earlier analogous measurements at PNPI [16], the result is

$$\alpha_{backgr} = (0.2 \pm 0.5) \cdot 10^{-8}.$$

This value can be used also for experiments with B, as the detector of charged particles, the ionization chamber, is the same. Thus, we can state that the effect of P-odd asymmetry in the presented experiment is associated with the reaction ^{10}B(n,α)^{7}Li.

Conclusion

The precision of measurement of P-odd asymmetry in the emission of α-particles in the reaction ^{10}B(n,α)^{7}Li ($\alpha_{P-odd}^{\alpha_0+\alpha_1}(^{10}B) = -(11.2 \pm 3.4) \cdot 10^{-8}$) is comparable with the precision of measurement of P-odd effect in the reaction ^{6}Li(n,α)^{3}H [13]. The non-zero result in the reaction ^{10}B(n,α)^{7}Li is obtained for the first time. ^{10}B is the second light nucleus, after ^{6}Li, where P-odd effect has been observed.

P-odd effect in the reaction ^{10}B(n,α)^{7}Li can be theoretically calculated within the cluster model; it would be of high importance to describe the considered reaction also from "first principles".

References

1. E. G. Adelberger and W. C. Haxton. *Ann. Rev. Nucl. Part. Sci.* **35** (1985) 501.
2. B. Desplanques, *Phys. Rep.* **297** (1998) 1.
3. B. Desplanques, J. F. Donoughe and B. R. Holstein. *Ann. Phys.* **124** (1980) 449.
4. N. Kaiser and U. G. Meissner, *Nucl. Phys. A* **489** (1988) 671.
5. N. Kaiser and U. G. Meissner, *Nucl. Phys. A* **499** (1989) 699.
6. S.-L. Zhu, C. M. Maekawa, B. R. Holstein *et al*, *Nucl. Phys. A* **748** (2005) 435.
7. M. J. Ramsey-Musolf, S. A. Page, *Ann. Rev. Nucl. Part. Sci.* **58** (2006) 1.
8. C.-P. Liu, *Phys. Rev. C* **75** (2007) 065501.
9. I. Balzer, R. Hennek, Ch. Jachquemart *et al*, *Phys. Rev. C* **30** (1984) 1409.
10. V. Yuan, H. Fraunfelder, R. W. Harper *et al*, *Phys. Rev. Lett.* **57** (1986) 1680.
11. P. A. Krupchitsky, *Fundamental Research with Polarized Slow Neutrons* [Springer Verlag Berlin Heidelberg, 1987].
12. M. M. Nesterov, I.S. Okunev, *JETP Lett.* **48** (1988) 621.
13. V. A. Vesna, Yu. M. Gledenov *et al*, *Phys. Rev. C* **77** (2008) 035501.
14. S. Yu. Igashov, A. V. Sinyakov *et al*, *Proc. ISINN-11, Dubna* (2004) 34.
15. V. A. Vesna, Yu.M. Gledenov *et al*, *Eur. Phys. J. A* **47** (2011) 43.
16. V. A. Vesna, Yu.M. Gledenov *et al*, *Phys. At. Nucl.* **59** (1996) 19.
17. O. P. Sushkov, V. V. Flambaum, *Sov. Phys. Usp.* **25** (1982) 1.
18. F. Ajzenberg-Selove, *Nucl. Phys. A* **506** (1990) 1.
19. I. S.Okunev. *In: "Time reversal invariance and parity violation in neutron reactions"* [Ed. C. R. Gould, J. D. Bowman, Yu. P. Popov. World Scientific, 1994, p.90-96].
20. V. A. Vesna, Yu. M. Gledenov *et al*, *JETP Lett.* **33** (1981) 411.
21. V. A. Vesna, Yu. M. Gledenov *et al*, *PNPI Preprint-2697* (Gatchina 2006) (in Russian).
22. V. A. Vesna, Yu. M. Gledenov *et al*, *JETP Lett.* **82** (2005) 463.
23. H. Abele, D. Dubbers, H. Häse *et al*, *Nucl. Instr. Meth. A* **562** (2006) 407.

MACROSCOPIC MANIFESTATION OF THE STRONG NUCLEAR INTERACTION IN THE OPTICAL SPECTRA OF SOLIDS

V.G. Plekhanov

Fonoriton Sci. Lab., Garon Ltd., Lasnamae 22 - 3, Tallinn 11413, Estonia

Abstract. Artifical activation of the strong interaction by adding of one neutron to the nucleus causes the global reconstruction of the macroscopic characteristics of solids.The experimental evidence of macroscopic manifestation of the strong interaction in optical spectra of solids which are differ by term of one neutron from each other has been presented. This evidence is based on two independent results: 1) The increase exciton energy on 103 meV is caused by the adding of one neutron (using LiD crystals instead LiH ones); 2) After increasing the amounts by one neutron the energy of LO phonons has decreased by 36 meV. The last one is directly seen from luminescence and scattering spectra. As far as the gravitation, electromagnetic and weak interactions are the same in both of kind crystals, it only changes the strong interaction. Therefore a logical conclusion is made that the renormalization of the energy of electromagnetic excitations (excitons, phonons) is carried out by the strong (nuclear) interaction. The Standard Model is insufficiently underlined.

I. Introduction

As is well known, the neutron is not only an investigation object but also a powerul instrument of the study of the nucleus and condensed matter properties. The neutron is one of the main particles of the Standard Model (SM) [1] which is perfectly described by Quantum Chromodynamics (QCD)[2]. Our present knowledge of physical phenomena suggests that there four types of forces between physical bodies (see, e.g. [3, 4]):

1) gravitational;
2) electromagnetic;
3) strong;
4) weak.

Both the gravitational and the electromagnetic forces vary in strength as the inverse square of the distance and so able to influence the state of an object even at very large distances whereas the strong and the weak forces fall off exponentially and so act only at extremely short distances. The strong forces does not act on leptons (electrons, positrons, muons and neutrinos), but only on protons and neutrons (more generally, on baryons and mesons - this is the reason for the collective name hadrons). It holds protons and neutrons together to form nuclei, and is insignificant at distances greater than 10^{-15} m [3]. Its macroscopic manifestations are restricted up to now to radioactivity and the release of nuclear energy. The three forces which are relevant to elementary particles can be recognized in the three kinds of radioactivity: α - radiation is caused by the strong force, β - radiation by the weak force, and γ - radiation by the electromagnetic force. The characteristics of these forces are summarized in Table 1.

Table 1. The four fundamental forces

Interaction	FQ	Mass	Range (m)	RS	Spin	TC - S (m^2)	TTS (s)
Strong	Gluon	0	10^{-15}	1	1	10^{-30}	10^{-23}
Weak	$W^{\pm}$, Z	81, 93 GeV/c^2	10^{-18}	10^{-5}	1, 1	10^{-44}	10^{-8}
Electromagnetic	Photon	0	∞	$\alpha = 1/137$	1	10^{-33}	10^{-20}
Gravity	Graviton	0	∞	10^{-38}	2	-	-

Here - FQ field quant, RS relative strength, TC - S Typical cross - section, TTS - Typical time scale.

This table given for the strength and range of the forces come from a comparison of the effects they produce on two protons. In some respect these resemble an ordinary Newtonian force between the protons, varying with the distance between them as if the force was derived from a potential function:

$$V(r) = \frac{ke^{-r/R}}{r^n} \qquad (1)$$

for some n. This is an inverse - power force which is diminished by an exponential factor at distances larger than a certain distance R, the range of the force. The strength of the force is measured by the constant k. The unit of strength is $hc/2\pi$ where h is Planck's constant and c the speed of light. We should add that the weak force does not appear to be particularly weak on this reckoning: the reason for its very short range (see Table 1) rather than its intrinsic strength. Since the protons and neutrons which make up the nucleus are themselves considered to be made up of quarks are considered to be held together by the color force [2], the strong force between nucleons may be considered to be a residual color force (see, also [1, 3]). In the SM, therefore the base exchange is the gluon which mediates the forces between quarks. The modern quantummechanical view of the three fundamental forces (all except gravity) is that particles of matter (fermions = neutrons, protons, electrons) do not directly interact with each other, but rather carry a charge, and exchange virtual particles (gauge bosons = photons, gluons, gravitons) which are the interaction carriers or force mediators. As can be see from Table 1, photons are the mediators of the interaction of electric charges (protons, electrons, positrons); and gluons are the mediators of the interaction of color charges (quarks). In our days, the accepted view is that all matter is made of quarks and leptons (see Table 2).

Table 2. Quarks and leptons

	Family 1 2 3	Electric charge (e)
Leptons	e^- μ^- τ^-	- 1
	ν_e ν_μ ν_t	0
Quarks	u c t	2/3
	d s b	- 1/3

As can be see, of the three pairs of quarks and leptons, one pair of each - the quark u and d and the leptons e^- and ν_e^- (electrons neutrino) - are necessary to make up the every day world, and a world which contained only these would seem to be quite possible.

The facts, summarized in the modern nuclear physics (see, e.g. [5, 6]) allow to draw several conclusions in regard to nuclear forces, most notably that the binding energy of a nucleus is

proportional to the number of nucleons and that the density of nuclear matter is approximately constant. This lead to conclude that nuclear forces have a "saturation property". It seems from the last conclusion it is enough to change the number of neutrons in nucleus to change strength of nuclear force. But the last one constitutes the main ideas of the isotope effect [4].
Below we will briefly describe the results of the optical spectroscopy of isotope - mixed solids. The apparatus used in our experiments has been described in several previous publications [7 - 9]. For clarity, we should mentioned here that immersion home - made helium cryostat and two identical double - prism monochromators were used . One monochromator was used for the excitation and the other, which was placed at right - angle to the first for analyzing the luminescence and scattering of light. In our experiments we investigated two kinds of crystals (LiH and LiD) which are differ by a term of one neutron.

II. Results

As demonstrated early (see, e.g. review [10]) most low - energy electron excitation in LiH crystals are the large - radius excitons [11]. Exciton luminescence is observed when LiH (LiD) crystals are excited in the midst of the fundamental absorption. The spectrum of exciton photoluminescence of LiH crystals cleaved in liquid (superfluid) helium consists of a narrow (in the best crystals, its half - width is $\Delta E \leq 10$ meV) phononless emission line and its broader phonon repetitions, which arise due to radiative annihilation of excitons with the production of one to five longitudinal optical (LO) phonons (see Fig. 1).

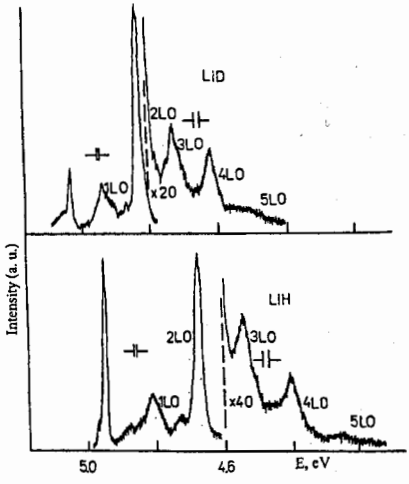

Fig. 1. Photoluminescence spectra of free excitons at 2 K in LiH and LiD crystals cleaved in superluid helium.

The phononless emission line coincides in an almost resonant way with the reflection line of the

exciton ground state which is indication of the direct electron transition X_1 - X_4 of the first Brillouin zone [12].The lines of phonon replicas form an equidistant series biased toward lower energies from the resonance emission line of excitons. The energy difference between these lines in LiH crystals is about 140 meV, which is very close to the calculated energy of the LO phonon in the middle of the Brillouin zone [13] and which was measured in [14]. The isotopic shift of the zero - phonon emission line of LiH crystals equals 103 meV. As we can see from Fig. 1 the photoluminescence spectrum of LiD crystals is largely similar to the spectrum of intrinsic luminescence of LiH crystals. There are, however, some distinctions one is related.

Firstly the zero - phonon emission line of free excitons in LiD crystals shifts to the short - wavelength side on 103 meV. The second difference concludes in less value of the LO phonon energy, which is equal to 104 meV.

At the excitation below the intrinsic absorption adge ($E_{n=1s}$ = 5.043 eV for LiD [10]) we have succeeded in observing the multiphonon resonance Raman scattering (RRS) with the creation of up four phonons (Fig. 2). Indeed, the energy difference between peaks in the RRS spectrum is equal the energy of the LO phonons in the center of the Brillouin zone [13].

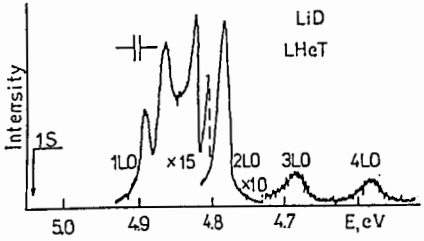

Fig. 2. Resonant Raman scattering of a LiD crystals at the excitation E = 4.992 eV at 4.2 K.

To pay attention the large half - width of observable lines in the RRS spectrum. As was shown in the paper [15] their half - width are always larger than of the excitation line. The proximity of the exciting light frequency to the energy of exciton transitions leads to an essential modification of the selection rules for light scattering. The presence of the second - order TO (Γ) ($\hbar\omega_{TO(\Gamma)}$ = 76 meV for LiH) in the RRS spectrum may be explained by a relatively strong scattering deformation mechanism in these crystals, where, however the main mechanism, as was seen from both figures, is Fröchlich mechanism of intraband scattering. The logwavelength displacement of the excitation line frequency relatively exciton resonance a monotonic decrease the intensity of RRS spectrum as whole more than 60 - fold in both LiH and LiD crystals. Comparison the experimental results on the luminescence and light scattering in the crystals which differ by a term of one neutron only is allowed to the next conclusions;

1. At the adding one neutron (using LiD crystals instead LiH ones) is involved the increase exciton energy on 103 meV.
2. At the addition one neutron the energy of LO phonons is decreased on the 36 meV, that is direct seen from luminescence and scattering spectra. Both characteristics are macroscopic.

III. Discussion

The modern concept of the atom emerged at the beginning of the 20th century , the particular as a result of Rutherford's experiments [5,6]. An atom is composed of a dense nucleus surrounded by an electron cloud. The nucleus itself can be decomposed into smaller particles. After the discovery by Chadvick of the neutron in 1932, there was no longer any doubt that the building blocks of nuclei are protons and neutrons (collectively called nucleons). The elementary particles came to considered the electron, proton and neutron [1, 4]. The primary aim of nuclear physics is to understand the force between nucleons, the structure of nuclei and how nuclei interact with each other and with other subatomic particles.

As say above, an atom consists of an extremely small, positively charged nucleus (see Fig. 3) surrounded by a cloud of negatively charged electrons. As can we see from Fig. 3 the nucleus is less than one ten - thousandth the size of atom, the nucleus contains more than 99.9% of the mass of the atom.

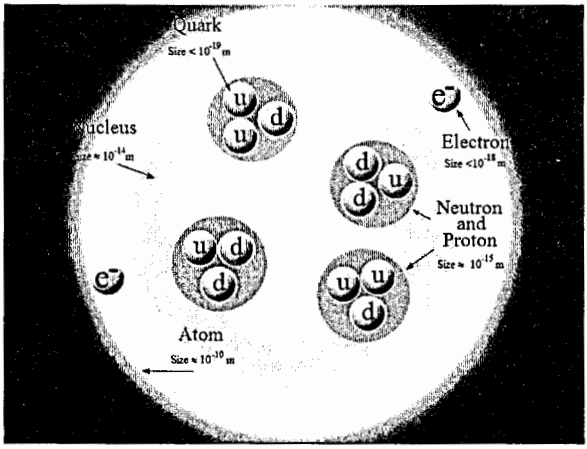

Fig. 3. Structure within the atom. If the protons and neutrons in this picture were 10 cm across, then the quarks and electrons would be less than 0.1 mm in size and the entire atom would be about 10 km across (after http://www.lbl.gov/abc/wallchart/).

Nucleus is central part of an atom consisting of A - nucleons, Z - protons and N - neutrons. The atomic mass of the nucleus is equal Z + N. A given element can have many different isotopes, which differ from one other by the number of neutrons contained in the nuclei [4 - 6]. Modern physics distinguishes three fundamental properties of atomic nuclei: mass, spin (and related magnetic moment) and volume (surrounding field strength) which are source of isotopic effect (see, also [16]). LiH (LiD) crystals with a lattice of NaCl type, whose parameters are close to cubic crystals, are dielectrics with band gap of E_g = 4.992 eV (E_g = 5.090 eV for LiD) at 2 K [7]. These crystals have

an identical electronic structure. The energy band structure of these substances is also identical. All three kinds of forces - gravitational, electromagnetic and weak are also the same for compounds above. The difference between these substances consists out at one neutron in the nucleus of deuteron. Below we should briefly consider some peculiarities of the physics of deuteron. Nucleons can combine to make four different few - nucleon systems, the deuteron (p + n), the triton (p + 2n), the helion (2p + n) and the α - particle (2p + 2n). These particles are grouped together because they are all stable (apart from triton which has a half - life of about twelve years and so may be treated as a stable entity for most practical purposes), have no bound excited states (except the α - particle which has two excited states at about 20 and 22 MeV [5]), and are frequently used as projectively in nuclear reactions. Few - nucleon systems provide the simplest systems to study nuclear structure (see, e.g. [17]). The deuteron provides important information about the nucleon - nucleon interaction. As was noted, the deuteron consists of a proton and a neutron and is the only bound state of two nucleons. Its binding energy is 2.2245 MeV and its total angular momentum J and parity are 1^+ [6]. Since the intrinsic parities of the neutron and the proton are positive parity of the deuteron implies that the relative orbital angular momentum of the neutron and the proton must be even. If the orbital angular momentum L is a good quantum number, states with lower orbital angular momentum generally have lower energy than states with higher angular momentum, and so we expect the ground state of the deuteron to have orbital angular momentum L = 0, so that it is in an S state. Then, if the spins of the proton and the neutron in the deuteron are parallel, we expect the magnetic moment of the deuteron to be approximately the sum of the magnetic moments of the proton and neutron, namely $\mu_p + \mu_n = (2.793 - 1.913)\mu_N = 0.880\mu_N$ ($\mu_N = \frac{eh}{2m_p}$) [5]. If, however, the spins are anti - parallel , we expect it to be $(2.793 + 1.913)\mu_N = 4.706\mu_N$. Experimentally it is $0.857\mu_N$ [5, 17] so the spins of the proton and neutron are parallel and so the total spin S of the deuteron is one, since J = L + S, J = 1. The small but definite difference between $\mu_d = 0.857\mu_N$ and $\mu_p + \mu_n = 0.880\mu_N$ is due, as will shown below, to tensor character of strong forces in deuteron. We thus conclude that the ground state of deuteron is a triplet S state. However this cannot the whole story because S states are spherically symmetrical and thus have no quadrupole moment. This is contradict to experiments. Experimentally the deuteron has a positive quadrupole moment of 0.29 fm^2 [18]. The deviation of the actual deuterium moment from the S state moment can be explained if it assumed that the deuteron ground state is a superposition of S and D states. Part of the time, the deuteron has orbital angular momentum L = 2. Independent evidence for this fact comes from the observation that, as was shown above, the deuteron has a small, but finite, quadrupole moment (see, also [18]). As is well - known, the electric quadrupole moment measures the deviation of a charge distribution from sphericity [4].

The quadrupole moment of a disk shaped (oblate) nucleus Q is negative. A positive quadrupole moment of Q = 0.29 fm^2 according experiment indicates that the deuteron is slightly elongated the z - axiz, like an olive (prolate). Quantum mechanical definition of quadrupole moment for a single proton [18] is described by:

$$eQ = e\int \Psi^* (3z^2 - r^2)\Psi dt . \qquad (2)$$

Thus, if the quadrupole moment is not equal to zero then the eigenfunction of the ground state of the deuteron assigns a probability of 0.04 to finding a $^3D_1$ state and a probability of a 0.96 to finding a $^3S_1$ state. The last one points to the tensor character of the nucleon - nucleon interaction (the more details see, e.g. [5, 6]). Nuclear magnetic dipole and electric quadrupole have a similar importance in helping us to interpret the deuteron structure.

The motion of the electrons produces a magnetic field $\overrightarrow{B_e}$ at the nucleus, which interacts with the nuclear magnetic moment μ_I (see, e.g. [19]):

$$E = -\overrightarrow{\mu_I} \cdot \overrightarrow{B_e}. \qquad (3)$$

Typical energy differences of hyperfine multiplets are only about 10^{-7} eV (in case of the deuteron it

is $3.16 \cdot 10^{-7}$ eV (see also [20, 21])). This value is by more than seven order less than we observe in experiments: the isotopic shift of the n = 1s excitons is equal to 0.103 eV.
The short range character of the strong interaction doesn't possess direct mechanism of the elementary excitation energy renormalization, which was observed in the experiments. However, there is one not very convincing possible hypothesis of the strong interaction mechanism - this is residual long range electromagnetic interaction of the electric charge quarks. The non - zero value of electric quadrupole moment indicates in favour of this hypothesis, for example, in deuterium. Such hypothesis doesn't contradict to the conclusion of the papers [1, 2, 3, 20, 21, 22] about the mass difference origin between the neutron and proton connected with electric charged u and d quarks. Moreover, the neutron mass diminishing in nuclei in comparison to the free state of neutron independently shows the actual residual electromagnetic interaction in nucleons between quarks (see, also [20] and references therein). Naturally, the origin of Van der Waals*) or new type forces are in need of more quantitative not only experimental but also theoretical investigations of observed effects.
Nevertheless, we have very close of the isotope shift exciton energy in the case $^{12}C_x^{13}C_{1-x}$ diamond crystals to the indicated value above in LiH crystals. Indeed, in such experiments we have isotope shift in $^{12}C_x^{13}C_{1-x}$ diamond crystals approximately 15 meV [4] per one neutron and on seven neutrons we get $15 \cdot 7 = 105$ meV. This value is very close to the observed one (103 meV) in LiH crystals.
Thus, the tentative interpretation of describing experimental results don't find consistent explanation at the change strong interaction leaving it to be another mystery of SM (see, also [20, 21]). We should remind that intrinsic contradiction of SM is already well - known. Really, the Lagrangian of QCD (theory of the strong interaction) describes both free motion and interaction between quarks and gluons, which is defined by the strength couple g, its eigenstates are the quarks and the gluons which are not observed in free states [2, 21, 22]. The observed hadrons in the experiment don't eigenstates in quantum chromodynamics. It is obvious to expect that the modern theory of QCD should finally overcome these difficulties [20]. We should add that the current theoretical and experimental evidence for the existence of electronic objects with a fractional of electron charge (e/2, e/3, etc) is reviewed in paper [23]. One more possible mechanism the influence of the strong interaction on the dynamics of elementary excitation connects with the zero - point vibration [4, 20, 21].

Conclusion

The experimental evidence of the macroscopic manifestation of strong (nuclear) interaction in optical spectra of solids which are differ by term of one neutron from each other has been presented for the first time. This evidence is based on two independent experimental results, which is directly seen from luminescence and scattering spectra. As far as the gravitation, electromagnetic and weak interactions are the same in both of kind crystals, it only changes the strong interaction. Therefore a logical conclusion is made that the renormalization of the energy of electromagnetic excitations (excitons, phonons) is carried out by the strong (nuclear) interaction. There is underlined the necessity consideration the strong (nuclear) interaction in quantum electrodynamics.

*) Estimation of the Van der Waals force, for example, dispersion character gives more than 25 times hydrogen polarization value decrease and this is not correct.

References

1. W.N. Cottingham, D.A. Greenwood, An Introduction to the Standard Model of Particle Physics (Cambridge University Press, Cambridge, 2007).
2. F.I. Yndurain, The Theory of Quark and Gluon Interactions (Springer, Berlin, 2013).
3. E.M. Henley, A. Garcia, Subatomic Physics (World Scientific Publishing Co., Singapore, 2007).
4. V.G. Plekhanov, Isotopes in Condensed Matter (Springer, Heidelberg, 2013).
5. K.S. Krane, Introductory Nuclear Physics (John Wiley & Sons, New York, Chichester, 1988).
6. E. Segre, Nuclei and Particles (W.A. Benjamin, Inc. , Reading, MA, 1977).
7. V.G. Plekhanov and V.I. Altukhov, J. Raman Spectr. **16** (1985) 358.
8. V.G. Plekhanov, Phys. Rev. **B53** (1996) 9558.
9. V.G. Plekhanov, Prog. Mat. Sci. **51** (2006) 287.
10. V.G. Plekhanov, Phys. - Uspekhi **40** (1997) 553.
11. R.S. Knox, Theory of Excitons (Academic Press, New York - London, 1963).
12. S. Baroni, G. Pastori Parravicini, G. Pezzics, Phys. Rev. **B32** (1985) 4077 .
13. J.L. Verble, J.L. Warren and J.L. Yarnell, ibid, **168** (1968) 980 .
14. V.G. Plekhanov, Isotope Efects in Solid State Physics (Academic Press, New York, 2001).
15. V.G. Plekhanov, Phys. - Uspekhi **46** (2003) 689.
16. V.G. Plekhanov, Giant Isotope Effect in Solids (Stefan University Press, La Jola, CA, 2004).
17. J Carlson R. Schivalia, Rev. Mod. Phys. **70** (1998) 743.
18. R.N. Zare, Angular Momentum (John Wiley & Sons, New York - Chichester, 1988).
19. H. Haken, H. Ch. Wolf, The Physics of Atoms and Quanta (Springer, Berlin, 2005).
20. V.G. Plekhanov, Universal J. Phys. & Appl. **11**, 6 (2017).
21. V.G. Plekhanov, Isotope Effect - Macroscopic Manifestation of the Strong Interaction (Lambert Academic Publishing, Saarbrücken, Germany) (in Russian).
22. I.M. Dremin, A.B. Kaidalov, Phys. - Uspekhi **49** (2006) 263 - 273 .
23. V.P. Bykov, Phys. - Uspekhi **49** (2006) 979 - 985.

Time-Dependent Long Range Nuclear Forces

Yu.L. Ratis

Institute of power engineering for special applications

Abstract

It was shown that the experimental results [1–5] provide an evidence for existence of time-dependent long range nuclear forces considered in [6]. Unfortunately, scientific community does not understand revolutionary results [1]–[5] since their interpretation was ambiguous. The original scheme of new "experimentum crucis" is proposed. The aim of this experiment is detection of time-dependent long range nuclear forces with effective radius $r_{\pi} > 17$ Å.

Keywords: nuclear forces, theory of exotic electroweak processes, experimentum crucis, exonuclear reactions

1. Introduction

Results [1]–[5] are in a formal contradiction with "the dogmas of modern nuclear physics which are reliably established". At the same time these results perfectly explained within a framework of the theory of exotic electroweak processes (TEEP) [6].

As the results of experiments [1–5] were published in the rare preprints, we will provide extensive cites from these works, accompanying them with comments from TEEP positions.

1.1. A.S. Roussetsky group experiments

International group of scientists investigated exothermic desorption of a deuterium from deuterated heterostructure Au/Pd/PdO:D. They systematically detected α-particles with the energy above 7.5 MeV [1]. The results of this work are presented in fig. 1

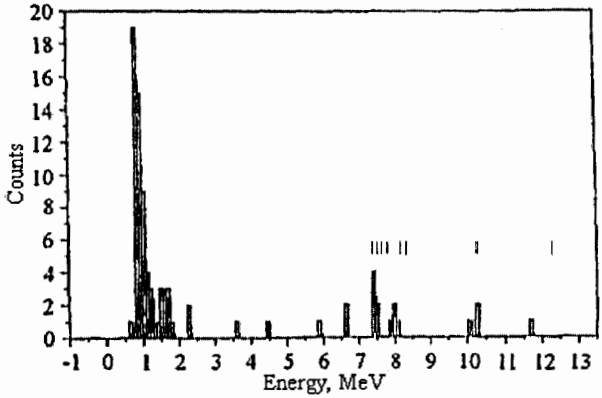

Fig. 1. The typical range of charged particles for Au/Pd/PdO:D samples thickness of l = 40 micron received for time t_D =24000 s. Strokes show the peak positions predicted by TEEP. The results of calculation are seen in Table 1. Peak at ~12 MeV corresponds to the α-particles from reaction $D_{\nu} + {}^{197}_{79}Au \rightarrow \alpha + {}^{195}_{78}Pt_{\nu}$.

Results [1] were processed by the TEEP methods [6]. It was established that

1) Exonuclear reaction $D_v + {}^{A}_{46}Pd \rightarrow \alpha + {}^{A-2}_{45}Rh_v$. A crystal lattice absorbs the recoil momentum. Corresponding energies see in Table 1.

Table 1

Energy of a - particles from $D_n + {}^{A}_{46}Pd$ ® $a + {}^{A-2}_{45}Rh_n$ reaction

Isotope	Abundance	Bound energy	Bound energy	E [MeV]
${}^{102}_{46}Pd$	0.96	875.246	857.550	8.377
${}^{104}_{46}Pd$	10.95	892.874	874.879	8.078
${}^{105}_{46}Pd$	22.23	899.947	884.189	10.315
${}^{106}_{46}Pd$	27.33	909.508	891.188	7.753
${}^{108}_{46}Pd$	26.80	925.275	906.750	7.548
${}^{110}_{46}Pd$	12.08	940.232	921.560	7.401

2) Reaction with ${}^{197}_{79}Au$. The recoil momentum is partially accepts by the affiliated nuclei ${}^{195}_{78}Pt$. Besides, α-particles, which are products of reaction $D_v + {}^{197}_{79}Au \rightarrow \alpha + {}^{195}_{78}Pt_v$, come from depth of heterostructure of Au/Pd/PdO:D (H), and lose a part of energy by passing through a foil.

$$D_v + {}^{197}_{79}Au \rightarrow \alpha + {}^{195}_{78}Pt_v + 12.397 \text{ MeV}$$

It is evident that TEEP allows to calculate correctly not only schemes of the "forbidden" reactions, but also predicts α-peaks positions (see fig. 1).

1.2. D.S. Baranov's experiments

D.S. Baranov detected [2–3] radioactive isotopes of bismuth and polonium at a spark electric discharge in solution of $({}^{209}_{83}BiNO_3) \times 10H_2O$ Место для формулы. (see fig. 2).

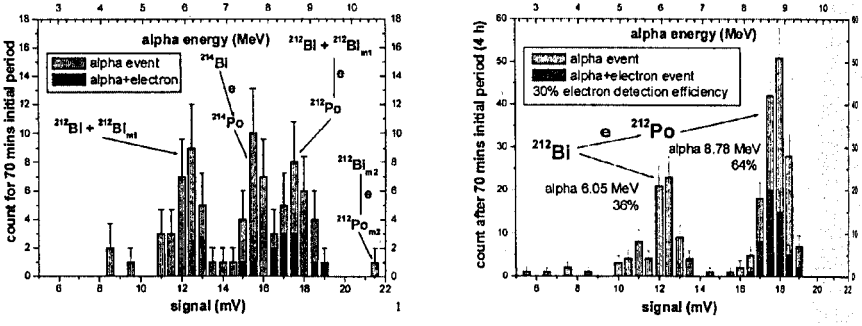

Fig. 2. Left histogram. The α-particles count rate at initial 70 minutes. Right histogram. The α-particles count rate after initial 70 minutes.

From the point of view of TEEP D.S. Baranov's reactions took place according to schemes

$$({}^{209}_{83}BiNO_3)_\nu \rightarrow {}^{210}_{84}Po + {}^{61}_{30}Zn_\nu + 31.645\ MeV \quad (1)$$
$$({}^{209}_{83}BiNO_3)_\nu \rightarrow {}^{212}_{84}Po + {}^{59}_{30}Zn_\nu + 22.287\ MeV \quad (2)$$
$$({}^{209}_{83}BiNO_3)_\nu \rightarrow {}^{214}_{84}Po + {}^{57}_{30}Zn_\nu + 22.259\ MeV \quad (3)$$
$$({}^{209}_{83}BiNO_3)_\nu \rightarrow {}^{212}_{83}Bi + {}^{59}_{31}Ga_\nu + 20.822\ MeV \quad (4)$$
$$({}^{209}_{83}BiNO_3)_\nu \rightarrow {}^{214}_{83}Bi + {}^{57}_{31}Ga_\nu + 19.765\ MeV \quad (5)$$

Index *n* in formulas (1)–(5) means that one of protons in the corresponding nuclei is replaced by neutroneum.

1.3. A.Yu. Didyk's experiments

One of the main puzzles of modern nuclear physics is carbon creation [4] in the high pressure helium irradiated by γ-quanta with energy of an order of 10 MeV.

The high pressure helium in the chamber (fig. 3) was irradiated by the bremsstrahlung γ-quanta with threshold energy of 10 MeV during $1.0 \cdot 10^5$ s [5].

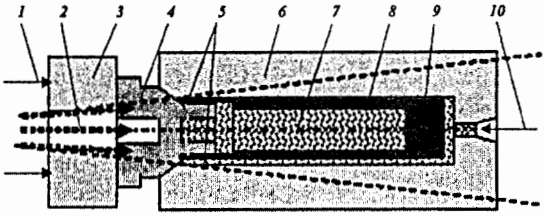

Fig. 3. The elements of a chamber of a high pressure of helium (HeHPC) used at radiation by bremsstrahlung γ- quanta. *1- screw* clamping consolidation (a cone 60°/58 °) which is not shown in this drawing; 2- stream γ- quanta with the section of 6 mm through passage; 3- $Cu_{1-X}Be_X$ - an entrance window into which the screw is inserted clamping; 4- entrance window γ- quanta; 5 - area in which were found "carbon" a foil; 6- chamber of a high pressure from $CuBe_2$ with the external protective steel cylinder, it is not shown in drawing; 7- helium; 8- copper reactionary chamber (99.99% copper); 9- copper collection of products of reaction closing a reactionary chamber; 10- device for loading and unloading of gas and for measurement of its pressure at control and in the course of radiation.

Initial pressure of gaseous helium was about 1.1 kbar. An electron beam current fluctuated in the range 22–24 mA.

When *HeHPC* had been opened after irradiation the residual pressure of helium was equal 426 bar. Inside *HeHPC* a foil of black color and other multiple objects were observed on internal surfaces of the reaction chamber. The chamber itself was made of high purity (99.99%) copper, its entrance window for γ-quanta was made of beryllium bronze and there was the copper collector for products of nuclear and chemical reactions. The materials collected from an internal surface of the chamber, the entrance window and the product collector have been studied by the x-ray analysis and other methods in two independent analytical centers: in NIIYaF of D.V. Skobeltsyn of Lomonosov Moscow State University (ATs-I) and FGBNU "Scientific research institute PMT"(ATs-II).

The performed measurements showed that foil consist generally of carbon, and, in smaller quantities, of other elements (from carbon to iron).

The most striking result of this experiment was that about 50% of initial helium turned into carbon!

From the point of view of orthodox nuclear physics there was simply impossible. However according to TEEP the exotic reaction of the induced electronic capture which is not followed the neutrino's emission (i.e., neutroneum creation reaction) "switched on" long range nuclear forces. As a result multinuclear fusion reactions become allowed, as it observed in this experiment.

The detailed analysis of experiments [4–5] showed that the effective radius of exonuclear forces exceeds

2. Description of the scheme of new experiment

To check the hypothesis on existence of the time-dependent long range nuclear forces the following reaction which is strictly forbidden by a Coulomb barrier is offered:

(6)

For its implementation there is necessary to make an electron beam tube (fig. 4) in which as the screen a chemically pure bismuth foil is used.

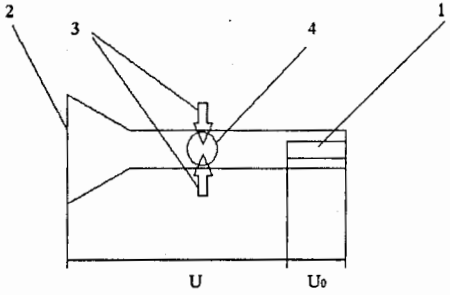

Fig. 4. Measuring part of installation. 1. Electron beam gun (cathode knot); 2. The bismuth foil screen. 3. Electrodes for checking of emergence of helium in volume of an electron beam tube; 4. A window for the analysis of optical spectra.

The recommended voltages are $U_0 \sim 30$ kV and $U \sim 1$ kV. Exposition time is more than 3 days. The vacuum in electron beam tube has to be of order 10^{-6} Torr. It is also, whenever possible, sustained under vacuum so the absence of helium in residual gases was guaranteed.

At an electric discharge between electrodes 3 a helium lines in an optical spectrum have to appear.

Experiment, as a matter of fact, repeats the well-known Rutherford–Soddi experiment in which transmutation of chemical elements was discovered.

Conclusion

It is necessary to wait for results of experimentum crucis.

Acknowledgments

I would like to thank all my fans and critics: V.I. Furman, A.V. Strelkov, A.A. Rukhadze, V.A. Zhigalov.

References

1. Lipson A.G., Roussetsky A.S., Takahashi A., Kasaagi J. Observation of long-range α-particles at desorption of a deuterium (hydrogen) from heterostructure of Au/Pd/PdO:D (H). *Short messages of FIAN (physics) number 10, 2001.*
2. Baranov D.S., Proceedings of the 6-th Russian Conference on Condensed Matter Nuclear Science. Dagomys, City of Sochi, p.121 (1999).
3. Baranov D.S., Baranova O.D. EXON - 2009. AIP CONFERENCE. PROCEEDINGS. V.**1224** p.241–246. http://proceedings.aip.org/proceedings (2010).
4. Didyk A.Yu., Vishnevsky R. Properties of the structures on the basis of carbon synthesized in nuclear reactions in helium with a pressure of 1.1 Kbar under the influence of radiation by brake γ quanta with threshold energy of 10 MEV. Preprint JINR R15-2014-38, JINR, Dubna, 2014.
5. Didyk A.Yu., Vishnevsky R. Nuclear reactions, synthesis of chemical elements and new structures in dense He with a pressure of 1.1 Kbar under the influence of radiation by brake γ quanta with threshold energy of 10 MEV. Preprint JINR R15-2014-50, JINR, Dubna, 2014.
6. Ratis Yu.L. Neutrino's exoatom neutroneum. Hypothesis or reality? Applied physics and mathematics (in russian), 2017, No. 1, pp. 28–73.

THE NEUTRON MATTER AS «THE BEGINNING» AND «THE END» OF THE PERIODIC SYSTEM OF D.I. MENDELEEV

Ryazantsev G.B.[1], Beckman I.N.[1], Lavrenchenko G.K.[2], Buntseva I.M.[1], Lavrik A.V.[3]

[1]Lomonosov Moscow State University, Leninskie Gory, Moscow, Russia,
[2]LLC «Institute of Low Temperature Energy Technology», POB188, Odessa, Ukraine

e-mails: [1]anis-mgu@rambler.ru ; [2]uasigma@mail.ru; [3]lavrikav@gmail.com

The formation of a neutron substance, in addition to gravitational neutronization, is considered, other mechanisms, such as the condensation of ultracold neutrons (UCN) and neutronization due to a critical increase in the atomic number in the periodic table (PS)

The stability of the neutron substance is substantiated already at the micro level due to Tamm interaction and not only at the macro level due to the gravitational interaction, as it is now considered in astrophysics. A neutron substance is a very concrete physical reality, urgently demanding its rightful place in the PS and studying not only physical, but also chemical, and possibly even in the near future, engineering and technical properties. We also consider the possibility of a "chemical" interaction of UCN with molecules of substances with an odd number of electrons. It is proposed to extend the PS beyond the limits of classical chemical substances and to cover a much wider range of matter in the universe, based on forgotten ideas of D.I. Mendeleev. Moreover, begins with neutron and its isotopes (dineutron, tetraneutron, etc.) and ends PS the neutron stellar substance.

Keywords: *neutron, neutron substance, Periodic system of elements, neutronization.*

Dmitri Ivanovich Mendeleyev assumed existence before the hydrogen elements X and Y. Element X (Mendeleev calls it **"Newtonium"**) got its place in the periodic system – in the zero period of the zero group, as the lightest analog of inert gases. In addition, Mendeleev allowed the existence of one more element lighter than hydrogen – the element Y, **"Koroniya"** [1, 2].

It should be noted that even after D.I. Mendeleev's question about "zero" elements was repeatedly raised by many authors both in the past and in the present centuries, however, for brevity we mention only the very first and famous: for example, Ernest Rutherford in 1920 [2,4] and Andreas von Antropoff in 1926 (before the discovery of the neutron itself) as a designation for a hypothetical element with an atomic number zero, which he placed at the beginning of the periodic table [3]. A. Antropoff also proposed the term "Neutronium" for the first time, although at that time this term was understood only by the yet not discovered, but already expected neutron. At the present time the dineutron, tetraneutron, and octaneutron can claim this place in the PS, the information about which has already appeared in the press [5,6] and which can formally be considered as neutron isotopes. It's not difficult to see that the very substance of neutron stars, which in 1937 predicted L.D. Landau and discovered in 1968 by astronomers from Cambridge, can be considered from the point of view of the isotope of the element Neutronium.

Thus, the zero position in the PS corresponds to the notion of it as a **"singular point"** in which to unite the micro- and mega-worlds, about the unity of which many philosophers and outstanding natural scientists have repeatedly spoken.

The process of transformation of ordinary matter into neutron under the influence of gravitational forces in the process of the evolution of certain stars was called **Neutronization**. The reaction of electron capture by atomic nuclei (A, Z) (A is the mass number, Z is the order number of the element) has the form:

$$(A, Z) + e^- \rightarrow (A, Z-1) + \nu, \quad (1)$$

The energy threshold of the reaction is large, therefore, only at high material densities, characteristic of the final stages of the evolution of some stars, the electron energy may exceed the critical value of the Neutronization threshold. Gravitational neutronization is widely described and discussed in detail, but other mechanisms for the formation of neutron matter are possible, for example, condensation of ultracold neutrons (UCN) and neutronization due to a critical increase in the atomic number of the elements in the PS.

First we turn to the consideration of neutronization due to a critical increase in the ordinal number of the elements in the PS. In general, the question of the "ultimate element" was repeatedly raised by different authors and has its interesting "intrigue". The final element was initially assumed to be from the "drip" model of the nucleus with Z slightly more than 100, then it was shifted to the "mysterious" number of 137, passionate admirers of many well-known physicists and among them Richard Feynman, through which 137 elements even got the unofficial name "Feynmanium ".

It was believed that this element is "finite" because of the uncritical use of the Bohr model of the atom for superheavy elements, when the light velocities for the orbital electrons were obtained at Z = 137. The development of the quantum theory shifted the finite element beyond Z > 170. Let's consider this question in more detail. The problem of the stability of superheavy atoms was described by Ya.B. Zeldovich and V.S. Popov back in 1971 [7]. The question of the electronic structure of an atom in a supercritical nuclear charge (Z > 170) is of great fundamental interest. In 1928, Paul Dirac showed [8] that in the Coulomb field of a point charge Ze the solution of the relativistic equation for an electron becomes singular for Z= 137. Introducing the finite dimensions of the I.Ya. Pomeranchuk and Ya.A. Smorodinsky [9] in 1945 showed that an accurate calculation leads to a critical charge (Zc = 170).

In the work of S.S. Gerstein and Ya.B. Zeldovich [10] in 1969 it was assumed that, with a supercritical charge Z > Zc, a bare nucleus Z spontaneously emits positrons. An atom with a filled K shell, with an increase in the charge of the nucleus Z > Zc (with increasing Z, the internal electronic levels continue to drop, and the size of the nuclei grow) directly passes to the critical state Z = Zc, not emitting positrons, but by trapping the electrons by the nucleus. The authors also consider the possible contribution of the phenomenon of vacuum polarization and the production of pairs of particles and antiparticles in the field of critical nuclei.

However, we make a few critical remarks:

1. With the unconditional heuristic value of the article by Zeldovich and Popov, they did not go any further - they did not make a direct conclusion about the almost complete neutronization of supercritical nuclei, although they laid the groundwork for this.

2. Their conclusion (the 4th conclusion on p. 410 [7]) that the properties of the outer shells of an atom (which determine, in particular, Mendeleev's periodicity of chemical properties) naturally continue to the supercritical region-is questionable.

3. They underestimated the role of vacuum polarization. Although there were papers [11], which state that the vacuum polarization grows unboundedly at Z→Zc. This contradicted their conclusions, however, in our opinion, this is closer to the truth and this leads to the inevitable and almost complete neutronization of supercritical nuclei.

Of the modern works specifying the value of the quantity Zc, we can indicate the work "New method for solving the problem" Z > 137 "and determining the energy levels of hydrogen-like atoms" V.P. Neznamov and I.I. Safronov in "Uspekhi Fizicheskikh Nauk" in 2014 [12].

The gradual neutronization of the element nuclei is observed long before the critical values of Zc are reached, the average index of the ratio of the number of neutrons and protons in the nuclei of chemical elements is steadily increasing already in all periods of the PS. Qualitatively, the growth of the neutronization degree of nuclei can be well observed by extrapolating the course of the curve on a proton-neutron diagram if from the whole set of known elements and their isotopes choose stable and long-lived ones.

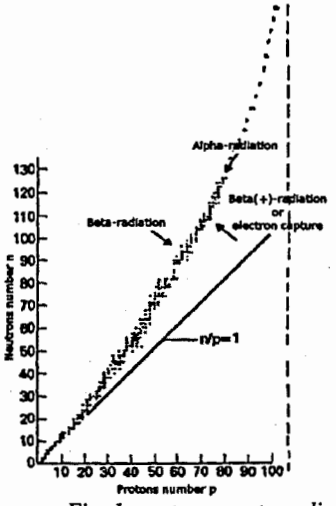

Fig. 1. proton - neutron diagram.

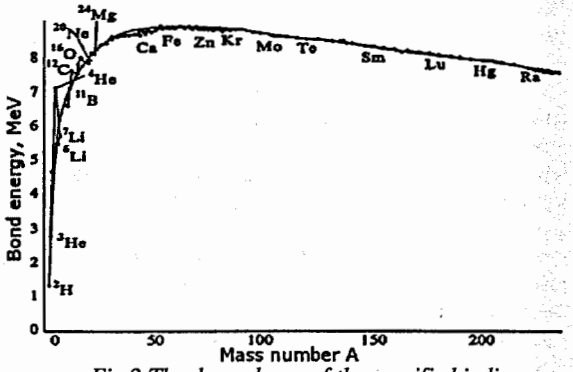

Fig.2.The dependence of the specific binding energy of the nucleus in atoms from their mass.

It's clear that for quantitative conclusions from the extrapolation of the diagram, it is necessary to carry out a thorough statistical analysis of the curve for the dependence p - n (Fig. 1) for a very wide range of nuclides. What is the nature of the mathematical dependence of p - n? It can be assumed that if in the limit a neutron substance is practically only a set of neutrons, then one should expect a hyperbolic dependence and an asymptotic tendency of the curve to some limit, if there always remains a definite, albeit decreasing, fraction of the protons in the neutron matter, then we should expect a parabolic or exponential dependence.

The statistical processing was carried out by **Mathcad** and **ORIGIN** programs: both methods yielded the same result. The proton-neutron diagram for stable and long-lived isotopes is best described by a quadratic polynomial: $y = ax^2 + bx + c$, where a = 0.004982, b = 1.122, c = –1.003 for Mathcad and a = 0.005, b = 1.126, c = –1.0034 by ORIGIN. Thus, the dependence of p - n best corresponds to a quadratic parabola, rather than to a hyperbola and an exponential, as one would expect from a "drip" nuclear model on the one hand, and on the other, indicates that there is always a residual in the neutron matter fraction of protons.

Additional information can be obtained from the dependence of the specific binding energy of nucleons in the atomic nucleus on their atomic mass A (Fig. 2), which is well described by the Weizsäcker formula.

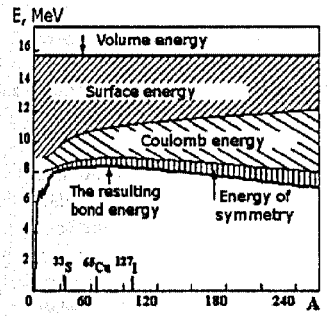

Fig.3. Contribution of different energy in the Weizsäcker's dependence.

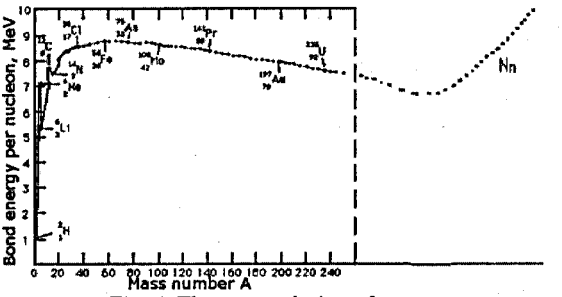

Fig. 4. The extrapolation of Weizsäcker's dependence.

Carl Friedrich von Weizsäcker obtained the semi-empirical equation for the binding energy:

$$E_B = \alpha A - \beta A^{2/3} - \gamma Z^2 A^{-1/3} - \xi (N-Z)^2/A + \delta A^{-3/4}, \qquad (2)$$

where, α = 15.75 MeV; β = 17.8 MeV; γ = 0.71 MeV; ξ = 22 MeV; δ = + 34 MeV for even-even, δ = 0 MeV for odd, δ = –34 Mev for odd-odd, A – atomic weight.

It can be seen (Fig. 3) that with increasing A, the Coulomb energy of repulsion of protons makes the largest contribution to the decrease in the binding energy, while the contribution of the surface energy decreases, and the energy of symmetry is not decisive. Let's try to continue Weizsäcker's dependence on supercritical nuclei (Fig. 4).

Because of the process of almost complete neutronization and growth of sizes for supercritical nuclei, the contribution of the surface energy will be leveled, and the Coulomb repulsion will cease to increase when supercriticality is reached, which will result in the stabilization of the neutron substance and reduce the probability of its decay by some mechanism (fission, β^+ decay). It is necessary to consider in more detail the β^- decay, which, it would seem, should be dominant with such "overloading" by neutrons.

However, the paradox of neutron matter leads to the fact that starting from a certain critical mass and size (when the path of β-electron in a neutron matter becomes smaller than the size of the matter), β^-- decay from the destabilizing factor becomes a significant factor of stability. There is always some residual content of the proton matter in the neutron matter, and beta-electron emitted by decayed neutron is not able to leave the neutron matter of sufficient size (larger than the path of beta-electron in it). The emitted electron is absorbed by the remaining protons, which in turn are converted into neutrons, thus the dynamic equilibrium of the system is maintained. In fact, it corresponds to the theory of Tamm [13], which he put forward in his time (1934) to explain the mechanism of nuclear forces for ordinary nuclei. It should be noted that his theory was not consistent for ordinary atoms (Tamm appreciated his "unsuccessful" theory of nuclear forces more than his Nobel work on Cherenkov radiation), but it can be realized for the neutron matter of appropriate scale (200–300 and more femtometers), giving it additional stability.

In strongly interacting systems, there are many virtual particles and all kinds of interactions that are allowed by considerations of invariance are realized. So, in our view, the

"age-old" theory of exchange β-nuclear forces Tamm (e-exchange of nucleons), and not just its modification by Hideki Yukawa (π-exchange of nucleons), still awaits its recognition (because besides the meson cloud around the nucleon there are certainly other particles) and "dominates" in the neutron matter of the Universe, ensuring its stability and wide space distribution.

A close examination of this problem was given by Frederick Hund in 1936 in the first microscopic description of the equation of state of nuclear matter in beta equilibrium in the article "The substance at very high pressures and temperatures" [14] only if Tamm has virtual electrons, Hund realizes a beta-equilibrium of completely real particles, but most importantly, both mechanisms contribute to the stability of supercritical nuclear matter, and in strongly interacting systems there is no fundamental difference between virtual and real particles.

Another factor of additional stability of the neutron matter during the significant increase of its mass (up to a macro scale) will be the ever-increasing contribution to the gravitational interaction. Thus, we obtain a modified Weizsäcker equation for the neutron matter, which describes the main factors of its stability and the real existence in the Universe:

$$E_B = \alpha A - \beta A^{2/3} + \tau A^t + \lambda A^l, \quad (3)$$

where α = 15.75 MeV; β = 17.8 MeV; τ – Tamm- interaction; λ – the gravitational interaction. The parameters of equation 3 (τ, λ, t, l) need to be clarified in the course of further research in this area.

It's namely Tamm interaction, due to nuclear β - force, confers resistance to neutron substance already on the micro-level, not just at the macro-level due to the gravitational interaction, as it is now considered to be in astrophysics!

The existence, in addition to the forces of Yukawa, of Tamm-interaction for a neutron substance, allows one to expect a technology for its production in terrestrial laboratory conditions, which, based on nuclear dimensions, can be called **Femtotechnology**. One of the directions of femtotechnology can be the study of collisions of nuclei of heavy elements, which in sum give a compound nucleus falling into the supercritical region, i.e. Zc >170–175, which, apart from fission, can be stabilized by the production of various pairs of particles and antiparticles in the field of supercritical nuclei, and in the case of electron-positron pairs, the electrons will be absorbed by the supercritical nucleus and positrons emit as the charge of the nucleus decreases to critical values of Zc. A detailed study of such systems will become possible after the implementation of the NICA Project (**NICA**, English Nuclotron-based Ion Collider facility) in Russia.

The possibility of the existence of superdense neutron nuclei was considered in the work of A.B. Migdal's *"Theory of finite Fermi systems and properties of atomic nuclei"* in the section: *"Application of TC FS in nuclear physics"* [15]. Migdal believed: *"... neutron nuclei can be stable with respect to beta decay and fission, with Z << N and N > 10^3 – 10^5. Such nuclei could be observed in cosmic rays in the form of large fragments."* Thus, A.B. Migdal proposed that neutron cores be searched for exotic tracks in photographic emulsions after exposure to cosmic rays.

From the Cosmos we will go down to Earth and once again we will see where it's possible to find a neutron substance here? Usually we are dealing with neutron radiation of various energies, but not with neutron matter. This was until 1968, when an experiment was conducted at the Laboratory of Neutron Physics under the guidance of the member of the USSR Academy of Sciences, Fyodor Lvovich Shapiro [16, 17], in which the phenomenon of retention in vessels of very slow neutrons, predicted by academician Ya.B. Zeldovich. The

behavior of neutrons held in vacuumed vessels is reminiscent of the behavior of a highly rarefied gas in the vessel. Such neutrons are called ultracold (UCN).

The retention of UCN in the vessels attracts researchers the opportunity (longer than a single neutron flight through the experimental volume) to observe longer after this elementary particle in the experimental setup, which gives a significant increase in the sensitivity and accuracy of experiments on the interaction of neutrons with fields and matter.

For example, the use of UCN has made it possible to significantly omit the limit of the existence of the electric dipole moment of a neutron, necessary for testing the law of conservation of time parity, to more accurately measure the lifetime of a free neutron to $\beta\beta$ decay. Working with UCN, the researcher, in fact, from femto- again comes back to nanotechnology, if we start from the sizes of objects! The most important feature of UCN is that they behave not as radiation, but as a substance and work with them as with a substance similar to a discharged inert gas. Moreover, one can study both physical and chemical properties. Physical properties are already being studied, but the question of the chemistry of UCN seems to be that the question is not even raised; by default somehow it seems obvious that they should be similar to inert gases.

It's look like the truth, but now we already know that inert gases, albeit with difficulty, enter into chemical reactions and form, albeit not stable, but chemical compounds. Can this happen with UCN? If one assumes that Chemistry is only the interaction of the electron shells of atoms, as many believe, a categorical negative answer follows. But if under Chemistry is understood, more generally, the ability of micro- (nano-, pico- or even femto-) objects to interact and form relatively stable compounds, then why not? Yes, neutrons do not have electric charge and free electrons, so that all ideas about possible classical chemical bonds (ionic, covalent, etc.) immediately disappear.

But, neutrons have exactly a magnetic moment and perhaps an electric dipole moment, cannot this serve the ability to interact with other objects and form, even if not stable, yet observable connections? For example, the interaction of a neutron with molecules of substances with an odd number of electrons is entirely possible [19, 21].

The development of new UCN sources is actively carried out worldwide, some of them are based on the use of solid deuterium at a temperature of 4.5 K (LANL, USA, PSI, Switzerland), and others on the accumulation of UCN in superfluid helium (KEK-RCNP-TRIUMF, Japan-Canada, ILL, France) [19]. Similar work is being intensively carried out in Russia: The neutron laboratory at the Joint Institute for Nuclear Research (Dubna), the Petersburg Nuclear Physics Institute (PNPI), in Gatchina, is working on the creation of a high-intensity UCN source. With its help, they hope to obtain data that will provide answers to the most important questions of modern physics.

The projected source will make it possible to obtain a flux of ultracold neutrons (UCN) with a density of 10^4 cm^{-3}, which is many times greater than the maximum density now reached [19]. This problem – obtaining intensive UCN fluxes – is now considered one of the priorities in neutron physics. An increasing and larger increase in the density of ultracold neutrons inevitably leads to the formulation of the question of their possible condensation and the production of a condensed neutron substance in laboratory conditions similar to the cosmic one. Not so long ago a decisive breakthrough was made to a new area: a radically new kind of matter, the so-called Bose condensates of the atoms of matter, was created.

Are condensate neutrons possible? Condensates, density and strength of which will be comparable to the density and strength of atomic nuclei. In other words, how close are we today to the point of creation of a cosmic neutron substance in the laboratory?

The Nobel Prize in Physics in 2001 was awarded to researchers Eric A. Cornell, Wolfgang Ketterle and Carl E. Wieman for obtaining and investigating the properties of the fifth state of matter – the Bose-Einstein condensate, they were able to get the first Bose condensate [20]. This could be done with the help of methods developed recently for the supercooling of particles by laser beams and a magnetic field.

The Bose condensate of atoms was obtained in a form convenient for research and laboratory analysis. Soon reports of the receipt of Bose condensates of various atoms showered from everywhere. The activity of scientists was also greatly facilitated by the fact that the facilities for obtaining Bose condensates turned out to be relatively inexpensive - experiments were in full swing in many countries. Soon, methods were also found for obtaining Bose condensates of particles of half-integer spin, fermions, whose class includes neutrons. In them, the particles are connected in pairs, then gathering in a Bose condensate. In many respects, neutrons are close to the lightest atoms. For example, the mass of a neutron is practically equal to the mass of a hydrogen atom, the Bose condensate of which was obtained by Ketterle in 1997.

But, in contrast to atomic Bose condensates, to natural compression of which under Bose condensation an electronic barrier is an irresistible obstacle, nothing can prevent the compression of the neutron Bose condensate. In such a condensate, UCN gas forms pairs with opposite spins, when the critical density and temperature are reached, will in itself shrink to near nuclear density when nuclear forces enter into the matter, forming a stable state-a condensed neutron matter.

CONCLUSION

Thus, the neutron matter in our time is a very concrete physical reality, urgently demanding its rightful place in the PS and studying not only physical, but also chemical, and possibly even in the near future, engineering and technical properties!

A neutron substance, or rather an element corresponding to it, begins (zero period) and ends (supercritical atoms) of the PS elements. The neutron substance is given stability already at the micro level due to Tamm-interaction, and not only at the macro level due to the gravitational interaction, as is now believed in astrophysics. The possibility of neutronization is shown not only because of the gravitational interaction, but also in other mechanisms (supercritical increase in the atomic number of the elements and UCN condensation), so there is a fundamental possibility of obtaining a neutron substance even under terrestrial conditions. The neutron substance is the necessary link connecting (throwing bridge) from micro- to macro- and mega- world, from a free neutron to neutron stars and black holes. **The neutron substance is consistent with the original concept of the Periodic Law and the system put forward by Dmitri Ivanovich Mendeleev [1, 2, 21–25]!**

REFERENCES

1. **Менделеев Д.И.** *Периодический закон* // Сочинения. Л.-М.,Т.2, 1934.; Под редакцией А.Н. Баха, Б.Н. Выропаева, И.А. Каблукова и др.- Л.: Госхимтехиздат.- 520с.
2. **Рязанцев Г.Б., Лавренченко Г.К.** *Современный взгляд на «нулевые» в Периодической системе элементов Д.И. Менделеева* // Технические газы. – 2014, **1**, С. 3–10.

3. **A.von Antropoff.** *Eineneue Form des Periodischen Systems der Elementen.//* Zeitschriftfur Angewandte Chemie **39** (23): 722–725. (1926) doi:10.1002/ange.19260392303.
4. **Кикоин А. К.** *За пределы таблицы* //Квант,1991,№ 1,С. 38, 39, 42–44.
5. **Marques F. M., Orr N. A., Achouri N. L., et al.** *Comment on "First Observation of Ground State Dineutron Decay":* ^{16}*Be//* Phys. Rev. Lett.,**109** (2012) 239201.
6. **Aleksandrov D. V., Nikol'skii E. Yu., Novatskii B.G. et al.** *«Search for Resonances in the Three- and Four-Neutron Systems in the* ^{7}*Li(*^{7}*Li,*^{11}*C)3n and* ^{7}*Li(*^{7}*Li,*^{10}*C)4n Reactions»//* JETP Letters, 2005. **81** (2): 43–46. DOI:10.1134/1.1887912.
7. **Зельдович Я.Б., Попов В.С.** *Электронная структура сверхтяжелых атомов // УФН* 105 403–440 (1971).
8. **Dirac P. A. M.** *The Quantum Theory of the Electron//* Proc. Roy. Soc. 117, 610; 118, 341 (1928).
9. **Pomeranchuk I.Ya., Smorodinsky Y.A.** *On energy levels in systems with Z >137 //* J. Phys. USSR **9**, 97 (1945).
10. **Gershtein S.S., Zel'dorovich Ya.B.** *Positron Production during the Mutual Approach of Heavy Nuclei and the Polarization of the Vacuum//* Soviet Physics JETP,1970, V.**30**. № 2, 358–361.
11. **Panchapakesan N.** *Charge Distribution around a Nucleus with Z>137//* Phys. Lett. **35B**, (1971) 522.
12. **Незнамов В.П., Сафронов И.И.** *Новый метод решения проблемы "Z >137" и определения уровней энергии водородоподобных атомов //* Успехи физических наук. 2014, Т. **184**, № 2, 200–205.
13. **Тамм И.Е.** *Теория ядерных сил и атомного ядра //* Собрание научных трудов, т.1, изд-во «Наука», М., 1975, с. 283–326.
14. **Hund F.** *Materieuntersehrhohen Drucken und Temperaturen//* Ergebn. Exakt. Naturwiss.**15**, (1936) 189.
15. **Мигдал А.Б.** *Теория конечных Ферми систем и свойства атомных ядер*, издание второе, переработанное и дополненное, М.: Наука, Главная редакция физико-математической литературы, 1983г., с.54.
16. **Шапиро Ф.Л.** *Нейтронные исследования //* Собрание трудов. Москва: Наука, 1976. Кн. 2: . - 1976. - 348 с.
17. **Игнатович В.К.** *Ультрахолодные нейтроны — открытие и исследование//* УФН, т. **166**, № 3, 1996, с. 303–324.
18. [Electronic resource]: *Ультрахолодные нейтроны//* http://femto.com.ua/articles/part_2/4211.html.
19. **Serebrov A.P., Boldarev S.T., Erykalov A.N. et al.** *Supersource of ultracold neutrons at WR-M reactor in PNPI and the research program on fundamental physics//* Physics Procedia, **17**, (2011) 251–258.
20. **Корнелл Э.А., Виман К.Э., Кеттерле В.** *"Нобелевские лекции по физике — 2001" // УФН* **173** 1319 http://ufn.ru/ru/articles/2003/12/c/.
21. **Рязанцев Г.Б., Лавренченко Г.К.** *Нейтронное вещество как «начало» и «конец» Периодической системы Д.И. Менделеева//* Технические газы. 2016, №4, С.41–49.
22. **Рязанцев Г.Б.** *Проблема "нулевых" в работах Менделеева //* Наука и жизнь, № 2, с. 76–80, 2014. http://www.nkj.ru/archive/articles/23734/.

23. **Ryazantsev G.B., Khaskov M.A., Beckman I.N.** *Chemical properties of the neutron matter and its place in the Periodic system of elements //* 24th International Seminar on Interaction of Neutrons with Nuclei: «Fundamental Interactions & Neutrons, Nuclear Structure, Ultracold Neutrons, Related Topics» Frank Laboratory of Neutron Physics, JINR, Dubna, Russia, Abstracts, 2016, E3-2016-32, p. 71.
24. **Ryazantsev G.B., Lavrenchenko G.K., Khaskov M.A., Beckman I.N.** *Chemical properties of the Neutron Matter and its place in the Periodic System of elements.//* 24th International Seminar on Interaction of Neutron with Nuclei. Dubna, JINR, Russia, E3-2017-8, 2017, P. 65–74.
25. **Ryazantsev G.B., Khaskov M.A., Beckman I.N., Lavrenchenko G.K.** *The Neutron Matter as "the Beginning" and "the End" of the D.I. Mendeleev Periodic System of Chemical Elements//* 25th International Seminar on Interaction of Neutron with Nuclei. Dubna, JINR, Russia, Abstracts, 2017, p.79.

Numerical Calculation of the Neutron Wave Packet Interaction with an Oscillating Potential Barrier

Maxim Zakharov[1, 2], *Alexander* Frank[1], *German* Kulin[1], and *Semyon* Goryunov[1]

[1]FLNP, JINR, Joliot-Curie 6, Dubna, Moscow region, Russian Federation, 141980
[2]MIPT, Institutskiy per. 9, Dolgoprudny, Moscow Region, Russian Federation, 141701

Abstract

It is assumed that in neutron optics the concept of an effective potential has a limited range of applicability at the accelerations of matter less than a certain critical value. The experiment intended to study the interaction of a neutron wave with matter moving with acceleration higher than the critical one was proposed. In this paper, in the framework of the proposed experiment, numerical calculations of the passage of a wave packet through the oscillating in space interference filter were carried out. The calculations were based on the assumption of the potential dispersion law validity.

1. Introduction

It is known that the theory of refractive index is valid for neutron waves, as well as for waves of a different nature. The physical nature of the refractive index is due to the interference of the incident wave and waves scattered by elementary scatterers in matter [1].

This interaction can be described by introducing an effective potential. The main contribution to neutron scattering in the medium is made by nuclei. The exact form of the strong interaction potential is unknown. However, since the wavelength of slow neutrons is much larger than the size of a nucleus, when calculating the scattering cross section, the radius of the nuclear interaction can be neglected and the potential describing the point interaction can be considered [2]. This is the so-called Fermi "pseudo-potential":

$$U(\vec{r}) = \frac{\hbar^2}{2\pi m} b\delta(\vec{r} - \vec{r}_0) \tag{1}$$

The quantity b is the coherent scattering length and is determined from the scattering cross section of slow neutrons $\sigma_{scat} = 4\pi b^2$.

For a slab with a nucleus density ρ, the averaging of the "pseudo-potential" with respect to the volume gives the following expression:

$$V = \rho \int U(\vec{r}) d^3r = \frac{\hbar^2}{2\pi m} \rho b. \tag{2}$$

The expression for the refractive index of a neutron wave in matter is written as follows [3]:

$$n^2 = 1 - \lambda^2 \frac{2m}{\hbar^2} V = 1 - \frac{4\pi\rho b}{k_0^2}. \tag{3}$$

Formulas (2) and (3) are equivalent to each other.

The legitimacy of using the concept of "effective potential" or an equivalent formula (3) for describing the optical properties of a uniformly moving medium is beyond argument due to the validity of the Galilean transformation for the wave function of a non-relativistic particle [4]. This motion affects only the value of the phase of the wave that has passed through the sample of matter. Neutron optics of moving media is described in [5-12].

The situation changes in case of accelerating motion of matter. It was found that in this case the frequency of the wave passing through the sample differs from the frequency of the incident wave [13, 14]. Based on the assumption of the validity of the potential dispersion law for accelerated motion of matter, it was shown that when the neutron escapes from the plate the neutron energy differs from the initial energy by an amount of

$$\Delta E \cong mwd\frac{1-n}{n}. \tag{4}$$

Here, m is the neutron mass, w is the plate acceleration directed along the neutron velocity, d is the plate thickness, and n is the refractive index of the plate material.

The first report on the experimental observation of the change in the ultracold neutron energy, when passing through the accelerating sample, appeared in 2006 [15], and the results of a more detailed study of the accelerating substance effect were published in [16]. The results of these experiments, in which the acceleration of the sample reached 75 m/s^2, were in good agreement with the theoretical predictions. It should be emphasized that the theory was based on an in non evident assumption of the validity of the potential dispersion law.

The question of the applicability of an "effective potential" for describing the optical properties of matter for all values of matter acceleration apparently remains open. The point is that in the theory of dispersion, which is, in fact, the theory of multiple scattering of waves, the assumption of the sphericity of the interfering scattered waves is rather significant. At the same time, in the non-inertial frame of reference associated with the accelerating substance, the idea of spherical waves is wrong and this can affect the condition of their interference.

This circumstance was pointed out in [16, 17], and a more detailed discussion of this problem was presented in [18]. Estimates of matter acceleration were made. At such estimates deviation from the potential dispersion law is possible by an amount of the same order as the phenomenon itself. For the case of ultracold neutrons (E = 100 neV), the value of the critical acceleration is $w_c = 8\cdot10^5\ m/s^2$. This acceleration is achievable in laboratory experiments.

Although the law of neutron wave dispersion in a substance moving with a very high acceleration is unknown, the information can be obtained from the experiment [19]. The experimental strategy of such investigation is as follows. It is planned to conduct two experiments to observe the interaction of neutrons with a potential oscillating in space. In one of them, the acceleration of the sample is less than the critical one, while in the other it exceeds the critical value. In both cases, the results are compared with a quantum calculation based on the assumption of the validity of the concept of effective potential. Obviously, to implement such a program, it is necessary to have software-mathematical tools for quantum calculations. In this paper, calculations of the wave packet passage through an oscillating interference filter were made.

2. Envisaged experimental implementation

Considering different possibilities of setting up the experiment, an experiment on the neutron wave passage through an oscillating interference filter was chosen. Such an experimental setting has the following advantage: the transmitted wave is time-modulated because of a periodic change in the neutron energy in the coordinate system of the moving

filter. This makes it possible to abandon a spectrometric experiment by starting to register the time oscillation of the stream that has passed through the sample. The disadvantage of this type of experiment is the limitation of the possible oscillation frequency, since the lifetime of the resonance state in the filter and, correspondingly, the tunneling time, are of the order of $10^{-7} sec$ [20, 21].

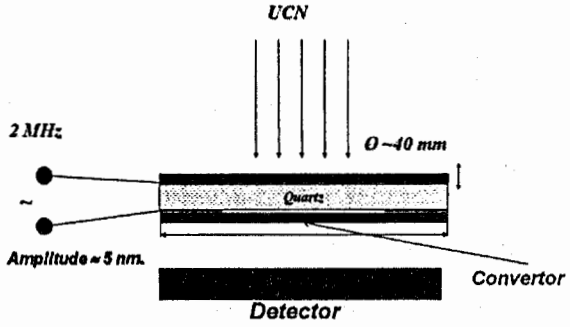

Fig.1. Scheme of the experiment on verification of the potential dispersion law for a substance in strongly non-inertial frames of reference.

A possible experimental realization of this study is illustrated in Fig.1. Three thin slabs forming a potential structure are applied to a quartz plate that acts as a resonant piezo driver [15]. On both surfaces of the plate, a thin aluminum foil serving as electrodes is preliminarily applied. Ultrasonic vibrations of the plate are excited when an alternating voltage is applied to the electrodes. The thickness of the plate should be equal to or multiples of half the length of the ultrasonic wave. For operation at a frequency of 2 *MHz*, it should be of the order of 0.3 *mm*. Such a quartz plate allows UCN to pass through sufficiently well. It is easy to estimate that the high-frequency oscillations of the flow that arise when the filter moves quickly disappear with distance because of the dispersion of the velocities. Therefore, the neutron detector should be as close as possible to the filter. It is assumed that this problem will be solved by applying to the exit surface of the plate a thin (0.2 μm) layer of the ^{10}B isotope converting a neutron flux into an α-particle flux as a result of the $^{10}B(n,\alpha)^{7}Li$ reaction. α-particles, which have a subluminal velocity, are detected by a semiconductor silicon detector located near the converter.

As a filter, it is planned to use neutron interference filters, which are quantum analogs of Fabry-Perot interferometers (Fig. 2). In the simplest case, the filter is three slabs of two kinds of matter deposited on a substrate transparent to neutrons. The materials of the layers are chosen in a way that the effective potential of the outer layers $V = \frac{\hbar^2}{2\pi m}\rho b$ considerably exceeds that for the inner slab and the substrate. Thus, the potential structure of the filter is two barriers with a well between them. With the parameters chosen in a certain way in the well region, a "quasibound" state can form, and the structure transmission function has a pronounced peak of resonant transmission at the energies corresponding to the position of the level of the "quasibound" state. The transmission function of such a structure can be found on the basis of the solution of the boundary-value problem, that is assuming the continuity of the wave functions and their derivatives at all interfaces.

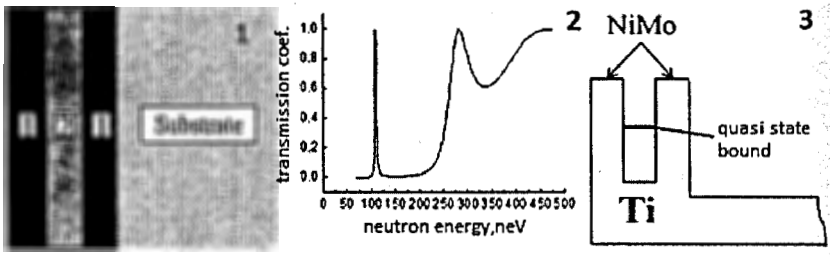

Fig. 2. Neutron interference filter. (1) is a schematic diagram of the simplest filter, (2) is the filter transmission function, (3) is the potential structure of the filter.

3. Interaction of neutrons with a potential barrier oscillating in space

The time evolution of a wave packet is described by a non-stationary Schrödinger equation:

$$i\hbar\frac{\partial}{\partial t}\Psi(x,t)=\hat{H}(t)\Psi(x,t). \tag{5}$$

The initial wave function was defined as follows:

$$\Psi_0(x,0)=\frac{\sqrt{\delta_p/\hbar}}{\sqrt[4]{\pi}}\exp(-ikx)\exp\left(-\frac{(x-x_0)^2}{2\delta_x^2}\right), \tag{6}$$

where δ_p is the width of the wave packet in the momentum space, δ_x is the width of the wave packet in the coordinate space, and k is the initial wave number of the neutron.
The potential $V(x, t)$ is bounded by a finite region, it is given by the expression:

$$V(x,t)=\bar{V}\left[x-A\cos(\omega t+\varphi)\right], \tag{7}$$

where $\bar{V}(x)$, in general, is any potential structure moving as a single whole:

$$\bar{V}(x)=\begin{cases}V_0(\xi), & 0\le x\le L\\ 0, & \textit{For other space}\end{cases}. \tag{8}$$

Here $V_0(\xi)$ determines the internal structure of the potential.

There are many methods for numerical solution of the non-stationary Schrödinger equation. To solve this problem, the splitting method of the evolution operator was used [22].

Numerical calculation was performed for a three-layer filter consisting of layers of *NiMo*, *TiZr*, *NiMo*, being 29.5, 23, 29.5 nm thick. The values of the effective potentials for these two materials are 226 and 0.26 neV. For simplicity, the substrate potential was assumed to be zero. In the numerical solution, the width of the wave packet was δE = 1 neV, the time step dt = 1 nsec, the discretization step of space dx = 4 nm.

This solution is compared with the classical solution based on the continuity equations, obtained as follows. For a plane wave, the recurrent method of Parrath [23] allowed calculating the transmission of a three-layer structure as a function of the plane wave energy, and its convolution was found with a spectrum corresponding to the parameters of the

wave packet used by our program. A comparison of the results obtained by the two methods is illustrated in Fig. 3.

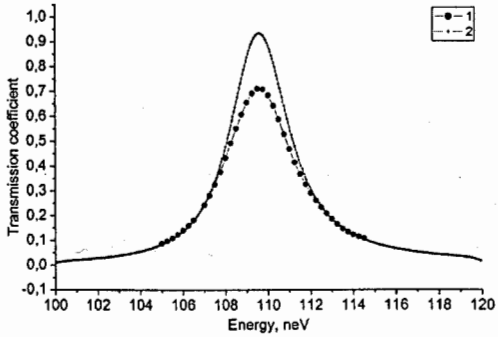

Fig.3. Interference filter transmission function obtained by two methods 1) Step-by-step numerical solution based on the splitting method of the evolution operator, 2) Solution of the boundary value problem.

The difference between the results can be explained by the presence of discretization in the coordinate and time, leading to some uncertainty in the position of the boundaries of the filter layers. It is known that the position of the resonance is very sensitive to the width of the well formed by two barriers. Fluctuations in the position of the barriers lead to line blurring, degrading the transmission characteristics.

The width of the wave packet was chosen in such a way that the transit time of the packet through the filter was much greater than the period of the oscillations. The restriction on the width of the wave packet is also imposed by the fact that the narrower the wave packet in the impulse representation is, the more space it occupies and the more time it takes to calculate. In the calculation, the width was assumed to be $\delta E = 1$ *neV*. A numerical calculation was made for the oscillation regime with a frequency of 2 *MHz* and amplitude of 5 *nm*.
The results of numerical calculations of the wave packet shape in the coordinate representation due to the intensity oscillation, as well as the spectra of the transmitted and reflected states, are given below. The wave packet evolution over time is shown in Figure 6.

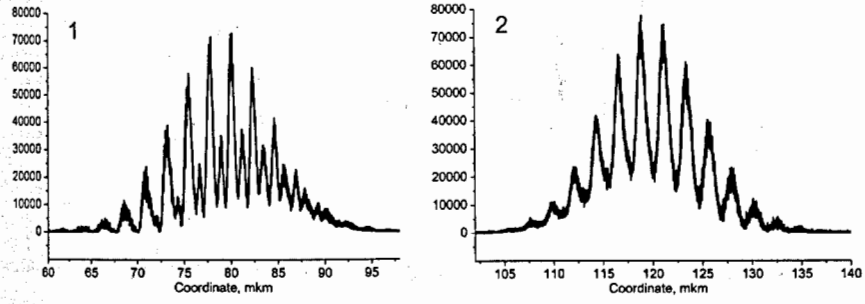

Fig. 4. Wave packets that were reflected (1) and that penetrated through (2).

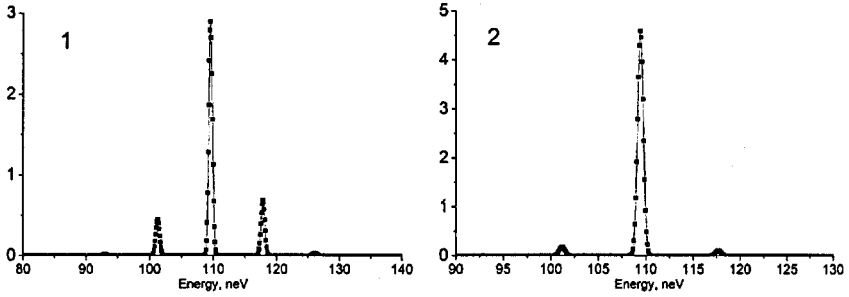

Fig. 5. Energy spectrum of the reflected (1) and transmitted (2) states of the wave function.

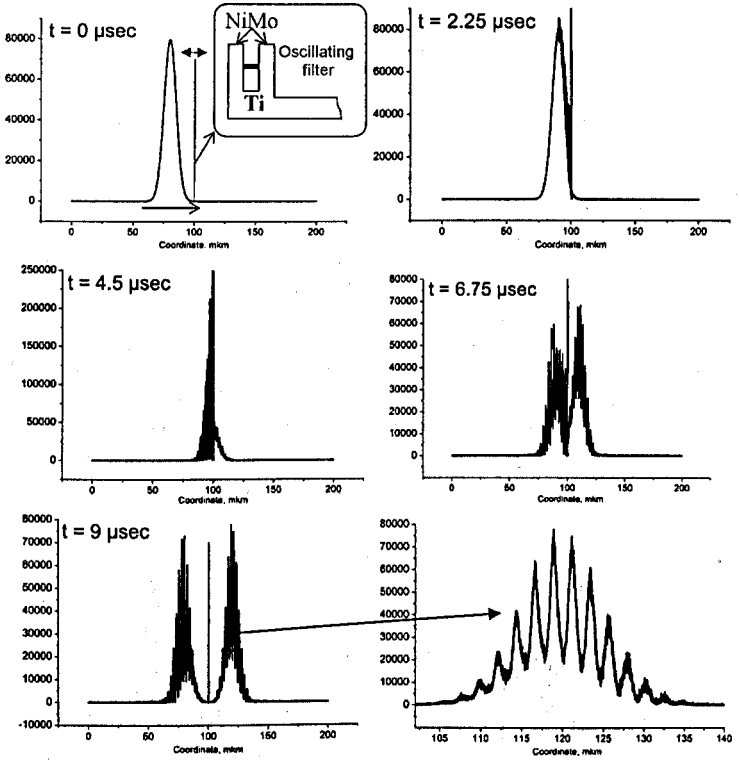

Fig. 6. Wave packet evolution in time when being reflected and passing through an oscillating interference filter.

4. Conclusion

The above-given result requires reflection and analysis. The fact is that, from general considerations, one should expect that the oscillation frequency of the stream should be twice as large as the spatial oscillation frequency of the filter, since the maximum transmission corresponds to the stopping times, that is, twice per period. However, the results of the calculation suggest that the frequencies of oscillations of the flow and the intensity are equal. This may be explained by a certain violation of the resonance conditions, when the scanning by the transmission line along the original spectrum occurs on the slope of the resulting function and does not capture the maximum. This may be due to a relatively large step in the coordinate $dx = 3$ *nm*, which is eroding the boundaries of the filter layers in the calculation. If this assumption is correct, the obvious solution to this problem is to decrease the step both in the coordinate dx and in the time dt. However, this will require the use of other hardware and other software. This task is a subject of future work.

References

1. I.I. Gurevich, V.P. Protasov. *Neutron physics.* (In Russian) M.: Energoatomizdat, 1997.
2. V.F. Turchin. *Slow neutrons.* (In Russian). Gosatomizdat, 1963
3. V.F. Sears. *Neutron Optics.* Oxford University Press, 1989.
4. L.D. Landau, E.M. Lifshitz. *Quantum mechanics.* (In Russian), M. Nauka, 1989.
5. M.A. Horn and A. Zeilinger. *Neutron Interferometry.*Eds. U. Bonse and H.Rauch, Clarendon Press, Oxford,1979, p. 350.
6. A. G. Klein, G.I. Opat, A. Cimmino et al. *Neutron propagation in moving matter: The Fizeau experiment with massive particles.* Phys. Rev.Lett. **46**, 1551 (1981).
7. M. Arif, H. Kaiser, S.A. Werner et al. *Observation of a motion-induced phase shift of neutron de Broglie waves passing through matter near a nuclear resonance.* Phys. Rev. A **31**, 1203 (1985).
8. U. Bonse and A. Rump. *Interferometric measurement of neutron Fizeau effect.* Phys. Rev. Lett. **56**, 2411 (1986).
9. M. Arif, H. Kaiser, R. Clothier et al. *Observation of a motion-induced phase shift of neutron de Broglie waves passing through matter near a nuclear resonance.* Phys. Rev. A **39**, 931 (1989).
10. M.A. Home, A. Zeilinger, A. G. Klein, and G.I. Opat. *Neutron phase shift in moving matter.* Phys. Rev. A **28**, 1 (1983).
11. V.F. Sears. *Fizeau effect for neutrons.* Phys. Rev. A **32**, 2524 (1985).
12. U. Bonse and A. Rump. *Thermal-neutron propagation in moving media.* Phys. Rev. A **37**, 1059 (1988).
13. F.V. Kowalski. *Interaction of neutrons with accelerating matter: test of the equivalence principle.* Phys. Lett. A **182**, 335 (1993).
14. V.G. Nosov и A.I. Frank. *Interaction of slow neutrons with a moving matter.* (In Russian). NuclPhys **61**, 686 (1998).
15. A.I. Frank et al. *The effect of an accelerating medium in neutron optics.* (In Russian). // JETF Letters. 2006. T.**84**. C. 485-489.

16. A.I. Frank, P. Geltenbort, M. Gentshel, D.V. Kustov, G.V. Kulin, V.G. Nosov, A.N. Strepetov. *Effect of accelerated matter in neutron optics.* NucleiExperiment. **71**, 1686 (2008).
17. A.I. Frank, P. Geltenbort, M. Gentshel, D.V. Kustov, G.V. Kulin, A.N. Strepetov. *A new experiment to observe the effect of an accelerating substance in neutron optics.* (In Russian). JETP Letters **93**, 403 (2011).
18. A.I. Frank. *On the law of dispersion in accelerating substances.* (In Russian). JETP Letters, **100**, 696 (2014)
19. A. I. Frank, D.V., Kustov , G.V. Kulin , S.V. Goryunov, D.V. Roshchupkin , D.V. Irzhak. *Experiment proposed for the observation of UCN interaction with matter moving with giant acceleration.* Journal of Physics:Conference Series 746 (2016) 012054.
20. A.I. Frank, I.V. Bondarenko, V.V.Vasilyev, I. Anderson, G. Eler, P. Hoghoy. *Measurement of the neutron interaction time with quantum objects.* (In Russian). JETP Letters, **75,** 2002, 729-733
21. A.I. Frank, V.A. Bushuev. *Bom-Wigner group time and neutron optics. (In Russian). Proceedings of the XXI International Symposium* «Nanophysics and Nanoelectronics», T. 1, 438-441.
22. Chin S A and Chen C R 2002 J. Chem. Phys. 117 1409.
23. L.G. Parratt. *Surface studies of solids by total reflection of x-rays.* Phys. Rev. **95**, 59 (1954).

Fast Neutron Induced Reactions

SILICON TWO-DIMENSIONAL POSITION-SENSITIVE FAST NEUTRON DETECTOR FOR BEAM PROFILE MEASUREMENT

F.A. Aliyev[1,2*], N.I. Zamyatin[1], V.M. Bystritsky[1], N.A. Fedorov[1,4], D.N. Grozdanov[1,3], C. Hramco[1,5], Yu.N. Kopatch[1], I.N. Ruskov[1,3], V.R. Skoy[1], V.M. Slepnev[1], D.I. Yurkov[6], Yu.N. Barmakov[6] and TANGRA collaboration

[1]*Joint Institute for Nuclear Research, Joliot Currie 6, 141980 Dubna, Moscow region, Russia*
[2]*Institute of Geology and Geophysics, Azerbaijan National Academy of Sciences, H. Javid av., 119 Baku, AZ1143 Azerbaijan*
[3]*Institute for Nuclear Research and Nuclear Energy of Bulgarian Academy of Sciences, Tsarigradsko chaussee 72, blvd., 1784 Sofia, Bulgaria*
[4]*Lomonosov Moscow State University, Leninskie Gory, 119991 Moscow, Russia*
[5]*Institute of Chemistry of the Academy of Sciences of Moldova Academiei str., 3; MD-2028 Chisinau, Republic of Moldova*
[6]*All-Russia Research Institute of Automatics (VNIIA), Sushchevskaya 22, 127055 Moscow, Russia*

Abstract

Recently, a new experimental setup named TANGRA (TAgged Neutrons and Gamma RAys), for studying the neutron-induced nuclear reactions, has been created and successfully tested in the Joint Institute for Nuclear Research (JINR) in Dubna, Russia.

In the present geometry TANGRA setup is used to investigate the angular and energy distributions of gamma rays from nuclear reactions induced by 14 MeV neutrons.

It consists of: a portable 14 MeV neutron generator ING-27 with a built-in 64-pixel position sensitive α-particle detector, an array of 22 Amcrys© NaI(Tl) gamma-ray detectors and a computerized 14bit, 100MHz, 32 channel JINR-AFI electronics data acquisition system.

Silicon (Si) two-dimensional position-sensitive fast neutron detector was constructed and used for adjusting the neutron beam and measuring its profile.

In the present article we briefly describe the neutron profile meter and report some results from the characterization of the ING-27 "tagged" neutron beams.

Keywords: Silicon strip detectors; Fast neutrons; Tagged neutrons and gamma rays; TANGRA.

* Corresponding author Tel.: + 7-496-216-2131; fax: +7-496-216-5085.
email: fuad.aliyev107@gmail.com.

1. Introduction

For detailed study of the inelastic scattering of neutrons with energy of 14.1 MeV on complex nuclei, within TANGRA project (TAgged Neutron and Gamma RAys), in 2014 an installation «TANGRA» was designed and created at the Joint Institute for Nuclear Research (Dubna, Russia) [1, 2].

The operation of the TANGRA facility is based on the use of the tagged neutron method (TNM), the essence of which consists in recording the characteristic radiation (gamma-quanta, neutrons) from the inelastic scattering reactions of 14.1 MeV fast neutrons on the nuclei A of the substance, A(n, n'γ)A, in coincidence with the α particle, formed in the following neutron producing reaction:

$$d + {}^3H \rightarrow {}^4He\ (3.5\ MeV) + n\ (14.1\ MeV). \quad (1)$$

Here, the kinetic energy of the incident deuteron beam on the tritium target is ~ 80–100 keV. The α-particle and neutron are emitted nearly in opposite directions and therefore, by recording the direction of the α-particle, using a multi-pixel alpha detector mounted inside the neutron generator, it is possible to determine with good accuracy the direction of the neutron.

For precise measurement of the angular distribution of the characteristic gamma radiation produced as a result of the inelastic scattering of fast neutrons on complex nuclei, one must have an unambiguous information about the spatial distribution of the tagged neutron beams incident on the investigated material.

Currently, there is a known method for obtaining information about the distribution of the tagged neutron beams in detector's XY plane, perpendicular to the direction of their propagation, consisting of a number of mutually parallel light-protected scintillation strips [3].

Using the coincidence of signals from one of the alpha-detector pixels inside the neutron generator with one of the profilometer scintillation strips, it is possible to obtain information about the profile of each of the tagged neutron beams along the X and Y axes.

In this case, it is necessary to make measurement with two mutually perpendicular positions of the profilometer (strips horizontally and vertically orientated), relative to the direction of tagged neutron beam.

2. Experimental Setup

The setup used for determination of the beam profile of fast neutrons is shown in Fig. 1. It includes: portable neutron generator with an energy of 14.1 MeV, a collimator made of iron for the protection of gamma detectors from the direct hit in them of the neutron radiation generated by ING-27 [4], spectrometric system for recording gamma radiation based on NaI(Tl) and double-sided silicon strip detectors.

As a source of tagged neutrons was used a portable neutron generator (NG), which was developed at All-Russia Research Institute of Automatics in Moscow (VNIIA) (Fig. 2). The maximum intensity of the neutrons flux created by NG in the solid angle 4π is 5×10^7 n/s.

The profilometer is a double-sided silicon strip neutron detector, in which the registration of fast 14.1 MeV tagged neutrons is done by detecting the charged products resulting from the neutron interaction with silicon nuclei: $^{28}Si(n,n')^{28}Si$; $^{28}Si(n,\alpha)^{25}Mg$; $^{28}Si(n,p)^{28}Al$; $^{28}Si(n,np)^{27}Al$; $^{28}Si(n,n\alpha)^{24}Mg$; $^{28}Si(n,d)^{27}Al$. The design of the profilometer is shown in Fig. 3.

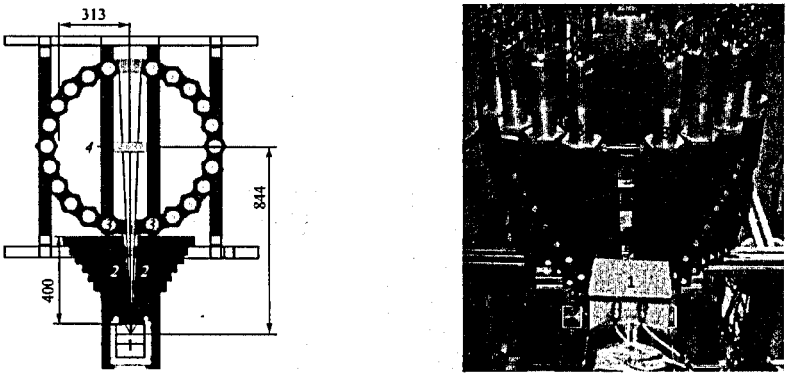

Fig. 1. Experimental setup: 1- the ING 27 neutron generator; 2 - the filter (passive shielding); 3 - the scintillation detector based on a NaI(Tl) crystal; 4 – the silicon two-dimensional position-sensitive fast neutron detector.

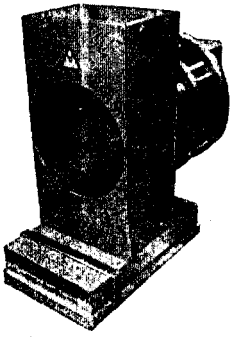

Fig. 2. The neutron generator ING 27.

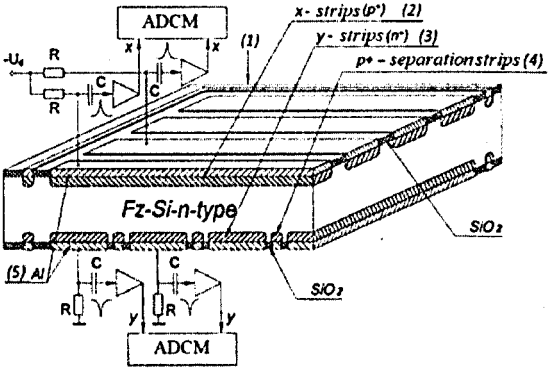

Fig. 3. The design of the integral double-sided silicon strip detector (DS-strip) and detector switching-on circuit with reading electronics.

Fig. 4 shows the mechanical design of the profilometer and its main elements. The specification of the two-coordinate plane with (64×64)-strips, consisting of 4 DS-strip/(32×32) detectors with strip's pitch of 1810 μm (1.81mm) and dimensions of each detector (60×60) mm^2, is given below:

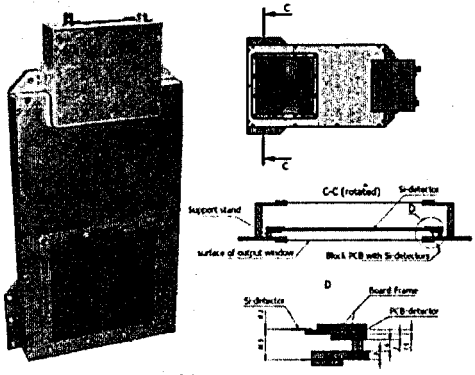

Fig. 4. Profilometer construction.

- Application – measurement of profiles and spatial distributions of neutron beams produced by fast neutron sources and dt-fusion generators (14.1 MeV);
- Detecting plane – 4 double-sided silicon strip detectors (DS-strip);
- Number of strips on the detecting plane: 64-X and 64-Y strips;
- Dimensions of each of the 4 detectors: (60×60) mm^2;
- Sensitive area: (58×58) mm^2;
- Number of strips in each detector: 32X+32Y;
- Strip pitch: 1810 μm;
- The thickness of the detector entrance window "dead" layer:
  -Al – 1.0 μm
  -(p+) – 0.3 μm (implanted layer of boron);
- Angle between the strips on the opposite sides of the detector: 90°;
- Thickness of the silicon detector: 300 +/- 15 μm;
- Dimensions of the profilometer detecting plane: (120×120) mm^2;
- The similar strips in all 4 detectors are combined in pairs on each side of the detector by ultrasonic welding (USW), forming a grid of (64×64) strips with a length of 120 mm;
- All 4 detectors are assembled on a printed circuit board (PCB), having contact pads for USW with the detector strips;
- 64 lines, on each side of the board, come out on two connectors, to which is connected the detector electronics (PA + PMT).

3. Energy calibration of the profilometer

For energy calibration of the silicon two-coordinate neutron beam profilometer, we used standard alpha sources of known activity and energy of alpha-particles (Table 1).

As an example, in Fig. 5 a) and b), are shows the calibration curves "amplitude-to-energy" of profilometer X and Y strips, correspondingly.

Using the calibration curves (Fig. 5), we calculate the energy spectra of the charged products (recoil silicon nuclei, protons, deuterons and alpha particles), produced in the reactions $^{28}Si(n, n')^{28}Si$, $^{28}Si(n, \alpha)^{25}Mg$, ($E_\alpha$=2.654 MeV), $^{28}Si(n, p)^{28}Al$ (E_p=3.860 MeV) and $^{28}Si(n, d)^{27}Al$ (E_d = 9.840 MeV), as a result of the interaction of ING-27 14.1MeV neutrons with the profilometer X and Y strips (Fig. 6).

Table 1.

Source	Activity (kBq)	Energy (MeV)
^{226}Ra	39.6	7.68
^{238}Pu	30	5.49
^{239}Pu	5	5.15

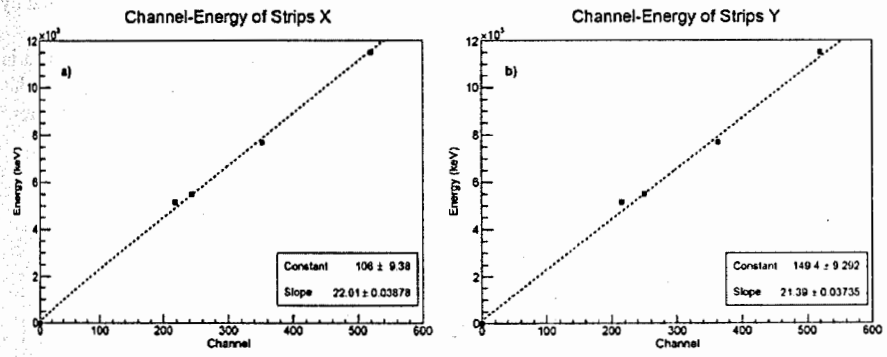

Fig. 5. Energy calibration of the profilometer X and Y strips, obtained with the following sources of alpha particles: ^{239}Pu (E_α = 5.2 MeV), ^{238}Pu (E_α = 5.5 MeV), ^{226}Ra (E_α = 7.8 MeV) and ^{28}Si (n, α) ^{25}Mg (E_α = 11.5 MeV).

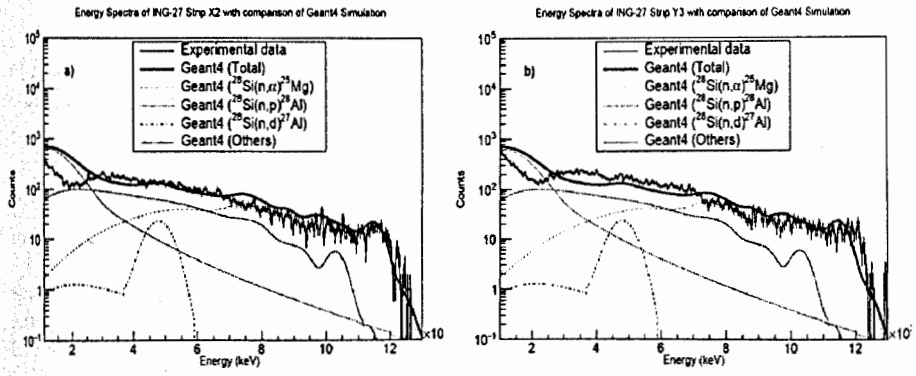

Fig. 6. Experimental and calculated energy spectra of the charged components obtained by irradiating X and Y strips with ING-27 tagged neutron flux. The calculated spectra are the result of simulation using Geant4 software.

At the Fig. 6 a) and b) show the calculated energy spectra obtained by Geant4 software [5] used for simulating the interaction of 14.1 MeV neutrons with silicon, as well as there is a fairly good agreement between our experiment data and the calculations. The registration energy threshold of the charged components is ~ 1 MeV.

4. Determination of tagged neutron beam profiles

As an example of the profilometer applications, its use to determine the profiles of 64 tagged neutron beam neutrons created by an ING-27 device is considered.

Fig. 7 shows the arrangement of the ING-27 neutron source and the profilometer, when measuring the space profiles of tagged neutron beams.

For clarity, in Fig. 7 is shown also a simplified scheme of the processes occurring during the measurement of the tagged beam profiles.

As a result of fusion reaction of a deuteron with a triton, an alpha particle and a neutron are formed, which fly apart in opposite directions. The alpha particle is detected by the ING-27 alpha detector and the neutron by the profilometer.

The intersection of strips perpendicular each other, both in the alpha detector and in the profilometer, forms the triggered pixels, which in Fig. 7 are highlighted in red. For this reason in the following text the term "pixels" is used when speaking about the alpha detector.

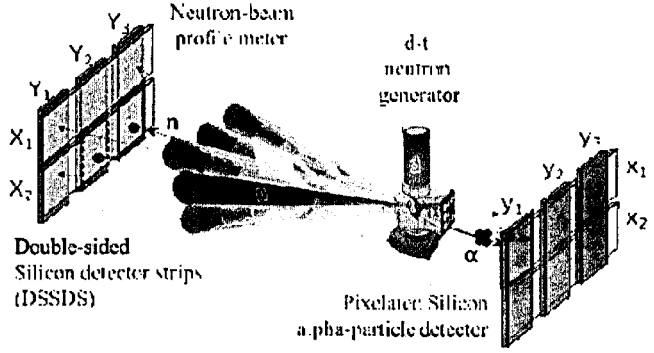

Fig. 7. The scheme of setup for measuring tagged neutron beam profiles.

In order to determine the profiles of neutron beams, the profilometer was installed in two different positions: directly at the exit window of the neutron generator ING-27 and at a distance of 40 cm from it.

Measurements of the beam profiles in two different positions make it possible to obtain correct information about all 64 tagged neutron beams.

The signals from the alpha detector in the neutron generator and from the profilometer were included in a scheme of 4-fold coincidence between the signals from x and y strips of the neutron generator α-detector and X and Y strips of the profilometer [6].

In this case, the selection of the recorded events was made only if all four of the above strips were triggered within 10 ns time interval. It corresponded to the full width of the measured distribution of the time intervals between the signals from the alpha detector and the profilometer (see Fig. 8).

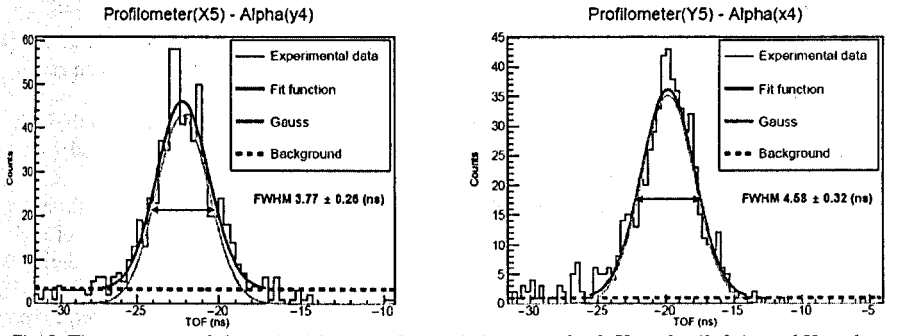

Fig. 8. Time spectra of the coincidences of signals between both X and y (left), and Y and x (right) strips of the neutron profile meter and alpha detector.

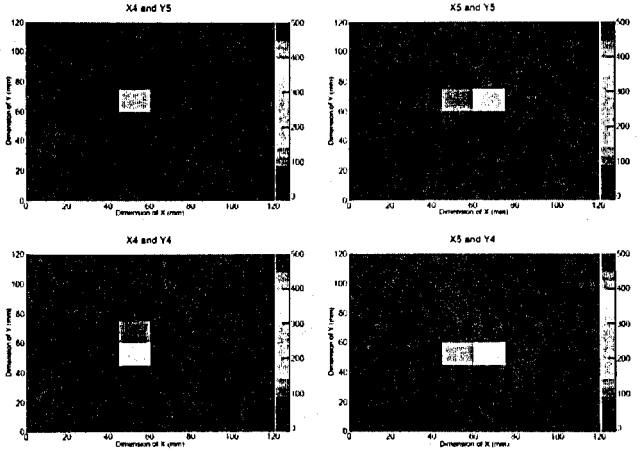

Fig. 9. Profile of the tagged neutron beam obtained at a distance of ~10 cm from ING-27 neutron producing target.

From the analysis of the results, it follows that the measured time resolution $(FWHM)_t$, averaged over all possible combinations of signals from strips of the alpha-detector and profilometer, is 5 ns.

A graphical representation of the statistics from the 4-fold coincidence of the signals, which reflects the profiles of the tagged beams corresponding to each pixel of the profilometer, is shown in Fig. 9.

Each two-dimensional histogram in Fig. 9 corresponds to a certain pixel of the alpha detector of the neutron generator; it shows the number of coincidences of signals from a given pixel of the alpha detector with each of the pixels of the profilometer. The colors of the points on the histograms reflect the number of such coincidences.

5. Conclusion

For measuring the profiles of tagged neutron beams produced by ING-27 neutron generator, we designed and created a two-coordinate detector of neutrons with an energy of 14.1 MeV.

The profilometer is a two-coordinate plane (64X×64Y), which is built on the basis of double-sided silicon strip detectors (DSSSD). The measurements were made with a configuration of the detector plane (8X×8Y).

The neutron registration is performed by detecting charged particles (silicon recoil nuclei, protons, deuterons and alpha particles) formed as a result of a number of nuclear reactions: $^{28}Si(n, n')^{28}Si$, $^{28}Si(n, \alpha)^{25}Mg$, $^{28}Si\ (n, p)^{28}Al$ and $^{28}Si(n, d)^{27}Al$, during the interaction of fast neutrons with the substance of the profilometer (silicon).

The measurement of the neutron beam profiles is carried out in a plane perpendicular to the direction of their propagation. The detecting plane consists of 4 double-sided silicon strip detectors.

The difference between the neutron profilometer based on silicon strip detectors and the scintillation profilometers is that the two coordinates (X and Y) of the interaction point of the neutron with silicon are measured simultaneously.

The design of the created profilometer allows its aperture to be increased by adding to it additional double-sided silicon strip detectors.

6. Acknowledgment

This work was partially supported by the RFBR grant N 16-52-45056.

References

[1] I. Ruskov et al., TANGRA – an experimental setup for basic and applied nuclear research by means of 14.1 MeV neutrons, European Physics Journal Web of Conferences, eISSN:2100-014X, https://www.epj-conferences.org/articles/epjconf/abs/2017/15/epjconf-nd2016_03024/epjconf-nd2016_03024.html

[2] V.M. Bystritsky, D.N. Grozdanov, A.O. Zontikov et al., Angular distribution of 4.43 - MeV γ-rays produced in inelastic scattering of 14.1 - MeV neutrons by ^{12}C nuclei, Physics of Particles and Nuclei Letters, 13 (2016) 504.

[3] V.M. Bystritsky et al., Proceedings of the international scientific and technical conference, The portable neutron generators and technologies of their basis, Moscow, Russia, 2013, p. 505, available at http://neutrontech.ru/img/papers/jinr4.pdf

[4] Neutron generator gas-filled neutron tube ING-27, available at http://vniia.ru/eng/production/incl/prospekt_element_eng.pdf

[5] Allison J., Amako K., Apostolakis J., et al. Geant4 developments and applications [J], IEEE Transactions on Nuclear Science, 53 (2006) 270-278.

[6] ADCM16 - A 16-channel, 14-bit, 100MHz, ADC board with signal processing core, available at http://afi.jinr.ru/ADCM16-LTC.

Angular Distribution of Gamma Rays from the Inelastic Scattering of 14 MeV Neutrons on Light Nuclei

N.A. Fedorov[1,2], T.Yu. Tretyakova[1,3], Yu.N. Kopatch[1], V.M. Bystritsky[1], D.N. Grozdanov[1,4], F.A. Aliyev[1,5], I.N. Ruskov[1,4], V.R. Skoy[1], C. Hramco[1,6] and TANGRA collaboration

[1]*Joint Institute for Nuclear Research (JINR), Dubna, Russia*
[2]*Faculty of Physics, Lomonosov Moscow State University (MSU), Moscow, Russia*
[3]*Skobeltsyn Institute of Nuclear Physics (SINP MSU), Moscow, Russia*
[4]*Institute for Nuclear Research and Nuclear Energy (INRNE) of Bulgarian Academy of Sciences (BAS), Sofia, Bulgaria*
[5]*Institute of Geology and Geophysics, Baku, Azerbaijan*
[6]*Institute of Chemistry, Academy of Science of Moldova, Chisinau, Republic of Moldova*

Abstract

An investigation of the angular and energy distributions of γ-rays from the inelastic scattering of ~14 MeV neutrons on a number of light nuclei was performed in the frame of the project TANGRA (TAgged Neutron & Gamma RAys). Using an experimental setup, which consists of an ING-27 portable generator producing ~14 MeV "tagged" neutrons and a Fe-shielded ring of 22 NaI(Tl) gamma-ray detectors, we have accomplished the measurements with C, O, Si and Al samples.

1. Introduction

The main purpose of the TANGRA project (TAgged Neutron & Gamma RAys) in JINR [1, 2] is the detailed studying the ~14 MeV neutron inelastic scattering on atomic nuclei using the tagged neutron method (TNM). The measurement of n-γ angular correlations in the 14.1 MeV neutron inelastic scattering is important from the point of view of understanding the mechanisms of interaction of the nucleus with the incident nucleon. In the literature, information on processes of this type involving neutrons is presented substantially less, compared to the results of experiments on inelastic scattering of charged particles by atomic nuclei. A comparison between the neutron and proton inelastic scattering is very important for theoretical nuclear physics and nuclear astrophysics, because it provides a possibility to investigate the isospin symmetry of the nucleon-nucleon interactions. Interest in the reactions (n, $n'\gamma$) on light and medium-weight elements is also dictated by the need to refine the previously obtained experimental data, since such reactions have wide practical applications in geology, in nuclear power engineering, in the detection of hidden dangerous substances [3].

The tagged neutron method is based on the registration of the α-particle with energy of 3.5 MeV from the reaction:

$$d + t \rightarrow n + \alpha \qquad (1)$$

The α-particle has practically the opposite direction of flight with respect to the direction of neutron emission. The energy of the neutron is 14.1 MeV. The α-particles are registered in

coincidence with the pulses from the characteristic nuclear γ-radiation, emitted during the neutron inelastic scattering reaction on the nuclei A in the sample.

$$A(n,n')A^* \xrightarrow{\gamma} A. \qquad (2)$$

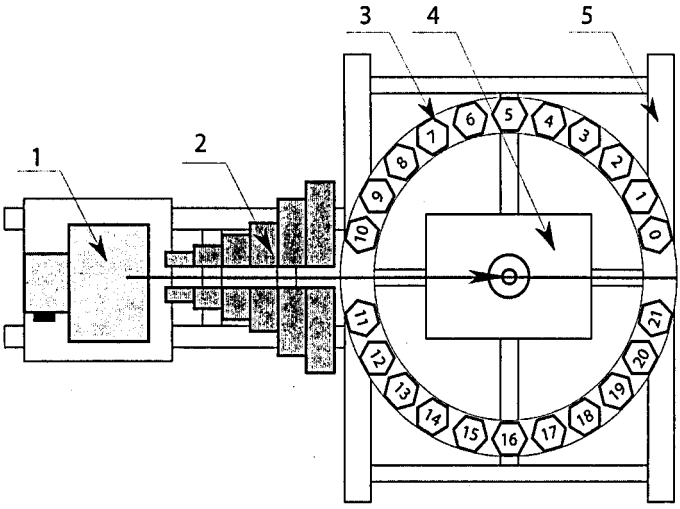

Fig. 1. Scheme of the TANGRA setup in the reaction plane: 1 – portable neutron generator ING-27, 2 – iron shielding, 3 – "Romashka" γ-ray registration system, 4 – sample holder, 5 – setup frame. Arrow of the longitudinal line shows the neutron beam direction.

So, it is possible to reconstruct the neutron flight direction by fixation of the alpha-particle emission angle, i.e. to "tag" each emitted neutron. Practically using a position-sensitive α-detector, embedded in the neutron generator, the "tagging" of the neutrons is achieved.

The information about the number of the emitted neutrons, the number of the n-γ coincidences and the efficiency of the γ-quanta registration, allows one to determine correctly the differential cross sections of inelastic scattering of neutrons by the nuclei of the investigated isotopes with the selected excitation states.

In our previous article [4] the γ-quanta angular distribution measurements of the 14.1 MeV neutron inelastic scattering on ^{12}C was considered. The use of tagged neutron method has made it possible to improve the accuracy of measurements, which is of fundamental importance, since the data available in the literature vary considerably. The chosen geometry of the experiment made it possible to carry out measurements with the emission of γ quanta at angles less than 10 ° for the first time. In this paper the results of γ-quanta angular distribution in reaction (n, $n'\gamma$) on ^{16}O, ^{27}Al и ^{28}Si are presented.

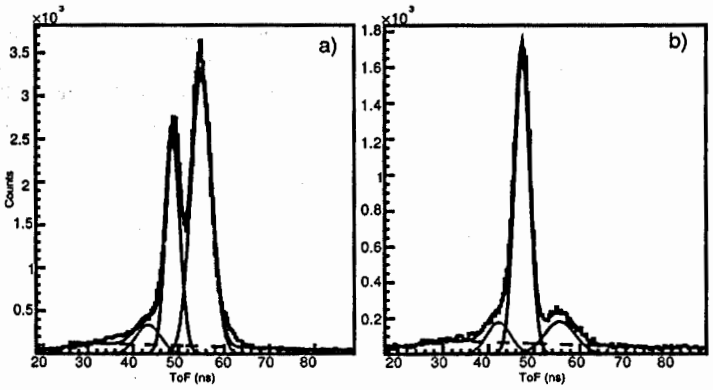

Fig. 2. Time-of-flight spectra and their approximations for γ-detectors placed at ~15° (a) and ~90° (b). The left peak corresponds to γ-quanta emitted from the neutron inelastic scattering in shielding, the central peak corresponds to the γ-quanta emitted from sample and the right peak is from the neutrons, which are elastically or inelastically scattered by the target.

2. Experimental setup

The detailed scheme of TANGRA-setup for studying the fast neutron scattering reactions is presented in [5] (Fig. 1). The neutron generator ING-27 is used as a neutron source. The neutrons are produced in the reaction (1), induced by the continuous deuteron beam with kinetic energy of 80–100 keV focusing on a tritium target. The products of this reaction are 14.1 MeV neutrons and 3.5 MeV α-particles. The maximal intensity of the "tagged" neutron flux in 4π–geometry is 5×10^7 c^{-1}. The α-particles are registered by a 64-pixel α-detector with a pixel dimensions or 6×6 mm^2. The detector is located at a distance of 100 mm from the tritium-enriched target.

The γ-quanta emitted after the neutron inelastic scattering by a target are registered by a system of 22 NaI(Tl) scintillator γ-detectors placed around the sample with ~15° step. To protect the detectors nearest to the generator from direct neutrons a compact steel collimator is used. The background events are separated using the Time-of-Flight (ToF) method. The "start" of the measurement time interval is given by the signal from the alpha-detector and the "stop" – by the signal from the γ-detector. The difference in speed between the neutron and the photon provides the possibility to separate the γ-rays from the neutrons. For data acquisition a personal computer with two ADCM-16 boards is used [6].

As targets in experiments on inelastic scattering of fast neutrons by oxygen and silicon, plastic containers filled with the test substances (water and chemically pure SiO_2 dust) with dimensions $10\times10\times10$ cm^3 were used. For experiment with aluminum a block with dimensions $10\times10\times5$ cm^3 was used. The optimal dimensions of the samples were determined by model simulations [4].

3. Experimental data analysis

The signals from the α- and γ-detectors, digitized by the ADCM, are written on the computer hard disk for creating the time and amplitude TOF neutron-gamma separated

spectra. The examples of time-spectra from the detectors at angles ~15° and ~90° relative to the neutron beam are presented in Fig. 2. There are three peaks visualized in each spectrum. The left peak corresponds to the γ-quanta emitted from neutron inelastic scattering in the shielding-collimator, the central peak corresponds to the γ-quanta emitted from the sample

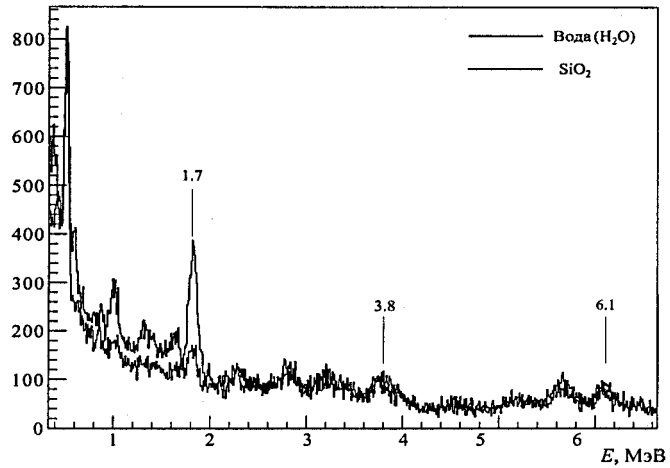

Fig. 3. Gamma-ray energy spectra emitted by SiO_2 and water from the 14.1 MeV neutron irradiation.

and the right peak is formed by neutrons that hit the γ-detector. Further, using the energy calibration of γ detectors, the energy spectra of the events occurring in a time window corresponding to γ-quanta are constructed.

The data from only one central pixel of the α-detector were taken into account in this experimental setup, which made it possible to substantially reduce the number of background events and simplify the algorithms for processing the experimental data. However, this technique leads to a reduction in the collected statistics and significantly increases the irradiation time.

The information on the number of events corresponding to the emission of the γ-quanta from the nucleus transition from a definite excited state to a lower state is extracted from the energy γ-spectra by evaluating the corresponding gamma-peak. This information is obtained from the events in the full energy absorption peak and/or single escape peak. The final angular distribution is normalized and fitted by a Legendre polynomial expansion. For quantitative description of γ-quanta emission angular distribution, an anisotropy parameter $W(\theta)$ is introduced:

$$\frac{d\sigma_j}{d\Omega} = AW(\theta) \tag{3}$$

$$W(\theta) = 1 + \sum_{i=2}^{2J} a_i P_i(\cos\theta), \tag{4}$$

where a_i are decomposition coefficients, J is the γ-transition multipolarity, the summation index i has only even values.

4. Results

In the inelastic scattering of 14 MeV neutrons by ^{12}C, the excitation of only one state that decays with the emission of a γ-ray with the energy of 4.43 MeV and the multipolarity of

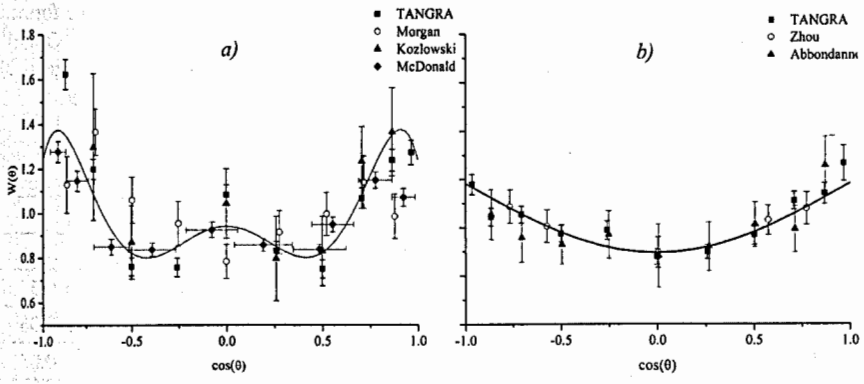

Fig. 4. The experimental angular distribution of γ-quanta with energy E_γ= 6.13 MeV, emitted during the neutron inelastic scattering on ^{16}O (a), and γ-quanta with energy E_γ= 1.78 МэВ, emitted by ^{28}Si (b). Solid lines are approximations by Legendre polynomials.

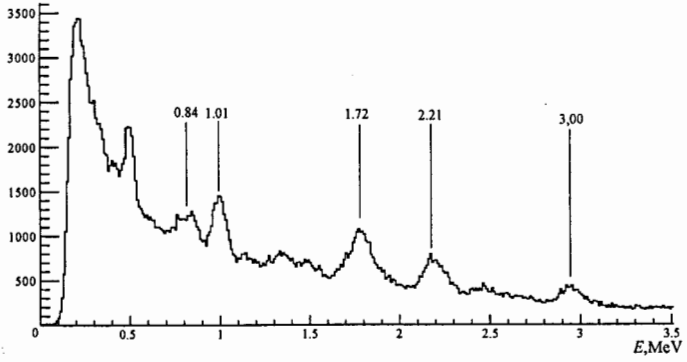

Fig.5. Gamma-ray energy spectrum emitted by ^{27}Al during 14.1 MeV neutron irradiation.

E2 is most pronounced. Many papers have been devoted to the study of this reaction and the angular distribution data are known with good accuracy [4]. With an increase in the number of nucleons, the spectra of the excited states of the nuclei become more complicated, which is reflected in the experimental data. In Fig. 3 the energy spectra from $(n, n'\gamma)$ reaction on water and SiO_2 are presented. In both spectra, the peak is most clearly distinguished at 6.1 MeV, corresponding to $E3$ transition from the state with spin and parity $J^\pi = 3^-$ to the ground state 0^+ ($3^- \rightarrow 0^+$) in ^{16}O. The structure of the energy spectra with E^* below ~ 6 MeV is more

complex for interpretation. In case of neutron inelastic scattering on SiO_2 γ-quanta emitted in $(n, n'\gamma)$ reaction make significant contribution to the photopeak at ~1.7 MeV, which also corresponds to the transition from state 2^- (8.87 MeV) to 1^-(7.12 MeV) in ^{16}O. The peaks near 2.7 and 3.8 MeV probably correspond to γ-transitions 2^- (8.87 MeV) → 3^-(6.13 MeV) and 2^+(9.84 MeV) → 0^+ (6.05 MeV) in oxygen. Also, the peak near 3.8 MeV could be formatted by the γ-quanta from deexcitation of ^{13}C, which could be produced in the reaction $^{16}O(n,\alpha)^{13}C$ [8]. A definite contribution to the structure of the spectrum in this energy range is also provided by annihilation γ-quanta, which arise from the pair production in the target.

Table 1. The Legendre coefficients fitted to the γ-quanta angular distributions from $(n, n'\gamma)$ reaction on ^{16}O and ^{28}Si

Experiment	a_2	a_4	a_6
^{16}O, 3^- (6.13 МэВ)			
Kozlowski (1965) [7]	0.2 ± 0.3	– 0.3 ± 0.5	– 0.7 ± 0.5
Morgan (1964) [7]	0.34 ± 0.04	0.01 ± 0.06	– 0.04 ± 0.06
McDonald (1966) [8]	0.22 ± 0.08	– 0,05 ± 0.10	– 0.32 ± 0.08
This work	0.39 ± 0.03	0.13 ± 0.04	– 0.28 ± 0.05
^{28}Si, 2^+ (1.78 МэВ)			
Zhou [9]	0.21 ± 0.02		
Abbondanno [10]	0.20 ± 0.09	0.11 ± 0.14	
This work	0.19 ± 0.02	0.02 ± 0.03	

As a result of an analysis of the events corresponding to the full absorption peak of γ rays with an energy of 6.13 MeV, the dependence of the anisotropy parameter $W(\theta)$ was obtained. The experimental values and the analytical approximation with formula (4) are shown in Fig.4. The Legendre coefficients are presented in Table 1 in comparison with the coefficients from our approximation of the results from [8] and the data from the CDFE SINP MSU database [7]. It should be noted that, in comparison with the number of experiments on inelastic neutron scattering by carbon, the data on the angular distribution of γ-radiation in the inelastic scattering of 14.1 MeV neutrons by ^{16}O nuclei are extremely poor. The data of our experiment are in accordance with the results of previous measurements, and they have a significantly higher accuracy. The contribution of the polynomials with higher degrees is very interesting because the behavior of the anisotropy is important not only for modeling or any practical application, but also needed for the theoretical description of the neutron inelastic scattering. In this case, a high multipolarity of the transition leads to a more complex angular dependence, which has not yet been qualitatively reproduced in theoretical approaches.

In 14.1 MeV neutron inelastic scattering by ^{28}Si a large number of states are excited, which can decay by emitting the γ-rays. The results of an experiment on scattering of neutrons with the energy of 14.9 MeV on natural silicon are presented in [9], and the structure of the formed γ–spectrum is considered in detail. According to ref. [9], the five of fifty identified γ-transitions occur during the $^{28}Si(n, n'\gamma)^{28}Si^*$ reaction. The most intensive γ-transition is the transition from the first excited state 2^+ (1.778 MeV) to the ground state. For this γ transition, the parameters of the anisotropy were determined (see Table 1).

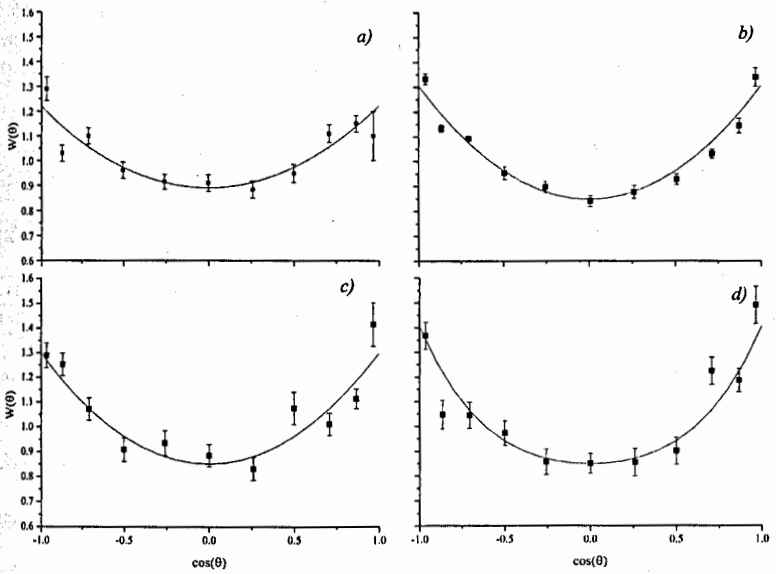

Fig. 6. The experimental angular distributions of γ-rays with energy E_γ= 1.014 MeV (a), E_γ= 1.72 MeV (b), E_γ= 2.21 MeV (c) and E_γ= 3,004 MeV (d) from inelastic scattering of 14.1 MeV neutrons by ^{27}Al. Solid lines are approximations by Legendre polynomials.

The data obtained in our experiment on the scattering of 14.1 MeV neutrons on a sample of SiO_2 make it possible to isolate γ–radiation for the transition from the first excited state 2^+ (1.778 MeV) to the ground state. Our results and their approximation are presented in Fig. 4 b). The Legendre coefficients, determined from our results in comparison with the coefficients from [9, 10] are presented in Table 1. The results of the approximation of the obtained angular distribution of γ-radiation agree with the data obtained in the previous experiments, within the limits of errors.

Interest in the inelastic neutron scattering reaction on ^{27}Al nuclei is explained by the fact that aluminum has only one stable isotope, and thus the experimental results must be in a good agreement with model calculations. An important factor is also the widespread use of aluminum as a constructing material.

However, ^{27}Al nucleus is even-odd, therefore the spectrum of the low-lying excited states is more complicated than that of the even-even nuclei. This feature makes the identification of the γ transitions more difficult. An additional uncertainty comes from mixing of γ-quanta with close energies from different reactions, for example, the γ-quanta from ^{27}Al(n, $n'\gamma$)^{27}Al and ^{27}Al(n, $p\gamma$)^{27}Mg* with consecutive β^- decay to ^{27}Al*. As a result, the accuracy of the obtained data is about 10% and only eight γ-transitions were identified. The most precisely the differential cross-section data for reaction ^{27}Al(n,$x\gamma$)^{27}Al were obtained in [11] at neutron energy of 14.9 MeV, 26 discrete γ-transitions were identified and ten of them in the energy range from 0.7921 to 3.004 MeV are related to the (n, $n'\gamma$) reaction. A lot of references for experimental works considered (n, $n'\gamma$) reaction cross-sections with neutron

energies near 14 MeV were collected in [11, 12]. It should be noted that the obtained experimental data fluctuate over a wide range and, despite the presence of γ-emission differential cross-section measurements at different angles, the angular dependences of the anisotropy are not presented.

Table 2. The Legendre coefficients fitted by γ-quanta angular distribution from ^{27}Al(n, $n'\gamma$)^{27}Al reaction. The energies and the multipolarities of the γ–transitions are also shown.

E_γ, MeV (Mult.)	1.01 ($M1$+$E2$)	1.72 ($M1$+$E2$)	2.21 ($M1$+$E2$)	3.00 ($E2$)
a_2	0.22 ± 0.02	0.30 ± 0.01	0.30 ± 0.03	0.35 ± 0.03
a_4				0.06 ± 0.04

The γ-spectrum of the photons, emitted during the neutron inelastic scattering on aluminum, obtained in our experiment is presented in Fig. 5. The γ-transitions with energies 0.84 MeV (transition from 1/2$^+$(0.844 MeV) to the ground state 5/2$^+$), 1.01 MeV (3/2$^+$(1.014 MeV) → 5/2$^+$, g.s.), 1.72 MeV (5/2$^+$(2.735 MeV) → 3/2$^+$(1.014 MeV)), 2.21 MeV (7/2$^+$(2.212 MeV) → 5/2$^+$, g.s.) and 3.00 MeV (9/2$^+$(3.004 MeV) → 5/2$^+$, g.s.) were identified with the highest reliability. The angular distributions of the gamma-quanta emitted during these transitions and their approximations are showed in Fig. 6. The coefficients of Legendre series approximation are written in Table 2. It is interesting to notice that for $E2$-transition 3.00 MeV (9/2$^+$(3.004 MeV) → 5/2$^+$, g.s.) a_4 is insignificant. In our experiment the parameters of anisotropy are quite similar for all observed transitions and it is completely different from the situation described in [13], where the γ-quanta angular distributions were investigated for ^{27}Al(n, $n'\gamma$)^{27}Al reaction with 3.5 MeV neutrons and a comparison with Hauser-Feshbach model was presented. For $J \leq 5/2$ the calculations predict $a_2 < 0.04$ and the experimental angular distributions for the gamma-transitions $E_\gamma = 1.01$ and 1.72 MeV are isotropic. The anisotropy coefficients for $E_\gamma = 2.21$ and 3.00 MeV have quite similar values, $a_2 = 0.22 \pm 0.04$. This value is comparable with our result for $E_\gamma = 3.00$ MeV transition. Such a discrepancy between the results of experiments at different neutron energies can indicate both the need for further refinement of the experimental data and a fundamental change in the dynamics of the reaction with increasing neutron energy.

Conclusion

At the TANGRA facility using the tagged neutron method on the beam of the ING-27 neutron generator, a study of the inelastic scattering of neutrons with the energy of 14.1 MeV on the nuclei of oxygen, silicon and aluminum was made. An important advantage of the experiment is a wide range of angles and a large number of points in which the registration of γ-quanta was simultaneously carried out.

The angular distributions of γ-quanta from the excited state of 6.13 MeV (3$^-$) in ^{16}O and from the first excited state of 1.78 MeV (2$^+$) in ^{28}Si were obtained with high accuracy. The values of the coefficients of the expansion of the anisotropy function in Legendre polynomials are in accordance with the results of the previous measurements. The angular distribution of γ-rays from the inelastic scattering of 14.1 MeV neutrons on ^{27}Al was measured for the first time.

This work was carried out with RFFR partial financial support (Grant 16-52-45056).

REFERENCES

1. Ruskov I.N., et al. // Phys. Procedia. 2015. **64**. 163.
2. Bystritsky V.M., et al. // Phys. Part. Nucl. Lett. 2015. **12**. 325.
3. Valković V. 14 MeV Neutrons. Physics and Applications. USA. CRC Press, 2016.
4. Bystritsky V.M., et al. // Phys. Part. Nucl. Lett. 2016. **13**. 504.
5. Ruskov I.N., et al.// EPJ Web of Conferences. 2017. **146**. 03024
6. ADCM – An universal Digital Pulse Processing System for nuclear physics experiments: http://afi.jinr.ru/ADCM16-LTC.
7. SINP MSU CDFE Data Base, http://cdfe.sinp.msu.ru/.
8. McDonald W.J., Robson J. M., Malcolm R. // Nucl. Phys. A. 1966. **75**. 353.
9. Hong-Yu Zhou, et al. // Nucl. Instr. and Meth. A. 2011. **648**. 192.
10. Abbondanno U., et al. // J. Nucl. Energy. 1973. **27**. 227.
11. Zhou H., Huang G. // Nucl. Sci. and Engineering. 1997. **125**. 61-74.
12. Hlaváč S., et al // Nucl. Sci. and Engineering. 1997. **125**. 196-204.
13. Chung K.C., et al // Nucl. Phys. 1968. **A115**. 476-480.

MEASUREMENTS OF GAMMA RAYS FROM THE INELASTIC SCATTERING OF 14.1 MeV NEUTRONS USING THE TAGGED NEUTRON METHOD

Grozdanov D.N.[1,2]*, Kopatch Yu.N.[1], Bystritsky V.M.[1], Fedorov N.A.[1,3], Aliyev F.A.[1,4], Hramco C.[1,5], Ruskov I.N.[1,2], Skoy V.R.[1], T.Yu. Tretyakova[6], Bogolyubov E.P.[7], Yurkov D.I.[7] and TANGRA collaboration

[1]*Joint Institute for Nuclear Research, Joliot Currie 6, 141980 Dubna, Moscow region, Russia*
[2]*Institute for Nuclear Research and Nuclear Energy of Bulgarian Academy of Sciences, Tzarigradsko chaussee, Blvd., 1784 Sofia, Bulgaria*
[3]*Lomonosov Moscow State University, Leninskie Gory, 119991 Moscow, Russia*
[4]*Institute of Geology and Geophysics, Azerbaijan National Academy of Sciences, Azerbaijan, AZ1143, Baku, H. Javid Av., 119*
[5]*Institute of Chemistry of the Academy of Sciences of Moldova Academiei str., 3; MD-2028 Chisinau, Republic of Moldova*
[6]*Skobeltsyn Institute of Nuclear Physics (SINP MSU), Moscow, Russia.*
[7]*All-Russia Research Institute of Automatics (VNIIA), Sushchevskaya 22, 127055 Moscow, Russia*

Abstract

At the Joint Institute for Nuclear Research, in the frame of the TANGRA project [1], we started the second set of measurements of the inelastic scattering (INS) of 14.1 MeV "tagged" neutrons on a number of isotopes. The 14.1 MeV neutrons are produced in the D(T,α)n reaction by the VNIIA ING-27 portable neutron generator [2], which has a 64 Si-pixel charge particle detector, incorporated into its vacuum chamber. By registering the alpha particles, we "tag" the corresponding neutrons which, according to the reaction kinematics, are emitted in the direction nearly opposite to that of the alpha particles.

We used an array of 22 hexagonal NaI(Tl) crystals for spectrometry of the coincided with α-particles characteristic γ-rays following the INS-reaction on the nuclei under investigation.

The signals from NaI(Tl) were fed to a computerized 32-channel data acquisition system from JINR AFI Electronics [3], which was used for digitizing the analog signals from the detectors and storing the waveforms on the computer hard-drive for further off-line analysis.

In current set of measurements, we succeed to measure the gamma-ray spectra from the INS of 14.1 MeV neutrons on a number of light elements. Here we report and discuss the preliminary results for some of the investigated samples.

Keywords: Gamma-rays, spectrometry, multichannel analyzer, neutron source.

* Corresponding author Tel.: + 7-496-216-2131; fax: +7-496-216-5085.
email: dimitar@nf.jinr.ru.

1. Experimental setup

The experimental setup consisted of the ING-27 and Fe-shielded NaI(Tl)-array. The scheme of the experimental setup is shown in Fig.1 (left) and the photo is in Fig.1 (right). The target is located at a distance of 805 mm from the neutron source. The gamma-ray detectors are placed around the target with a step of 15 degrees at a distance of 320 mm from the target. The 40cm thick iron shielding was used to protect the gamma detectors from the direct neutron beam. Only one central pixel of the alpha-particle detector was used for producing the tagged neutron beam.

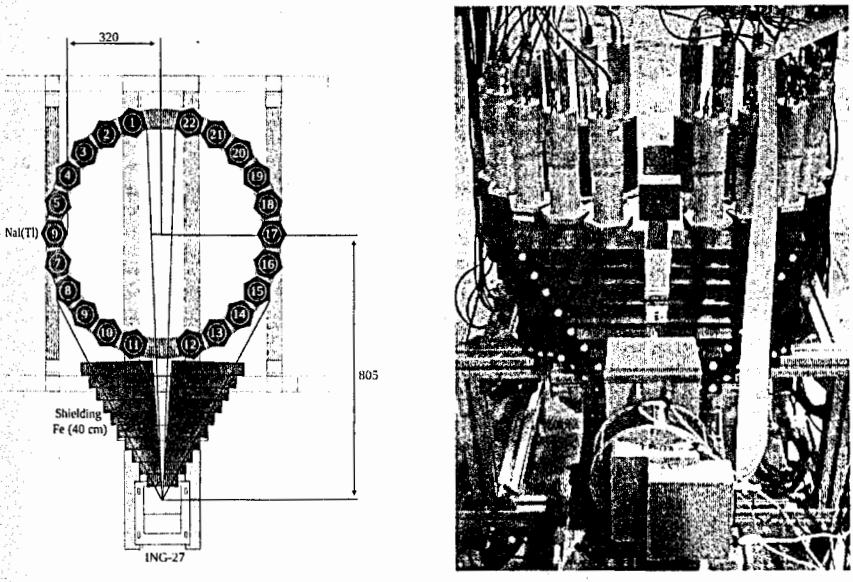

Fig. 1 The scheme (left) and the photo (right) of the experimental setup

In Fig. 2 are shown the samples from Lead (^{208}Pb), Carbon (^{12}C), Iron (^{56}Fe), Bismuth (^{209}Bi) and Aluminum (^{27}Al) of the same size – 100×100×50 mm.

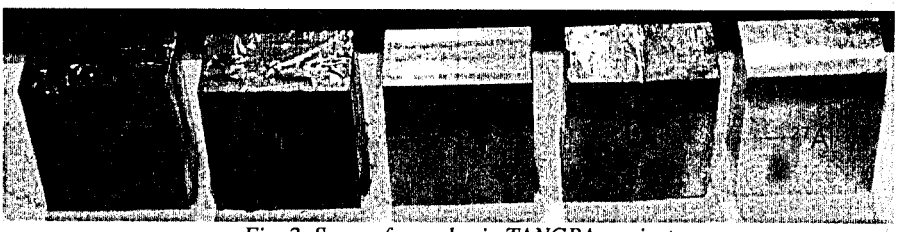

Fig. 2. Same of samples in TANGRA-project

2. Data acquisition and analysis

Data taking lasted 8h/sample. In Fig. 3 one can see a (triple) coincidence – the signals from the x-coordinate (ch # 23) and y-coordinate (ch # 22) of the ING-27 α-detector with a signal from the γ-detector (ch # 3). The data were saved on the computer hard disk as list-mode data and were analyzed offline in the ROOT environment [4].

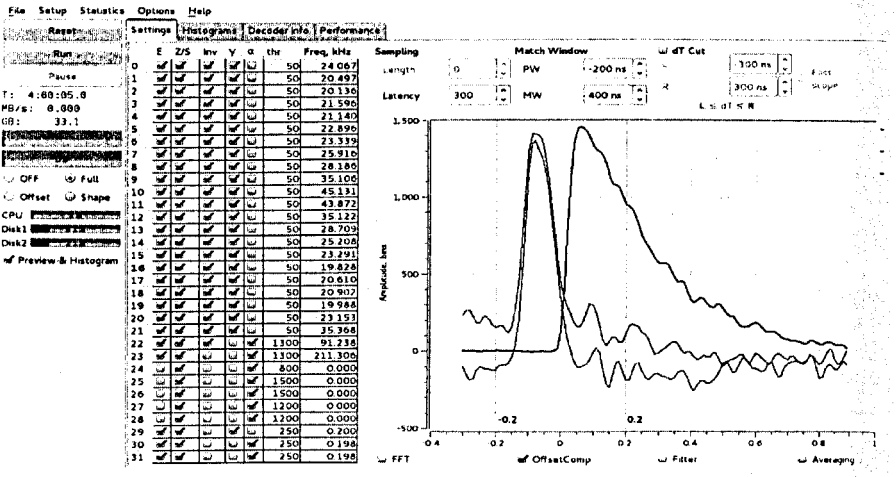

Fig. 3. DAQ system software main panel

The energy calibration of the collected amplitude spectra was done using standard (calibration) "point"-type gamma-sources. The time-spectra ('start' from α-detector and 'stop' from any of the γ-detectors) from the Al-sample are shown in Fig. 4. The first peak is arising from the neutrons scattered on the Fe-shielding (A), the second is from the inelastic scattering of neutrons on the sample (B) and the last one is from the interaction of the fast neutrons with the detector nuclei (C).

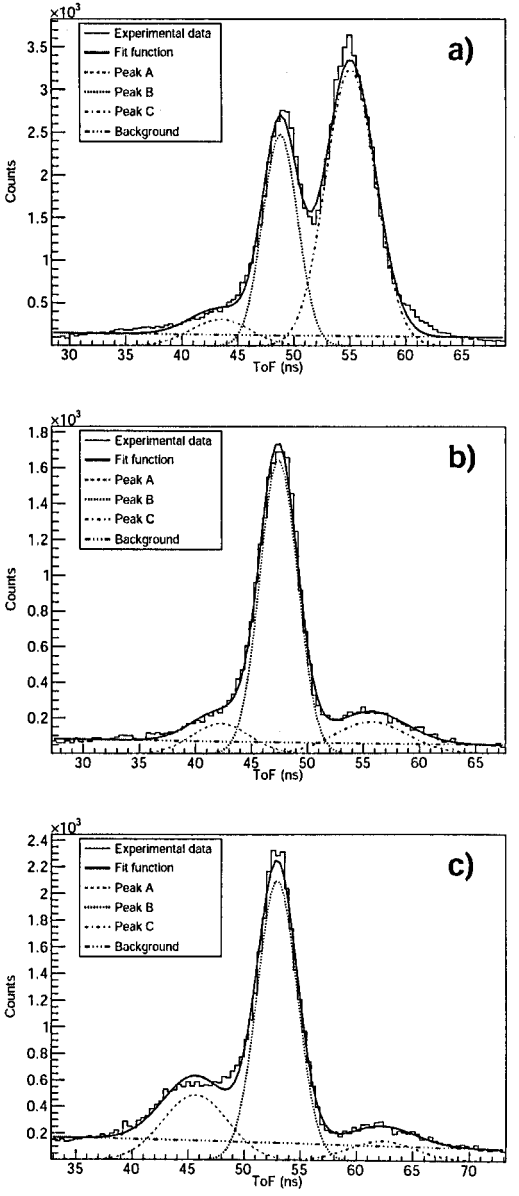

Fig. 4. ^{27}Al sample: the time spectra from the detectors at 15° (a), 90° (b) and 165° (c).

In Fig. 5 to 6 we show the comparison of the total energy spectra of gamma-rays (top spectra) and the spectra obtained within a time-window corresponding to 3σ width of the central gamma-peak in of time-of-flight spectra (see Fig.4, peak B). In this way, the radiation background in the "untagged" spectra was reduced by about 70%.

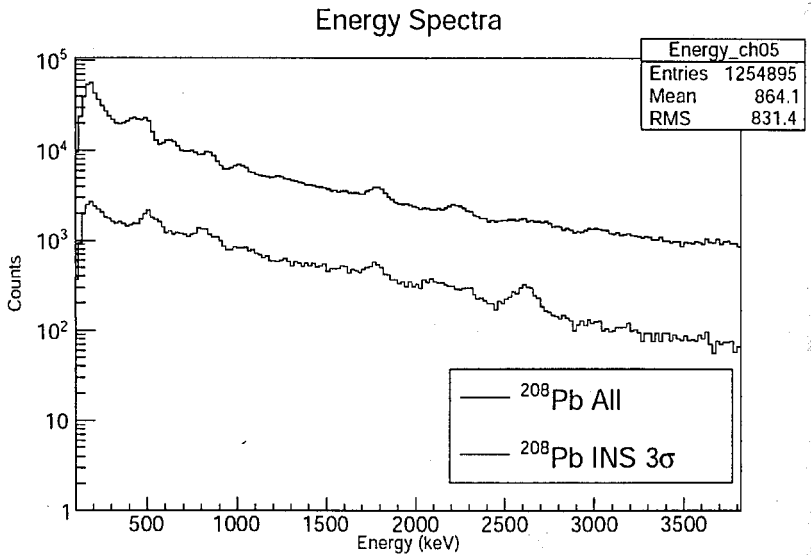

Fig. 5. ^{208}Pb sample: energy spectra from the detector at 90°

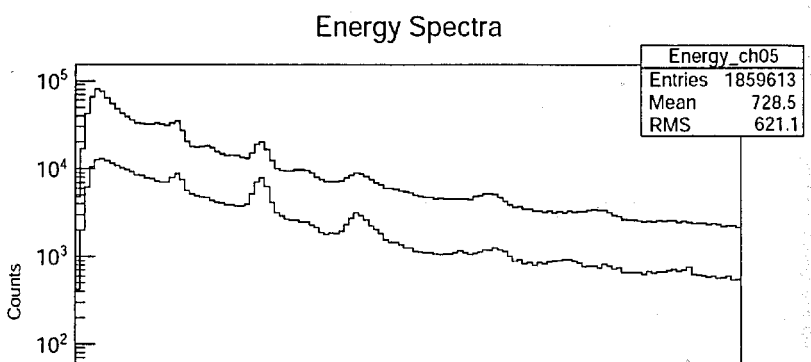

Fig. 6. ^{56}Fe sample: energy spectra from the detector at 90°

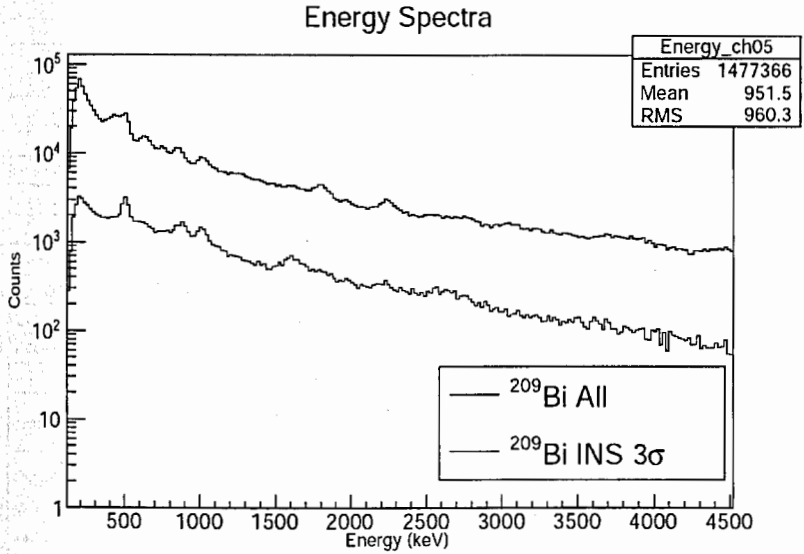

Fig. 7. ^{209}Bi sample: energy spectra from the detector at 90°

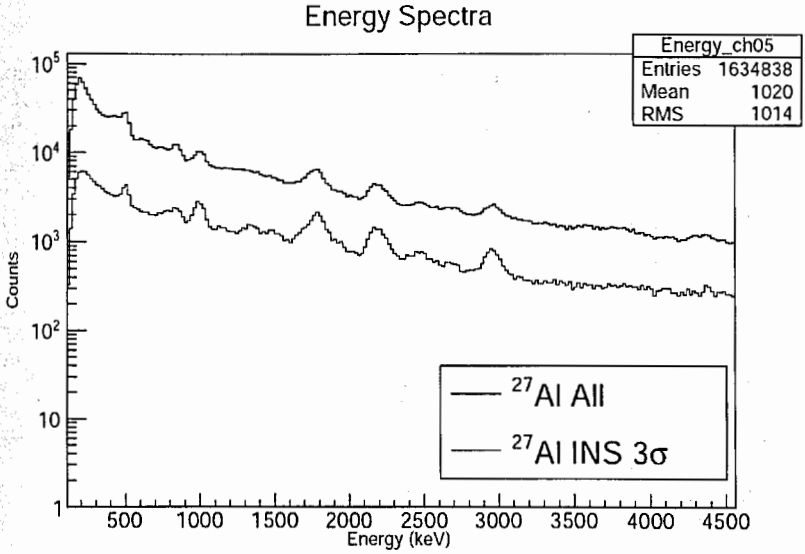

Fig. 5. ^{27}Al sample: energy spectra from the detector at 90°

In the table below are listed the main characteristics of the identified γ-lines from the INS of 14.1 MeV neutrons on the target nuclei. The gamma-lines data are taken from ref. [5].

Table 1.

Samples (Isotope)	E (keV)	Jπ	Eγ (keV)	M (γ)	Final level	
^{208}Pb	3708.45	5-	510.74	M1+E2	3197.71	5-
	3961.16	5-	763.43	M1+E2	3197.71	5-
	4962.43	4(-),5(+)	1764.71	M1+E2	3197.71	5-
	2614.52	3-	2614 51	E3	0	0+
^{12}C	4438.91	2-	4438.03	E2	0	0+
^{56}Fe	846.77	2+	846.76	E2	0	0+
	2085.10	4+	1238.27	E2	846.77	2+
	2657.59	2+	1810.75	M1+E2	846.77	2+
	3369.95	2+	2523.06	M1+E2	846.77	2+
^{209}Bi	896.28	7/2-	896.28	M1+E2	0	9/2-
	1603.5	19/2-	1603.50	M2+E3	0	9/2-
	2564.12	(9/2)-	2564.12	E1+E3	0	9/2-
^{27}Al	843.76	1/2+	843.76	E2	0	5/2+
	1014.52	3/2+	1014.52	M1+E2	0	5/2+
	2734.90	3/2+	1720.30	M1+E2	1014.52	3/2+
	2212.01	(7/2+)	2212.01	M1+E2	0	5/2+
	3004	9/2+	3004	E2	0	5/2+

3. Conclusions

By using the target neutron method (TNM) we reduced by ~70% the radiation background in the collected pulse-height spectra. As a result of this we were able to identify the main characteristic gamma-lines from the INS of 14.1 MeV neutrons by the investigated elements.

4. Acknowledgment

This work was partially supported by the RFBR grant N 16-52-45056.

References

1. Kopatch Yu.N., Bystritsky V.M., Grozdanov D.N., Zontikov A.O., Ruskov I.N., Skoy V.R., Rogov Yu.N., Sadovsky A.B., Barmakov Yu.N., Bogolyubov E.P., Ryzhkov V.I., Yurkov D.I., Angular Correlation of Gamma-Rays in the Inelastic Scattering of 14.1 MeV Neutrons on Carbon, Proc. of ISINN-23, 2015, http://isinn.jinr.ru/proceedings/isinn-23/pdf/Kopatch.pdf
2. ING-27 neutron generator based on a gas filled neutron tube. http://www.vniia.ru/ng/element.html.
3. A digital pulse processing system for nuclear physics experiments ADCM16-LTC http://afi.jinr.ru/ADCM.
4. ROOT Data Analysis Framework, https://root.cern.ch/
5. NuDat 2.7b, http://www.nndc.bnl.gov/nudat2/

Nuclear Reactions with 14 MeV Neutrons on Molybdenum Isotopes

C. Oprea, A.I. Oprea

Frank Laboratory of Neutron Physics (FLNP), Joint Institute for Nuclear Researches (JINR)
141980 Dubna, Moscow Region, Russian Federation

Abstract. Molybdenum and Niobium are important chemical elements in many fundamental and applicative researches. The cross sections of fast neutron induced reactions with emission of charged particles in the ^{94}Mo(n,p)^{94}Nb reaction were evaluated. For each process, the contribution of compound, direct and pre-equilibrium nuclear reaction mechanism and the corresponding nuclear data (parameters of nuclear potential, density states and others) were extracted. The present evaluations were done in order to realize new fast neutron measurements at IREN neutron source from FLNP JINR Dubna.

INTRODUCTION

Molybdenum is a chemical element with protons number, Z= 42, it has a total number of 33 isotopes with six natural ones (A= 92, 94, 95, 96, 97, 98) and four isomers. The Mo isotope with mass A= 100 is a fission product and is very important for medicine [1,2].

Nuclear reactions induced by fast neutrons with emission of charged particles like (protons and alphas) are of interest for fundamental and applicative researches. Relative to fundamental studies, these reactions furnish new information about structure of atomic nuclei and nuclear reactions mechanisms. In the applicative researches, (n,p) and (n,α) reactions are of great importance in the material sciences. Due to these processes, in time, in the walls and vessels take place a process of accumulation of Hydrogen and Helium which will modify their physical properties. Further, these reactions provide precise data for nuclear technology, reprocessing of U and Th for future projects of transmutation and energy, processing of long live waste, accelerated driven systems, fast neutron activation analysis etc [3,4].

In the present work the ^{94}Mo(n,p)^{94}Nb reactions with fast neutrons, starting from protons threshold (Q= –1.26 MeV) up to 20 MeV will be analyzed. Residual nucleus ^{94}Nb, obtained in this reactions, has the time of life $T_{1/2}$= 20300 years and can be found in the radioactive waste. Due to its large time of life, the ^{94}Nb isotope contributes to the low level activity of environment caused by buried waste [5]. For this reaction, cross sections were evaluated with Talys. Contributions to the cross sections of different nuclear reactions mechanisms given by discrete and continuum states were separated. Using cross sections theoretical evaluations, isomer ratios were also calculated, parameters of nuclear potential were extracted and finally, some activities were obtained for planned experimental measurements.

THEORETICAL BACKGROUND

Talys represents a freeware computer codes destined for nuclear reactions and structure of atomic nuclei evaluations, working mainly under Linux operation system. In Talys are implemented the main nuclear reaction mechanisms (compound, direct and pre-equilibrium) and large nuclear database which includes information about levels, states densities and parameters of nuclear potentials. This software allows to calculate inclusive and exclusive cross sections. Considering a binary nuclear reaction, A(a,b)B, inclusive cross

sections are defined as those cross sections in which are taken into account emergent "b" particles coming not only from the channel "b+B" but from other channels also involving the "b" particles. If in the cross sections are considered emergent "b" particles only from "b+B" channel than the cross section is defined as exclusive. Extensive information about Talys and its possibility is given in the reference [6].

In the cross sections calculations, the compound, direct and pre-equilibrium nuclear reaction mechanisms were taken into account for incident neutrons energy starting from the proton threshold up to 20 MeV. Compound processes are described by Hauser–Feshbach formalism [7], direct processes by Distorted Wave Born Approximation (DWBA) [8] and pre-equilibrium by two-component exciton model [9]. Discrete and continuum states of the residual nuclei were considered together with corresponding nuclear densities based on Fermi gas model [6].

In the incident and emergent channels, the interaction is described by all type of Woods–Saxon potentials like volume, surface, spin-orbit with real and imaginary part. For a very large number of nuclei, in Talys, there are the nuclear potential parameters extracted from experimental data (local parameters). In the situation when for some nuclei the potential parameters do not exist it is possible to obtain them using the global parameters according to the approach described in [6,10].

Another physical values of interest, which can be measured by activation method, are the isomer ratios. Usually, in the experiment, the isomer ratio is defined like [11]:

$$R = \frac{Y_m}{Y_g} = \frac{\int_{Eihr}^{E\max} N_0 \phi(E) \sigma_m(E) dE}{\int_{Ethr}^{E\max} N_0 \phi(E) \sigma_g(E) dE}, \quad (1)$$

where $Y_{m,g}$ are yields of isotope in isomer (m) and ground (g) states; N_0 is number (concentration) of nuclei in the target; ϕ is the flux of incident beam; $\sigma_{m,g}$ are the cross sections production of m and g states respectively; E_{thr} is the threshold energy of emergent particle emission; E_{max} is the maximum energy of incident beam.

For the evaluation of isomer ratio, by activation method, the following relation for observed activity is used [12]:

$$A_{obs} = \frac{N\sigma\varphi a\varepsilon}{\lambda}[1 - Exp(-\lambda t)]Exp(-\lambda T)[1 - Exp(-\lambda \Delta T)] \quad (2)$$

N is the number of atoms of the isotope of the element; σ is cross section; a is γ-ray abundance; φ is neutron flux; ε is detector efficiency; λ is decay constant; t, T, ΔT are the irradiation time, cooling time and counting times respectively.

RESULTS AND DISCUSSIONS

In the Figure 1, the inclusive cross sections for ^{94}Mo(n,p) process with the separation on different nuclear reaction mechanisms and residual nucleus states, are represented.

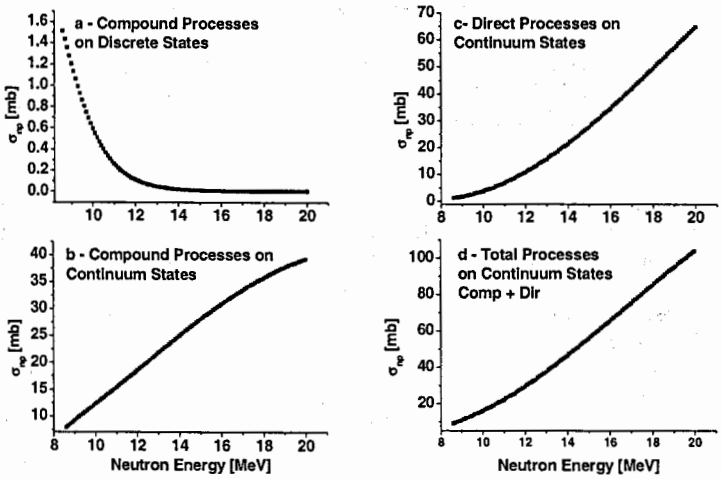

Figure 1. Inclusive cross section in ^{94}Mo(n,p) reaction.

Compound processes on discrete states are with order of magnitude lower than compound processes on continuum states (Figure 1.a and 1.b). Direct processes on discrete states can be neglected and therefore they are not shown in Figure 1. If at low energy, in the threshold region can be considered that the compound processes are dominant, with the increasing of incident energy direct mechanism gives more contribution to the cross section in comparison with compound mechanisms (Figure 1.b and 1.c). In the Figure 1.d, the total inclusive cross section is represented. Both processes (direct and compound) are generated by pre-equilibrium mechanism as is resulting from Talys evaluations.

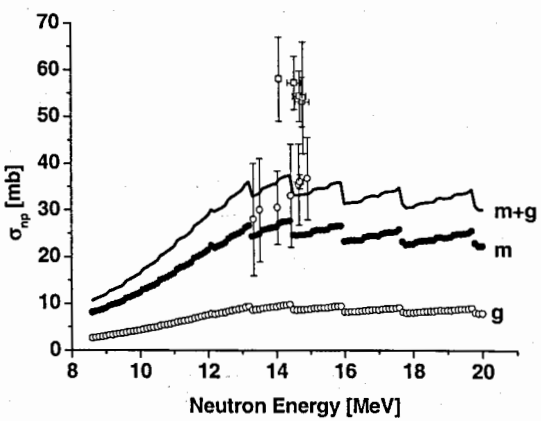

Figure 2. Exclusive cross section in ^{94}Mo(n,p)^{94m,g}Nb reaction. g. – ground; m – isomer; m+g – total; points – two sets of experimental data

The incident neutrons energy dependence of cross section production of ^{94}Nb, from proton threshold, up to 20 MeV, in ^{94}Mo(n,p)^{94m,g}Nb is represented in the Figure 2. The isomer and ground states cross sections production are represented by the curve m) and g) respectively from Figure 2. The total production of ^{94}Nb is given by m+g) in Figure 2. Talys allows to evaluate the exclusive cross section on other levels of residual nucleus but their values are much lower than the contribution of ground and first isomer states and they are neglected.

The total cross section production of ^{94}Nb isotope, obtained with Talys, is compared with experimental data from literature [13]. From Figure 2 it is noticed that there are two sets of experimental data in the 12–16 MeV region, where the cross section has higher value. It is easy to describe one of the experimental set but as a first step is better to use the default Talys input and to consider a satisfactory agreement between theory and experiment.

For the isomer ratios calculations (1), evaluated cross sections and some model for incident neutrons source are necessary. Further characteristic of the ground and isomer states, like spin, parity and time of life are: $(J^{\Pi})_g = 6^+$, $\tau_g = 20300$ y, and $(J^{\Pi})_m = 3^+$, $\tau_m = 6.23$ min, with a low energy gamma transition $\Delta E_\gamma = 40.902$ keV [14]. Below are given the isomer ratios R, for incident neutron flux: a) $\phi = 1$ and b) $\phi \sim (E_n)^{-0.9}$

$$R_a = 2.852 \pm 0.1 \quad \text{and} \quad R_b = 2.860 \pm 0.130 \tag{3}$$

Isomer ratios can be measured in an activation type of experiment. Considering a target of Mo with dimensions 1×1×1 cm^3, irradiated by a neutron flux of type b) ($\phi \sim (E_n)^{-0.9}$), with irradiation time, t= 3 min, cooling time T= 3 min, counting time ΔT= 6 min then, the observed activities (2) for different energies are in Table 1.

Table 1. Observed activities

^{94}Mo(n,p)^{94m}Nb			^{94}Mo(n,p)^{94g}Nb	
E_n[MeV]	σ_m[mb]	A_{obs}[dez]	σ_g[mb]	A_{obs}[dez]
14.1	27.1	$8.75 \cdot 10^{6}$	9.48	$6.4 \cdot 10^{-3}$
20	22.2	$7.17 \cdot 10^{5}$	7.83	$4.3 \cdot 10^{-3}$

Isomer state of ^{94m}Nb requires a short live type of measurement but not enough to evidence the ground state. Nevertheless, a short time measurement can provide new data of isomer state, ^{94m}Nb. Pure target of ^{94}Mo is very difficult to produce then is necessary also to investigate other reactions in which the residual nucleus ^{94}Nb is obtained or in those processes where protons in the emergent channel coming from other isotopes of Mo are obtained.

The parameters of optical nuclear potential, in the incident and emergent channels, which have the most influence on the cross sections, are the volume Woods–Saxon (WS) potential with real and imaginary part and the real part of spin–orbit interaction. The results are in the Table 2.

Table 2. Parameters of Woods–Saxon optical potential

Channel	WS volume						Spin-orbit		
	Real part			Imaginary part			Real part		
	V [MeV]	r_v [fm]	a_v [fm^{-1}]	W [MeV]	r_w [fm]	a_w [fm^{-1}]	V_{so} [MeV]	r_{so} [fm]	a_{vso} [fm^{-1}]
n+^{94}Mo	50.99	1.220	0.658	0.16	1.220	0.658	5.99	1.050	0.58
p+^{94}Nb	61.94	1.215	0.664	0.13	1.215	0.664	6.03	1.043	0.59

Because cross sections are not so influenced by Woods–Saxon surface potential (real and imaginary) and imaginary part of spin-orbit interaction their values are not shown here. The expressions of all Woods–Saxon optical potential can be found in [6].

CONCLUSIONS

The $^{94}Mo(n,p)^{94}Nb$ reaction with fast neutrons from protons threshold up to 20 MeV, was analyzed. Target and residual nuclei are of great interest in many applications. The inclusive and exclusive cross sections were obtained with default input of Talys. The contribution of each nuclear reaction mechanism related to discrete and continuum states were extracted together with parameters of Woods–Saxon optical potential. Because in this process the isomer state ^{94m}Nb is obtained the isomer ratios, using different model of incident neutrons flux, were determined. The cross sections and isomer ratios can be measured in an activation experiment and therefore observed activities were evaluated. In a short time measurement, in principle it is possible to extract new nuclear data on ^{94m}Nb isotope. Taking into account that a pure ^{94}Mo target is very difficult to obtain, in the future it is necessary to evaluate the influence of other Mo isotopes on the $^{94}Mo(n,p)^{94}Nb$ process.

The theoretical results on the (n,p) reactions with fast neutrons on ^{94}Mo nucleus can be effectuated at the FLNP JINR Dubna basic facilities and the present work can be considered a starting point for future proposals.

Acknowledgement. *The work was supported by Cooperation Program between JINR Dubna and Romanian Research Institutes coordinated by JINR Dubna Romanian Plenipotentiary Representative on 2016 – 2017 years and FLNP Thematic Plan.*

REFERENCES

[1] G. Audi, A.H. Wapstra, Nucl. Phys. A, **565**, p. 1–65 (1993).
[2] G. Audi, A.H. Wapstra, Nucl. Phys. A, **595**, p. 408–490 (1993).
[3] M. Salvatores, I. Slessarev, A. Tchistiakov, Nucl. Sci. Eng. p. 130, 309–319 (1998).
[4] M. Salvatores, A. Zaetta, C. Girard, M. Delpech, I. Slessarev, J. Tomassi, Appl. Radiat. Isot. **46** (6), p. 681–687 (1995).
[5] Y. Ikeda, C. Konno, IAEA Vienna, INDC(NDS)-**286**, p. 27–31 (1993).
[6] A.J. Koning, S. Hilaire and M.C. Duijvestijn,TALYS-1.0., Proceedings of the International Conference on Nuclear Data for Science and Technology, April 22–27, 2007, Nice, France, editors O.BERSILLON, F.GUNSING, E.BAUGE, R.JACQMIN, S.LERAY, EDP Sciences, p. 211 (2008).
[7] W. Hauser, H. Feshbach, Phys. Rev., **87**, 2, p. 366 (1952).
[8] G.R. Satchler, Direct Nuclear Reactions, Oxford University Press, New York (1983).
[9] A.J. Koning and M.C. Duijvestijn, Nucl. Phys. A, **744**, p. 15 (2004).
[10] S. Hilaire , S. Goriely, A.J. Koning, M. Sin, R. Capote, Phys. Rev. C **79**, 024612 (2009).
[11] B.S. Ishkhanov, V.V. Varlamov, Physics of Atomic Nuclei, **67**, 9, p. 1664 (2004).
[12] H.Naik, P.M. Prajapati, S.V. Surayanarayana, K.C. Jagadeesan, S.V. Thakare, D. Raj, V.K. Mulik, B.S. Sivashankar, B.K. Nayak, S.C. Sharma, S. Mukherjee, S. Singh, A Goswami, S. Ganesan, V.K. Manchanda, European Physics Journal A, **47** (4) p. 1–9 (2011).
[13] Experimental data EXFOR – http://www-nds.iaea.org[14] R.B. Firestone, V.S. Shirley, S.Y.F. Chu, C.M. Baglin, J. Zipkin, Tables of Isotopes. CD ROM Edition, Wiley-Interscience (1996).

Nuclear Structure, Nuclear Data

About the Flaky Structure of Atomic Nucleus. Further Development of Analysis

Yu.A. Alexandrov[1], G.V. Anikin[2], V.G. Anikin[2]

[1]*FLNP. Joint Institute for Nuclear Research, Dubna, Russia*
[2]*Institute of Physics and Power Engineering, Obninsk, Russia*

Abstract. The Neutron-optical model is some remarkable microscope for the investigation of gross-structural elements of atomic nuclei. In paper [1] the detail structure of potential of the neutron interaction with ^{208}Pb nuclei (for 0.1 Mev < E_n < 15 MeV) was presented. The experimental cross sections σ_{tot} from [2] in comparison with the results of calculation are presented. The real part of potential (peripheral area) was $-V_r = 0.38/r^8+0.05/r^4+0.02/r$ (Mev). We may especially underline the role of quantity C/r^8 in description of spectrum of scattered neurons with $E_n > 5\div6$ MeV.

There exist another experimental data about σ_{tot} for interaction of neutron with ^{208}Pb in more wide energetic diapason. In work [3] the cross sections for En < 1MeV was measured. We have used these data in our estimation of σ_{tot} for ^{208}Pb. The results are presented at Fig 1. Cross section has a rise at $E_n \leq 0.1$ MeV.

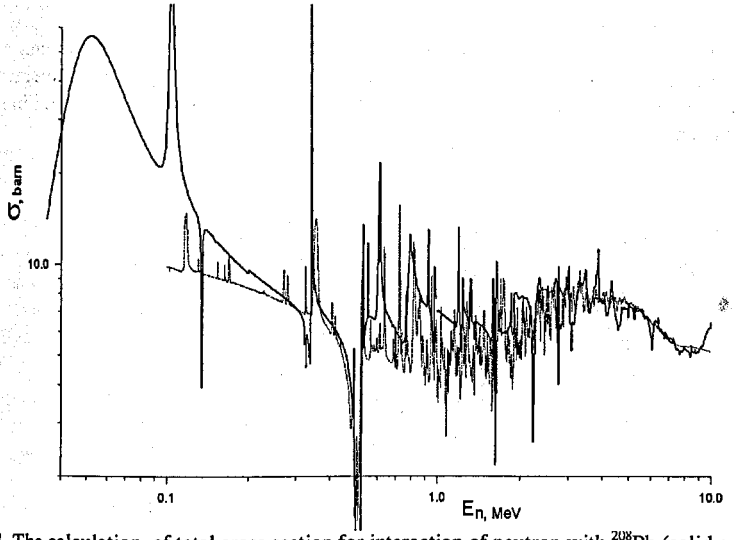

Fig. 1. The calculation of total cross section for interaction of neutron with ^{208}Pb (solid curve) in comparing with experimental data of the work [2] (dotted curve).

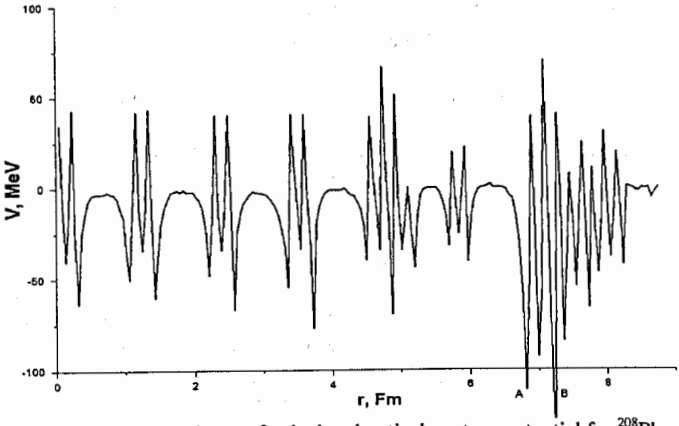

Fig. 2. The real part of calculated optical neutron potential for ^{208}Pb.

The real part of potential is presented in Fig.2. This part is very close to that published in [1]. The receiving of spin-orbital and imaginary component of potential is described in paper [1].

In this paper we start the description of neutron scattering by stannum nuclei. In IPPE (Obninsk) some interesting measurement of σ_{tot} for 12 isotopes of Sn was performed. Every isotope has the mass difference of one neutron from neighbour isotope [4].

We have searched the potential parameters for ^{120}Sn. The starting set of parameters was fitted early for Pb. The results for real part of potential is presented in Fig.3. Some elements of this potential are very close to that of ^{208}Pb. The more significant difference is found in peripheral part of nucleus (4 fm < r < 8 fm).

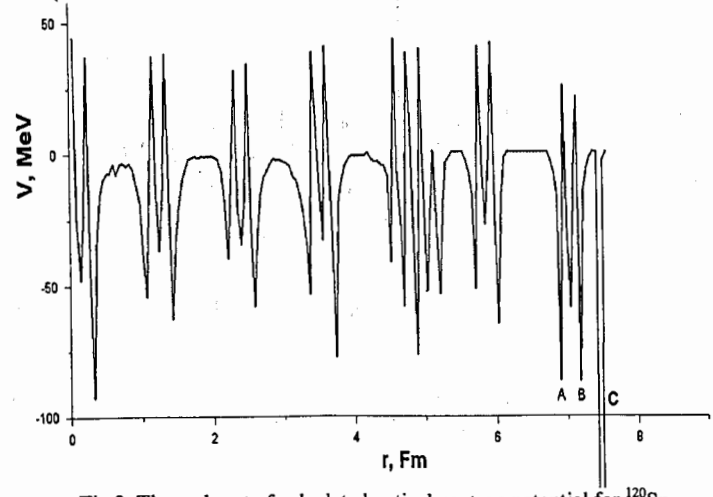

Fig.3. The real part of calculated optical neutron potential for ^{120}Sn.

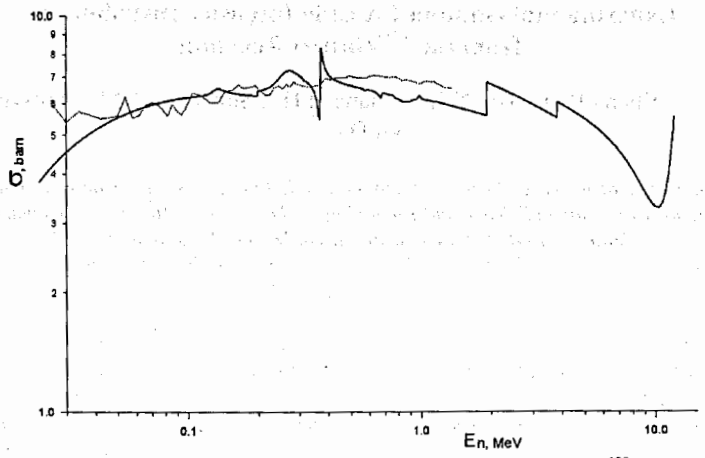

Fig.4. The calculation of total cross section for interaction of neutron with ^{120}Sn (solid curve) in comparing with experimental data of the work [4] (dotted curve).

It is interesting to note that maximums A and B (Figs. 2 and 3) have the same positions for Pb and Sn. But for Sn fitting procedure found a great extremum at radius $r \approx 7.5$ (point C at Fig.3). At these radius neutron forms orbit with greatest probability.

Outside the central part, given discretely, all components of the potential for ^{120}Sn are represented by smooth curves:

$$-V_r = 0.38/r^8 + 0.04/r^4 + 0.03/r,$$

$$V_{so} = 0.0012/r^3,$$

$$-V_{im} = 0.2/r^2$$

All ordinate the internal and external parts of the potential are multiplied by energy dependency coefficients:

EDr – coefficient for the real part.
EDim – for the imaginary part,
EDso – for the spin-orbital part of potential.
EDr = 1.15
EDso = $1/\sqrt{E_n}+2.62E_n$
EDim = 0.00023,
where E_n – energy of scattering neutron, integration step - 0.0464 Fm.

References

[1] Yu. Alexandrov, G. Anikin, V. Anikin. About the flaky neutron-optical potential. Further development of approach. ISINN-24, E3-2017-8, Dubna June 2016.
[2] R.F. Carlton, R.R. Winters and J.A. Harvey at al. Bull of Am. Phys.,**36** (1991), p.1349.
[3] A. Laptev, Yu. Alexandrov, I. Guseva at al. Journal of Nuclear Science and Technology Supplement **2**, p.327 (August 2002).
[4] Tihonov V.M., Kononov V.N. at al. Journal of Nuclear Physics **50**, 3(9), 1989.

Experimental Gamma Cascade Intensity Distributions from the ^{171}Yb(n,γ) Reaction

Anh N.N.[1], Khang P.D.[2], Hai N.X.[1], Thang H.H.[1], Sukhovoj A.M.[3], Mitsyna L.V.[3], Vu D.C.[3,4]

[1]*Dalat Nuclear Research Institute, Vietnam Atomic Energy Institute, Hanoi, Vietnam*
[2]*Hanoi University of Science and Technology, 1 Dai Co Viet, Hanoi city, Vietnam*
[3]*Joint Institute for Nuclear Research, Dubna, 141980, Russia*
[4]*Vietnam Academy of Science and Technology Institute of Physics, Hanoi, Vietnam*

Abstract

In the present paper, the gamma cascade intensity distributions of ^{172}Yb from the ^{171}Yb(n,γ) reaction are determined. The obtained gamma cascade intensity distributions can be used to simultaneously extract the nuclear level density and radiative strength function of ^{172}Yb excited nucleus by means of the Dubna method. The latter has been applied to 43 nuclei, whose atomic number ranges from 28 to 200, but ^{172}Yb. Thanks to the high quality gamma-gamma coincidence spectrometer and the high statistics achievement, the gamma cascade intensity distributions obtained for ^{172}Yb within the present work is the most accurate in comparison to all the 43 investigated nuclei.

Introduction

We have already known that the nuclear level density and radiative strength function are all together important quantities, which describe the average properties of excited nuclei in the high-excitation-energy region [1]. As ^{172}Yb is an even-even, deformed, and heavy nucleus, its nuclear properties are useful information for confirming as well as improving the nuclear models of high-mass nuclei near the stability line.

In the excited energy below the neutron binding energy, the Dubna method [2] is widely used to simultaneously extract the nuclear level density and radiative strength function from the measured gamma cascade intensity distributions. Although this method has been applied to 43 nuclei whose atomic number ranges between 28 and 200 [3], the ^{172}Yb nucleus has not been studied yet.

Within the Dubna method, the gamma cascade intensity distributions are determined from the two-step-cascade (TSC) spectra, corresponding to the gamma cascades from the compound state to the different final excited states. The events, which are due to the Compton scattering, are significantly suppressed, particularly in the TSC spectra corresponding to low-energy final states. Therefore, the obtained gamma cascade intensities are highly reliable.

In the present paper, we present the experimental gamma cascade intensity distributions of the excited ^{172}Yb nucleus measured via the thermal neutron capture reaction. A nuclear level scheme, which is constructed from the resolved cascade decays using the maximum likelihood method, is also given.

Experimental

The gamma-gamma coincidence experiment was carried out on the neutron beam No.3 of Dalat Nuclear Research Reactor. The latter provided a neutron beam whose flux and diameter were 1.7 ×10^5 n/cm^2/sand 2.5 cm, respectively. The target was 0.56 g Yb_2O_3 powder sealed in a plastic bag. The enrichment of ^{171}Yb in this target is more than 95.5%, that is, the ^{171}Yb mass is about 0.48 g. The percentages of the other impurities in the target is small

enough to not cause net influences on the obtained spectroscopic data of ^{172}Yb nucleus. The cascade decay data were recorded for about 830 hours using two HPGe detectors whose relative efficiency equal to 35% of the standard NaI(Tl) scintillator detector (3 in×3 in× 3 in). The measurement was performed using the "close" geometry as given in Fig. 1, in which the distance from the target to the detector windows are only 5 cm. The energy threshold of the spectrometer was set to 520 keV.

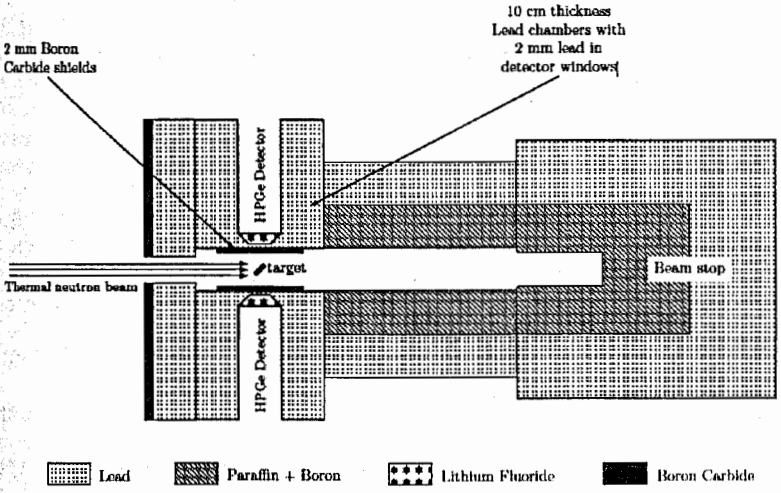

Fig. 1. The "close" geometry used for measuring the gamma – gamma coincidences.

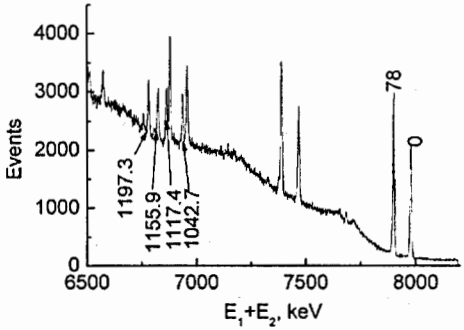

Fig. 2. The most informative part of the spectrum of sums of coincident pulse's amplitudes for ^{171}Yb(n_{th},2γ) reaction. The energies of the final levels of cascades (in keV) are pointed near peaks of the full energy capture.

The most informative part of the spectrum of sums of coincident pulse's amplitudes for ^{172}Yb is shown in Fig. 2. It can be easily seen from this figure that there is almost no Compton background under the summation peaks corresponding to the ground state and the final state E_f = 78.8 keV. However, the Compton background is rather high under the other summation peaks corresponding to the other four final states. A number of peaks caused by single- and double-escape events can also be clearly seen.

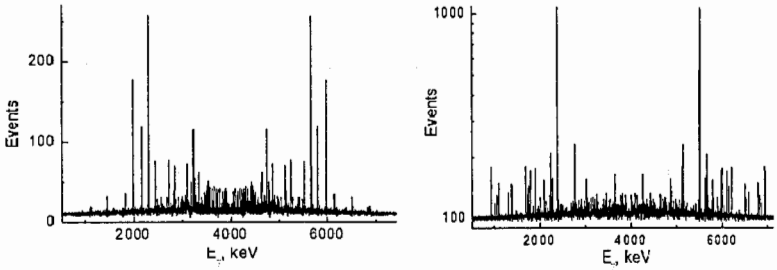

Fig. 3. TSC spectra corresponding to the cascade decays from the compound state to the ground state (left panel) and the final state $E_f = 78.8$ keV (right panel) of ^{172}Yb.

Fig. 3 shows the TSC spectra corresponding to the cascades decays from the compound state to the ground state and the first excited state $E_f = 78.8$ keV of ^{172}Yb. Within these TSC spectra, more than 66% of the collected events are belongs to the resolved cascade decays; consequently, the contribution of the unresolved cascade decays in the obtained gamma cascade intensity distributions are not larger than 33%. It is noted that the energy resolution and the symmetry of the TSC spectra are improved since the algorithm for digitally improving the energy resolution [4] were applied.

In order to determine the absolute intensity of the primary transitions within the investigated reaction, the gamma-rays intensities of 5538 keV transition were measured via the prompt gamma spectrum of a complex ^{27}Al+^{171}Yb target. The intensity of 5538 keV transition obtained within the present work is in agreement with that in Ref. [5] within the experimental uncertainty.

Data Analysis

Resolved cascade decays

A pair of gamma transition corresponding to the cascade decay from the compound state to a certain final state is represented as a pair of peak in the corresponding TSC spectrum. These two peaks are symmetrical via the center of the TSC spectrum, and their peak area is proportional to the cascade transition intensity. By determining the position and area of all the peaks in all the obtained TSC spectra, one can achieve a list of cascade transitions together with their relative intensities. These relative intensities are then converted to the absolute intensities using the intensity of a well-known primary transition, such as 5538 keV transition in the case of ^{172}Yb experiment.

Construction of the gamma cascade scheme

It is obvious that the gamma – gamma coincidence spectrometer does not provide information to identify the primary and secondary transitions of a certain cascade decay, therefore a method is needed to construct the gamma cascade scheme from the obtained list of cascade transitions. The maximum likelihood method [2] was known as an efficient one. Consequently, within the present work, the gamma cascade scheme is built by means of themaximum likelihood method.

Since the result obtained by using the maximum likelihood can be false in case of cascade transitions which appear in only one TSC spectrum, the data in Ref. [5] and the ENSDF library are also used as additional information to construct the gamma cascade scheme.

Unresolved cascade decays

A TSC spectrum consists of three components [6]:

1. a set of discrete peaks corresponding to the resolved transitions;
2. A number of low intensity transitions, also known as unresolved cascade decays;
3. And a noise line, which has zero average value.

As the resolved part of a TSC spectrum, which is caused by the resolved transitions, can be easily recreated using the list of resolved cascade decays, one can obtain the unresolved part of the TSC by subtracting the resolved part from the TSC spectrum. After that, the unresolved part of the TSC spectrum is averagely smoothed to remove the noise.

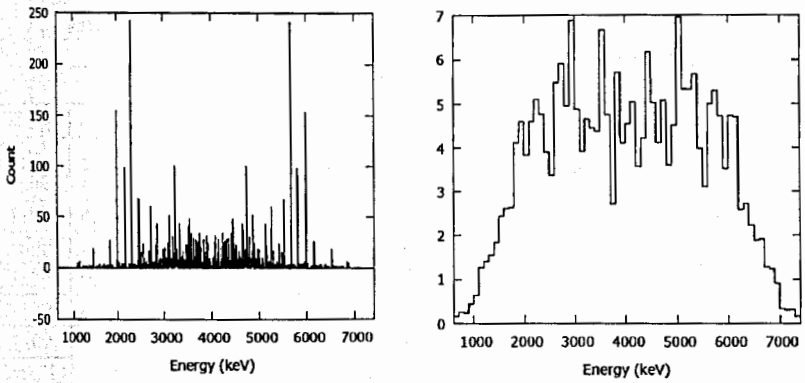

Fig. 4. The resolved part (left panel) and the unresolved part (right panel) of the TSC spectrum corresponding to cascade decay from the compound state to the ground state of ^{172}Yb (Fig.3, left panel). The unresolved part is averaged over 100 channels to remove the noise line.

Gamma cascade intensity distributions $I_{\gamma\gamma}(E_1)$

Since both primary and secondary transitions are accumulated in the TSC spectrum, the TSC spectrum is the sum of the primary gamma intensity distributions $I_{\gamma\gamma}(E_1)$ and secondary gamma intensity distributions $I_{\gamma\gamma}(E_2)$. Within the Dubna method, it is necessary to determine the $I_{\gamma\gamma}(E_1)$ as accurately as possible.

The resolved part of the $I_{\gamma\gamma}(E_1)$ can be easily determined as the maximum likelihood method allows us to determine a reliable nuclear level scheme based on the experimental list of discrete cascade transitions. However, the determination of the unresolved part of $I_{\gamma\gamma}(E_1)$ is complex because for this part, there is no information to separate the primary and secondary transitions. Because of the latter, in order to determine the unresolved part of $I_{\gamma\gamma}(E_1)$ we assume that the unresolved parts of $I_{\gamma\gamma}(E_1)$ and $I_{\gamma\gamma}(E_2)$ are identical in the unresolved part of the TSC spectrum (Fig. 4, right panel) [6]. Since this assumption can cause some distortions in the medium energy of the $I_{\gamma\gamma}(E_1)$ distributions, one should reduce the distortions by increasing the contribution of the resolved part. Besides, effects of the distortions on the nuclear level scheme and radiative strength function obtained using the Dubna method is insignificant in many cases [6].

Results and Discussion

Gamma cascade scheme

Table 1 present the list of obtained gamma cascades together with their intensity. These cascades decay from the compound state to the ground state and five low-lying states whose energies are 78.8, 1042.7, 1117.4, 1155.9 and 1197.3 keV. The uncertainty of the gamma cascade intensity is almost less than 30%. From this table, we can see that most of the resolved cascade are belongs to the decay to the ground state and the first excited state E_f = 78.8 keV. It is obvious that the spectroscopic data corresponding to these two final states are in high quality because of the very low Compton background under the corresponding summation peaks together with their large statistics. For the other final states, the spectroscopic data are worse due to the high Compton background. Additionally, the statistical count of the summation peaks corresponding to these final states are much less than those of the ground state and 78.8 kev state. For these reasons, only 79 cascades presented in the Table 1 belongs to the TSC spectra of 1042.7, 1117.4, 1155.9 and 1197.3 keV states.

Table 1. The gamma cascade scheme of ^{172}Yb. E_i is energy of intermediate states. $i_{\gamma\gamma}$ is absolute intensity of the cascade, normalized to 10^6 decays.

E_1+E_2=8020 keV									
E_1	E_i	$i_{\gamma\gamma}\pm\delta i_{\gamma\gamma}$	E_1	E_i	$i_{\gamma\gamma}\pm\delta i_{\gamma\gamma}$	E_1	E_i	$i_{\gamma\gamma}\pm\delta i_{\gamma\gamma}$
6902.6	1117.4	90±16	6864.6	1155.4	123± 25	6553.8	1466.2	180± 33
6542.9	1477.1	361± 41	6419.5	1600.5	66± 16	6410.9	1609.1	66±25
6312.1	1707.9	74±25	6240.9	1779.1	49±16	6170.5	1849.5	549± 66
6025.0	1995.0	107±33	6010.0	2010.0	3214± 139	5982.1	2037.9	139±33
5966.2	2053.8	107±33	5961.3	2058.7	107±33	5917.0	2103.0	98±33
5859.5	2160.5	98±33	5825.4	2194.6	2099±123	5708.4	2311.6	98±33
5691.7	2328.3	5158±197	5666.5	2353.5	98±33	5645.1	2374.9	90±33
5556.0	2464.0	180±33	5539.7	2480.3	1451±90	5531.7	2488.3	123±33
5516.2	2503.8	213±41	5495.1	2524.9	344±49	5481.9	2538.1	107±33
5445.1	2574.9	525±57	5437.8	2582.2	123±33	5421.6	2598.4	213±41
5398.7	2621.3	115±33	5381.4	2638.6	156±41	5353.6	2666.4	82
5272.7	2747.3	1328±107	5240.7	2776.3	131±41	5233.6	2786.4	164±41
5208.0	2812.0	115±41	5191.2	2828.8	156±41	5185.1	2834.9	279±57
5175.2	2845.4	484±74	5147.2	2872.8	976±90	5147.2	2872.8	139±41
5035.8	2984.2	205±49	4986.3	3033.7	230±49	4982.0	3038.0	443±57
4960.9	3059.1	139±33	4952.3	3067.7	221±41	4899.0	3121.0	377±49
4889.9	3130.1	1148±82	4881.9	3138.1	230±41	4867.0	3153.0	115±33
4860.1	3159.9	213±41	4854.3	3165.7	205±41	4835.3	3184.7	197±49
4814.5	3205.5	713±90	4805.6	3214.4	336±20	4798.6	3221.4	164±49
4789.5	3230.5	180±49	4765.2	3254.8	279±66	4758.9	3261.1	2255±164
4739.3	3280.7	287±66	4723.6	3296.4	435±82	4718.5	3301.5	328±74
4711.4	3308.6	205±57	4673.3	3346.7	968±90	4664.2	3355.8	172±41
4637.3	3382.7	238±49	4614.0	3406.0	254±66	4596.3	3423.7	377±57
4560.6	3459.4	180±41	4537.4	3482.6	533±66	4523.5	3496.5	385±90
4499.5	3520.9	533±74	4476.0	3544.0	910±90	4462.0	3558.0	1107±98

E_1+E_2=8020 keV								
E_1	E_i	$i_{\gamma\gamma}\pm\delta i_{\gamma\gamma}$	E_1	E_i	$i_{\gamma\gamma}\pm\delta i_{\gamma\gamma}$	E_1	E_i	$i_{\gamma\gamma}\pm\delta i_{\gamma\gamma}$
4449.5	3570.5	517±74	4427.3	3592.7	344±74	4421.6	3598.4	115±41
4414.8	3605.9	180±41	4385.0	3635.0	541±74	4360.4	3659.6	238±49
4351.1	3668.9	262±49	4344.8	3675.2	246±49	4338.2	3682.2	640±80
4321.1	3698.9	156±41	4304.8	3715.2	615±90	4299.2	3720.8	279±57
4278.5	3741.5	492±82	4272.3	3747.7	582±82	4263.6	3756.4	197±49
4252.2	3767.8	771±90	4220.2	3799.8	484±74	4210.9	3809.1	148±49
4172.7	3847.3	148±49	4154.5	3865.5	123±49	4144.0	3876.0	353±57
4124.5	3895.5	107±33	4111.9	3908.1	246±49	4102.5	3917.5	730±74
4093.6	3926.4	213±41	4063.1	3956.9	180±41	4057.4	3962.6	131±41
4046.7	3973.3	107±33	4040.9	3979.1	230±49	4036.0	3984.0	172±49
3941.3	4078.7	574±66	3857.2	4162.8	640±90	3788.7	4231.3	131±49
3641.3	4378.7	656±82	3588.2	4431.8	771±98	3491.8	4528.2	230±74
3440.2	4579.8	189±41	3429.6	4590.4	238±49	3409.8	4610.2	254±66
3388.3	4631.7	131±41	3337.9	4682.1	205±41	3289.3	4730.7	172±49
3245.4	4774.6	328±57	3191.4	4828.6	82±33	3177.9	4842.1	221±57
3146.8	4873.2	394±49	3098.0	4922.0	566±57	3071.9	4948.1	123±33
3022.8	4997.2	369±49	3004.0	5016.0	410±66	2997.1	5022.9	123±41
2942.2	5077.8	221±57	2919.1	5100.9	205±41	2866.9	5153.1	213±49
2839.8	5180.2	115±49	2818.2	5201.8	115±41			

E_1+E_2=7942 keV								
E_1	E_i	$i_{\gamma\gamma}\pm\delta i_{\gamma\gamma}$	E_1	E_i	$i_{\gamma\gamma}\pm\delta i_{\gamma\gamma}$	E_1	E_i	$i_{\gamma\gamma}\pm\delta i_{\gamma\gamma}$
6977.2	1042.8	1635±73	6902.6	1117.4	317±37	6864.6	1155.4	720±61
6821.5	1198.5	976±61	6656.9	1363.1	49±12	6615.5	1404.5	659± 61
6553.8	1466.2	451±49	6542.9	1477.1	988±73	6226.1	1793.9	1464±98
6170.5	1849.5	817±73	6125.7	1894.3	1671±98	6111.9	1908.1	85±24
6062.0	1958.0	183±49	6010.0	2010.0	1696±122	5973.0	2047.0	171±49
5946.6	2073.4	159±49	5917.0	2103.0	573±73	5825.4	2194.6	854±98
5792.5	2227.5	403±73	5743.5	2276.5	20724	5708.4	2311.6	476±73
5691.7	2328.3	2098±159	5678.2	2341.8	659±85	5645.1	2374.9	1196±134
5633.8	2386.2	195±61	5556.0	2464.0	268±61	5539.7	2480.3	22216± 537
5516.2	2503.8	366±61	5460.1	2559.9	207±49	5445.1	2574.9	232±49
5415.5	2604.5	183±49	5392.3	2627.7	195±49	5365.1	2654.9	146±49
5353.6	2666.4	122±49	5338.6	2681.4	171±49	5272.7	2747.3	146±49
5240.7	2776.3	220±61	5237.8	2782.2	146±61	5233.6	2786.4	171±49
5208.0	2812.0	256±61	5198.6	2821.4	220±49	5185.1	2834.9	390±61
5175.2	2845.4	220±60	5157.4	2862.6	378±73	5147.2	2872.8	2867±171
5140.2	2879.8	146±49	5131.8	2888.2	427±73	5060.0	2960.0	220±49

5035.8	2984.2	329±61		5028.7	2991.3	268±61		5007.2	3012.8	244±61
4989.2	3003.8	195±61		4982.0	3038.0	134±49		4952.3	3067.7	195±61
4926.6	309.4	281±61		4911.6	3108.4	195±61		4899.0	3121.0	1074±110
4889.9	3130.1	525±85		4881.9	3138.1	220±61		4805.6	3214.4	159±31
4779.4	3240.6	171±49		4771.3	3248.7	122±37		4758.9	3261.1	427±73
4739.3	3280.7	329±61		4728.7	3291.3	415±61		4718.5	3301.5	598±73
4685.2	3334.8	256±49		4673.3	3346.7	671±73		4637.3	3382.7	244±61
4623.7	3396.3	159±49		4596.3	3423.7	207±49		4560.6	3459.4	146±49
4527.0	3493.0	305±122		4523.5	3496.5	305±122		4499.5	3520.9	122±40
4493.4	3526.6	232±61		4476.0	3544.0	488±73		4462.0	3558.0	415±73
4442.2	3577.8	476±85		4433.7	3586.3	207±61		4421.6	3598.4	232±61
4414.8	3605.9	171±61		4393.2	3626.8	329±73		4338.2	3682.2	317±90
4321.1	3698.9	30573		4315.1	3704.9	317±73		4304.8	3715.2	378±110
4278.5	3741.5	159±61		4272.3	3747.7	1061±110		4263.6	3756.4	464±73
4252.2	3767.8	378±73		4220.2	3799.8	281±61		4210.9	3809.1	293±61
4195.0	3825.0	220±61		4172.7	3847.3	256±61		4165.8	3854.2	293±73
4144.0	3876.0	805±98		4138.9	3881.1	183±61		4124.5	3895.5	146±49
4111.9	3908.1	439±85		4102.5	3917.5	610±98		4060.4	3959.6	232±61
4036.0	3984.0	415±85		4031.1	3988.9	586±98		4020.1	3999.9	195±61
3975.5	4044.5	171±49		3941.3	4078.7	98±37		3857.2	4162.8	305±73
3788.7	4231.3	110±49		3641.3	4378.7	342±98		3579.1	4440.9	378±73
3491.8	4528.2	659±98		3473.9	4546.1	122±49		3429.6	4590.4	354±61
3409.8	4610.2	305±73		3388.3	4631.7	378±61		3337.9	4682.1	98±49
3289.3	4730.7	366±73		3233.0	4787.0	159±49		3191.4	4828.6	378±61
3177.9	4842.1	500±85		3146.8	4873.2	512±73		3098.0	4922.0	293±73
3071.9	4948.1	134±61		3022.8	4997.2	293±61		3004.0	5016.0	244±61
2997.1	5022.9	512±85		2942.2	5077.8	671±85		2919.1	5100.9	220±61
2866.9	5153.1	488±73		2839.8	5180.2	171±49		2818.2	5201.8	183±49

E_1+E_2=6977 keV									
E_1	E_i	$i_{\gamma\gamma}\pm\delta i_{\gamma\gamma}$	E_1	E_i	$i_{\gamma\gamma}\pm\delta i_{\gamma\gamma}$	E_1	E_i	$i_{\gamma\gamma}\pm\delta i_{\gamma}$
6012.3	2007.7	220±41	5825.4	2194.6	142±43	5539.7	2480.3	562±113
5495.1	2524.9	110±41	5392.3	2627.7	376±97	5028.7	2991.3	344±119
4968.0	3052.0	214±90	4577.4	3442.6	767±349	4523.5	3496.5	535±275
4338.2	3682.2	171±67	4220.2	3799.8	259±81	3513.6	4506.4	198±74
3491.8	4528.2	257±83	3245.4	4774.6	166±76	3233.0	4787.0	328±99

E_1+E_2=6902 keV								
E_1	E_i	$i_{\gamma\gamma}\pm\delta i_{\gamma\gamma}$	E_1	E_i	$i_{\gamma\gamma}\pm\delta i_{\gamma\gamma}$	E_1	E_i	$i_{\gamma\gamma}\pm\delta i_{\gamma}$
6194.4	1825.6	118±27	6111.9	1908.1	55±19	6010.0	2010.0	92±29
5825.4	2194.6	937±132	5604.0	2416.0	164±71	5539.7	2480.3	850±172
5412.3	2607.7	231±74	5392.3	2627.7	399±97	5175.2	2845.4	130±48
5131.8	2888.2	122±48	4877.0	3143.0	309±84	4523.5	3496.5	386±151

4501.8	3518.2	708±227		4338.2	3682.2	250±82		4252.2	3767.8	132±63

E_1+E_2=6864 keV									
E_1	E_i	$i_{\gamma\gamma}\pm\delta i_{\gamma\gamma}$		E_1	E_i	$i_{\gamma\gamma}\pm\delta i_{\gamma\gamma}$		E_1	E_i	$i_{\gamma\gamma}\pm\delta i_{\gamma\gamma}$
5825.4	2194.6	905±107		5743.5	2276.5	128±44		5708.4	2311.6	113±40
5691.7	2328.3	71±29		5539.7	2480.3	605±134		5028.7	2991.3	273±92
4758.9	3261.1	225±80		4637.3	3382.7	441±120		4534.2	3485.8	223±113
4462.0	3558.0	483±176		4269.3	3750.7	218±78		3588.2	4431.4	229±90
3579.1	4440.9	397±109		3409.8	4610.2	225±90				

E_1+E_2=6823 keV									
E_1	E_i	$i_{\gamma\gamma}\pm\delta i_{\gamma\gamma}$		E_1	E_i	$i_{\gamma\gamma}\pm\delta i_{\gamma\gamma}$		E_1	E_i	$i_{\gamma\gamma}\pm\delta i_{\gamma\gamma}$
5825.4	2194.6	1410±177		5539.7	2480.3	1413±237		5028.7	2991.3	459±144
4982.0	3038.0	378±132		4782.0	3238.0	183±84		4758.9	3261.1	345±135
4637.3	3382.7	525±171		4493.4	3526.6	348±129		4462.0	3558.0	327±120
4418.3	3601.7	681±273		4278.5	3741.5	261±183		3878.4	4141.6	342±117
3612.4	4407.6	414±120		3588.2	4431.8	414±120		3579.1	4440.9	321±108
3289.3	4730.7	303±111								

In general, most of our obtained data are in agreement with data in Ref. [5] and in the ENSDF library [7]. The consistency proves the reliability of the obtained gamma cascade scheme within our work.

Gamma cascade intensity distributions

The gamma cascade intensity distributions of ^{172}Yb determined from all six measured TSC spectra are shown in Fig. 5. The large statistics of counts allow us to determine the gamma cascade intensity distributions over a 250 keV energy interval. This energy interval is twice less than the interval of all 43 investigated nuclei [3]. Therefore, the analysis of the data of ^{172}Yb obtained in the present work is more precise than for all the previous investigated nuclei [3].

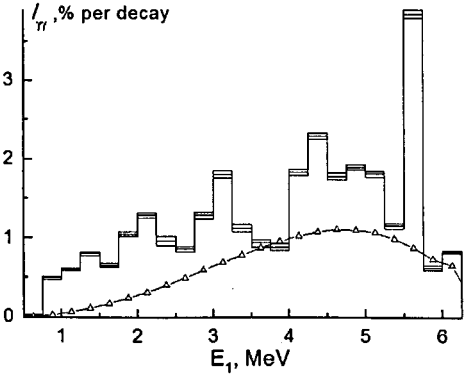

Fig. 5. The gamma cascade intensity via primary gamma energy (E_1). The triangle is $I_{\gamma\gamma}(E_1)$ calculated from the combination of models [8] for nuclear level scheme and [9] for radiative strength function.

In the Fig. 5, the experimental $I_{\gamma\gamma}(E_1)$ is compared with the $I_{\gamma\gamma}(E_1)$ calculated from the combination of nuclear level density [8] and radiative strength function [9] models. There is a clear discrepancy between the experimental $I_{\gamma\gamma}(E_1)$ and that obtained by calculation. Thus, it is needed to use other models for both the nuclear level density and radiative strength function, such as those proposed in Ref. [10].

Conclusion

Within the present work,the gamma cascade intensity distributions of ^{172}Yb was determined for 250 keV energy intervals. Thanks to the large statistics of counts, the obtained data of ^{172}Yb is more precise than any other nuclei, which we have investigated earlier using the Dubna method. The forthcoming studies are to analyze the obtained data here by means of the Dubna method in order to extract the nuclear level density and radiative strength function of ^{172}Yb.

References

1. *Reference Input Parameter Library RIPL-2, Handbook for calculations of nuclear reaction data*, IAEA-TECDOC (2002).
2. S.T. Boneva et al., Sov. J. Part. Nucl. **22** (1991)232.
3. A.M. Sukhovoj, L.V. Mitsyna, N. Jovancevic, Phys. Atom. Nucl. **79** (2016)313.
4. A.M. Sukhovoj, V.A. Khitrov, Instrum. Exp. Tech., **27** (1984)1071.
5. R.C. Greenwood, C.W. Reich, and S.H. Egors, Jr. Nucl. Phys., **262** (1975)260.
6. S.T. Boneva, A.M. Sukhovoj, V.A. Khitrov, and A.V. Voinov, Nucl. Phys. **589** (1995)293.
7. http://www-nds.iaea.org/ENDSF
8. W. Dilg, W. Schantl, H. Vonach, and M. Uhl, Nucl. Phys. A **217** (1973)269.
9. S.G. Kadmenskij, V.P. Markushev and W.I. Furman, Sov. J. Nucl. Phys. **37** (1983)165.
10. A.M. Sukhovoj, Phys. Atom. Nucl. **78** (2015)230.

TWO METHODS OF THE DETERMINATION OF THE PARITIES OF LOW-LYING STATES IN ^{159}Gd FROM ANALYSIS OF THE γ-RAY INTENSITIES FROM REACTION ^{158}Gd$(n_{res},\gamma)^{159}$Gd

C. Granja [a], *J. Kubasta* [b], *S. Pospisil* [a], *S.A. Telezhnikov* [c 1]

[a]Institute of Experimental and Applied Physics, Czech Technical University, 128 00 Prague 2, Czech Republic

[b]Faculty of Nuclear Sciences and Physical Engineering, Czech Technical University, CZ-11819 Prague 1, Czech Republic

[c]Frank Laboratory of Neutron Physics, JINR, 141980 Dubna, Moscow reg, Russia

ABSTRACT

Energy levels and transitions in ^{159}Gd were studied by means of radiative capture of resonance neutrons at 12 isolated resonances of ^{158}Gd. The time-of-flight technique was used on an enriched target at the IBR-30 reactor at JINR Dubna. A total of 80 primary gamma-transitions were recorded and their absolute intensities were determined resulting in the observation of $1/2^{\pm}$, $3/2^{\pm}$ levels up to 2.4 MeV. Parities of found levels were recalculated using two methods: the first method consists in analyzing of intensities averaging in 12 resonances and in the second method individual intensities are analyzed. The second method is described for the first time.

1. INTRODUCTION

We extensively studied spectroscopic properties of ^{159}Gd by resonance neutrons [1,2], by neutrons from neutron filters [3], by thermal neutrons and from (d,p) and (d,t) reactions. Full information was published in [4].

In [2] together with the other information the determination of parities of low lying levels of ^{159}Gd was obtained. Due to big volume of information in that work description of the method of this determination is very short. In this work we must to give more detailed description of procedure of parity determinations. During preparation of this work we recalculated all data and there are some differences between results of previous work ([2], Table 3) and new results. Analysis of these differences will be done later.

2. EXPERIMENT

Energy levels and transitions in ^{159}Gd were studied by means of radiative capture of resonance neutrons at 12 isolated resonances of ^{158}Gd. The time-of-flight technique was used on an enriched target at the IBR-30 reactor at JINR Dubna. A total of 80 primary gamma-transitions were recorded and their absolute intensities were determined. Absolute intensities of 80 transitions in 12 resonances of ^{158}Gd are presented in [2] (Table 1).

As ^{158}Gd is even-even nucleus all resonances in measured range of neutron energy have $J^{\pi} = 1/2^{+}$. Primary γ-rays usually are E1 (transitions on the levels with the

[1]Corresponding author.

E-mail address: telezhni@nf.jinr.ru (S.A.Telezhnikov)

opposite parity) and M1 (transitions on the levels with the same parities). Levels on which transitions pass have J=1/2, 3/2 with parity + if transition is M1 or - if transition is E1. M1 transitions have energy dependence E_γ^3 and dependence of E1 transitions is more sharply namely about E_γ^5. It is known that intensities of E1 transitions in measured range of energies are in 5-7 times more than of M1 transitions. From spectroscopic data 8 M1 transitions and 9 E1 transitions are known.

3. TASK OF PARITY DETERMINATION

Using the difference in intensities of E1 and M1 transitions we formulated and decided quantitative conditions of parity determination of low lying levels in ^{159}Gd. Two methods of the parity determination were used by us: the first method consists in analyzing of intensities averaging in 12 resonances and in the second method individual intensities are analyzed. The second method is described for the first time.

3a. The first method

80 intensities averaged in 12 resonances were obtained. From these data dependence E_γ^3 was excluded and reduced data were normalized on mean value of reduced intensities of 8 known M1 transitions. Here formula of reducing is shown:

$$\xi_{\gamma f} = \{< I_{\gamma\lambda f} >_\lambda / E_\gamma^3\} / \{<< I(M1)_{\gamma\lambda f} >_\lambda / E_\gamma^3 >_{M1}\}, \quad (1)$$

where λ is sign of resonance and f is sign of final state.

Values $\xi_{\gamma f}$ of 80 transitions are presented in Fig. 1. There are two curves and straight line in this Figure: curves are dependences of E1 transitions (E_γ^5) which normalization was from 9 known E1 transitions - upper curve and from 8 known E1 transition - lower curve. Straight line is mean of 8 known M1 transitions, its y = 1.

As point about energy 5400 keV (transition 5384.70 keV) is very high two curves for E1 normalizing are plotted: upper curve with use this point and lower curve is without this point. Later meaning of these two curves will be discussed.

It is clearly seen that intensities of E1 transitions are good separated from intensities of M1 in range 4700-6000 keV. This fact gives opportunity to use intensities for separation all intensities in two groups. For this we use statistical properties of intensities. It is known that intensities of transitions from resonances of one type to the levels with certain J^π follow Porter-Thomas (PT) law of distribution [5]. This distribution is from class of χ^2 distributions, namely χ^2 distribution with ν=1. Mean value of intensities from 12 resonances will obey χ^2 distribution with ν=12. To determine that some transition is E1 we must show that it can not be from distribution which describe M1 transitions.

For deciding if point of examined transition obeys or not obeys analyzed distribution the confidence level must be chosen. In our works we use two confidence levels: 1% and 0.1%. For these two confidence levels critical values must be found. These are values of x integrals to which from the left or from the right are equal to confidence level. When event falls in the piece p1 with confidence level 0.1% this hypothesis is abandoned hardly and result of other hypothesis is set without parentheses and when event falls in the piece p2 with confidence level 1% other hypothesis is set in parentheses. We shell use term reability which determines integral of the distribution from the left to the tested point. This value

will be close to 0 if point is to the left from maximum of the distribution or close to 1 if point is to the right from maximum.

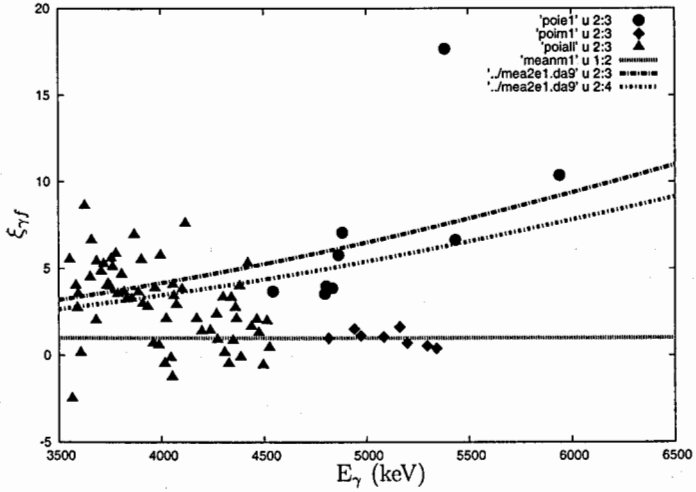

Fig. 1. Values $\xi_{\gamma f}$ of 80 γ-transitions (points), 2 curves – dependences of E1 and stright line – dependence of M1; • –known E1, ♦ – known M1, ▲ – unknown parities.

We must create statistical distribution which picture this hypothesis and see how point of examined transition is far from the center of distribution. As distribution is normalized on 1 probability to appear accidentally in any piece of this distribution is equal to area of distribution within this piece. For events far to the left and far to the right from the center of distribution probabilities are integrals from the beginning of distribution to this event for events far to the left and from this event to the end of distribution for events far to the right. An example of arbitrary distribution is shown in Fig.2.

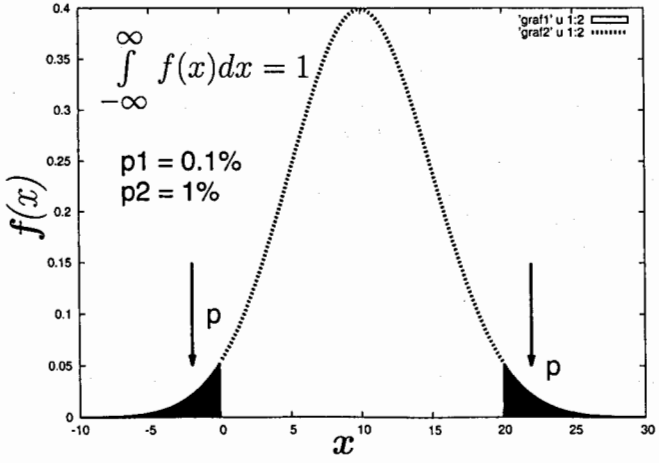

Fig. 2. Arbitrary function $f(x)$ normalyzed on 1

It was said that mean value of intensities from 12 resonances will obey χ^2 distribution with ν=12. But apart of this distribution each intensity of transition has its statistical error which obeys Gaussian distribution. Hence χ^2 distribution with ν=12 must be convoluted with Gaussian with individual statistical error of each intensity.

To find E1 transitions it is need:

- to normalize all experimental intensities on mean M1 value;
- to obtain χ^2 distribution with ν=12;
- to make convolution of this distribution with Gaussian which is individual for each point;
- to find critical values for two confidence levels;
- to find value reability which will be integral from the left, this value will be close to 1 as E1 transitions are greater than M1;
- to compare this value with two critical values.

To find M1 transitions we must compare intensities which are normalized on mean of E1 transitions after excluding of energy dependance of these transitions with χ^2 distribution. For this dependence of E1 transitions must be eliminated. In [2] two dependences of E1 transitions were discussed: Lorencian and Markushev-Furman model. But in this work we use simple dependence E_γ^5 because this dependence is more sharply than others and this gives more reliable results in energy range from 3.5 to 4.5 MeV as curve E_γ^5 is more near to M1 points.

Now we must discuss about two curves in Fig.1. Upper curve is obtained with use point 5384.70 keV. During analysis of points with normalizing on E1 with lower curve this point was very big and it was determined as doublet. At next doublets will be marked as D or (D). In view of this upper curve did not used and all calculations were made with lover curve. Using method described upper points which are lover than critical values can be determined as M1 or (M1) and points which are higher than critical values with integrals near 1 can be determined as D or (D).

3b. The second method

This method consists in analysis of absolute intensities of each transition from resonances to each level. As number of resonances is 12 we have twelve distributions for each level. Statistical distribution of these values is PT distribution. This distribution must be convoluted with Gaussian from the statistical error of transition. By such way twelve values of reability can be obtain. These values must be analyzed. They represent 12 points on [0,1] cut. Now we try to obtain quantitative conditions to refuse hypothesis that twelve transitions on one level belong to obtained distributions.

Divide [0:1] cut by point on two pieces p and q. We know that p is small part of cut [0:1].

$$p + q = 1$$

From 12 resonances we have 12 independent probabilities and whole probability is:

$$(p + q)^{12} = 1$$

It is Newton's binomial. Reveal parenthesis:

$$p^{12}+12p^{11}q+66p^{10}q^2+220p^9q^3+495p^8q^4+792p^7q^5+924p^6q^6+792p^5q^7+495p^4q^8+$$
$$220p^3q^9+66p^2q^{10}+12pq^{11}+q^{12}=1$$

Now analyze some member of this expression, for instance, the forth: $220p^9q^3$. This member is the probability that 9 points fall to part p. If we solve the equation $220p^9q^3 = 0.001$ or $220p^9q^3 = 0.01$ we can obtain critical values which say that probability to have 9 point in piece p is 0.1% or 1%.

By such way we can obtain all 12 pairs of critical values for all members with p of this expression. Now for all 80 transitions it is need to do convolutions of one function of PT with the individual Gaussian from experimental errors and to find set of 12 reability values. These data can be compared with critical values.

4. CALCULATIONS

We must:

- to obtain Gaussian, χ^2 distribution with ν=1, χ^2 distribution with ν=12;
- to make convolution of χ^2 distributions with Gaussians which are individual for each intensity;
- to find critical values for two confidence levels for χ^2 distribution with ν=12;
- to find reability values for ν=12;
- to calculate critical values for 12 pairs of confidence levels for ν=1;
- to analyze all data and obtain parities by two methods.

It is seen in Fig. 2 that bounds of p pieces are set far from maxima of distributions and integrating must be to the area with small values of functions.

For better precision all calculations were made in Fortran codes with variables REAL*16. Calculations with such variables give precision of results with about 33 right signs.

For making of convolution all curves were replaced by piecewise continuous polynomials of the third power throw each 4 points of x coordinates with different steps which were determined as gave high precision of replacing. Precision of replacing was tested by integrating of curves and comparing of integrals with 1. In Table 1 parameters of fit of some functions by polynomials are shown: N – numbers of points of x coordinates, Area – integrals and NR – number of right signs in integrals obtained. It is seen that precision depends on number of points x.

Table 1. Parameters of polynomials for 4 functions: N – number of points x, Area – integral, NR – number of right signs in integrals

Function	N	Area	NR
Gaussian	2031	0.999999999897369E+00	9
χ^2 with $\nu = 1$	1463	0.999999991390689E+00	8
χ^2 with $\nu = 2$	5594	0.999999999999126E+00	12
χ^2 with $\nu = 12$	1950	0.999999998204125E+00	8

Function χ^2 with $\nu = 2$ is very simple function: $exp(-x)$. It was not used and provides as example. The most computer time is spent for convolutions. In [2] these calculations were provided in old system UNIX or SANOS and time of calculations was limited. Because of this calculations were made with smaller precision of convolutions: namely, 5 or 6 signs.

Now calculations were made on modern desktop computer and 8 signs of precision were achieved. This is source of differences between old and new results which will be discussed later. The most time was spent in method 2 as there must be 12 convolutions for each of 80 levels.

Borders of reability for 4 confidence levels were calculated and are shown in Table 2. These borders were tested by Monte-Carlo simulation. In Monte-Carlo 12 random numbers were generated and events which fall to pieces with borders from Table 2 were added in four counters. Results are shown in Table 3.

Table 2. Borders of reability for 4 confidence levels (Led) at the end of the cut [0,1].

Led n	20%	10%	1%	0.1%
1	0.97893530	0.99077201	0.99915892	0.99991661
2	0.91343027	0.94958514	0.98684847	0.99602932
3	0.83148438	0.89147431	0.95961344	0.98253584
4	0.74358207	0.82471770	0.92095554	0.95900744
5	0.65528965	0.75295264	0.87335509	0.92642683
6	0.57046992	0.67804360	0.81823516	0.88558257
7	0.49108195	0.60097700	0.75631922	0.83685452
8	0.41670281	0.52218020	0.68779033	0.78017426
9	0.34546533	0.44160458	0.61227202	0.71491122
10	0.27519742	0.35861242	0.52855957	0.63952595
11	0.20343767	0.27143469	0.43368423	0.55049646
12	0.12551473	0.17459582	0.31870794	0.43765867

Table 3. Monte-Carlo test of 4 borders of confidence levels (Led). 1 billion of 12 random numbers was generated.

Led n	20%	10%	1%	0.1%
1	199988356	99997723	9999206	1000541
2	200003147	99993970	10001449	1001716
3	199990133	100008878	9997067	1000800
4	199982567	100009826	9999704	999397
5	199995607	100006117	9996229	1001007
6	199991386	100020255	10002878	1001937
7	200022638	100009744	9999832	1002330
8	200021065	100013733	9995901	1001405
9	200017754	100004531	10001494	1000768
10	200010661	99996432	10001575	1000500
11	200009661	100005569	9998226	1000163
12	200001707	100005309	10003698	1000244

5. RESULTS AND DISCUSSION

Results of the determination of parities are lead in Table 4. This Table is similar to Table 3 in [2]. Only when in the second column of Table 3 in [2] f_γ are listed here in

column 5 values $\xi_{\gamma f}$ from the expression (1) are lead and when in that Table there was column Resonance here number of points on [0,1] cut for which appropriate confidence level was performed are listed. The more of these groups results are reliable.

Now results which are worse than in [2] will be listed. As for transition 4474.4 keV in [2] was parity (+) now parity is not determined. For transitions 4348.4, 4308.0 and 4053.5 keV results from + became (+).

For some transitions now results are better: for 4381.7 and 3720.6 keV results are changed from (-) to - without parenthesis. In Table 3 in [2] there are 3 columns with the determination of *XL*. For 5384.7 keV in these columns there are E1 determinations. Now all 3 values of *XL* of transition 5384.7 keV are changed from E1 to D. This indicates probability of non-statistical big intensity of this transition. For transitions 3780.4, 3720.6, 3662.1 and 3655.0 keV values of *XL* became (D).

These results demonstrate importance of precision of calculations for more reliable determination of parities.

Now analysis of differences in parity determination by two methods will be obtained. Schematic comparison of results is shown in Fig. 3.

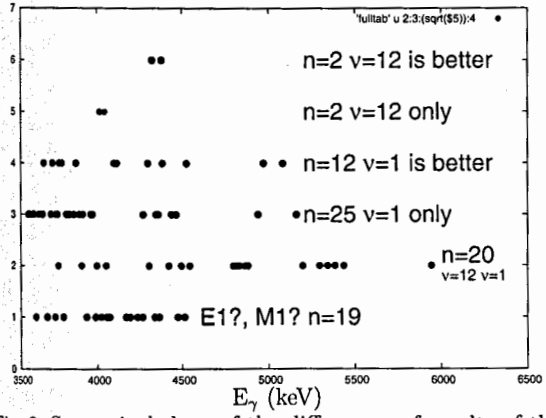

Fig. 3. Scematical show of the differences of results of the determination of parities by two methods (method 1 and method 2).

In this scheme is seen that for 19 transitions parities were not determinated. For 20 transitions determinations by two methods coincide. For 25 transitions determinations are obtained only by the second method and for two transitions determination by the second method is more precise. For two transitions determination is obtain only by the first method and for two transitions this method gave more precise result. This demonstrate that method 2 is more hard criterion then method 1.

There are many D and (D) determinations for transitions in the region 3500 - 4500 keV. This can demonstrate that E_γ^5 is very sharp and Lorencian or Markushev-Furman model may be more real.

Table 4. Final assignments of transition multipolarity XL are based on the analysis of analytically averaged (a) and of individual (b) γ-ray intensities. All observed levels have either spin 1/2 or 3/2 with parity as indicated. Assignments are made within 0.1% significance level (assignments within 1% are indicated in parenthesis)

E_γ [keV]	ΔE_γ	$\xi_{\gamma f}$	$\Delta\xi_{\gamma f}$	Groups[a]	Multipolarity[b] $XL(a)$	$XL(b)$	XL	E_f [keV]	j^π $\frac{1}{2}^\pi, \frac{3}{2}^\pi$
5943.0	0.2	10.4	0.3	1 2 3 4 5 6 7 8 9 10 11	E1	E1	E1	0.0	-
5434.7	0.2	6.6	0.3	1 2 3 4 9 10 11 12	E1	E1	E1	508.3	-
5384.7	0.2	17.7	0.6	2	D	D	D	558.3	-
5341.1	0.3	0.4	0.3	9 10 11 12	M1	M1	M1	601.9	+
5295.9	0.5	0.6	0.3	11 12	M1	M1	M1	647.1	+
5198.1	0.2	0.7	0.3	10 11 12	M1	M1	M1	744.9	+
5161.0	0.5	1.6	0.3	11		M1	M1	782.0	+
5083.0	0.6	1.1	0.3	11	(M1)	M1	M1	860.0	+
4971.0	1.3	1.1	0.5	11	(M1)	M1	M1	972.0	+
4939.7	1.0	1.5	0.4	12		(M1)	(M1)	1003.3	(+)
4881.7	0.3	7.1	0.5	1 2 3 4 5 6 10	E1	E1	E1	1061.3	-
4863.5	0.2	5.8	0.4	1 2 3 4 5 6 7	E1	E1	E1	1079.5	-
4832.2	0.3	3.9	0.5	3	E1	E1	E1	1110.8	-
4814.4	0.3	1.0	0.4	2 10	(M1)	(M1)	(M1)	1128.6	(+)
4803.3	0.2	4.0	0.5	3 4 5 6	E1	E1	E1	1139.7	-
4796.9	0.2	3.5	0.5	2 3 4 5	E1	E1	E1	1146.1	-
4543.7	1.1	3.7	0.6	7 8 9	E1	E1	E1	1399.3	-
4526.1	1.3	0.5	0.6	11	(M1)	M1	M1	1416.9	+
4513.4	1.2	2.0	0.6					1429.6	
4495.2	1.3	-0.6	0.6	3 5 12	M1	M1	M1	1447.8	+
4474.4	1.2	1.3	0.6					1468.6	
4464.7	0.3	2.1	0.6	5		(E1)	(E1)	1478.3	(-)
4438.6	0.8	1.7	0.6	10		(M1)	(M1)	1504.4	(+)
4421.7	0.5	5.3	0.7	1 4 5 6 7 8	E1	E1	E1	1521.3	-
4385.9	1.0	-0.1	0.8	10	(M1)	M1	M1	1557.1	+
4381.7	0.5	4.0	0.8	1 6 7 8 9 11	E1	(E1)	E1	1561.3	-
4366.0	1.4	2.1	0.8					1577.0	
4360.7	0.9	2.8	0.8	5 9 10 11		(E1)	(E1)	1582.3	(-)
4348.4	1.5	0.9	0.8	10 11 12		(M1)	(M1)	1594.6	(+)
4340.4	1.5	3.3	1.4					1602.6	
4327.9	0.6	-0.5	0.8	6 7 9 10 11 12	M1	(M1)	M1	1615.1	+
4308.0	1.0	0.2	0.8	9 10 11	(M1)	(M1)	(M1)	1635.0	(+)
4301.4	0.8	3.3	0.8	9	(E1)	E1	E1	1641.6	-
4273.2	1.5	0.9	0.9	10		(M1)	(M1)	1669.8	(+)
4268.8	0.8	2.4	0.9					1674.2	
4238.4	1.0	1.4	0.8					1704.6	
4197.0	1.0	1.4	0.9					1746.0	
4172.7	0.9	2.1	0.9					1770.3	
4118.5	0.4	7.6	1.0	10	E1	D	D	1824.5	-
4102.1	1.5	3.8	1.0	10	(E1)	E1	E1	1840.9	-
4074.5	0.3	2.9	1.0					1868.5	
4062.3	1.0	3.4	1.2					1880.7	

(cont.)

Table 4 (continued)

E_γ [keV]	ΔE_γ	$\xi_{\gamma f}$	$\Delta\xi_{\gamma f}$	Groups[a]	Multipolarity[b]			E_f [keV]	j^π $\frac{1}{2}^\pi, \frac{3}{2}^\pi$
					XL(a)	*XL(b)*	*XL*		
4057.7	1.5	4.1	1.3					1885.3	
4053.5	2.0	-1.2	1.2	5 9 10 11 12	(M1)	(M1)	(M1)	1889.5	(+)
4046.2	3.0	-0.2	1.0		(M1)		(M1)	1896.8	(+)
4024.5	1.0	2.1	1.1					1918.5	
4017.0	0.9	-0.5	1.1		(M1)		(M1)	1926.0	(+)
3997.6	0.8	5.7	1.2	2 3 4 5 6 7 8 9	E1	E1	E1	1945.4	-
3988.6	0.5	0.6	1.2					1954.4	
3970.9	0.3	3.9	1.3	1 2		(E1)	(E1)	1972.1	(-)
3961.4	1.0	0.7	1.3	12		(M1)	(M1)	1981.6	(+)
3934.9	2.5	2.8	1.4					2008.1	
3911.3	1.7	3.0	1.3	2 6		(E1)	(E1)	2031.7	(-)
3904.7	1.7	5.5	1.3	3 4 5 6 8	E1	E1	E1	2038.3	-
3890.0	2.5	3.6	1.3	4 5 6		E1	E1	2053.0	-
3870.4	0.4	6.9	1.4	12	E1	(D)	(D)	2072.6	-
3856.8	1.7	3.3	1.4	1		(E1)	(E1)	2086.2	(-)
3831.6	0.7	3.2	1.5	6		(E1)	(E1)	2111.4	(-)
3821.1	1.7	3.6	1.5	9 10		(E1)	(E1)	2121.9	(-)
3808.7	1.7	4.7	1.5	5 6		(E1)	(E1)	2134.3	(-)
3789.6	1.0	3.5	1.5					2153.4	
3780.4	1.0	5.8	1.6	12	(E1)	(D)	(D)	2162.6	-
3764.3	1.0	5.1	1.5	2 3 4 5	(E1)	E1	E1	2178.7	-
3758.0	1.0	5.6	1.6	2 7 9 10 11 12	(E1)	(E1)	(E1)	2185.0	(-)
3752.2	1.4	4.0	1.6	3 7		(E1)	(E1)	2190.8	(-)
3742.2	1.0	4.1	1.6	8		(E1)	(E1)	2200.8	(-)
3736.4	1.6	4.0	1.7					2206.6	
3720.6	0.8	5.3	1.7	11	(E1)	(D)	(D)	2222.4	-
3709.0	1.0	4.8	1.7	11		(E1)	(E1)	2234.0	(-)
3686.9	1.0	5.4	2.0					2256.1	
3683.2	0.8	2.0	2.0					2259.8	
3662.1	0.7	6.6	2.0	8 9	(E1)	(D)	(D)	2280.9	-
3655.0	1.0	4.5	1.9	7		(D)	(D)	2288.0	-
3628.7	0.7	8.6	3.7	12		(D)	(D)	2314.3	-
3607.6	0.8	0.2	2.1					2335.4	
3596.0	0.5	3.5	2.2	1		(E1)	(E1)	2347.0	(-)
3591.7	1.7	2.7	2.1	1		E1	E1	2351.3	-
3585.2	0.5	4.0	2.2	1		(E1)	(E1)	2357.8	(-)
3565.4	0.8	-2.5	2.1	7		(M1)	(M1)	2377.6	(+)
3554.4	0.8	5.5	2.2	1 2 3 4		(E1)	(E1)	2388.6	(-)

[a] Numbers of points on [0,1] cut for which appropriate confidence level was performed

[b] Transitions with unusually strong intensities are labelled by D to indicate the possibility of a doublet or of a non-statistically large fluctuation.

SUPPLEMENT

As we have software toolkit to calculate integrals of some functions we prepared some tables. We hope that these data will have more wide set of arguments and more precise values than that which usually can be received from the Internet.

S1 Table of values of $\Phi(x) = \frac{1}{\sqrt{2\pi}} \int_x^\infty exp(-\frac{z^2}{2})dz$ for integer values of argument.

x	$\Phi(x)$
1.00	1.5865525E-01
2.00	2.2750132E-02
3.00	1.3498980E-03
4.00	3.1671242E-05
5.00	2.8665157E-07
6.00	9.8658764E-10
7.00	1.2798125E-12
8.00	6.2209606E-16
9.00	1.1285884E-19
10.00	7.6198530E-24
11.00	1.9106596E-28
12.00	1.7764821E-33
13.00	6.1171566E-39

S2 Table of reverse values for $\Phi(x) = \frac{1}{\sqrt{2\pi}} \int_x^\infty exp(-\frac{z^2}{2})dz$ for values of 10^{-n} of $\Phi(x)$

$\Phi(x)$	x
1.0E-01	1.2815516E+00
1.0E-02	2.3263479E+00
1.0E-03	3.0902323E+00
1.0E-04	3.7190165E+00
1.0E-05	4.2648908E+00
1.0E-06	4.7534243E+00
1.0E-07	5.1993376E+00
1.0E-08	5.6120012E+00
1.0E-09	5.9978070E+00
1.0E-10	6.3613409E+00
1.0E-11	6.7060232E+00
1.0E-12	7.0344838E+00
1.0E-13	7.3487961E+00
1.0E-14	7.6506281E+00
1.0E-15	7.9413453E+00
1.0E-16	8.2220822E+00
1.0E-17	8.4937932E+00
1.0E-18	8.7572903E+00
1.0E-19	9.0132712E+00
1.0E-20	9.2623401E+00
1.0E-21	9.5050250E+00
1.0E-22	9.7417899E+00
1.0E-23	9.9730456E+00
1.0E-24	1.0199157E+01
1.0E-25	1.0420452E+01
1.0E-26	1.0637224E+01

REFERENCES

- *Pospisil S., Becvar F., Granja Bustamante C., Kubasta J. and Telezhnikov S.A.* Secondary γ Transitions in ^{159}Gd After Neutron Capture at Isolated Resonances J. Res. Natl. Inst. Stand. Technol. 2000.V.105.P.173.

- *Granja C., Pospisil S., Kubasta J.and Telezhnikov S.A.* Primary gamma transitions in ^{159}Gd after isolated resonance neutron capture Nuclear Physics A 2003.V.724.P.14-28.

- *Granja C., Pospisil S., Telezhnikov S.A. and Chrien R.E.* Levels of ^{159}Gd populated in average resonance neutron capture Nuclear Physics A 2003.V.729.P.679-698.

- *Granja C., Pospisil S., Aprahamian A., Borner H., Lehmann H., von Egidy T., Wirth H.-F. Graw G., Hertenberger R., Eisermann Y., Nosek D., Rubacek L. and Telezhnikov S.A.* Nuclear structure of ^{159}Gd Physical Review C 2004.V.70.P.034316.

- *Porter C. E. and Thomas R. G.* Fluctuations of Nuclear Reaction Widths Physical Review 1956.V.104.P.483.

CROSS SECTIONS STRUCTURE RESEARCH AT INR SPALLATION NEUTRON SOURCE INSTALLATION INES

Khliustin D.V., Djilkibaev R.M., Vasilev I.A.

Institute for Nuclear Research Russian, Academy of Sciences
117312, Russia, Moscow, prospect 60-letiya Oktyabrya, 7A

Abstract. Calibration results of installation INES are presented. Research carried out by TOF method on 50 meter flight base of the pulsed neutron source RADEX. Measurements were performed using the 8-sectional liquid (n,gamma) detector. Proton linac was operating with parameters: energy of protons 209 MeV, repetition rate 50 Hz, pulse current 8 mA, pulse duration 1 microsecond. Average neutron flux 13000 n/cm^{2}sec on target was measured. As spectrometric data acquisition system, new single-channel high speed modules were used. Proportional He-3 counter with new fast amplifier was used as accelerator's proton beam intensity monitor.

1. INTRODUCTION

Installation INES is created to investigate neutron cross sections and make measurements of effective group cross sections for metal alloys and other nuclear reactor materials, which were made using enriched isotopes.

Effectiveness of measurements grow due to making two types of experiments: both absolute cross sections measurements and comparable measurements, using as a calibration pattern the same alloy material, made using usual chemical elements of natural isotope composition.

There are 62 chemical elements in nature which are mixtures of stable isotopes, which can be separated and used in nuclear technics as alloys with perfected qualities. Among them 23 two-isotope chemical elements and 39 elements with even 'Z' value, each of those has 3 and more stable isotopes. Group cross sections of materials and alloys, based on separated isotopes, depend on separation quality and must be measured experimentally.

INES allows to get experimental group cross sections for alloys, produced by industry for usage in cores of nuclear reactors. This gives an opportunity to compare and check precise theoretical calculation results.

2. EXPERIMENTAL PROCEDURE

The experiment was carried out at the 50-meter flight path of the INR RADEX pulsed neutron source. Proton linac was operating with energy of protons 209 MeV, repetition rate 50 Hz, pulse current 8 mA, pulse duration 1 microsecond which corresponds to 1.6 MW pulsed power and averaged value 13000 n/cm^{2}sec on the surface of the detector's surface. The 209 MeV proton beam is injected into tungsten target, resonance neutron spectrum is formed using water moderator.

The gamma rays were detected using 8-sectional liquid scintillator contained in 40-liter tank equipped with FEU-110 photomultiplier. The total gamma detection efficiency of the liquid scintillator amounts to about 30%.

Detector has pulse length 30 nanoseconds and allows usage of coincidence multiplicity method to extract (n, γ) cross sections also in energy region upper then resolved resonances. Effect and background can be distinguished also in upper energy groups.

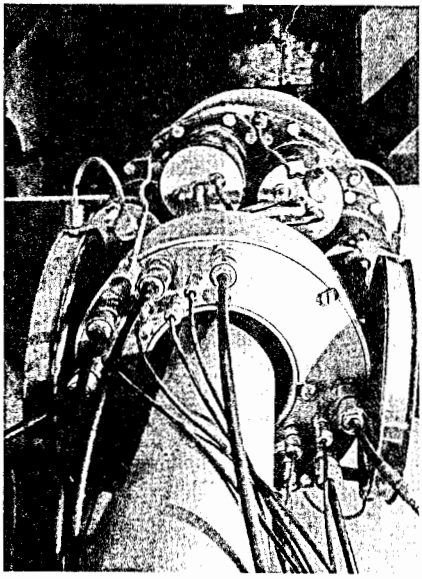

Fig.1. 8-sectional liquid (n, γ) detector.

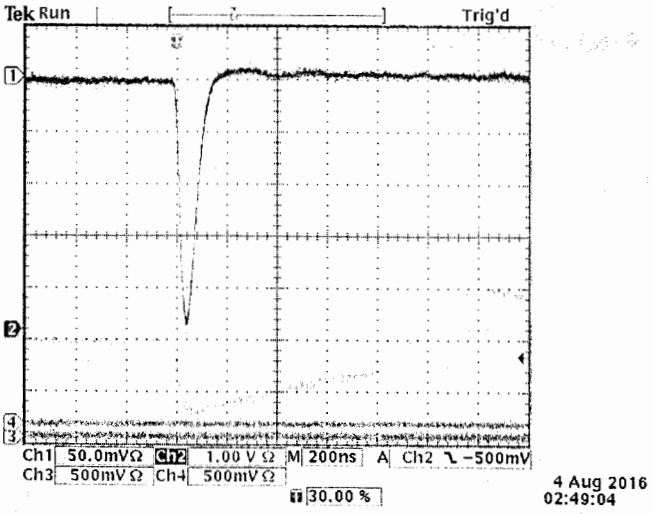

Fig.2. Test signals of the He^3 monitor's preamplifier.

Previously used He^3 monitor's front end electronics provided pulse length 6 mcs and maximum load 80 kHz.For measurements with accelerators which provide smaller pulse length compared to IBR-30 which had 4 mcs, in cooperation with John Scarley (New York University) we created new front-end electronics.

New amplifier design uses modern electronic element base. He-3 detector, equipped with it, provides pulse length 350 nanoseconds, the same as the shortest INR proton linac beam. Maximum work load of He^3 monitor with new front-end electronics was measured using Cf-252 neutron source, its value is approximately 900 kHz.

Metal plates of Au^{197}, Ta^{181} and U^{238} were used during INES calibration measurements. Beam length was 1 mcs, data acquisition system's channel width was chosen 133 nanoseconds. This choice provided energy resolution of 22 nanosec/meter and acceptable measurement time. All 50 Hz spectrum includes 150375 histogram channels.

DATA ANALYZIS AND RESULTS

Resulting product of TOF measurements is a table of 28 (or 299 in BNAB-93 standard) group cross section values, which are used by reactor calculation programs as initial data.

To get these group cross sections values using TOF spectra as a raw material, few new programs (on language C++) during current year were written.

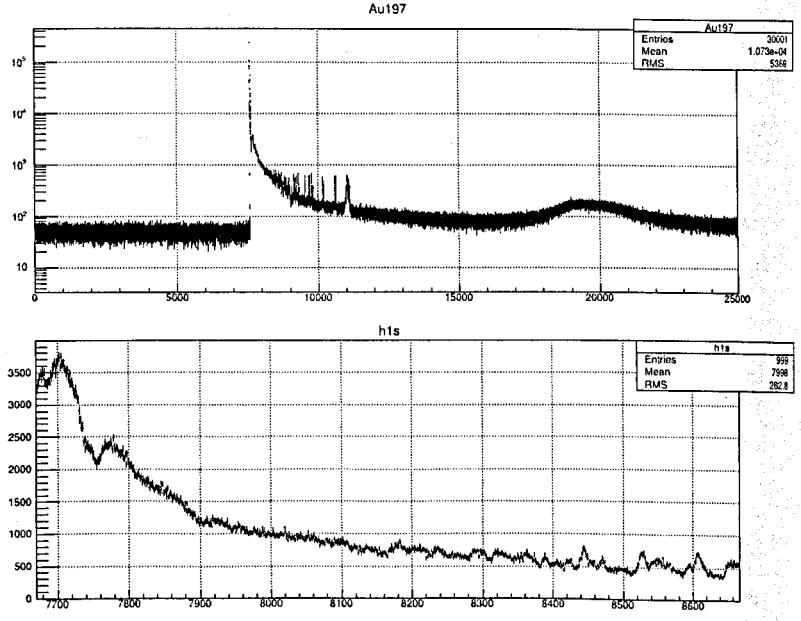

Fig.3. Screen of the program for preliminary observation of experimental TOF spectra.

Each experimental TOF spectra is automatically analyzed by method of form, considering that form of resonance in ideal case is determined by Breit-Wigner formulae. Program marks candidate peaks by red markers, and after that,it is trying to find resonance

parameters for them. For the case when calculation converges, program is painting red curve above candidate peaks, which are recognized as resonances by chosen parameter which can be changed inside program.

Example of TOF Au-197 spectra recognition process on fig.4 is shown. At chosen analysis parameters, resonances at 57.92 eV, 60.1 eV and 78.27 eV and their resonance parameters are automatically determined.

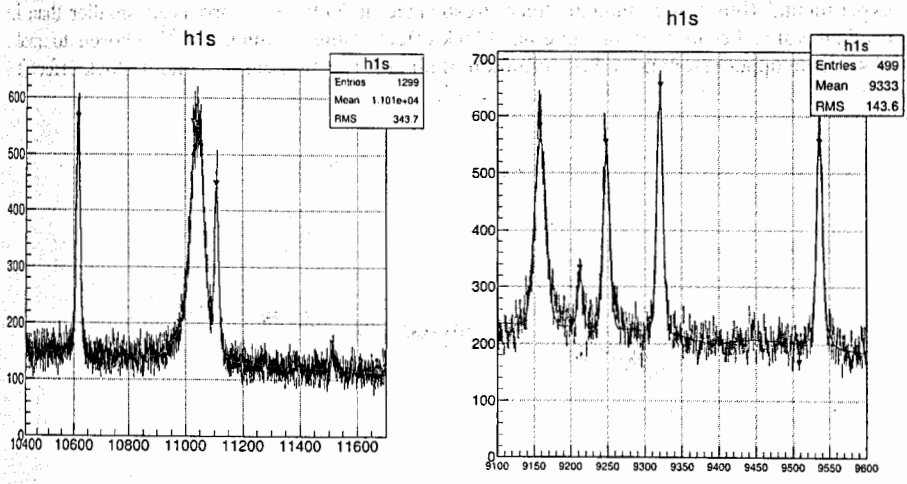

Fig.4. Screens of the program for extracting resonance parameters.

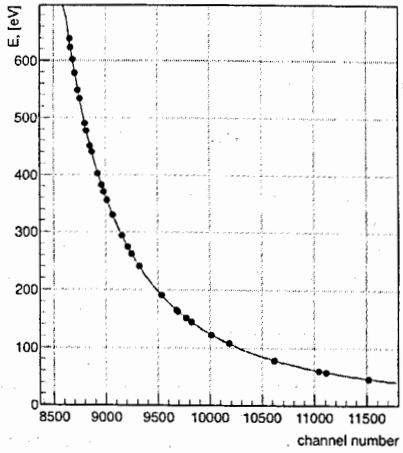

Fig.5. Calibration results for energy axis of installation INES.

One of tasks during present measurements was precise calibration in energy axis of installation INES. Calibration was made by 30 recognized peaks, using ENDF-BVII data as standard. Red curve is theoretical correlation between channel number and resonance energy, blue markers are BNL data.

Experimental TOF spectra before deletion of background, was compared with curve of capture cross section for Au^{197}. We can see coincidence in the energy axis between experimental (blue) and standard lines. Resonance at 59.9 eV is observed smaller than its original value because of big internal block-effect value in thick Au^{197}, chosen to make observable upper resonances. For definition of all cross section curve without block-effect it's necessary to measure plates of patterns with different thicknesses.

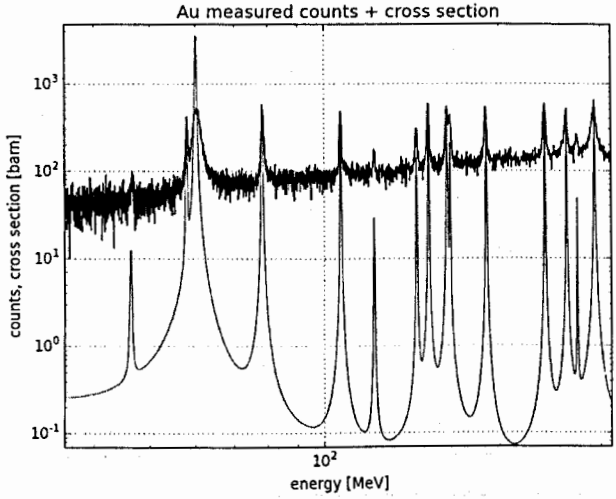

Fig.6. Experimental counts with background (blue) and standard cross section for Au^{197}.

4. CONCLUSION

During work cycle of the proton accelerator TOF spectrums of total and capture cross sections were measured. Calibration of energy axis for installation INES was provided using neutron capture cross sections of Au^{197}, Ta^{181} and U^{238} as standard data.

During measurements few created in INR new blocks of equipment were used. Among them fast preamplifiers for He^3 counters, single-channel coders, HV sources, fast data acquisition system. Their stable work was proven.

New programs for data analysis were written for computer in LINUX operation system. They provide resonance parameters definition and group cross sections extraction using experimental TOF spectrums as entering data.

Experimentally shown, that installation INES is able to make measurements of isotope compositions and group cross sections for alloys of structural and fissile materials. INES is able to determine both isotope enrichment of selected isotope in alloy, and alloy's group cross sections. This applied direction of work becomes an important supplement to previous research program [1].

ACKNOWLEDGMENTS

The authors would like to express their sincere thanks to INR director Kravchuk L.V. for the strong support of nuclear spectrometry investigations among INR accelerator facility [2] work plan, and to the staff of the INR Accelerator Department for excellent operation and high stability of the proton beam during measurements.

REFERENCES

1. Yu.V. Grigoriev, D.V. Khliustin, et al. The Investigation of the Resonance Neutron Cross Sections Structure and the Spectrometer Parameters for the Pulsed Neutron Sources RADEX and IREN-1. 61th International Conference 'Nucleus-2011', p. 65, Russian Federal Nuclear Center – All-Russian Institute of Experimental Physics. 10 - 14 October 2011, Sarov.

2. G.N. Vyalov, Yu.V. Ryabov, Yu.V. Grigoriev, D.V. Khliustin, Zh.V. Mezentseva, S.B. Borzakov. Proton Beam Separation for Simultaneous Operation of Two Installations at the INR Linear Accelerator. ISINN-20, May 2012, E3-2013-22, p.216, JINR, Dubna.

NEUTRONS IN LIGHT NUCLEI AND NEUTRON TRANSFER IN REACTIONS WITH LIGHT NUCLEI

Naumenko M.A.[1,*], Samarin V.V.[1,2]

[1]Joint Institute for Nuclear Research, Dubna, Russian Federation
[2]Dubna State University, Dubna, Russian Federation
[*]E-mail: anaumenko@jinr.ru

Abstract. The energies and the probability densities for the ground states of ^{3,6}He nuclei have been calculated by Feynman's continual integrals method. The contribution of neutron transfer to experimental cross sections for formation of isotopes ^{44,46}Sc in reaction ^{3}He + ^{45}Sc, ^{46}Sc in reaction ^{6}He + ^{45}Sc, ^{65}Zn in reaction ^{6}He + ^{64}Zn, ^{196,198}Au in reactions ^{3,6}He + ^{197}Au has been evaluated. For this purpose, the time-dependent Schrödinger equation for the external neutrons of ^{3,6}He, ^{45}Sc and ^{197}Au nuclei has been solved. The contribution of fusion-evaporation is taken into account using the NRV evaporation code. Results of calculation are in satisfactory agreement with the experimental data.

Keywords: Nuclear structure; Few-body systems; Feynman's continual integrals; Clusters in light nuclei; Nuclear reactions; Neutron transfer; Time-dependent Schrödinger equation; Fusion-Evaporation.

Introduction

The properties of the ground states of light nuclei (e.g., ^{3,6}He) may be calculated by Feynman's continual integrals method in Euclidean time [1–3]. The few-body nucleus ^{3}He may be considered as consisting of two protons and a neutron, whereas the cluster nucleus ^{6}He may be considered as an α-cluster and two neutrons. Knowledge of the properties and the wave functions of the ground states of helium isotopes is necessary for the theoretical description of reactions involving them, and is also of interest from the point of view of studying the cluster structure and halos in light nuclei.

The processes of neutron transfer are widely studied both experimentally and theoretically. In this work, we show that in the low-energy reactions ^{3,6}He + ^{197}Au, ^{3,6}He + ^{45}Sc, ^{6}He + ^{64}Zn neutron transfer is one of the most important channels. These calculations are based on the numerical solution of the time-dependent Schrödinger equation (TDSE) [4, 5] for the external neutrons of ^{3,6}He, ^{45}Sc and ^{197}Au nuclei. Fusion-evaporation was taken into account using the statistical model code available in the NRV knowledge base [6]. Results of calculation demonstrate overall satisfactory agreement with the experimental data.

Ground states of ^{3,6}He nuclei

The details of Feynman's continual integrals method are given in Refs. [1–3]. The parallel Monte Carlo algorithm for numerical calculations within Feynman's continual integrals method in Euclidean time was developed and implemented in C++ programming language using NVIDIA CUDA technology [7]. The calculations were carried out on the heterogeneous cluster [8] of the Laboratory of Information Technologies, Joint Institute for Nuclear Research, Dubna.

The calculations were performed in the center of mass system using Jacobi coordinates. For a system of three particles, two of which have equal masses $m_1 = m_2 = m$ (two protons in ^{3}He or two neutrons in ^{6}He)

$$\mathbf{q}=\{\mathbf{x},\mathbf{y}\},\ \mathbf{x}=\mathbf{r}_2-\mathbf{r}_1,\ \mathbf{y}=\mathbf{r}_3-\frac{1}{2}(\mathbf{r}_1+\mathbf{r}_2). \quad (1)$$

Neutron-neutron, proton-proton and neutron-proton two-body strong interaction potentials $V_{i-j}(r)$ $(i,j=n,p)$ similar to the M3Y potential have been used

$$V_{i-j}(r)=\sum_{k=1}^{3}u_k\exp\left(-r^2/b_k^2\right). \quad (2)$$

The values of the parameters of these potentials are given in Ref. [3].

The probability density distribution $\Psi_0(x,y,\cos\theta)$ for the different configurations of the ^{3}He nucleus with the angle θ between the vectors $\mathbf{x}$ and $\mathbf{y}$ is shown in Fig. 1.

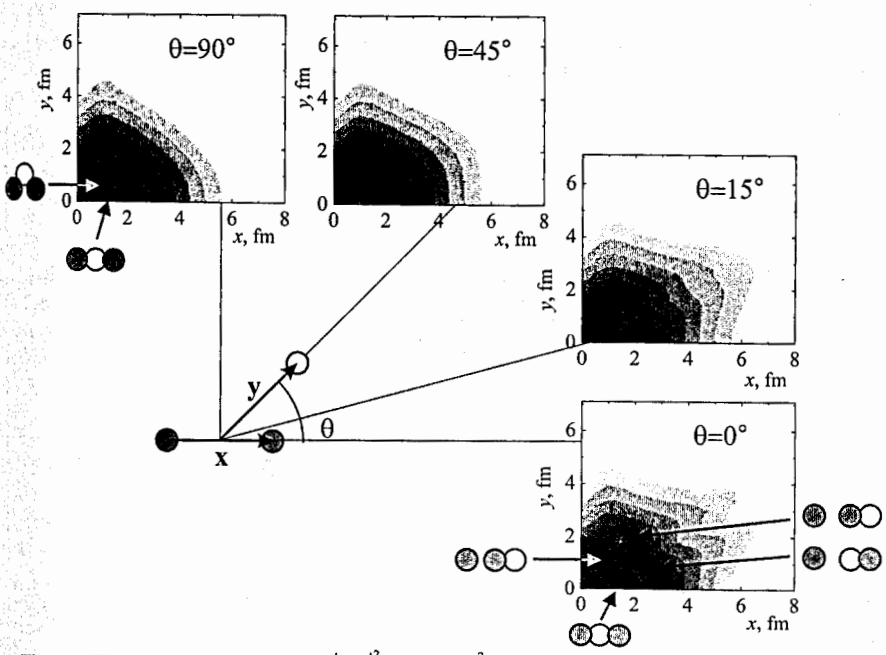

Fig. 1. The probability density $|\Psi_0|^2$ for the ^{3}He nucleus and the vectors in Jacobi coordinates; neutrons and protons are denoted as small empty circles and filled circles, respectively.

For the ^{3}He nucleus there are experimental data on the charge distribution [9]. The results of calculations of the charge distribution in the framework of the Feynman's continual integrals method for the ^{3}He nucleus in comparison with the experimental data [9] taken from the NRV knowledge base [6] are shown in Fig. 2. It can be seen that the calculations are in good agreement with the experimental data.

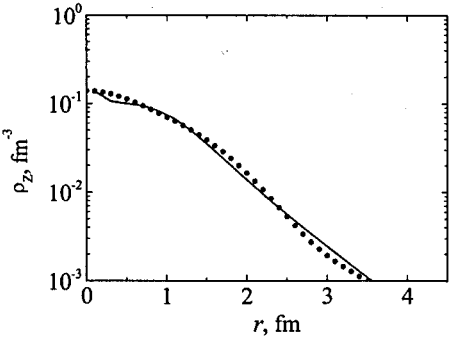

Fig. 2. A comparison of the theoretical charge distribution for the ^{3}He nucleus (solid line) with experimental data (circles) [9] taken from the NRV knowledge base [6].

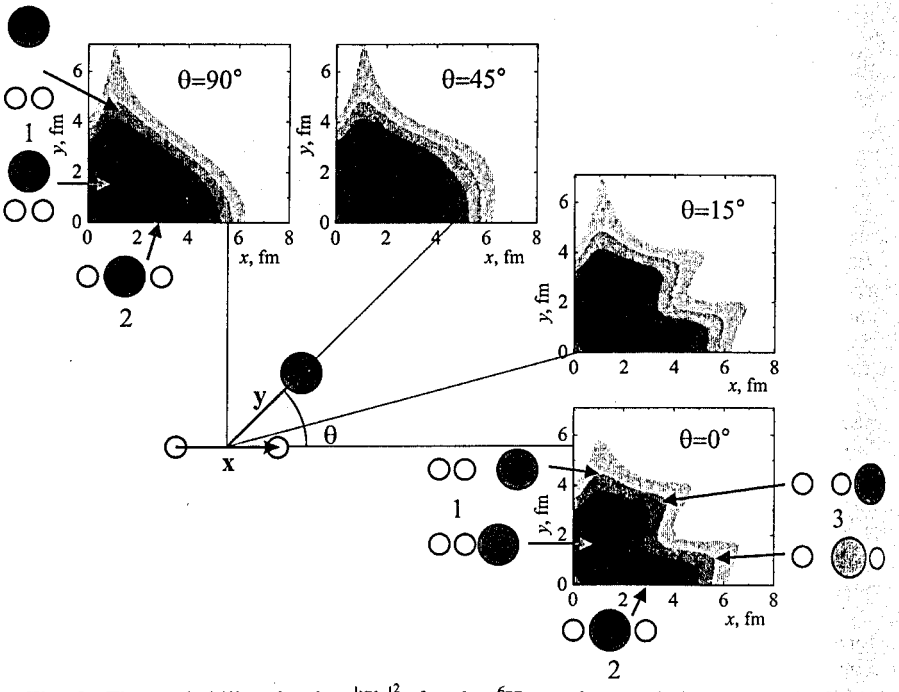

Fig. 3. The probability density $|\Psi_0|^2$ for the ^{6}He nucleus and the vectors in Jacobi coordinates; neutrons and α-clusters are denoted as small empty circles and large filled circles, respectively. The most probable configurations are α-cluster + dineutron (1) and the cigar configuration (2). The configuration n + ^{5}He (3) has low probability.

Momentum distributions after breakup in nuclear reactions show that ^{6}He nucleus consists of an α-cluster core and a two-neutron cluster (e.g., [10]). The α-cluster-neutron interaction potential $V_{\alpha-n}(r)$ in the form of the combination of Woods-Saxon potentials was used

$$V_{\alpha-n}(r)=\sum_{i=1}^{s}U_i\left[1+\exp\left((r-R_i)/a_i\right)\right]^{-1}, \tag{3}$$

where $s = 2, 3$. The values of the parameters of these potentials are given in Ref. [3].

The probability density distribution $\Psi_0(x, y, \cos\theta)$ for the different configurations of the ^{6}He $(\alpha + n + n)$ nucleus with the angle θ between the vectors **x** and **y** is shown in Fig. 3.

The obtained theoretical binding energies $E_B = -E_0$ are listed in Tab. 1 together with the experimental values taken from the NRV knowledge base [6]. For the ^{6}He nucleus the energy required for separation into an α-particle and two neutrons $E_S = -E_0$ is given. It is clear that the theoretical values are close enough to the experimental ones.

Table 1. Comparison of theoretical and experimental binding energies for the ground states of the studied few-body and α-cluster nuclei.

Atomic nucleus	Experimental value [6], MeV	Theoretical value, MeV
^{3}He	7.718	7.37 ± 0.3
^{6}He	0.97542	0.96 ± 0.05

Time-dependent Schrödinger equation approach

For theoretical description of neutron transfer during collisions of heavy atomic nuclei we used the time-dependent Schrödinger equation (TDSE) approach [4, 5] for the external neutrons combined with the classical equations of motion of atomic nuclei

$$m_1\ddot{\vec{r}}_1=-\nabla_{\vec{r}_1}V_{12}\left(\left|\vec{r}_1-\vec{r}_2\right|\right),\ m_2\ddot{\vec{r}}_2=-\nabla_{\vec{r}_2}V_{12}\left(\left|\vec{r}_2-\vec{r}_1\right|\right). \tag{4}$$

Here $\vec{r}_1(t)$, $\vec{r}_2(t)$ are the centers of nuclei with the masses m_1, m_2 and $V_{12}(r)$ is the potential energy of nuclear interaction. We may assume that before contact of the surfaces of spherical nuclei with the radii R_1, R_2 the potential energy of a neutron $W(\vec{r},t)$ is equal to the sum of its interaction energies with both nuclei.

The evolution of the components ψ_1, ψ_2 of the spinor wave function $\Psi(\vec{r},t)$ for the neutron with the mass m during the collision of nuclei was determined by Eq. (5) with the operator of the spin-orbit interaction $\hat{V}_{LS}(\vec{r},t)$

$$i\hbar\frac{\partial}{\partial t}\Psi(\vec{r},t)=\left\{-\frac{\hbar^2}{2m}\Delta+W(\vec{r},t)+\hat{V}_{LS}(\vec{r},t)\right\}\Psi(\vec{r},t). \tag{5}$$

The initial conditions for the wave functions were obtained using the shell model calculations with the parameters providing neutron separation energies close to the experimental values. Based on the obtained results of Feynman's continual integrals method new parametrization of the mean field in the shell model for neutrons inside ^{3,6}He nuclei was proposed [1, 4].

The solution of the time-dependent Schrödinger equation provides the neutron transfer probability $p(b, E)$ [4, 5], where b is an impact parameter and E is the center-of-mass energy. The transfer cross section was calculated as an integral of $p(b, E)$ over the impact parameters of grazing collisions $b > b_{min}$

$$\sigma(E) = \int_{b_{min}}^{\infty} p(b,E) b db . \quad (6)$$

In the analysis of experimental cross sections for formation of isotopes one must also take into account the possibility of their formation via fusion of colliding nuclei with the subsequent evaporation of nucleons and α-particles. For this purpose, we used computational code of the statistical model available in the NRV knowledge base [6].

Neutron transfer in reactions with ^{3,6}He

^{3}He + ^{45}Sc. Comparison of theoretical calculations with experimental cross sections for formation of isotopes ^{44}Sc and ^{46}Sc in reaction ^{3}He + ^{45}Sc is shown in Fig. 4*a* and Fig. 4*b*, respectively. Due to the low charge of the formed compound nucleus, the cross sections for the fusion with the subsequent evaporation of an α-particle and 2*p* are high enough and are respectively comparable with neutron pickup (^{44}Sc, Fig. 4*a*) and stripping (^{46}Sc, Fig. 4*b*) cross sections. The corresponding sums of neutron transfer and fusion-evaporation channels provide overall satisfactory agreement of calculation results with experimental data.

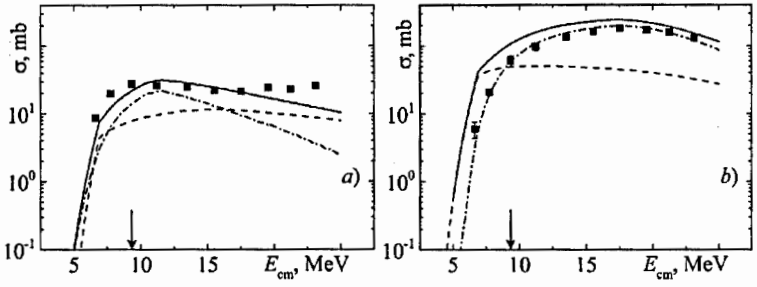

Fig. 4. The cross sections for formation of isotopes ^{44}Sc (*a*) and ^{46}Sc (*b*) in reaction ^{3}He + ^{45}Sc. Symbols are the experimental data from Refs. [11, 12], dash-dotted curves are the results of calculation of fusion-α-evaporation (*a*) and fusion-2*p*-evaporation (*b*) within the NRV knowledge base [6], dashed curves are the results neutron transfer calculations within the TDSE approach, solid curves are the sums of the corresponding transfer and fusion-evaporation channels. Here and below arrows indicate the position of the Coulomb barrier.

^{3}He + ^{197}Au. The experimental data on the formation of isotopes ^{196}Au and ^{198}Au in the reaction ^{3}He + ^{197}Au [13, 14] are compared to the theoretical calculations in Fig. 5*a* and Fig. 5*b*, respectively. The cross section for formation of the isotope ^{196}Au via fusion with the subsequent evaporation of an α-particle from the compound nucleus at energies above the Coulomb barrier is substantially (about two orders of magnitude) lower than the experimental data because the high Coulomb barrier prevents the emission of the α-particle from the compound nucleus with the high charge. Formation of ^{198}Au via fusion with the evaporation of 2*p* from the compound nucleus was not observed in calculations. The calculated neutron pickup (^{196}Au, Fig. 5*a*) and stripping (^{198}Au, Fig. 5*b*) cross sections are in satisfactory agreement with the experimental data.

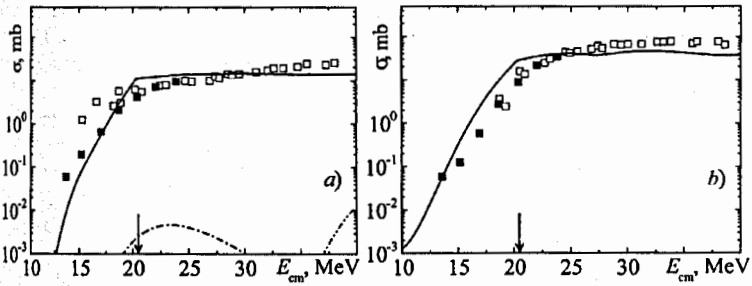

Fig. 5. The cross sections for formation of isotopes ^{196}Au (*a*) and ^{198}Au (*b*) in reaction ^{3}He + ^{197}Au. Symbols are the experimental data from Ref. [13] (filled squares) and Ref. [14] (empty squares), dash-dotted and dash-dot-dotted curves are respectively the results of calculation of fusion-α-evaporation and fusion-2*p*2*n*-evaporation within the NRV knowledge base [6], solid curves are the results neutron transfer calculations within the TDSE approach.

^{6}He + ^{45}Sc, ^{6}He + ^{64}Zn. Comparison of experimental data on the formation of isotopes ^{46}Sc in reaction ^{6}He + ^{45}Sc and ^{65}Zn in reaction ^{6}He + ^{64}Zn with the theoretical calculations is shown in Fig. 6*a* and Fig. 6*b*, respectively.

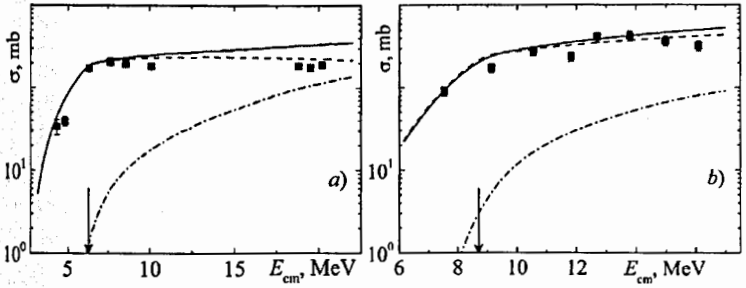

Fig. 6. The cross sections for formation of isotopes ^{46}Sc in reaction ^{6}He + ^{45}Sc (*a*) and ^{65}Zn in reaction ^{6}He + ^{64}Zn (*b*). Symbols are the experimental data from Ref. [15] (*a*) and Ref. [16] (*b*), dash-dotted curves are the results of calculation of fusion-α*n*-evaporation within the NRV knowledge base [6], dashed curves are the results neutron transfer calculations within the TDSE approach, solid curves are the sums of the corresponding transfer and fusion-evaporation channels.

The cross sections for the formation of the isotopes ^{46}Sc and ^{65}Zn via fusion with the subsequent evaporation of α*n* is significant at energies above the Coulomb barriers due to the low charge of the formed compound nucleus. In both cases, the corresponding sums of neutron transfer (stripping) and fusion-evaporation channels provide a satisfactory agreement between the calculated results and the experimental data.

^{6}He + ^{197}Au. Comparison of experimental data on the formation of isotopes ^{196}Au and ^{198}Au in the reaction ^{6}He + ^{197}Au with the theoretical calculations is shown in Fig. 7*a* and Fig. 7*b*, respectively. It can be seen that in this case the contribution of fusion with the subsequent

evaporation to the experimental data is negligible due to the high Coulomb barrier of the formed compound nucleus preventing the evaporation of α-particles. It is an interesting fact that the experimental yield of the isotope ^{196}Au in the higher-energy region is comparable and even exceeds the yield of the isotope ^{198}Au.

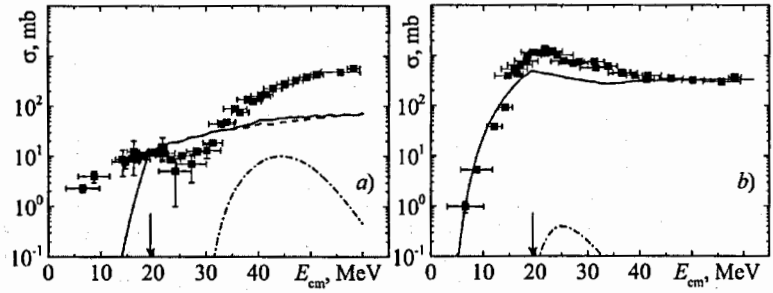

Fig. 7. The cross sections for formation of isotopes ^{196}Au (*a*) ^{198}Au (*b*) and in reaction ^{6}He + ^{197}Au. Symbols are the experimental data from Ref. [17], dash-dotted curves are the results of calculation of fusion-$\alpha 3n$-evaporation (*a*) and fusion-αn-evaporation (*b*) within the NRV knowledge base [6], dashed curves are the results neutron transfer calculations within the TDSE approach, solid curves are the sums of the corresponding transfer and fusion-evaporation channels.

Conclusions

The results of calculation within Feynman's continual integrals method in Euclidean time demonstrate that the theoretical values are close enough to the experimental ones for the studied nuclei. The obtained probability densities were used to propose new parametrization of mean field for neutrons inside ^{3,6}He nuclei within the shell model. The results of the shell model calculations served as the initial conditions in the time-dependent calculations of neutron transfer cross sections in reactions with the considered nuclei. The sums of neutron transfer and fusion-evaporation channels provided overall satisfactory agreement of calculation results with experimental data on formation of isotopes ^{44,46}Sc in reaction ^{3}He + ^{45}Sc, ^{46}Sc in reaction ^{6}He + ^{45}Sc, ^{65}Zn in reaction ^{6}He + ^{64}Zn, ^{196,198}Au in reactions ^{3,6}He + ^{197}Au. The statistical model calculations were performed using the computational code of the NRV knowledge base.

Acknowledgments

Authors thank Yu. E. Penionzhkevich, N. K. Skobelev, A. S. Denikin, and A. V. Karpov for fruitful discussions. The work was supported by Russian Science Foundation (RSF), grant No. 17-12-01170.

References

1. V. V. Samarin and M. A. Naumenko, Study of ground states of ^{3,4,6}He nuclides by Feynman's continual integrals method, *Bull. Russ. Acad. Sci.: Phys.* **80**, 283 (2016).
2. M. A. Naumenko, V. V. Samarin, Application of CUDA technology to calculation of ground states of few-body nuclei by Feynman's continual integrals method, *Supercomp. Front. Innov.* **3**, 80 (2016).
3. V. V. Samarin and M. A. Naumenko, Study of ground states of ^{3}H, ^{3,4,6}He, ^{6}Li, and ^{9}Be nuclei by Feynman's continual integrals method, *Phys. Atom. Nucl.* **80**, 877 (2017).

4. M. A. Naumenko, V. V. Samarin, Yu. E. Penionzhkevich, N. K. Skobelev, Near-barrier neutron transfer in reactions with ^{3}He nucleus, *Bull. Russ. Acad. Sci.: Phys.* **80**, 264 (2016).
5. M. A. Naumenko, V. V. Samarin, Yu. E. Penionzhkevich, N. K. Skobelev, Near-barrier neutron transfer in reactions ^{6}He + ^{45}Sc, ^{64}Zn, and ^{197}Au, *Bull. Russ. Acad. Sci.: Phys.* **81**, 710 (2017).
6. V. I. Zagrebaev, A. S. Denikin, A. V. Karpov, A. P. Alekseev, M. A. Naumenko, V. A. Rachkov, V. V. Samarin, V. V. Saiko, *NRV web knowledge base on low-energy nuclear physics*. URL: http://nrv.jinr.ru/.
7. NVIDIA CUDA. URL: http://developer.nvidia.com/cuda-zone/.
8. Heterogeneous cluster of LIT, JINR. URL: http://hybrilit.jinr.ru/.
9. G. A. Retzlaff, D. M. Skopik, ^{3}He charge form factors by nuclear recoil detection, *Phys. Rev.* C **29**, 1194 (1984).
10. Yu. E. Penionzhkevich, Reactions involving loosely bound cluster nuclei: heavy ions and new technologies, *Phys. Atom. Nucl.* **74**, 1615 (2011).
11. N. K. Skobelev, A. A. Kulko, Yu. E. Penionzhkevich *et al.*, Cross sections for production of ^{43}Sc, ^{44}Sc, and ^{46}Sc isotopes in the ^{45}Sc + ^{3}He reaction, *Phys. Part. Nucl. Lett.* **10**, 410 (2013).
12. N. K. Skobelev, A. A. Kulko, Yu. E. Penionzhkevich *et al.*, Cross sections of ^{43}Sc, ^{44}Sc, ^{46}Sc isotopes formed in the ^{45}Sc + ^{3}He reaction, *Bull. Russ. Acad. Sci.: Phys.* **77**, 795 (2013).
13. N. K. Skobelev, Yu. E. Penionzhkevich, E. I. Voskoboinik *et al.*, Fusion and transfer cross sections of ^{3}He induced reaction on Pt and Au in energy range 10-24.5 MeV, *Phys. Part. Nucl. Lett.* **11**, 114 (2014).
14. Y. Nagame, K. Sueki, S. Baba, and H. Nakahara, Isomeric yield in proton, ^{3}He, and α-particle induced reactions on ^{197}Au, *Phys. Rev. C* **41**, 889 (1990).
15. N. K. Skobelev, A. A. Kulko, V. Kroha *et al.*, Excitation functions for the radionuclide ^{46}Sc produced in the irradiation of ^{45}Sc with deuterons and ^{6}He, *J. Phys. G: Nucl. Part. Phys.* **38**, 035106 (2011).
16. V. Scuderi, A. Di Pietro, P. Figuera et al., Fusion and direct reactions for the system ^{6}He + ^{64}Zn at and below the Coulomb barrier, *Phys. Rev. C* **84**, 064604 (2011).
17. Yu. E. Penionzhkevich, R. A. Astabatyan, N. A. Demekhina *et al.*, Excitation functions of fusion reactions and neutron transfer in the interaction of ^{6}He with ^{197}Au and ^{206}Pb, *Eur. Phys. J. A* **31**, 185 (2007).

SYMMETRY MOTIVATED ANALYSIS OF PARTICLE MASS DATA

S.I. Sukhoruchkin , Z.N. Soroko, D.S. Sukhoruchkin

B.P. Konstantinov Petersburg Nuclear Physics Institute of NRCKI 188300 Gatchina

1. General remarks

Neutron resonance spectroscopy is a part of nuclear physics which is based on QCD - Quantum Chromodynamics. In its turn QCD is a part of the Standard Model (SM) - a theory of all interactions. Y. Nambu suggested [1] the SM development taking into account all existing particle masses. The analysis of particle masses and nuclear data revealed an existence of the tuning effect in these data [2-12]. It consists in correlations between such fundamental SM–parameters as lepton masses, QED parameters α, α_Z, masses of vector/scalar fields and parameters of QCD–based NRCQM (Constituent Quark Model) corresponding to mass generation due to the gluon quark dressing effect [13-15]. Data from compilations PDG–2016 and CODATA [16,17] were used for analysis of correlations between particle masses. For the analysis of nuclear data 3 collected in PNPI files: Neutron Resonance File NRF, Nuclear Excitation File CRF and Mass Difference File MDF [18] were used. Combined consideration of data in all these files resulted in common representation of particle masses and stable nuclear intervals shown in Table 1. Tuning effects in nucleon and electron masses were observed in CODATA relations:

$$m_n = 115 \cdot 16m_e - m_e - \delta m_N/8 \qquad m_p = 115 \cdot 16m_e - m_e - 9\delta m_N/8. \quad (1)$$

Here a shift in neutron mass relative to integer number of m_e ($115{\cdot}16m_e - m_e$) accounts δm_n=161.65 keV that is exactly rational to nucleon mass splitting $\delta m_N/\delta m_n$=8(1.000(1)) with δm_N from the CODATA. Values δm_n, δm_N and both NRCQM-parameters, standard constituent quarks masses M_q=m_Ξ/3=441 MeV and $M''_q = m_\rho/2$=388 MeV, are given in Table 1. Both values are in the lepton ratio L=$m_\mu/m_e = 13{\cdot}16-1 = 207$ with vector boson masses (M_W/388 MeV=207.4 and M_Z/441 MeV=206.8) connected with symmetry motivated estimations. An important role of particle mass analysis for the SM–development concerns NRCQM- and SM - parameters M_q, M''_q, m_e, m_μ, M_Z, M_W.

Table 1. Representation of parameters of tuning effects in particle masses (top) and nuclear data (bottom) with the expression $n{\cdot}16m_e(\alpha/2\pi)^X$M and different values of the X–power of factor $\alpha/2\pi$ and integers M,n. Boxed are groups of values differing with QED correction $\alpha/2\pi$.

X	M	n = 1	n = 13	n = 16	n = 17	n = 18	Comm.
-1	3/2	$16M_q$=δ°		m_t=172.0			
GeV	1	δ°=7.06	M_Z=91.2	M'_H=115		M_H=125	
	1/2	(m_b-M_q)		M^{L3}=58			
0	1	$16m_e$=δ=$8\varepsilon_o$	m_μ=106	f_π=130.7	m_π-m_e	ΔM_Δ=147	
MeV	3			M"$_q$=m_ρ/2		M_q=441=ΔE_B	NRCQM
1	1	CODATA			kδ-m_n-m_e=161.65	170 = m_e/3	Part.
keV	8				δm_N=1293.332		CODATA
1	1	9.5=δ'=$8\varepsilon'$	123	152	Δ^{TF}=161	170 (Sn)	Nuclear
keV	8,3		984	1212	1289-1293 (D,E^*)	512 (Pd)	data
2	1,4	11=δ''=$8\varepsilon''$	143	176	749 (Br,Sb)		Neutr.res.
eV	4,8		570 (Sb)		1500 (Pd,Hf)		data

2. Particle masses in the international particle data file PDG–2016

The tuning effect includes relations with integers n of the period δ=16m_e introduced in 70-ties [19] from the proximity of the pion charge mass splitting δm_π to 9m_e ($2\delta m_\pi$-$2m_e \approx 16m_e$=δ), see lines X=0, M=1-8 in Table 1 for masses of the muon (n=13), the pion (n=17) and the nucleon (n=115=13+6·17) noticed earlier by Y. Nambu [20], A. Hautot and others [19-24]. The tuning effect extends into the high–mass region, to the mass values of heavy quarks (m_b, m_t) and bosons (M_Z, M_W, M_H). They are multiple with the analogous period $\delta^\circ = 2m_b - 2M_q$=$16M_q$=7.056 GeV due to relations m_d/m_b=m_e/M_q=$116\cdot10^{-5}$ similar to the ratio m_μ/M_Z=$115.9\cdot10^{-5}$ coinciding with the QED-radiative correction $\alpha/2\pi$=$115.9\cdot10^{-5}$.

Confirmation of the distinguished character of mass intervals close to masses of heavy fermions M_q=441 MeV and m_b=4.18(4) GeV [16] was obtained with the analysis of spacing distribution between masses presented n Table 2 taken directly from summary tables of PDG–2016 compilation [16]. Selection of the material was considered in [3]: 1) values with uncertainties larger than 0.6 MeV are marked with one asterisk (in PDG–2016 they are given without rounding up of 0.1 MeV); 2) values with uncertainties less than 6 MeV (given in PDG–2016 without rounding up of MeV) are marked here **; corresponding numbers of mass values are 169 (total number of mass values), 87 (accurately known), 54 and 28 values (less certain, with one or two asterisks, respectively); 3) to avoid a grouping effect at small mass differences (ΔM) due to proximity of masses of multiplet members (n–p mass difference 1.3 MeV, $\pi^\pm$-π°=4.6 MeV etc.) 30 values (out of n=169) were excluded from the analysis (charged baryon and neutral meson masses, namely, proton mass, π° mass etc.). These masses are marked with ***. A necessity of exclusion of small mass differences inside multiplets can be seen from unwanted maximum at small ΔM in the distribution between all values given in PDG–2016 (Fig. 2 bottom, n=169, Δ=3 MeV).

Distribution of differences between all remaining 137 values (for three differing averaging intervals Δ=3, 5 and 9 MeV of the ideohistograms) are presented in three upper parts of Fig. 1 and 2 (separately for regions 0–1500 and 1500–4500 MeV).

In Table 2, intervals forming maxima with values ΔM=16,48,104,142 MeV are given (for the interested reader) together with the sequence number of such interval in the list of these intervals forming maximum obtained in the analysis (in case of averaging interval 5 MeV in Fig. 1 center). Exclusion from the consideration less accurate values (marked **) results in the distribution for remaining n=139-28=111 values shown in the bottom line of Fig. 1, where one can notice, that some maxima disappeared (for example, maximum at 114 MeV in the central distribution of Fig. 1), but the maximum at 104 MeV (containing the muon mass 106 MeV) remains to be seen.

Maxima in obtained distributions of mass differences could be considered in line of earlier performed in the literature theoretical or empirical observations. For illustration of relations between stable intervals discussed in the literature we use in Fig. 3 two–dimensional mass presentation with units along the horizontal line $16\cdot16m_e = 16\delta$ close to pion's β-decay parameter f_π. It allows to see integer relations in masses of the charged pion and three hyperons (Λ, Ξ and Ω on the straight line in the center of Fig. 3) that contains Y. Nambu relation m_Λ=8π [20].

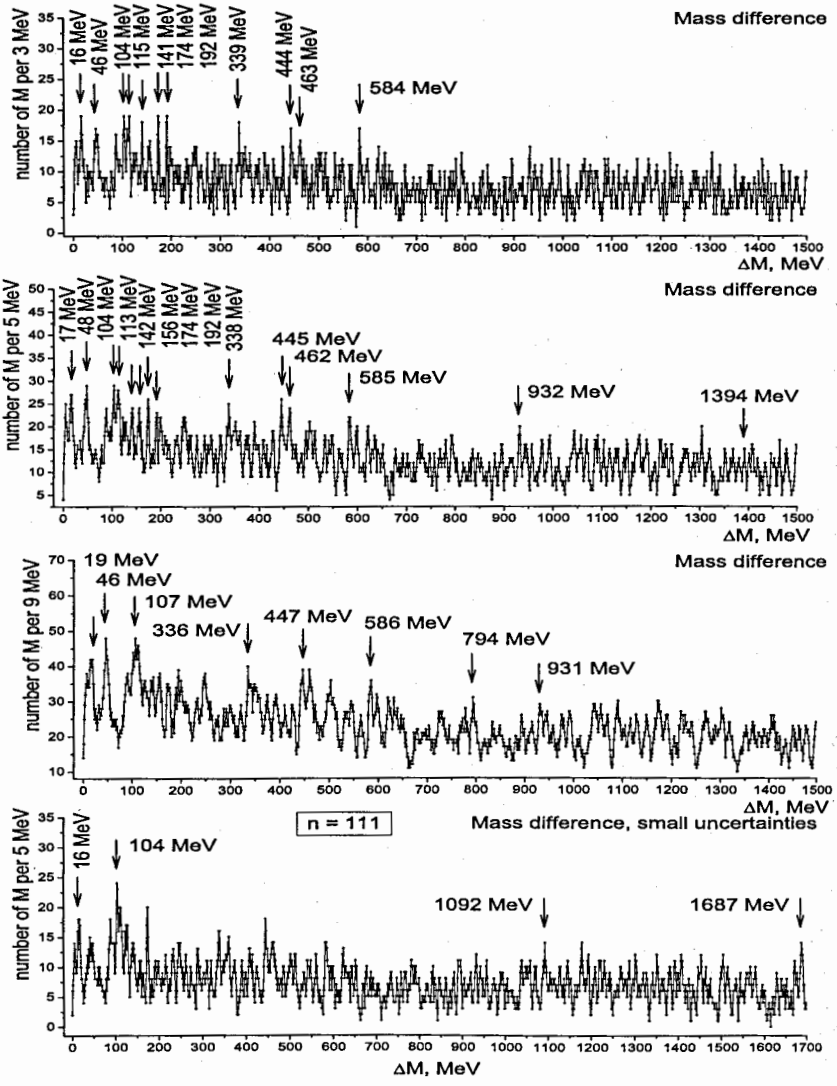

Fig. 1. *Top:* Distribution of differences between particle masses ΔM in the region 0–1500 MeV and averaging interval of the histogram 3 MeV. Stable intervals (discussed in the text) are marked with arrows.

Center: The same for averaging intervals 5 MeV and 9 MeV. Intervals 16 MeV, 48 MeV, 107 MeV$\approx m_\mu$ and 141 MeV$=m_{\pi^\pm}$ are close to integer numbers of the parameter $\delta = 16m_e$ found in CODATA relations with the masses of nucleons.

Bottom: Distribution of differences between particle masses known relatively accurate (including marked *), averaging interval of the histogram 5 MeV. Stable intervals 104 MeV close to m_μ are discussed in the text and Table 1 (marked with arrow).

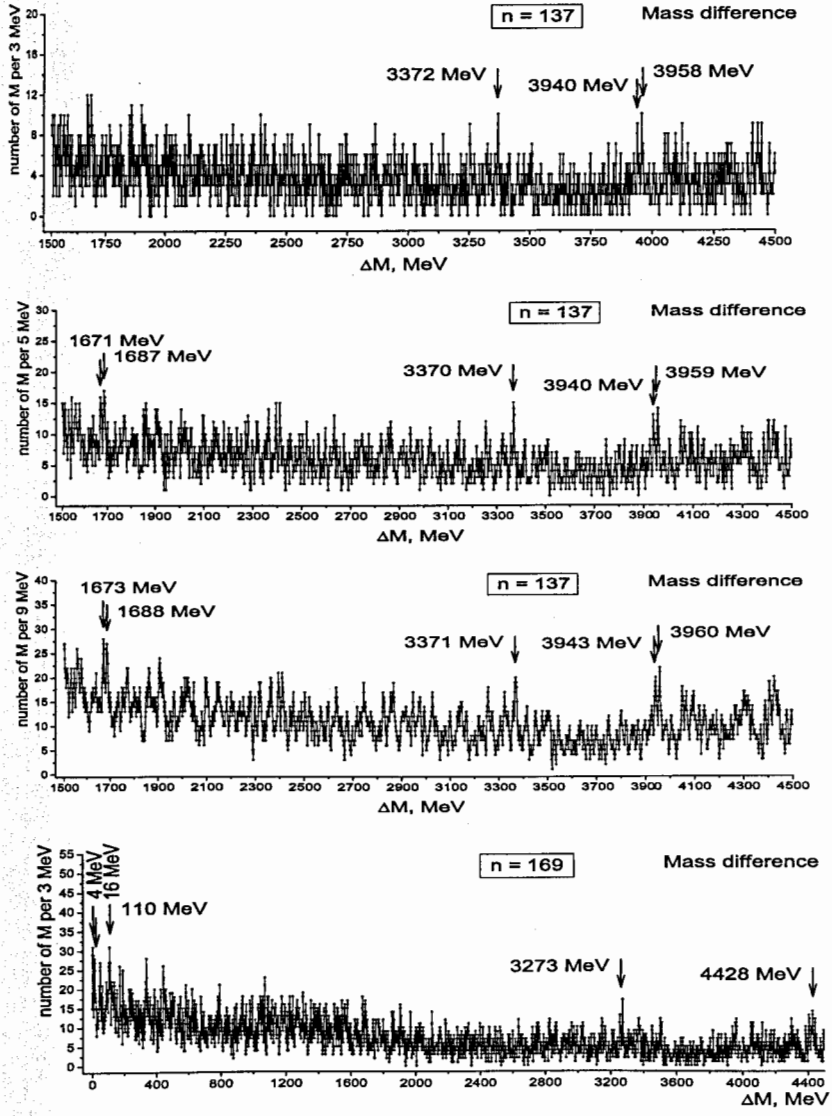

Fig. 2 (from [3]). *Top:* Distribution of differences between particle masses ΔM in the region 1500–4500 MeV and averaging interval of the histogram 3 MeV. Stable intervals (discussed in the text) are marked with arrows.

Center: The same for averaging intervals 5 MeV and 9 MeV. Intervals 3943 MeV, 3960 MeV are close to the bottom quark mass estimation 4.2 GeV [16].

Bottom: Distribution of differences between all particle mass values presented in PDG–2016 compilation.

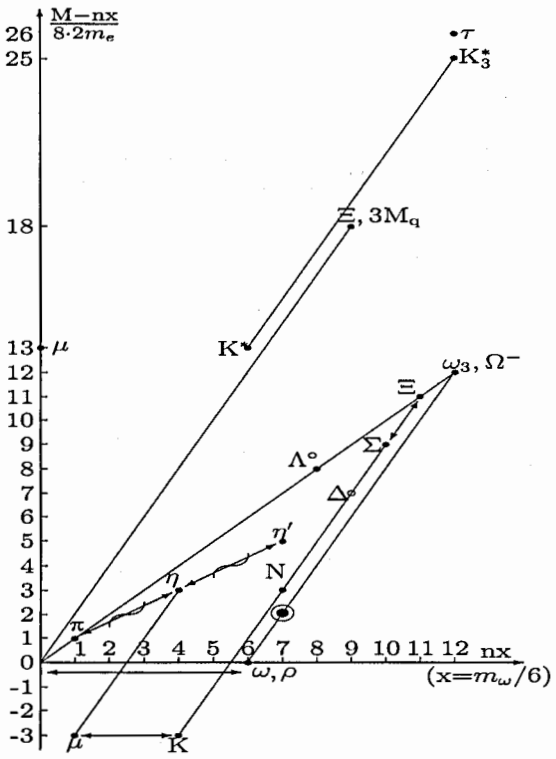

Fig. 3. Two-dimensional representation of particle masses as the period (somewhat less than pion's mass) f_π=16·16m_e=130.4 MeV≈ $m_\omega/6$ along the x–axis and the remainder – in units δ=16m_e. Four different slopes correspond to different mass systematics including noticed by Y. Nambu (line π-Λ-Ξ-Ω) and by T. Takabayashi – equidistance in scalar mesons masses (crossed arrows, π-η-η' intervals, 547.9-139.6=408.3 MeV and 957.8-547.9=409.9 MeV, close to 50δ=408.8 MeV) are seen in the center. Difference between masses of η' meson and the neutron (957.8-939.6=18.2 MeV) is close to 2δ=16.3 MeV Δn = 2 =(117=17+2·50) - 115 and boxed in column 17 of Table 1 (at η' and n).

Other intervals are considered in the text and [5-12]. Intervals ω_3-ω (1667(4)-782.7=884 MeV=2×442 MeV) and K_3^*-K^* (1776(7)-891.7=2×442 MeV) are close to $2M_q$=2×54δ, with M_q = $m_\Xi/3$=441 MeV=3·18δ being the estimate of the constituent quark mass value in NRCQM (due to the gluon quark-dressing effect [13-15]).

Mass of the third τ-lepton is shown at the top (12·16δ+26δ). Distance between this value and close to each other masses of π_2-meson and Ω^--hyperon (1672.2-1673.5 MeV) is close to 104 MeV and m_μ (see boxed values in column 104 in Table 1).

Neutron mass is a member of the sequence K-N-Δ-Σ-Ξ (parallel with the line μ-η) noticed by R. Sternheimer after observation by G. Wick [22] that there are stable intervals close to a half of ω-meson mass (horizontal lines in Fig 3).

Table 2. Particle masses [16] (in MeV) known with the uncertainty less than 6-10 MeV.

	Particle		m_l	Δ	17	48	104	142	156	174
1	leptons	electron, ν	0.0				106 (1)	140 (1)		
	μ		105.658				106 (1)			
	τ		1776.82			46 (15)	105 (7,8)			
2	Unflav.	mesons								
	f_π		130.7	0.4	***					
	π°	$1^-(0^-)$	134.977		***					
	$\pi^\pm$	$1^-(0^-)$	139.570					140 (1)		
	η	$0^+(0^{-+})$	547.86							
	$\rho(770)$	$1^+(1^{--})$	775.26							
	$\omega(782)$	$0^-(1^{--})$	782.65						157 (1)	175 (1)
	$\eta'(958)$	$0^+(0^{-+})$	957.78		18 (1)				159 (2)	175 (1)
	$\phi(1020)$	$0^-(1^{--})$	1019.46							173 (3)
	$b_1(1235)$*	$1^+(1^{+-})$	1229.5	3.2		46 (2)			154 (4)	174 (4,5)
	$f_2(1270)$*	$0^+(2^{++})$	1275.5	0.8	19 (2)	46 (2,5)				
	$f_1(1285)$	$0^+(1^{++})$	1282.0	0.5			102 (2)	142 (2,3)		
	$\eta(1295)$**	$0^+(0^{-+})$	1294	4	19 (2)					
	$a_2(1320)$	$1^-(2^{++})$	1318.3	0.5		46 (3)			138 (7)	
	$\eta(1405)$*	$0^+(0^{--})$	1408.8	1.8	18 (4,5)					
	$f_1(1420)$*	$0^+(1^{++})$	1426.4	0.9	18 (5)	47 (8,9)	105 (4,6)	142 (3)	154 (6)	
	$\eta(1475)$**	$0^+(0^{-+})$	1476	4		50 (7,9)		141 (5)	156 (7,8)	
	$f_0(1500)$**	$0^+(0^{++})$	1504	6	16 (6)				158 (9)	
	$f_2'(1525)$**	$0^+(2^{++})$	1525	5		49 (11)		142 (4,7)		
	$\pi_1(1600)$**	$1^-(1^{-+})$	1662	8				142 (6)	158 (9)	
	$\eta_2(1645)$**	$0^+(0^{-+})$	1617	5		50 (12)		141 (5)	156 (12)	
	$\omega_3(1670)$**	$0^-(3^{--})$	1667	4		45 (12)		142 (7)	156 (13)	
	$\pi_2(1670)$*	$1^-(2^{-+})$	1672.2	3.0	17 (7)		105 (7)	140 (8)		
	$\rho_3(1690)$*	$1^+(3^{--})$	1688.8	2.1	17 (7,8)				157 (11)	176 (6)
	$f_0(1710)$**	$0^+(0^{++})$	1723	6		50 (13)		142 (10)		
	$\phi_3(1850)$**	$0^-(3^{--})$	1854	7	16 (9)			142 (11)	156 (14)	
	$a_4(2040)$**	$1^-(4^{++}$	1995	8	15 (10)	50 (17)		142 (11)		172 (7)
3	strange	mesons								
	$K^\pm$	$1/2(0^-)$	493.677							
	$K^*(892)^{*\pm}$	$1/2(1^-)$	891.66			48 (1)				
	$K^*(892)^{*\circ}$	$1/2(1^-)$	895.81		***					
	$K_1(1270)$**	$1/2(1^+)$	1272	7		46 (3,4)			156 (3,5,6)	
	$K_1(1400)$**	$1/2(1^+)$	1403	7	19 (3)					174 (4)
	$K_0^*(1430)^{\pm *}$	$1/2(2^+)$	1425.6	1.5	17 (4)	47 (6,7)	104 (3,5)	142 (2)	154 (5)	
	$K_0^*(1430)^{\circ *}$	$1/2(2^+)$	1432.4	1.3	***					
	$K_2(1770)$**	$1/2(2^-)$	1773	8					156 (12)	
	$K_3^*(1780)$**	$1/2(3^-)$	1776	7		47 (14)				
	$K_4^*(2045)$**	$1/2(4^+)$	2045	9		50 (17)				175 (8)
4	charmed	mesons								
	D°	$1/2(0^-)$	1864.83				103 (9)	142 (10)		176 (6)
	$D^\pm$	$1/2(0^-)$	1869.58		16 (9)	47 (16)		141 (12)	155 (15)	175 (8)
	$D^*(2007)^\circ$	$1/2(1^-)$	2006.85		***					
	$D^*(2010)^\pm$	$1/2(1^-)$	2010.28		15 (10,11)		102 (10)	141 (12)	156 (14)	
	$D_1(2420)^\circ$	$1/2(1^+)$	2420.8	0.5		50 (18,19)	103 (11)		157 (16)	
	$D_2^*(2460)^\circ$	$1/2(2^+)$	2460.57		***					
	$D_2^*(2460)^{\pm *}$	$1/2(2^+)$	2465.4	1.3			104 (12)			
5	charmed	strange	mesons							
	$D_s^\pm$	$0^+(0^-)$	1968.27				103 (9)	144 (13)		
	$D_s^{*\pm}$	$0(?^?)$	2112.1	0.4			102 (10)	144 (13,14)		174 (9)
	$D_{s0}^*(2317)^\pm$	$0(0^+)$	2317.7	0.6			103 (11)	142 (15)		
	$D_{s1}(2460)^\pm$	$0(1^+)$	2459.5	0.6				142 (15)		174 (10)
	$D_{s1}(2536)^\pm$	$0(1^+)$	2535.10		17 (14)					173 (13)
	$D_{s2}^*(2573)^*$	$0(2^+)$	2569.1	0.8			104 (12)			
	$D_{s1}^*(2700)^{\pm *}$	$0(1^-)$	2708.3	3.4						173 (13,16)

Table 2. Continued.

	Particle		m_l	Δ	17	48	104	142	156	174
6	bottom	mesons								
	$B^{\pm}$	$1/2(0^-)$	5279.31							
	B°	$1/2(0^-)$	5279.62		***					
	B^*	$1/2(1^-)$	5324.65							
	$B_1(5721)^{+*}$	$1/2(1^+)$	5725.9	2.7			106 (17,18,19)			
	$B_1(5721)^{\circ *}$	$1/2(1^+)$	5726.0	1.3	***					
	$B_2^*(5747)^{+*}$	$1/2(2^+)$	5737.2	0.7			103 (20)			175 (23)
	$B_2^*(5747)^{\circ}$	$1/2(2^+)$	5739.5	0.7	***					
	$B_J(5970)^+$	$1/1(?^?)^{**}$	5964	5	15 (24)					172 (24)
	$B_J(5970)^{\circ}$	$1/1(?^?)^{**}$	5971	5	***					172 (24)
7	bottom	strange	mesons							
	B_s°	$0(0^-)$	5366.82			49 (27)				
	B_s^{**}	$0(1^-)$	5415.4	1.5		49 (27)				
	$B_{s1}(5830)^{\circ}$	$0(1^+)$	5828.63		17 (22)		103 (18,21)			
	$B_{s2}^*(5640)^{\circ}$	$0(2^+)$	5839.84			48 (28)	103 (20)			
8	bottom	charmed	mesons							
	B_c^{**}	$0(0^-)$	6275.1	1.0						
9	$c\bar{c}$	mesons								
	$\eta_c(1S)$	$0^+(0^{-+})$	2983.4	0.5	15 (16)		102 (14)			
	$J/\psi(1S)$	$0^-(1^{--})$	3096.90		17 (17)				158 (18)	
	$\chi_{c0}(1P)$	$0^+(0^{++})$	3414.75					141 (18)		
	$\chi_{c1}(1P)$	$0^+(1^{++})$	3510.66		14 (18)	46 (22)				174 (21)
	$h_c(1P)$	$?^?(0^{+-})$	3525.38		14 (18)					
	$\chi_{c2}(1P)$	$0^+(2^{++})$	3556.20			46 (22)		141 (18)		
	$\eta_c(2S)^*$	$0^+(0^{-+})$	3639.2	1.2		47 (23)				
	$\psi(2S)$	$0^-(1^{--})$	3686.10			47 (23)				173 (21)
	$\psi(3770)$	$0^-(1^{--})$	3773.13			49 (24)			154 (19)	
	$\psi(3823)^*$	$?^?(2^{--})$	3822.2	1.2		49 (24)	105 (15)			
	$X(3872)$	$0^+(1^{++})$	3871.69		15 (19)	49 (25)				
	$X(3900)^*$	$1^+(1^{+-})$	3886.6	2.4	15 (19)					
	$X(3915)^*$	$0^+(?^{++})$	3918.4	1.9		47 (26)	106 (16)			
	$\chi_{c2}(1P)^*$	$0^+(2^{++})$	3927.2	2.6			105 (15)		154 (19)	
	$X(4020)^*$	$1(?^?)$	4024.1	1.9	15 (20)		106 (16)			
	$\psi(4040)^{**}$	$0^-(1^{--})$	4039	1	15 (20)					
	$X(4140)^*$	$0^+(?^{?+})$	4146.9	3.1						
	$\psi(4160)^{**}$	$0^-(1^{--})$	4191	5					156 (20)	
	$X(4260)^{**}$	$?^?(1^{--})$	4251	9						
	$X(4360)^{**}$	$?^?(1^{--})$	4346.9	6					156 (20)	
	$\psi(4415)^{**}$	$0^-(1^{--})$	4421	4						
	$X(4660)^{**}$	$?^?(1^{--})$	4643	9						
10	$b\bar{b}$	mesons								
	$\eta_b(1S)^*$	$0^+(0^{-+})$	9399.0	2.3						
	$\Upsilon(1S)$	$0^-(1^{--})$	9460.30							
	$\chi_{b0}(1P)$	$0^+(0^{++})$	9859.44							
	$\chi_{b1}(1P)$	$0^+(0^{++})$	9892.78		19 (25)					
	$h_b(1P)^*$	$?^?(1^{+-})$	9899.3	0.8						
	$\chi_{b2}(1P)$	$0^+(2^{++})$	9912.21		19 (25)					
	$\Upsilon(2S)$	$0^-(1^{--})$	10023.26					140 (21)		
	$\Upsilon(1D)^*$	$0^-(2^{--})$	10163.7	1.4			105 (23)	140 (21)		
	$\chi_{b0}(2P)$	$0^+(0^{++})$	10232.5	0.4						
	$\chi_{b1}(2P)$	$0^+(1^{++})$	10255.46							
	$\chi_{b2}(2P)$	$0^-(2^{+-})$	10268.65				105 (23)			
	$\Upsilon(3S)$	$0^-(1^{--})$	10355.2	0.5					157 (22)	174 (25)
	$\chi_{b1}(3P)^*$	$0^+(1^{++})$	10512.1	2.3	17 (26)				157 (22)	
	$\Upsilon(4S)^*$	$0^-(1^{--})$	10529.4	1.2	17 (26)					174 (25)
	$X(10610)^{\pm *}$	$1^+(1^+)$	10607.2	2.0						
	$X(10610)^{\circ **}$	$1^+(1^+)$	10609	6						
	$\Upsilon(10860)^{**}$	$0^-(1^{--})$	10891	6						
11		baryons								
	p	$1/2(1/2^+)$	938.2721		***	48 (1)				
	n	$1/2(1/2^+)$	939.5654		18 (1)				157 (1)	176 (2)
	Λ	$0(1/2^+)$	1115.683						158 (2,3)	176 (2)

Table 2. Continued.

	Particle		m_i	Δ	17	48	104	142	156	174
	$\Lambda(1405)1/2^{-}$*	$0(1/2^{-})$	1405.1	1.3						176 (5)
	$\Lambda(1520)3/2^{-}$*	$0(3/2^{-})$	1519.5	1.0	16 (6)	47 (10)		142 (6)	154 (10)	
	Σ^{+}	$1(1/2^{+})$	1189.37	0.07	***					
	Σ°	$1(1/2^{+})$	1192.642							173 (3)
	Σ^{-}	$1(1/2^{+})$	1197.45	0.03	***					
	$\Sigma(1385)^{+}$	$1(3/2^{+})$	1382.80	0.35	***					
	$\Sigma(1385)^{\circ}$*	$1(3/2^{+})$	1383.7	1.0	19 (3)		102 (2)	144 (3)	154 (4)	
	$\Sigma(1385)^{-}$	$1(3/2^{+})$	1387.2	0.5	***					
	Ξ°	$1/2(1/2^{+})$	1314.86	0.20						
	Ξ^{-}	$1/2(1/2^{+})$	1321.71	0.07		50 (4,5)	105 (3,4)		154 (8)	
	$\Xi(1530)3/2^{+\circ}$	$1/2(3/2^{+})$	1531.80	0.32			106 (5,6)	140 (8,9)	157 (11)	
	$\Xi(1530)3/2^{-}$	$1/2(3/2^{+})$	1535.0	0.6	***					
	$\Xi(1820)3/2^{-}$	$1/2(3/2^{-})$**	1823	5		47 (14)			156 (13)	172 (7)
	$\Xi(2030)$**	$1/2(\geq 3/2^{?})$	2025	5	18 (11)				155 (15)	
	Ω^{-}	$0(3/2^{+})$	1673.45		15 (8)	50 (13)	103 (8)	141 (9)	153 (10)	
	$\Omega(2250)^{-}$**	$0(?^{?})$	2252	9				140 (14)		
12	charmed	baryons								
	Λ_c^{+}	$0(1/2^{+}$	2286.46							174 (9,10)
	$\Lambda_c(2595)^{+}$	$0(1/2^{-})$	2592.25				103 (13)			174 (14)
	$\Lambda_c(2625)^{+}$	$0(3/2^{-})$	2628.11		18 (15)	50 (20)			157 (17)	174 (11)
	$\Lambda_c(2880^{+})$	$0(5/2^{+})$	2881.53				102 (14)			173 (16,19)
	$\Lambda_c(2940^{+})$*	$0(5/2^{+})$	2939.3	1.5				141 (17)	158 (18)	173 (17)
	$\Sigma_c(2455)^{++}$	$1(1/2^{+})$	2453.97		***					174 (11)
	$\Sigma_c(2455)^{+}$	$1(1/2^{+})$	2452.9	0.4	***					
	$\Sigma_c(2455)^{\circ}$	$1(1/2^{+})$	2453.75		17 (12)					
	$\Sigma_c(2520)^{+-}$	$1(3/2^{+})$	2518.41		***					
	$\Sigma_c(2520)^{+}$*	$1(3/2^{+})$	2517.5	2.3	***					
	$\Sigma_c(2520)^{\circ}$	$1(3/2^{+})$	2518.48		17 (14)	48 (19)				
	$\Sigma_c(2800)^{+-}$**	$1(3/2^{+})$	2801	6	***					
	$\Sigma_c(2800)^{\circ}$**	$1(3/2^{+})$	2906	7				140 (16)		174 (20)
	Ξ_c^{+}	$1/2(1/2^{+})$	2467.93		***	50 (17)				
	Ξ_c°	$1/2(1/2^{+})$	2470.85		17 (12)	50 (18)			157 (17)	175 (12)
	$\Xi_c'^{+}$*	$1/2(1/2^{+})$	2575.7	3.0	***					
	$\Xi_c'^{\circ}$*	$1/2(1/2^{+})$	2577.9	2.9	16	50 (20)			157 (16)	
	$\Xi_c(2645)^{+}$	$1/2(3/2^{+})$	2645.9	0.5	***					
	$\Xi_c(2645)^{\circ}$	$1/2(3/2^{+})$	2645.9	0.5	18 (15)	49 (21)				175 (12,15)
	$\Xi_c(2790)^{+}$*	$1/2(1/2^{-})$	2789.1	3.2	***					
	$\Xi_c(2790)^{\circ}$*	$1/2(1/2^{-})$	2791.9	3.3						176 (18)
	$\Xi_c(2815)^{+}$*	$1/2(3/2^{-})$	2816.6	0.9	***					
	$\Xi_c(2815)^{\circ}$*	$1/2(3/2^{-})$	2819.6	1.2						174 (15)
	$\Xi_c(2970)^{+}$*	$1/2(?^{?})$	2970.7	2.2	***					
	$\Xi_c(2970)^{\circ}$*	$1/2(?^{?})$	2968.0	2.6	15 (16)					176 (18)
	$\Xi_c(3055)$*	$1/2(?^{?})$	3055.1	1.7						173 (19)
	$\Xi_c(3080)^{+}$	$1/2(?^{?})$	3076.94		***					
	$\Xi_c(3080)^{\circ}$*	$1/2(?^{?})$	3079.9	1.4	17 (17)			141 (17)		174 (20)
	Ω_c°*	$0(1/2^{+})$	2695.2	1.7		49 (21)	103 (13)			
	$\Omega_c(2770)^{\circ}$*	$0(3/2^{+})$	2765.9	2.0				140 (16)		174 (14,17)
13	bottom	baryons								
	Λ_b°	$0(1/2^{+})$	5619.51				106 (17)			172 (22)
	$\Lambda_b(5912)^{\circ}$	$0(1/2^{-})$	5912.11							175 (23)
	$\Lambda_b(5920)^{\circ}$	$0(3/2^{-})$	5919.81		15 (23)					
	Σ_b^{+}*	$1(1/2^{+})$	5811.3	1.9	17 (21,22)			144 (20)		
	Σ_b^{-}	$1(1/2^{+})$	5815.5	1.8	***					
	Σ_b^{*+}*	$1(3/2^{+})$	5832.1	1.9			106 (19,22)			
	Σ_b^{*-}*	$1(3/2^{+})$	5835.1	1.9	***					
	Ξ_b^{-}*	$1/2(1/2^{+})$	5794.5	1.4	***					
	Ξ_b°	$1/2(1/2^{+})$	5791.9	0.5	19 (21)	48 (28)		143 (19)	157 (21)	172 (22)
	$\Xi_b'(5935)^{-}$	$1/2(1/2^{+})$	5935.02		15 (23)		106 (21,22)	143 (19)		
	$\Xi_b(5945)^{\circ}$*	$1/2(3/2^{+})$	5948.9	1.6	15 (24)				157 (21)	
	$\Xi_b^{*}(5955)^{-}$	$1/2(1/2^{+})$	5955.33					144 (20)		
	Ω_b^{-}*	$0(3/2^{+})$	6046.4	1.9						
14	exotic	baryons								
	$P_c(4450)^{+}$*		4449.8	3.0						

3. Analysis of data in the file PDG–2016

The groping of ΔM at 104 MeV includes muon mass m_μ=106 MeV and is close to estimated s-quark mass m_s=98 MeV [16]. It was noticed by R. Sternheimer [22] that the difference (due to strangeness) between masses of K^* and ω meson 892 MeV-783 MeV=109 MeV (marked as K^* and ω in Fig. 3, on the horizontal axis and near the line from 0 up to Ξ=3M_q), is close to the muon mass μ which is shown at n=13 of the period $\delta = 16m_e$ (along the vertical axis) and again at n=-3 (plus one period 16δ=130.4 MeV) along horizontal axis of two–dimensional mass representation. The real value of the m_{K^*}-m_ω=109 MeV is 3 MeV away from m_μ and hence not included in Table 1.

Observed maxima in spacing distribution ΔM at 17, 104 and 142 MeV connected with well–known particles (see Fig. 3) were used for obtaining information on some aspects of the common dynamics within particle masses. Developed in PNPI method of data analysis AIM (Adjacent Interval Method) consists in fixating of distinguished intervals in the spectrum (pairs of masses which differ one from another with stable intervals, close to each other within averaging interval Δ) and plotting sum distribution to all other levels of the spectrum (distance D^{AIM} from both sides of fixed intervals). For example, fixating some parts of the rotational sequence with expression E^*=a·J(J+1), we can expect an appearance of traces of this expression in adjacent interval distributions. Hidden common dynamics in particle masses was found in cases discussed below.

Stable character of the interval close to the mass of the charged pion is clearly seen with Δ=5 MeV (central distribution). It was noticed by many authors (Y. Nambu, M.H. Mac Gregor and others). Intervals forming maximum at ΔM=142 MeV in spacing distribution between masses from PDG–2016 (Fig.1) are given in the corresponding column (142) of Table 2.

In unflavored and charmed mesons there is a clear excess of such intervals (boxed). According to Mac Gregor [24] a probability of an accidental grouping of mass intervals close to m_π is very low. First time small probability of accidental appearance of the observed periodicity with the interval m_π was found in data for masses of Λ and Ω hyperons [19,23]. In Fig. 3 it is seen as a straight–line (π-Λ-Ξ-Ω, k=1,8,11,12). Straight line connecting three pseudoscalar masses (π, η, η') corresponds to the interval Δ^T=409 MeV=50δ close to $2m_\pi+f_\pi$ (n=2·17+16=50). Independently, there is a grouping effect of mass differences at ΔM=1688 MeV, close to $12m_\pi$ (including masses of Ω-hyperon and ω_3 meson) and similar groupings at ΔM=1672 MeV (shifted from the first one with 16 MeV, close to 2δ).

Application of AIM method to the pion mass (x=142 MeV, upward AIM-direction, Δ=5 MeV) results in the maximum at ΔM=493 MeV exactly coinciding with the kaon mass (Fig. 4, top left). Application of the same method to the intervals equal to the kaon mass (Fig. 4, top right) results in confirmation of the pion mass and appearance of interval 388 MeV exactly equal to a half of the ρ-meson mass ΔM=389 MeV=$m_\rho/2$=M''_q, which is a standard estimate of the constituent quark mass. In Fig. 4 (2-nd line, Δ=5 and 9) the distributions for x=389 MeV contain maxima at 143 and 493 MeV confirming the distinguished character and interconnection of these three discussed well–known intervals and masses. We see in Fig. 3, that intervals close to $3f_\pi$=$m_\omega/2$ ≈390 MeV (horizontal line, n=3·16), the above mentioned interval $2m_\pi+f_\pi$ (n=50) and the periodicities with m_π (n=17) and ΔM_Δ=147 MeV (n=18) correspond to a common dynamics connected

with the pion. Discussed correlations with m_π are corresponding to the real particle masses and to the standard estimate of the meson constituent quark (a half of the mass of vector meson with parallel spins) and three–fold value of the f_π (as an example of the manifestation of pions parameters with n=16,17,18). An expression $16 \times 16 m_\pi$ shows the basic parameter for this symmetry–motivated dynamics.

The AIM method was used to find out intervals in the spectra (of the energies or the masses) which are situated close to each other (or adjacent). Fixating in the mass spectrum all small interval x=ΔM=16(2) MeV we plot sum spacing distribution of all intervals Δ^{AIM} from low–lying masses, of the interval x, up to all larger masses (upwards direction in AIM method). Appearance of eleven intervals Δ^{AIM}=463(2) MeV (Fig. 4 center left) can be checked with the presence of the maximum at 444 MeV in the downwards distribution for x=463 MeV (Fig. 4 center, right). It means that both intervals 444–463 MeV are systematically appear together (adjacent) in the different parts of the particle mass spectrum. These intervals are close to the parameter in the NRCQM–model 441 MeV=3·18δ=m_Ξ-/3 [14,15,20,21].

Observed maximum at 445 MeV (Fig. 1, center) includes two pairs of intervals between masses of $K°$, the neutron, $\Sigma°$ and $\omega°$, b_1-meson and Ω^-. The stable character of such intervals was noticed by R. Sternheimer and P. Kropotkin [21,22]. Now it is explained as the QCD effect in the Nonrelativistic Constituent Quark Model [13-15].

We continue comparison of obtained distributions in Fig. 1, 2 with stable intervals in particles with low mass. Interval ΔM=174 MeV includes differences between masses of Λ-hyperon and the neutron (1115.7–939.6 MeV=176.1 MeV). These two values are shown as Λ and N in Fig. 3 and correspond to n=8·17=136 and n=115 in the tuning effect considered here (and noticed by Y. Nambu as relations m_Λ=8m_π). Value 174 MeV is larger than expected 21δ=171.7 MeV due to the fact that Λ-hyperon mass is very close to $8m_\pi^\pm$=8·139.57 MeV=1116.6 MeV which is somewhat larger than 8·17δ=1111.9 MeV (charged pion mass is close, but larger than 17δ). Value m_Λ deviates from 136δ with the values about 8m_e=4 MeV. Possibly it is connected with the fact that 174 MeV in the total mass spacing distribution deviates from 172 MeV. Other intervals should be considered.

Three doublets of maxima in ΔM-distribution at 444–463 MeV (ΔM=3 MeV, Fig. 1 top) at 1673–1688 MeV, 3943–3960 MeV (Fig. 2, 3rd line, ΔM=9 MeV), at 4406–4425 MeV could be connected with the manifestation of three well-known dynamics, namely:
1) generation of the constituent quark mass within NRCQM-model (M_q=441 MeV=m_Ξ/3 [13-15] due to the gluon quark dressing effect based on QCD;
2) stable intervals ΔM multiple with m_π (k=12 and 24) resulted in the doublet at 1688 MeV=12m_π and the maximum at 3370 MeV=24m_π, and
3) the spectroscopy of the bottom quark – one of the heaviest fundamental component of the Standard Model with the estimated value m_b=4180(40) MeV [16]. Now we show that mass parameters of all effects are interconnected.

Stable interval Δ^{AIM}=460 MeV (close to M_q=441 MeV) appears also in the adjacent interval AIM-distribution (the AIM upward direction) for the fixed large stable intervals x=3960 MeV seen as the strongest maxima in all parts of Fig. 2 right (namely, ΔM=3957(1) MeV, 3959(2) MeV and 3960(4) MeV, for averaging intervals 3–5–9 MeV). These intervals are seen as a part of systems of maxima separated with small intervals close to 16 MeV=2δ. Such a system consisting out of Δ^{AIM}=3926 MeV and 3946 MeV in Δ^{AIM}–distribution (adjacent upwards distribution) for x=3960 MeV is shown in Fig. 4,

2nd line, right. Maximum in this system with the energy 3957(1) MeV (on the top distribution in Fig. 2 right) contains two sequences of exactly coinciding intervals:
1) the value ΔM=3957.4 MeV between the $b\bar{b}$ meson $\chi_{b0}(2P)$ with M=10232.5(4) MeV ($\chi_{b0}(2P)$, $0^+(0^{++})$) and the bottom charmed meson with M=6275.1(10) MeV (B_c^*, $0(0^-)$), and practically the same value ΔM=3957.4 MeV between the latter value and the mass of the charmed strange meson ($D_{sc}^*(2317)^{\pm}$, $0(0^+)$) M=2317.7(6) MeV ; and
2) value ΔM=3957.2 MeV between $b\bar{b}$ meson $\chi_{b2}(1P)$ with M=9912.5(4) MeV ($0^+(2^{++})$) and the bottom baryon with M=5955.33(13) MeV (Ξ_b^*, $1/2(1/2^+)$), and close to it (but uncertain) value ΔM=3960(8) MeV between the latter value and the mass value of the unflavored meson ($a_4(2040)^{\pm}$, $1^-(4^{++})$) M=1995(8) MeV.

Observed exact coincidence of three independent accurately measured intervals clearly connected with the presence of two and one bottom quarks in the structure of the relevant particles could be compared with the observed exact relation in CODATA data (exact multiplicity with the period $16m_e = \delta$=8.176 MeV). The ratio n=484.026 between the large interval under consideration (3957.4 MeV) and the universal parameter δ of the tuning effect, is close to n=484=486-2 (as well as n=486-4 and 486-6 for masses of other two members of the above discussed system of masses, situated within the region of the bottom quark mass m_b=4.18 GeV [16]). It allows to notice that n=486=9·54 corresponds to the mass 3974 MeV=9M_q with M_q=441 MeV, introduced empirically long ago by R. Sternheimer and P. Kropotkin [21,22]. The ratio between the vector boson mass (M_Z) and discussed stable interval is $M_Z/\Delta M$=91187(2) MeV/3957.4 MeV=23.042. It corresponds to the proximity of the ratio between M_Z and M_q to the lepton ratio L=207=16·13-1=9·23 (a reflection of the empirically found coincidence of ratios m_μ/M_Z and m_e/M_q with the QED radiative correction $\alpha/2\pi$ [3-12]). Theoretical and empirical analysis of discussed here coincidence of mass intervals associated with m_b is needed.

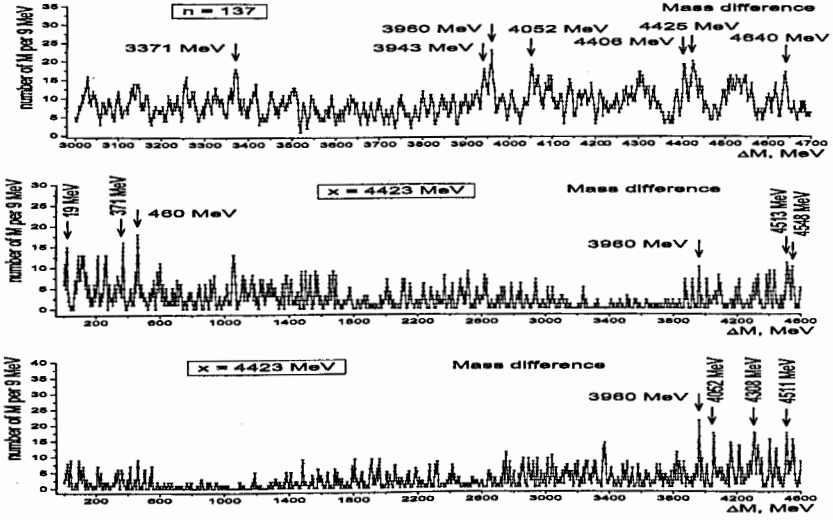

Fig. 3. *Top*: Spacing distribution in mass spectrum in high-energy region. *Central and Bottom*: Application of AIM to x=4423 MeV (AIM upward and downward directions, separately).

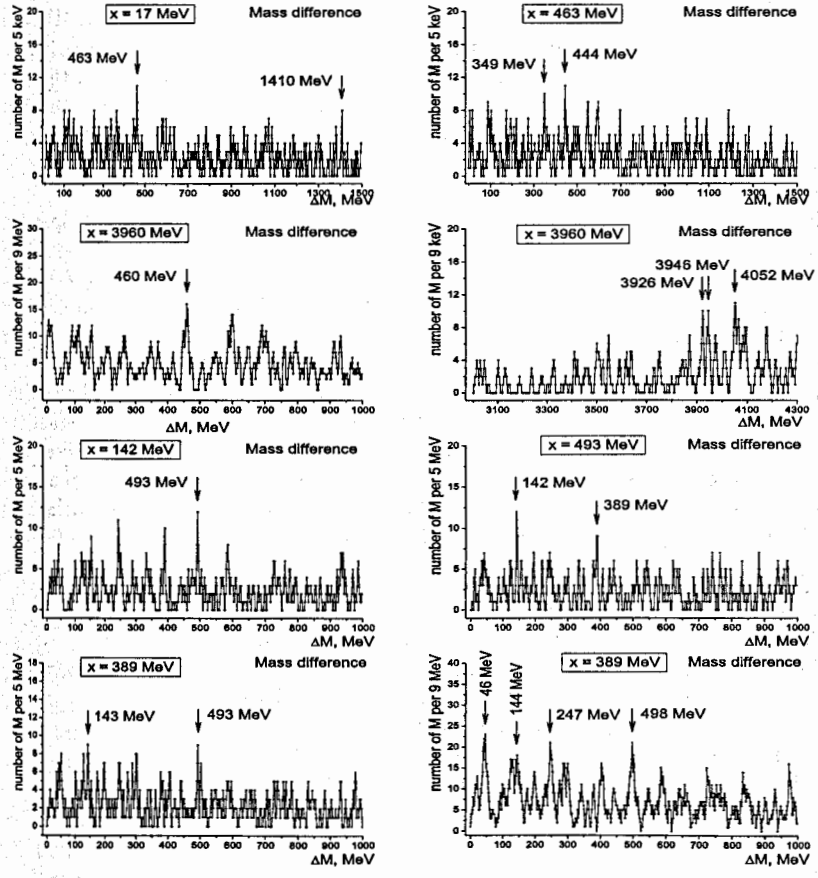

Fig. 4. *Top:* Application of AIM Method to show a systematic character of the appearance of intervals 444–463 MeV. Maximum at 463 MeV in left distribution (AIM upward x=16 MeV) corresponds to the maximum at 444 MeV in right distribution (AIM for x=463 MeV).
2nd line: The same to show a systematic character of intervals 3960–3946-3926 MeV (differing with 16 MeV=2δ). Maximum at 460 MeV in left distribution (upward, x=3960 MeV) corresponds to 463 MeV in upper left distribution (x=17 MeV).
Center: D^{AIM}–distribution for x=142 MeV=m_π. Maximum at 493 MeV correspond to the kaon mass (at left). The same for x=493 MeV to check the left distribution.
Bottom: D^{AIM}–distribution (Δ=5 MeV and 9 MeV) for the interval 389 MeV close to the meson constituent quark mass equal to a half of the ρ–meson mass. Presence of maxima at 143 MeV and 493 MeV is in agreement with maxima in the distribution for x=493 MeV (center right). These relations are needed to be confirmed and analyzed.

4. Conclusions

The distinguished character of mass values of the pion and the muon and clearly seen integer relations with the pion mass should be considered together with the fact that the constituent quark masses in NRCQM-model are close to three-fold values of both pions parameters, $M_q'' = 3f_\pi$ and M_q=3(ΔM_Δ=147 MeV). We have found here that observed long range correlation in CODATA relations with the parameter $\delta = 16m_e$ is supported by analysis of spacing distribution in the spectrum of particle masses.

Splitting in the vector boson masses ($8 : 9 = M_W : M_Z$) and the same splitting between the scalar field masses ($8 : 9 = M_H' : M_H$) are interconnected with splitting in the pion parameters f_π:m_π:ΔM_Δ (n=16:17:18 with the CODATA period $\delta = 16m_e$, Table 1) and ($8 : 9 = M_q'' : M_q$) between the constituent quark masses. Ratio between these two systems could be extrapolated to the fine structure parameters 161 keV=$\delta m_N/8$ and 170 keV=$m_e/3$ with the QED factor $\alpha/2\pi \approx 1/(32 \cdot 27)$ used in Table 1.

A role of similar QED correction with α_Z=1/129 for short distances should be considered together with a notice by R. Feynman about the universality of vector interaction. Symmetry motivated estimation of relations of the type 1:13 and 1:17 [7-12], and confirmation of the discreteness in particle masses with the analysis of nuclear binding energies could be useful. Presence of common tuning effect allows to use nuclear and particle mass spectra for the development of the Standard Model (see these Proceedings).

REFERENCES

1. Y. Nambu, Nucl. Phys. A **629** (1998) 3c.
2. S.I. Sukhoruchkin *et al*, Int. Rev. Phys. (IREPHY) **7** (2013) 135.
3. S.I. Sukhoruchkin *et al.*, Proc. ISINN-24, Dubna, 2016. JINR E3-2017-8, pp.86,98,110.
4. S.I. Sukhoruchkin, Nucl. Phys. B (Proc. Suppl.) **234** (2013) 241.
5. S.I. Sukhoruchkin, J. Phys.: Conf. Ser. **447** (2013) 012056.
6. S.I. Sukhoruchkin, Nucl. Part. Phys. Proc. **270-272** (2016) 211.
7. S.I. Sukhoruchkin, J. Phys.: Conf. Series **678** (2016) 012052.
8. S.I. Sukhoruchkin, PoS (EPS-HEP2015) 527.
9. S.I. Sukhoruchkin, Nucl. Part. Phys. Proc. **258-259** (2015) 268.
10. S.I. Sukhoruchkin, Nucl. Part. Phys. Proc. (in press).
11. S.I. Sukhoruchkin *et al.*, Proc. ISINN-23, 2015. JINR E3-2016-12, pp. 251,263,275,287.
12. S.I. Sukhoruchkin, *Tuning effect in particle masses*, Chicago. PoS (ICHEP2016) 1198.
13. T. Horn and G. Roberts, J. Phys. G: Nucl. Part. Phys. **43** (2016) 073061.
14. C. Itoh *et al.*, Phys. Rev. D **40** (1989) 3660.
15. L.A. Glozman, Nucl. Phys. A **629** (1998) 121c.
16. C. Patrignani *et al.* (Part. Data Group) Chin. Phys. C **40** (2016) 100001.
17. P. Mohr, B. Naylor, D.B. Neeell, Rev. Mod. Phys. 84 (2012) 1527 (CODATA).
18. H. Schopper (Ed.), Landoldt-Boernstein NS **vol. I/24,25,26**. Springer, 2000-2016.
19. S.I. Sukhoruchkin, *Stat. Prop. Nuclei.* Ed. G. Garg, (Pl. Press) p. 215 (1972).
20. Y. Nambu, Progr. Theor. Phys. **7** (1952) 595.
21. P. Kropotkin, *Field and Matter* (in Russian, Moscow Univ.) p. 106 (1971).
22. R. Sternheimer, Phys. Rev. **136** (1964) 1364; **170** (1968) 1267.
23. S.I. Sukhoruchkin, Proc. Symm Subatom. Phys., Adelaida, p. 142. AIP 539 (2000).
24. M.H. Mac Gregor, Nuovo Cimento A **103** (1990) 983.

COMBINED ANALYSIS OF NUCLEAR DATA AND PARTICLE MASSES

S.I. Sukhoruchkin, Z.N. Soroko, M.S. Sukhoruchkina

Petersburg Nuclear Physics Institute named by B.P.Konstantinov of NRC Kurchatov Institute 188300 Gatchina

1. Introduction

Neutron resonance spectroscopy could play an important role in the development of the Standard Model - a modern theory of all interactions [1] except gravitation and dark matter problem. A specific position of scalar and vector field masses among masses of other particles and constituent quarks was considered in [2]. Between masses of these fields (boxed in Table 1, top), other particle masses and stable nuclear intervals a correlation (named fine– and superfine structure) was established. Recently performed analysis [3] of mass spectra of all particles from the compilation PDG–2016 [1] confirmed discussed earlier "tuning effect" in particle masses and relations [4] between masses of nucleons and the electron (CODATA relations [2]).

Presence of stable intervals of 104 MeV and 142 MeV close to masses of the muon and the pion (n=13 and 17 of the CODATA period $\delta = 16m_e$) in the particle mass spectrum was noticed earlier by different authors [5,6]. The value δ=8.176 MeV was connected [5,6] with the proximity of d-quark mass estimate m_d=4.78 MeV [1] and pion charge splitting 4.594 MeV to $9m_e$=4.599 MeV = Δ. Simultaneously, there is a proximity of pions parameters f_π, m_π-m_e and ΔM_Δ=147 MeV (quark interaction in NRCQM, Nonrelativistic Constituent Quark Model) to integers n=16,17,18 of the common period δ. It is shown in [7] that QCD dynamics is based on gluon quark–dressing effect (from the Dyson–Schwinger equations and lattice QCD calculations) and is resulted in the constituent quark mass $M_q \approx 400$ MeV close to the standard estimates of constituent quark masses in NRCQM $M_q = m_\Xi/3$=441 MeV=3ΔM_Δ (n=3×18) and $M''_q = m_\rho/2$=388 MeV$\approx 3f_\pi$ (n=3×16). The ratio between masses of two fermions, namely, the electron and constituent quark m_e/M_q=(0.511 MeV/441 MeV)=115.8·10^{-5} is close to the ratio 1/27·32 = 115.7 · 10^{-5} in the tuning effect and to the QED radiative correction $\alpha/2\pi = 115.9 \cdot 10^{-5}$. V. Belokurov, D. Shirkov and R. Feynman [8,9] suggested that similar factor close to $\alpha/2\pi$ (correction to the electron magnetic moment) is contained also in the electron mass itself.

The fundamental origin of observed tuning effects (including common fine structure in particle masses and in unclear data) is connected with an important role of QCD as SM-component. We observe the fine structure and long–range correlations with m_e, $\Delta = 9m_e$ and $\Delta M_\Delta = 32\Delta$ [6] in nuclear data because the hadronization and mass generation in QCD is a base for the nuclear physics. Intervals of common fine structure in CODATA relations (n=17,18) and in nuclear data (n=13,14-18 [6]) are expressed as:

$$D = \Delta M = n \times 9.5\ keV; \quad n = 13, 14, 16, 17, 18 \tag{1}$$

The value of the period δ'=9.5 keV=8ε' is boxed in the central left part of Table 1. Manifestation of this parameter in positions of neutron resonances in light nuclei (top) and in the near-magic nuclei with N=82 (^{141}Ce and ^{142}Pr, center of Table 2 left) and in low-lying excitations of neighbour ^{143}Ce is presented in Table 2 together with the position of resonances at integer values of 1/8 part of the δ' , namely, at integers of the parameter ε'=1.188 keV, found earlier [5,6] in nonstatistical effects in many nuclei.

In the distribution of differences (ΔM) between all accurately known particle masses the grouping effect was found at the muon mass (ΔM=104 eV, 13δ-m_e), the pion mass (ΔM=142 MeV, 17δ+m_e), in regions of the constituent quark mass in NRCQM (ΔM=445-460 MeV) and at the bottom quark mass (ΔM=3959 MeV close to 9M_q=3969 MeV). It allows to represent as a single mass sequence the vector boson masses M_Z=91.19 GeV=13$\delta°$-M_q=L·M_q and M_W=80.38 GeV=13 · 16M''_q, the top quark mass m_t=172 GeV (close to 3×16$\delta°$=169 GeV), and finally, scalar field mass, M_H=125 GeV (close to 18$\delta°$=126 GeV) with the period $\delta°$=16M_q=$(\alpha/2\pi)^{-1}\delta$. Rapidly increasing number of accurately estimated values of particle masses allows to check CODATA relation with the forthcoming file PDG–2018. Besides nuclear fine structure effects with intervals multiple to 161–170 keV (n=17,18), additional systems of stable intervals corresponding to n=13,14,16 with the same period δ=9.5 keV were found [6]. Simultaneously, in neutron resonance spacing distributions second order effects with the same above mentioned small QED parameter $\alpha/2\pi$ were found as superfine structure with the period δ''=11 eV=$(\alpha/2\pi)^2\delta$=$(\alpha/2\pi)^3\delta°$. It is shown in Table 1, where above discussed intervals of the tuning effect (starting from NRCQM parameters, line X=0, M=3), stable spacing in particle masses spectrum 104 MeV≈ m_μ and m_π (n=13,17, line X=0, M=1) and corresponding intervals of fine and superfine structures (lines X=1 and 2) are presented as different power X of discussed factor $\alpha/2\pi \approx 1/32 \times 27$ and numbers n=1,13,16,17,18 in the expression n·16$m_e(\alpha/2\pi)^X$M.

Table 1. Representation of parameters of tuning effects in particle masses (top) and nuclear data (bottom) with the expression n·16$m_e(\alpha/2\pi)^X$M and different values of the X–power of QED factor $\alpha/2\pi$ and integers M,n. Boxed are groups of values differing with $\alpha/2\pi$.

X	M	n = 1	n = 13	n = 16	n = 17	n = 18	n = 18·6
-1	3/2			m_t=172.0			
GeV	1	$16M_q=\delta°$	M_Z=91.2	M'_H=115		M_H=126	
	1/2	(m_b-M_q)		M^{L3}=58			
0	1	$16m_e=\delta=8\varepsilon_o$	m_μ=106	f_π=130.7	m_π-m_e	ΔM_Δ=147	$2M_q$
MeV	3	NRCQM		M"$_q$=m_ρ/2		M_q=441=ΔE_B	
1	1				kδ-m_n-m_e=	170 = m_e/3	
		CODATA			=161.65		
keV	8				δm_N=1293.3		
1	1	9.5=δ'=8ε'	123	152	Δ^{TF}=161	170 (Sn)	ε_o=2m_e
keV	3				484 (E^*)	512 (Pd)	
	4		492		648 (Pd)	682(Co)	
	6					1023 (Os)	
	8		984	1212	1293 (E^*)	1360 (Te)	
2	1	11=δ''=8ε''	143	176	186 (Nd)		ε'=1188
eV	2				377 Nd)		
	4,6		570 (Sb)		749 (Br,Sb,Rh)	1205 (Os)*	
	8				1500 (Pd,Hf,Sb,Rh)		
	8×5				7498 (Pd)	M=3	ε''=1.35

* Before recoil correction

2. Fine structure in nuclear excitations

General character of the QCD dynamics is reflected in proximities to QED correction of ratios of fine structure parameters in nuclear data and particle masses to well-known parameters of strong interaction m_π=140 MeV and ΔM_Δ=147 MeV (161 keV/m_π=115·10^{-5} and 170.3 keV/147 MeV=116·10^{-5}). We should mention here three aspects.

1) Position of neutron resonance is a difference between excitation energy and neutron separation energy, hence, now one can assign nonstatistical effects in neutron resonance positions to the common structure in particle masses (CODATA) and nuclear data (n=17,18 of the period 9.5 keV=δ'). This interval δ' was directly observed by M. Ohkubo in the position of strong resonances of near-magic ^{141}Ce [10] (Table 2).

2) Observed by K. Ideno [11] superfine structure in ^{124}Sb with the period 11 eV=δ'' (see Table 1, Fig. 8 in [12]) could serve as a second example of a role of neutron spectroscopy in SM-development due to the fact that a ratio between these parameters δ''/δ'=11 eV/9.5 keV=115.8·10^{-5} is close to $\alpha/2\pi$. In Table 1 (bottom) similar ratios between superfine intervals D=373–570–1501 eV in ^{124}Sb (Fig. 186 in [6]), D=748–1495 eV in ^{104}Rh, D=749 eV in ^{80}Br, D=1497-7498 eV in ^{107}Pd (Fig. 191 [6]), D=757–1509 eV in ^{127,179}Hf, D=186–377 eV in ^{146,149}Nd (Fig. 192 [6]), D=1205 eV in ^{187,188}Os (Fig. 193 [6]), and corresponding stable fine structure excitations in the same or neighbour nuclei are presented. Such relation could provide an indirect confirmation of QED factor $\alpha/2\pi$.

Table 2. Comparison of positions and spacing in light and near-magic nuclei with the integer values of the parameter of the fine structure $\varepsilon' = \delta'/8 = 1.188$ keV [6].
Top: Positions E'_n of strong neutron resonances in light and magic nuclei and the periodicity in spacing distributions in resonances of ^{61}Ni (top right).
Center: Values E_n in nuclei with N=83=82+1, maxima in spacing distributions of ^{141}Ce.
Bottom left: Positions of strong neutron resonances in isotopes with Z=35–39 are compared with integer number of the period ε'=1.188 keV=9.505 keV/8 found in positions of strong resonances in Z=57–59, N=83 nuclei (center). *Bottom right:* Excitation energies E^* of ^{143}Ce.

Nucl.	Ca-Ni	^{61}Ni	^{61}Ni	^{61}Ni	^{61}Ni	^{61}Ni
E_n, l_n=0, D(keV)	18.8	4.8	9.3	14.1	19.0	24.7
k(ε')	16	4	8	12	16	20
k×ε'	19.0	4.8	9.6	14.4	19.0	24.7
Nucl.	^{141}Ce	^{141}Ce	^{142}Pr	^{141}Ce	^{141}Ce	^{141}Ce
J_i^π	$1/2^+$	$1/2^+$	$(5/2^-)$			
Γ_n^o,meV	660*	3060*	160	D	D	D
E_n	9.573	21.570	9.598	21.7	43.1	86.2
E^*,E'_n	9.505	21.418	9.530			
m($8\varepsilon'$)	1	9/4	1	9/4	9/2	9
m×$8\varepsilon'$	9.504	21.384	9.504	21.4	42.5	85
Nucl.	^{140}La	^{80}Br	^{82}Br	^{86}Rb	^{143}Ce	J_o^π=3/2$^-$
J_i^π	3^+	l_n=0	l_n=0	l_n=0	$7/2^-$	$5/2^-$
Γ_n^o,meV	54	72.0	120	159	E^*	E^*
E_n	1.179	1.201	1.209	2.398		
E^*,E'_n	1.170	1.186	1.194	2.370	18.9	42.3
m($8\varepsilon'$)	1/8	1	1	2	2	9/2
m×$8\varepsilon'$	1.188	1.188	1.188	2376	19.0	42.77

In Fig. 1 and Table 3, new results of fine structure analysis in recently published data are presented. Boxed are excitations in light nuclei which belong to fine structure with n=17 ($E^*=\delta m_N$ etc. [12]). Such excitations in ^{59}Co, ^{41}K and ^{116}Sn were noticed by O.I. Sumbayev [13] in data from γ-ray compilation [14]. Presence of the fine and superfine structures simultaneously in low-lying excitations and in neutron resonances was found in the regions around N=50, Z=51 and Z=72 (Hf, Os). Proximity of intervals of both structures in different nuclei could be assigned to meson exchange dynamics [6,15].

Neutron resonances correspond to a part of nuclear excitation spectra. In compilation ENSDF appearance of neutron resonances in the spectra of states can be seen as the groping effect. Such groupings were found by S.L. Sakharov [16] (periodicity in positions of these groupings). Results are similar to the correlation noticed earlier in [5].

Returning to the check of CODATA with files of nuclear data (CRF, NRF, MDF), we should notice that combined analysis of these files is important for development of truly microscopic models based on QCD. Quantum numbers of nuclear states should be measured. This time most of neutron resonances have uncertain spin/parity assignment. For example, in new data for excitations in near-magic ^{57}Ni spacing distributions (shown in Fig. 1) could be determined only for groups of states (see partial distributions which contain maxima at D=342 keV=36δ', of low-lying levels), 510 keV=3×18δ' (negative parity levels), 481–510 keV with small $J < 9/2$ and 680 keV (all positive parity levels).

Marked values in Table 3 [6] belong to the discussed system k(m_e/3) or k(δm_N/8).

Table 3. Excitations (in keV) in nuclei N=21,22 (top), N=28,27 and the period of 161 keV.

(Z-14)/2	3		2	1	1	1	1	0	0
$^A Z$	^{41}Ca		^{39}Ar	^{37}S	^{38}S	^{33}S	^{43}S	^{32}Si	^{35}Si
E^*	0.0	1943	1267	646.2	1292	322	320.7	1942	973.9
$2J^\pi$	7^-	3^-	3^-	3^-	2^+	D	7^-	2^+	(3^+)
k$\frac{\delta m_N}{8}$	0.0	1941	1293	646	1293	322	322	1941	971
$^A Z$	^{53}Ni $2J_o$=7-			^{58}Ni	^{59}Ni	^{61}Ni	^{53}Co	^{59}Co	
E^*	320(3)	1292*	1456*	1454.2	339.4	1454.8	646.2*	1291.6)	1459
$2J^\pi$	(5^-)	(3^-)	(11^-)	2^+	3^-–5^-	7^-	7^-	3^-	11^-
k$\frac{\delta m_N}{8}$	322	1293	1454	1454	322	1454	647	1293	1454

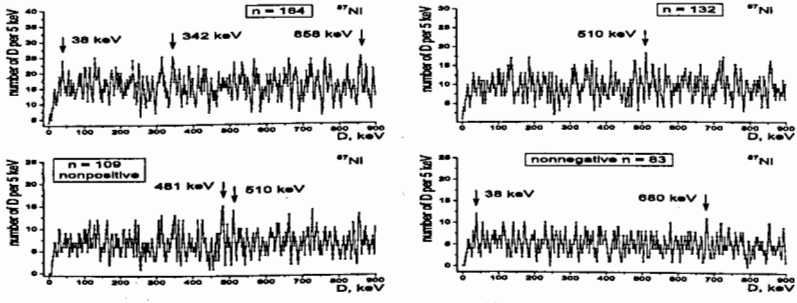

Fig. 1. *Top:* Spacing distribution in all levels of ^{57}Ni (*at left*) and in negative parity levels. *Bottom:* The same for negative parity levels with small spins and for nonnegative parity levels.

3. Analysis of particle masses in PDG–2016 file

In Tables 4–6, a continuation of the analysis [3] of particle masses from PDG–2016 [1] is presented. Table 7 contains new file PDG–2017. Values are given in the same order as they appear in Summary Tables and marked according to their uncertainty ΔM (as it was done in [6,12]. In this work, distributions for averaging intervals Δ=5 MeV and 9 MeV (Tables 4–6) were used.

Table 4. Particle masses [4] (in MeV) known with the uncertainty less than 6 MeV (intervals 193–1304 MeV).

	Particle		m_i	Δ	193	584	794 Δ=9	932	1092	1304
1	leptons	electron	0.0							
	μ		105.658					931 (13)		1303 (1)
	τ		1776.82		191 (11)	584 (4)	792 (18)			1304 (12)
2	Unflav.	mesons								
	$\pi^{\pm}$	$1^-(0^-)$	139.570						1090 (1)	
	η	$0^+(0^{-+})$	547.86							1306 (2)
	$\eta'(958)$	$0^+(0^{-+})$	957.78							
	$\phi(1020)$	$0^-(1^{--})$	1019.46						1093 (4)	
	$b_1(1235)$*	$1^+(1^{+-})$	1229.5	3.2			796 (2)		1090 (1)	1306 (4)
	$f_2(1270)$*	$0^+(2^{++})$	1275.5	0.8						1302 (6)
	$f_1(1285)$	$0^+(1^{++})$	1282.0	0.5	194 (2)	583 (6)				
	$a_2(1320)$	$1^-(2^{++}$	1318.3	0.5			794 (4)	934 (5)		
	$\eta(1405)$*	$0^+(0^{--})$	1408.8	1.8		587 (8)				1303 (1)
	$f_1(1420)$*	$0^+(1^{++})$	1426.4	0.9	191 (4)	584 (10)		933 (2)	1092 (7)	
	$\eta(1475)$**	$0^+(0^{-+})$	1476	4	194 (2,5)	584 (1)				
	$f_2'(1525)$**	$0^+(2^{++})$	1525	5		585 (2)	793 (7)	934 (9)		
	$\pi_1(1600)$**	$1^-(1^{-+})$	1662	8	192 (7)		794 (8,9)	930 (11)		1306 (10)
	$\eta_2(1645)$**	$0^+(0^{-+})$	1617	5	191 (3,4)					
	$\omega_3(1670)$**	$0^-(3^{--})$	1667	4	191 (5)	585 (11)	794 (10,11)			
	$\pi_2(1670)$*	$1^-(2^{-+})$	1672.2	3.0	192 (7)		793 (12)		1094 (8)	
	$\rho_3(1690)$*	$1^+(3^{--})$	1688.8	2.1			797 (1)			
	$f_0(1710)$**	$0^+(0^{++})$	1723	6	191 (6)		795 (15)			
	$\phi_3(1850)$**	$0^-(3^{--})$	1854	7	192 (7,11)	582 (5)	791 (19)			1306 (2)
	$a_4(2040)$**	$1^-(4^{++}$	1995	8		587 (8,13)	797 (21)			
3	strange	mesons								
	$K^{\pm}$	$1/2(0^-)$	493.677					932 (1,2)		
	$K^*(892)^{*\pm}$	$1/2(1^-)$	891.66			584 (1)	797 (1)	931 (3)		
	$K_1(1270)$**	$1/2(1^+)$	1272	7		582 (5)				1306 (5)
	$K_1(1400)$**	$1/2(1^+)$	1403	7						1305 (8)
	$K_2^*(1430)^{\pm}$*	$1/2(2^+)$	1425.6	1.5	191 (3)	585 (9)		932 (1)	1093 (6)	
	$K_2(1770)$**	$1/2(2^-)$	1773	8			796 (16)			
	$K_3^*(1780)$**	$1/2(3^-)$	1776	7	192 (10)	583 (3)	793 (17)	932 (12)		1304 (11)
	$K_4^*(2045)$**	$1/2(4^+)$	2045	9	191 (12)	583 (15)				
4	charmed	mesons								
	D°	$1/2(0^-)$	1864.83		192 (8,9)	583 (6)			1090 (2)	
	$D^{\pm}$	$1/2(0^-)$	1869.58			584 (12)		930 (4)	1094 (3)	
	$D^*(2010)^{\pm}$	$1/2(1^-)$	2010.28			585 (9,10,14)				
	$D_1(2420)^{\circ}$	$1/2(1^+)$	2420.8	0.5					1090 (10)	1305 (3)
	$D_2^*(2460)^{\pm}$*	$1/2(2^+)$	2465.4	1.3			798 (11,12,13)	934(10)	1091 (11)	
5	charmed,	strange	mesons							
	$D_s^{\pm}$	$0^+(0^-)$	1968.27		192 (10,11)	586 (7)	798 (20)			
	$D_s^{*\pm}$	$0(?^?)$	2112.1	0.4		583 (16)	797 (3,4,5,23)		1093 (4)	1303 (13)
	$D_{s0}^*(2317)^{\pm}$	$0(0^+)$	2317.7	0.6			794 (6,7)	934 (7)		
	$D_{s1}(2460)^{\pm}$	$0(1^+)$	2459.5	0.6			798 (9,10)	934 (9)		
	$D_{s1}(2536)^{\pm}$	$0(1^+)$	2535.10							1306 (4)
	$D_{s2}^*(2573)^*$	$0(2^+)$	2569.1	0.8			794 (16,17,18)			1303 (17)
	$D_{s1}^*(2700)^{\pm}$**	$0(1^-)$	2708.3	3.4	190 (14)			932 (12,13,16)		1304 (8,9)
6	bottom	mesons								
	$B^{\pm}$	$1/2(0^-)$	5279.31					932 (19)		
	$B_1(5721)^{+}$**	$1/2(1^+)$	5725.9	2.7	194 (20)					1305 (18)
7	bottom	strange	mesons							
	B_s°	$0(0^-)$	5366.82			582 (20)				
9	$c\bar{c}$"	mesons								
	$\eta_c(1S)$	$0^+(0^{-+})$	2983.4	0.5	191 (16)		790 (26)			
	$J/\psi(1S)$	$0^-(1^{--})$	3096.90		191 (17)		790 (28)			
	$\chi_{c0}(1P)$	$0^+(0^{++})$	3414.75					932 (18)		1303 (13)
	$\chi_{c1}(1P)$	$0^+(1^{++})$	3510.66					933 (14)	1090 (10)	

Table 4. Continued.

	Particle		m_l	Δ	193	584	794 Δ=9	932	1092	1304
	$h_c(1P)$	$?^?(0^{+-})$	3525.38			586(18)		933(15)		
	$\chi_{c2}(1P)$	$0^+(2^{++})$	3556.20				790(25,29)		1091(11)	1304 (14)
	$\eta_c(2S)$*	$0^+(0^{-+})$	3639.2	1.2		584(19)		931(16)		
	$\psi(2S)$	$0^-(1^{--})$	3686.10						1094(12)	
	$\psi(3770)$	$0^-(1^{--})$	3773.13				790(26)			1302 (15)
	$\psi(3823)$*	$?^?(2^{--})$	3822.2	1.2						1304 (16)
	$X(3872)$	$0^+(1^{++})$	3871.69				792(27)	932(17)		1303 (17)
	$X(3900)$*	$1^+(1^{+-})$	3886.6	2.4			790(28)			
	$X(4140)$*	$0^+(??+)$	4146.9	3.1					1092(13)	
	$X(4140)$*	$0^+(??+)$	4146.9	3.1					1092(13)	
	$X(4360)$**	$?^?(1^{--})$	4346.9	6			791(29)	932(18,19)		
	$\psi(4415)$**	$0^-(1^{--})$	4421	4						1305 (18)
	$X(4660)$**	$?^?(1^{--})$	4643	9	193(18)					1306 (19)
10	$b\bar{b}$	mesons								
	$\eta_b(1S)$*	$0^+(0^{-+})$	9399.0	2.3						
	$\Upsilon(1S)$	$0^-(1^{--})$	9460.30				795(30)			
	$\Upsilon(1D)$*	$0^-(2^{--})$	10163.7	1.4	192(21)					
	$\chi_{b0}(2P)$	$0^+(0^{++})$	10232.5	0.4		584(21)				
	$\chi_{b1}(2P)$	$0^+(1^{++})$	10255.46				795(30)			
	$\Upsilon(3S)$	$0^-(1^{--})$	10355.2	0.5	192(21)					
	$X(10610)^{\pm}$*	$1^+(1^+)$	10607.2	2.0		584(21)				
11		baryons								
	n	$1/2(1/2^+)$	939.5654			585(2)		930(4)		
	Λ	$0(1/2^+)$	1115.683							1305 (3)
	$\Lambda(1405)1/2^-$*	$0(1/2^-)$	1405.1	1.3						1303 (9)
	$\Lambda(1520)3/2^-$*	$0(3/2^-)$	1519.5	1.0			798(6)	934(8)		
	Σ°	$1(1/2^+)$	1192.642		191(1)	584(3,4)			1094(5)	
	$\Sigma(1385)^\circ$*	$1(3/2^+)$	1383.7	1.0	191(1)	586(7)		934(7)		
	Ξ°	$1/2(1/2^+)$	1314.86	0.20			797(3)			
	Ξ^-	$1/2(1/2^+)$	1321.71	0.07			797(5)	930(6)		1306 (7)
	$\Xi(1530)3/2^+{}^\circ$	$1/2(3/2^+)$	1531.80	0.32	191(6)			945(10)		
	$\Xi(1820)3/2^-$	$1/2(3/2^-)$**	1823	5				931(3)		
	$\Xi(2030)$**	$1/2(\geq 3/2^?)$	2025	5			786(2,22)			
	Ω^-	$0(3/2^+)$	1673.45		191(9)		794(13,14)		1092(9)	
	$\Omega(2250)^-$**	$0(?^?)$	2252	9		585(11)		932(5,6)		1304 (14)
12	charmed	baryons								
	Λ_c^+	$0(1/2^+$	2286.46				793(24)		1094(5)	
	$\Lambda_c(2595)^+$	$0(1/2^-)$	2592.25			583(14)		930(11,15)	1094(12)	
	$\Lambda_c(2625)^+$	$0(3/2^-)$	2628.11		191(15)	583(15)				1306 (7)
	$\Lambda_c(2940^+)$*	$0(5/2^+)$	2939.3	1.5		586(18)		932(17)		
	$\Sigma_c(2455)^\circ$	$1(1/2^+)$	2453.75		192(13)	584(12)	792(8)	934(8)		
	$\Sigma_c(2520)^\circ$	$1(3/2^+)$	2518.48		190(14)		795(15)		1092(6,7)	1304 (16)
	$\Sigma_c(2800)^\circ$**	$1(3/2^+)$	2906	7	190(17)		794(23)			
	Ξ_c°	$1/2(1/2^+)$	2470.85			584(17)	797(14)			1302 (15)
	$\Xi_c'^\circ$*	$1/2(1/2^+)$	2577.9	2.9		583(13)		933(14)		1304 (5,6)
	$\Xi_c(2645)^\circ$	$1/2(3/2^+)$	2645.9	0.5	192(13)		792(19)			
	$\Xi_c(2790)^\circ$*	$1/2(1/2^-)$	2791.9	3.3	192(16)		797(21)			
	$\Xi_c(2815)^\circ$*	$1/2(3/2^-)$	2819.6	1.2	191(15)		795(22)			
	$\Xi_c(2970)^\circ$*	$1/2(?^?)$	2968.0	2.6						1306 (10)
	$\Xi_c(3055)$*	$1/2(?^?)$	3055.1	1.7		584(17,19)			1092 (13)	
	$\Xi_c(3080)^\circ$*	$1/2(?^?)$	3079.9	1.4			794(24,27)			1304 (11,12)
	Ω_c°*	$0(1/2^+)$	2695.2	1.7		583(16)				
	$\Omega_c(2770)^\circ$*	$0(3/2^+)$	2765.9	2.0			798(20,25)		1092 (8,9)	
13	bottom	baryons								
	Λ_b°	$0(1/2^+)$	5619.51		192(19)					
	$\Lambda_b(5920)^\circ$	$0(3/2^-)$	5919.81		194(20)					
	Σ_b^{+}*	$1(1/2^+)$	5811.3	1.9	192(19)					
	$\Xi_b(5945)^\circ$*	$1/2(3/2^+)$	5948.9	1.6		582(20)				1306 (19)
	$P_c(4450)^+$*		4449.8	3.0	193(18)					

Table 5. Particle masses [4] (in MeV) known with the uncertainty less than 6 MeV (intervals 336–3371 MeV).

	Particle		m_l	Δ	336	447	460	1673	1688	3371
1	leptons	el., ν	0.0					1673 (1,2)	1688 (1)	
	μ		105.658					1673 (3,4)		
	τ		1776.82		336 (22)		460 (7,9)	1673 (4)		

Table 5. Continued.

	Particle		m_l	336	447	460	1673	1688	3371
2	Unflav.	mesons							
	$\pi^{\pm}$	$1^-(0^-)$	139.570						3371(1)
	η	$0^+(0^{-+})$	547.86						
	$\rho(770)$	$1^+(1^{--})$	775.26	336(1)				1688(2,3)	3371(3)
	$\omega(782)$	$0^-(1^{--})$	782.65	336(2)	447(2)		1673(5,6)	1688(4)	
	$\eta'(958)$	$0^+(0^{-+})$	957.78	336(6)	447(4,5,6)	460(1)	1673(8)	1688(7)	3371(2)
	$\phi(1020)$	$0^-(1^{--})$	1019.46			460(3)	1673(9)	1688(8)	
	$b_1(1235)$*	$1^+(1^{+-})$	1229.5	336(3)	447(2,7,8)	460(4)	1673(11)		
	$f_2(1270)$*	$0^+(2^{++})$	1275.5	336(5)	447(10)			1688(10)	3371(5)
	$f_1(1285)$	$0^+(1^{++})$	1282.0	336(9)				1688(11)	
	$\eta(1295)$**	$0^+(0^{-+})$	1294	336(6)			1673(12)	1688(1)	
	$a_2(1320)$	$1^-(2^{++}$	1318.3			460(8,9)			
	$\eta(1405)$*	$0^+(0^{--})$	1408.8		447(6,14)	460(13,14)	1673(17)	1688(14)	
	$f_1(1420)$*	$0^+(1^{++})$	1426.4		447(16)		1673(19)		
	$\eta(1475)$**	$0^+(0^{-+})$	1476			460(3)			
	$f_0(1500)$**	$0^+(0^{++})$	1504			460(15)			
	$f_2'(1525)$**	$0^+(2^{++})$	1525	336(7,13)	447(18)				
	$\pi_1(1600)$**	$1^-(1^{-+})$	1662	336(10,16)	447(19)				
	$\eta_2(1645)$**	$0^+(0^{-+})$	1617	336(9)					
	$\omega_3(1670)$**	$0^-(3^{--})$	1667		447(20)				
	$\pi_2(1670)$*	$1^-(2^{-+})$	1672.2	336(17)	447(7)		1673(1)		
	$\rho_3(1690)$*	$1^+(3^{--})$	1688.8	336(19)		460(4)		1688(1)	
	$f_0(1710)$**	$0^+(0^{++})$	1723	336(11)	447(9,10)			1688(15)	
	$\phi_3(1850)$**	$0^-(3^{--})$	1854	336(12)	447(12,13,14)	460(18)	1673(20)		
	$a_4(2040)$**	$1^-(4^{++}$	1995	336(16)		460(16,19,21)		1688(19)	3371(6)
3	strange	mesons							
	$K^{\pm}$	$1/2(0^-)$	493.677		447(1)	460(1)			
	$K^*(892)^{*\pm}$	$1/2(1^-)$	891.66	336(3)			1673(7)	1688(5)	
	$K_1(1270)$**	$1/2(1^+)$	1272	336(4)	447(9)				3371(4)
	$K_1(1400)$**	$1/2(1^+)$	1403		447(4,12)	460(2,10)	1673(15)		
	$K_2^*(1430)^{\pm}$*	$1/2(2^+)$	1425.6		447(15)		1673(12)		
	$K_2(1770)$**	$1/2(2^-)$	1773	336(20)	447(11)	460(5)			
	$K_3^*(1780)$**	$1/2(3^-)$	1776	336(21)		460(6,8)	1673(3)		
	$K_4^*(2045)$**	$1/2(4^+)$	2045						3371(7)
4	charmed	mesons							
	D^0	$1/2(0^-)$	1864.83	336(13,14)		460(10,11,13)		1688(17)	
	$D^{\pm}$	$1/2(0^-)$	1869.58	336(15)	447(15,16,21)	460(12,14)		1688(18)	
	$D^*(2010)^{\pm}$	$1/2(1^-)$	2010.28	336(17,18)	447(22,23)	460(21)	1673(22)		
	$D_1(2420)^0$	$1/2(1^+)$	2420.8			460(24)			3371(9)
	$D_2^*(2460)^{\pm}$*	$1/2(2^+)$	2465.4					1688(3)	3371(13,14)
5	charmed,	strange	mesons						
	$D_s^{\pm}$	$0^+(0^-)$	1968.27		447(17,18)	460(15)	1673(12)		
	$D_s^{*\pm}$	$0(?^?)$	2112.1	336(20,21,22)	447(19,20)	460(22)			
	$D_{s0}^*(2317)^{\pm}$	$0(0^+)$	2317.7		447(21,26)	460(18)			
	$D_{s1}(2460)^{\pm}$	$0(1^+)$	2459.5	336(25)	447(23,27)	460(20)	1673(6)	1688(2,20)	3371(11,12)
	$D_{s1}(2536)^{\pm}$	$0(1^+)$	2535.10		447(29)				
	$D_{s2}^*(2573)$*	$0(2^+)$	2569.1	336(26)		460(22)	1673(7)		
	$D_{s1}^*(2700)^{\pm}$*	$0(1^-)$	2708.3			460(23)		1688(8)	
6	bottom	mesons							
	$B^{\pm}$	$1/2(0^-)$	5279.31	336(32)					
	B^*	$1/2(1^-)$	5324.65					1688(22)	
	$B_1(5721)^{+*}$	$1/2(1^+)$	5725.9		447(33)			1688(24)	
	$B_2^*(5747)^{+*}$	$1/2(2^+)$	5737.2			460(31)			
	$B_J(5970)^+$	$1/1(?^?)$**	5964						3371(17)
7	bottom	strange	mesons						
	B_s^0	$0(0^-)$	5366.82		447(34)	460(32)			3371(6)
	B_s^{**}	$0(1^-)$	5415.4						3371(7)
	$B_{s1}(5830)^0$	$0(1^+)$	5828.63	447(35)	460(32)			3371(10,11)	
	$B_{s2}^*(5640)^0$	$0(2^+)$	5839.84					3371(14,15)	
8	bottom	charmed	mesons						
	B_c^{**}	$0(0^-)$	6275.1	336(34)	447(35,36)	460(33)			3371(18)
9	$c\bar{c}$"	mesons							
	$\eta_c(1S)$	$0^+(0^{-+})$	2983.4	336(28)	447(29)		1673(13)	1688(12)	
	$J/\psi(1S)$	$0^-(1^{--})$	3096.90		447(30)	460(27)	1673(18,19)	1688 (13.14)	
	$\chi_{c0}(1P)$	$0^+(0^{++})$	3414.75	336(29)	447(31)	460(28)		1688(15)	
	$\chi_{c1}(1P)$	$0^+(1^{++})$	3510.66			460(26)		1688(16)	3371(1)
	$h_c(1P)$	$?^?(0^{+-})$	3525.38		447(32)		1673(20)		

Table 5. Continued.

	Particle		m_i	336	447	460	1673	1688	3371
	$\chi_{c2}(1P)$	$0^+(2^{++})$	3556.20			460(27)		1688(17,18)	
	$\eta_c(2S)$*	$0^+(0^{-+})$	3639.2				1673(21)	1688(22)	
	$\psi(2S)$	$0^-(1^{--})$	3686.10	336(30)		460(29)	1673(26)	1688(19)	
	$X(3872)$	$0^+(1^{++})$	3871.69			460(28)			
	$X(3900)$*	$1^+(1^{+-})$	3886.6			460(30)			
	$X(3915)$*	$0^+(?^{++})$	3918.4	336(31)					3371(2)
	$\chi_{c2}(1P)$*	$0^+(2^{++})$	3927.2				1673(23)	1688(23)	
	$X(4020)$*	$1(?^?)$	4024.1	336(30)					
	$\psi(4040)$**	$0^-(1^{--})$	4039					1688(24)	
	$X(4140)$*	$0^+(??+)$	4146.9			460(29)	1673(24)	1688(20,25)	3371(3)
	$\psi(4160)$**	$0^-(1^{--})$	4191				1673(25)		
	$X(4260)$**	$?^?(1^{--})$	4251	336(31)			1673(28,26)	1688(26)	
	$X(4360)$**	$?^?(1^{--})$	4346.9			460(30)			
	$X(4660)$**	$?^?(1^{--})$	4643				1673(27)		3371(4,5)
10	$b\bar{b}$	mesons							
	$\eta_b(1S)$*	$0^+(0^{-+})$	9399.0			460(34)			
	$\chi_{b0}(1P)$	$0^+(0^{++})$	9859.44			460(34)			
	$\chi_{b1}(1P)$	$0^+(0^{++})$	9892.78	336(35)		460(35)			
	$h_b(1P)$*	$?^?(1^{+-})$	9899.3	336(36)		460(36)			
	$\chi_{b2}(1P)$	$0^+(2^{++})$	9912.21		447(37)				
	$\Upsilon(2S)$	$0^-(1^{--})$	10023.26	336(37)					
	$\Upsilon(1D)$*	$0^-(2^{--})$	10163.7		447(38)				
	$\chi_{b0}(2P)$	$0^+(0^{++})$	10232.5	336(35,36)					
	$\chi_{b2}(2P)$	$0^-(2^{+-})$	10268.65	336(38)					
	$\Upsilon(3S)$	$0^-(1^{--})$	10355.2	336(37)	447(37)	460(35,36)			
10	$X(10610)^{\pm}$*	$1^+(1^+)$	10607.2	336(38)	447(38)				
11		baryons							
	n	$1/2(1/2^+)$	939.5654	336(4,5)	447(1,3)	460(2)		1688(6)	
	Λ	$0(1/2^+)$	1115.683	336(1,2)			1673(10)		
	$\Lambda(1405)1/2^-$*	$0(1/2^-)$	1405.1		447(5,13)	460(11,12)	1673(16)	1688(13)	
	$\Lambda(1520)3/2^-$*	$0(3/2^-)$	1519.5	336(12)	447(17)				
	Σ°	$1(1/2^+)$	1192.642	336(7,8)				1688(9)	
	$\Sigma(1385)^\circ$*	$1(3/2^+)$	1383.7	336(11)	447(3)		1673(14)		
	Ξ°	$1/2(1/2^+)$	1314.86			460(5,6,7)	1673(13)		
	Ξ^-	$1/2(1/2^+)$	1321.71	336(10)	447(11)				
	$\Xi(1530)3/2^+{}^\circ$	$1/2(3/2^+)$	1531.80	336(8,14,15)		460(16)			
	$\Xi(1820)3/2^-$	$1/2(3/2^-)$**	1823			460(17)		1688(16)	
	$\Xi(2030)$**	$1/2(\geq 3/2^?)$	2025	336(19)	447(24)				
	Ω^-	$0(3/2^+)$	1673.45	336(18)	447(8)		1673(2)		
	$\Omega(2250)^-$**	$0(?^?)$	2252	336(23)	447(25)	460(21)	1673(23)		3371(8)
12	charmed	baryons							
	Λ_c^+	$0(1/2^+$	2286.46			460(17)			
	$\Lambda_c(2595)^+$	$0(1/2^-)$	2592.25	336(23)		460(25)			3371(17)
	$\Lambda_c(2625)^+$	$0(3/2^-)$	2628.11	336(27)			1673(8)	1688(6)	
	$\Lambda_c(2880^+)$	$0(5/2^+)$	2881.53					1688(9)	
	$\Sigma_c(2455)^\circ$	$1(1/2^+)$	2453.75	336(24)	447(22)	460(19)	1673(5)		3371(10)
	$\Sigma_c(2520)^\circ$	$1(3/2^+)$	2518.48		447(28)		1673(12)		
	$\Sigma_c(2800)^\circ$**	$1(3/2^+)$	2906	336(26)	447(27)		1673(11)		3371(18)
	Ξ_c°	$1/2(1/2^+)$	2470.85		447(24)	460(21)	1673(24)	1688(4)	3371(15)
	$\Xi_c'^\circ$*	$1/2(1/2^+)$	2577.9				1673(26)	1688 (5)	3371(16)
	$\Xi_c(2645)^\circ$	$1/2(3/2^+)$	2645.9	336(28)	447(30)			1688(7)	
	$\Xi_c(2790)^\circ$*	$1/2(1/2^-)$	2791.9	336(24,25)			1673(10)		
	$\Xi_c(2970)^\circ$*	$1/2(?^?)$	2968.0	336(27)	447(28,31)		1673(12,27)	1688(10,11)	
	$\Xi_c(3055)$*	$1/2(?^?)$	3055.1			460(25,26)	1673(14)		
	$\Xi_c(3080)^\circ$*	$1/2(?^?)$	3079.9	336(29)	447(32)		1673(15,16,17)		
	Ω_c°*	$0(1/2^+)$	2695.2		447(25)		1673(9)		
	$\Omega_c(2770)^\circ$*	$0(3/2^+)$	2765.9		447(26)			1688(21)	
13	bottom	baryons							
	Λ_b°	$0(1/2^+)$	5619.51	336(32,33)				1688(23)	3371(8)
	Σ_b^{+}*	$1(1/2^+)$	5811.3		447(34)	460(33)			
	Σ_b^{*+}*	$1(3/2^+)$	5832.1		447(36)			1688(25)	3371(12,13)
	Ξ_b°	$1/2(1/2^+)$	5791.9						3371(9)
	$\Xi_b'(5935)^-$	$1/2(1/2^+)$	5935.02	336(34)				1688(26)	
	$\Xi_b(5945)^\circ$*	$1/2(3/2^+)$	5948.9						3371(16)
	$\Xi_b^*(5955)^-$	$1/2(1/2^+)$	5955.33	336(33)					
14	exotic	baryons							
	$P_c(4450)^+$*		4449.8					1688(21)	

Table 6. Particle masses [4] (in MeV) known with the uncertainty less than 6 MeV (intervals 4425–3959 MeV).

	Particle		m_i	Δ	4425	4640	3943	4406	4052	3959
1	leptons	el., ν	0.0		4425(1)	4640(1)				
	$\boxed{\mu}$		105.658							
	τ		1776.82						4052(13,14)	3960(11)
2	Unflav.	mesons								
	$\pi^{\pm}$	$1^-(0^-)$	139.570						4052(1)	
	η	$0^+(0^{-+})$	547.86							
	$\rho(770)$	$1^+(1^{--})$	775.26			4640(2)				
	$\eta'(958)$	$0^+(0^{-+})$	957.78					4406(1)		
	$b_1(1235)^*$	$1^+(1^{+-})$	1229.5	3.2					4052(2)	
	$f_2(1270)^*$	$0^+(2^{++})$	1275.5	0.8		4640(6,7)			4052(4)	
	$f_1(1285)$	$0^+(1^{++})$	1282.0	0.5		4640(8)				
	$\eta(1295)^{**}$	$0^+(0^{-+})$	1294	4		4640(9)				
	$a_2(1320)$	$1^-(2^{++}$	1318.3	0.5		4640(11)		4406(2)	4052(6)	3960(3)
	$\eta(1405)^*$	$0^+(0^{--})$	1408.8	1.8	4425(10)	4640(15)		4406(7)		3960(7)
	$f_1(1420)^*$	$0^+(1^{++})$	1426.4	0.9			3940(3)	4406(10,11)		
	$\eta(1475)^{**}$	$0^+(0^{-+})$	1476	4			3939(4)			
	$f_0(1500)^{**}$	$0^+(0^{++})$	1504	6				4406(12)		
	$f_2'(1525)^{**}$	$0^+(2^{++})$	1525	5	4425(12)			4406(13)		
	$\pi_1(1600)^{**}$	$1^-(1^{-+})$	1662	8						3960(1)
	$\eta_2(1645)^{**}$	$0^+(0^{-+})$	1617	5	4425(14)					
	$\pi_2(1670)^*$	$1^-(2^{-+})$	1672.2	3.0			3947(5)		4052(7)	
	$\rho_3(1690)^*$	$1^+(3^{--})$	1688.8	2.1					4052(9)	
	$\phi_3(1850)^{**}$	$0^-(3^{--})$	1854	7	4425(15)					3960(12)
	$a_4(2040)^{**}$	$1^-(4^{++}$	1995	8			3940(10)		4052(17)	3960(16)
3	strange	mesons								
	$K^{\pm}$	$1/2(0^-)$	493.677							3960(1)
	$K_1(1270)^{**}$	$1/2(1^+)$	1272	7		4640(5)			4052(3)	
	$K_1(1400)^{**}$	$1/2(1^+)$	1403	7	4425(6,7)	4640(13)		4406(5)		3960 (5)
	$K_2^*(1430)^{\pm *}$	$1/2(2^+)$	1425.6	1.5			3941(2)	4406(8,9)		
	$K_2(1770^{**}$	$1/2(2^-)$	1773	8					4052(10)	3960(9)
4	charmed	mesons								
	D°	$1/2(0^-)$	1864.83				3046(7)	4406(15)	4052(15)	3960(13)
	$D^{\pm}$	$1/2(0^-)$	1869.58				3942(8)	4406(16)	4052(16)	3960(14,15)
	$D^*(2010)^{\pm}$	$1/2(1^-)$	2010.28				3943(11,12)			
5	charmed,	strange	mesons							
	$D_s^{\pm}$	$0^+(0^-)$	1968.27				3944(9)			
	$D_{s1}^*(2700)^{\pm *}$	$0(1^-)$	2708.3	3.4						
6	bottom	mesons								
	$B^{\pm}$	$1/2(0^-)$	5279.31						4052(2)	3960(2)
	B^*	$1/2(1^-)$	5324.65				3941(1)		4052(3,4)	
	$B_1(5721)^{+*}$	$1/2(1^+)$	5725.9	2.7				4406(2,3)	4052(7,8)	
	$B_2^*(5747)^{+*}$	$1/2(2^+)$	5737.2	0.7	4425(4,16)				4052(9)	3960(9,10,11)
	$B_J(5970)^+$	$1/1(?^?)^{**}$	5964	5		4640(12,17)	3939(13)			
7	bottom	strange	mesons							
	B_s°	$0(0^-)$	5366.82		4425(2)		3941(2,3)	4406(1)	4052(5,6)	3960(5,6,7)
	B_s^{**}	$0(1^-)$	5415.4	1.5		4640(2)	3939 (4)			
	$B_{s1}(5830)^{\circ}$	$0(1^+)$	5828.63		4425(6,8,18)	4640(1)		(8,10,18)	4052(10,11,13)	3960(13,14)
	$B_{s2}^*(5640)^{\circ}$	$0(2^+)$	5839.84		4425(20)				4052(19)	
8	bottom	charmed	mesons							
	B_c^{**}	$0(0^-)$	6275.1	1.0	4425(15)			4406(15,16)		3960(17,22)
9	$c\bar{c}$"	mesons								
	$\psi(4160)^{**}$	$0^-(1^{--})$	4191	5					4052(1)	
	$\psi(4415)^{**}$	$0^-(1^{--})$	4421	4	$\boxed{4425(1)}$					
	$X(4660)^{**}$	$?^?(1^{--})$	4643	9		$\boxed{4640(1)}$				
10	$b\bar{b}$	mesons								
	$\chi_{b0}(1P)$	$0^+(0^{++})$	9859.44				3943(14,15)		4052(18)	
	$\chi_{b1}(1P)$	$0^+(0^{++})$	9892.78				3944(16)		4052(19)	3960(18)
	$h_b(1P)^*$	$?^?(1^{+-})$	9899.3	0.8			3944(17)			3960(19)
	$\chi_{b2}(1P)$	$0^+(2^{++})$	9912.21							3960(20,21)
	$\Upsilon(2S)$	$0^-(1^{--})$	10023.26		4425(17)			4406(17)		
	$\Upsilon(1D)^*$	$0^-(2^{--})$	10163.7	1.4	4425(1)					
	$\chi_{b0}(2P)$	$0^+(0^{++})$	10232.5	0.4				4406(18)		3960(22)
	$\chi_{b1}(2P)$	$0^+(1^{++})$	10255.46		4425(18,19)	4640(16)				

Table 6. Continued.

	Particle		m_i	Δ	4425	4640	3943	4406	4052	3959
	$\chi_{b2}(2P)$	$0^-(2^{+-})$	10268.65		4425(20)					
	$\Upsilon(3S)$	$0^-(1^{--})$	10355.2	0.5				4406(19)		
	$X(10610)^{\pm}$*	$1^+(1^+)$	10607.2	2.0		4640(17)				
11		baryons								
	n	$1/2(1/2^+)$	939.5654		4425(2)					
	Λ	$0(1/2^+)$	1115.683							
	$\Lambda(1405)1/2^-$*	$0(1/2^-)$	1405.1	1.3	4425(8,9)	4640(14)		4406(6)		3960(6)
	$\Lambda(1520)3/2^-$*	$0(3/2^-)$	1519.5	1.0	4425(11)					
	Σ°	$1(1/2^+)$	1192.642		4425(3)	4640(3,4)				
	$\Sigma(1385)^{\circ}$*	$1(3/2^+)$	1383.7	1.0	4425(5)		3941(1)	4406(4)		
	Ξ°	$1/2(1/2^+)$	1314.86	0.20	4425(4)	4640(9)			4052(5)	3960(2)
	Ξ^-	$1/2(1/2^+)$	1321.71	0.07		4640(12)		4406(3)		3960(4)
	$\Xi(1530)3/2^{+\circ}$	$1/2(3/2^+)$	1531.80	0.32	4425(13)			4406(14)		
	$\Xi(2030)$**	$1/2(\geq 3/2^?)$	2025	5			3939(13)			
	Ω^-	$0(3/2^+)$	1673.45				3946(6)		4052(8)	
13	bottom	baryons								
	Λ_b°	$0(1/2^+)$	5619.51		4425(3)	4640(16)	3947(5,6)	4406(17)		3960(8)
	$\Lambda_b(5912)^\circ$	$0(1/2^-)$	5912.11			4640(5,6)	3944(9,14)	4406(12)		
	$\Lambda_b(5920)^\circ$	$0(3/2^-)$	5919.81			4640(7,8)	3940(15)		4052(15,16)	
	Σ_b^{+}*	$1(1/2^+)$	5811.3	1.9	4425(5,17)		3943(7,8)	4406(5,6,7)	4052(18)	3960(12)
	Σ_b^{*+}*	$1(3/2^+)$	5832.1	1.9	4425	4640(4)		4406(9,11)	4052(12,14)	3960(15)
					(7,9,10,18)					
	Ξ_b°	$1/2(1/2^+)$	5791.9	0.5				4406(4)		
	$\Xi_b'(5935)^-$	$1/2(1/2^+)$	5935.02			4640(9)	3940(10)	4406(13,14)		3960(18,19)
	$\Xi_b(5945)^{\circ}$*	$1/2(3/2^+)$	5948.9	1.6	4425(11,12)		3938(11,16)	4406(19)		3960(20)
	$\Xi_b^*(5955)^-$	$1/2(1/2^+)$	5955.33		4425(13)	4640(10,11)	3945(12,17)			3960(16,21)
	Ω_b^-*	$0(3/2^+)$	6046.4	1.9	4425(14)	4640(13,14.15)			4052 (17)	
14	exotic	baryons								
	$P_c(4450)^+$*		4449.8	3.0						3960(1)

4. General conclusions

Performed confirmation of CODATA relations between masses of nucleons and the electron provides a base for the Symmetry Motivated Electron–Based approach to the Standard Model development with the dominant role of two parameters of the electron: the mass value m_e and QED radiative correction [8,9]. This approach requires collection and analysis of new accurately measured data on particle masses and nuclear states.

Three parts of CODATA relations were considered:

1) The period $\delta = 16m_e$ common for many different particles, including leptons and hadrons; this period is confirmed with the analysis of data from PDG reviews. Distinguished position of the pions parameters $f_\pi, m_\pi, \Delta M_\Delta$ with n=16,17,18 provide a direct confirmation of symmetry motivated origin of the common period δ.

2) Fine structure with values of shifts 161 keV and 8×161 keV coinciding with nucleon mass splitting was earlier observed in nuclear excitations. Only recently this splitting was estimated theoretically within very large uncertainty, but its appearance in nuclear data was noticed long ago.

Now members of fine structure in nuclear data are determined within 1 keV uncertainty.

3) Similar situation exists with the parameter 170 keV=$m_e/3$ frequently seen as the analog of above mentioned fine structure. A possibility to study directly this common fine structure is a unique opportunity of the nuclear and neutron resonance spectroscopies which should not be ignored (taking into account a possibility to study position of nucleon mass within the first just discussed correlation).

4) Confirmation of CODATA relations suggested by Y. Nambu should be supplement with efforts from neutron resonance spectroscopy to check the role of the QED correction.

Table 7. Particle masses (MeV) from PDG–2017 known with an uncertainty <30 MeV given without rounding up; values with one and two meaningful numbers after the point are given directly; values with uncertainty < 8 MeV are marked by *; values with uncertainty > 8 MeV are marked by **; values which belong to members of multiplets excluded from the analysis (see text and [3,6,12]) are marked by ***.

		Particle		m_i	Δ
1	1	leptons	electron, ν	0.511	
	2		μ	105.658	
	3		τ	1776.82	
2		Unflav.	mesons		
		f_π		130.7	0.4
	4	π°***	$1^-(0^-)$	134.977	
	5	$\pi^{\pm}$	$1^-(0^-)$	139.571	
	6	η	$0^+(0^{-+})$	547.862	
	7	$\rho(770)$	$1^+(1^{--})$	775.26	
	8	$\omega(782)$	$0^-(1^{--})$	782.65	
	9	$\eta'(958)$	$0^+(0^{-+})$	957.78	
	10	$\phi(1020)$	$0^-(1^{--})$	1019.46	
	11	$b_1(1235)$*	$1^+(1^{+-})$	1229.5	3.2
	12	$f_2(1270)$*	$0^+(2^{++})$	1275.5	0.8
	13	$f_1(1285)$	$0^+(1^{++})$	1281.9	0.5
	14	$\eta(1295)$*	$0^+(0^{-+})$	1294	4
	15	$a_2(1320)$	$1^-(2^{++})$	1318.3	0.5
		$\pi_1(1400)$	$1^-(1^{--})$	1354	25
	16	$\eta(1405)$	$0^+(0^{--})$	1408.8	1.8
	17	$f_1(1420)$	$0^+(1^{++})$	1426.4	0.9
	18	$\eta(1475)$*	$0^+(0^{-+})$	1476	4
		$a_o(1450)$**	$1^-(0^{++})$	1474	19
	19	$f_0(1500)$*	$0^+(0^{++})$	1504	6
	20	$f_2'(1525)$*	$0^+(2^{++})$	1525	5
	21	$\pi_1(1600)$*	$1^-(1^{-+})$	1662	8
	22	$\eta_2(1645)$*	$0^+(2^{-+})$	1617	5
	23	$\omega_3(1670)$*	$0^-(3^{--})$	1667	4
	24	$\pi_2(1670)$	$1^-(2^{-+})$	1672.2	3.0
	25	$\rho_3(1690)$	$1^+(3^{--})$	1688.8	2.1
		$\rho(1700)$	$1^+(1^{--})$	1720	20
	26	$f_0(1710)$*	$0^+(0^{++})$	1723	6
	27	$\phi(1800)$**	$1^-(0^{-+})$	1812	12
	28	$\phi_3(1850)$*	$0^-(3^{--})$	1854	7
	29	$\pi_2(1880)$**	$1^-(2^{-+})$	1895	16
	30	$f_2(1950)$**	$0^+(2^{++})$	1944	12
	31	$a_4(2040)$*	$1^-(4^{++}$	1995	8
	32	$f_2(2050)$**	$0^+(4^{++})$	2018	11
	33	$\psi(2170)$**	$0^-(1^{--})$	2188	10
3		strange	mesons		
	34	$K^{\pm}$	$1/2(0^-)$	493.677	
	35	K°***	$1/2(0^-)$	497.01	0.013
	36	$K^*(892)^{*\pm}$	$1/2(1^-)$	891.76	0.29
	37	$K^*(892)^{*\circ}$***	$1/2(1^-)$	895.85	0.20
	38	$K_1(1270)$*	$1/2(1^+)$	1272	7
	39	$K_1(1400)$*	$1/2(1^+)$	1403	7
	40	$K^*(1410)$*	$1/2(1^-)$	1421	9
	41	$K_0^*(1430)^{\pm}$	$1/2(2^+)$	1425.6	1.5
	42	$K_2^*(1430)^{\circ}$***	$1/2(2^+)$	1432.4	1.3
		$K^*(1680)$**	$1/2(1^-)$	1718	18
	43	$K_2(1770)$*	$1/2(2^-)$	1773	8
	44	$K_3^*(1780)$*	$1/2(3^-)$	1776	7
	45	$K_2^*(1820)$**	$1/2(2^-)$	1819	12
	46	$K_4^*(2045)$*	$1/2(4^+)$	2045	9
4		charmed	mesons		
	47	D°	$1/2(0^-)$	1864.83	
	48	$D^{\pm}$	$1/2(0^-)$	1869.59	0.20
	49	$D^*(2007)^{\circ}$***	$1/2(1^-)$	2006.85	
	50	$D^*(2010)^{\pm}$	$1/2(1^-)$	2010.28	
	51	$D_1(2420)^{\circ}$	$1/2(1^+)$	2420.8	0.5
	52	$D_2^*(2460)^{\circ}$***	$1/2(2^+)$	2460.7	0.4
	53	$D_2^*(2460)^{\pm}$**	$1/2(2^+)$	2465.4	1.3
5		charmed	strange	mesons	
	54	$D_s^{\pm}$	$0^+(0^-)$	1968.18	
	55	$D_s^{*\pm}$	$0(?^?)$	2112.1	0.4
	56	$D_{s0}^*(2317)^{\pm}$	$0(0^+)$	2317.7	0.6
	57	$D_{s1}(2460)^{\pm}$	$0(1^+)$	2459.5	0.6
	58	$D_{s1}(2536)^{\pm}$	$0(1^+)$	2535.10	
	59	$D_{s2}^*(2573)$*	$0(2^+)$	2569.1	0.8
	60	$D_{s1}^*(2700)^{\pm}$**	$0(1^-)$	2708.3	3.4
6		bottom	mesons		
	61	$B^{\pm}$	$1/2(0^-)$	5279.32	
	62	B°***	$1/2(0^-)$	5279.63	
	63	B^*	$1/2(1^-)$	5324.65	
	64	$B_1(5721)^{+}$**	$1/2(1^+)$	5725.9	2.7
	65	$B_1(5721)^{\circ}$***	$1/2(1^+)$	5726.0	1.3
	66	$B_2^*(5747)^{+}$**	$1/2(2^+)$	5737.2	0.7
	67	$B_2^*(5747)^{\circ}$***	$1/2(2^+)$	5739.5	0.7
	68	$B_J(5970)^{+}$	$1/1(?^?)$**	5964	5
	69	$B_J(5970)^{\circ}$***	$1/1(?^?)$**	5971	5
7		bottom	strange	mesons	
	70	B_s°	$0(0^-)$	5366.89	
	71	B_s^{*}*	$0(1^-)$	5415.4	1.5
	72	$B_{s1}(5830)^{\circ}$	$0(1^+)$	5828.63	
	73	$B_{s2}^*(5640)^{\circ}$	$0(2^+)$	5839.85	
8		bottom	charmed	mesons	
	74	B_c^{+}*	$0(0^-)$	6274.9	1.0
9		$c\bar{c}$	mesons		
	75	$\eta_c(1S)$	$0^+(0^{-+})$	2983.4	0.5
	76	$J/\psi(1S)$	$0^-(1^{--})$	3096.90	
	77	$\chi_{c0}(1P)$	$0^+(0^{++})$	3414.75	
	78	$\chi_{c1}(1P)$	$0^+(1^{++})$	3510.66	
	79	$h_c(1P)$	$?^?(1^{+-})$	3525.38	
	80	$\chi_{c2}(1P)$	$0^+(2^{++})$	3556.20	
	81	$\eta_c(2S)$	$0^+(0^{-+})$	3639.2	1.2
	82	$\psi(2S)$	$0^-(1^{--})$	3686.10	
	83	$\psi(3770)$	$0^-(1^{--})$	3773.13	
	84	$\psi(3823)$	$?^?(2^{--})$	3822.2	1.2
	85	$X(3872)$	$0^+(1^{++})$	3871.69	
	86	$X(3900)$	$1^+(1^{+-})$	3886.6	2.4
	87	$X(3915)$	$0^+(?^{++})$	3918.4	1.9
	88	$\chi_{c2}(1P)$	$0^+(2^{++})$	3927.2	2.6
	89	$X(4020)$	$1(?^?)$	4024.1	1.9
	90	$\psi(4040)$*	$0^-(1^{--})$	4039	1
	91	$X(4140)$	$0^+(?^{1+})$	4146.8	3.1
	92	$\psi(4160)$*	$0^-(1^{--})$	4191	5
	93	$X(4260)$*	$?^?(1^{--})$	4230	8
	94	$X(4360)$*	$?^?(1^{--})$	4341	8
	95	$\psi(4415)$*	$0^-(1^{--})$	4421	4
	96	$X(4430)$**	$?^?(1^{+})$	4418	15
	97	$X(4660)$*	$?^?(1^{--})$	4643	9
10		$b\bar{b}$	mesons		
	98	$\eta_b(1S)$	$0^+(0^{-+})$	9399.0	2.3
	99	$\Upsilon(1S)$	$0^-(1^{--})$	9460.30	
	100	$\chi_{b0}(1P)$	$0^+(0^{++})$	9859.44	
	101	$\chi_{b1}(1P)$	$0^+(0^{++})$	9892.78	
	102	$h_b(1P)$	$?^?(1^{+-})$	9899.3	0.8
	103	$\chi_{b2}(1P)$	$0^+(2^{++})$	9912.21	
	104	$\Upsilon(2S)$	$0^-(1^{--})$	10023.26	
	105	$\Upsilon(1D)$	$0^-(2^{--})$	10163.7	1.4
	106	$\chi_{b0}(2P)$	$0^+(0^{++})$	10232.5	0.4

Table 7. Continued.

	Particle		m_i	Δ		Particle		m_i	Δ
107	$\chi_{b1}(2P)$	$0^+(1^{++})$	10255.46		143	$\Sigma_c(2520)^{++***}$	$1(3/2^+)$	2518.41	
108	$\chi_{b2}(2P)$	$0^-(2^{+-})$	10268.65		144	$\Sigma_c(2520)^{+***}$	$1(3/2^+)$	2517.5	2.3
109	$\Upsilon(3S)$	$0^-(1^{--})$	10355.2	0.5	145	$\Sigma_c(2520)^{\circ}$	$1(3/2^+)$	2518.48	
110	$\chi_{b1}(3P)$	$0^+(1^{++})$	10512.1	2.3	146	$\Sigma_c(2800)^{++***}$	$1(3/2^+)$	2801	6
111	$\Upsilon(4S)$	$0^-(1^{--})$	10579.4	1.2	147	$\Sigma_c(2800)^{+**}$	$1(3/2^+)$	2792	14
112	$X(10610)^{\pm}$	$1^+(1^+)$	10607.2	2.0	148	$\Sigma_c(2800)^{\circ *}$	$1(3/2^+)$	2806	7
113	$X(10610)^{\circ}$	$1^+(1^+)$	10609	6	149	Ξ_c^{+***}	$1/2(1/2^+)$	2467.87	
114	$\Upsilon(10860)$	$0^-(1^{--})$	10889.9	3.2	150	Ξ_c°	$1/2(1/2^+)$	2470.87	
115	$\Upsilon(11020)^*$	$0^-(1^{--})$	10993	10	151	$\Xi_c'^{+***}$	$1/2(1/2^+)$	2577.4	1.2
11		baryons			152	$\Xi_c'^{\circ}$	$1/2(1/2^+)$	2577.8	0.3
116	p^{***}	$1/2(1/2^+)$	938.2721		153	$\Xi_c(2645)^{+***}$	$1/2(3/2^+)$	2645.53	
117	n	$1/2(1/2^+)$	939.5654		154	$\Xi_c(2645)^{\circ}$	$1/2(3/2^+)$	2646.32	
118	Λ	$0(1/2^+)$	1115.683		155	$\Xi_c(2790)^{+***}$	$1/2(1/2^-)$	2792.0	0.5
119	$\Lambda(1405)1/2^{-*}$	$0(1/2^-)$	1405.1	1.3	156	$\Xi_c(2790)^{\circ}$	$1/2(1/2^-)$	2792.8	1.2
120	$\Lambda(1520)3/2^{-*}$	$0(3/2^-)$	1519.5	1.0	157	$\Xi_c(2815)^{+***}$	$1/2(3/2^-)$	2816.67	0.31
121	Σ^{+***}	$1(1/2^+)$	1189.37	0.07	158	$\Xi_c(2815)^{\circ}$	$1/2(3/2^-)$	2820.22	0.32
122	Σ°	$1(1/2^+)$	1192.642		159	$\Xi_c(2970)^{+***}$	$1/2(?^?)$	2969.4	0.8
123	Σ^{-***}	$1(1/2^+)$	1197.45	0.03	160	$\Xi_c(2970)^{\circ}$	$1/2(?^?)$	2967.8	0.8
124	$\Sigma(1385)^{+***}$	$1(3/2^+)$	1382.80	0.35	161	$\Xi_c(3055)$	$1/2(?^?)$	3055.9	0.4
125	$\Sigma(1385)^{\circ}$	$1(3/2^+)$	1383.7	1.0	162	$\Xi_c(3080)^{+***}$	$1/2(?^?)$	3077.2	0.4
126	$\Sigma(1385)^{-***}$	$1(3/2^+)$	1387.2	0.5	163	$\Xi_c(3080)^{\circ}$	$1/2(?^?)$	3079.9	1.4
127	Ξ°	$1/2(1/2^+)$	1314.86	0.20	164	Ω_c°	$0(1/2^+)$	2695.2	1.7
128	Ξ^-	$1/2(1/2^+)$	1321.71	0.07	165	$\Omega_c(2770)^{\circ}$	$0(3/2^+)$	2765.9	2.0
129	$\Xi(1530)3/2^{+\circ}$	$1/2(3/2^+)$	1531.80		13	bottom	baryons		
130	$\Xi(1530)3/2^{-***}$	$1/2(3/2^+)$	1535.0		166	Λ_b°	$0(1/2^+)$	5619.58	
131	$\Xi(1820)3/2^{-*}$	$1/2(3/2^-)$	1823	5	167	$\Lambda_b(5912)^{\circ}$	$0(1/2^-)$	5912.18	0.21
132	$\Xi(2030)^*$	$1/2(\geq 3/2^?)$	2025	5	168	$\Lambda_b(5920)^{\circ}$	$0(3/2^-)$	5919.90	0.19
133	$\boxed{\Omega^-}$	$0(3/2^+)$	$\boxed{1673.45}$		169	Σ_b^{+*}	$1(1/2^+)$	5811.3	1.9
134	$\Omega(2250)^{-**}$	$0(?^?)$	2252	9	170	Σ_b^{-***}	$1(1/2^+)$	5815.5	1.8
12	charmed	baryons			171	Σ_b^{*+*}	$1(3/2^+)$	5832.1	1.9
135	Λ_c^+	$0(1/2^+$	2286.46		172	Σ_b^{*-***}	$1(3/2^+)$	5835.1	1.9
136	$\Lambda_c(2595)^+$	$0(1/2^-)$	2592.25		173	Ξ_b^{-***}	$1/2(1/2^+)$	5794.5	1.4
137	$\Lambda_c(2625)^+$	$0(3/2^-)$	2628.11		174	Ξ_b°	$1/2(1/2^+)$	5791.9	0.5
138	$\Lambda_c(2880^+)$	$0(5/2^+)$	2881.53		175	$\Xi_b'(5935)^-$	$1/2(1/2^+)$	5935.02	
139	$\Lambda_c(2940^+)^*$	$0(5/2^+)$	2939.3	1.5	176	$\Xi_b(5945)^{\circ}$	$1/2(3/2^+)$	5949.8	1.4
140	$\Sigma_c(2455)^{++***}$	$1(1/2^+)$	2453.97		177	$\Xi_b^*(5955)^-$	$1/2(1/2^+)$	5955.33	
141	$\Sigma_c(2455)^{+***}$	$1(1/2^+)$	2452.9	0.4	178	Ω_b^-	$0(3/2^+)$	6046.1	1.9
142	$\Sigma_c(2455)^{\circ}$	$1(1/2^+)$	2453.75						

REFERENCES

1. C. Patrignani *et al.* (Particle Data Group) Chin. Phys. C **40** (2016) 100001.
2. S.I. Sukhoruchkin, *Tuning effect in particle masses*, PoS (ICHEP2016) 1198.
3. S.I. Sukhoruchkin, these Proceedings.
4. P. Mohr, D.B. Newell, B.N. Taylor, Rev. Mod. Phys. (2016) **88** 035009.
5. S.I. Sukhoruchkin, *Stat. Prop. Nuclei.* Ed. G. Garg, (Pl. Press) p. 215, 1972.
6. S.I. Sukhoruchkin, *Discreteness in particle masses.* (Lambert Ac. Publ.) 2017.
7. T. Horn and G. Roberts, J. Phys. G: Nucl. Part. Phys. **43** (2016) 073061.
8. V.V. Belokurov, D.V. Shirkov, *Theory of Part. Interactions.* AIP, N.-Y, 1991.
9. R. Feynman, *QED-Strange Theory of Light/Matter*, 1986. Princ. Univ. Press.
10. M. Ohkubo *et al.*, Rept. JAERI-M-93112, 1993.
11. K. Ideno, Proc. Conf. Neutrons in Res., Crete. SPIE Proc. **2867**, 1997, p. 398.
12. S.I. Sukhoruchkin, Proc. of the L Winter School of PNPI SPb, 2017, pp. 45–119.
13. O.I. Sumbayev, Doklady AN SSSR **316** (1991) 1116.
14. B.S. Dzhelepov, S.F. Koksharova, *Tables of γ-rays energies* p.215. L., Nauka, 1970.
15. T. Otsuka et al., Nucl. Phys. A **805** (2008) 127c; Phys. Scr. T **152** (2013) 014007.
16. S.L. Sakharov, Izv. RAS ser. fis. **64** (2000) 930.

ON FEATURES OF A METHOD FOR THE SUPERFLUIDITY INVESTIGATION AT NUCLEAR EXCITATIONS BELOW THE NEUTRON BINDING ENERGY

Sukhovoj A.M.[1], Mitsyna L.V.[1], Vu D.C.[1,2], Anh N.N.[3], Hai N.X.[3], Khang P.D.[4], Thang H.H.[3]

[1]*Joint Institute for Nuclear Research, Dubna, 141980, Russia*
[2]*Vietnam Academy of Science and Technology Institute of Physics, Hanoi, Vietnam*
[3]*Dalat Nuclear Research Institute, Vietnam Atomic Energy Institute, Hanoi, Vietnam*
[4]*Hanoi University of Science and Technology, 1 Daicoviet, Hanoi, Vietnam*

Abstract. A simultaneous determination of the nuclear level density (NLD) and the radiative γ-ray strength functions (RSF) is a way to investigate the nuclear superfluidity. The empirical method, proposed for this purpose, is based on analysis of the two-step γ-ray cascades (TSC), which are resulted from a capture of thermal neutrons. At that, different valid assumptions and phenomenological representations of NLD and RSF parameterizations were used and tested for the experimental TSC intensities description. Investigation of 44 nuclei with masses in the region $28 \le A \le 200$ showed an influence of the nuclear shape on the dynamics of a change of a phase of nuclear matter.

1. Introduction

By analogy with the superfluidity effect in metals due to pairing of electrons [1, 2] a pairing of nucleons results in the superfluidity of nuclear matter [3]. As information about pair correlations, thermodynamic characteristics and properties of electromagnetic transitions [4, 5] can be extracted from NLD and RSF values, so in order to understand the process of phase change in nuclear matter it is necessary to determine these two values experimentally.

As it is impossible to resolve all individual levels and to determine probabilities of transitions between them by available now spectrometers, information on the superfluidity can be obtained from indirect experiments only. The method of TSC measuring has been developed at FLNP JINR [6]. In this method TSC of γ-decay following a thermal neutron capture are recorded, and then their intensities are described by functions of some fitted parameters (chosen for NLD and RSF according to appropriate theoretical representations) at the excitation energies from the ground state to neutron resonance [7].

Up to now, the experiment was carried out on 44 nuclei of mass region $28 \le A \le 200$: ^{28}Al, ^{40}K, ^{52}V, ^{60}Co, ^{64}Cu, ^{71}Ge, ^{74}Ge, ^{114}Cd, ^{118}Sn, ^{124}Te, ^{125}Te, ^{128}I, ^{137}Ba, ^{138}Ba, ^{139}Ba, ^{140}La, ^{150}Sm, ^{156}Gd, ^{158}Gd, ^{160}Tb, ^{163}Dy, ^{164}Dy, ^{165}Dy, ^{166}Ho, ^{168}Er, ^{170}Tm, ^{172}Yb, ^{174}Yb, ^{176}Lu, ^{177}Lu, ^{181}Hf, ^{182}Ta, ^{183}W, ^{184}W, ^{185}W, ^{187}W, ^{188}Os, ^{190}Os, ^{191}Os, ^{192}Ir, ^{193}Os, ^{196}Pt, and ^{198}Au.

TSC is determined by the energies of initial, intermediate and final levels as well as the probabilities of electromagnetic transitions between them. In a small interval ΔE of energies of primary transitions the sum of the intensities of TSC from initial states λ to a group of low-lying final states f through intermediate levels i is determined by an equation:

$$I_{\gamma\gamma}(E_1 \pm \Delta E/2) = \sum_{\lambda,f}\sum_{i} \frac{\Gamma_{\lambda i}}{\Gamma_{\lambda}} \frac{\Gamma_{if}}{\Gamma_{i}} = \sum_{\lambda,f}\sum_{j} \frac{\Gamma_{\lambda j}}{<\Gamma_{\lambda j}> M_{\lambda j}} n_j \frac{\Gamma_{jf}}{<\Gamma_{jf}> m_{jf}}, \qquad (1)$$

where $n_j = \langle\rho_j\rangle \cdot \Delta E$ is the number of excited levels of the cascades in the ΔE energy bin, $\langle\rho_j\rangle$ is a mean value of NLD in the ΔE energy bin, a sum of the partial widths of the primary transitions $\Sigma_j \Gamma_{\lambda j}$ to $M_{\lambda j}$ intermediate levels is $\langle\Gamma_{\lambda j}\rangle M_{\lambda j}$, and a sum $\Sigma_j \Gamma_{jf}$ for the secondary transition to m_{jf} final levels is $\langle\Gamma_{jf}\rangle m_{jf}$, inasmuch as $\langle\Gamma_{\lambda j}\rangle = \Sigma_j \Gamma_{\lambda j}/M_{\lambda j}$ and $\langle\Gamma_{jf}\rangle = \Sigma_j \Gamma_{jf}/m_{jf}$.

The system of equations (1) is nonlinear and strongly correlated. Its solving (by maximum likelihood method) allows to obtain the NLD and RSF values simultaneously. The required NLD and RSF values, which are expressed as functions $\rho(E_{ex})=\varphi(p_1,p_2\ldots)$ and $\Gamma(E_1)= \psi(q_1,q_2\ldots)$ using different valid representations, can be evaluated from the fits of p_1, p_2, ... and q_1, q_2, ... parameters to the experimental intensities for all observed γ-transitions.

Now NLD is commonly represented by Gilbert-Cameron formula [8], what combines the Fermi gas model [9] and the constant temperature model [4], the backshift Fermi gas model (BSFM) [10] or phenomenological version of generalized superfluid model (GSM) [11]. Parameters of these models are founded by fitting to the experimental data of cumulative numbers of low-lying levels and the average distance between neutron resonances [12]. As these data cover only an interval of the excitation energies $E_{ex}<E_d$ (E_d is an upper energy of the region of discrete levels) and energies in the vicinity of B_n (B_n is the neutron binding energy), so calculated by these models NLD values will contain unexpected errors in energy region $E_d < E_{ex} < B_n$. There is a similar problem for phenomenological RSF models, as the Kadmenskij-Markushev-Furman model (KMF) [13] or the generalized Lorentzian model (GLO) [14].

However, calculations using abovementioned models of the NLD and RSF indicate that calculated TSC intensities, ${}^{cal}I_{\gamma\gamma}$, are significantly lower than the experimental TSC intensities, ${}^{exp}I_{\gamma\gamma}$. Average values of ratio ${}^{exp}I_{\gamma\gamma}/{}^{cal}I_{\gamma\gamma}$ over 40 nuclei are 1.4–2.6 for different models of NLD and RSF [15]. Moreover, it must be said that a strong correlation between NLD and RSF was not taken into account in these models.

2. Experiment

The TSC method with recording of gamma-quanta coincidences following a thermal neutron capture was described in detail in [6]. The spectrometer includes two semiconductor detectors of high efficiency at face-to-face close geometry. TSC to a group of final levels are observed as a group of peaks in the spectrum of sums of amplitudes of coincident pulses (SACP) (see Figure 1.1). Distortion of TSC because of noise coincidences is inhibited and removed by follows:

- coincident events due to γ-quanta backscattering between the detectors are reduced by lead filters 2.5 g/cm^2 in front of each detector's window;
- coincidences with a small energy of γ-quanta are completely eliminated by the threshold for detectors at 520 keV;
- coincidences due to the Compton scattering and random coincidences are removed at an appropriate background subtraction.

Amplitude's codes of coincident pulses are recorded and processed off-line. This procedure brings the possibility to improve the energy resolution of TSC spectra by the numerical algorithm without a loss of efficiency, which was presented in [16].

In order to obtain the experimental TSC intensities we have to determine efficiency of both detectors in the energy region $0.5 < E_\gamma < 9$ MeV. It was done using areas of full-capture peaks of the single γ-ray spectra, which were recorded from ${}^{35}Cl(n,\gamma){}^{36}Cl$ reaction, and known for them γ-ray intensities [17].

After efficiency correction TSC distributions are obtained. Any intensity distribution of two-step cascades contains only peaks of the full capture of the cascade energy and a noise background with a zero average. A dispersion of a background line is effectively diminished at an increase in the number of events of recording of the total energy of the cascade (see Figure 1.2). Each of TSC spectra includes couples of mirror-symmetrical peaks, their center positions correspond to the energies of primary transition (E_1) and secondary transition (E_2). Areas of these mirror-symmetrical peaks are equal to each other. *FWHM* of all resolved peaks is not more than 2–4 keV.

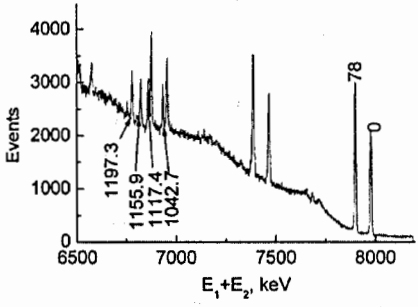

Figure 1.1. A part of SACP spectrum of nucleus ^{172}Yb, the energies of final levels (in keV) of the cascades are written nearby.

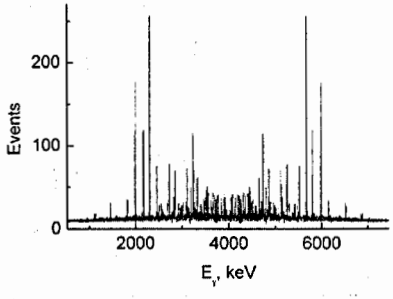

Figure 1.2. The distribution of TSC to the ground state of ^{172}Yb.

Relative intensities $i_{\gamma\gamma}$ of the strongest cascades with intensity i_1 are used for a determination of absolute values of the sum $I_{\gamma\gamma}$ of all cascades: $I_{\gamma\gamma}=i_1 \cdot B_r \cdot 100/i_{\gamma\gamma}$, where the branching ratio B_r is determined from the set of γ-γ coincidences, accumulated in the experiment. And an absolute intensity i_1 (in percent per decay) of primary transitions is usually taken from PGAA [18] or ENDSF [19] files.

3. Determination of the $I_{\gamma\gamma}(E_1)$ distribution

Structure of each TSC spectrum was described in detail in [20], and it consists of three components:

1. a set of pairs of resolved peaks (see Figure 2.1, part A);
2. overlapping distribution of unresolved peaks (Figure 2.1, part B);
3. noise background with zero average line.

Each TSC distribution (as in Figure 1.2) depends on both E_1 and E_2 energies of the cascade quanta. We can consider this distribution as a sum of two mirror-symmetrical distributions, $I_{\gamma\gamma}(E_1)$ and $I_{\gamma\gamma}(E_2)$. For the experimental data analysis by proposed Dubna method it is need to separate $I_{\gamma\gamma}(E_1)$ intensity distribution from the total $I_{\gamma\gamma}(E_1,E_2)$ one. Taking into account that a background is almost absent, an equality of areas of the peaks of primary and secondary transitions (for each individual cascade) and a mirror-symmetry of their positions in relation to the spectrum center at $0.5(E_1+E_2)$, we subtracted all peaks of intense low-energy secondary transitions from the energy interval of the intermediate levels $E_i \geq 0.5B_n$. The rest of intensity in this interval (a continuous distribution of intensity of large number of low-energy primary cascade gamma-quanta) in sum with intense resolved primary transitions from the energy interval $E_i \leq 0.5B_n$ is just the most probable distribution $I_{\gamma\gamma}(E_1)$.

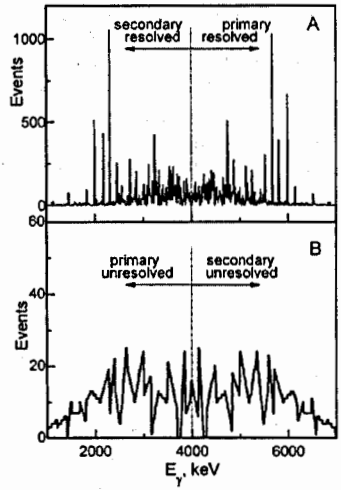

Figure 2.1.Illustration of the $I_{\gamma\gamma}(E_1)$ separation procedure for TSC to the ground state of ^{172}Yb nucleus (the percentage of resolved peaks is 70%).

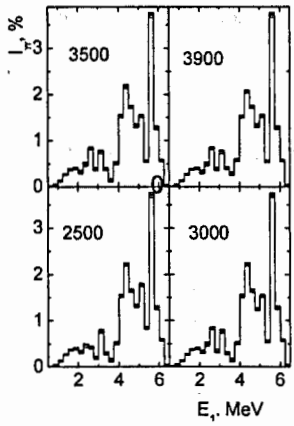

Figure 2.2. Evaluation of the effect of systematic errors for ^{172}Yb in 4 fits at chosen boundary points of "zero primary transitions" at 2500, 3000, 3500, 3900 keV. The spectra were obtained for a sum of intensities of the cascades to the ground state and to the level with $E_f = 78$ keV.

Of course, if a part of peaks near the energy $0.5(E_1+E_2)$, where there is a mixture of inseparable primary and secondary transitions, is inaccurately identified, the obtained function $I_{\gamma\gamma}= f(E_1)$ distorts. But the part of the intensity of secondary transitions, which are mistakenly included into $I_{\gamma\gamma}(E_1)$, and the part of the intensity of primary transitions, mistakenly included into $I_{\gamma\gamma}(E_2)$, are equal to each other. At that, a possible distortion of a shape of $I_{\gamma\gamma}(E_1)$ distribution in a small energy region of the primary transitions near $0.5B_n$ decreases with an increase in statistics. If TSC are recorded with a sufficient statistic (more than ~ 4000 events at the sum peak), percentage contribution of the unresolved peaks in the total intensity distribution is small. Three of quarter of all investigated nuclei had a minimal required statistic, and it was some times more for the rest of nuclei (in the case of ^{172}Yb, for example, the percentage of resolved TSC to the ground state was 70%). So, a high statistics allows to obtain $I_{\gamma\gamma}(E_1)$ distribution with an accuracy not worse than 10–20% in any energy bins.

In Figure 2.2 the $I_{\gamma\gamma}(E_1)$ distributions are shown, obtained at four chosen boundary points (it is supposed that the intensity of primary transitions decreases to zero in these points): 2500, 3000, 3500 and 3900 keV. As the shape of the $I_{\gamma\gamma}(E_1)$ distribution does not change, so an extension and a shape of the "tail" of unresolved primary transitions, which were taken into account inaccurately, have no influence on the fitting. It means that an uncertainty of such determination of the partial distribution $I_{\gamma\gamma}(E_1)$ is acceptable.

4. The empirical Dubna model

There is a potential for simultaneous estimation of the most probable NLD and RSF values even by model-free method [15] using the Monte-Carlo technique. However, it would be preferable if the NLD and RSF values should be built on a kind of physical assumptions. These assumptions have to take into account shell effects, pairing correlations, collective phenomena of NLD, and also a dependence of width giant dipole resonance on temperature.

The presence of the step-like structure at the fitted NLD curves (this structure was noticed even in [15]) confirms a validity of the superfluid nucleus theory, which interprets the step-like structure as the consequence of breaking Cooper pairs. In the RIPL projects [12] the GSM [11] model has also been considered as a preeminent model. But the GSM model needs in more precise description of the level density below a point of the phase transition.

Description of the NLD function

For a description of the nuclear level density in the empirical Dubna model [21,22] the representations were used:

1) Gaussian distribution $G_n(J)$ for the J-spin-dependent expansion of NLD,
2) a dependence on excitation energy of $\Omega_n(E_{ex})$density ofn-quasi-particle states[23] in the nucleus,
3) a modified (see [24]) phenomenological coefficient C_{coll} [12] for collective effects included the effect of an enhancement of the level density due to vibrational and rotational (for deformed nuclei) excitations.

So, the NLD function was expressed as $\rho(E_{ex}) = G_n(J) \times \Omega_n(E_{ex}) \times C_{coll}$. The fitted parameters, included in the NLD function $\rho(E_{ex})=\varphi(U_l,g,A_l,\beta,E_u)$, are: the breaking thresholds U_l (l is a number of Cooper pair) from both $\Omega_n(E_{ex})$ and C_{coll} distributions, the density of single-particle states g near the Fermi-surface from $\Omega_n(E_{ex})$distribution and also parameters of density of vibrational levels A_l above each breaking point, the nuclear deformed parameter β and a rate $E_u$of a change in densities of quasi-particle and phonon levels from C_{coll}.

The shell inhomogeneities of a single-particle spectrum were taken into account (as in [24]) through a dependence on excitation energy of the parameters $g=6\cdot a(E_{ex})/\pi^2$, where $a(E_{ex})$ is described in detail in [13].

Description of the RSF function

RSF functions both for E1- and M1-transitions are predicted by the model [13] to be smooth, the analysis of the experimental database showed an absolute necessity of an addition of one or two peaks to the smooth parts of them for the better description of TSC intensities [25].

In the Dubna model RSF functions of E1- and M1-transitons are presented by the smooth parts from KMF model [13] in a sum with one or two peaks, each of which is described by asymmetrical Lorentzian curve.

Parameters of the RSF functions (normalized parameter w for the total radiative width Γ_γ, a parameter κ for a possible change of the thermodynamic temperature and also position, width, amplitude and asymmetric parameter of each local i-th peak [24]) of E1- and M1-transitons are fitted separately.

5. The results and discussion

The results of the best $I_{\gamma\gamma}(E_1)$ fits of the radiative widths and the level densities for 43 investigated nuclei are presented in [24] in comparison with their calculations using generally accepted models. In Fig.4 there is an example of $I_{\gamma\gamma}(E_1)$ description for the ^{172}Yb nucleus.

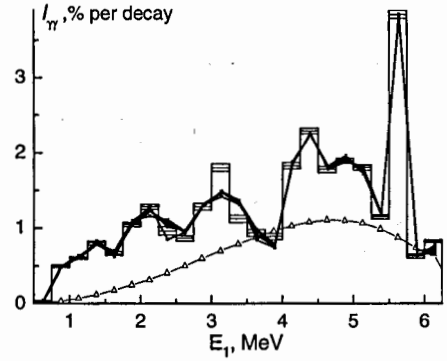

Figure 4.1. The $I_{\gamma\gamma}(E_1)$ distribution for the ^{172}Yb nucleus. Histogram is the experiment with its errors. Broken lines are the results of 5 the best fits. Triangles are the cascade intensity calculated using models [11] and [10].

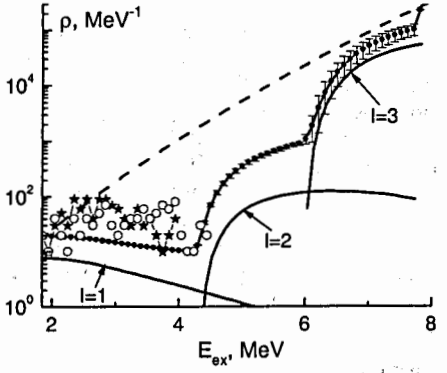

Figure 4.2. Dependence of the level density for ^{172}Yb on the excitation energy. Dased line is the level density predicted by the model [10] for spins $0 \leq J \leq 3$ and both parities; open points and stars are numbers of "discrete" levels obtained by TSC method and other experiment [26] corresponding; black points with errors are the densities from the best fits to the experimental cascade intensities; solid lines noted by numbers are densities of vibrational levels above the breaking thresholds of 3 Cooper pairs, calculated with fitted parameters.

Using fitted parameters, the NLD and RSF values are simultaneously determined with help of the presented empirical model. Obtained distributions of the NLD for ^{172}Yb nucleus are shown in Figure 5, as an example. For ^{172}Yb, as for all investigated nuclei, the $\rho(E_{ex})$ distributions have a step-wise structure. At the first step (it is usually at excitation energies from 1–2 to 3–4 MeV), above the first breaking point, NLD distribution is mostly constant and is even lowered with an increase of excitation energy (see Figure 5). And energy dependences of NLD above breaking points of the second and the third Cooper pairs rapidly increase as it was predicted by the model [23].

The NLD dependencies on the excitation energy obtained from the Dubna model were compared with ones of the BSFG model, which is considered as a standard model for NLD description in low-energy region and nearby B_n. The comparison showed an agreement between the results in the area near the breaking point of the first Cooper pair and B_n, but at an increase of excitation energy there is a strong divergence between the results of the compared models. However, a plateau, or even a little fall of NLD distributions of Dubna model in the region of excitation energies of 2 – 4 MeV is not in discrepancy with the density of discrete levels obtained from some different experiments (see Figure 5).

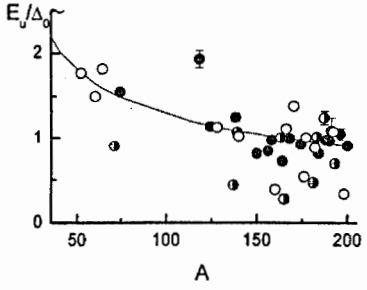

Figure 6. Mass dependencies of E_u fitted parameter for even-even nuclei (black points), even-odd nuclei (half-black points) and odd-odd compound- nuclei (open points).

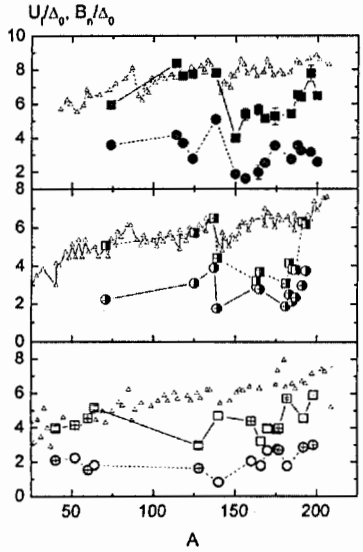

Figure 7. Mass dependencies of breaking thresholds of the second (points) and of the third (squares) Cooper pairs for even-even nuclei (black points), even-odd nuclei (half-black points) and odd-odd compound- nuclei (open points). Triangles are mass dependencies of B_n/Δ_0.

In Figures 6, 7 the mass dependences of fitted parameters for the investigated nuclei are shown: E_u/Δ_0 ratios ($\Delta_0=12.8\cdot A^{1/2}$ is the mean pairing energy of the last nucleon in the nucleus) as well asthe breaking thresholds of the second and of the third Cooper pairs. It is seen that the mean value of E_u/Δ_0 ratios was approximately 1 for about 30 nuclei, and the breaking thresholds of Cooper pairs for spherical nuclei (A<150) have values higher than those for deformed nuclei (see Figure 7). It is obvious that for spherical nuclei the breaking thresholds of the 3-rd Cooper pair are about B_n, and for deformed nuclei they are far less.

5. Conclusions

The Dubna empirical model has an ability to describe the experimental $I_{\gamma\gamma}(E_1)$ distributions with a high accuracy. The experimental intensity distributions were measured for 44 nuclei

precisely enough to assert that in case under consideration of the used phenomenological representations the obtained results are reliable:

- ✓ an existence of the superfluid phase of nuclear matter was established at an observation of the behavior of the NLD dependences on the excitation energy during the phase transition process;
- ✓ it was obtained that the energies of the breaking thresholds of Cooper pairs in spherical nuclei are larger than ones for deformed nuclei, i.e. the dynamics of the phase transition in the nuclear matter depends on a shape and a parity of the nucleus.

In order to obtain a more detailed picture of the dynamics of a transition between the fermion and the boson states in the nucleus one should to expand the number of the studied nuclei.

A validity of obtained results depends also on a reliability of the used phenomenological descriptions of NLD and RSF functions, so model evolution is necessary. And, first of all, a replacement of the phenomenological coefficient of enhancement of collective levels by a modern appropriate model must be done.

REFERENCES

1. J. Bardeen, L.N. Cooper, and J.R. Schrieffer, Phys. Rev. **108** (1957)1175.
2. N.N. Bogolyubov, Zh. Ehksp. Teor. Fiz. **34**, 58(1958); Usp. Fiz. Nauk. **67** (1959)549.
3. V.G. Solov'ev, Zh. Ehksp. Teor. Fiz. **36** (1959)1869.
4. T. Ericson, Adv. Phys. **9** (1960)425.
5. J. M. Blatt and V. F. Weisskopf, *Theoretical Nuclear Physics* (Wiley, New York, 1952).
6. S.T. Boneva, É.V. Vasil'eva, Y.P. Popov, A.M. Sukhovoi, and V.A. Khitrov, Sov. J. Part. Nucl. **22** (1991)232.
7. S.T. Boneva *et al.*, Sov. J. Part. Nucl. **22** (1991)698.
8. Gilbert and A.G.W. Cameron, Can. J. Phys. **43** (1965)1446.
9. H. Bethe, Rev. Mod. Phys. **9** (1937)69.
10. W. Dilg, W. Schantl, H. Vonach, and M. Uhl, Nucl. Phys. **A217** (1973)269.
11. A.V. Ignatyuk, *Statistical Properties of Excited Atomic Nuclei* (in Russian). Energoatomizdat, Moscow 1983); Translated by IAEA, Report INDC-233(L) (IAEA Vienna 1985).
12. *Reference Input Parameter Library RIPL-2, Handbook for calculations of nuclear reaction data*, IAEA-TECDOC (2002).
13. S.G. Kadmenskij, V.P. Markushev, and V.I. Furman, Yad. Fiz. **37** (1983)277 [Sov. J. Nucl. Phys. **37** (1983)165].
14. J. Kopecky and R. E. Chrien, Nucl. Phys. **A468** (1987)285.
15. E.V. Vasilieva, A.M. Sukhovoj, V.A. Khitrov, Nucl. Phys. At. Nucl. **64** (2001)153.
16. A.M. Sukhovoj, V.A. Khitrov, Instrum. Exp. Tech. **27** (1984)1071.
17. B. Krusche, K.P. Lieb, H. Daniel et al., Nucl. Phys. **A386** (1982)245.
18. http://www-pub.iaea.org/MTCD/publications/PDF/Pub1263_web.pdf
19. http://www-nds.iaea.org/ENDSF
20. S.T. Boneva, V.A. Khitrov, A.M. Sukhovoj, and A.V. Vojnov, Nucl. Phys. **A589** (1995)293.
21. A.M. Sukhovoj, Phys. Atom. Nucl. **78** (2015)230.
22. L.V. Mitsyna, A.M. Sukhovoj, in Proc. XXII International Seminar on Interaction of Neutrons with Nuclei, Dubna, Russia, May 27-30, 2014 , Preprint № E3-2015-13 (JINR Dubna 2015) p. 245; http://isinn.jinr.ru/past-isinns.html.
23. V.M. Strutinsky, in Proc. International Congress on Nucl. Physics, Paris, France, 1958, p.617.
24. D.C. Vu *et al.*, Phys. Atom. Nucl. **80** (2017)237.
25. A.M. Sukhovoj, V.A. Khitrov, W.I. Furman, Phys. Atom. Nucl. **71** (2008)982.
26. R.C. Greenwood, C.W. Reich, and S.H. Egors, Jr., Nucl. Phys. **262** (1975)260.

The Features of the Cascading Decay of ^{172}Yb Nucleus in the ^{171}Yb(n_{th},2γ) Reaction

Sukhovoj A.M.[1], Mitsyna L.V.[1], Hai N.X.[2], Anh N.N.[2], Khang P.D.[3], Thang H.H.[2], Vu D.C.[1,4]

[1]*Joint Institute for Nuclear Research, Dubna, 141980, Russia*
[2]*Dalat Nuclear Research Institute, Vietnam Atomic Energy Institute, Hanoi, Vietnam*
[3]*Hanoi University of Science and Technology, 1 Dai Co Viet, Hanoi city, Vietnam*
[4]*Vietnam Academy of Science and Technology Institute of Physics, Hanoi, Vietnam*

Abstract. For the purpose of an enhancement of the experimental data set on the cascade intensities of two gamma quanta emitted step by step after radiative capture of thermal neutrons, the ^{171}Yb(n_{th},2γ)-reaction was investigated. In the analysis of the cascade intensities a structure change of the observed levels of the ^{172}Yb nucleus was discovered depending on the excitation energy, and the most probable breaking thresholds were obtained for four Cooper pairs of neutrons below the neutron binding energy.

1. INTRODUCTION

A nucleus with even number of neutrons (and protons) is, in the ground state, a system of pairing nucleons, and it becomes a system of excited fermions at its excitation in a process of pair breaking. An investigation of the dynamics of this process promotes obtaining the principally new information about fundamental interactions occurred in the nucleus.

In representation about the nuclear superfluidity, which is generally accepted among experimenters, an excited nucleus is considered as a statistic fermion system. And now as before, this representation is applied in the experimental analysis, even at using a state-of-the-art instrumentation and at a modern status of theory of the nucleus. Theorists exploit a representation about "pair correlations of superconductive type", at least, in an excitation region above the experimentally obtained energies of rotational and vibrational excitations.

Unfortunately, a multiple increase in errors of the extracted experimental parameters (level density ρ and widths Γ of emission of gamma-quanta), which exists due to large coefficients of transfer to them of errors of the measured spectra (or cross-sections), hamper the progress in understanding of the intranuclear processes.

In the realized in Dubna method [1] of measuring the intensities of two-step cascades at γ-decay of neutron resonances, the most probable values of both the level density ρ of intermediate levels in compound-nucleus and the partial widths Γ of emission of reaction products are determined simultaneously. It allows to study a change dynamics in behavior of superfluid phase of the nuclear matter at an increase in the excitation energy of the nucleus, since the energies of three cascade levels (initial, intermediate and final ones) as well as the probabilities of transmissions between them are determined in the investigated (n,2γ)-reaction with a high accuracy.

The correlation always exists between the obtained parameters ρ and Γ (or radiative strength functions $k = \Gamma/(A^{2/3} \cdot E_\gamma^3 \cdot D_\lambda)$, where A is a mass of nucleus, D_λ is an average space

between its levels, and E_γ is an energy of emitted γ-quantum). Nevertheless, at an existence of the total system of equations, which connect the ρ and Γ values in each point of the excitation energy E_{ex}, these two values could be calculated exactly. But because of a deficiency of experimental information, a simultaneous determination of ρ and Γ values from the experimental data is possible only with use of different appropriate model representations about $\rho(E_{ex})$ and $\Gamma(E_\gamma)$ functions. At that, an uncertainty, which exists due to a correlation between ρ and Γ values, is converted into systematical errors in the tested correlated models for $\rho(E_{ex})$ and $\Gamma(E_\gamma)$ functions.

At the analysis of the $I_{\gamma\gamma}(E_\gamma)$ intensities of the two-step cascades of γ-transitions, measured by now for 43 nuclei in the mass region $28 \leq A \leq 200$, it turned out, that the experimental information for each investigated nucleus is individual. It completely corresponds to the modern theories about dynamics of fragmentation of nuclear states (the wave functions of excited nuclear levels are formed in the fragmentation process of states of nuclear potential with different quantum numbers and various positions relative to Fermi surface) [2, 3].

The theoretical description of a structure change of the complex nuclei in the energy range from the ground state up to neutron resonances one can inquire for in [4], for example. Although there is no yet a comprehensive knowledge about an interaction between Fermi- and Bose-states in the nucleus, but on a base of the analysis of the cascades' intensities $I_{\gamma\gamma}(E_\gamma)$ measured for stable nuclei-targets with different *P/N* ratio (*P* is a number of protons, *N* is a number of neutrons) the quite realistic picture of nuclear changeover to fermion system at the excitation energy $E_{ex} < B_n$ (B_n is a neutron binding energy in the nucleus) already exists. In particular, the strength functions, obtained for pairs of nuclei with the same *P* and various *N* (^{156}Gd and ^{158}Gd, ^{188}Os and ^{190}Os), are essentially different, and the level densities for such pairs of nuclei differ to a lesser degree.

An existence of two phases of nuclear matter in the nucleus and their interaction indicate that the partial widths of gamma-transitions are determined by the wave functions with different contributions of vibrational and quasi-particle components, so regarding to them the Porter-Thomas hypothesis [5] cannot be applied, by a definition.

The investigations [6–10] resulted that both a number of breaking Cooper pairs of nucleons and a shape of excited nucleus [8] have an influence on the dynamics of superfluid phase of the nuclear matter. Widening of the region of investigated nuclei and, in that way, a numerical growth of experimental data will help to make clear the details of interaction between fermion and boson nuclear states.

2. EXPERIMENT

The experiment with the sample of ytterbium as a nucleus-target was carried out at the DDNR reactor (Dalat, Vietnam). The sample of 0.5 g mass contained 0.45 g of ^{171}Yb and was irradiated during 830 hours in "closed" [1] geometry with a distance between the target and the detector of about 5 cm. Cascades were recorded by HPGe-detectors with an efficiency of 35% relative to efficiency of NaI(Tl) crystal (with 72 mm in diameter and the same height). The recording threshold for a cascade gamma-transition was chosen 0.52 MeV.

An informative part of the spectrum of amplitudes' sums of coincided pulses for ^{171}Yb$(n_{th},2\gamma)^{172}$Yb reaction is presented in fig. 1. In figs. 2 and 3 the spectra of the cascades to the ground state and to the first excited level with the energy $E_f = 78$ κeV are shown. The algorithm is used for a digital improvement of resolution [11], according to which a deviation of the sum of γ-quanta energies from its average for any cascade is divided proportionally to

widths of the cascade peaks and then subtracted from (or added to) the energies of primary E_1 and secondary E_2 transitions of each recorded event of the total absorption of the cascade energy by the detectors. The spectra of the intensities (figs. 2 and 3) are normalized by the recording efficiency of corresponding cascades with a storing of the total number of events. The energies and the relative intensities were determined for all experimentally resolved peaks for 386 cascades.

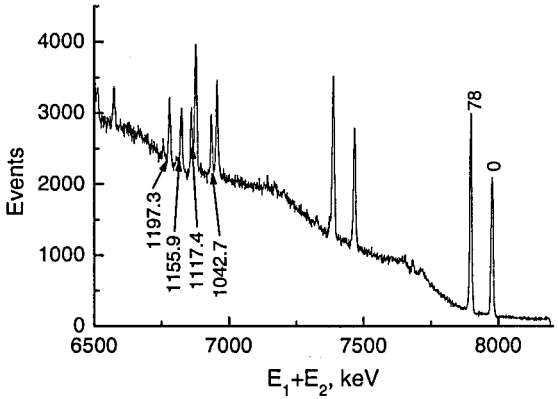

Fig. 1. Spectrum of the sums of amplitudes of coincident pulses for ^{171}Yb(n_{th},2γ)-reaction. Along X-axis: energy of the cascades, Y-axis: number of recorded events with the total energy $E_1+E_2 > 6500$ кеV. The energies of the final levels of the cascades (in keV) are pointed near the peaks of the total energy absorption.

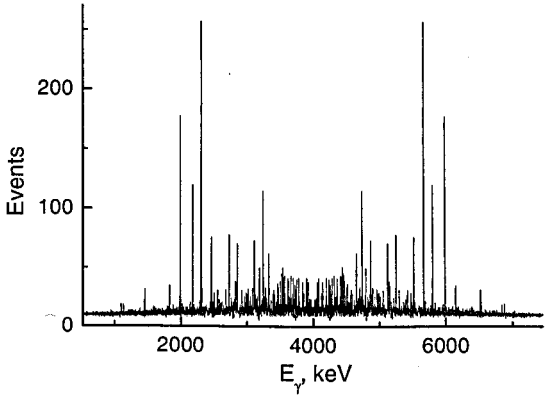

Fig. 2. Intensity distribution for the cascades to the ground state of the ^{172}Yb nucleus depending on the energies of the primary and the secondary quanta. An efficiency of the cascade recording is taken into account.

At the analysis the spectra of the experimental intensities of the cascades (figs. 2, 3), using the technique [1, 12] and the nuclear spectroscopy methods [13], are transformed [14] into two mirror-symmetrical distributions of intensities of primary $I_{\gamma\gamma}(E_1)$ and secondary $I_{\gamma\gamma}(E_2)$ transitions. The parameters p and q of the most probable functions $\rho=\varphi(p_1, p_2, ...)$ and

$\Gamma=\psi(q_1, q_2,...)$ were determined by fitting of a model description of the cascade intensity $I_{\gamma\gamma}(E_1)$ to the experimental one. The physical information about the nucleus is obtained from the experiment analysis at a comparison of some of the model representations. There are no other ways to obtain simultaneously the level density and the radiative strength functions from the gamma-spectra of the decay of high-excited levels. Any gamma-spectrum can be described, if only the energies, quanta numbers in the cascades and the total number of gamma-transitions are correctly determined.

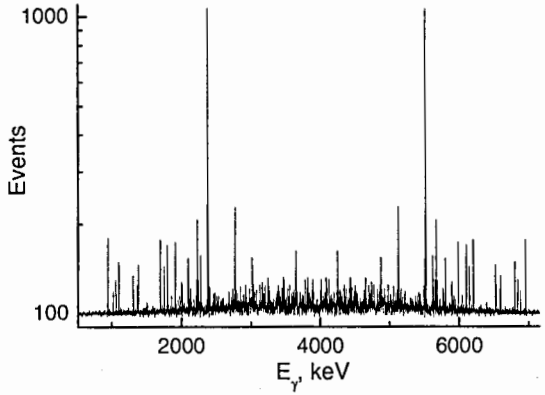

Fig. 3. Intensity distribution for the cascades to the level with the energy E_f=78 κeV of ^{172}Yb depending on the energy of the primary and the secondary quanta.

A cascade decay of a neutron resonance (or any compound-state) λ occurs through the intermediate levels *i* to the final levels *f*. Spins and parities of the intermediate levels of different cascades are determined by the selection rules on multipolarity. The part of primary transitions $I_{\gamma\gamma}(E_1)$ for any small energy interval ΔE_j of cascades may be presented by an equation:

$$I_{\gamma\gamma}(E_1)=\sum_{\lambda,f}\sum_{i}\frac{\Gamma_{\lambda i}}{\Gamma_{\lambda}}\frac{\Gamma_{if}}{\Gamma_{i}}=\sum_{\lambda,f}\sum_{j}\frac{\Gamma_{\lambda j}}{<\Gamma_{\lambda j}>M_{\lambda j}}n_j\frac{\Gamma_{jf}}{<\Gamma_{jf}>m_{jf}}. \qquad (1)$$

A sum of the partial widths of the primary transitions $\Sigma_j\Gamma_{\lambda j}$ to $M_{\lambda j}$ intermediate levels is $<\Gamma_{\lambda j}>M_{\lambda j}$, and a sum $\Sigma_j\Gamma_{jf}$ for the secondary transition to m_{jf} final levels is $<\Gamma_{jf}>m_{jf}$, inasmuch as $<\Gamma_{\lambda j}> = \Sigma_j\Gamma_{\lambda j}/M_{\lambda j}$ and $<\Gamma_{jf}> = \Sigma_j\Gamma_{jf}/m_{jf}$. In the small energy interval ΔE_j a number of intermediate levels of all types is $n_j = \rho\Delta E_j$.

As equipment possibilities to determine the parameters of all cascades are absent, the necessary information for the system (1) solving is extracted from the fits of model descriptions of the intensities for all observed γ-transitions to their experimental intensities. Any intensity distribution of two-step cascades (see figs. 2 and 3) contains only peaks of the full capture of the cascade energy and a noise background with a zero average [1]. A dispersion of a background line is effectively diminished at an increase in the number of events of recording the total energy of the cascade.

Taking into account a practical absence of a background, an equality of areas of the peaks of primary and secondary transitions (for each individual cascade) and a mirror-symmetry of their positions in relation to the spectrum center $0.5(E_1+E_2)$ of all cascades, we

subtracted all peaks of intense low-energy secondary transitions from the energy interval of the intermediate levels $E_i \geq 0.5B_n$. The rest of intensity in this interval (a continuous distribution of intensity of large number of low-energy primary cascade gamma-quanta) in sum with intense resolved primary transitions from the energy interval $E_i \leq 0.5B_n$ is just the most probable distribution $I_{\gamma\gamma}(E_1)$.

Of course, if a part of peaks near the energy $0.5(E_1+E_2)$, where there is an mixture of inseparable the primary and the secondary transitions, is inaccurately identified, the obtained function $I_{\gamma\gamma} = f(E_1)$ distorts. But the part of the intensity of secondary transitions, which are mistakenly included into $I_{\gamma\gamma}(E_1)$, and the part of the intensity of primary transitions, mistakenly included into $I_{\gamma\gamma}(E_2)$, are equal to each other. At that, a possible distortion of a shape of $I_{\gamma\gamma}(E_1)$ distribution in a small energy region of the primary transitions near $0.5B_n$ decreases with an increase in statistics.

At the system (1) solving the average partial width of transitions of the same type and the level density in the branching coefficients ($\Gamma_{\lambda j}/(<\Gamma_{\lambda j}>M_{\lambda j})$ for the primary transitions and $\Gamma_{jf}/(<\Gamma_{jf}>m_{\lambda j})$ for the secondary transitions) were fitted in small energy intervals ΔE_j. A large statistics of events and a small background under peaks of full capture of the cascades' energies $E_1 + E_2 = 8020$ keV and $E_1 + E_2 = 7942$ keV allowed us to accept for ^{172}Yb the width of energy interval for summation of experimental intensity $\Delta E_j = 250$ keV (two times less than for all nuclei investigated before). So, a shape of $I_{\gamma\gamma}(E_1)$ function was obtained with a better accuracy for ^{172}Yb in comparison with the other 43 nuclei [8, 10].

The resolved peaks with the widths of ~ 2 – 4 keV for the cascades with $E_f = 0$ and $E_f = 78$ keV were 70% and 67% of the total area of the spectra, correspondingly (see figs. 2 and 3). According to [12], the primary quantum in two or more cascades with different E_f, as a rule, is the cascade transition of a bigger energy. This condition with use of the likelihood method allowed us to make an independent and correct scheme of the decay of initial cascade level, in addition to the data of the ENDSF file.

The absolute intensity of primary transitions of the investigated reaction was determined from the intensities of gamma-rays of ^{171}Yb+ ^{27}Al complex target. The obtained data for the cascade $E_1+E_2 = 5540+2402$ keV coincide with the data of [15] within some percents.

3. THE DECAY SCHEME FOR ^{172}Yb

Spectra of the sums of amplitudes of coincided pulses were obtained not only for the cascades to the ground state and to the first excited level of ^{172}Yb, but also for final levels of the cascades with the energies E_f = 1042.7; 1117.4; 1155.9 and 1197.3 кеV. Unfortunately, a large background under peaks of the cascades with $E_f > 78$ keV (because of events of recording of only a part of the cascade energy) did not allow to obtain for them such quality spectroscopic information as it was done for the cascades with $E_f = 0$ and $E_f = 78$ кеV.

In the presented experiment for the cascades of the biggest intensity the errors in the determination of $I_{\gamma\gamma}$ values were mainly much lower than 30% (at that error the cascade peak was assumed to be resolved). In a majority of cases, the procedure [12] shows that the primary transition triggers some (at least, two) secondary transitions, what (taken together with the data of [15]) allowed to identify the primary transitions with a strong probability.

In order to determine the parameters of the nuclear superfluidity in excited nucleus [16] the independent ρ values at two energy regions are needed: at $E_{ex} \approx$ 1–3 MeV and at $E_{ex} \approx B_n$. The accuracy of ρ determination at these energies is bounded because of a loss of resonances with small neutron widths and an omission of low-lying levels, which are weakly

excited in the nuclear reaction or have a big background. But it is worthy of being noted, that in the method of the two-step cascades' investigation there are no the main sources of background, which exist in the ordinary (one-step) experiments. So, background conditions in the case two-step cascades are practically not dependent on the excitation energy of the nucleus, what allows to determine the density of its "discrete" levels with a smaller (if to compare with other nuclear reactions [13]) threshold of gamma-quanta recording.

Radiative capture of thermal neutrons by the stable nucleus-target ^{172}Yb limits a number of spins of levels, which density is needed to determine, by the interval $0 \leq J \leq 3$. The obtained from different experiments densities of "discrete" levels of ^{172}Yb for all spins and parities are presented in fig. 4 in the energy region 2 – 4 MeV. Approximation of ρ and Γ values was done here for the cascades with the total energies 8020 and 7982 keV only. Up to excitation energy of E_{ex}=3 MeV the densities of low-lying intermediate levels of the cascades to the final levels with E_f = 0 and E_f = 78 keV from the presented experiment coincide quite good with the values predicted by the back shifted Fermi-gas model [17]. The same one could say about level densities from ENDSF file and from the experiment [15] with the neutron beam of 2 keV energy. But at a growth of the excitation energy a number of "discrete" levels descend faster than it is predicted by the Fermi-gas model.

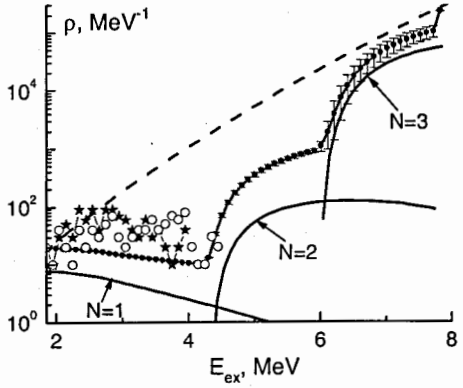

Fig.4. The dependences of the level density for ^{172}Yb on the excitation energy. Dased line – level density predicted by the model from [17]] for spins $0 \leq J \leq 3$ and both parities. Open points – number of "discrete" levels obtained in the present experiment. Full points with errors – densities from the best fits to the experimental cascade intensities. Stars – calculation from the spectrum of resolved gamma-transitions after a capture of neutrons with the energy E_n= 2 keV [15]. Solid lines noted by numbers are density of vibrational levels above the breaking thresholds of three Cooper pairs, calculated according to (3) with fitted parameters.

In the framework of existing theoretical representations about deformed heavy nucleus the excitation energy of 2 – 2.5 MeV is approximately equal to the breaking energy of the first Cooper pair 2Δ (Δ is a pairing energy of the last nucleon in the nucleus). But a small level density at the energy about 2Δ prevents to notice the breaking threshold of the first Cooper pair, which is expected at this energy (according to a redistribution of the excitation energy). Nevertheless, for a quantitative description of the total cascade intensity, it is necessary to take into account in the fittings an existence of vibrational levels below the breaking threshold of the second Cooper pair.

4. THE EMPIRICAL MODEL OF THE GAMMA-DECAY

In order to extract reliable experimental information about a behavior of a superfluid phase of the nuclear matter it is necessary:

1) to measure an intensity of gamma-cascades to the low-lying levels of investigated nucleus (to the ground state and to a group of levels with small energies);
2) to ensure the best description of measured spectra at a simultaneous fitting of the parameters of both the level density and the partial radiative widths.

The principal problem for a study of superfluidity in the excited nucleus is a choice of model representations for reliable description of the investigated process. To obtain the level density and the partial widths of the products of the nuclear reaction, in a majority of the world's experiments, the models are used, which are based on the calculations of different spectra and cross-sections at the large excitation energies [17–19]. The analysis of the created by now experimental data on the intensities of the two-step cascades for 43 nuclei showed a worthlessness (for a valid description of the processes in the nucleus) of an obsolete representation, that the nucleus is a system of uninteractive Fermi-particles.

In the absence of correct theoretical models we used our empirical model, including the different realistic phenomenological representations into it. But it is illegal to use even generally accepted representations about the parameters of the investigated process without experimental testing. Otherwise, the principle errors will inevitably appear.

For the level density description in the present analysis the model of density of n-quasi-particle nuclear excitations [19, 20], which is commonly used in a study of the preequlibrium reactions, was parameterized. The density ρ_l of levels of fermion type above the expected breaking threshold of the l-th Cooper pair was written by an expression:

$$\rho_l = \frac{(2J+1)\cdot\exp(-(J+1/2)^2/2\sigma^2)}{2\sqrt{2\pi}\sigma^3}\Omega_n(E_{ex}), \qquad \Omega_n(E_{ex}) = \frac{g^n(E_{ex}-U_l)^{n-1}}{((n/2)!)^2(n-1)!}. \tag{2}$$

Here Ω_n is a density of n-quasi-particle states, σ is a factor of spin cutting, J is a spin of the compound-state of nucleus, g is a density of singe-particle states near Fermi-surface, and U_l – the breaking energy of the l-th Cooper pair (or the energy of an excitation of pair of quasi-particles).

For a description of the coefficient C_{coll} of an increase of a density of collective levels a phenomenological relation between entropies of phases of the nuclear matter was used [16] IGN] with taking into account a cyclical break of Cooper pairs:

$$C_{col} = A_l\exp(\sqrt{(E_{ex}-U_l)/E_u} - (E_{ex}-U_l)/E_u) + \beta. \tag{3}$$

Here A_l are fitting parameters of vibrational level density above the breaking point of each l-th Cooper pair, parameter $\beta \geq 0$ can differ from 0 for deformed nuclei. Parameter E_u (a rate of a change in densities of quasi-particle and phonon levels) is practically equal to the average pairing energy of the last nucleon in the majority of investigated nuclei [6–10].

As it was experimentally determined earlier [21], a correct description of the intensities of the two-step cascades is possible only if to add one or two peaks to the smooth energy dependence of the radiative strength functions of $E1$- and $M1$-transitions. The smooth parts of the energy dependences $k(E1,E_\gamma)$ and $k(M1,E_\gamma)$ were described as in the model [18] with addition fitted parameters of weight w_E (or w_M) and of a change of derivatives of the strength function κ_E (or κ_M) (indexes E and M refer to $E1$- or $M1$-transitions, correspondingly). And in order to take into account the local peaks one or two summands

were added to the smooth parts of the strength function. In the presented analysis the asymmetric Lorentzian curve was used for description of the shape of each local peak. So, $k(E1,E_\gamma)$ and $k(M1,E_\gamma)$ strength functions were expressed similarly as:

$$k(E1,E_\gamma) = w_E \frac{\Gamma_{GE}^2(E_\gamma^2 + \kappa_E 4\pi^2 T_E^2)}{(E_\gamma^2 - E_{GE}^2)^2 + E_{GE}^2\Gamma_{GE}^2} + \sum_i W_{Ei} \frac{(E_\gamma^2 + (\alpha_{Ei}(E_{Ei} - E_\gamma)/E_\gamma))\Gamma_{Ei}^2}{(E_\gamma^2 - E_{Ei}^2)^2 + E_\gamma^2\Gamma_{Ei}^2}, \quad (4)$$

$$k(M1,E_\gamma) = w_M \frac{\Gamma_{GM}^2(E_\gamma^2 + \kappa_M 4\pi^2 T_M^2)}{(E_\gamma^2 - E_{GM}^2)^2 + E_{GM}^2\Gamma_{GM}^2} + \sum_i W_{Mi} \frac{(E_\gamma^2 + (\alpha_{Mi}(E_{Mi} - E_\gamma)/E_\gamma))\Gamma_{Mi}^2}{(E_\gamma^2 - E_{Mi}^2)^2 + E_\gamma^2\Gamma_{Mi}^2}, \quad (5)$$

where E_{GE} (or E_{GM}) and Γ_{GE} (or Γ_{GM}) are location of the center and width of the maximum of the giant dipole resonance, T_E (or T_M) is a varied nuclear thermodynamic temperature, for $E1$- (or $M1$-) transitions. And for each i-th peak ($i \leq 2$) of the strength functions of $E1$- (or $M1$-) transition: E_{Ei} (or E_{Mi}) is a center position, Γ_{Ei} (or Γ_{Mi}) – width, W_{Ei} (or W_{Mi}) – amplitude, and α_{Ei} (or α_{Mi}) ~ T^2 is an asymmetry parameter. A necessity of taking into account a peak asymmetry in the radiative strength function results both from the model [18] and from the theoretical analysis of features of the fragmentation of single-particle states in the nuclear potential [2]. At the fitting the functions (4) and (5) are appreciably varied.

The shell inhomogeneties of a single-partial spectrum were also taken into account in the presented analysis (as in [9]).

A comparison of the level density obtained from spectra of evaporated nucleons [22] with the data of analysis of the cascade intensities [23] shows their sizeable distortion in the energy points of the Cooper pairs' breaking. A phonon disappearance and an appearance of additional pair of quasi-particles must noticeably change the level density. From the existence of the smooth evaporated spectra results that a change in the level density (at breaks of the Cooper pairs in the nucleus) must be compensated by a change in the strength functions at the same excitation energies. And a resonance structure of the strength functions, experimentally discovered [24] near the point of the second Cooper pair breaking (at the excitation energy of about 3 – 4 MeV), which was interpreted by an existance of a "pygmy"-resonance in the nucleus, must be accompanied by a change in the level density. For a verification of this reasonable assumption we introduced into equations (4) and (5) the compensation coefficients M [6,25]:

$$M = \rho_{mod}/\rho_{exp}. \quad (6)$$

Here ρ_{mod} is the level density calculated using Fermi-gas model, ρ_{exp} – the level density obtained at the experimental intensity description. For the strength functions (4) and (5) coefficients M are fitted separately.

The compensation parameters M introduce some unaccounted anti-correlation between ρ and Γ, which was not completely included in used model representations for ρ and Γ. At a high enough quality of the experimental data on the two-step cascades on ^{172}Yb there is a real possibility to evaluate an influence of compensation parameters M on determination of the breaking thresholds of Cooper pairs.

5. RESULTS

5.1. On a stability of obtained parameters

The results of analysis of the cascade gamma-decay of ^{172}Yb using the empirical model describe with a high accuracy the intensity of the cascades with the total energies from $E_1 + E_2$

= 8020 keV to $E_1 + E_2 = 6823$ keV including the resolved local peaks above $E_{ex} \approx 5$ MeV (see fig. 5).

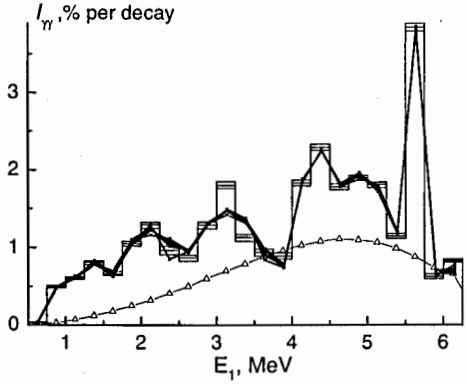

Fig. 5. The dependence of the total intensity of the cascades of ^{172}Yb to 6 final levels with $E_f \leq 1197$ keV on the energy of primary transition. Histogram is the experimental intensity with its errors obtained by the procedure [14]. Broken lines are the results of the best fits with different M coefficients. Triangles are intensity calculations using models [17] and [18].

In figs. 6 – 8 there are the best seven fits of the intensity of the cascades with different compensation parameters M. The initial M values were chosen in the interval $1 \leq M \leq 10$. The results of a description of the cascades' intensities with different initial M values showed that their fitted values are always bounded above (for $E1$-strength function $M \leq 5$, and for $M1$-strength function $M \leq 3$).

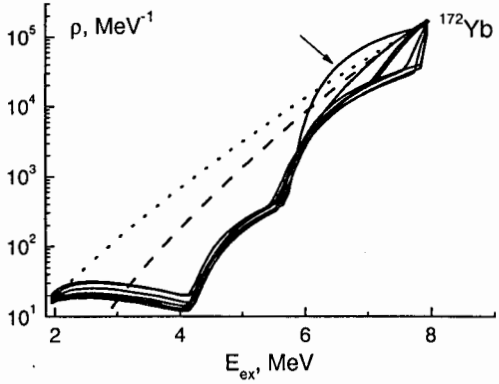

Fig. 6. The excitation energy dependences of the level densities for ^{172}Yb. Solid lines are the level densities obtained from approximations of the total intensity $I_{\gamma\gamma}$ of the cascades to 6 final levels with $E_f \leq 1197$ keV at varied M (6). Dashed and dotted lines are calculations of ρ value using the model [17] with and without taking into account the shell inhomogeneities of a single-particle spectrum [16], correspondingly. Fit without taking into account the parameter M is shown by an arrow.

For ^{172}Yb, as in [8, 10], the stepwise structure in the level density at a growth of the excitation energy was discovered (fig. 6), at a decrease of the density of the levels of vibrational type between the breaking thresholds of Cooper pairs. This result is in qualitative agreement with the model representations both from [16] about the behavior of the density of vibrational levels (see fig. 4), and from [20], where a rapid rise of density of the quasi-particle levels at each Cooper pairs' breaking threshold was predicted.

The probable values of $E1$- and $M1$-radiative strength functions for ^{172}Yb nucleus in dependence on the energies of primary transitions of the cascades (with taking into account a contribution of a negative (below neutron binding energy) resonance) are presented separately in fig. 7. In fig. 8 the sums of $E1$- and $M1$-radiative strength functions are shown. The results were obtained by a condition that a part of decays of the compound-state with the spin $J = 1$ is 60%.

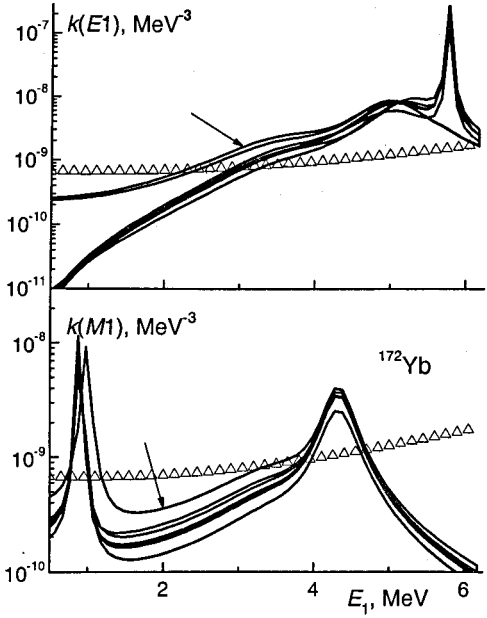

Fig. 7. The strength functions $k(E1)$ and $k(M1)$ of $E1$-transitions (upper picture) and $M1$-transitions (bottom picture) obtained for the energy of primary transition in the interval $0.52 < E_1 < 6$ MeV at varied parameter M (6). Triangles – calculation of the strength function of $E1$-transitions using the model [18] in a sum with c $k(M1)$= const. Two fits without taking into account the parameter M are shown by arrows.

Figs. 5 and 6 results that the compensation coefficients M have almost no influence on the calculated cascade intensities and relatively weakly change the level density near the breaking thresholds of the first, the second and the third Cooper pairs. And figs.7 and 8 shows that the fittings with parameter M noticeably change the strength functions. More essential fact is that at $M > 2$ in the fitted spectra of radiative strength functions the local peak with the center at $E_1 \approx 1$ MeV appears (near excitation energy, where there is the breaking point for the fourth Cooper pair). An increment of the strength function in the point of breaking the 4-th

Cooper pair, as for ^{172}Yb, would be expected also for a number of nuclei with noticeable excess intensity of the cascades near $E_1 = 1 - 2$ MeV [8, 10].

At the fits with $M > 2$ the positions of both the peak of the electrical strength functions at the energy of primary transitions near 6 MeV and the peak of the magnet strength functions near $E_1 = 4$ MeV (see fig.7) correspond to the breaking points of Cooper pairs of ^{172}Yb nuclear.

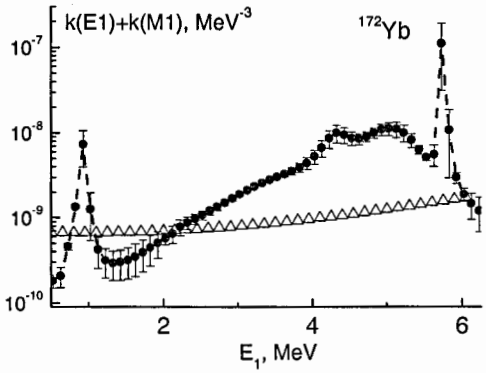

Fig. 8. Dependences of the sums of $E1$- and $M1$- radiative strength functions on the energy of primary transition. Points with errors connected by dashed line are the best 7 fits with varied M (6). Triangles – $E1$-strength function calculated using the model [18] in a sum with $k(M1)$=const.

At the fits with $M = 1$, in the energy dependence of the $E1$- radiative strength function, the peak of the strongest resolved cascade 5540+2402 keV near $E_1 = 6$ MeV is not observed (according to [15], its relatively strong intensity is due to existing negative resonance). Nevertheless, such intense peak is not observed at a capture of 2 keV neutrons, so it would be a large random deviation.

5.2. On a connection between the parameters of the gamma decay and the compound-state spin

Cascading γ-decay of the neutron resonance of a target with odd number of neutrons (or/and protons) is happened through dipole $E1$- and $M1$-transitions practically in 100% of decays. Mixtures of dipole and quadrupole gamma-transitions are present at the γ-decay process and have an influence on the values of the strength functions, but their existence in the two-step cascades of all nuclei investigated earlier was not identified.

A high resolution of the detectors for the cascade recording allows to investigate a dependence of the parameters of the nuclear superfluidity on the spins of the excited levels and on their parities at varied excitation energy. At the fitting an unknown ratio of the densities of levels with different parities in the interval of excitation energy $E_d \le E_{ex} \le B_n$ (E_d is upper energy boundary of the area of discrete levels) was taken as $r = \rho(\pi-)/(\rho(\pi-)+\rho(\pi+))$, where $\rho(\pi-)$ and $\rho(\pi+)$ are the densities of levels with negative and positive parities, correspondingly. In all calculations for ^{172}Yb, at $B_n = 8$ MeV $r = 0.5$ (it is generally accepted now hypothesis) and at $E_{ex} = E_d$ r varied from 0 to 1 (at $E_d < E_{ex} < B_n$ r value was taken from corresponding linear extrapolations).

A capture cross sections of thermal neutron by ^{171}Yb nucleus composed by known resonances to the compound states $J = 1$ и $J = 0$ are $\sigma_1 = 4$ b and $\sigma_0 = 1.8$ b, correspondingly.

And capture cross section from the negative resonance is 42.8 b [26]. An existence of the negative resonance with unknown spin influences on the fitting results (and on the calculated values of the breaking thresholds). Under selection rules on multipolarity, at the decay of compound-state with the spin $J = 0$ the two-step cascade excites the final levels with spins $I = 0, 1, 2$, and at the decay of the compound-state with $J = 1$ the final levels with $I = 0, 1, 2$ and 3 are excited.

It is possible to evaluate an influence of a spin of the compound-state on the fitted parameters, which describe the experimental intensities in the present experiment, from calculated dependences of intensities on a ratio $\sigma_1/(\sigma_1+\sigma_0)$. This ratio determines a contribution of a neutron capture by the compound states with spin $J = 1$ to the total capture cross section $\sigma_1+\sigma_0$. The calculated total intensities for a given ratios $\sigma_1/(\sigma_1+\sigma_0)$ (points connected by lines) are shown in fig. 9 for the cascades to 8 final levels of ^{172}Yb. Six of the final levels presented in fig. 9 have energy $E_f > 1$ MeV. The best fits for the level density and for the strength functions (figs. 6–8) are used in calculations of $I_{\gamma\gamma}$ for these cascades. The obtained from the experiment parts of intensities for the sums of two strongest cascades and of four cascades with the energies 1043; 1118; 1155 and 1198 keV are 0.203(11) and 0.078(11), correspondingly.

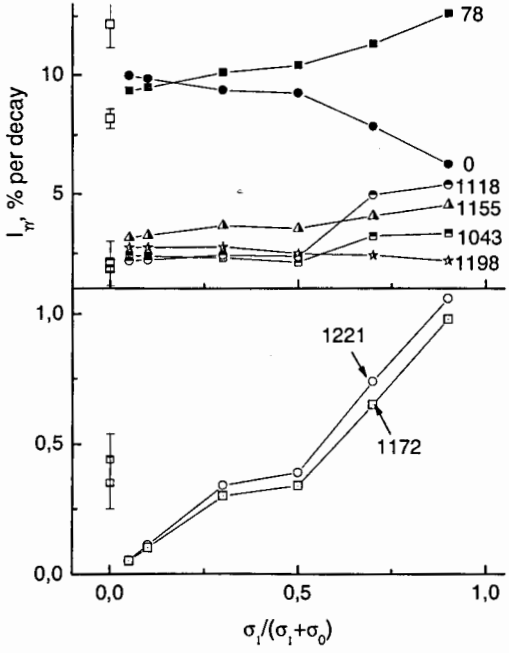

Fig. 9. The calculated total intensities of the cascades for a given ratios $\sigma_1/(\sigma_1+\sigma_0)$ of a capture cross section by the compound states with spin $J = 1$ to the total capture cross section (points connected by lines). The energies of the final levels are denoted by arrows (in keV). Points with errors are the experimental intensities of the explored cascades.

If the negative resonance have a spin $J = 0$, the calculations (fig. 9) show that the levels with $E_f = 1172$ keV ($I = 3^+$) and $E_f = 1221$ keV ($I = 3^-$) cannot be excited often than in

1 case per 1000 decays. If the negative resonance has a spin $J = 1$, these cascades have intensities up to 1 % per a decay. From a comparison of calculations, which are presented in fig. 9, the ratio $\sigma_1/(\sigma_1+\sigma_0)$ can be evaluated by a value 30 to 60 %.

In dependence on a spin of negative resonance the calculated sum of the intensities of the cascades to the ground and the first exciting states changes from 18.8 to 19.6% per decay.

The obtained intensities of the cascades with $E_f = 0$ ($I = 0$) and $E_f = 78$ keV ($I = 2$) clearly demonstrate an anti-correlation between calculated intensities of the cascades to these final levels, when the part of cross-section of a capture to the state with $J = 1$ changes.

6. CONCLUSION

In the present experiment the specific behavior of the gamma-decay, discovered by us earlier for 43 nuclei, was confirmed for ^{172}Yb nucleus. The intensities of the two-step cascades in the ^{172}Yb nucleus were determined with the best accuracy among all investigated even-even nuclei.

From the experimental distributions $I_{\gamma\gamma}(E_1)$ of the cascades to different final levels at a capture of thermal neutrons by ^{171}Yb nucleus the most probable value of the breaking threshold for the second Cooper pair was obtained with an uncertainty less than 0.5 MeV, and the breaking thresholds for the 3-rd and the 4-th Cooper pairs were determined with some bigger uncertainties. A demonstrable connection between the breaking thresholds and the spin of the neutron resonance was not discovered in the analysis. For ^{172}Yb (as for all investigated deformed nuclei) the obtained value of the breaking thresholds for 4-th Cooper pair satisfies the condition $U_4 \leq B_n$.

All obtained dependencies ($k(E1)$, $k(M1)$ and $\rho(E_{ex})$) for ^{172}Yb have the similar shapes if to compare with ones for ^{174}Yb [9, 10]. An existence of the stepwise structure in the $\rho(E_{ex})$ distribution with the closed for two ytterbium isotopes breaking thresholds of Cooper pairs can be considered as an observation of common pattern of the gamma-decay for these deformed nuclei. A comparison of the level density ρ obtained from approximation of the intensity of the cascades to two final levels (fig. 4) and analogous data for 6 cascades (fig. 6) showed a weak dependency of ρ on a structure of the wave functions of rotation and vibrational final levels of ^{172}Yb. An accuracy of the $I_{\gamma\gamma}(E_1)$ experimental distribution allows us to declare that the superfluid phase of the nuclear matter exists and we can observe its change with a growth of the excitation energy.

For ^{172}Yb the energy dependencies of $E1$- and $M1$-radiative strength functions are similar, on the whole, with ones obtained earlier for the other even-even deformed nuclei. Some difference can be explained by both errors of the experiment and imperfection of the model representations about ρ and Γ parameters of the investigated nucleus.

For a further research of the cascade gamma-decay of the compound-states the new models are needed, which would be able to describe the dipole radiative strength function and the level density at all excitation energies of investigated nucleus. First of all, it is necessary to change a phenomenological coefficient of vibrational enhancement of the level density by a modern appropriate model. The new models had to take into account a dependency of ρ and Γ on spin, parity, quantum number K etc., and, for an objectivity of obtained results at a study of the change dynamics of superfluid nuclear properties, the required models had to have a possibility the descriptions of the nucleus both as a pure fermion system and as a pure boson one, as special cases.

A heavy potential for investigation of the superfluidity of exited nuclei one can expect, if for the cascades' intensity recording the system of great number of HPGe-detectors would

be used (for a separation of the cascades with different multiplicity of quanta and with the intensities up to 90% of the total intensity of primary transitions), and at a study of the decay of compound-states with emission of two divers reaction products.

References

1. S.T. Boneva et al., Sov. J. Part. Nucl. **22** (1991)232.
2. L.A. Malov, V.G. Soloviev, Sov. J. Nucl. Phys. **26** (1977)384.
3. V.G. Soloviev, Theory of Atomic Nuclei. Quasi-particle and Phonons, IPP, Bristol and Philadelphia, 1992.
4. V.G. Soloviev, Sov. J. Phys. Part. Nucl., **3** (1972)390.
5. C.F. Porter and R.G. Thomas, Phys. Rev. **104** (1956)483.
6. A.M. Sukhovoj, Phys. Atom. Nucl. **78** (2015)230.
7. A.M. Sukhovoj and L.V. Mitsyna, in *Proceedings of XXII International Seminar on Interaction of Neutrons with Nuclei, Dubna, May 2014,* Preprint № E3-2015-13 (Dubna, 2015), p. 245; http://isinn.jinr.ru/past-isinns.html.
8. A.M. Sukhovoj, L.V. Mitsyna, N. Jovancevich, Phys. Atom. Nucl. **79** (2016)313.
9. D.C. Vu et al., ЯФ **80** (2017)113 [Phys. Atom. Nucl. **80** (2017)237].
10. D.C. Vu et al., JINR preprint E3-2016-43, Dubna, JINR, 2016.
11. A.M. Sukhovoj, V.A. Khitrov, Instrum. Exp. Tech., **27** (1984)1071.
12. Yu.P. Popov et al., Izv. Acad. Nauk SSSR, Ser, Fiz., **48** (1984)1830.
13. http://www-nds.iaea.org/ENDSF.
14. S.T. Boneva, A.M. Sukhovoj, V.A. Khitrov, and A.V. Voinov, Nucl. Phys. **589** (1995)293.
15. R.C. Greenwood, C.W. Reich, and S.H. Egors, Jr., Nucl. Phys., **262** (1975)260.
16. A.V. Ignatyuk, Report INDC-233(L), IAEA (Vienna, 1985).
17. W. Dilg, W. Schantl, H. Vonach, and M. Uhl, Nucl. Phys. A **217** (1973)269.
18. S.G. Kadmenskij, V.P. Markushev and W.I. Furman, Sov. J. Nucl. Phys. **37** (1983)165.
19. *Reference Input Parameter Library RIPL-2, Handbook for calculations of nuclear reaction data*, IAEA-TECDOC (2002).
20. V.M. Strutinsky, in *Proceedings of the International Congress on Nuclear Physics, Paris, France, 1958*, p. 617.
21. A.M. Sukhovoj, V.A. Khitrov, Phys. Atom. Nucl. **76** (2015)68.
22. V. G. Pronyaev et al., Phys. Atom. Nucl. **30** (1979)310.
23. A.M. Sukhovoj, V.A. Khitrov, Phys. Atom. Nucl. **73** (2010)1554.
24. D. Bohle et al., Phys. Lett. **137B** (1984)27.
25. N. Jovancevic, A.M. Sukhovoj, W.I. Furman, and V.A. Khitrov, in *Proceedings of XX International Seminar on Interaction of Neutrons with Nuclei, Dubna, May 2012,* Preprint № E3-2013-22 (Dubna, 2013), p. 157; http://isinn.jinr.ru/past-isinns.html.
26. S.F. Mughabhab, Neutron Cross Sections, BNL-325. V. **1** Part B, NY, Academic Press. 1984.

Nuclear Analytical Methods in the Life Sciences

APPLICATION OF NONDESTRUCTIVE NEUTRON RESONANCE ANALYSIS FOR INVESTIGATION OF METAL COMPOSITION OF RESKUPORID V STATERS (3 CENTURY AD) FROM PHANAGORIA'S TREASURE

Bazhazhina N.V.[1], Abramzon M.G.[2], Ergashov A.M.[1], Mareev Yu.D.[1], Mazhen S.T.[1], Saprykina I.A.[3], Sedyshev P.V.[1], Shvetsov V.N.[1]

[1]Frank Laboratory of Neutron Physics, Joint Institute for Nuclear Research, Dubna, Russia
[2]Nosov Magnitogorsk State Technical University, Magnitogorsk, Russia
[3]Institute of Archaeology of Russian Academy of Sciences, Moscow, Russia

Abstract

The method of Neutron Resonance Capture Analysis (NRCA) is currently being developed in the Frank Laboratory of Neutron Physics (FLNP) for the purpose of determination of the element composition of samples. The method is based on registration neutron resonances in radiative capture and measurement the yield of reaction products in these resonances. To test the capabilities of this method, such investigations were carried out in collaboration with Institute of Archaeology of RAS at the pulsed neutron source IREN of FLNP for the ancient coins from Phanagoria's treasure. A cylindrical multi-sectional liquid scintillator detector was used as a detector of γ-quanta.

Introduction

The method of Neutron Resonance Capture Analysis (NRCA) is currently being developed in the Frank Laboratory of Neutron Physics for the purpose of determination of the element composition of samples [1,2]. The method is based on registration neutron resonances in radiative capture and measurement the yield of reaction products in these resonances. The resonance parameters were determined to date for practically all stable nuclei in the neutron energy region up to several tens of keV [3, 4], that allows us to solve an inverse problem. The investigations are carried out at the IREN facility by time-of-flight method. To test the capabilities of this method such investigations were carried out in collaboration with Institute of Archaeology RAS for the ancient coins from Phanagoria's treasure [5].

The main part of a treasure (more than two thirds) is staters of Reskuporid V (242/243–276/277). These coins are of special interest for studying of economic climate and inflationary processes which are followed by degradation of coinage alloy of staters. We selected to this study the staters of the following years AD (Fig. 1): 242/243 (catalog № 2), 249/250 (№ 183), 250/251 (№ 271), 251/252 (№ 355), 252/253 (№ 482), 262/263 (№ 709, 732), 263/264 (№ 860, 961), 264/265 (№ 1025). A more detailed description and photographs of coins can be found in the publication of the results of archaeological research in Phanagoria [5].

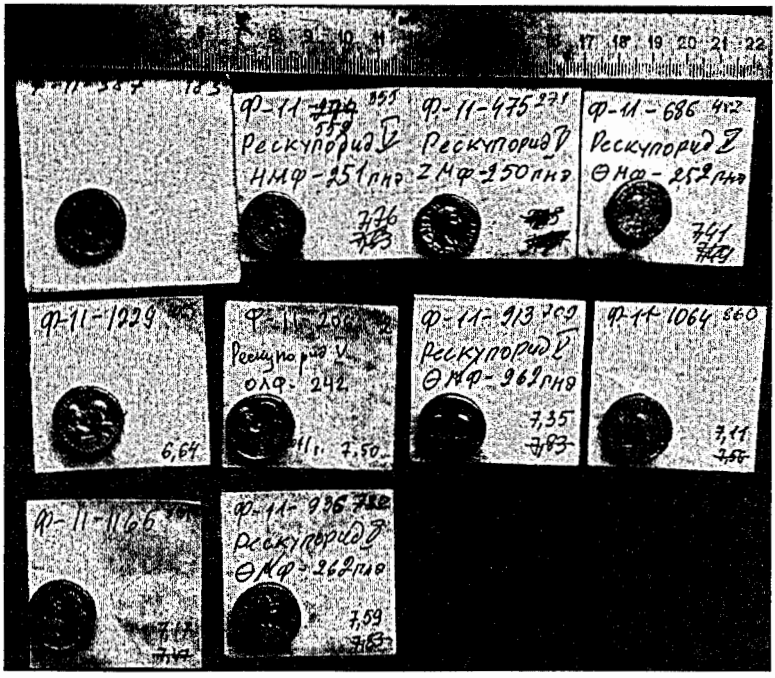

Fig. 1. Bosporan staters (3 century AD) from the Phanagoria's treasure found in 2011.

Previously, the X-ray fluorescence analysis was applied for determination the elemental composition of coins [6]. The applied type of a spectrometer allows to make measurements of a surface on depth to 10 μm. Most of the metal archaeological finds are inhomogeneous. The investigation of such objects requires a different approach. The NRCA is non-destructive and gives a possibility to study samples through all its volume. Therefore, such analysis was carried out at IREN facility.

Experiment

The main part of the IREN facility is a linear electron accelerator LUE-200 with non-multiplying neutron-producing target of the VNZH-90 alloy [7, 8]. The facility parameters in which the investigation was made are: the average energy of electrons ~ 40 MeV, the peak current ~ 1.5 A, the width of electron pulse ~ 100 ns, the repetition rate – 25 Hz. The total neutron yield is about ~ $3 \cdot 10^{11}$ s^{-1}. The measurements were carried out at the 58.6 meters flight path of the 3rd channel of the IREN. The big liquid scintillator detector was used for the registration of γ-quanta [9]. The neutron flux was permanently monitored by a neutron counter located on the 4th neutron channel of the IREN facility. The signals from the detector and the monitor counter were simultaneously fed to the two independent inputs of TDC. The time-of-flight spectra were stored on a computer disk for later processing off-line. A more detailed description of experimental setup can be found in Ref. [1].

To evaluate of the method the investigations were carried out in the "bulk-form", for all coins at once. The coins were placed in an aluminum cassette, which was placed in a beam inside the detector channel. The total mass of coins was 73.033 g. The measurements with the sample lasted about 13 hours. Only silver and copper resonances were identified on the time-of-flight spectrum (Fig. 2). The measurements with standard samples of silver and copper were made in addition to the measurement with the investigated sample.

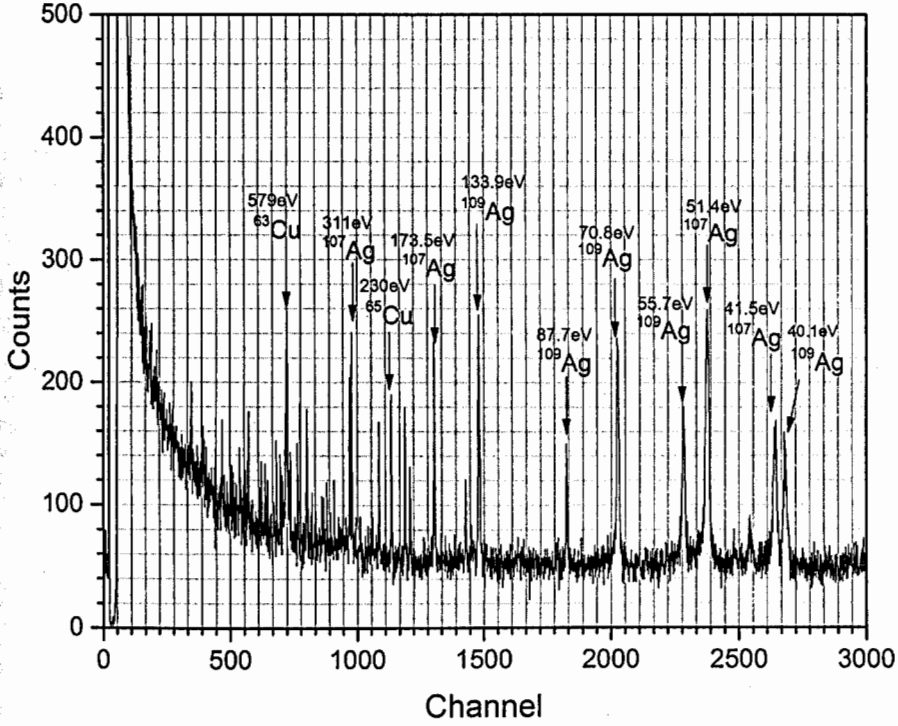

Fig. 2. Part of time-of-flight spectrum, obtained from measurement with ancient coins from the Phanagoria's treasure.

Results

The number of nuclei of the element in the sample was determined by the measurement of the yield of gamma-quanta in the resonances. The sum of events in the resonance is related with resonances parameters and experimental values by the expression [1, 10]:

$$\sum N = f(E_0) \cdot S \cdot t \cdot \varepsilon_\gamma \cdot \frac{\Gamma_\gamma}{\Gamma} A \qquad (1)$$

Here, $f(E_0)$ is the energy density of the neutron flux at the resonance energy E_0, S – the area of the sample, t – measuring time, ε_γ – the detection efficiency of radiative capture by the detector, Γ_γ, Γ – the radiative and total widths of the resonance.

$$A = \int_{-\infty}^{+\infty} [1 - T(E)] dE \tag{2}$$

is resonance area on the transmission curve.

$$T(E) = e^{-n\sigma(E)} \tag{3}$$

is the energy dependence of the neutron transmission by the sample; $\sigma(E)$ – the total cross section at a given energy, n – the number of isotope nuclei per unit area. The value A for investigated sample was determined from experimental data by the formula:

$$A_x = \frac{\sum N_x \cdot M_s \cdot S_s}{\sum N_s \cdot M_x \cdot S_x} \cdot A_s . \tag{4}$$

Here the indices x and s refer to the investigated and standard samples, respectively; M – the number of monitor counts during the measurement time. The value A_s for the standard was determined by well-known parameters of resonances and the standard sample using a program based on the algorithm of Ref. [11]. The number of nuclei per unit area of isotope was determined from the value A_x by the same program.

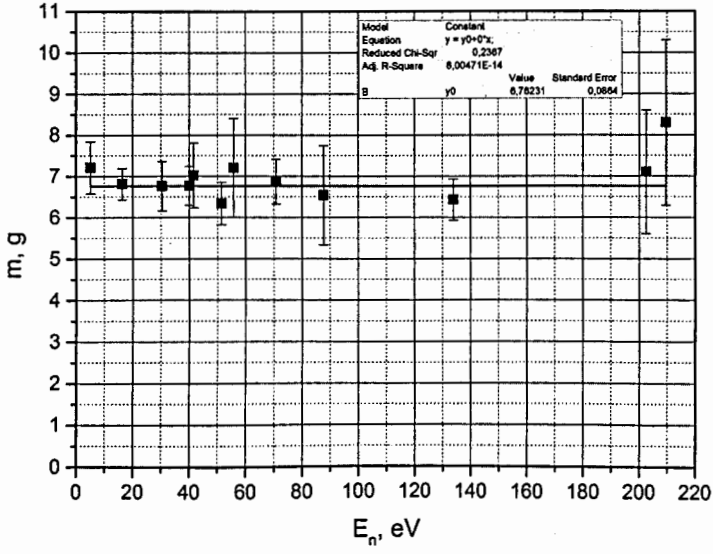

Fig. 3. The values of the mass of silver in coins obtained from individual resonances and the weighted-average value.

The twelve resonances of ^{107}Ag and ^{109}Ag were processed for determination the mass of silver in coins. The results are shown in Fig. 3. The weighted-average value of silver content in the samples was (6.762 ± 0.086) g or (9.26 ± 0.12) wt. %. The copper content was estimated only by one resonance of ^{65}Cu at 230 eV. Another observed resonance of ^{63}Cu at 579 eV is covered by closely spaced silver resonances, and it can't be used for processing. The result for copper is 62.0 ± 3.1.

Conclusion

The total mass of the elements in coins, determined from the resonances, is 68.76 ± 3.1 g. The mass of coins determined by weighing is 73.033 g. The difference does not exceed two standard deviations, in that way the result can be considered satisfactory.

We can make preliminary estimation of the possibilities of method, if it would be necessary to analyze the isotope composition of each coin separately. The weighted-average value of silver content in ten coins is 6.76 ± 0.09 g. The statistical error is about 1 %. In the case when each coin is measured separately, the statistics will be in 10 times less during the same measurement time and the error will increase by 3 times (up to 4–5 %). In that way if the difference in the silver content in coins is more than 12 % we can define it with high degree of confidence.

Acknowledgements. The authors express their gratitude to the staff of the IREN facility and to the head of the development of the facility A.P. Sumbaev for the supporting with uninterrupted operation of the facility in the process of measurements.

References

1. N.V. Bazhazhina, Yu.D. Mareev, L.B. Pikelner, P.V. Sedyshev, V.N. Shvetsov. Analysis of element and isotope composition of samples by neutron spectroscopy at the IREN facility. Physics of Particles and Nuclei Letters **12** (2015) 578–583.
2. H. Postma, P. Schillebeeckx. Non-destructive analysis of objects using neutron resonance capture. J. of Radioanalytical and Nuclear Chemistry. **265** (2005) 297–302.
3. S.F. Mughabghab. Neutron Gross Sections, Neutron Resonance Parameters and Thermal Gross Sections. Academic Press, New York, 1984.
4. S.I. Sukhoruchkin, Z.N. Soroko, V.V. Deriglazov. Low Energy Neutron Physics. Landolt-Bornstein.V. I/16B, Berlin: Springer Verlag, 1998.
5. M.G. Abramzon, V.D. Kuznetsov. Treasure of Bosporan stators III-IV centuries from Phanagoria. In the collection: Phanagoria. Results of archaeological research. V. 5. Ed. by V.D. Kuznetsova (Moscow: Institute of Archeology RAS, 2017) 3-271 (in Russian).
6. I.A. Saprykina, O.L. Gunchina. The chemical metal composition of Bosporan stators of Phanagoria's treasure in 2011. In the collection: Phanagoria. Results of archaeological research. V. 5. Ed. By V.D. Kuznetsova (Moscow: Institute of Archeology RAS, 2017), 272–483 (in Russian).
7. O.V. Belikov, A.V. Belozerov, Yu. Becher, Yu. Bulycheva, A.A. Fateev, A.A. Galt, A.S. Kayukov, A.R. Krylov, V.V. Kobetz, P.V. Logachev, A.S. Medvedko, I.N. Meshkov, V.F. Minashkin, V.M. Pavlov, V.A. Petrov, V.G. Pyataev, A.D. Rogov, P.V. Sedyshev, V.G. Shabratov, V.A. Shvec, V.N. Shvetsov, A.V. Skrypnik,

A.P. Sumbaev, A.V. Ufimtsev, V.N. Zamrij. Physical start-up of the first stage of IREN facility. Journal of Physics: Conf. Ser. 205 (2010) 012053.
8. E.A. Golubkov, V.V. Kobets, V.F. Minashkin, K.I. Mikhailov, A.N. Repkin, A.P. Sumbaev, K.V. Udovichenko, V.N. Shvetsov. The first results of adjustment of the second accelerating section of the LUE-200 accelerator at IREN facility. Communication of JINR P9-2017-77 (Dubna, JINR, 2017) 1–8 (in Russian).
9. H. Maletsky, L.B. Pikel'ner, K.G. Rodionov, I.M. Salamatin, E.I. Sharapov. Detector of neutrons and gamma rays for work in the field of neutron spectroscopy. Communication of JINR 13-6609 (Dubna, JINR, 1972) 1–15 (in Russian).
10. D. Zeliger, N. Iliescu, Kim Hi San, D. Longo, L.B. Pikel'ner, E.I. Sharapov. Neutron resonances in Bromine. Sov. Phys. JETP **18** (1964) 189–214.
11. V.N. Efimov, I.I. Shelontsev. Calculation for graphs of determining the parameters of neutron resonances by the transmission method. Communications of the JINR P-641 (Dubna, 1961) 1–19 (in Russian).

ASSESSMENT OF CHANGES IN THE MINERAL COMPOSITION OF THE BROWN ALGA *CYSTOSEIRA BARBATA* (TURN.) C.AG., COLLECTED ALONG THE COAST OF ANAPA

Bunkova O.M.[1], Kamnev A.N.[2], Kravtsova A.V.[3], Ermakov I.P.[2], Rudchenko M.N.[2], Stukolova I.V.[2], Yakovlev A.S.[1]

[1]*Moscow State University, Faculty of Soil Science, 1-12 Leninskie Gory, 119991 Moscow, Russia*
[2]*Moscow State University, Faculty of Biology, 1-12 Leninskie Gory, 119991 Moscow, Russia*
[3]*Joint Institute for Nuclear Research, 6, Joliot-Curie str., 141980 Dubna, Russia*

Introduction

The study of the biology and ecology of marine benthic microalgae due to their importance to the world's oceans as one of the major primary producers of the shelf zone, where their products are comparable to the products of temperate forests. Moulded macrophytes coastal thickets are, on the one hand, and spawning habitat for fish and invertebrates, and on the other - a natural barrier to anthropogenic pollution coming from coastal runoff. Currently, one of the most important areas of research of macroalgae is to assess their contribution to the exchange of biogeochemical ocean.

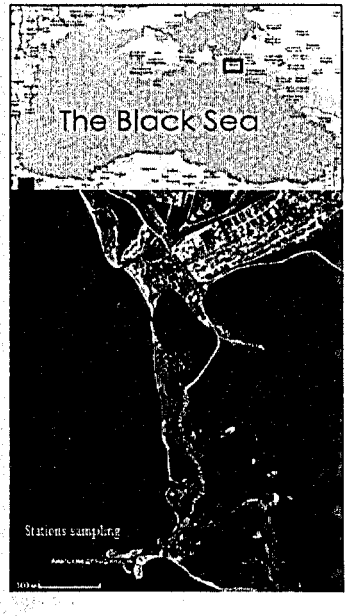

Fig. 1. Field sampling (Anapa district)

Objects and methods

Object of this research are representatives of one of dominant trade views of the Black Sea - *Cystoseira barbata* (Turn.) C. Ag. *Cystoseira barbata* (Stachouse) of C. Agardh – large (to 1 m of height) the attached sea brown alga living on a solid substratum: stony terraces, boulders, stones. Absorbs all difficult differentiated surface of a thallus. The root system is absent.

Collecting material was carried out in 1980 - 2015 on various shallow sites of the Black Sea. As model sites from 2001 to 2015 served the sites around Anapa which are settling down from the settlement of Sukko to the cape Utrish. The algae were collected at depths of 0,5; 2; 4; 6 and 8 meters (fig. 1).

Determination of content of Na, Rb, Cs, Ba, Sc, La, Ce, Th, U, Au, Cr, Fe, Co, Zn, Hg, As, Se, Sb, Br in thalli*Cystoseira barbata* were determined by neutron activation, and K, Mg, Ca, Mn, Cu, Ni, Cd, Pb by atomic absorption and x-ray fluorescence analysis.

Results and its discussion

Figure 2 shows the long-term (over 20 years), these changes of mineral composition *Cystoseira barbata* (Bunkova et al, 2014; Kamnev et al, 2014). Only such long-term data allow relatively correctly judge the actual concentration opportunities *Cystoseira barbata* (Stachouse) C. Agardh.

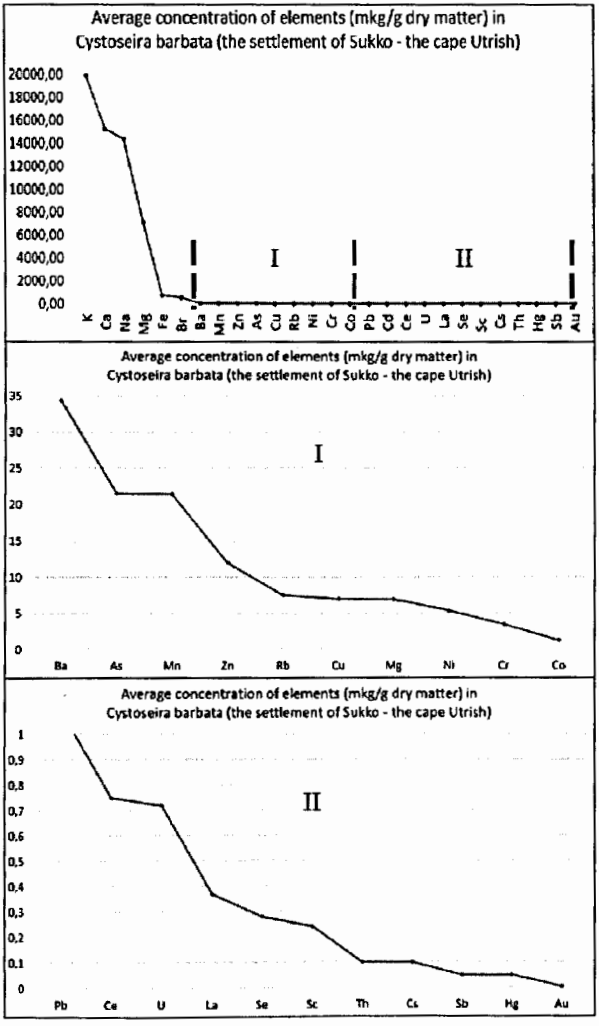

Fig. 2. Average concentration of elements in Cystoseira barbata.

As a result, our research has received several patterns of different chemical elements in the thallus of the brown alga *Cystoseira barbata*, collected in the waters of the river to the Sukko – the cape Utrish. Within chemical group we analyzed alkali metals (Na, K, Rb), alkaline earth metals (Mg, Ca, Ba), and IV group metals of the B subgroup (Pb), and V group B subgroups (Sb) of the periodic table.

Figure 2 shows that the mineral elements in their average content in thallus *cystoseira barbata* can be arranged in the following descending order: K> Ca> Br> Na> Fe> Mg> Ba> As> Mn> Zn> Ni> Rb> Cu> Cr> Co> Pb> U> Ce> La> Se> Sc> Cs> Sb> Th> Hg> Au.

As can be seen, the content of the same mineral elements in the algae contemporaneous depending on various factors can vary from 2 to 99 times (depending on the item). The reason for such fluctuations may be changing as the concentration of a particular element in the mineral water and the complex environmental factors environment, affecting

the accumulation of this element of the vegetable organism and the physiological condition of the macrophytes.

The ratio of the maximum and minimum macronutrients concentrations, such as the Na, K, Mg, Ca in thallus *Cystoseira barbata* can vary from 2 (Mg) 5 (K) times, and trace elements - 22 (Zn) and 99 (Fe) times. Similar fluctuations are also characteristic of physiologically "unimportant" items. These results, on the one hand, to some extent, show absorption physiological selectivity of chemical elements *Cystoseira barbata* and confirm the presence of physiological regulatory mechanisms of accumulation of nutrients. Perhaps this is due to the fact that the availability of these elements in different geological epochs changed and, accordingly, the physiological mechanisms of accumulation are different ranges. On the other hand, these results indicate the existence of a particular pool is able to accumulate these elements. In the case of Cystoseira - a storage pool such minerals may be alginic acid and fucoidan forming intercellular spaces and cell walls, and excessive penetration of the delay elements in the cell concentration.

These results, summarizing long-term observations, may indicate the potential need algae in certain elements, as well as the carrying capacity of the cell walls C. barbata in relation to the accumulation of the individual elements.

Seasonal variations

The study changes depending on the mineral composition of C. barbata on the degree of contamination of the habitat and its depth has been found that in general, the content of the majority of these elements in the thallus in the river above the removal area - "conditionally dirty" stations. This is most clearly seen at a depth of 2 m, which is probably due to the immediate removal of the various elements of the drain of the river, and the higher the metabolic activity of the algae in shallow water. An exception is the concentration of non-metals arsenic and selenium contents of which are higher value-added station. It is possible that this is due to local pollution by these elements of the "value-added" station.

On the "value-added" the station the mineral elements are also generally higher in the algae at a depth of 2 m. The exception to both stations is Ba, Sb and Br.

At a depth of about 4 meters of both stations, metal concentrations in thallus vary slightly. Nevertheless, a number of active elements is stored at this depth. Thus, in place of the river removal have high concentrations of bromine, the content of which is almost 1,4 times higher than that at a depth of 2 m the same station and 2-4 times higher than 4 m and 2 m, respectively "value-added" station. Furthermore, at a depth of 4 m "conditionally dirty" stations are the highest concentrations of uranium and gold.

As for the "heavy" metals, some of the general laws fall Pb, whose concentration decreases with depth, but the maximum on the "value-added" station, and Mn, m. To. Its concentration is also higher on the "value-added" station. It can be concluded that to "conditionally dirty" river station takeaway clearly affects the accumulation of minerals, and in the value-added station may have some local flooded contaminants (As, Se, Pb, Mn).

Seasonal variations

To study the content of mineral elements in the daylight saving time following contact was chosen mineral elements: Fe, Mn, Cu, Zn, Pb, Cd. When harvesting season, summer or winter (within a limited time period), the picture is somewhat different (even if the collection

was carried out at several stations, several depths, located a few kilometers from each other). Especially clearly this is manifested in the analysis of changes in the content of macro and micro elements (fig.3).

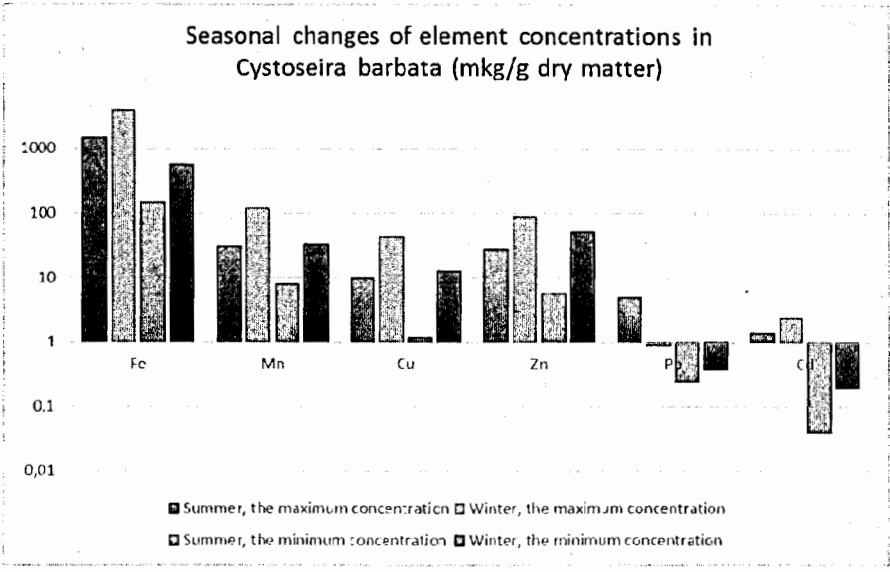

Fig. 3. Seasonal changes of element concentrations in Cystoseira barbata.

The ratio of the maximum and minimum contents of macronutrients (Na, K, Mg, Ca) in the algal thallus varies 1,5 – 4,3 times, trace elements (Fe, Mn, Zn, Cu) – 3,8 – 9,9 times, heavy "physiologically insignificant" heavy metals in the 20,8 – 34,6 times.

The results clearly demonstrate the selectivity of the physiological absorption of chemical elements macroalgae and confirm the presence of the physiological regulatory mechanisms of accumulation of biogenic elements.

The difference in concentrations in the winter, namely an increase in 2-3 times, probably due to a change in the length growth rate, growth prevailing in thickness, and accordingly, changes in the structure and functioning of the cell walls. Reducing Pb content, probably due to its level of change in the environment. Reducing Pb content, probably due to its level of change in the environment.

Age-related changes

Defined contribution is age-related changes in the accumulation of elements of different ages algae and their parts. In order to study the dependence of change in the content of mineral elements of the age part thallus contact 8 elements (Ca, Na, K, Mg, Fe, Mn, Zn, Cu). In age-related changes are most clearly traced to the copper, magnesium, sodium, potassium, iron and manganese (fig.4, fig. 5, fig. 6).

According to our research stations clear age-related changes can be traced, and the minimum content of the elements characteristic of the axis 0 of the order, and the maximum - for axis II and higher orders.

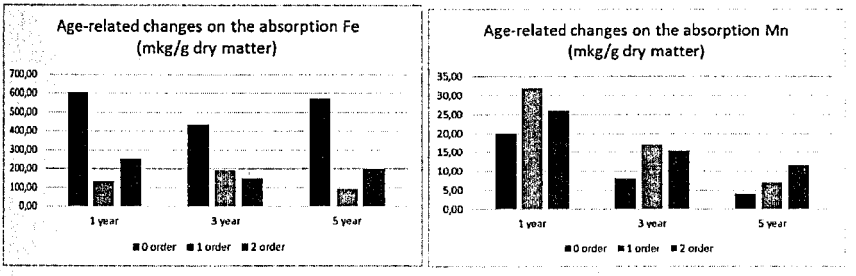

Fig. 4 Age-related changes on the absorption Fe and Mn (mkg/g dry matter)

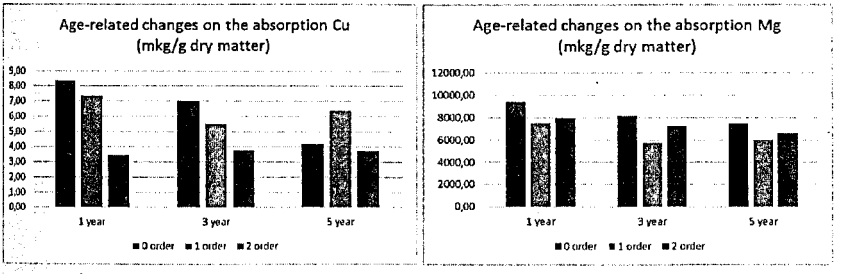

Fig. 5 Age-related changes on the absorption Cu and Mg (mkg/g dry matter)

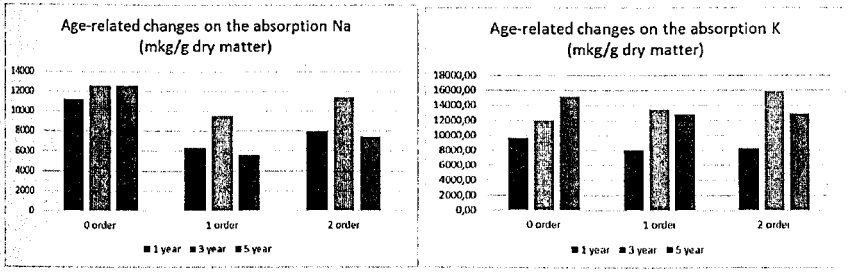

Fig. 6 Age-related changes on the absorption Na and K (mkg/g dry matter)

Coefficients of concentration and biological absorption

One of the most important areas in biogeochemistry is the concept of biogeochemical provinces, based on the separation of which is the specificity of the behavior of certain elements within the areas associated with excess or deficiency of elements in the environment. Therefore, the establishment of the content in relation to a particular standard

element is one of the most important techniques in biogeochemistry (Perelman, Kasimov, 1999; Bogatyrev, 2008).

There are approaches integral consideration of the content of the most important macro- and microelements data. These approaches include the construction of geochemical spectra of the elements. With their construction are guided by the following procedure. Usually, on the x-axis successively placed elements according to their serial number. The ordinate axis represents the ratio of the content of each element in the investigated object to the average content in the earth's crust, or lithosphere (Clarke). Then the indices greater than 1 indicate concentration of the element is smaller - about the dispersion (Bogatyrev, 2008).

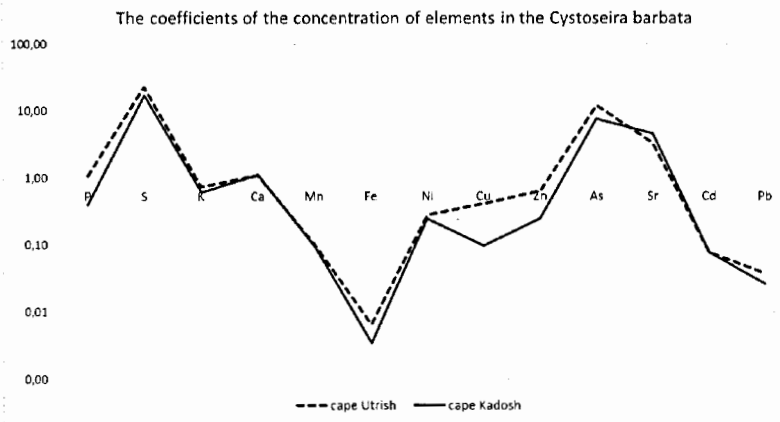

Fig. 7. The coefficients of the concentration of elements in the Cystoseira barbata.

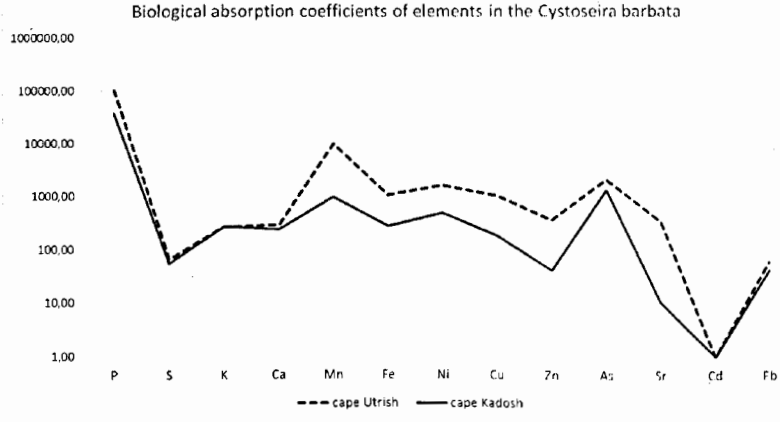

Fig. 8. The biological absorption coefficients of Cystoseira barbata.

When man-made pollution of the environment is not only a dangerous excess of MPC members (maximum permissible concentration), but also changes in the relations of elements to each other, and this should be taken into account when carrying out this kind of work. Clarke values set by AP were used to calculate the concentration factor Vinogradov (Vinogradov, 1962). By geochemical spectra presented above clearly shows that the resulting study data show the graphic elements of the same type of behavior accumulated in macrophytes collected in one region (fig. 7, fig. 8).

Conclusions

1. The availability of these elements to different geological ages varied and accordingly accumulation physiological mechanisms have different ranges. Over the past 100 years, the situation with the availability of many nutrients change, and anthropogenic pollution has led to the fact that some elements of the power plant inaccessible (Cu, Zn, Fe, Co) steel contaminants, which are classified as "heavy toxic metals." Experimental study of the accumulation of some elements of the algae leads to the assumption that a number of elements not found the upper accumulation physiological range, which can lead to a variety of toxic effects on algae.
2. The study changes depending on the mineral composition of C. barbata on the degree of contamination of the habitat and its depth has been found that in general, the content of the majority of these elements in the thallus in the river above the removal area - "conditionally dirty" stations.
3. Seasonal changes of mineral element concentrations in the axes of various orders in the winter becomes less pronounced, which is likely to be associated with reduced metabolism.
4. According to our research stations clear age-related changes can be traced, and the minimum content of the elements characteristic of the axis 0 of the order, and the maximum - for axis II and higher orders.
5. By geochemical spectra clearly it shows that the resulting study data show the graphic elements of the same type of behavior accumulated in macrophytes collected in one region.
6. Only long-term data, including various stations and depth allow relatively correctly judge the real possibilities of uneven concentration of brown algae *Cystoseira barbata.*

Bibliography

1. Bogatyrev L.G. Geochemical spectra as a form of environmental objects analysis environment // Professional lectures National Youth Science Forum "Step into the Future". Symposium 2. Natural Sciences and the Modern World. - ROO NTA APFN, Moscow, 2008, p. 36-39.
2. Bunkova O., Kamnev A., Yakovlev A., Suhova T., Shahpenderyan E. Studying of mineral structure of Cystoseira barbata in a sublittoral zone of the northeast coast of the Black Sea. // World Conference on Marine Biodiversity, Qingdao, China, 12-16 October 2014, p. 76.
3. Bunkova O.M., Kamnev A.N., Yakovlev A.S. Evaluation of the biogeochemical status of protected areas of Anapa region // Proceedings of the International scientific conference devoted to the 100th anniversary of the Southern Federal University "The role of botanic gardens in the conservation and monitoring of biodiversity," May 27-30, 2015, Rostov-on-Don, p. 492-495.
4. Bunkova O. Pollution of coastal waters of the Black sea by mineral elements, with Cystoseira barbata use as the type-indicator of pollution // Marine research horizon 2020. Abstract Book, Helix Press Ltd Varna, p. 70.

5. Bunkova O.M. Evaluation of diffuse pollution of coastal areas of the Black sea with heavy metals, using macroalgae and higher aquatic plants as pollution indicators // XX International Conference of students, graduate students and young scientists "Lomonosov-2013", a series of Soil Science. -M., MAKS Press, 2015, p. 92-94.
6. Kamnev A.N. Structure and function of brown algae. – M.: Publishing. Moscow State University, 1989. – 200 p.
7. Kamnev A.N., Messineva E.M., Rudchenko M.N., Silkin V.A. Age-related changes of morphological and functional characteristics of the genus of brown algae Cystoseira Black and Sea of Japan // Problems of modern algology. 2012. № 2 (2). URL: http://algology.ru/148.
8. Kamnev A.N., Bunkova O.M., Bogatyrev L.G., Stukolova I.V., Yakovlev A.S. Ideas Sabinina D.A. and their implementation: The mineral composition of macrophytes as a key indicator of their contribution to the exchange of the oceans biogeochemical // Proceedings of the International Conference "Environmental physiology of aquatic phototrophic: distribution, reserves, chemical composition and use» III Sabininskie reading. Part2. URL: http://algology.ru/557.
9. Perelman A.I., Kasimov N.S. Geochemistry of landscape. M.: Astrea 2000, 1999 - 764 p.
10. Vinogradov A.P. Average content of chemical elements in the main types of igneous rocks of the crust // Geochemistry. 1962. № 7, p. 555-571.

ASSESSING THE ENVIRONMENTAL POLLUTION USING NEUTRON ACTIVATION ANALYSIS – K_0 METHOD ON MOSSES

Bucsa Adrian Florinel

Institute for Nuclear Research Pitesti – No.1, Campului Street, 115400, Mioveni, Romania

ABSTRACT

The problem of toxic pollutant agents that exists in environment was and still is a main interest subject for nowadays health protection issues. Evaluating the impact of these agents on human health can influence major decisions that are to be taken by the authorities concerning the industrial activities developed in the inhabited areas or from the surrounding areas that directly impact the environment and inferentially the man. Precise measurements of toxic particles in the environment at the level of microelements are essential for exact and correct evaluations of the pollution degree. In order to determine the chemical elements that have negative effects on human health, we used as vegetal indicator, the ground moss. This plant has the ability to retain in the tissue the chemical elements precipitated from the atmosphere, because it is missing the cuticle that would normally prevent the elements from penetrating the cell interior. In order to determine the elements' concentration in the samples, it was employed as analysis method the neutron activation (NAA-k_0) using k_0 standardization. The neutron activation analysis is an analytic technique based on measuring the number and energy of gamma radiation emitted by the radioactive isotopes produced in the sample matrix by irradiation with thermal neutrons in a nuclear reactor. After the irradiation and the specific radioactive decay, the energy spectrum of gamma rays is obtained by measuring the sample with a detection system for high-resolution gamma spectrometry. The sample irradiation was processed in the TRIGA ACPR reactor in the rabbit (D10 location). The study was conducted on a total of four samples of ground moss from the environment (rough samples) and these were processed, irradiated and studied and the results obtained were recorded in a database. The thermal neutron flux supplied by the ACPR reactor in the rabbit location was fair enough for activating elements like manganese, potassium, bromine, europium, lanthanum, arsenic, scandium, antimony, iron. During the entire irradiation period, the presence of the sample in the irradiation location did not disturb the average value of the thermal neutron flux. The differences showed between the elements concentrations in the samples are actually because of the pollution more or less intense in the areas from which they were taken. Hence the quality of the ground moss as a good monitor. From the analysis of the results obtained on these samples and following the comparison with the reference values, it was noticed a slight excess concentration for arsenic and antimony. These overhauls are smaller than 2 ppm. Nevertheless, the alert value is not reached.

Key words: Neutron activation analysis, K_0 method, moss, ACPR

Introduction

The purpose of this paper is to determine the concentrations of the chemical elements that affect the human health, toxic agents that are present in the air and that are retained through fallout in the earth moss used as a genuine pollution indicator.In order to determine these chemical elements that negatively affect the human health, we used the moss as

indicator. This plant has the ability to retain in the vegetative tissue the chemical elements precipitated from the atmosphere, because it lacks the cuticle that would stop the penetration of elements in the cells.In the urban areas, the air's quality is strongly influenced by many human activities. The high population density, the heavy traffic and the house heating system in winter and various industrial activities in the outskirts, influence the concentration of trace elements and radionuclide in the atmosphere. Consequently, the population is exposed to potential adverse effects of changes in the composition of urban air. Thus, monitoring of air quality has become a standard of quality control procedures in the urban environment.This plant has the ability to retain in the tissue the chemical elements precipitated from the atmosphere, because it is missing the cuticle that would normally prevent the elements from penetrating the cell interior.

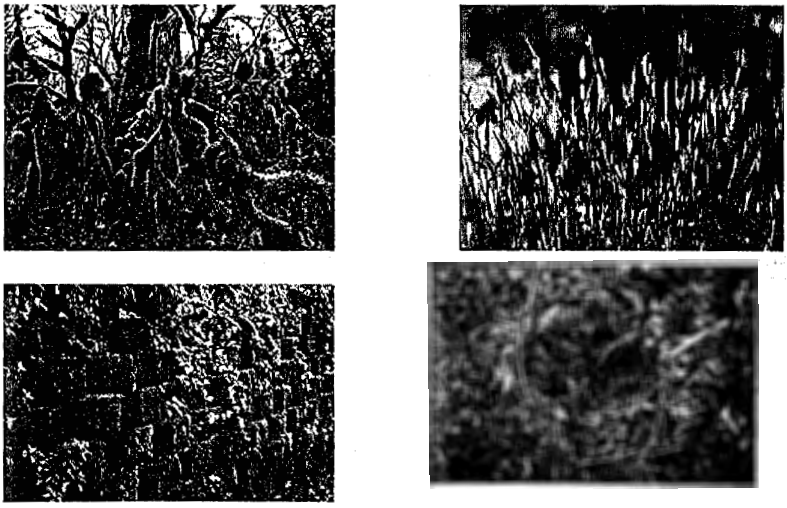

Figure 1. Samples of mosses

Moss samples were picked-up from certain locations (the locations considered with an upper degree regarding environment pollution), and then these were processed (burned in an industrial oven) and finally their residual solid state was inserted in polypropylene vial. These vials were exposed to a neutron flux in TRIGA ACPR rabbit. After been activated in the neutron field, the samples were measured via high resolution gamma ray detection system. The system consists of hyper-pure germanium detector crystal, electronic system (preamplifier, pulsating source, detector polarization unit and amplifier) and a multichannel analyser which was delivered with software specially used for radiation spectrum analysis. This system was used in order to obtain the qualitative analysis of the sample (which are the elements contained in the samples) and the quantitative analysis (determination of the concentrations of the elements discovered) using NAA-k0 standardization method. The results can be used to make a graphical representation of the areas with a high degree of pollution and based on this map decisions can be taken to reduce environment pollution.

Sampling

For the experimental part of this research work there have taken a total of 9 samples from different locations of the Pitesti city.Out of the total samples we choose to analyse only 4 samples due to the lack of time.

Table 1. Samples selected for irradiation in the TRIGA ACPR

Sample no.	Sampling location	Sample weight (g)	Mapping indicative
1	TRIGA Reactor stack	4470E-5	P1
2	Pitesti South train station	6715E-5	P4
3	ARPECHIM Petrochemical Factory	10884E-5	P6
4	ROLAST S.A. (Gavananeighbourhood)	12113E-5	P7

The samples and the flux monitor preparation. Irradiation experiment

After collecting the samples, they were stored in polyethylene bags at room temperature for 10 days after which they were weighed and then placed in an oven at a temperature of 40°C. There were made regular measurements of the masses and then the work continued with drying them in the oven until the land moss's mass remained constant.

The samples burning took place in CTD 2 oven type at a temperature of 450° C until a white coloured ash was obtained. This step was made for the following reasons:

- Water evaporation from the vegetative tissue of mosses; and
- Chemical elements concentration; thru this method it will be easier to determine the chemical elements resulted from neutron activation in TRIGA ACPR rabbit.

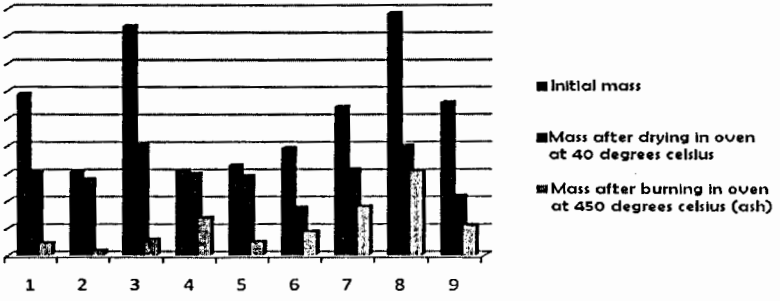

Figure 2. Moss mass evolution from initial sampling until burning (ready to be irradiated in reactor core)

For irradiation experiment, we have chosen a quantity approximately equal from the all four samples; these were weighted in polypropylene vials with small dimensions and then were sealed. The samples irradiation was processed in the TRIGA ACPR reactor in the rabbit (D10 location). The study was conducted on a total of four samples of ground moss from the environment (rough samples) and these were processed, irradiated and studied and the results obtained were recorded in a database.The samples together with flux monitor (foil of Au-197) were irradiated in ACPR rabbit for 4142 seconds. During the entire irradiation period, the presence of the sample in the irradiation location did not disturb the average value of the thermal neutron flux.The calculus made after irradiation showed that the mean value of neutron thermal flux was about 9.47E+11 neutrons / (cm^2·sec).It should be mentioned that the

short irradiation period of time did not allow the activation of heavy metal elements. Hence, in 4142 seconds of irradiation we succeed in activation of short life-time isotopes: ^{55}Mn, ^{41}K, ^{45}Sc, ^{121}Sb, ^{139}La, ^{151}Eu, ^{75}As, ^{81}Br, ^{58}Fe.

Qualitative-quantitative measurements of the elements retained in mosses; NAA-k_0 standardization method

Accurate measurements of toxic particles in the environment at the level of microelements are essential for exact and correct evaluations of the pollution degree.In order to determine the elements' concentration in the samples, it was employed as analysis method the neutron activation (NAA-k_0) using k_0 standardization.The neutron activation analysis is an analytic technique based on measuring the number and energy of gamma radiation emitted by the radioactive isotopes produced in the sample matrix by irradiation with thermal neutrons in a nuclear reactor. Usually, the sample matrix together with specific flow monitors, duplicates and standards for items of interest are irradiated for a selected period of time in a neutron flux in the core of the research reactor. After the irradiation and the specific radioactive decay, the energy spectrum of gamma rays is obtained by measuring the sample with a detection system for high-resolution gamma spectrometry.It was made a set of eight measurements on gamma ray HPGe detector for each one of the four samples irradiated. For chemical elements concentrations determination it was used NAA-k_0 standardization method.The high resolution gamma ray detector is shown in the following figure.

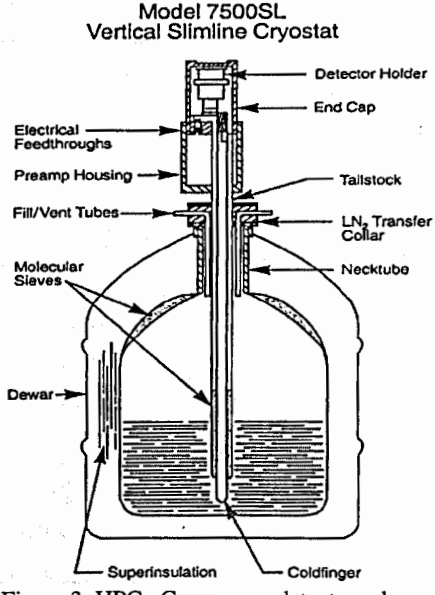

Figure 3. HPGe Gamma ray detector scheme

For this experiment it were used the following samples, apparatus and installations: ground mosses samples, polypropylene vials, TRIGA ACPR reactor (rabbit) and detection system consisted of bin and power supply, high resolution germanium γ-rays detector, amplifier, detector bias supply, pulsating source, multichannel analyser (MCA) and personal computer.

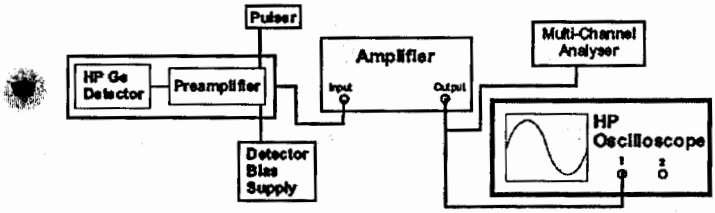

Figure 4: Block diagram for high resolution gamma ray measurement chain

According to NAA-k_0 method, element concentration in a sample is obtained as follows:

$$\rho_a(\mu g/g) = \frac{\left(\frac{N_p/t_c}{SDCW}\right)_a}{A_{sp,m}} \cdot \frac{1}{k_{0,m}(a)} \cdot \frac{G_{th,m}\cdot f + G_{e,m}\cdot Q_{0,m}(\alpha)}{G_{th,a}\cdot f + G_{e,a}\cdot Q_{0,a}(\alpha)} \cdot \frac{\varepsilon_{p,m}}{\varepsilon_{p,a}} \cdot 10^6$$

where,

analysed element concentration - "a" (μg/g);

m – co-irradiated monitor for neutron thermal flux value determination;

N_p – measured net peak aria;

t_c – counting time [s];

S – saturation factor; = 1 – exp(-λt_{ir}), where t_{ir}– irradiation time and λ= (ln2)/$T_{1/2}$ with $T_{1/2}$ – half-life time;

D – decay factor; = 1-exp(-λt_d), where t_d– decay time (starting from the end of irradiation until the measuring start);

C – counting factor; = [1-exp(-λt_c)]/λt_c;

W – sample mass [g];

A_{sp} – (N_p/t_c)/SDCw, specific counting rate, w – monitor element mass [g];

$k_{0,m}(a)$– k_0 factor of analysed element "*a*" experimental determined relative to mmonitor, defined as: $k_{0,m}(a) = (M_m\theta_a\sigma_{0,a}\gamma_a)/(M_a\theta_m\sigma_{0,m}\gamma_m)$, with M – molar mass, θ – isotopic abundance, σ_0– cross section of (n,γ) reaction at 2200 $m\cdot s^{-1}$, γ – absolute intensity of gamma ray;

G_{th} – correction factor for thermal neutrons self-shielding;

G_e– correction factor for epithermal neutrons self-shielding;

f – Φ_{th}/Φ_e, thermal neutron fluency rate and epithermal neutron fluency rate ratio; (for ACPR reactor the *f* parameter value at irradiation date was 17.12);

$Q_0(\alpha)$ – , where ,

with - resonance integral, defined as

– resonance effective energy in eV;

A – the value for the epithermal neutrons fluency rate distribution deviation from ideal shape 1/E, approximated as ; (for ACPR reactor the α parameter value at irradiation date was 0.01159);

– Full-energy peak detection efficiency.

Figure 5 shows the concentration of each detected element by samples, resulted after making the calculus using the NAA-k_0 standardization method.

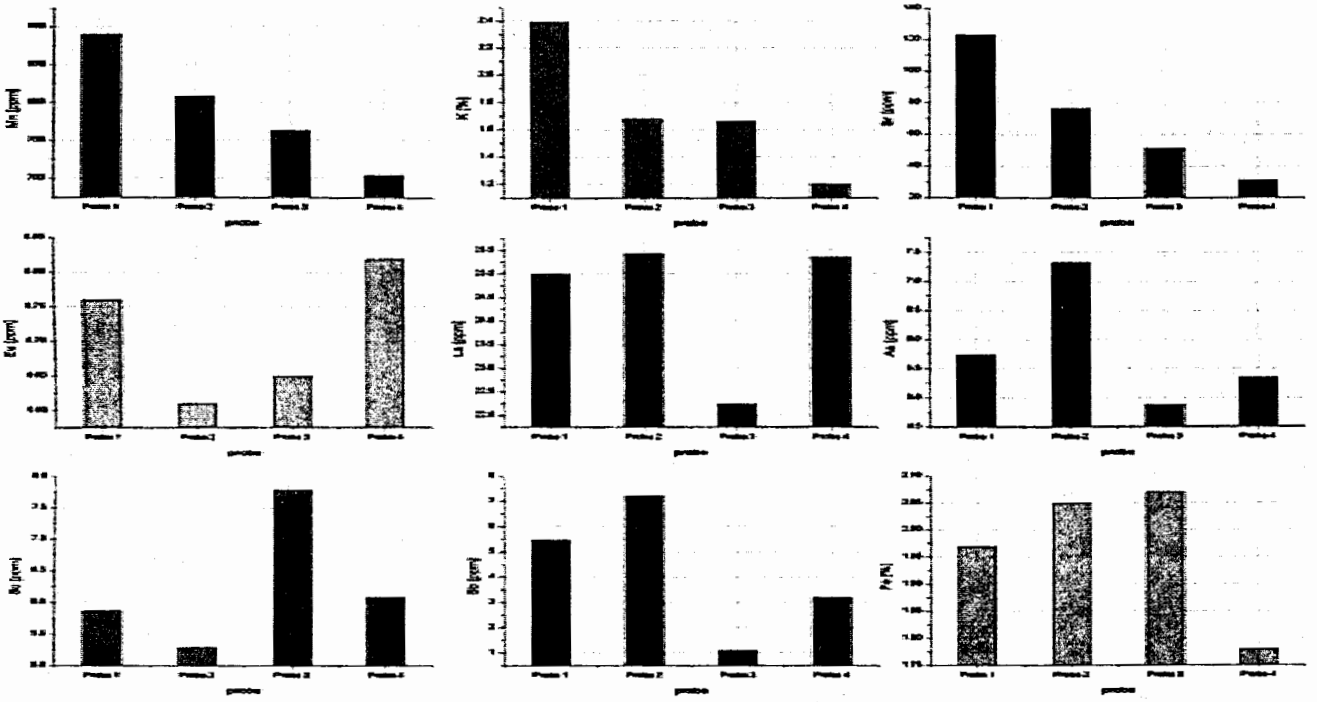

Figure 5. Chemical elements concentrations from each analyzed sample

Conclusion

Thermal neutron flux provided by ACPR reactor in rabbit point had an experimental determined value of 9.47E+11 n/(cm^2·sec). During irradiation period, the presence of samples in irradiation location did not influence the mean flux value. The results indicated the presence of the following elements contained in samples: manganese, potassium, bromine, europium, lanthanum, arsenic, scandium, antimony and iron. The differences showed between the elements concentrations in the samples are actually because of the pollution more or less intense in the areas from which they were taken. Hence the quality of the ground moss as a good bio-monitor.After analysing the results of the samples and after comparing them with reference values from Environmental Protection Agency database, it is noticed a slight excess concentration for arsenic (accepted reference value = 5 ppm) in P1 (TRIGA Reactor stack), P2 (Pitesti South train station) and P4 (ROLAST S.A.) samples. These exceeding are less than 2 ppm. Nevertheless, the alert value is not reached.Another identified element in the samples and for which there is a reference value from EPA is antimony (accepted reference value = 5ppm). In two of four analysed samples there is an exceeding for antimony in P1 (TRIGA Reactor stack) and P2 (Pitesti South train station). For manganese the threshold is 900 ppm but it is not reached. For the other elements found in samples there is no exceeding. It is worth mentioning the fact that no sample showed elements like cadmium, cobalt, mercury, selenium, or zinc.

References

[1] D. Popovic, "Trace elements and radionuclides in urban air monitored by moss and tree leaves", INTECH, Air Quality, ISBN 978-953-307-131-2.

[2] J. Weaver, "Determination of metals in ambient particulate matter using neutron activation analysis gamma spectrometry", EPA/625/R-96/010a.

[3] F. De Corte, "The K_0 standardization method", Science Direct, Atomic data and nuclear data tables **85** (2003) p. 47-67.

[4] Zs. Molnár, "Neutron Activation Analysis".

[5] A. Simonits et al., "K_0 –measurements and related nuclear data compilation for (n,γ) reactor neutron activation analysis".

ATMOSPHERIC DEPOSITION STUDY IN SOUTHERN BULGARIA BASED ON MOSS BIOMONITORS, NEUTRON ACTIVATION ANALYSIS ANDINDUCTIVELY COUPLED PLASMA ATOMIC EMISSION SPECTROSCOPY

G. Hristozova[1,2] , S. Marinova[1], M.V. Frontasyeva[2]

[1]*Faculty of Physics, 'Paisii Hilendarski' University, Plovdiv, Bulgaria*
[2]*FLNP, Joint Institute for Nuclear Research, Dubna, Russia*

Abstract. For the fifth time Bulgaria participates in the moss survey carried out in the framework of the International Cooperative Programme on Effects of Air Pollution on Natural Vegetation and Crops (the UNECE ICP Vegetation). In the summer of 2015, 115 moss samples (*Hypnum cupressiforme, Pleurozium schreberi* and *Pseudoscleropodium purum*) were collected in accordance with the sampling strategy. Concentrations of a total of 37 elements were determined in moss biomonitoring species using instrumental epithermal neutron activation analysis (Na, Mg, Al, Cl, K, Ca, Sc, Ti, V, Cr, Mn, Fe, Ni, Co, Zn, As, Se, Br, Rb, Sr, Sb, I, Ba, Cs, La, Ce, Nd, Eu, Tb, Tm, Yb, Lu, Hf, Ta, W, Th, U). Three additional environmentally important elements were analysed using inductively coupled plasma atomic emission spectroscopy (Cd, Cu, Pb). The determined concentrations were compared with data from previous moss surveys conducted in Bulgaria, as well as with data from other European countries participating in the ICP Vegetation programme.

INTRODUCTION

Mosses obtain nutrients primarily through wet and dry deposition, and possess a certain set of morphological and physiological properties (such as rudimentary root system and lack of vascular tissues), which make them suitable for biomonitoring of atmospheric depositions of metals [1]. Their wide geographical distribution facilitates large scale monitoring. The moss technique is a well-established method for monitoring in Europe. Several moss species have been thoroughly studied and accepted as biomonitors in air pollution monitoring programs conducted in more than 25 countries under the auspices of United Nations Economic Commission for Europe (UNECE) - International Cooperative Programme on Effects of Air Pollution on Natural Vegetation and Crops (ICP Vegetation) [2]. Surveys have been conducted in parallel at five-year intervals in all participating counties since 1990.

Bulgaria was involved in the program in 1995. Sampling was performed regularly, and the predominant biomonitoring species was *Hypnum cupressiforme*. The sampling networks were non-uniform throughout the years because of the climate conditions (hot and dry summers unfavourable for moss growth), mountainous terrains, and different member groups partaking in the sampling.

In previous moss surveys, it was ascertained that there were several persistent local hotspots corresponding to contemporary and historical non-ferrous and ferrous facilities, mining and smelting activities. Over the past three decades, the country has undergone a shift from a highly centralized, planned economy to an open market-based economy, characterized by slow economic restructuring and growth. The largest industrial enterprises have been closed down, which has lead to a reduction in local pollution emissions. Still, continuous and systematic exceeding of limit values for daily and annual particulate matter concentrations (PM10) is being reported via state air quality monitoring stations in over 20 towns. This is attributed to domestic heating (especially burning wood and coal),

vehicle emissions (obsolete fleets lacking catalytic converters), and to a lesser extent, electricity production and industrial activities.

SAMPLES AND METHODS

Object of study

For the purpose of the study, 115 moss samples were collected in Bulgaria the summer and autumn of 2015. The predominant species was *Hypnum cupressiforme.* In its absence *Pleurozium schreberi* and *Pseudoscleropodium purum* were collected instead. Sampling was performed in accordance with the requirements of the ICP Vegetation Programme [3]. A map of the sampled sites is presented in Fig. 1. All collected samples were put into paper bags for storage and transportation.

Fig. 1. Sampling sites

Methodology and equipment

After removal of extraneous plant material, the unwashed samples were sorted, so that only the green living part of the moss was subjected to analysis. The samples were air-dried to constant weight at 40 °C for 48 h.

Instrumental epithermal neutron activation analysis was performed in the radioanalytical laboratory REGATA at the reactor IBR-2 of FLNP, JINR. Moss samples of about 0.3 g were packed in polyethylene foil bags for short-term irradiation and in aluminum cups for long-term irradiation [4]. Neutron activation analysis was performed in the radioanalytical laboratory at the fast pulsed reactor IBR-2 of the Frank Laboratory of Neutron Physics, Joint Institute for Nuclear Research (FLNP JINR), Dubna, Russia. Qualitative and quantitative analysis were conducted on the basis of certified reference materials.

Inductively coupled plasma atomic emission spectroscopy was carried out in Plovdiv, Bulgaria. 0.5 g of moss were treated with 7ml concentrated NHO_3 and 2 ml H_2O_2 overnight. Microwave digestion was performed. Digests were filtered and transferred quantitavely to 25 ml flasks.

RESULTS AND DISCUSSION

Concentrations of 34 elements in total were determined using instrumental epithermal neutron activation analysis (NAA) (Al, As, Ba, Br, Ca, Ce, Cl, Co, Cr, Cs, Eu, Fe, Hf, I, K, La, Lu, Mg, Mn, Na, Nd, Ni, Rb, Sb, Sc, Se, Sr, Ta, Tb, Th, Ti, Tm, U, V, W, Yb, and Zn). Three additional elements (Cd, Cu, and Pb) were analysed by means of inductively coupled plasma atomic emission spectroscopy (ICP-ES).

Summarized results of the determined elemental contents are presented in Table 1. A comparison with NAA and AAS data of 2005 and 2000 for Bulgaria shows a decrease in the concentration of element pollutants. This could be explained by the shutdown of several major industrial facilities, the implementation of better filtering technologies, and emission control introduced in the functional operational factories. A comparison with background values for regions of Norway where the influence of air pollution is considered minor [5] shows that As, Cr, Fe, and V contents are still high.

Multivariate statistics (factor analysis) was applied to identify associations between the determined elements. Four factors were determined, of which one was interpreted as anthropogenic. Factor 1 is mixed, characterized by earth crust elements (Na (0.66), Mg (0.81), Al (0.74), Sc (0.80), Ti (0.65), V (0.84,) and Fe (0.82)) and marine aerosols (Cl (0.53), Br (0.53), and I (0.61)). Factor 2 contains REEs, U (0.61), and Th (0.84) – typical crust components, indicating presence of soil particles in the samples. Factor 3 has high loadings for As (0.75), Se (0.73), Sb (0.72), and Cu (0.74), which are found in ores. The highest loadings for this factor were for sites located near Cu-Ag mines. Factor 4 has high values for K (0.67) and Ca (0.65), characterizing wet deposition by higher vegetation.

Fig. 1 shows the temporal trends for metals reported in the moss surveys, with the exception of Sb. Data for this element determined in mosses using INAA in 2000/2001 is available elsewhere [6], and in the thematic report in 2005/2006 as additional data. Median values for Sb decreased by 52% (from 0.23 mg/kg in 2000, 0.29 mg/kg in 2005, to 0.11 mg/kg in 2015).

A comparison between the median values submitted in the ICP Vegetation reports for Bulgaria shows that with the exception of As, all reported metals have decreased atmospheric depositions between 1995 and 2010.

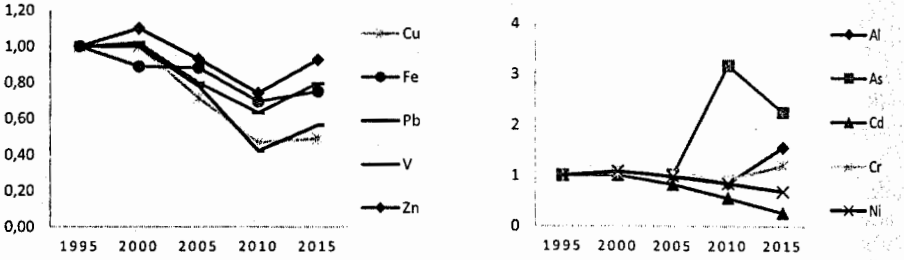

Fig. 1. Temporal trends – median values for concentrations of 10 metals, normalized to their values for 1995

The median value for As increased sharply in 2010 but has decreased again in 2015 (from 0.2 mg/kg in 1995, 0.21 mg/kg in 2000, 0.2 mg/kg in 2005, 0.63 mg/kg in 2010 and 0.44 mg/kg in 2015).

The maximal values for As in 2015 could be attributed to operation activities in cement plants and fossil fuel power stations.

Table 1. Results and comparison. Descriptive statistics

	Bulgaria, 2015 N=115 [mg/kg]		Bulgaria, 2005 [5] N=99 [mg/kg]		Bulgaria, 2000 [5] N=103 [mg/kg]		Norway [7] [mg/kg]	
	median	range	median	range	median	range	median	range
Na	225	79-1560	725	189-8210	523	155-5580	-	-
Mg	2080	514-8550	-	-	-	-	1730	940-2370
Al	2310	569-10900	6930	1532-43600	3843	1111-46400	200	67-820
Cl	78.8	16.6-861	232	84-1330	161	59-1180	-	-
K	5670	3250-14200	6020	2750-13800	5760	3270-20500	-	-
Ca	6630	606-14200	8960	4530-32200	7280	2270-19700	2820	1680-5490
Sc	0.408	0.104-3.13	0.92	0.21-7.20	0.65	0.2-6.4	0.052	0.009-0.220
Ti	143	46.4-764	340	94-2590	-			12.4-66.4
V	3.89	1.3-22.7	8.7	2.23-64	8.4	2.2-113	0.92	0.39-5.1
Cr	2.73	0.219-25	3.8	1.18-55	3.2	0.5-26.9	- -	0.10-4.2
Mn	180	39-551	243	45-1270	251	32-986	256	22-750
Fe	1190	376-7240	3000	689-19400	2310	692-147	209	77-1370
Co	0.585	0.197-3.29	1.49	0.35-28	1.08	0.23-10.6	0.202	0.065-0.654
Ni	2.11	0.451-13.5	5	1.08-29	4.1	0.5-18.6		0.12-6.6
Cu	7.36*	3.2-46.88*	6.84**	0.1-63.9**	14.5**	5.34-1860**		-
Zn	27.8	9.52-101	45	23-774	41	19-379		7.9-173
As	0.447	0.201-3.57	0.97	0.27-8.76	1	0.35-59	0.093	0.020-0.505
Se	0.2	0.00753-0.671		0.09-4.71	0.24	0.01-1.18	0.33	0.05-1.30
Br	2.76	1.21-9.39		1.33-18				-
Rb	7.38	2.24-50.7	15	5.16-68	12	3-69	7.7	1.3-51.5
Sr	25	11.3-122	36	14-170	25	7-106	15.8	3.6-43.3
Cd	0.1*	0.02-1.56*	0.23**	0.1-5.56**	-	-	-	-
Sb	0.113	0.0397-0.511	0.29	0.07-8.7	0.23	0.07-20.2	0.033	0.004-0.240
I	1.28	0.48-2.99	2.6	0.85-6.31	1.4	0.6-4.4	2.5	0.6-41.7
Cs	0.207	0.0716-1.8	0.52	0.18-5.71	0.4	0.10-2.96	0.072	0.016-0.88
Ba	46	14.2-309	79	21-294	68	17-517	17.1	5.6-50.5
La	1.35	0.399-22.6	3.3	1-61.79	2.9	0.8-23.7	0.189	0.045-2.56
Ce	2.41	0.49-29.2	6.8	1.75-143	-	-	0.342	0.095-4.61
Nd	1.33	0.22-24.1	3.15	0.01-47	-	-	-	-
Eu	0.0701	0.00972-0.918	-	-	-	-	-	-
Tb	0.0258	0.00531-0.422	0.076	0.02-0.98	0.068	0.016-0.610	0.003	<0.002-0.030
Tm	0.0137	0.00147-0.214	0.057	0.02-0.67	-	-	-	-
Yb	0.094	0.0248-1.08	0.22	0.05-3.32	-	-	-	-
Lu	0.0198	0.0003-1.45	-	-	-	-	-	-
Hf	0.158	0.0404-1.44	0.45	0.11-12.1	0.46	0.11-4.78	-	-
Ta	0.0355	0.00921-0.284	0.127	0.03-1.52	0.076	0.018-0.563	0.01	<0.01-0.07
W	0.0994	0.0244-1.44	1.22	0.25-13	0.193	0.03-1.39	0.127	0.009-1.23
Pb	10.72*	3.72-102.8*	11.7**	0.5-368**	18.9**	4.55-887**	-	-
Th	0.39	0.091-2.8	0.86	0.27-23	0.56	0.11-4.53	0.033	0.004-0.240
U	0.124	0.0327-3.2	0.3	0.09-6.28	0.2	0.03-1.87	0.015	0.001-0.138

It should be noted that due to the analytical methods applied (ICP-ES until 2010, NAA in 2015), some differences in the results are anticipated. They arise from the sample preparation and sensitivities, and in ICP-ES, refractory compounds in the samples may potentially be omitted. Still,

the trends for decreasing in Ni and Cd atmospheric depositions are retained in 2015. Fe and Cu have a slightly higher median value in 2015 than in 2010.

Bulgarian mosses had the highest concentration of Pb (maximal values) in the European moss survey in 1995. Since then, leaded petrol has been phased out. Open quarries and tailings, and an explosion in an ordnance plant in Iganovo (VMZ Sopot) explain the observed maximal values for Pb in 2015.

In 2015, the highest concentrations for the elements Al, V, Ni and Fe were determined in three of the border crossing posts with Greece (Kulata, Ivaylovgrad, Zlatograd), along the nearest major roads, and in a site located relatively close to a fossil fuel power station.

CONCLUSIONS

Concentrations of a total of 37 elements were determined in 115 moss samples using instrumental epithermal neutron activation analysis (Na, Mg, Al, Cl, K, Ca, Sc, Ti, V, Cr, Mn, Fe, Ni, Co, Zn, As, Se, Br, Rb, Sr, Sb, I, Ba, Cs, La, Ce, Nd, Eu, Tb, Tm, Yb, Lu, Hf, Ta, W, Th, and U). Three additional environmentally important elements were analysed by means of inductively coupled plasma atomic emission spectroscopy (Cd, Cu, and Pb). The concentrations determined are comparable with data from other European countries, reported in the 2010 moss survey. In 2010 there was an observation that, in general, since the beginning of Bulgaria's participation in the ICP Vegetation programme in 1995, concentrations of metals deposited from the atmosphere have steadily decreased by about 30%. The most recent survey data does not show continuation of that trend for all elements reported. Following the shutdown of several major industrial facilities and the implementation of better filtering technologies, a vehicle fleet renewal and more strict environmental and safety regulations are required to improve air quality. The results obtained supplement state monitoring air quality data, which is limited to a small number of sites and pollutants. They could provide for a better estimation of health and environmental risks, and aid risk-management decisions.

REFERENCES

1. D. Čeburnis, D. Vailiulis, Investigation of absolute metal uptake efficiency from precipitation in moss, Sci. Total Environ. 226 (1999) 247-253
2. The International Cooperative Programme on Effects of Air Pollution on Natural Vegetation and Crops, United Nation Economic Commission for Europe (UNECE) Convention on Long-Range Transboundary Air Pollution (LRTAP). http://icpvegetation.ceh.ac.uk/
3. H. Harmens, D. Norris, G. Mills, Heavy metals and nitrogen in mosses: spatial patterns in 2010/2011 and long-term temporal trends in Europe, ICP Vegetation Programme Coordination Centre, WGE of the Convention on Long-range Transboundary Air Pollution
4. M.V. Frontasyeva, Neutron activation analysis for the Life Sciences. A review, Phys. of Part. and Nucl. 42 (2011) 332-378
5. H. Harmens, D. Norris, Spacial and temporal trends in Heavy metal accumulation in mosses in Europe (1990-2005), ICP Vegetation Programme Coordination Centre, WGE of the Convention on Long-range Transboundary Air Pollution
6. J. Stamenov et al. New results from air pollution studies in Bulgaria (moss survey 2000-2001). E14-2002-204, JINR, Dubna, Russia, 2002
7. E. Steinnes et al., Atmospheric Deposition of Heavy Metals in Norway, Nation-Wide Survey in 2005, State Program for Pollution Monitoring, Report 980/2007. Norwegian State Pollution Control Authority, Oslo, 2007. (in Norwegian)

DETERMINATION OF THE COSMIC DUST FROM THE ISON COMET IN THE MOSCOW REGION

N.S. Gustova, O.D. Maslov, M.V. Gustova, T.P. Drobina, A.G. Belov

The Flerov Laboratory of Nuclear Reactions of the Joint Institute for Nuclear Research, Joliot Curie 6, Dubna, Russia, 141980

Abstract

Attention of astronomers from all over the world at 2012-2013 was focused on the comet C/2012 S1 (ISON). It came at a distance of 1.17 million km near the Sun at 28.11.13 and fall to pieces. Snow samples were collected around the Dubna city at the period when Earth came through the comet dust cloud. Melted water fractions with less than1 μm and more than 1 μm particles were analyzed separately. Snow samples contained increased compared with normal for this region content of Os, Ir, Au, Pt, U.

Introduction

The ISON comet was discovered on 21 September 2012 by Russian astronomers Vitali Nevski and Artyom Novichonok. ISON passed at a distance of 1.17 million kilometers from the Sun's surface on 28.11.13 at 22:30 on Moscow time. With the passage of the perihelion, the comet disintegrated into pieces. According to the calculations of most astronomers [1, 2], the dust cloud with smaller than 10 μm particles resulting from the comet collapse has covered the Earth in the period from 12.01.2014 to 17.01.2014.

The study of the substance of the comet has of great scientific interest. Some scientists believe that comets may be carriers of life in the Universe (the hypothesis of space panspermia). The comet first flew in the inner region of the Solar system from the Oort cloud, so the volatile substances of it ice core have not been disturbed and has not been seriously affected by heat and gravity. The age of the comet was estimated at 4.5 billion years and the study of dust particles from the ISON comet may answer on questions about the substance at the time of formation of our planetary system.

Experimental

To conduct the study, samples of snow were taken in the vicinity of the Dubna city in the period of Earth passage through the dust cloud of the comet, few days before it and few days after it. Upper layer of snow less than 5 cm was collected and melted. Melted water samples were filtrated through the polymer nuclear filter with pore size 1 μm (F-fraction was stay on the filter). Less than 1 μm particles were co-precipitated with $Fe(OH)_3$ (OH-fraction): 50 μg/dm^3 Fe^{3+} solution was added and NaOH solution was added dropwise to pH=8. Received precipitates were filtered through the polymer nuclear filter.

Also, evaluation of potential ^{137}Cs technogenic pollution of snow samples was conducted. After precipitation with $Fe(OH)_3$ and following filtration, solutions were boiled down to 50 ml and acidified by HNO_3 to pH=5 [3]. ^{137}Cs was sorbed at the dynamic conditions with the m(sorbent)/V(solution) = 10^{-2} g/ml ratio at the granulated $K_2Ni[Fe(CN)_6]$ sorbent.

Solution and precipitate samples were analyzed by nuclear physics methods.

X-ray fluorescent analysis (XRF). Multi-element analysis of dried precipitates on filter was conducted by the X-ray fluorescent spectometer at FLNR JINR. Radioisotope ^{109}Cd

(E=22.16 keV, $T_{1/2}$=453 d) and ^{241}Am (E=59.6 keV, $T_{1/2}$=458 y) sources were used for excitation of X-ray radiation. Characteristic radiation was registered by a semiconductor Si(Li) detector with 145eV resolution on Fe line (6.4 keV). Element contents at the explored samples were determined by the simultaneous determination method in saturated layer [4].

Gamma-activation analysis (GAA). Standards of Au, Ir, Pt, Os, U, Th and dried precipitates on filter, which put on 5 mm high and Ø=35mm polyethylene cassettes covered by 6-10 μm lavsan film, were irradiated 2-5 h by gamma-rays with energy Eγ = 24 MeV on the compact electron accelerator MT-25 microtron at FLNR JINR. Electron current was 15 μA. Methods similar with [5, 6] were used.

Gamma-spectroscopy. Natural activity of precipitates on filters and sorbents as well as activity of irradiated samples were measured by Canberra gamma-spectrometer with a HP Ge detector, which has 1.5 keV resolution and 1% efficiency on 1.33 MeV (^{60}Co) line. Measurement time was 1-24h.

Results and discussion

The content of elements in 1 dm^3 of thawed water on the average corresponds to the content of elements in 5 liters of snow collected from a five-centimeter of 0.1 m^2 surface layer.

Plenty of elements, such as Mg, K, Ca, Cr, Fe, Ni, Cu, Zn etc., may be contained in cosmic particles [7, 8]. However, for sparse and platinum-group elements (Os, Ir, Au, Pt, U) a difference between their content in cosmic particles and the earth's crust should be more noticeably. It is considered that iridium is a precise indicator of cosmic matter presence in the samples, since its content in meteorites is approximately 20,000 times higher than in rocks of the earth's crust. Therefore, to these components was paid attention.

Contents of macro components were determined by XRF. The XRF spectrum is shown in Fig.1.

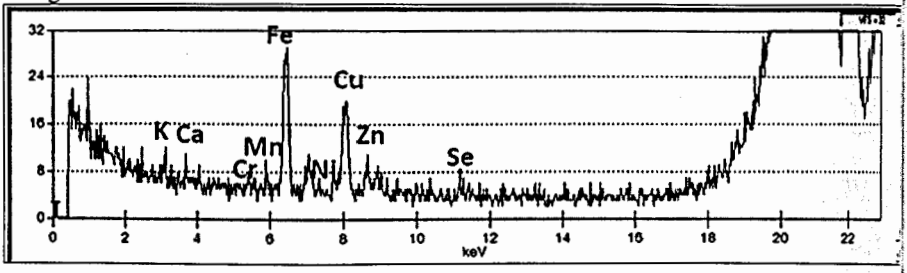

Fig.1. The X-ray spectrum of F-fraction (>1 μm particles on filter) of sample 17.01.14 obtained by ^{109}Cd source.

Ir, Au, Pt, Os, U and Th were determined by GAA. Nuclear reactions, which interesting to this research, are shown in the Table 1.

The spectrum of irradiated OH-fraction of sample 17.01.2014 was shown in Fig. 2. Visible content differences of Fe, Ni, Cu, Cr, Zn, Th, Pt in various samples not found. However, elevated contents compared to usual levels of elements such as Ir, Os, Au, U were found in the snow samples in the period of the Earth passage through the dust cloud.

Table 1. Reactions of interest to this research for GAA

El	Isotope	$T_{1/2}$	Eγ, KeV (%)	Reaction
Ir	Ir-190	11.8d	605 (41.3), 187(53.4)	$^{191}Ir(\gamma,n)^{190}Ir$
Au	Au-196	6.2d	333 (23), 355.7 (86.9)	$^{197}Au(\gamma,n)^{196}Au$
Pt	Pt-197	18.3h	77 (17.1)	$^{198}Pt(\gamma,n)^{197}Pt$
Os	Os-183	13h	114.59 (20), 381.7 (89.6)	$^{184}Os(\gamma,n)^{183}Os$
U	U-237	6.75d	208 (21.14)	$^{238}U(\gamma,n)^{237}U$
Th	Th-231	25.5h	25.65 (14.6), 84 (6.65)	$^{232}Th(\gamma,n)^{231}Th$

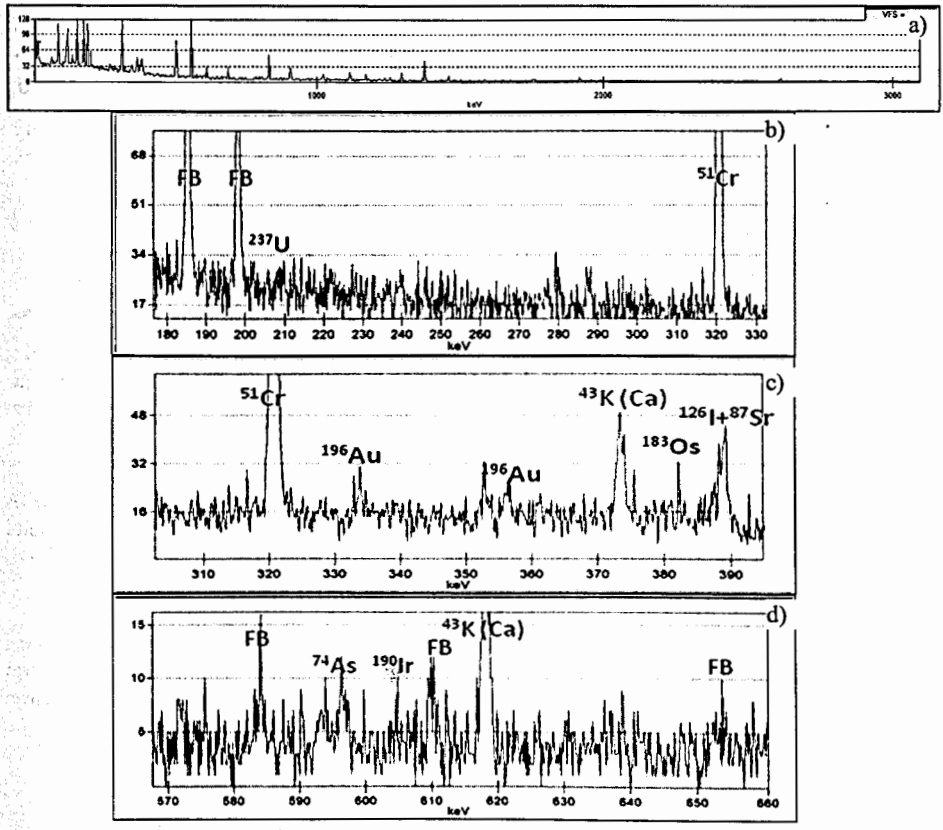

Fig.2. The spectrum of irradiated OH-fraction of sample 17.01.2014 (a) and fragments of spectrum (b), (c), (d). Filter background (FB) peaks concern to irradiated filter without a sample.

The change of Ir, Os, Au and U content in melted water samples in the period of the Earth passage through the dust cloud is shown at the Fig.3. White bars correspond with a more than 1 μm particle size fraction (F-fraction) and grey bars correspond with a less than 1 μm particle size fraction (OH-fraction).

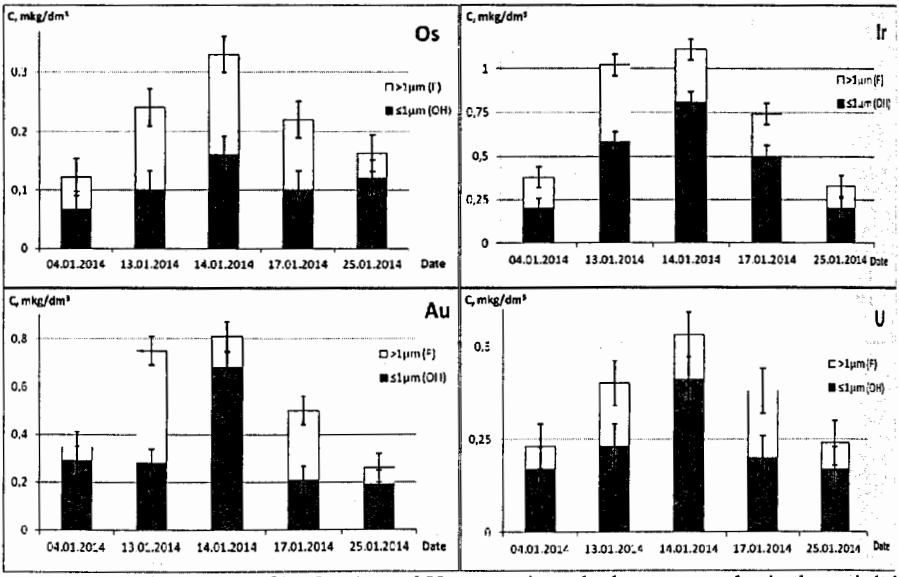

Fig.3. The change of Ir, Os, Au and U content in melted water samples in the period of the Earth passage through the dust cloud. White bars correspond with a more than 1 μm particle size fraction (F-fraction) and grey bars correspond with a less than 1 μm particle size fraction (OH-fraction).

Determination of ^{137}Cs was conducted for evaluation of the environmental state. A content of radio-Cs was less than 0.0049 Bq/dm^3 in all samples. Accordingly an obtained result indicates on unpolluted region by cesium.

Conclusion

Elevated compared to usual levels of Ir, Os, Au and U in the snow samples from Moscow region at the period of the Earth passage through the cosmic dust cloud was determined. Obtained results indicates the possibility of a comet observation by snow cover samples (and dust samples) research at Moscow region.

Acknowledgements

The authors are grateful for the help in the work to Semina V.K., Levkovich N.V., Voronyuk M.G.

References

1. Asteroids, Comets, Meteors, 2014. Helsinki, Finland. Book of Abstracts.
2. *Steckloff J. K. et al.* The size and fragmentation of the nucleus of comet C/2012 S1 (ISON) // 46th Lunar and Planetary Science Conference, 2015. 2723.
3. *Panasjugin A.S. et al* // Radiochemistry. 1995. V. 37, N.6, P. 537–541. (RUS)
4. Standard of the enterprise. Multicomponent instrumental X-ray fluorescent analysis soil and other objects of an environment on toxical and attendant elements, STP 104-2002, JINR 6-8092. Dubna, 2002, 16 p. (RUS)
5. *Gustova M.V., Maslov O.D., Molokanova L.G., Dmitriev S.N.* // Radiochemistry. 2004. V. 46, N. 4. P. 403–405.
6. Standard of the enterprise. Multicomponent instrumental gamma-activation analysis soil and other objects of an environment on toxical and attendant elements, STP 105-2004, JINR 6-8233. Dubna. 2004. 15 p. (RUS)
7. *Kolesnikov E.M., Hou Q.L., Xie L.W., Kolesnikova N.V.* // Astron. and Astrophys. Transactions. 2005. V. 24. N. 2. P. 101–111.
8. *Kolesnikov E.M., Kolesnikova N.V.* // Astronomichesky Vestnik. 2010. V. 44, N. 2. P. 123–134. (RUS)

STUDY OF NEUTRON IRRADIATION-INDUCED COLOR IN TOPAZ AT THE PULSED REACTOR IBR-2

Yu. Khatchenko[1], T. Enik[2], M. Kovalenko[1], O. Ryabukhin[1], M. Bulavin[2], A. Verkhoglyadov[2], S. Borzakov[2], K. Khramko[2], S. Kulikov[2], S. Tyutyunnikov[2], B. Yuldashev[2]

[1]Ural Federal University, 620002 Yekaterinburg, Russia
[2]Joint Institute for nuclear research, 141980 Dubna, Russia

e-mail: yulya.khatchenko@mail.ru

Abstract

In the present work, a method of a blue topaz production at the reactor IBR-2 is studied. To obtain deep blue color the fast neutron fluence needs to be about 10^{18} cm^{-2}. The optimal sample position in the channel №3 was determined. The special irradiation containers filled with boron carbide were created to reduce activation by thermal and resonance neutrons.

1. Introduction

Most of the natural topazes $Al_2SiO_4(F,OH)_2$ are colorless. To enhance these gemstones various types of radiation are widely used [1]. The irradiation forms the color centers in the crystal structure which change the mineral's color and, thereby, increase its consumer value. Reactor neutron irradiation is commonly applied to create an attractive deep blue color, called «London Blue», in the almost colorless topazes (Fig. 1). The production of blue centers is established to be caused by fast neutrons, while thermal and resonance neutrons lead to induced radioactivity of trace-element in topaz. This induced radioactivity doesn't allow using topazes in jewelry immediately after irradiation, because it can harm the health. The irradiated topazes can be used only after several years, when the radiation level will decrease to appropriate levels. Fast reactor IBR-2 makes it possible to achieve effective color modification with a minimum of induced activity.

This work is devoted to the optimization of the irradiation conditions in the channel №3 of the reactor IBR-2 [2] for production of «London Blue» topazes. In addition, the mechanism of blue centers formation were investigated by the optical absorption and Raman spectroscopy methods.

Fig. 1. Color changes of Ural topazes before (a) and after (b) neutron irradiation at the reactor IBR-2. Fast neutron fluence was about 10^{18} cm^{-2}.

2. Experiment

Topazes of different deposits were irradiated by neutrons at the reactor IBR-2. Samples were placed on the I-bar in the research channel №3 in the aluminum capsules (Fig. 2).

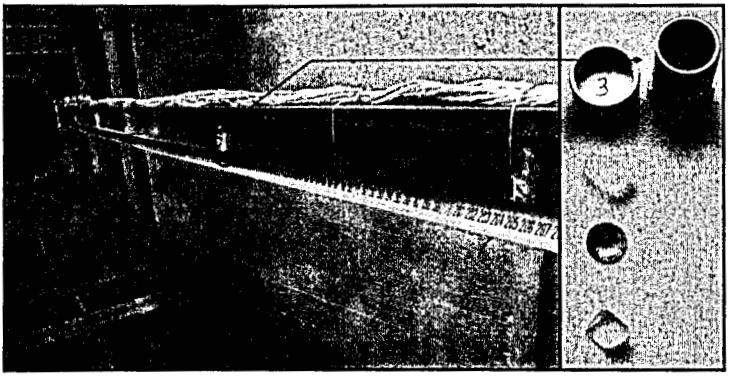

Fig. 2. Capsules for samples in the research channel №3 at IBR-2.

Fluence value was varied by positioning the samples at different distances from the moderator. Fast (>1 MeV) fluence value was measured by the method of the neutron activation analysis. Threshold detectors based on the reaction $^{58}Ni(n,p)^{58}Co$ were positioned near each samples group. The reactor operation cycle was 264 hours. The activity of irradiated samples was analyzed using gamma spectrometer with HPGe detector (Canberra) with relative efficiency of 40 %, an energy resolution of 1.8 keV at 1332 keV for ^{60}Co. The annealing was carried out in a furnace in air.

3. Results and discussion

Sample positions in channel №3 and the color changes depending on the fast neutron (>1 MeV) fluence value are presented in Fig. 3.

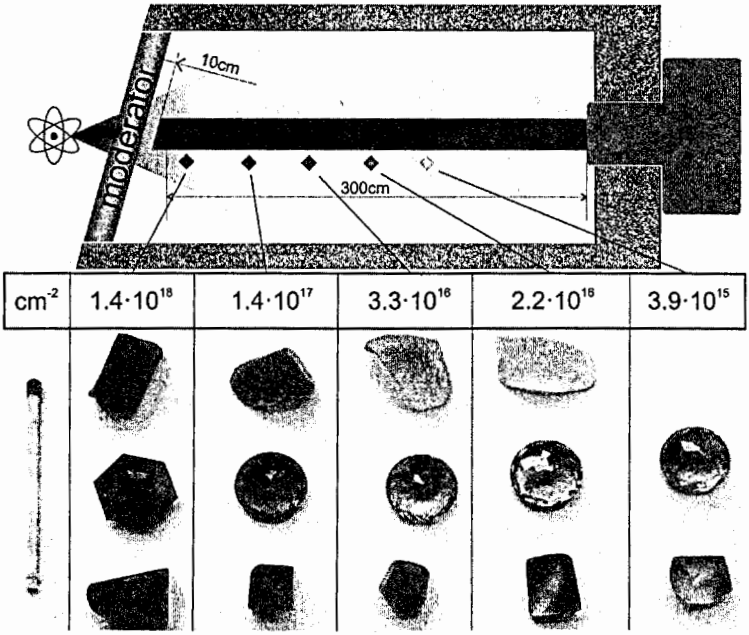

Fig. 3. Sample positions in channel №3 and the color changes depending on the fast neutron (>1 MeV) fluence value.

It can be seen that «London blue» color can be obtained with the fast neutron fluence of about 10^{18} cm^{-2}. This fluence value is reached at the I-bar end.

Some samples have a brown tint which is easy removed by heating in air at the temperature (200÷300)°C (Fig. 4). Various annealing modes at temperatures above 500 °C give any shade of blue color (the optical absorption band is centered at 620 nm). Achieved color remains stable at room temperature for a long time.

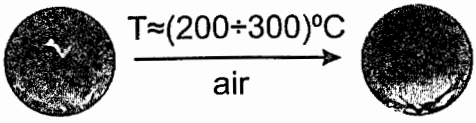

Fig. 4. Removing a brown tint by heat treatment.

Gamma-ray spectroscopy detected the presence of different radionuclides in the irradiated topazes. To reduce activation the special irradiation containers were created. The containers sides were made of boron carbide placed between two aluminum layers (Fig. 5). These containers significantly reduced the residual activity level. The residual activity values of two Ural samples at the end of irradiation are stated in Table 1.

Table 1. Residual activity of two Ural samples at the end of irradiation.

Nuclide	Half-life	Residual activity (Bq/g)	
		Sample №1	Sample №2
^{134}Cs	753.6 d	0.51±0.04	8.17±0.13
^{54}Mn	312.3 d	14.53±0.08	49.58±0.28
^{110m}Ag	249.79 d	0.27±0.04	9.85±0.18
^{65}Zn	244.26 d	8.70±0.09	42.06±0.37
^{182}Ta	114.43 d	22.94±0.25	59.58±0.79
^{46}Sc	83.79 d	28.27±0.11	39.91±0.24
^{58}Co	70.86 d	1.52±0.03	11.53±0.14
^{160}Tb	72.3 d	8.88±0.13	97.09±0.69
^{124}Sb	60.2 d	2.94±0.10	19.60±0.42
^{59}Fe	44.5 d	11.28±0.13	37.88±0.43
^{181}Hf	42.39 d	3.39±0.04	42.22±0.22
^{141}Ce	32.5 d	3.36±0.03	23.07±0.17
^{51}Cr	27.7 d	35.92±0.29	281.79±1.38
^{233}Pa	26.96 d	70.59±0.19	798.57±1.12
^{86}Rb	18.63 d	5.71±0.52	1267.60±5.85
^{122}Sb	2.72 d	37.94±0.87	251.87±2.65
^{198}Au	2.69 d	11.45±0.39	4041.18±6.55
^{239}Np	2.35 d	906.7±3.69	13107.59±18.00
^{140}La	1.67 d	269.08±7.40	2152.36±23.72
^{99}Mo	65.94 h	2.69±0.19	85.36±1.76
^{153}Sm	46.28 h	2516.38±9.27	27414.81±37.09
^{24}Na	14.95 h	(7.07±0.10)E+06	(8.44±0.07)E+06

Fig. 5. The irradiation containers filled with boron carbide between aluminum layers

To optimize this method, we need to investigate the mechanism of blue centers formation. The preliminary results of Raman spectroscopy showed intensity decreasing of peaks, associated with the OH stretching mode (3650 cm^{-1}), after neutron irradiation. Taking into account that natural blue topazes have a low OH-content [3], we can suppose that the blue centers formation is caused by collision mechanism of hydroxyl destruction by fast neutrons. The same effect is observed with an electron beam irradiation, but it is much less pronounced.

4. Conclusion

The optimal irradiation conditions for blue topazes production were determined: To obtain «London blue» color the fast neutron fluence needs to be about 10^{18} cm^{-2}. This fluence value is reached at the I-bar end in the channel №3 of the reactor IBR-2 with operation cycle of 264 hours. The containers with double sides filled with boron carbide significantly reduce the residual activity level. Based on the preliminary results of Raman spectroscopy we can suppose that the formation of blue centers is caused by collision mechanism of hydroxyl destruction by fast neutrons.

References

[1] W. Ying, G. Yong-Bao. Research on radiation-induced color change of white topaz. Radiation Physics and Chemistry, **63** (2002) 223–225.

[2] M. Bulavin, A. Cheplakov, V. Kukhtin, E. Kulagin, S. Kulikov, E. Shabalin, A. Verkhoglyadov. Irradiation facility at the IBR-2 reactor for investigation of material radiation hardness. Nuclear Instruments and Methods in Physics Research B, **343** (2015) 26–29.

[3] A.N. Platonov, M.N. Taran, B.S. Balitsky. Природа окраски самоцветов. M., Nedra, 1984, 196 p. (in Russian).

NEUTRON ACTIVATION ANALYSIS FOR ECOLOGICAL STATE ASSESSMENT OF COASTAL ECOSYSTEMS OF THE BLACK SEA

Pavel Nekhoroshkov[1], Alexandra Kravtsova[1], Marina Frontasyeva[1], Octavian Duliu[2], Alexander Kamnev[3], Nikita Yushin[1], Inga Zinicovscaia[1]

[1]*Frank Laboratory of Neutron Physics of Joint Institute for Nuclear Research, Dubna*
[2]*Department of the Structure of Matter, Earth and Atmospheric Physics, and Astrophysics, Faculty of Physics, University of Bucharest, Bucharest, Romania*
[3]*Biological and Soil Science Faculties of Moscow State University, Moscow*

Abstract

The concentration of majority of elements in soils and bottom sediments of chosen model recreational zone are corresponded to values reported for non-polluted zones except the area, which close to city dump. Cl, Br and I, the atmospheric supply from the marine environment is the predominant source for aquatic plants. The root-biomonitor for assessing accumulation of the majority of elements in plants from soils and bottom sediments, and in contrast the good leaf-biomonitor were found and analyzed. Translocation of elements varies depending on the physiological property of elemental uptake and is generally more intense through plant tissues than from sediments to plants. Cu, Zn, Sb, As, Ag, Au accumulated in phytoplankton due to coastal flows from anthropogenic sources.Obtained results could be used in ecological monitoring studies of the coastal zones.

Introduction

The coastal ecosystems with sources of natural runoff evolved from the estuarine areas towards complex shore with beaches, cliffs, wetlands et al. The vegetation and phytoplankton play the key role in elemental flows in these objects.

The aim of this complex study was to determine the ranges of variability of concentrations of different groups of elements in connection with affinity of pollution sources and properties of autotrophic biota in a typical recreational coastal zone.

We were solved several tasks during the study:

- Selection of model coastal zones
- Checking of organisms-biomonitors and choosing
- Determination the elements in different parts of organisms
- Analysis of elemental groups in substrates (soils and bottom sediments)
- Estimation of the levels of accumulation of elemental groups in these organisms by different zones
- The comparative analysis of data with reference values

Material and methods

First of all we were divided the coastal zones into 3 main groups: natural reserves, recreational zones and industrial regions.

In the coastal zone of Anapa city aquatic plants such as cane Phragmites australis, sedge Carex canescens, macroalgae such as Cladophora sericea were analyzed as a biomonitors. As a substrate the bottom sediments and soils from different layers (0, 20, 40 cm) were studied.

For analysis of elemental concentrations the neutron activation analysis performed at the reactor IBR-2 of the Frank Laboratory of Neutron Physics, Joint Institute for Nuclear

Research, Dubna in 2014-2016 were used. The main analytical technique was described in Frontasyeva (2011) with additions based on latest studies of aquatic biota and phytoplankton (Nekhoroshkov et al., 2015, Kravtsova et al., 2014).

Among the aquatic biomonitors we were chosen macrophytes, aquatic vegetation and phytoplankton as different organisms which exist under natural and anthropogenic conditions.

Macroalgae and aquatic plants were dried and prepared by using standards technique which was performed for vegetation. The filters with phytoplankton were divided into two equal portions. The concentrations of elements in filter blanks were taken into account. All samples were packed in plastic bags (to determine the short-lived isotopes) and into aluminum cups (to determine the long-lived isotopes). Quality control was provided by using standard reference materials of different origin: 433, 690CC, 1547, 1572, 1632b, 1633b, 2709, 2710.

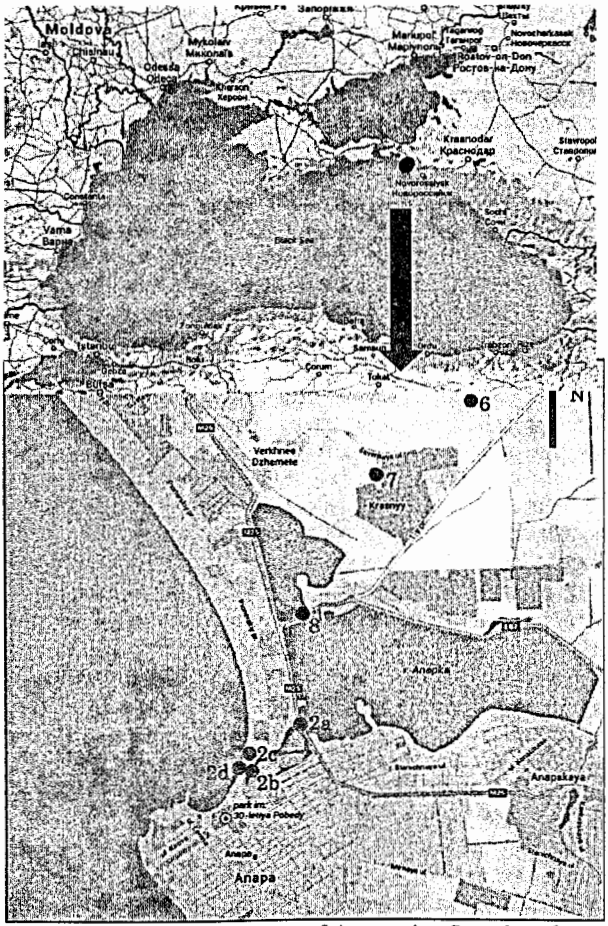

Fig. 1. Sampling sites in coastal zone of Anapa city. Samples of aquatic vegetation, macrophytes, soils, bottom sediments.

The results and discussion

The majority of the results and more detailed discussion were presented in our previous papers (Nekhoroshkov et al., 2015; Kravtsova et al., 2014; Nekhoroshkov et al., 2017).Several references could be find in this sources.

Such elements as Cr, Zn, As and Ba, which contained in soils and sediments and could be translocate and accumulate in aquatic vegetation, had the bigger concentrations than maximum permissible levels established for several developed countries. But these values corresponded to station which situated close to city dump and connected with anthropogenic sources of pollution such as fuel, solid domestic waste combustion and others.

Our data were also compared to results of Kolesnikov et al. (2012) who determined in laboratory conditions the levels of several elements for non-polluted, low polluted and moderate polluted soil from the Southern part of Russia using the integral index of biological state of soil (Table 1). It helps to realize the level of local differences in elemental content of soils from the standard levels for whole region. The maximal concentrations of Cr, Zn, As, Se and Sr in soils of Anapa region that were determined at the stations 6 and 7 (the nearest to city dump) were similar with the values reported for moderate polluted soils.

Table 1. Maximal and median elemental concentrations (μg/g dry weight) in soils from Anapa region (our data) and values for non-polluted and polluted soils from the Southern part of Russia

Elements	Soils in Anapa region		Soils in the Southern part of Russia[1]		
	Max	Median	Non-polluted	Low polluted	Moderate polluted
V	150	30	<200	200-300	300-850
Cr	**105**	30	<70	70-90	90-170
Mn	900	370	<1000	1000-1600	1600-1800
Co	24	4	<18	18-36	36-250
Ni	80	12	<50	50-100	100-700
Zn	**270**	50	<125	125-200	200-850
As	**36.8**	7.1	<17	17-30	30-160
Se	**2.31**	0.25	<0.7	0.7-1.4	1.4-9
Sr	**840**	510	<250	240-450	450-3200
Mo	15.7	1.1	<8	8-400	>400
Sb	2.1	0.6	<5	5-12	12-200
Ba	690	250	<900	900-1500	1500-4000

[1]elements insoil according to (Kolesnikov et al., 2012)

The concentration of elements which relate to moderate polluted range are given in **bold**

The obtained results were compared to the available data for Phragmites, Carex, and Cladophora, reported by other authors (Table 2) to represent the variability of concentrations in different regions. The concentrations of most elements in leaves and roots of *Phragmites australis* sampled in the mountain lake in Italy (Baldantoni et al., 2009) and in the mouth of the longest Sicilian river (Bonanno et al., 2010) are higher compared to our results. The exceptions are Ti, Mn, As, Sb and Ti, V, As, Se, which values in roots and leaves,

respectively, are higher in the present study. The values of Co, Zn, Rb, and Th in *Carex pendula* sampled in Germany in botanical garden (Horovitz et al., 1974) are higher than our data; the reverse trend is observed for Sc, Cr, Fe and Cs. The elemental content of *Cladophora* reported by different authors varies in a wide range depending on the sampling region and the species.

Table 2. Elemental content of different species of *Phragmites*, *Carex* and *Cladophora* ($\mu g \cdot g^{-1}$ dry weight).

El.	*Phragmitesaustralis*			*Carex pendula*	*Cladophora sp.*	*Cladophoraglomerata*	
	Roots[1]	Roots[2,3]	Leaves[2,3]	Whole plant[4]	Whole plant[5]	Whole plant[6]	Whole plant[7]
Na	–	–	–	–	17100	–	3000
Mg	1550	–	–	–	7800	–	23000
Al	–	3153	389	–	–	–	–
K	17000	–	–	–	24500	–	11000
Ca	–	–	–	–	8500	–	170000
Sc	–	–	–	0.19	–	–	–
Ti	–	<0.05	<0.05	–	–	–	–
V	14.5	9.2	<0.05	–	–	–	–
Cr	3.06	6.97	0.69	0.12	–	–	–
Mn	300	475.8	308	–	470	500	18000
Fe	2990	5561	453	460	2400	10000	2300
Co	–	8.0	0.22	0.03	0.5	–	–
Ni	6.52	9.12	1.69	–	3.1	–	6.3
Zn	54	104	28.4	595	60	200	–
As	–	<0.05	<0.05	–	–	–	5
Se	–	<0.5	<0.5	–	–	–	–
Rb	–	–	–	3.8	–	–	–
Sr	–	48.5	82.3	–	90	–	–
Mo	–	16.8	8.5	–	–	–	–
Sb	–	<0.05	<0.05	–	–	–	–
Cs	–	–	–	0.01	–	–	–
Ba	–	47.3	20.1	–	–	–	–
Th	–	–	–	0.45	–	–	–

1-Baldantoni et al., 2009; 2-Bonanno et al., 2010; 3-Bonanno, 2011; 4-Horovitz et al., 1974; 5-Bojanowski, 1973; 6-Ravera, 2001; 7-Maltsev et al., 2014

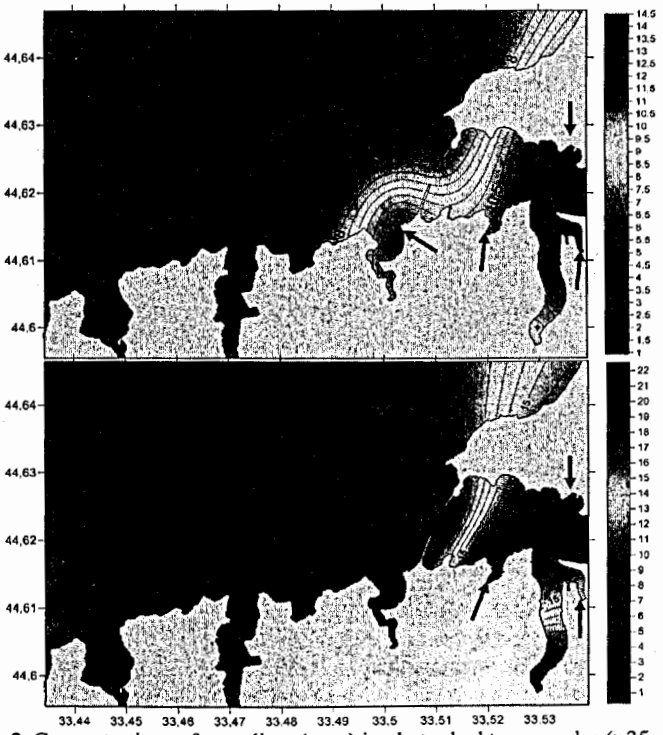

Fig. 2. Concentrations of vanadium (ppm) in phytoplankton samples (>35 μm) in summer and winter period of 2013-2014 from the coastal zone of Sevastopol. Red strings – sources of the coastal runoff and sources of pollution.

The different composition of *Cladophora sericea* and *Phragmites australis* with *Carex canescens* is explainable by different elemental uptake, either mainly by entire surface of plant from water (*Cladophora*) or by roots from sediments (*Phragmites australis* and *Carex canescens*).

The results, which were obtained for the largest phytoplanktonic organisms (>35 μm) in coastal polluted zones, showed that the elements with anthropogenic origin were accumulated in phytoplankton communities high concentrations relate to terrigenous along-coastal flows.

The accumulation of elements (for example vanadium) that could be anthropogenic origin corresponded to sources of terrigenous and anthropogenic flows (Fig. 2, red strings).

Conclusions

Neutron Activation Analysis fits well to assessment of elemental accumulation in organisms from coastal ecosystems. Coastal water objects could be analyzed by using NAA in complex study.

By using NAA we concluded that such elements as Al, Sc, Ti, Zr, REE, Th can be used as markers of terrigenous suspension. The normalizing concentrations in phytoplankton

matter reflect the accumulative features of organisms with the higher accuracy excluding the effect of adsorbed mineral particles.

Roots and leaves of *Phragmitesaustralis* are good accumulators of Na, Ti, and Br and, in contrast, contain lower levels of Zn, Rb, and Ba than in RP. In *Carexcanescens* roots and leaves the levels of Na, Ti, As, Th, and U are one order of magnitude higher than in RP. In contrast, Mg, K, Mn, Zn, Rb, Cs, and Ba show lower levels in comparison to RP concentrations.

Cladophora sericea accumulated Cl in small relative amounts in comparison to Br and I. *Phragmites australis* in the major cases selected I and Cl regardless Br. In that sense the *Carex canescens* demonstrated the most flexible ability for accumulation of these halogens.

The environmental levels of the 19 trace elements in *Cystoseiraspp.* From relatively clean waters from marine protected areas, determined in this study, could be used for the further biomonitoring objectives in the Black Sea region.

The revealed peculiarities of elemental accumulation in different morphostructural parts of Cystoseira spp. and the relationship between the concentrations of some trace elements in algae with geological composition of the coast (that is, the type of rocks) improved our knowledge regarding the use of *Cystoseira spp.* as a biomonitor of coastal waters pollution.

Using such organisms as phytoplankton, macroalgae and aquatic vegetation (as basic elements forming primary production) in biomonitoring studies the environmental states of coastal zones and special fingerprints in different regions should be analyzed.

References

[1] Baldantoni, D., Ligrone, R. and Alfani, A. (2009) Macro- and Trace-Element Concentrations in Leaves and Roots of Phragmitesaustralis in a Volcanic Lake in Southern Italy. Journal of Geochemical Exploration, 101, 166-174.

[2] Bojanowski, R. (1973) The Occurrence of Major and Minor Chemical Elements in the More Common Baltic Seaweed. Oceanologia, 2, 81-152.

[3] Bonanno, G. and Lo, G.R. (2010) Heavy Metal Bioaccumulation by the Organs of Phragmitesaustralis (Common Reed) and Their Potential Use as Contamination Indicators. Ecological Indicators, 10, 639-645.

[4] Bonanno, G. (2011) Trace Element Accumulation and Distribution in the Organs of Phragmitesaustralis(Common Reed) and Biomonitoring Applications. Ecotoxicology and Environmental Safety, 74, 1057-1064.

[5] Frontasyeva, M. V. (2011). Neutron activation analysis in the life sciences. Physics of Particles and Nuclei, 42(2), 332-378.

[6] Horovitz, C.T., Schock, H.H. and Horovitz-Kisimova, L.A. (1974) The Content of Scandium, Thorium, Silver, and Other Trace Elements in Different Plant Species. Plant and Soil, 40, 397-403. https://doi.org/10.1007/BF00011522

[7] Kravtsova A. V., Milchakova N. A., Frontasyeva M. V. The features of trace elements accumulation by macroalgaeCystoseira in the coastal zone of marine protected areas of the Crimea (the Black Sea)// Optimization and Protection of Ecosystems. Simferopol: TNU, 2014. Iss. 10. P. 146–158.

[8] Kolesnikov, S.I., Kazeev, K.S., Denisova, T.V. and Dadenko, E.V. (2012) Development of Regional Ecological Regulations of Content of Contaminants in Soils of Southern Russia. Polythematic Online Scientific Journal of Kuban State Agrarian University, 82, 1-17. (In Russian)

1. Maltsev, A.E., Leonova, G.A., Bogush, A.A. and Bulycheva, T.M. (2014) Ecogeochemical Assessment of Anthropogenic Pollution of Flooded Open Pits Ecosystems in Novosibirsk. Ecology of Industrial Production, 2, 44-53. (In Russian)
2. Markert, B. (1992) Establishing of "Reference Plant" for Inorganic Characterization of Different Plant Species by Chemical Fingerprinting. Water, Air, and Soil Pollution, 64, 533-538. https://doi.org/10.1007/BF00483363
3. Nehoroshkov P. S., Frontaseva M. V., Tokarev Yu. N. Biophysical parameters and multi-element composition of the Black Sea phytoplankton communities in the Crimea coastal area // Water: chemistry and ecology. 2015. Vol. 8. pp. 11-20. (http://watchemec.ru/en/article/27469/)
4. Nekhoroshkov, P., Kravtsova, A., Kamnev, A., Bun'kova, O., Duliu, O., Frontasyeva, M., &Yermakov, I. (2017). Assessment of Minor and Trace Elements in Aquatic Macrophytes, Soils and Bottom Sediments Collected along Different Water Objects in the Black Sea Coastal Zone by Using Neutron Activation Analysis// American Journal of Analytical Chemistry, 8(04), 225.
5. Ravera, O. (2001) Monitoring of the Aquatic Environment by Species Accumulator of Pollutants: A Review. Journal of Limnology, 60, 63-78. https://doi.org/10.4081/jlimnol.2001.s1.63

INAA AND ICP-MS IN THE INVESTIGATION OF CADMIUM/TRACE ELEMENT CONTENT RATIOS IN MALIGNANT PROSTATE GLAND

V. Zaichick[1], S. Zaichick[1,2]

[1]*Medical Radiological Research Centre, Korolyev St., 4, Obninsk, 249036, Russia, e-mail: vezai@obninsk.com*

[2] *Feinberg School of Medicine, Northwestern University, Chicago, IL 60611-4296, USA*

Introduction

Prostate cancer (PCa) is the most common non-cutaneous male cancer in most populations. Although the etiology of PCa is unknown, several risk factors including age, diet, and environment (Cd and some other trace element) have been well determined. It is also reported that the risk of having PCa drastically increase with age, being three orders of magnitude higher for the age group 40–79 years than for those younger than 39 years. Trace elements are involved in regulation of cell membrane and cell function, gene regulation, activation or inhibition of enzymatic reactions. Essential or toxic (mutagenic, carcinogenic) properties of trace elements depend on tissue-specific need or tolerance, respectively. Excessive accumulation or an imbalance of the trace elements may disturb the cell functions and may result in cellular degeneration, death or, on the contrary, intensive uncontrolled proliferation, and malignancy.

Some trace elements have been highlighted in the literature in relation to the development of PCa.[1-20] However, questions on the role of trace elements in etiology and pathogenesis of PCa are far from being answered. First of all, it is necessary to establish the normal level and changes of trace element contents in PCa tissue, and relationships of trace elements in norm and disease. To that end, we determined the ratio to Cd of 42 trace element (Ag, Al, Au, B, Be, Bi, Br, Ce, Co, Cr, Cs, Dy, Er, Fe, Gd, Hg, Ho, La, Li, Mn, Mo, Nb, Nd, Ni, Pb, Pr, Rb, Sb, Sc, Se, Sm, Sn, Tb, Th, Ti, Tl, Tm, U, Y, Yb, Zn, and Zr) in normal and cancerous prostate gland.

All studies were approved by the Ethical Committee of the Medical Radiological Research Center, Obninsk.

Experimental

The 60 patients aged 40-79 years (M±SD 65±10) suffered from PCa (stage T1-T4) were hospitalized in the Urological Department of the Medical Radiological Research Centre (Obninsk, Russia). Transrectal puncture biopsy of suspicious indurated regions of the prostate was performed for every patient, to permit morphological study of prostatic tissue at these sites and to estimate their chemical element contents. In all cases the diagnosis has been confirmed by clinical and morphological results obtained during studies of biopsy and resected materials.

Intact prostates (N) were removed at necropsy from 37 men aged 41-87 who had died suddenly. Their mean age was 55±11 (M±SD) years. The majority of deaths were due to trauma. Tissue samples were collected from the peripheral zone of dorsal and lateral lobes of their prostates, within 2 days of death. A histological examination was used to control the age norm conformity, as well as to confirm the absence of microadenomatosis and latent cancer.[6,7,12,20]

All tissue samples were divided into two portions. One was used for morphological study while the other was intended for trace element analysis. After the samples intended for trace element analysis were weighed, they were freeze-dried and homogenized. The sample weighing about 10 mg (for biopsy materials) and 50-100 mg (for resected materials) was used for trace element measurement by INAA-LLR. The samples for INAA-LLR were wrapped separately in a high-purity aluminum foil washed with double rectified alcohol beforehand and placed in a nitric acid-washed quartz ampoule.

After INAA-LLR investigation, the prostate samples were taken out and used for ICP-MS method. The samples were decomposed in autoclaves; 1.5 mL of concentrated HNO_3 (nitric acid at 65 %, maximum (max) of 0.0000005 % Hg; GR, ISO, Merck) and 0.3 mL of H_2O_2 (pure for analysis) were added to prostate tissue samples, placed in one-chamber autoclaves (Ancon-AT2, Ltd., Russia) and then heated for 3 h at 160–200 °C. After autoclaving, they were cooled to room temperature and solutions from the decomposed samples were diluted with deionized water (up to 20 mL) and transferred to the plastic measuring bottles. Simultaneously, the same procedure was performed in autoclaves without tissue samples (only HNO_3+H_2O_2+ deionized water), and the resultant solutions were used as control samples.

A vertical channel of a nuclear reactor was applied to determine the trace element mass fractions by INAA-LLR. The quartz ampoule with prostate samples and certified reference materials was soldered, positioned in a transport aluminum container, and exposed to a 24-hour neutron irradiation in a vertical channel with a neutron flux of $1.3 \cdot 10^{13}$ $n \cdot cm^{-2} \cdot s^{-1}$. Ten days after irradiation samples were reweighed and repacked. The samples were measured for period from 10 to 30 days after irradiation. The duration of measurements was from 20 min to 10 hours subject to pulse counting rate. The gamma spectrometer used for INAA-LLR included the 100 cm^3 Ge(Li) detector and on-line computer-based multichannel analyzer. The spectrometer provided a resolution of 1.9 keV on the ^{60}Co 1332 keV line. Other details of the INAA-LLR analysis were presented in our previous publication.[7]

An ICP-MS Thermo-Fisher "X-7" Spectrometer (Thermo Electron, USA) was used to determine the content of trace elements by ICP-MS. The element concentrations in aqueous solutions were determined by the quantitative method using multi elemental calibration solutions ICP-MS-68A and ICP-AM-6-A produced by High-Purity Standards (Charleston, SC 29423, USA). Indium was used as an internal standard in all measurements. Information detailing with the ICP-MS method used was presented in our previous publication.[10]

For quality control, ten subsamples of the certified reference materials (CRM) IAEA H-4 Animal muscle and IAEA HH-1 Human hair from the International Atomic Energy Agency (IAEA), and also five sub-samples INCT-SBF-4 Soya Bean Flour, INCT-TL-1 Tea Leaves and INCT-MPH-2Mixed Polish Herbs from the Institute of Nuclear Chemistry and Technology (INCT, Warszawa, Poland) were analyzed simultaneously with the investigated prostate tissue samples. All samples of CRMs were treated in the same way as the prostate samples. Detailed results of this quality assurance program were presented in earlier publications.[7,10]

A dedicated computer program for INAA mode optimization was used.[21] All prostate samples for INAA-LLR were prepared in duplicate and mean values of trace element contents were used in final calculation. For elements investigated by both INAA-LLR and ICP-MS methods the mean of all results was used. Using the Microsoft Office Excel software Cd/trace element contents for each trace element in every sample were calculated. Then arithmetic mean ± standard error of mean was calculated for trace element mass fraction and for ratios of Cd/trace element mass fraction in normal and cancerous prostate. The difference in the results between PCa and N was evaluated by parametric Student's *t*-test and non-parametric Wilcoxon-Mann-Whitney *U*-test.

Results and discussion

As was shown by us[6,7,9,10], the use of CRM IAEA H-4 Animal muscle, IAEA HH-1 Human hair, INCT-SBF-4 Soya Bean Flour, INCT-TL-1 Tea Leaves, and INCT-MPH-2Mixed Polish Herbs as certified reference materials for the analysis of samples of prostate tissue can be seen as quite acceptable. Good agreement of the trace element contents in these CRMs, measured by us using INAA-LLR and ICP-MS methods, with the certified data[6,7,9,10] indicates an acceptable accuracy of the results obtained in the present study.

Table 1 represents mean values ± standard error of mean (M±SEM) of the Ag, Al, Au, B, Be, Bi, Br, Cd, Ce, Co, Cr, Cs, Dy, Er, Fe, Gd, Hg, Ho, La, Li, Mn, Mo, Nb, Nd, Ni, Pb, Pr, Rb, Sb, Sc, Se, Sm, Sn, Tb, Th, Ti, Tl, Tm, U, Y, Yb, Zn and Zr mass fraction, as well as the ratio to Cd of Ag, Al, Au, B, Be, Bi, Br, Ce, Co, Cr, Cs, Dy, Er, Fe, Gd, Hg, Ho, La, Li, Mn, Mo, Nb, Nd, Ni, Pb, Pr, Rb, Sb, Sc, Se, Sm, Sn, Tb, Th, Ti, Tl, Tm, U, Y, Yb, Zn, and Zr mass fraction in normal and cancerous prostate.

The mean values and standard error of mean (±SEM) were calculated for 43 trace element contents including Cd, as well as for 42 ratios of Cd/trace element mass fractions (Table 1). The mass fraction of Cd and other 42 trace elements were measured in all, or a major portion of normal prostate samples. The masses of PCa samples varied very strong from a few milligrams (sample from needle biopsy material) to 100 mg (sample from resected material). Therefore, in PCa prostates mass fraction ratios to Cd of other trace element content were determined in 11 samples.

The ratios of means and the difference between mean values of the Cd/trace element mass fraction ratios in normal and cancerous prostate are presented in Table 2.From Table 2, it is observed that in cancerous tissue the all Cd/trace element mass fraction ratios investigated in the study are significantly lower, than in normal prostate, with the exception of Cd/Nb, Cd/Sc, and Cd/Zn ratios.

Analysis of the mass fraction ratios for trace element in prostate tissue could become a powerful diagnostic tool[22-26]. To a large extent, the resumption of the search for new methods for early diagnosis of PCa was due to experience gained in a critical assessment of the limited capacity of the prostate specific antigen (PSA) serum test. In addition to the PSA serum test and morphological study of needle-biopsy cores of the prostate, the development of other highly precise testing methods seems to be very useful. Experimental conditions of the present study were approximated to the hospital conditions as closely as possible. In PCa cases we analyzed a part of the material obtained from a puncture transrectal biopsy of the indurated site in the prostate. Therefore, our data allow us to evaluate adequately the importance of Cd/trace element mass fraction ratios for the diagnosis of PCa.

Table 1: Mean values (M±SEM) of the trace element mass fraction (mg/kg, dry mass basis) and the Cd mass fraction/ trace element mass fraction ratios in normal (N), benign hypertrophic (BPH) and cancerous prostate (PCa)

	Mass fraction			Ratio	
Symbol	N	PCa	Symbol	N	PCa
Ag	0.038±0.006	0.252±0.030	Cd/Ag	69.5±21.0	1.06±0.22
Al	34.2±3.5	328±73	Cd/Al	0.0437±0.0076	0.0013±0.0005
Au	0.0041±0.0008	0.0297±0.0056	Cd/Au	496±120	12.2±2.9
B	1.04±0.18	12.6±3,7	Cd/B	1.79±0.37	0.0309±0.0051
Be	0.00094±0.00007	0.0137±0.0022	Cd/Be	1384±188	28.8±5.9
Bi	0.029±0.011	1.75±0.27	Cd/Bi	285±87	0.153±0.030
Br	27.9±2.9	99.9±8.9	Cd/Br	0.0528±0.0086	0.00388±0.00085
Cd	1.12±0.13	0.425±0.099	Cd/Cd	1.00	1.00
Ce	0.0309±0.0050	0.101±0.013	Cd/Ce	65.4±16.9	4.02±1.01
Co	0.0467±0.0064	0.0336±0.0040	Cd/Co	31.4±4.5	9.83±1.90
Cr	0.56±0.08	2.34±0.32	Cd/Cr	5.91±2.78	0.138±0.037
Cs	0.0339±0.0033	0.0389±0.0039	Cd/Cs	43.8±7.2	14.9±5.1
Dy	0.00293±0.00049	0.00771±0.00110	Cd/Dy	724±162	74.2±24.6
Er	0.00148±0.00023	0.00297±0.00038	Cd/Er	1219±235	151±45
Fe	111±9	165±15	Cd/Fe	0.0106±0.0013	0.00344±0.00097
Gd	0.00290±0.00041	0.00945±0.00173	Cd/Gd	654±151	37.1±8.5
Hg	0.052±0.008	0.122±0.019	Cd/Hg	34.9±6.2	2.56±1.01
Ho	0.00057±0.00008	0.00178±0.00022	Cd/Ho	3100±584	196±35
La	0.080±0.020	0.969±0.537	Cd/La	55.8±11.9	1.30±0.50
Li	0.0419±0.0055	0.251±0.054	Cd/Li	39.1±7.4	1.62±0.53
Mn	1.34±0.08	6.99±1.35	Cd/Mn	0.967±0.139	0.108±0.034
Mo	0.282±0.038	0.298±0.035	Cd/Mo	5.69±1.05	2.10±1.15
Nb	0.0054±0.0012	0.0052±0.0002	Cd/Nb	475±109	148±92
Nd	0.0137±0.0021	0.0413±0.0065	Cd/Nd	146±38	10.0±2.4
Ni	3.10±0.51	6.96±1.04	Cd/Ni	0.810±0.213	0.0555±0.0128
Pb	2.39±0.56	1.81±0.35	Cd/Pb	1.98±0.68	0.209±0.034
Pr	0.00353±0.00053	0.00973±0.00174	Cd/Pr	565±134	34.7±7.6
Rb	13.3±0.9	8.71±0.66	Cd/Rb	0.101±0.014	0.0473±0.0085
Sb	0.043±0.006	0.490±0.059	Cd/Sb	58.2±12.8	1.62±0.33
Sc	0.0294±0.0053	0.0116±0.0015	Cd/Sc	62.3±16.9	40.2±17.1
Se	0.75±0.05	0.56±0.08	Cd/Se	1.63±0.23	0.601±0.112
Sm	0.0027±0.0004	0.0095±0.0029	Cd/Sm	773±182	95.9±30.1
Sn	0.32±0.06	1.28±0.24	Cd/Sn	9.45±2.14	0.430±0.155
Tb	0.00039±0.00006	0.00089±0.00012	Cd/Tb	6314±1729	361±84
Th	0.0033±0.0007	0.0495±0.0123	Cd/Th	727±145	9.41±3.81
Ti*	2.82±0.64	8.60±2.20	Cd/Ti*	0.848±0.184	0.0938±0.0438
Tl	0.0014±0.0001	0.0219±0.0056	Cd/Tl	1134±195	13.2±2.2
Tm	0.00024±0.00003	0.00054±0.00011	Cd/Tm	6818±1129	439±80
U	0.0070±0.0021	0.0068±0.0013	Cd/U	659±150	81.5±20.0
Y	0.0187±0.0043	0.0340±0.0038	Cd/Y	340±204	15.5±4.9
Yb	0.00141±0.00025	0.00174±0.00039	Cd/Yb	1787±537	314±113
Zn	1031±129	136±10	Cd/Zn	0.00200±0.00045	0.00295±0.00034
Zr	0.036±0.006	2.13±0.89	Cd/Zr	55.1±10.7	0.454±0.133

M – arithmetic mean, SEM – standard error of mean, * Titanium tools were used for sampling and sample preparation.

Table 2: Ratio of means and the difference between mean values of the Cd mass fraction/ trace element mass fraction ratios in normal (N) and cancerous prostate (PCa)

Symbol	Ratio PCa/N	$p\leq$, t-test	p, U-test
Cd/Ag	0.015	**0.0034**	**≤0.01**
Cd/Al	0.029	**0.00001**	**≤0.01**
Cd/Au	0.025	**0.00069**	**≤0.01**
Cd/B	0.017	**0.00009**	**≤0.01**
Cd/Be	0.021	**0.00001**	**≤0.01**
Cd/Bi	0.001	**0.0032**	**≤0.01**
Cd/Br	0.073	**0.00002**	**≤0.01**
Cd/Ce	0.061	**0.0014**	**≤0.01**
Cd/Co	0.313	**0.00014**	**≤0.01**
Cd/Cr	0.023	0.052	**≤0.01**
Cd/Cs	0.340	**0.0024**	**≤0.01**
Cd/Dy	0.102	**0.00059**	**≤0.01**
Cd/Er	0.124	**0.00016**	**≤0.01**
Cd/Fe	0.325	**0.00011**	**≤0.01**
Cd/Gd	0.057	**0.00046**	**≤0.01**
Cd/Hg	0.073	**0.00003**	**≤0.01**
Cd/Ho	0.063	**0.00005**	**≤0.01**
Cd/La	0.023	**0.00011**	**≤0.01**
Cd/Li	0.041	**0.00006**	**≤0.01**
Cd/Mn	0.112	**0.00001**	**≤0.01**
Cd/Mo	0.369	**0.039**	>0.05
Cd/Nb	0.312	0.067	>0.05
Cd/Nd	0.068	**0.0017**	**≤0.01**
Cd/Ni	0.069	**0.0020**	**≤0.01**
Cd/Pb	0.106	**0.016**	**≤0.01**
Cd/Pr	0.061	**0.00065**	**≤0.01**
Cd/Rb	0.468	**0.0030**	**≤0.01**
Cd/Sb	0.028	**0.00022**	**≤0.01**
Cd/Sc	0.645	0.391	>0.05
Cd/Se	0.369	**0.00044**	**≤0.01**
Cd/Sm	0.124	**0.0013**	**≤0.01**
Cd/Sn	0.046	**0.00036**	**≤0.01**
Cd/Tb	0.057	**0.0023**	**≤0.01**
Cd/Th	0.013	**0.00001**	**≤0.01**
Cd/Ti*	0.111	**0.00058**	**≤0.01**
Cd/Tl	0.012	**0.00001**	**≤0.01**
Cd/Tm	0.064	**0.00002**	**≤0.05**
Cd/U	0.124	**0.00089**	**≤0.01**
Cd/Y	0.046	0.126	**≤0.05**
Cd/Yb	0.176	**0.013**	**≤0.05**
Cd/Zn	1.48	0.104	>0.05
Cd/Zr	0.008	**0.00004**	**≤0.01**

t-test - Student's *t*-test, U-test - Wilcoxon-Mann-Whitney *U*-test, ***Bold*** significant differences

Conclusions

The combination of nondestructive INAA-LLR and destructive ICP-MS methods is satisfactory analytical tool for the precise determination of 43 trace element mass fractions in the tissue samples of normal and carcinomatous prostate glands. The sequential application of these methods allowed precise quantitative determinations of mean mass fraction of Ag, Al, Au, B, Be, Bi, Br, Cd, Ce, Co, Cr, Cs, Dy, Er, Fe, Gd, Hg, Ho, La, Li, Mn, Mo, Nb, Nd, Ni, Pb, Pr, Rb, Sb, Sc, Se, Sm, Sn, Tb, Th, Ti, Tl, Tm, U, Y, Yb, Zn and Zr. It was observed that the ratio to Cd of Ag, Al, Au, B, Be, Bi, Br, Ce, Cr, Cs, Dy, Er, Gd, Ho, La, Li, Mn, Nd, Ni, Pb, Pr, Sb, Sm, Sn, Tb, Th, Ti, Tl, U, Y, Yb, and Zr mass fraction were significantly lower in cancerous tissues than in normal prostate. Further studies on larger number of samples are required to confirm our findings and to investigate the impact of the trace element relationships on prostate cancer etiology.

Acknowledgements

We are grateful to Dr. Karandaschev V., Dr. Nosenko S., and Moskvina I., Institute of Microelectronics Technology and High Purity Materials, Chernogolovka, Russia, for their help in ICP-MS analysis.

References

1. Waalkes M.P., Rehm S. (1994) Cadmium and prostate cancer. J. Toxicol. Environ. Health **43**: 251-269.
2. Zaichick V., Zaichick S. (1999) Role of zinc in prostate cancerogenesis. In: Anke M., et al., editors. Mengen und Spurenelemente. 19. Arbeitstagung. Friedrich-Schiller-Universitat. Jena: 104-115.
3. Platz E.A., Helzlsouer K.J. (2001) Selenium, zinc, and prostate cancer. Epidemiol. Rev. **23**: 93-101.
4. Zaichick V. (2004) INAA and EDXRF applications in the age dynamics assessment of Zn content and distribution in the normal human prostate. J. Radioanal. Nucl. Chem. **262**(1): 229-234.
5. Gray M.A., Centeno J.A., Slaney D.P., Ejnik J.W., Todorov T., et al. (2005) Environmental exposure to trace elements and prostate cancer in three New Zealand ethnic groups. Int. J. Environ. Res. Public Health **2**: 374-384.
6. Zaichick S., Zaichick V. (2011) INAA application in the age dynamics assessment of Br, Ca, Cl, K, Mg, Mn, and Na content in the normal human prostate. J. Radioanal. Nucl. Chem. **288**(1): 197-202.
7. Zaichick S., Zaichick V. (2011) The effect of age on Ag, Co, Cr, Fe, Hg, Sb, Sc, Se, and Zn contents in intact human prostate investigated by neutron activation analysis. Appl. Radiat. Isot. **69**: 827-833.
8. Zaichick S., Zaichick V. (2011) The Br, Fe, Rb, Sr, and Zn content and interrelation in intact and morphologic normal prostate tissue of adult men investigated by energy dispersive X-ray fluorescent analysis. X-Ray Spectrom. **40**(6): 464-469.
9. Zaichick V., Nosenko S., Moskvina I. (2012) The effect of age on 12 chemical element contents in intact prostate of adult men investigated by inductively coupled plasma atomic emission spectrometry. Biol. Trace Elem. Res. **147**(1): 49-58.

10. Zaichick S., Zaichick V., Nosenko S., Moskvina I. (2012) Mass Fractions of 52 Trace Elements and Zinc Trace Element Content Ratios in Intact Human Prostates Investigated by Inductively Coupled Plasma Mass Spectrometry. Biol. Trace Elem. Res. **149**(2): 171-183.
11. Zaichick V., Zaichick S. (2014) Age-related histological and zinc content changes in adult nonhyperplastic prostate glands. Age **36**(1): 167-181.
12. Zaichick V., Zaichick S. (2014) INAA application in the assessment of chemical element mass fractions in adult and geriatric prostate glands. Appl. Radiat. Isot. **90**: 62-73.
13. Zaichick V., Zaichick S. (2014) Determination of trace elements in adults and geriatric prostate combining neutron activation with inductively coupled plasma atomic emission spectrometry. Open Journal of Biochemistry **1**(2): 16-33.
14. Zaichick V., Zaichick S. (2014) Use of INAA and ICP-MS for the assessment of trace element mass fractions in adult and geriatric prostate. J. Radioanal. Nucl. Chem. **301**(2): 383-397.
15. Zaichick V. (2015) The variation with age of 67 macro- and microelement contents in nonhyperplastic prostate glands of adult and elderly males investigated by nuclear analytical and related methods. Biol. Trace Elem. Res. **168**(1): 44-60.
16. Zaichick V., Zaichick S. (2015) Dietary intake of minerals and prostate cancer: insights into problem based on the chemical element contents in the prostate gland. J. Aging Res. Clin. Practice **4**(3): 164-171.
17. Zaichick V., Zaichick S. (2015) Global contamination from uranium: insights into problem based on the uranium content in the human prostate gland. J. Environ. Health Sci. **1**(4): 1-5.
18. Zaichick V., Zaichick S. (2016) Variations in concentration and distribution of several androgen-dependent and -independent trace elements in nonhyperplastic prostate gland tissue throughout adulthood. J. Androl. Gynaecol. **4**(1): 1-10.
19. Zaichick V., Zaichick S. (2016) Age-related changes in concentration and histological distribution of Br, Ca, Cl, K, Mg, Mn, and Na in nonhyperplastic prostate of adults. European Journal of Biology and Medical Science Research **4**(2): 31-48.
20. Zaichick V., Zaichick S. (2016) Variations in concentration and histological distribution of Ag, Co, Cr, Fe, Hg, Rb, Sb, Sc, Se, and Zn in nonhyperplastic prostate gland throughout adulthood. Jacobs Journal of Cell and Molecular Biology **2**(1): 011.
21. Korelo A.M., Zaichick V. (1993) Software to optimize the multielement INAA of medical and environmental samples. In: Activation Analysis in Environment Protection. Joint Institute for Nuclear Research, Dubna, Russia: 326-332.
22. Zaichick V., Zaichick S. (2017) Trace element levels in prostate gland as carcinoma's markers. Journal of Cancer Therapy **8**, 131-145.
23. Zaichick V., Zaichick S. (2017) Ratios of Zn/trace element contents in prostate gland as carcinoma's markers. Cancer. Rep. Rev. 2017, **1**(1), 1-7.
24. Zaichick V., Zaichick S. (2017) Ratios of Calcium/Trace Elements as Prostate Cancer Markers. J. Oncol. Res. Ther. 2017(4): J116.
25. Zaichick V., Zaichick S. (2017). Ratios of Mg/trace element contents in prostate gland as carcinoma's markers. SAJ Canc. Sci. **2**(1): 102.
26. Zaichick V., Zaichick S. (2017) Ratios of cobalt/trace element contents in prostate gland as carcinoma's markers. IJCER 1(1): 21-27.

RELATIONSHIP BETWEEN Ca, Cl, K, Mg, Mn, Na, P, AND Sr CONTENTS IN THE INTACT ROOTS OF MALE TEETH INVESTIGATED BY NEUTRON ACTIVATION ANALYSIS

V. Zaichick[1], S. Zaichick[1,2]

[1]*Medical Radiological Research Centre, Korolyev St., 4, Obninsk, 249036, Russia, e-mail: vezai@obninsk.com*

[2] *Feinberg School of Medicine, Northwestern University, Chicago, IL 60611-4296, USA*

Introduction

To use chemical element composition as estimation of bone and teeth health in stomatological, geographical, environmental and occupational medicine, paleoanthropology, and other directions, it is necessary to know normal levels and age- and gender-related changes of chemical element contents and their ratios.[1-22]

In our previous studies it was shown that samples are contaminated by trace elements from stainless steel tools during the sample preparation.[23] There is evidence that some chemical elements are lost if tooth samples are treated with solvents in order to remove the organic matrix, and are then ashed and acid digested.[24, 25]

This work had three aims. The first was to determine the Ca, Cl, K, Mg, Mn, Na, P, and Sr mass fractions in the intact roots of male teeth by instrumental neutron activation analysis with high resolution spectrometry of short-lived radionuclides (INAA-SLR) and to calculate some statistical parameters of Cl/Ca, K/Ca, Mg/Ca, Mn/Ca, Na/Ca, P/Ca, Sr/Ca, Ca/P, Cl/P, K/P, Mg/P, Mn/P, Na/P, Sr/P, Ca/Mg, Cl/Mg, Mn/Mg, Na/Mg, P/Mg, Sr/Mg, Ca/Cl, K/Cl, Mg/Cl, Mn/Cl, Na/Cl, P/Cl, Sr/Cl, Ca/K, Cl/K, Mg/K, Mn/K, Na/K, P/K, Sr/K, Ca/Na, Cl/Na, K/Na, Mg/Na, Mn/Na, P/Na, and Sr/Na mass fraction ratios. The second aim was to evaluate the effect of age on mean values of ratios of chemical element mass fractions.The third aimwas to estimate the inter correlations between Ca, Cl, K, Mg, Mn, Na, P, and Sr mass fractions in the intact roots of male teeth.

All studies were approved bythe Ethical Committee of the Medical Radiological Research Center, Obninsk.

Experimental

Tooth root samples were obtained at postmortems from intact cadavers (46male, 16–58 years old) within 24 h of death. Samples were freeze dried until constant mass was obtained. All subjects died mainly due to trauma. A titanium tool was used to cut and to scrub samples as well as to cut teeth roots. The samplesweighing about 100 mg for INAA-SLR were sealed separately in thin polyethylene film washed beforehand with acetone and rectified alcohol. The sealed samples were placed in labeled polyethylene ampoules.

To determine contents of the elements by comparison with a known standard, biological synthetic standards (BSS) prepared from phenol–formaldehyde resins and chemically pure compounds were used.[26] Ten certified reference materials (CRM) IAEA H-5 (Animal Bone)

and standard reference materials (SRM) NIST 1486 (Bone Meal) sub-samples weighing about 50–100mg were analyzed in the same conditions as teeth samples to estimate the precision and accuracy of results.

The mass fractions of Ca, Cl, K, Mg, Mn, Na, P, and Sr were determined by INAA-SLR using a horizontal channel equipped with the pneumatic rabbit system of the WWR-c research nuclear reactor. The information of used nuclear reactions, radionuclides, gamma-energies, neutron flux, spectrometer and other details of the analysis including the quality control of results were reported by us before.[6, 26]

A dedicated computer program of NAA mode optimization was used.[27] Using the Microsoft Office Excelsoftware, the summary of statistics were calculated for different ratios of chemical element mass fractions. The reliability of difference in the results between two age groups of females was evaluated by Student's *t*-test. The Pearson's correlation analysis was used to identify relationships between elements.

Results and discussion

Table 1 represents certain statistical parameters (arithmetic mean, standard deviation, standard error of mean, minimal and maximal values, median, percentiles with 0.025 and 0.975 levels) of 42 different ratios of Ca, Cl, K, Mg, Mn, Na, P, and Sr mass fractions in the intact roots of male teeth.

The obtained values for Ca/P ratio, as shown in Table 1, agree well with median of means cited by other researchers for the teeth enamel.[28, 29] No published data referring to ratios of Ca/P or other chemical element mass fractions in the intact roots of male teeth was found.

To estimate the effect of age on the chemical element ratios in the intact roots of male teeth we examined two age groups: one comprised a younger group with ages from 15 to 35 years and the other comprised older people with ages ranging from 36 to 55 years (Table 2).In the intact roots of male teeth it was not found thestatistically significant age-related changes of the mass fraction ratios of chemical elements investigated in the study.

No published data referring to age-related differences of ratios of chemical element mass fractions in the intact roots of male teethwere found.

Table 3 depicts the inter-correlation calculations including all chemical elements identified by us. For example, the positive inter-correlations of Ca mass fractions with P ($p<0.001$), Cl($p<0.001$), and Mn ($p<0.01$) mass fractions were found in male teeth roots. If some correlations between the elements were predictable (e.g., Ca–P), the interpretation of other observed relationships requires further study for a more complete understanding.

Conclusions

INAA-SLRis a satisfactoryanalytical tool for the non-destructive precise determination of mass fraction of 8 chemical elements (Ca, Cl, K, Mg, Mn, Na, P, and Sr) in the root samples of permanent teeth. It was not found the statistically significant changes of chemical element mass fraction ratios in the intact roots of male teeth with age. All the deceased were citizens of Obninsk, a small city of non-industrial region near Moscow. None of those who died a sudden death had suffered from any systematic or chronic disorders before. Thus, our data for element mass fraction ratios in the intact roots of male teethmay serve as indicative normal values for residents of the Central European region of Russia.

Table 1. Some statistical parameters of 42 different ratios of Ca, Cl, K, Mg, Mn, Na, P, and Sr mass fractions in the intact roots of male teeth

Ratio	M	SD	SEM	Min	Max	Med	P0.025	P0.975
(Cl/Ca)×10^3	3.83	2.34	0.36	0.880	14.2	3.43	1.27	7.63
(K/Ca) ×10^3	3.46	1.13	0.19	0.587	6.69	3.10	1.59	6.11
(Mg/Ca) ×10^2	2.97	0.83	0.13	0.692	4.55	3.09	1.42	4.29
(Mn/Ca) ×10^6	5.20	3.25	0.51	1.25	15.8	3.99	1.49	11.3
(Na/Ca) ×10^2	2.59	1.13	0.18	1.69	7.98	2.28	1.74	5.90
P/Ca	0.543	0.056	0.009	0.427	0.714	0.541	0.454	0.635
(Sr/Ca) ×10^3	1.79	1.00	0.15	0.231	5.36	1.61	0.511	3.59
Ca/P	1.86	0.19	0.03	1.40	2.34	1.85	1.58	2.20
(Cl/P) ×10^2	0.713	0.430	0.066	0.164	2.52	0.658	0.233	1.35
(K/P) ×10^2	0.626	0.202	0.034	0.129	1.24	0.575	0.349	1.05
(Mg/P) ×10^2	5.54	1.71	0.27	1.22	8.92	5.46	2.62	8.57
(Mn/P) ×10^6	9.56	6.04	0.96	2.53	29.5	6.90	2.78	21.9
(Na/P) ×10^2	4.79	1.98	0.31	2.81	13.5	4.30	3.07	10.6
(Sr/P) ×10^3	3.30	1.81	0.27	0.467	8.97	3.03	0.845	7.26
Ca/Mg	38.1	19.9	3.10	22.0	145	32.4	23.3	70.6
Cl/Mg	0.158	0.180	0.028	0.0254	1.11	0.114	0.0384	0.482
K/Mg	0.136	0.072	0.012	0.0179	0.419	0.126	0.0455	0.273
(Mn/Mg) ×10^4	2.04	1.51	0.24	0.320	6.90	1.40	0.428	5.60
Na/Mg	0.952	0.503	0.079	0.457	3.11	0.789	0.504	2.58
P/Mg	20.8	11.5	1.8	11.2	82.0	18.3	11.7	38.2
Sr/Mg	0.0680	0.0487	0.0070	0.0059	0.275	0.0592	0.0152	0.159
Ca/Cl	355	210	32	70.7	1136	292	131	791
K/Cl	1.30	0.93	0.16	0.213	4.41	1.03	0.354	3.68
Mg/Cl	11.0	7.8	1.2	0.904	39.4	8.75	2.07	26.0
(Mn/Cl) ×10^4	19.6	27.9	4.4	2.32	180	13.9	3.75	53.3
Na/Cl	9.41	7.82	1.21	1.69	47.1	7.07	2.34	24.5
P/Cl	194	119	18	39.5	610	152	74.2	430
Sr/Cl	0.645	0.658	0.099	0.0698	3.98	0.447	0.0757	1.65
Ca/K	344	250	42	149	1704	322	164	737
Cl/K	1.20	0.89	0.15	0.227	4.69	0.973	0.274	2.95
Mg/K	9.94	8.77	1.51	2.39	55.8	7.95	3.82	25.8
(Mn/K) ×10^4	16.2	11.3	1.9	7.02	49.4	10.9	7.40	42.1
Na/K	8.69	7.39	1.25	4.24	48.6	6.67	4.83	20.0
P/K	185	111	19	80.7	774	174	95.4	335
Sr/K	0.529	0.271	0.042	0.172	1.31	0.468	0.187	1.25
Ca/Na	42.4	9.8	1.5	12.5	59.1	43.9	17.0	57.6
Cl/Na	0.165	0.114	0.018	0.0212	0.593	0.141	0.0409	0.428
K/Na	0.141	0.043	0.007	0.0206	0.236	0.150	0.0602	0.208
Mg/Na	1.23	0.42	0.07	0.322	2.19	1.27	0.388	1.98
(Mn/Na) ×10^4	2.24	1.66	0.26	0.415	7.33	1.68	0.520	6.37
P/Na	23.0	5.9	0.9	7.38	35.6	23.3	9.42	32.6
Sr/Na	0.746	0.405	0.061	0.0766	1.67	0.641	0.231	1.61

M arithmetic mean, *SD* standard deviation, *SEM* standard error of mean, *Min* minimum value, *Max* maximum value, *Med* median, *P0.025* percentile with 0.025 level, *P0.975* percentile with 0.975 level

Table 2. Effect of age on mean values (M±SEM) of ratios of chemical element in the intact roots of male teeth (Student's *t*-test)

Ratio	Age			Ratio
	15-35 year (M_1)	36-55 year (M_2)	$p\leq$	M_2/M_1
(Cl/Ca)×10^3	3.99±0.41	3.70±0.56	0.67	0.93
(K/Ca) ×10^3	3.41±0.34	3.50±0.22	0.83	1.03
(Mg/Ca) ×10^2	2.88±0.19	3.03±0.18	0.55	1.05
(Mn/Ca) ×10^6	4.74±0.62	5.57±0.79	0.41	1.18
(Na/Ca) ×10^2	2.79±0.38	2.44±0.12	0.37	0.87
P/Ca	0.534±0.012	0.550±0.012	0.37	1.03
(Sr/Ca) ×10^3	1.78±0.18	1.80±0.24	0.94	1.01
Ca/P	1.89±0.05	1.84±0.04	0.41	0.97
(Cl/P) ×10^2	0.745±0.072	0.690±0.104	0.67	0.93
(K/P) ×10^2	0.625±0.056	0.627±0.043	0.98	1.00
(Mg/P) ×10^2	5.46±0.39	5.59±0.37	0.81	1.02
(Mn/P) ×10^6	6.16±1.20	10.2±1.5	0.46	1.66
(Na/P) ×10^2	5.23±0.65	4.46±0.22	0.27	0.85
(Sr/P) ×10^3	3.30±0.34	3.30±0.43	0.99	1.00
Ca/Mg	37.5±2.8	38.5±5.0	0.86	1.03
Cl/Mg	0.157±0.027	0.159±0.045	0.97	1.01
K/Mg	0.131±0.015	0.139±0.019	0.75	1.06
(Mn/Mg) ×10^4	2.00±0.40	2.07±0.31	0.88	1.04
Na/Mg	1.02±0.14	0.905±0.090	0.50	0.89
P/Mg	20.1±1.7	21.3±2.9	0.72	1.06
Sr/Mg	0.065±0.008	0.071±0.012	0.70	1.09
Ca/Cl	320±44	382±46	0.34	1.19
K/Cl	1.12±0.23	1.45±0.21	0.30	1.29
Mg/Cl	9.79±1.66	11.9±1.7	0.38	1.22
(Mn/Cl) ×10^4	13.4±1.8	24.7±7.8	0.17	1.84
Na/Cl	9.75±2.5	9.15±1.05	0.83	0.94
P/Cl	169±22	214±27	0.21	1.27
Sr/Cl	0.551±0.096	0.731±0.169	0.36	1.33
Ca/K	394±91	301±14	0.32	0.76
Cl/K	1.34±0.17	1.08±0.24	0.39	0.81
Mg/K	11.6±3.3	8.67±0.71	0.41	0.75
(Mn/K) ×10^4	16.2±3.3	16.2±2.2	0.99	1.00
Na/K	10.5±2.7	7.15±0.35	0.23	0.68
P/K	202±40	170±9	0.44	0.84
Sr/K	0.541±0.058	0.515±0.064	0.76	0.95
Ca/Na	41.8±2.9	42.8±1.6	0.75	1.02
Cl/Na	0.173±0.023	0.160±0.026	0.71	0.92
K/Na	0.136±0.014	0.145±0.007	0.56	1.07
Mg/Na	1.15±0.09	1.29±0.09	0.28	1.12
(Mn/Na) ×10^4	2.06±0.38	2.38±0.37	0.54	1.16
P/Na	22.3±1.7	23.5±1.0	0.55	1.05
Sr/Na	0.736±0.085	0.755±0.089	0.88	1.03

M arithmetic mean, *SEM* standard error of mean, ***bold*** statistically significant

Table 3. Intercorrelations of the chemical element mass fractions in the intact roots of male teeth (r – coefficient of correlation)

Element	Ca	Cl	K	Mg	Mn	Na	P	Sr
Ca	**1.00**	0.594[c]	0.126	0.205	0.393[b]	-0.049	0.903[c]	0.137
Cl	0.594[c]	**1.00**	0.279	0.022	0.260	0.091	0.516[c]	0.058
K	0.126	0.279	**1.00**	-0.175	0.240	-0.088	0.205	0.209
Mg	0.205	0.022	-0.175	**1.00**	0.002	-0.018	0.138	-0.142
Mn	0.393[b]	0.260	0.240	0.002	**1.00**	-0.112	0.368[a]	0.223
Na	-0.049	0.091	-0.088	-0.018	-0.112	**1.00**	-0.018	-0.032
P	0.903[c]	0.516[c]	0.205	0.138	0.368[a]	-0.018	**1.00**	0.111
Sr	0.137	0.058	0.209	-0.142	0.223	-0.032	0.111	**1.00**

Statistically significant values: [a]$p \leq 0.05$, [b]$p \leq 0.01$, [c]$p \leq 0.001$.

References

1. Zaichick V. (1993) The *in vivo* neutron activation analysis of calcium in the skeleton of normal subjects, with hypokinesia and bone diseases. J. Radioanal. Nucl. Chem. **169**(2): 307–316.
2. Zaichick V. (1994) Instrumental activation and *X*-ray fluorescent analysis of human bones in health and disease. J. Radioanal. Nucl. Chem. **179**(2):295–303.
3. Zaichick V., Ovchjarenko N.N. (1996) *In vivo* X-ray fluorescent analysis of Ca, Zn, Sr, and Pb in frontal tooth enamel. J. Trace and Microprobe Techniques **14**(1):143–152.
4. Zaichick V., Morukov B. (1998) *In vivo* bone mineral studies on volunteers during a 370-day antiorthostatic hypokinesia test. J. Appl. Radiat. Isot. **49**(5/6): 691–694.
5. Zaichick V., Ovchjarenko N., Zaichick S. (1999) *In vivo* energy dispersive x-ray fluorescence for measuring the content of essential and toxic trace elements in teeth. J. Appl. Radiat. Isot. **50**(2):283–293.
6. Zaichick V., Dyatlov A., Zaichick S. (2000) INAA application in the age dynamics assessment of major, minor, and trace elements in the human rib. J. Radioanal. Nucl. Chem. **244**:189–193.
7. Zaichick V., Tzaphlidou M. (2002) Determination of calcium, phosphorus, and the calcium/phosphorus ratio in cortical bone from the human femoral neck by neutron activation analysis. J. Appl. Radiat. Isot. **56**:781–786.
8. Tzaphlidou M., Zaichick V. (2002) Neutron activation analysis of calcium/phosphorus ratio in rib bone of healthy humans. J. Appl. Radiat. Isot. **57**: 779–783.
9. Tzaphlidou M., Zaichick V. (2003) Calcium, phosphorus, calcium-phosphorus ratio in rib bone of healthy humans. Biol. Trace Elem. Res. **93**:63–74.
10. Zaichick V., Tzaphlidou M. (2003) Calcium and phosphorus concentrations and calcium/phosphorus ratio in trabecular bone from femoral neck of healthy humans as determined by neutron activation analysis. J. Appl. Radiat. Isot. **58**:623–627.
11. Zaichick V. (2004) INAA application in the age dynamics assessment of Ca, Cl, K, Mg, Mn, Na, P, and Sr contents in the cortical bone of human femoral neck. J. Radioanal. Nucl. Chem. **259**:351–354.
12. Tzaphlidou M., Zaichick V. (2004) Sex and age related Ca/P ratio in cortical bone of iliac crest of healthy humans. J. Radioanal. Nucl. Chem. **259**(2): 347–349.
13. Zaichick V. (2006) NAA of Ca, Cl, K, Mg, Mn, Na, P, and Sr contents in the human cortical and trabecular bone. J. Radioanal. Nucl. Chem. **269**:653–659.

14. Zaichick V. (2007) INAA application in the assessment of selected elements in cancellous bone of human iliac crest. J. Radioanal. Nucl. Chem. **271**:573–576.
15. Zaichick V., Zaichick S. (2009) Instrumental neutron activation analysis of trace element contents in the rib bone of healthy men. J. Radioanal. Nucl. Chem. **281**:47–52.
16. Zaichick V. (2009) Neutron activation analysis of Ca, Cl, K, Mg, Mn, Na, P, and Sr contents in the crowns of human permanent teeth. J. Radioanal. Nucl. Chem. **281**(1):41–45.
17. Zaichick S., Zaichick V. (2010) The effect of age and gender on 38 chemical element contents in human iliac crest investigated by instrumental neutron activation analysis. J. Trace Elements. Med. Biol. **24**: 1–6.
18. Zaichick S., Zaichick V. (2010) The effect of age and gender on 38 chemical element contents in human femoral neck investigated by instrumental neutron activation analysis". Biol. Trace Elem. Res. **137**: 1–12.
19. Zaichick S., Zaichick V. (2012) Neutron activation analysis of Ca, Cl, Mg, Na, and P content in human bone affected by osteomyelitis or osteogenic sarcoma. J. Radioanal. Nucl. Chem. **293**: 241–246.
20. Zaichick V. (2013) Chemical elements of human bone tissue investigated by nuclear analytical and related methods. Biol. Trace Elem. Res. **153**: 84–99.
21. Zaichick V. (2013) Data for the Reference Man: skeleton content of chemical elements. Radiat. Environ. Biophys. **52**(1): 65–85.
22. Zaichick V., Zaichick S. (2014) The Ca, Cl, Mg, Na, and P mass fractions in human bone affected by Ewing's sarcoma. Biol. Trace Elem. Res. **159**(1-3):32–38.
23. Zaichick V., Zaichick S. (1996) Instrumental effect on the contamination of biomedical samples in the course of sampling. J. Anal. Chem. **51**(12):1200–1205.
24. Zaichick V. (1997) Sampling, sample storage and preparation of biomaterials for INAA in clinical medicine, occupational and environmental health. In: Harmonization of Health-Related Environmental Measurements Using Nuclear and Isotopic Techniques. IAEA, Vienna, pp 123–133.
25. Zaichick V. (2004) Losses of chemical elements in biological samples under the dry ashing process. Trace Elements in Medicine **5**(3): 17–22.
26. Zaichick V. (1995) Application of synthetic reference materials in the Medical Radiological Research Centre. Fresenius J. Anal. Chem. **352**:219–223.
27. Korelo A.M., Zaichick V. (1993) Software to optimize the multielement INAA of medical and environmental samples. In: Activation Analysis in Environment Protection. Join Institute on Nuclear Research, Dubna, Russia, pp 326–332.
28. Antunes A., Salvador V.L.R., Scapin M.A., de Rossi W., Zezell D.M. (2005) Nanosecond Nd: YAG laser on dental enamel: compositional analysis by X-ray fluorescence. Laser Phys. Lett. **2**(6): 318–323.
29. Liu H., Chao J., Chuang C., Chiu H., Yang C., Sun Y. (2013) Study of P, Ca, Sr, Ba and Pb levels in enamel and dentine of human third molars for environmental and archaeological research. Advances in Anthropology **3**: 71–77.

APPLICATION OF NEUTRON ACTIVATION ANALYSIS FOR THE MEASUREMENT OF Br, Ca, Cl, K, Mg, Mn, AND Na CONTENTS IN THE INTACT THYROID OF FEMALE

V. Zaichick[1], S. Zaichick[1,2]

[1]*Medical Radiological Research Centre, Koroleva St., 4, Obninsk, 249036, Russia, e-mail: vezai@obninsk.com*

[2]*Feinberg School of Medicine, Northwestern University, Chicago, IL 60611-4296, USA*

Introduction

A large proportion of the world and European populations has some evidence of thyroid dysfunction. For example, the prevalence of goiter in areas of severe iodine deficiency can be as high as 80%. In Germany, an area of relative iodine deficiency, thyroid nodules or goiter were found in 33% of working adults aged 18–65 years. Another problem is thyroid cancer. In the last decades, thyroid cancer incidence has continuously and sharply increased all over the world. Moreover, thyroid cancer mortality, in spite of earlier diagnosis and better treatment, has not decreased but is rather increasing. The reasons for this increase are not well understood, but some environmental carcinogens in the industrialized lifestyle may have specifically affected the thyroid. Among potential carcinogens, the increased iodine and some other chemical elementintake isone of the most likely risk factors. Excessive accumulation or an imbalance of the chemical elements may disturb the cell functions and may result in cellular degeneration, death or, on the contrary, intensive uncontrolled proliferation, and malignancy. Questions on the role of chemical elements in etiology and pathogenesis of thyroid cancer are far from being answered. First of all, it is necessary to establish the normal level and changes of chemical element contents in thyroid tissue, and their relationships in intact gland.

In our previous studies the high mass fraction of I and some other chemical element were observed in intact human thyroid gland when compared with their levels in non-thyroid soft tissues of the human body.[1-9] However, some questions about the chemical element mass fraction in thyroid of adult and, particularly, elderly females still remain unanswered

This study aimed to perform a nondestructive method to evaluate the Br, Ca, Cl, K, Mg, Mn, and Na mass fraction in thyroid parenchyma and present data on relationships of these element contents in intact thyroid of females.

All studies were approved bythe Ethical Committee of the Medical Radiological Research Center, Obninsk.

Experimental

Samples of the human thyroid were obtained from randomly selected autopsy specimens of 33 females (European-Caucasian) aged 3.5 to 87 years. All the deceased were citizens of Obninsk and had undergone routine autopsy at the Forensic Medicine Department of City Hospital, Obninsk. Age ranges for subjects were divided into two age groups, with group 1, 3.5-40 years (30.9±3.1 years, M±SEM, n=11) and group 2, 41–87 years (66.3±2.7 years,

M±SEM, n=22). These groups were selected to reflect the condition of thyroid tissue in the children, teenagers, young adults and first period of adult life (group 1) and in the second period of adult life as well as in old age (group 2). The available clinical data were reviewed for each subject. None of the subjects had a history of an intersex condition, endocrine disorder, or other chronic disease that could affect the normal development of the thyroid. None of the subjects were receiving medications or used any supplements known to affect thyroid chemical element contents. The typical causes of sudden death of most of these subjects included trauma or suicide and also acute illness (cardiac insufficiency, stroke, embolism of pulmonary artery, alcohol poisoning). All right lobes of thyroid glands were divided into two portions using a titanium scalpel.[10]One tissue portion was reviewed by an anatomical pathologist while the other was used for the chemical element content determination. A histological examination was used to control the age norm conformity as well as the unavailability of microadenomatosis and latent cancer.

After the samples intended for chemical element analysis were weighed, they were transferred to -20°C and stored until the day of transportation in the Medical Radiological Research Center, Obninsk, where all samples were freeze-dried and homogenized.[11] The pounded sample weighing about 100 mg was used for chemical element measurement by INAA-SLR. The samples for INAA-SLR were sealed separately in thin polyethylene films washed beforehand with acetone and rectified alcohol. The sealed samples were placed in labeled polyethylene ampoules.

To determine contents of the elements by comparison with a known standard, biological synthetic standards (BSS) prepared from phenol-formaldehyde resins were used.[12] In addition to BSS, aliquots of commercial, chemically pure compounds were also used as standards. Ten certified reference material (CRM) IAEA H-4 (animal muscle) sub-samples weighing about 100 mg were treated and analyzed in the same conditions that thyroid samples to estimate the precision and accuracy of results.

The content of Br, Ca, Cl, I, K, Mg, Mn, and Na were determined by INAA-SLR using a horizontal channel equipped with the pneumatic rabbit system of the WWR-c research nuclear reactor. The neutron flux in the channel was 1.7×10^{13}n cm^{-2} s^{-1}. Ampoules with thyroid tissue samples, SSB, intralaboratory-made standards, and certified reference material were put into polyethylene rabbits and then irradiated separately for 180 s. Copper foils were used to assess neutron flux.

The measurement of each sample was made twice, 1 and 120 min after irradiation. The duration of the first and second measurements was 10 and 20 min, respectively. A coaxial 98-cm3 Ge (Li) detector and a spectrometric unit (NUC 8100), including a PC-coupled multichannel analyzer, were used for measurements. The spectrometric unit provided 2.9-keV resolution at the ^{60}Co 1,332-keV line. Details of used nuclear reactions, radionuclides, and gamma-energies were presented in our earlier publications concerning the INAA chemical element contents in human scalp hair.[13,14]

A dedicated computer program for INAA mode optimization was used.[15] All thyroid samples were prepared in duplicate, and mean values of chemical element contents were used in final calculation. Using Microsoft Office Excel, a summary of the statistics, including, arithmetic mean, standard deviation, standard error of mean, minimum and maximum values, median, percentiles with 0.025 and 0.975 levels was calculated for chemical element contents. For the estimation of the Pearson correlation coefficient between different chemical elements the Microsoft Office Excel programs was also used.

Results and discussion

Good agreement of the Br, Ca, Cl, I, K, Mg, Mn, and Na contents analyzed by INAA-SLR with the certified data of CRM IAEA H-4 (Table 1) indicates an acceptable accuracy of the results obtained in the study of chemicalelements of the thyroid presented in Tables 2–4.

The obtained means for Br, Ca, Cl, I, K, Mg, Mn, and Na mass fraction, as shown in Table 3, agree well with the medians of mean values cited by other researches for the human thyroid, including samples received from persons who died from different non-thyroid diseases.[16-27] A number of values for chemical element mass fractions were not expressed on a dry mass basis by the authors of the cited references. However, we calculated these values using published data for water (75%)[28] and ash (4.16% on dry mass basis)[29] contents in thyroid of adults.

Table 1. INAA-SLR data of chemical element contents in the IAEA H-4 (animal muscle) reference material compared to certified values (mg/kg, dry mass basis)

Element	Certified values			This work results
	Mean	95% confidence interval	Type	Mean±SD
Br	4.1	3.5 – 4.7	N	5.0±0.9
Ca	188	163 – 213	N	238±59
Cl	1890	1810 – 1970	N	1950±230
I	0.08	-	N	<1.0
K	15800	15300 – 16400	C	16200±3800
Mg	1050	990 – 1110	C	1100±190
Mn	0.52	0.48 – 0.55	C	0.55±0.11
Na	2060	1930 – 2180	C	2190±140

Mean - arithmetical mean, SD -standard deviation, C- certified values, N -non-certified values.

Table 2. Some statistical parameters of Br, Ca, Cl, I, K, Mg, Mn, and Na mass fraction (mg/kg, dry mass basis) in intact thyroid of female

Gender	Element	Mean	SD	SEM	Min	Max	Median	P 0.025	P 0.975
Females	Br	22.4	16.1	3.2	5.00	66.9	16.3	5.00	59.2
n=33	Ca	1663	570	198	461	3640	1170	670	3600
	Cl	3317	1480	290	1200	6000	3375	1388	5906
	I	1956	1199	219	114	5061	1562	309	4662
	K	5395	3245	723	1740	13700	4835	2120	13230
	Mg	212	97	24	66.0	364	215	67.5	356
	Mn	1.50	0.84	0.22	0.550	4.18	1.37	0.603	3.41
	Na	6421	1721	320	3800	10450	6700	4122	9924

Mean – arithmetic mean, SD – standard deviation, SEM – standard error of mean, Min – minimum value, Max – maximum value, P 0.025 – percentile with 0.025 level, P 0.975 – percentile with 0.975 level.

Table 3. Median, minimum and maximum value of means Br, Ca, Cl, I, K, Mg, Mn, and Na contents in normal thyroid according to data from the literature in comparison with our results (mg/kg, dry mass basis)

Element	Published data [Reference]			This work
	Median of means (n)*	Minimum of means M or M±SD, (n)**	Maximum of means M or M±SD, (n)**	M±SD
Br	18.1 (11)	5.12 (44) [16]	284±44 (14) [17]	22±16
Ca	1600 (17)	840±240 (10) [18]	3800±320 (29) [18]	1663±570
Cl	6800 (5)	804±80 (4) [19]	8000 (-) [20]	3317±1480
I	1888 (95)	159±8 (23) [21]	5772±2708 (50) [22]	1956±1199
K	4400 (17)	46.4±4.8 (4) [19]	6090 (17) [23]	5395±3245
Mg	390 (16)	3.5 (-) [24]	840±400 (14) [25]	212±97
Mn	1.82 (36)	0.44±11 (12) [26]	69.2±7.2 (4) [19]	1.50±0.84
Na	8000 (9)	438 (-) [27]	10000±5000 (11) [25]	6421±1721

M –arithmetic mean, SD – standard deviation, (n)* – number of all references, (n)** – number of samples.

A significant direct correlation between the Br-K, Br-Mn, Cl-Mg, Cl-Na, I-Na, K-Mg, and Mn-Na mass fractions as well as an inverse correlation between Ca-Cland Na-Mnmass fractions was seen in female thyroid. No correlation was demonstrated between any other chemical elements (Table 4).If some correlations between the elements were predictable (e.g., Na-Cl), the interpretation of other observed relationships would require further study.No published data referring to inter-correlations of Br, Ca, Cl, I, K, Mg, Mn, and Namass fractions in thyroid of females was found.

Table 4. Intercorrelations of the chemical element mass fractions in the intact thyroid of female (r – coefficient of correlation)

Element	Br	Ca	Cl	I	K	Mg	Mn	Na
Br	**1.00**	0.246	0.073	-0.053	0.398^{a}	-0.179	0.727^{c}	0.179
Ca	0.246	**1.00**	-0.658^{c}	0.132	0.125	0.021	0.341	-0.184
Cl	0.073	-0.658^{c}	**1.00**	0.159	-0.367	0.563^{b}	-0.207	0.389^{a}
I	-0.053	0.132	0.159	**1.00**	-0.319	0.191	-0.090	0.446^{a}
K	0.398^{a}	0.125	-0.367	-0.319	**1.00**	0.774^{c}	-0.194	-0.152
Mg	-0.179	0.021	0.563^{b}	0.191	0.774^{c}	**1.00**	-0.266	0.313
Mn	0.727^{c}	0.341	-0.207	-0.090	-0.194	-0.266	**1.00**	-0.410^{a}
Na	0.179	-0.184	0.389^{a}	0.446^{a}	-0.152	0.313	0.410^{a}	**1.00**

Statistically significant values: $^{a}p\leq0.05$, $^{b}p\leq0.01$, $^{c}p\leq0.001$.

All the deceased were citizens of Obninsk. Obninsk is the small nonindustrial city not far from Moscow in unpolluted area. None of those who died a sudden death had suffered from any systematic or chronic disorders before. The normal state of thyroid was confirmed by morphological study. Thus, our data for Br, Ca, Cl, I, K, Mg, Mn, and Na mass fractions in intact thyroid may serve as indicative normal values for females of urban population of the Russian Central European region.

Conclusions

The instrumentalneutron activation analysis with high resolution spectrometry of short-lived radionuclides is a useful analytical tool for the non-destructive determination of chemical element content in the thyroid tissue samples. This method allows determine means for 8 chemical elements:Br, Ca, Cl, I, K, Mg, Mn, and Na.

The good agreement with the medians of mean values cited by other researches for Br, Ca, Cl, I, K, Mg, Mn, and Na mass fraction in the human thyroid allows accept data obtained in the study for these elements as indicative normal values for female thyroid of urban population of the Russian Central European region.

Acknowledgements

We are grateful to Dr. Yu. Choporov, Head of the Forensic Medicine Department of City Hospital, Obninsk, for supplying thyroid samples.

References

1. Zaichick V., Tsyb A., Vtyurin B.M. (1995) Trace elements and thyroid cancer. Analyst 120: 817-821.
2. Zaichick V., Choporov Yu. (1996) Determination of the natural level of human intra-thyroid iodine by instrumental neutron activation analysis. J Radioanal. Nucl. Chem. **207**(1): 153-161.
3. Zaichick V., Zaichick S. (1997) Normal human intrathyroidal iodine. Sci. Total. Environ. **206**(1): 39-56.
4. Zaichick V. (1998) Iodine excess and thyroid cancer. J. Trace Elements in Experimental Medicine **11**(4): 508-509.
5. Zaichick V. (1998) In vivo and in vitro application of energy-dispersive XRF in clinical investigations: experience and the future. J. Trace Elements in Experimental Medicine **11**(4): 509-510.
6. Zaichick V., Iljina T. (1998) Dietary iodine supplementation effect on the rat thyroid ^{131}I blastomogenic action. In: Die Bedentung der Mengen- und Spurenelemente. 18. Arbeitstangung. Anke M., et al., editors. Friedrich-Schiller-Universität, Jena, 294-306.
7. Zaichick V., Zaichick S. (1999) Energy-dispersive X-ray fluorescence of iodine in thyroid puncture biopsy specimens. J. Trace and Microprobe Techniques **17**(2): 219-232.
8. Zaichick V. (1999) Human intrathyroidal iodine in health and non-thyroidal disease. In: New aspects of trace element research. Abdulla M., et al., editors. Smith-Gordon and Nishimura London and Tokyo, 114-119.
9. Zaichick V. (2000) Relevance of and potentiality for in vivo intrathyroidal iodine determination. In: In Vivo Body Composition Studies. Yasumura S., et al., editors. Annals of the New York Academy of Sciences 904: 630-632.
10. Zaichick V., Zaichick S. (1996) Instrumental effect on the contamination of biomedical samples in the course of sampling. The Journal of Analytical Chemistry **51**(12): 1200-1205.
11. Zaichick V., Zaichick S. (1997) A search for losses of chemical elements during freeze-drying of biological materials. J. Radioanal. Nucl. Chem. **218**(2): 249-253.
12. Zaichick V. (1995) Applications of synthetic reference materials in the medical Radiological Research Centre. Fresenius J. Anal. Chem. **352**: 219-223.

13. Zaichick V., Choporov Yu. (1996) Determination of the natural level of human intra-thyroid iodine by instrumental neutron activation analysis. J. Radioanal. Nucl. Chem. **207**(1): 153-161.
14. Zaichick S., Zaichick V. (2010) The effect of age and gender on 37 chemical element contents in scalp hair of healthy humans. Biol. Trace Elem. Res. **134**(1): 41-54.
15. Korelo A.M., Zaichick V. (1993) Software to optimize the multielement INAA of medical and environmental samples. In: Activation Analysis in Environment Protection. Joint Institute for Nuclear Research, Dubna, Russia: 326-332.
16. Zhu H., Wang N., Zhang Y., et al. (2010) Element contents in organs and tissues of Chinese adult men. Health Phys. **98**(1): 61–73.
17. Salimi J., Moosavi K., Vatankhah S., et al. (2004) Investigation of heavy trace elements in neoplastic and non-neoplastic human thyroid tissue: A study by proton – induced X-ray emissions. Iran J. Radiat. Res. **1**(4): 211-216.
18. Boulyga S.F., Zhuk I.V., Lomonosova E.M., et al. (1997) Determination of microelements in thyroids of the inhabitants of Belarus by neutron activation analysis using the k0-method. J. Radioanal. Nucl. Chem. **222** (1-2): 11-14.
19. Reddy S.B., Charles M.J., Kumar M.R., et al. (2002) Trace elemental analysis of adenoma and carcinoma thyroid by PIXE method. Nucl. Instr. Meth. Phys. Res. B**196**(3-4): 333-339.
20. Woodard H.Q., White DR (1986) The composition of body tissues. Brit. J. Radiol. **708**: 1209-1218.
21. Neimark I.I., Timoschnikov V.M. (1978) Development of carcinoma of the thyroid gland in person residing in the focus of goiter endemic. Problemy Endocrinilogii **24**(3): 28-32.
22. Zabala J., Carrion N., Murillo M., et al. (2009) Determination of normal human intrathyroidal iodine in Caracas population. J. Trace Elem. Med. Bio. **23**(1): 9-14.
23. Forssen A. (1972) Inorganic elements in the human body. Annales Medicinae Experimentalis et Biologiae Fenniae **50**(3): 99-162.
24. Kortev A.I., Donthov G.I., Lyascheva A.P. (1972) Bioelements and a human pathology. Middle-Ural publishing-house, Sverdlovsk, Russia, 302 p.
25. Soman S.D., Joseph K.T., Raut S.J., et al. (1970) Studies of major and trace element content in human tissues. Health Phys. **19**(5): 641-656.
26. Teraoka H. (1981) Distribution of 24 elements in the internal organs of normal males and the metallic workers in Japan. Arch. Environ. Health **36**(4): 155-165.
27. Boulyga S.F., Becker J.S., Malenchenko A.F., et al. (2000) Application of ICP-MS for Multielement Analysis in Small Sample Amounts of Pathological Thyroid Tissue. Microchimica Acta **134**(3-4): 215-222.
28. Katoh Y., Sato T., Yamamoto Y. (2002) Determination of multielement concentrations in normal human organs from the Japanese. Biol. Trace Elem. Res. **90**(1-3): 57-70.
29. Schroeder H.A., Tipton I.H., Nason A.P. (1972) Trace metals in man: strontium and barium. J. Chron. Dis. **25**(9): 491-517.

Methodical Aspects

EVALUATION OF NEUTRON INDUCED CROSS SECTION DATA USING EMPIRE 3.2.2 AND TALYS 1.8 CODES

A. Gandhi[1], B.J. Roy[2], V. Mishra[1], N.K. Rai[1], V. Kumar[1], Y. Sawant[2], B.K. Nayak[2], A. Saxena[2], S. Mukherjee[3], N.L. Singh[3], Yu.N. Kopatch[4], I.N. Ruskov[4] and A. Kumar[1]

[1]*Department of Physics, Banaras Hindu University, Varanasi-221005, India*
[2]*Nuclear Physics Division, Bhabha Atomic Research Centre, Mumbai-400085, India*
[3]*Department of Physics, Maharaja Sayajirao University of Baroda, Vadodara-390002, India*
[4]*Joint Institute for Nuclear Research (JINR), Dubna, Russia*

E-mail: gandhiaman653@gmail.com

Key Words: fast neutrons, nuclear reactions, nuclear data, nuclear model codes

Abstract

The cross sections of ^{67}Zn,^{92,96}Mo,^{208}Pb(n,p) and ^{70}Zn,^{100}Mo(n,2n) reactions have been evaluated using statistical nuclear model codes EMPIRE 3.2.2 and TALYS 1.8 at the neutron energy range from reactions threshold to 20 MeV. The variation in cross section with different optical model potential, level density models, and nuclear reaction models have been investigated at neutron energy 14.5 MeV. In this work, the pre-equilibrium emission contribution in the total cross section has also been verified in the neutron energy of 14.5 MeV. The calculated results were also compared with the experimental data being taken from EXFOR database.

Introduction

The need of precise and accurate neutron induced cross section data is very important in nuclear technologies, such as designing of nuclear reactors, accelerator driven subcritical systems (ADS), transmutation of nuclear waste and medical applications (production of radioisotopes, radiotherapy) etc. The neutron induced reaction cross section data in the fast neutron energy region ~ 14 MeV for the structural material (Zinc and Molybdenum) has many applications in fusion and fission reactors. Similarly, neutron induced cross section data of Lead is also important for shielding materials. The reactions induced by fast neutrons such as, (n, 2n) and (n, p) were used to study the neutron multiplicity and charge particle emission in reactor structure wall that causes micro-structural defects. This neutron data can be generated experimentally by using the neutron activation technique (NAA) over the neutron energy range. For those isotopes where the experimental measurements are not feasible, the cross section data can be generated by using standard nuclear models.

This neutron induced cross section data obtained from theoretical models are important for the study of nuclear reaction mechanism and it can be used by evaluators to interpolate or extrapolate data for the energy range where the data does not exists. EMPIRE and TALYS are two such computer codes based on the statistical model which are used to estimate the cross section data on the basis of three major nuclear reactions mechanism i.e., direct reaction (DR), pre-equilibrium emission (PE) and compound nucleus (CN) decay. Thus the mechanism of the nuclear reactions changes with the incident neutron energy.

In order to study the different reaction mechanisms, the EMPIRE and TALYS model codes were used with different parameters which are defined at particular energy range and elements [1–2].

EMPIRE Calculations

Empire is a modular nuclear reactions code, comprising various nuclear theoretical models in order to estimate the probability of the emitted particles such as photons, nucleons, deuterons and tritons etc., in the energy range up to several hundred MeV.

In the EMPIRE code, the direct reaction is calculated with default spherical optical model that uses the ECIS06 code and which have been used to calculate the particle transmission coefficient. In this calculation, the OM potential parameter has used which is proposed by A.J Koning and J.P. Delaroche [3].The Statistical Hauser-Feshbach model is used for the calculation of the compound nucleus decay. For pre-equilibrium emission, the exciton model (PCROSS code) has been used which describes particle and gamma-emission and also calculate pre-equilibrium emission with default mean free path multiplier PCROSS 1.5.
The contribution from all three mechanisms make total cross-section and maximum contribution comes from the CN decay with an addition of some pre-equilibrium mechanism. The effect of pre-equilibrium contribution increases with increase in incident energy.
Cross section is very sensitive to the level density parameters and EMPIRE incorporated four level density models to calculate them which are as follow:

(i) LEVDEN 0 is the EMPIRE-specific level densities (EGSM RIPL-3) and it is a default model used in EMPIRE, adjusted to RIPL- 3 experimental D_{obs} and to discrete levels. This is Enhanced Generalized Super fluid Model (EGSM). The model uses super fluid model below critical excitation energy and the Fermi gas model above.

(ii) LEVDEN 1 is the Generalized Super fluid Model (GSM, Ignatyuk et al.), adjusted to RIPL-2 experimental D_{obs} and to discrete levels which use constant temperature model below critical energy (Ucrt) and Fermi gas model above critical energy (depend on the compound nucleus excitation energy).

(iii) LEVDEN 2 is Gilbert-Cameron level densities (parameterized by Ijinov et al), which adjusted to RIPL-2 experimental D_{obs} and to discrete levels recommended for CN exited up to about 20 MeV.

(iv) LEVDEN 3 is the RIPL-3 microscopic HFB level densities (where D_{obs} is neutron resonance spacing).

The calculations have been done with the all four choices to check how the cross section is changing with different level density models at 14.5 MeV.

Apart from PCROSS model, the cross section has also been calculated for multi-step direct and multi-step compound (MSD/MSC) pre-equilibrium model.

For emission of charged particle or photons (gamma-ray) the exciton model (PCROSS code) is considered while for the neutron emission a combination of MSD/MSC model is preferred. The required parameters for the nuclear models to calculate the excitation functions have been taken from the RIPL-3 library. The RIPL-3 includes the nuclear masses, discrete levels and decay schemes, neutron resonances, optical model parameters, level densities, gamma-ray strength function and fission barriers [4].

TALYS Calculations

TALYS is another computer code for the analysis and prediction of nuclear reactions. The objective of this code is to reproduce the nuclear reactions that involve neutrons, photons, protons, deuterons, tritons, and ^{3}He particles in the energy range of 1 keV – 200 MeV and for target nuclides of mass 12 and heavier. To achieve this, TALYS code implements a suite of nuclear reaction models into a single code system. This enables us to evaluate nuclear reactions from the unresolved resonance range up to intermediate energies.

TALYS generate nuclear data for all open reaction channels, on a user-defined energy and angle grid, beyond the resonance region. In the present study, calculations have been done with the default set of input parameters, where only we have changed the different level density models and pre-equilibrium models.

In TALYS six level density models are defined for calculating level density parameters, which are as follows:

1. ldmodel 1 Constant temperature and Fermi gas model
2. ldmodel 2 (default) Back-shifted Fermi gas model
3. ldmodel 3 Generalised super fluid model
4. ldmodel 4 Microscopic level densities (Skyrme force) from Goriely's tables
5. ldmodel 5 Microscopic level densities (Skyrme force) from Hilaire's combinatorial tables
6. ldmodel 6 Microscopic level densities (temperature dependent HFB, Gogny force) from Hilaire's.

The calculations have been performed using the optical model potential as proposed by A.J Koning [1]. For the contribution of pre-equilibrium emission in total reaction cross section, the Exciton (preqmode 2) (default) and MSD/MSC models (preqmode 4) were used. The pre-equilibrium contribution in (n, p) and (n, 2n) reaction cross sections have also been performed with and without including the pre-equilibrium channel.

Results and Discussion

From the available options of the level density models , OM potential in the EMPIRE 3.2.2 code, the cross section for the reaction $^{67}Zn(n,p)^{67}Cu$, $^{92}Mo(n,p)^{92m}Nb$, $^{96}Mo(n,p)^{96}Nb$, $^{208}Pb(n,p)^{208}Tl$ and $^{70}Zn(n,2n)^{69m}Zn$, $^{100}Mo(n,2n)^{99}Mo$ have been evaluated over the energy range from threshold to 20MeV. The calculation was done by using exciton model, the combination of multi-step direct and multi-step compound model (MSD/MSC) and all four level density models which are given in Table 1 and 2. Similarly, evaluation has been done with TALYS 1.8 code using ldmodel 1–6 and considering both exciton model and MSD/MSC model are shown in Table 3 and 4.

It can be observed in Tables 1–4, that the cross section is changed for different level density models. The contribution of pre-equilibrium emission in (n, p) and (n, 2n) reactions have been studied at neutron energy of 14.5 MeV and it is found that the effect of pre-equilibrium emission is larger for (n, p) as compared to (n, 2n) reaction as given in Table 6.

From the literature survey, it was found that the contribution from the pre-equilibrium emission is dominated when one particle is emitted whereas in the case of two particle emission the effect of pre-equilibrium on the second emitted particle is very less that's why in our calculations the contribution of pre-equilibrium of (n,2n) reaction is less than (n,p) reaction [6–7].

Calculations have also been done with different choices of OM potential and the cross section for different choices of OM potentials are observed to vary within 10% in all reactions except for ^{208}Pb (n,p) where the variation is as large as ~35% was observed.

The theoretical model calculations for $^{67}Zn(n,p)^{67}Cu$, $^{92}Mo(n,p)^{92m}Nb$, $^{96}Mo(n,p)^{96}Nb$, $^{208}Pb(n,p)^{208}Tl$ and $^{70}Zn(n,2n)^{69m}Zn$, $^{100}Mo(n,2n)^{99}Mo$ reactions are given in Table 1–5. However, Table 5 contains only those data that reproduces the experimental results.

For $^{67}Zn(n,p)^{67}Cu$ reaction

The graph between theoretical and experimental cross section data of $^{67}Zn(n,p)^{67}Cu$ reaction from threshold to 20 MeV has been plotted in Fig. 1. The theoretical cross section data for the

above reaction have calculated by using different models of EMPIRE and TALYS, which are following as, for EMPIRE code: (i) Exciton model with HFB level density model and Koning OM potentials have been used and for TALYS code: (i) Exciton model with Back-shifted Fermi gas level density model and Koning local OM potential have opted.

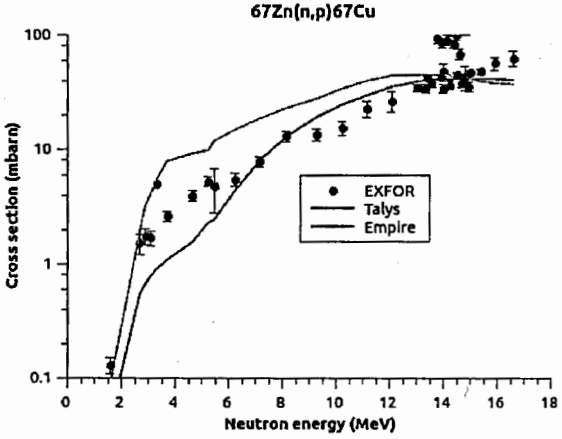

Fig. 1. Cross section of $^{67}Zn(n,p)^{67}Cu$ reaction at different neutron energies estimated in present work and experimental data taken from EXFOR database.

Table 1: Cross section estimated through exciton model by using different level density options of EMPIRE 3.2.2 code at neutron energy 14.5 MeV

Reactions	LEVDEN 0 (mb)	LEVDEN 1 (mb)	LEVDEN 2 (mb)	LEVDEN 3 (mb)
$^{67}Zn(n,p)^{67}Cu$	110.97	74.62	25.982	43.13
$^{92}Mo(n,p)^{92m}Nb$	121.18	79.411	258.36	100.36
$^{96}Mo(n,p)^{96}Nb$	28.332	14.374	288.19	19.081
$^{208}Pb(n,p)^{208}Tl$	0.1943	0.1079	5.3704	0.2148
$^{70}Zn(n,2n)^{69m}Zn$	610.56	737.79	25.846	730.46
$^{100}Mo(n,2n)^{99}Mo$	1641.3	1680	182.54	1670.5

Table 2: Cross section estimated through MSD/MSC model by using different level density options of EMPIRE 3.2.2 code at neutron energy 14.5 MeV

Reactions	LEVDEN 0 (mb)	LEVDEN 1 (mb)	LEVDEN 2 (mb)	LEVDEN 3 (mb)
$^{67}Zn(n,p)^{67}Cu$	94.91	59.62	12.53	29.42
$^{92}Mo(n,p)^{92m}Nb$	104.32	63.13	239.41	84.01
$^{96}Mo(n,p)^{96}Nb$	21.39	8.12	268.60	12.58
$^{208}Pb(n,p)^{208}Tl$	0.1011	0.0171	5.1307	0.1211
$^{70}Zn(n,2n)^{69m}Zn$	583.85	692.17	71.88	687.18
$^{100}Mo(n,2n)^{99}Mo$	1524.9	1559.8	193.9	1551.3

For $^{92}Mo(n,p)^{92m}Nb$ reaction

The graph between theoretical and experimental cross section data of $^{92}Mo(n,p)^{92m}Nb$ reaction from threshold to 20 MeV has been plotted in Fig. 2. The theoretical cross section data for the above reactions have calculated by using different models of EMPIRE and

TALYS. For EMPIRE code (i) MSD/MSD model with Generalized Super fluid level density Model and Koning OM potentials have been used and for TALYS (i) exciton model with back-shifted Fermi gas level density model and Koning local OM potential have opted.

Table 3: Cross section estimated through exciton model by using different level density options of TALYS 1.8 code at neutron energy 14.5 MeV

Reactions	ldmodel 1 (mb)	ldmodel 2 (mb)	ldmodel 3 (mb)	ldmodel 4 (mb)	ldmodel 5 (mb)	ldmodel 6 (mb)
^{67}Zn(n,p)^{67}Cu	33.36	41.83	22.14	72.11	51.44	65.73
^{92}Mo(n,p)^{92m}Nb	84.84	62.20	36.07	65.66	87.49	166.85
^{96}Mo(n,p)^{96}Nb	30.66	21.14	22.38	30.41	33.84	35.02
^{208}Pb(n,p)^{208}Tl	0.7687	0.5836	159.30	0.8936	1.068	0.9120
^{70}Zn(n,2n)^{69m}Zn	686.53	667.44	512.49	512.49	667.44	686.53
^{100}Mo(n,2n)^{99}Mo	1536.3	1524.6	1323.04	1518.8	1537.2	1309.1

Table 4: Cross section estimated through MSD/MSC model by using different level density options of TALYS code at neutron energy 14.5 MeV

Reactions	ldmodel 1 (mb)	ldmodel 2 (mb)	ldmodel 3 (mb)	ldmodel 4 (mb)	ldmodel 5 (mb)	ldmodel 6 (mb)
^{67}Zn(n,p)^{67}Cu	63.38	68.76	61.82	102.34	81.53	96.25
^{92}Mo(n,p)^{92m}Nb	85.29	65.56	38.55	64.61	89.78	180.09
^{96}Mo(n,p)^{96}Nb	46.51	39.10	36.80	45.86	50.26	51.62
^{208}Pb(n,p)^{208}Tl	9.77	9.86	201.7	9.86	10.47	10.52
^{70}Zn(n,2n)^{69m}Zn	700.70	687.36	561.85	681.62	747.35	593.62
^{100}Mo(n,2n)^{99}Mo	1588.2	1582.0	1486.2	1568.5	1587.3	1332.2

For ^{96}Mo(n,p)^{96}Nb reaction

The graph between theoretical and experimental cross section data of ^{96}Mo(n,p)^{96}Nb reaction from threshold to 20 MeV have been plotted and shown in Fig. 3. The theoretical cross section data for the above reactions have calculated by using different models of EMPIRE and TALYS. For EMPIRE code (i) MSD/MSD model with EGSM level density Model and Koning OM potential have been used and for TALYS (i) exciton model with back-shifted Fermi gas level density model and Koning local OM potential have opted.

For ^{208}Pb(n,p)^{208}Tl reaction

The graph of theoretical and experimental cross section data of ^{208}Pb(n,p)^{208}Tl from the reaction threshold to 20 MeV has been plotted and shown in Fig. 4.The theoretical cross section data for the above reactions have calculated by using different models of TALYS. For EMPIRE code (i) exciton model with microscopic level densities (temperature dependent HFB, Gogny force) from Hilaire's and Koning local OM potential.

During calculations with EMPIRE, it was found that for ^{208}Pb(n,p) case the EMPIRE 3.2.2 was not suitable to calculate fission cross section due to the absence of fission barrier parameters in EMPIRE data library for reaction product ^{209}Pb and since EMPIRE considers ^{209}Pb to be fissile and due to missing of parameters, it shows error in the output file without calculating any cross section. So, to calculate the ^{208}Pb(n,p) cross section we edit the input file with optional input keyword FISSHI 2.0 which is used to ignore the fission channel.

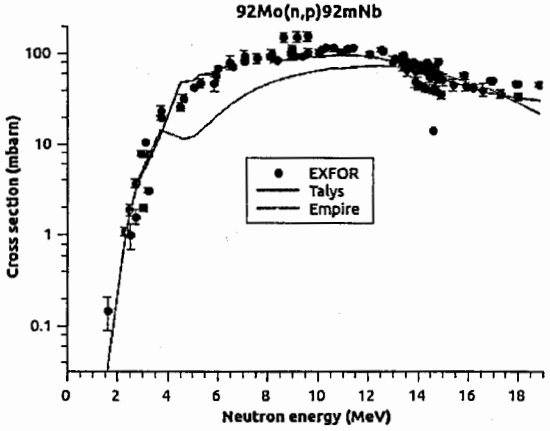

Fig. 2. Cross section of ^{92}Mo(n,p)^{92m}Nb reaction at different neutron energies estimated in present work and experimental data taken from EXFOR database.

For ^{70}Zn(n,2n)^{69m}Zn reaction

Fig. 5 shows the graph of theoretical and experimental cross section data of ^{70}Zn(n,2n)^{69m}Zn reaction from threshold to 20 MeV. The theoretical cross section data for the above reaction has been calculated by using different models of EMPIRE and TALYS. For EMPIRE code (i) MSD/MSD model with EGSM level density Model and Koning OM potentials and for TALYS (i) exciton model with Generalised super fluid level density model and Koning local OM potential.

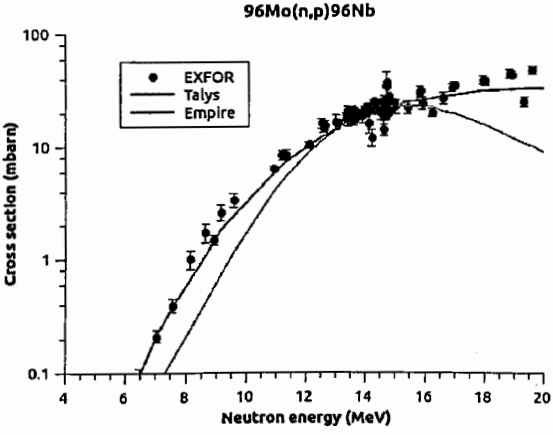

Fig. 3. Cross section of ^{96}Mo(n,p)^{96}Nb reaction at different neutron energies estimated in present work and experimental data taken from EXFOR database.

Table 5: Comparison of all reactions cross section data at neutron energy 14.5 MeV

Reactions	Experimental data (mb)	EMPIRE 3.2.2 (mb)	TALYS 1.8 (mb)
$^{67}Zn(n,p)^{67}Cu$	44.9±2.1	43.13	41.83
$^{92}Mo(n,p)^{92m}Nb$	56.3±8	63.13	62.20
$^{96}Mo(n,p)^{96}Nb$	20±2.7	21.39	21.14
$^{208}Pb(n,p)^{208}Tl$	0.94±0.18	0.2148	0.9120
$^{70}Zn(n,2n)^{69m}Zn$	547±22	583.85	512.49
$^{100}Mo(n,2n)^{99}Mo$	1377±86	1524.9	1323.04

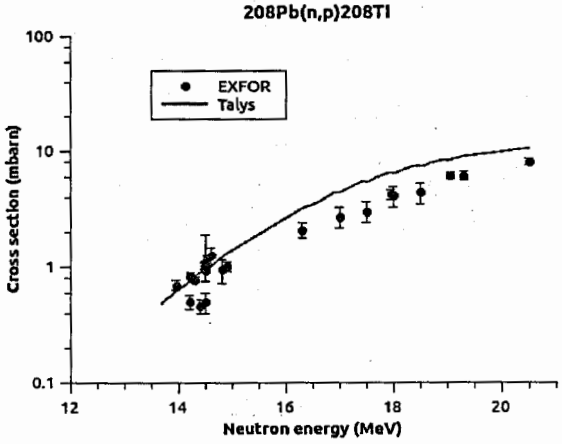

Fig. 4. Cross section of $^{208}Pb(n,p)^{208}Tl$ reaction at different neutron energies estimated in present work and experimental data taken from EXFOR database.

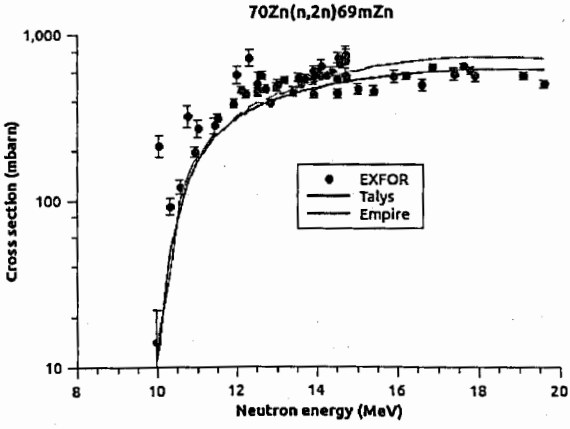

Fig. 5. Cross section of $^{70}Zn(n,2n)^{69m}Zn$ reaction at different neutron energies estimated in present work and experimental data taken from EXFOR database.

For ^{100}Mo (n, 2n) ^{99}Mo reaction

The graph of theoretical and experimental cross section data of ^{100}Mo(n,2n)^{99}Mo reaction from threshold to 20 MeV has been shown in Fig. 6. The theoretical cross section data for the above reactions have calculated by using different models of EMPIRE and TALYS. For EMPIRE code (i) MSD/MSD model with EGSM level density Model and Koning OM potentials and for TALYS (i) exciton model with Generalised super fluid level density model and Koning local OM potential.

Table 6: Contribution of pre-equilibrium in (n, p) and (n, 2n) reactions which is calculated through TALYS code at neutron energy 14.5 MeV

Reactions	TALYS 1.8 (with PE) (mb)	TALYS 1.8 (without PE) (mb)
^{67}Zn(n,p)^{67}Cu	41.83	13.58
^{92}Mo(n,p)^{92m}Nb	62.20	49.63
^{96}Mo(n,p)^{96}Nb	21.14	4.55
^{208}Pb(n,p)^{208}Tl	0.9120	0.2125
^{70}Zn(n,2n)^{69m}Zn	512.49	641.834
^{100}Mo(n,2n)^{99}Mo	1323.04	1652.5

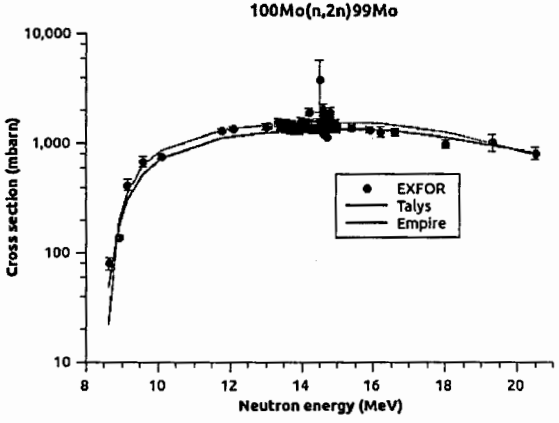

Fig. 6. Cross section of ^{100}Mo(n,2n)^{99}Mo reaction at different neutron energies estimated in present work and experimental data taken from EXFOR database.

Summary and Conclusions

1. We have calculated the neutron induced reaction cross section for the reactions ^{67}Zn(n,p)^{67}Cu, ^{92}Mo(n,p)^{92m}Nb, ^{96}Mo(n,p)^{96}Nb, ^{208}Pb(n,p)^{208}Tl and ^{70}Zn(n,2n)^{69m}Zn, ^{100}Mo(n,2n)^{99}Mo over the neutron energy range from threshold to 20 MeV.
2. In this model calculation, it was observed that the cross section is very sensitive to the optical model potential, level density model, and nuclear reaction models.
3. The result of calculations by TALYS 1.8 and EMPIRE 3.2.2 codes with allowance for pre-equilibrium processes are in best agreement with experimental data.

4. This comparison of theoretical data and experimental data is important in fusion/fission reactors and medical application technologies.

Acknowledgments

This work has been done under the research project sponsored by DAE-BRNS, Government of India (sanction no. 36(6)/14/23/2016-BRNS) and DST, Government of India (sanction no. INT/RUS/RFBR/P-250)

References

1. Herman M., et al. "EMPIRE-3.2 Malta modular system for nuclear reaction calculations and nuclear data evaluation." *International Atomic Energy Agency and Brookhaven National Laboratory Report* (2013). https://www.nndc.bnl.gov/empire/
2. Koning A., Hilaire S., and Goriely S. "TALYS-1.8, A Nuclear Reaction Program, NRG-1755 ZG Petten the Netherlands. (2015)." http://www.talys.eu/home/
3. Koning A.J., and Delaroche J.P. "Local and global nucleon optical models from 1 keV to 200 MeV." *Nuclear Physics A* **713**.3-4 (2003): 231–310
4. Capote R., et al. "RIPL–reference input parameter library for calculation of nuclear reactions and nuclear data evaluations." *Nuclear Data Sheets* **110**.12 (2009): 3107–3214.
5. IAEA Nuclear Data Services, https://www-nds.iaea.org/exfor/exfor.htm
6. Qaim S.M. "Total (n, 2n) cross sections and isomeric cross-section ratios at 14.7 MeV in the region of rare earth." *Nuclear Physics A* **224**.2 (1974): 319–330.
7. Kadenko A., et al. "Cross Sections of Neutron Reactions (n, p), (n, α), (n, 2n) on Isotopes of Dysprosium, Erbium, and Ytterbium at ~ 14 MeV Neutron Energy." *arXiv preprint arXiv:1306.6210* (2013).

NEUTRON DIFFRACTOMETRY CHANNEL OPTIMIZATION TO OBTAIN THE HIGHEST NEUTRON FLUX AND THE LEAST FAST NEUTRON NOISE

Gholamzadeh1 Z. *, Bavrngin E., Lamei Rashti M., Mirvakili S.M., Joze-Vaziri A.

Reactor Research School, Nuclear Science and Technology Research Institute, Tehran, Iran

Abstract

Neutron powder diffraction (NPD) is complementary to many other materials characterization techniques. Some material analyses are not possible using the other procedures such as investigation of magnetic properties of materials or distinguishing between the adjacent elements in the periodic table. In overall, neutron diffraction could involve many unique advantages: the neutron scattering strength is not dependent on the atomic number. In the present work, NPD system of 5 MW Tehran Research Reactor was modeled using MCNPX2.6.0 and Vitess 3.3a codes in details. The system uses a PG reflector to reflect 0.02–0.33 eV neutrons through the second collimator. The neutron spectra achieved by Vitess 3.3a code at sample position was compared with the available experimental data. Impact of Al_2O_3 filter on fast neutron noise at the sample position was investigated. The obtained data from the simulations showed good conformity with the experimental measurements. Our simulations showed registration of an adequate thickness of Al_2O_3 inside the NPD facility could decrease the fast neutron noise drastically.

Keywords: Tehran research reactor, neutron powder diffraction, MCNPX2.6.0, Vitess 3.3a

Introduction

Whereas the large capital costs associated with intense neutron sources, neutron diffraction is rarely the first technique used to study a particular material or a highly specialized way to provide critical information or facilitate a critical in situ experiment. It is possible to observe the effect of light elements in the presence in heavy ones in neutron diffraction patterns. Neutrons are deeply penetrating so they can diffract off specimens contained in cryo-refrigerators or furnaces, making it easy to examine materials under special conditions and in special environments. Unlike the case for X-Rays, the scattering of neutrons from materials can be accurately calculated making comparison to theoretical [1]. Today neutron diffraction plays a vital role in vast domains of science and technology while it makes ability of observation and analysis of many materials which was not possible by XRD or other diffraction techniques.

Mazzochi et al. reported a powder diffractometer has been recently installed on the IEA-R1 reactor at IPEN-CNEN/SP. IEA-R1 is a light-water open-pool research reactor. At present it operates at 4.5 MW thermal with the possible maximum power of 5 MW. At 4.5 MW the in-core flux is ca. 7×10^{13} $cm^{-2}s^{-1}$. In spite of this low flux, installation of both a position-sensitive detector (PSD) and a double-bent silicon monochromator has turned possible to design the new instrument as a high-resolution powder diffractometer [2].

Material and methods

TRR is a 5 MW pool-type light water research reactor. Its fuel assemblies contain low enriched uranium fuel plates in the form of U_3O_8Al alloy. The users apply two sections of the reactor pool. One of the sections contains experimental facilities like beam tubes, rabbit system, and thermal column. The other section is an open area for bulk irradiation studies. Fig. 1 shows the schematic view of TRR pools and irradiation facilities. TRR was simulated in

details using MCNPX 2.6.0[3] code as shown in Fig.1.

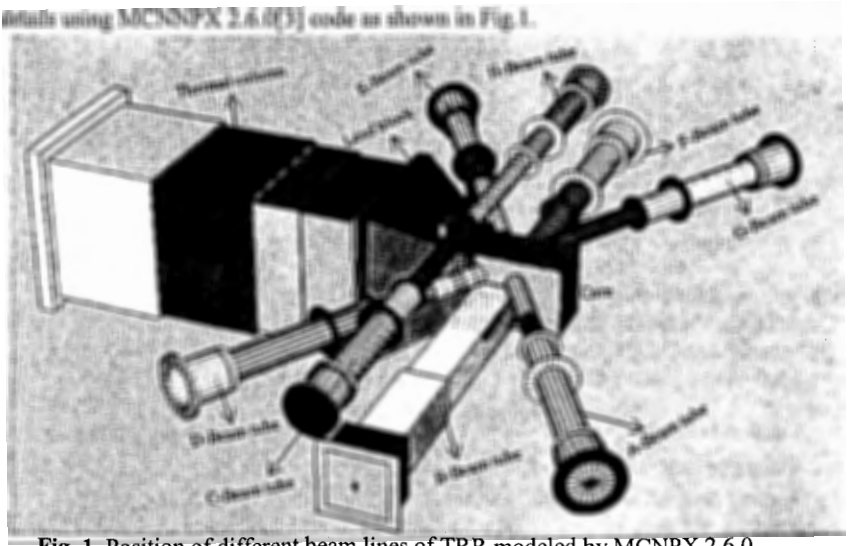

Fig. 1. Position of different beam lines of TRR modeled by MCNPX 2.6.0

In this facility D channel was allocated to NPD system. The equipped D channel was modeled using the Monte Carlo-based computation code (Fig.2).

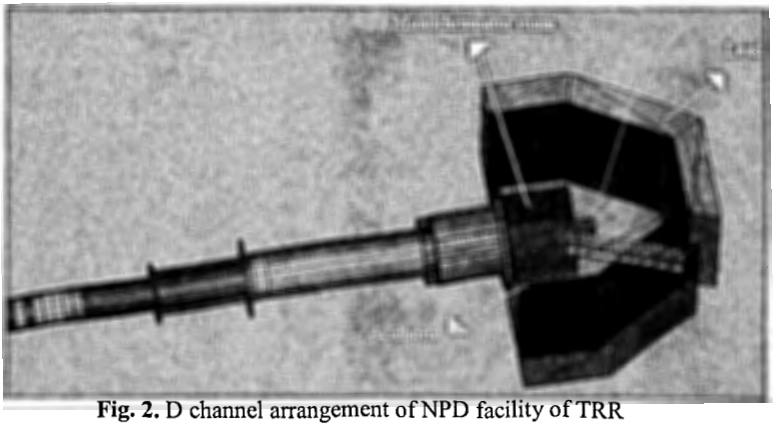

Fig. 2. D channel arrangement of NPD facility of TRR

Neutron and photon flux distributions were calculated along the NPD channel using the computational code. In addition, neutron spectra at the beginning of the NPD channel obtained from the MCNPX2.6.0 code was introduced as an input source for the Vitess 3.3a code [4] to investigate the reflected neutron spectra from the NPD system monochromator.

The PG monochromator is used in the current NPD facility of TRR was introduced in the Vitess 3.3a code according to Table 1.

Table 1- PG monochromator characteristics

d-spread	PG(002): 0.2 - 2′ 10^{-3}
d-spacing	PG(002): 3.332 Å
Thickness, with, height	0.2, 7.5, 5
Mosaic factor	2
d range factor	3

In pyrolytic graphite the crystallites are aligned to a high degree with their hexagonal c-axes parallel, whereas the a-axes are oriented at random. Therefore, the reflected neutrons are from the (00l) planes satisfying the Bragg equation:

$$n\lambda = 2d_{hkl}Sin\theta_{00l} \quad (1)$$

Where, n is the order of reflection, θ_{00l} is the glancing angle to the (00l) plane [5].

Neutron flux on wavelength was calculated after the PG monochromator and at the sample position, which is located 100 cm far from the second collimator exit.

The code uses F4 tally card to calculate neutron flux via the following equation [6]:

$$F4 = \frac{1}{V}\int_V dV \int_E dE \int_{4\pi} d\Omega\Phi(r,E,\Omega)\left(\frac{\#}{\frac{cm^2}{source\ particle}}\right) \quad (2)$$

Neutron noise was determined in the pathway of the neutrons flying directly from the second collimator to the sample position. The calculated neutron flux at the sample position was compared with the experimental data.

Al_2O_3 filter application inside the NPD facility was investigated to decrease the fast neutron noise at the sample position.

Result and discussion

D channel of the 5 MW reactor has a 305 cm length, at the final section of the channel a collimator was placed. The first collimator is a rectangular Soller-type collimator made of steel with the dimension of 6×11×120 cm. Neutron spectra was calculated using MCNPX2.6.0 at the beginning of the D channel (Fig.3).

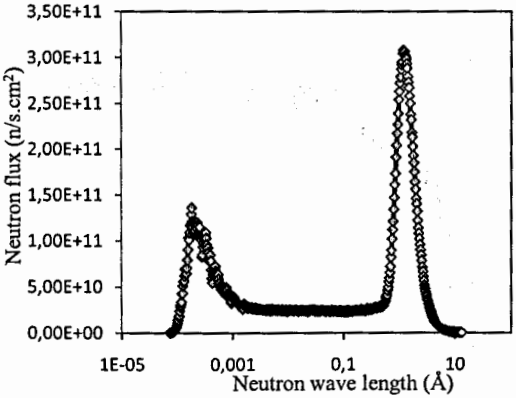

Fig. 3. Neutron spectra on wavelength at the beginning of NPD D channel facility of TRR

As the figure shows, there is a thermal neutron flux in order of 10^{11} n/s·cm^2 at the beginning of D channel. The obtained spectra from the MCNPX2.6.0 code exported to Vitess 3.3a code and the departing neutrons from the first collimator were investigated. According to Fig.4, the thermal neutron intensity drops 10^3 orders during its flight along the 3-meter D channel and its equipped collimator.

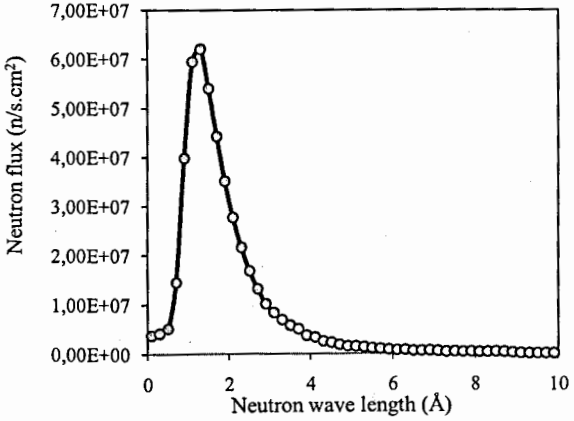

Fig. 4. Neutron spectra on wavelength at the exit of first collimator

Also fast neutrons with an intensity in order of 10^6 n/s·cm^2 are exiting from the first collimator toward the PG monocromator of the NPD system (Fig.5).

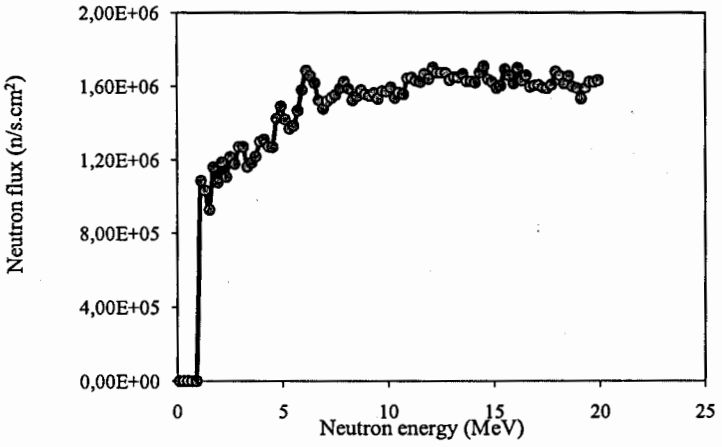

Fig. 5. Neutron spectra on energy at the exit of first collimator

The collimated neutrons collide on the PG monochromator positioned 15 cm far from the first collimator exit. The channel arrangement simulation by Vittes3.3a code showed the reflected neutrons from the monochromator would have a peak intensity of 1×10^6 n/s·cm^2. The monochromatic neutrons have 1–1.5 Å wavelength (Fig.6).

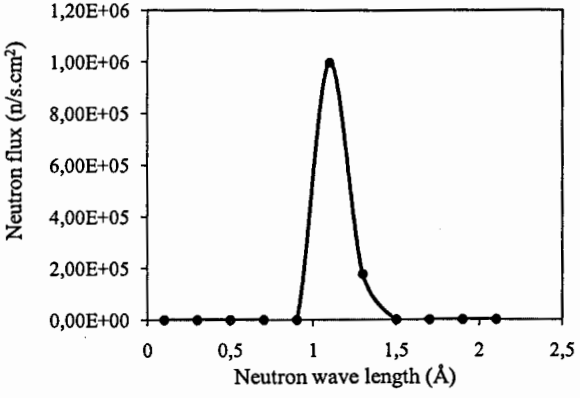

Fig. 6. Neutron flux intensity on wavelength after monochromator reflection

After reflection of low-energy neutrons (1–1.5 Å), the other neutrons available in the incident neutron spectra pass through the monochromator and follow their track approximately directly. Hence, as the Vitess code calculations show there is not fast neutron noise in the second collimator track. As illustrated before, a 60 cm long soller-type collimator was placed in the pathway of neutrons. The sample Table was placed at 122 cm interval than the second collimator exit. Vitess 3.3a code calculations showed the thermal neutron flux intensity at the

sample position is 0.5×10^3 n/s·cm^2 which has 40.5% relative discrepancy than the measured value; 0.84×10^3 (Fig.7).

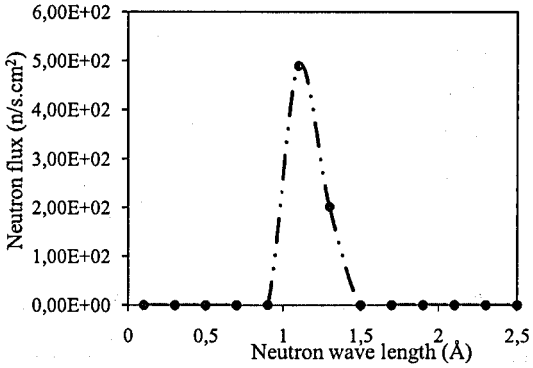

Fig. 7. Neutron flux intensity on wavelength at the sample position (122 cm from the second collimator)

Paraffin was filled around the monochromator room and an iron box with $10\times10\times10$ cm^3 (Fig. 8) was placed in the fast neutron pathway, the results showed higher thickness causes the fast neutron enhancement (Fig.9,10). The optimized dimension decreases the fast neutron flux up 36%. Al_2O_3 was investigated also but the obtained results showed the material positioning at this place is not effective than the iron box. Application of Al_2O_3 at the beginning of the channel resulted in 55% reduction of fast neutrons. Another iron box application after the shielding of monochromator room resulted in 66% reduction of the leaked fast neutrons. Application of Al_2O_3 after the monochromator room was not as efficient as iron box because it causes only 17% reduction of the fast neutrons.

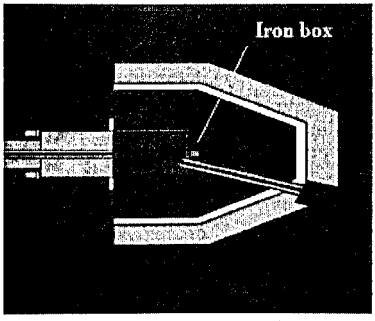

Fig. 8. Iron box view after monochromator room

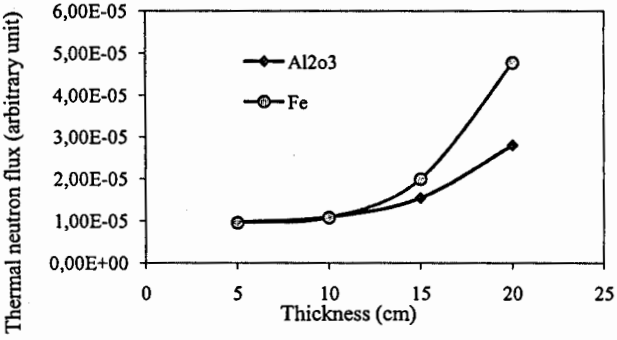

Fig. 9. Thermal neutron flux variation on filter thickness

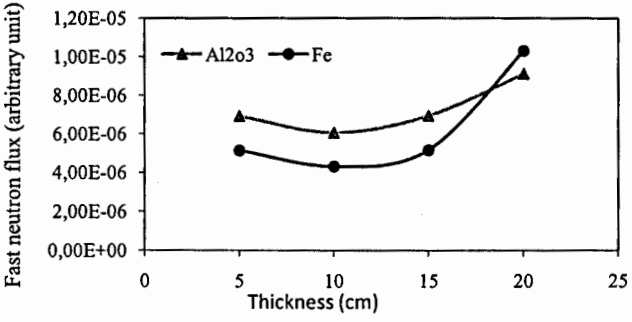

Fig. 10. Fast neutron flux variation on filter thickness

Conclusion

Vitess code application could desirably estimate the different structures of the system. This study showed Al_2O_3 and Fe application in different parts of the system can decrease the fast neutron flux considerably.

References

1. E.H. Kisi, C.J. Howard, Application of neutron powder diffraction, Oxford New York, 2008.
2. V.L. Mazzocchi, C.B.R. Parente, J. Mestnik-Filho, Y.P. Mascarenhas, Neutron diffraction patterns measured with a high resolution powder diffractometer installed on a low-flux reactor, IAEA.
3. Pelowitz D.B., "Users' manual versión of MCNPX2.6.0 ", LANL, LA-CP-07-1473, 2008.
4. K. Lieutenant, G. Zsigmond, M. Fromme, S. Manoshin, General features of the neutron instrument simulation package VITESS.
5. M. Adib, N. Habib, M.S. El-Mesiry and M. Fathallah, CHARACTERISTICS OF PYROLYTIC GRAPHITE AS A NEUTRON MONOCHROMATOR Proceedings of the 8th Conference on Nuclear and Particle Physics, 20-24 Nov. 2011, Hurghada, Egypt.
6. Briesmeister J.F., MCNP-A General Monte Carlo N-Particle Transport code Version4C, Los Alamos National Laboratory Report, USA, LA-13709-M, 2000.

POTENTIAL INVESTIGATION OF ^{99}Mo PRODUCTION VIA UO_2SO_4 LIQUID TARGETS CONTAINING ^{NAT}U IN A 5 MW RESEARCH REACTOR

Gholamzadeh Z., Davari A., Joze-Vaziri A., Mirvakili S.M.

Reactor Research School, Nuclear Science and Technology Research Institute, Tehran, Iran

Abstract

The most routine methods of ^{99}Mo production are either by ^{98}Mo(n,γ)^{99}Mo reaction or by ^{235}U(n,f)^{99}Mo fission process; the highest specific activity of ^{99}Mo among all production methods is achieved by the second process. However, recently some research centers have directed their attention toward liquid target application instead of the previously mentioned solid ones. Therefore, this work investigates the production potential of ^{99}Mo using uranyl sulphate liquid target irradiation in a 5 MW nuclear research reactor. Irradiation of four liquid targets involving natural uranium was theoretically investigated in the TRR irradiation boxes. The most optimize uranyl sulfate concentration was determined to fulfill convection condition of the TRR irradiation box cooling. The burn up calculations using the MCNPX 2.7.0 code showed about 5 Ci of ^{99}Mo is produced after 7-days irradiation at 4 MW power. Application of an enforced cooling inside the irradiation boxes could easily increase the radioisotope production rate to >100 Ci. Low cost of such liquid targets, extraction of gaseous fission products, short-time chemically separation of the proposed products and reusability of the irradiated liquid target are the main attractions of such method for ^{99}Mo production.

Keywords: ^{99}Mo production, ^{nat}Uranyl sulfate, MCNPX, Reactor irradiation

Introduction

The medical community has been weighed down by ^{99}Mo shortages due to aging of reactors such as the NRU (National Research Universal) reactor in Canada. There are currently no US producers of ^{99}Mo, and NRU is scheduled for shutdown in 2016, which means that another ^{99}Mo shortage is needed unless a potential domestic ^{99}Mo producer fills the void [1–2]. Currently solid target plates are used for the production of ^{99}Mo. The targets are generally either miniature Al-clad fuel plates or pins containing U–Al alloy or a thin film of UO_2 coated on the inside of a stainless steel tube [3]. In these targets, separation of ^{99}Mo from the other fission products produced inside the target after irradiation is started by the target dissolution either with alkali or acid material. However, aqueous homogenous reactors inspirit such imitation by modeling a liquid target instead of the pervious mentioned solid ones.

Hence, feasibility and economically study of such liquid target irradiation in research reactor in order to ^{99}Mo and possibly other radioisotopes production was proposed in this work.

Material and methods

In this work, MCNPX 2.6.0 has been used as a powerful particle transport code with the ability to calculate steady-state reaction rates, normalization parameters, neutronic

parameters, as well as fuel burn up using CINDER90 to calculate the time-dependent parameters [4–5].

A cylindrical aluminum container involved uranyl sulfate solution was modeled using the MCNPX 2.6.0 code. A 3D neutronic model was set up using the MCNPX 2.6.0 code in cold zero power situations by means of ENDF/B-VI continuous-energy cross section. The cross sections of S(α,β) was used for the fuel solution and light water. KCODE card of the computational code was used for neutronic parameter calculations. 1500000 particle histories were transported to decrease the calculation errors to less than 2%. The modeled liquid target specifications are presented in Table 1.

Table 1 Liquid target material and dimensions modeled using MCNPX 2.6.0

sample specifications	value	unit
Fuel solution ($^{Nat}UO_2SO_4$): ^{235}U, ^{238}U, O, H, S	1.2-1.3	g/cm^3
Aluminum container: Al, Fe, Cu, Mn, Si	2.70	g/cm^3
Target dimension	0.55×8	cm
Al clad thickness	0.2	cm

Four modeled targets containing about 7.5 cm^3 of the liquid solution were positioned at the irradiation boxes of the 5 MW Tehran Research Reactor (Fig.1).

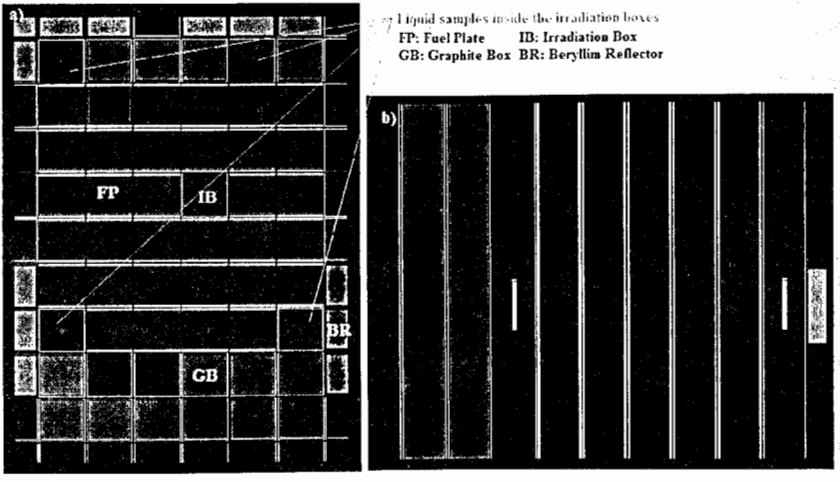

Fig. 1. Cross sectional view of TRR containing the liquid targets a) radial b) axial

Three types of sulfate solutions containing different concentrations of dissolved uranium were considered to be used as liquid solution to produce ^{99}Mo and other possible radioisotopes. Deposited power inside the modeled solution targets was calculated separately. Different concentrations of fissionable component of the liquid sample were investigated and an optimum concentration was suggested. Radial and axial deposited power was determined inside an optimum selected liquid sample using mesh tally card of the used code. ^{99}Mo, ^{131}I and ^{133}Xe production yield after 7-days irradiation of the different liquid samples comprised the optimum concentration of the fissionable isotopes were investigated. BURN card of the computational code was used to calculate fission process inside the irradiated samples. The calculations were repeated for a shell-type cylindrical geometry involves 227 cm^{3}of the liquid sample.

Results and discussion

Considering natural convection of the irradiation boxes, maximum bearable heat should be kept less than 50 W to avoid boiling of the liquid target during the 7-days irradiation. According to Table 2, a concentration of 180 g/lit will result in maximum deposited power <40 W.

Table 2 Deposited heat inside the liquid targets, the calculation errors <2%

Channel No	Uraniumconcentration: 30 g/l	Uraniumconcentration: 90 g/r	Uraniumconcentration: 180 g/l
		Depositedpower (W)	
1	8.87	17.18	32.99
2	6.25	12.28	24.11
3	10.31	19.77	38.34
4	9.89	19.27	35.41

Axial calculated deposited heat inside the cylindrical target with 7.5 cm^3 uranyl sulfate showed maximum value is <1 W/cm^3 (Fig.2a), while radial sectioning of the sample with height of 8 cm shows the value is <3 W/cm^3 (Fig.2b).

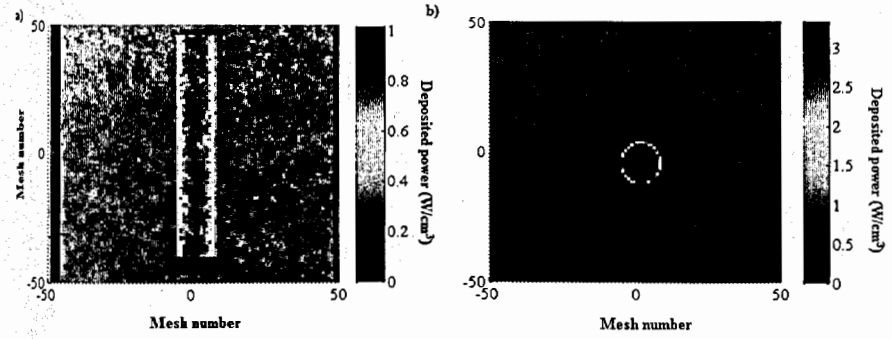

Fig. 2. Deposited heat inside the liquid target a)axial b)radial

Burn-up calculations showed about 1 Ci of ^{99}Mo is produced inside the 7.5 cm^3 liquid samples involved natural uranium (Table 3).

Table 3 Activity of different produced radioisotopes in 7.5 cm^3 targets after 7-days irradiation, Uranium concentration: 180 g/l

Channel No	^{99}Mo (Ci)	^{131}I (Ci)	^{133}Xe (Ci)
1	1.306	0.328	0.897
2	0.873	0.218	0.600
3	1.418	0.357	0.976
4	1.337	0.336	0.920

Total produced ^{99}Mo at the EOC is 4.93 Ci. About 1 Ci of ^{131}I and 3 Ci of ^{133}Xe is produced at the EOC.

By geometry optimization and an enforced cooling with 0.5 m/s flow in the irradiation boxes, 1000 W deposited power is easily removed during the sample irradiation. The calculations showed about 90 Ci of ^{99}Mo is produced inside the liquid irradiated sample at EOC.About 62 Ci of ^{131}I and 22 Ci of ^{133}Xe is produced too (Table 4).

Table 4 Activity of different produced radioisotopes in 227 cm^3 targets after 7-days irradiation, Uranium concentration: 180 g/l

Channel No	^{99}Mo (Ci)	^{131}I (Ci)	^{133}Xe (Ci)
1	23.93	6.02	16.45
2	17.48	4.39	12.00
3	26.56	6.7	18.27
4	24.57	6.19	16.89

Axial calculated deposited heat inside the cylindrical target with 227 cm^{3}volume showed maximum value is <2 W/cm^3 (Fig.2a), while radial sectioning of the sample with height of 14 cm shows the value is <3 W/cm^3 (Fig.2b).

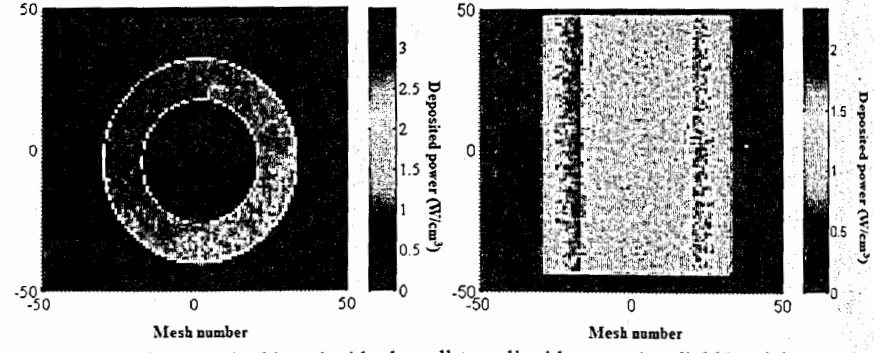

Fig. 3. Deposited heat inside the sell-type liquid target a) radial b) axial

Thermal-hydraulic calculations showed the investigated target maximum temperature is less than 70 °C by application of 0.13 m/s flow rate.

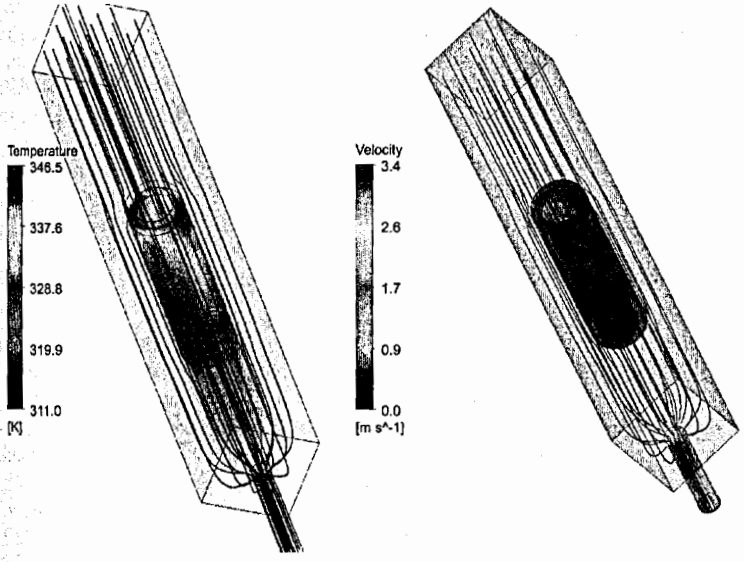

Fig. 4. Temperature profile along the liquid target length

Conclusion

The manuscript findings show that application of the liquid target with an optimized geometry opens an attractive method for simultaneously production of ^{99}Mo because of potentially production of several radioisotopes along with, minimization of radio-biologically hazardous nuclear effluent, reusable potential of the liquid target and its low cost.

References

1. Rao, A., Kumar Sharma, A., Kumar, P., Charyulu, M.M., Tomar, B.S., & Rama Kumar, K.L. (2014) Studies on separation and purification of fission ^{99}Mo from neutron activated uranium aluminum alloy. J. Appl. Radiat. Isot., 89, 186–191.
2. Muenze, R., Juergen Beyer, G., Ross, R., Wagner, G., Novotny, D., Franke, E., Jehangir, M., Pervez, S., & Mushtaq, A. (2013). The fission-based ^{99}Mo production process ROMOL-99 and its application to PINSTECH Islamabad. Sci. Technol. Nucl. Install., 2013.
3. Ali, K.L., Ahmad Khan, A., Mushtaq, A., Imtiaz, F., MaratabZiai, A., Gulzar, A., Farooq, M., Hussain, N., Ahmed, N., Pervez, S., Zaidi, J.H., 2013. Development of low enriched uranium target plates by thermo-mechanical processing of UAl2–Al matrix for production of ^{99}Mo in Pakistan. J. Nucl. Eng. and Des. 255, 77– 85.
4. Pelowitz, D.B., 2008. MCNPX User's Manual. Version 2.6.0.s.l.: Los Alamos National Laboratory (LANL), LA-CP-07-1473.
5. Fensin, M.L., 2008. Development of the MCNPX Depletion Capability: A Monte Carlo Depletion Method that Automates the Coupling between MCNPX and CINDER90 for High Fidelity Burnup Calculations. Florida University.

GEOMETRY OPTIMIZATION OF URANYL NITRATE LIQUID TARGET SYSTEM FOR ^{99}Mo PRODUCTION USING 30 MeV PROTON CYCLOTRON

Z. Gholamzadeh[1], S. Mohammadi[2], S.M. Mirvakili[1], F. Faghihi[2]

[1]Reactor Research School, Nuclear Science and Technology Research Institute, Atomic Energy Organization of Iran (AEOI), Tehran 14399-51113, Iran

[2]Department of Nuclear Engineering, School of Mechanical Engineering, Shiraz University 71936-16548 Shiraz, Iran

Abstract

^{99}Mo radioisotope is widely demanded by world community for both therapy and imaging purposes. Accelerator and reactor-based routine procedures are applied to produce this radioisotope. Newly proton-fission production method has been taken in attention by some research centers. In the present work, computationally investigation of the ^{99}Mo production yield in uranyl nitrate liquid targets irradiated by 30 MeV proton particles was aimed. In the present work, height and radius of the chamber of the liquid target are optimized considering minimum required solution for production of an adequate amount of ^{99}Mo. The obtained results showed uranyl nitrate liquid targets could be efficiently used to produce 18.83 Ci yield of ^{99}Mo using 30 MeV proton irradiation of the optimized-dimension target after 150 μA current application for 24 hours irradiation. Also this accelerator-based procedure using proton-fission induction in the natural uranium dissolved in nitrate solution presents a potentially competitive alternative in comparison with the reactor-based or other accelerator-based methods to produce ^{99}Mo and some other fission products simultaneously.

Keywords: ^{99}Mo production, ^{nat}Uranyl nitrate, MCNPX, Accelerator irradiation

Introduction

Technetium-99m is a principal radioisotope used for medical diagnostic imaging and accounts for approximately 80% of all nuclear medicine procedures. ^{99m}Tc is the daughter product of ^{99}Mo, and it is usually supplied in the form of a ^{99}Mo/^{99m}Tc generator to make diagnostic radiopharmaceuticals [1]. The global supply chain of ^{99}Mo used for generator production has several complex difficulties, which makes the system fragile and unreliable. Aging reactors, limited suppliers and transportation obstacles are all challenges faced with the supply chain. ^{99}Mo has been exclusively produced in 7 nuclear reactors, with an average age of these reactors being more than 40 years old. These 7 nuclear reactors are the Belgian Reactor 2 (BR-2) in Belgium, High Flux Reactor in The Netherlands, LVR-15 REZ Reactor in the Czech Republic, Maria Research Reactor in Poland, National Research Universal (NRU) in Canada, Open Pool Australian Light water reactor in Australia, and South African Fundamental Atomic Research Installation in South Africa [2].

After being produced in nuclear reactors, is ^{99}Mo transported to a processing facility to be chemically separated and purified. There are currently only 5 ^{99}Mo -processing facilities in

Australia, the Institute for Radio Elements (IRE) in Belgium, Mallinckrodt in the Netherlands, Nordion in Canada, and Nuclear Technology Products (NTP) Radioisotopes SOC Ltd. in South Africa. The finished ^{99}Mo product material is then isolated and shipped to 1 of 8 generator-manufacturing facilities that supply ^{99}Mo in the form of a ^{99}Mo/^{99m}Tc generator to send users, such as nuclear pharmacies and hospitals [2].

Currently other new methods for production of this important radioisotope are studied by approach of eliminating HEU targets and supplement in small scales for region and central use. In this way solid target plates are used for the production of ^{99}Mo. The targets are generally either miniature Al-clad fuel plates or pins containing U–Al alloy or a thin film of UO_2 coated on the inside of a stainless steel tube [3]. Hence, feasibility and economically study of such liquid target irradiation by proton accelerators in order to ^{99}Mo production was proposed in this work.

Material and methods

In this study, MCNPX 2.6.0 was used for investigation of feasibility of productionusing proton-fission induction and optimization of geometrical condition of utilized uranyl nitrate liquid target. MCNPX^{TM} is a general purpose Monte Carlo radiation transport code designed to track many particle types over broad ranges of energies. MCNPX 2.6.0 is the latest Radiation Safety Information Computational Center (RSICC) release of the code that includes many new capabilities, particularly in the areas of transmutation, burnup and delayed particle production [4]. ^{99}Mo production yield was determined according to the MCNPX results obtained by HISTP card of the input file. HISTP solves Batman decay chain equations using CINDER90 package involved in the MCNPX code.

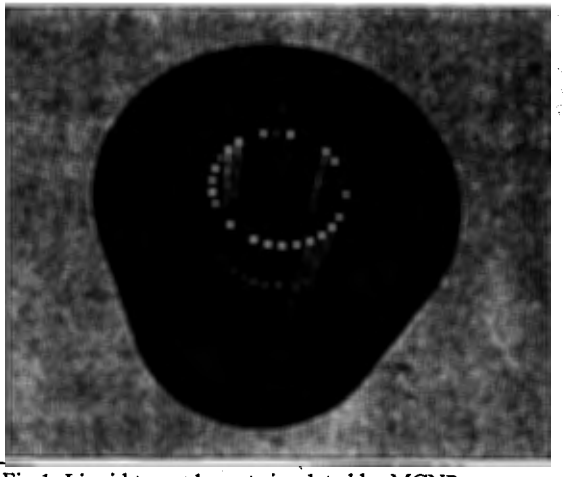

Fig.1. Liquid target layout simulated by MCNP.

In this study, the liquid target system is simulated according to the targetry used at both Duke University Medical Cyclotron and Wisconsin Medical Cyclotron for F-18 production (see Fig.1) [5]. General scheme of the simulated target is shown in Fig. 2. This target system includes the main body which made of ZnCu (target holder), cooling channels, beam line and

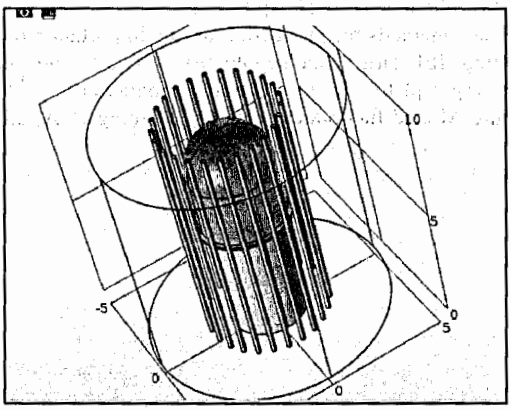

Fig.2. 3D view of liquid target without container (Target holder).

target container (Target chamber). Beam window of the target system is a 500-micron aluminum layer and helium cooling layer with a thickness of 1 mm was considered to cool the lateral surfaces of the container. Next, the ^{99}Mo production has been investigated in various radiuses of cylindrical liquid target, and height changes and an optimized dimension was suggested.

Results and discussion

Our liquid target solution contains 20 grams per liter concentration of natural uranium. It is assumed that this target is irradiated by a 30 MeV proton beam energy with 150 A current that produced by a cyclotron accelerator. The target radius changed as 2 mm, 4 mm, 6 mm and 8 mm and deposited heat power and molybdenum production yields were investigated in any different situations. According to Fig. 3 it can be seen that ^{99}Mo yield has max value of 193.4898 Mbq/μAh using 2 mm radius. Other results such as deposited heat power and proton flux that obtained by calculations were given in Table1.

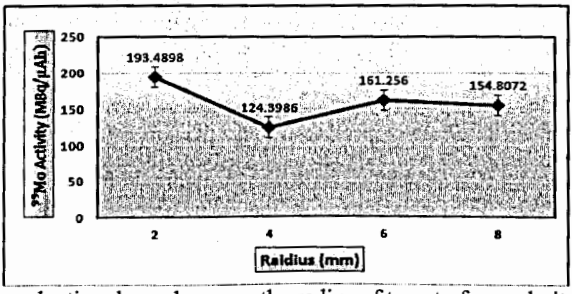

Fig.3. ^{99}Mo production dependence on the radius of target of uranyl nitrate solution.

Table 1. Some of important information in liquid target, the calculation errors <1%.

Radius (mm)	Neutron Flux ($n/cm^2 \cdot s$)	Proton Flux ($p/cm^2 \cdot s$)	Total Deposited Heat Power (W)	Neutron fission heat power (W)	Target Volume (cm^3)
2	1.61E+12	4.18E+14	6.52E+01	1.62E-04	1.42E-01
4	1.24E+12	2.99E+14	9.37E+02	5.52E-04	6.37E-01
6	9.60E+11	1.91E+14	3.71E+03	1.05E-03	1.58E+00
8	7.56E+11	1.17E+14	8.62E+03	1.58E-03	3.08E+00

First, we discuss about the total deposited heat power in liquid target. We know that by increasing the radius of the target, the solution proton-exposure is increased. By volume increasing more fission could occur in the solution and obviously more total and also neutron-fission deposited heat power in solution is experienced so that from 65.2 W in a radius of 2 mm reaches to the extra-large value of 8.62 kW in radius of 8 mm. However, in this case (kW heat power) the jet cooling is applicable, but taken attention to working with radioactive materials we are interested to minimize other problems such as difficulties related to the heat transfer. So by regarding both terms of production yield and heat transfer, the radius of 2 mm is really more desirable than others.

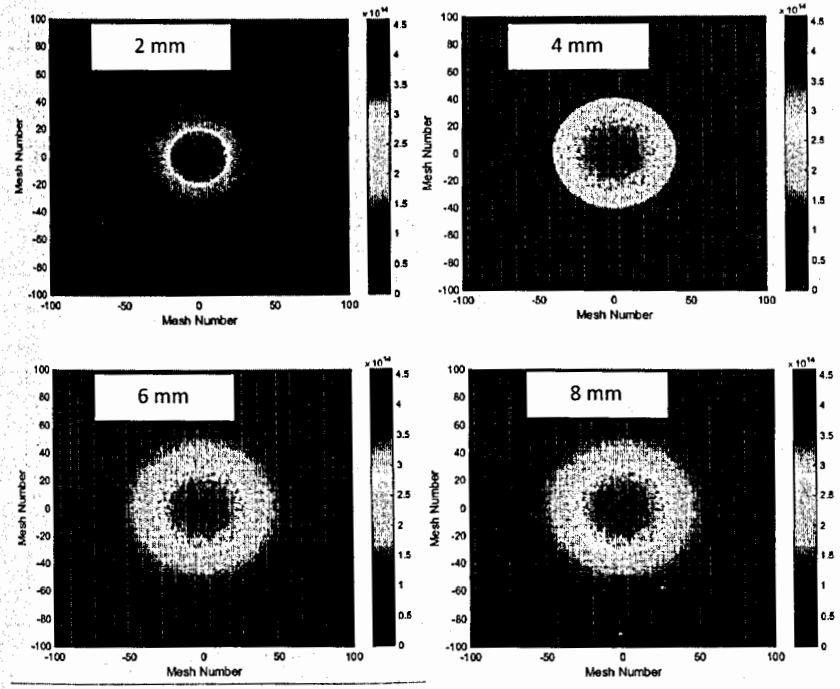

Fig. 4. Proton flux distribution inside the targets with different radii.

It was expected that by the radius increasing, the production yield increases because a Gaussian distribution with a FWHM (Full Width Half Maximum) of 0.8 was used to irradiate the cylindrical liquid target. However it should be illustrated the chain reactions involving absorption, decay and production determine the final yield of the product. Enhancement of neutron flux could decrease ^{99}Mo yield because of n+^{99}Mo reaction rate. According to Fig. 1 clearly higher radius experience higher proton flux availability and thereby higher deposited heat. The carried out calculations showed 2 mm radius is desirable to produce the highest ^{99}Mo yield and the least deposited power.

In the next step different height of the target was investigated. According to our calculation results, height variation does not cause a significant change in the production of ^{99}Mo (Table 2).

Table 2. Some of important information in liquid target, the calculation errors <1%.

Height (mm)	Neutron Flux (n/cm^2·s)	Proton Flux (p/cm^2·s)	Total Deposited Heat Power (W)	Neutron fission heat power (W)	Target Volume (cm^3)
8	1.84E+12	5.08E+14	5.37E+01	1.53E-04	1.17E-01
12	1.43E+12	3.56E+14	7.68E+01	1.69E-04	1.68E-01
16	1.17E+12	2.73E+14	9.98E+01	1.80E-04	2.18E-01
20	9.89E+11	2.22E+14	1.23E+02	1.86E-04	2.68E-01

Height of 8mm, 12 mm, 16 mm and 20 mm have been checked and according to Table 2 by increasing the volume and mass of the irradiated solution, total and neutron-fission deposited heat power enhances. But the protons and neutrons flux is reduced as a result of absorption process. Axial distribution of neutron and proton flux is shown in Fig.5. According to the figure there is an intense distribution at the beginning of the target.

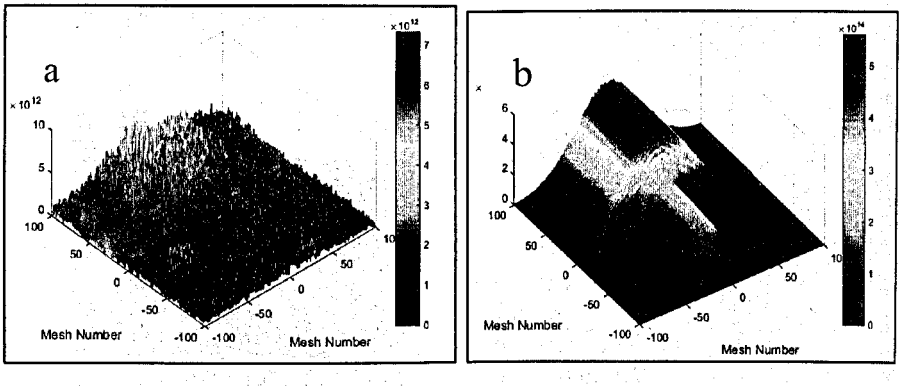

Fig.5. Distribution of a) neutron flux and b) proton flux in liquid target.

According to the results, as well as the fact that none of the investigated heights have no preference in terms of the production yield. The height can be selected arbitrary. Because better heat transfer occurs in bigger target area so we choose a height of 20 mm. For 24 hours

irradiation the ^{99}Mo yield is about 18.83 Ci. Therefore, we would account the number of required uranium atoms by A=λN equation. So, the necessary number of atoms is equal to 4E+15 while the available atoms inside the solution are 7.43E+18 for2.68E–1 cm^3 target volume (according to a radius of 20 mm). So this tiny target could be used to produce desirable amount of ^{99}Mo in low-cost condition with minimum nuclear waste and independency to rector-based procedures.

Conclusion

The liquid target containing natural uranium can customize and develop our prospects for the peaceful use of the nuclear industry and also be regarded as excellent replacement of HEU solid target. In the same time this procedure reduces our dependency to high-cost operation nuclear reactors. Our funding showed about 18.83 Ci/week of ^{99}Mo is producible by means of the optimized target.

References

1. Radioisotopes in medicine. World Nuclear Association website.http://www.world-nuclear.org/information-library/non-power-nuclear-applications/radioisotopes-research/radioisotopes-in-medicine.aspx. Updated December 28, 2016. Accessed January 30, 2017.
2. Nuclear imaging: global Mo-99 supply chain. Mallinckrodt Pharmaceuticals website. http://www2.mallinckrodt.com/nuclear_imaging//global_mo-99_supply.aspx. Updated 2015. Accessed January 11, 2017.
3. Ali, K.L., Ahmad Khan, A., Mushtaq, A., Imtiaz, F., MaratabZiai, A., Gulzar, A., Farooq, M., Hussain, N., Ahmed, N., Pervez, S., Zaidi, J. H., 2013. Development of low enriched uranium target plates by thermo-mechanical processing of UAl2–Al matrix for production of 99Mo in Pakistan. J. Nucl. Eng. and Des. 255, 77– 85.
4. Pelowitz, D.B., 2008. MCNPX User's Manual. Version 2.6.0.s.l.: Los Alamos National Laboratory (LANL), LA-CP-07-1473.
5. Peeples, J. L., Stokely, M. H., & Doster, J. M. (2011). Thermal performance of batch boiling water targets for 18 F production. Applied Radiation and Isotopes, 69(10), 1349–1354.

The Ion and Gamma Backgrounds in the Experiment on Radiative Neutron Decay

Khafizov R.U.[a], Kolesnikov I.A.[a], Nikolenko M.V.[a], Tarnovitsky S.A.[a], Tolokonnikov S.V.[a], Torokhov V.D.[a], Trifonov G.M.[a], Solovei V.A.[a], Kolkhidashvili M.R.[a], Konorov I.V.[b]

[a]NRC «Kurchatov Institute», Russia
[b]Technical University of Munich, Munich, Germany

Annotation

The aim of the new experiment on radiative neutron decay is the measurement of its main characteristic, the branching ratio - BR. The methodology is focused on measuring the spectra of triple coincidences of radiative gamma-quantum, beta electron, and recoil proton and double coincidences of beta electron and recoil proton. The peak on the spectrum of triple coincidences shows the number of radiative neutron decays, while the peak on the spectrum of double coincidences shows the number of regular neutron beta-decays. This methodology enabled us to become the first team to measure the branching ratio of radiative neutron decay B.R. = $(3.2 \pm 1.6)\cdot 10^{-3}$ (where C.L. = 99.7% and gamma quanta energy exceeds 35 keV) in 2005 on our old experimental equipment.

The precision of branching ratio measurement is determined using the value of the ion and gamma backgrounds. The spectrum of double coincidences obtained in our experiment shows a fairly significant ion background, the fluctuations of which indicate the precision of measurement for the number of recoil protons. The spectrum of triple coincidences shows a significant gamma background, the fluctuations of which determine the precision of measurement for the number of triple coincidences. Because the ion background specifically is quite significant, it appears even under super deep vacuum as beta electrons ionize the highly rarified air inside the chamber. Besides, we discovered an additional wide peak on the spectrum of triple coincidences. This peak consists of delayed gamma quanta created during the ionization of rare gas by beta-electrons.

Thus, this experiment allows us to study another important phenomenon, the ionization of rarified gas by beta electrons with emission of gamma quanta. Our last experiment showed that these two phenomena, radiative neutron decay and ionization with gamma quanta emission, are distinguishable in the case of high time resolution and can be studied separately. This is another important result of our last experiment and in this report we mention that the authors of articles registered namely the ionization with gamma radiation events.

From this it follows that the research of the ion and gamma backgrounds is a critically important task for this experiment. This report is dedicated to a discussion of the computer experiment we conducted using the well-known GEANT4 software package. One of the main goals of these Monte-Carlo calculations is to obtain the ion and gamma background conditions for conducting the experiment. The report presents the results of these calculations along with a comparison of our measurements of double coincidence and triple coincidences, with two other experimental groups. One of the main results of our computer experiment is the evaluation of background conditions, which shows that the geometry and materials we selected allow us to measure the branching ratio with precision of several percentage points.

Introduction

Presently, the characteristics of the ordinary decay mode are measured with precision of tenths of a percentage point. Under these circumstances, the experimental data obtained by different groups of experimentalists can be reconciled only by taking into account the

corrections calculated within the framework of the standard theory of electroweak interactions. This means that the experimental research of the ordinary mode of neutron decay have exhausted their usefulness for testing the standard model. To test the theory of electroweak interaction independently, it is necessary to move from the research of the ordinary branch of decay to the next step, namely, to the experimental research of the radiative decay branch.

The radiative decay branch of elementary particles, where an additional particle, a radiative gamma quantum is formed along with the regular decay products, has been discovered for practically all elementary particles. This has been facilitated by the fact that among the rare decay branches the radiative branch is the most intensive, as its value is proportional to the fine structure constant α and is only several percent of the intensity of the regular decay mode (in other words, the relative intensity B.R. of the radiative decay branch has the value of several hundredths of a unit.)

However, for the neutron this decay branch had not been discovered until recently and considered theoretically only [1–4]. Our first attempt to register the radiative neutron decay events was made on intensive cold neutron beam at ILL [5]. But our experiment conducted in 2005 at the FRMII reactor of Munich Technical University became the first experiment to observe this elementary process [6]. We initially identified the events of radiative neutron decay by the triple coincidence, when along with the two regular particles, beta electron and recoil proton, we registered an additional particle, the radiative gamma quantum

$$n \rightarrow p + e^- + \nu + \gamma,$$

and so could measure the relative intensity of the radiative branch of neutron decay B.R.= $(3.2 \pm 1.6)\cdot 10^{-3}$ (with C.L.= 99.7% and gamma quanta energy over 35 keV; before this experiment we had measured only the upper limit on B.R. at ILL [5]).

The main characteristic of any rare mode of elementary particle decay is its relative intensity, branching ratio (BR). By definition, BR is equal to the ratio between the intensity of the rare decay mode and the intensity of the ordinary mode. In the case of neutron, this intensity ratio can be reduced to the ratio between the number of triple coincidences between the registration of beta-electrons, radiative gamma-quantum and the delayed proton N_T to the number of double coincidences between the registration of the ordinary decay products, beta electron and recoil proton N_D:

$$BR = I(\text{radiative decay}) / I(\text{ordinary decay}) = N(e,p,\gamma) / N(e,p) = N_T / N_D$$

These two values can be determined only from the analysis of double and triple coincidences spectra, which form corresponding peaks. Identifying these peaks and distinguishing them from the significant background is the central problem in the methodology of BR measurements for neutron radiative decay.

Further, this experimental BR value needs to be compared with the theoretical value, estimated within the framework of the electroweak model. Any difference between these two values would mean that we are observing a deviation from the electroweak interaction theory.

Our group calculated the neutron radiative spectrum in the framework of standard electroweak theory in the following papers [1–4]. The calculated branching ratio for this decay mode as a function of the gamma energy threshold was published in these papers. BR value for the energy region over 35 keV was calculated to be about $2.1\cdot 10^{-3}$.

It follows that to measure the main characteristic of radiative neutron decay it is necessary to obtain and analyze the spectra of double and triple coincidences. So, it is necessary to consider the main particularity of these spectra – the ion and gamma backgrounds.

Let us consider in detail the question around the value of ion background in the experiment on radiative neutron decay, namely, its value in the spectrum of double coincidences of electron and proton. Theory makes it clear that the number of ions created by an electron that spreads in the media of its path with length of L is equal to $N_{ion} = L/\lambda$. Here λ is the length of the electron's free path in media with molecular density n. If ionization cross section of media is σ_i, then the length of the free path is inversely proportional to the product of media density to the cross section $\lambda = (n\sigma_i)^{-1}$. On the other hand, if the probability of the one media atom ionization is $P(n)$, then the number of ions N_{ion} created when the electron cross the media equals the product of this probability to the total number N of atoms on the electron trajectory length L. This number is equal to the ratio of the trajectory length L to the average distance between nearest atoms of media $\ell = n^{-1/3}$ with density n: $N = L/\ell$. Thus, we arrive at the following chain of equations:

$$N_{ion} = \frac{L}{\lambda} = Ln\sigma_i = P(n)N = P(n)\frac{L}{\ell} = P(n)Ln^{1/3}$$

Thus, the classic probability of ion creation per one media atom with density n is equal to the ratio between the two areas – that of ionization cross section σ_i to area $S = n^{-2/3}$, the area per one media atom: $P(n) = \sigma_i/S = \sigma_i n^{2/3}$.

This formula occurs in the simplest model of a "perfectly black sphere". Introducing a random value, aim distance ρ, leads to the probability of ionization dependent on that aim distance of $P(\rho) = 1$ for all aim distances shorter than the atom radius $a = (\sigma_i/\pi)^{1/2}$ while for greater aim distances probability of ionization is 0 (see Fig. 1).

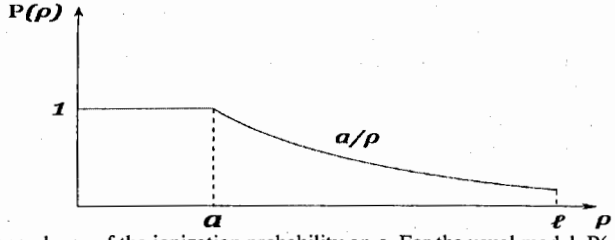

Fig. 1. The dependence of the ionization probability on ρ. For the usual model: $P(\rho)=1$ for $\rho<a$ and $P(\rho)= 0$ for $a < \rho < \ell$; for Coulomb interaction model $P(\rho) = 1$ and $P(\rho) = a/\rho$ for $a < \rho < \ell$.

However, in the case of ionization process in highly rarefied media this simple model becomes inaccurate as it does not take into account Coulomb interaction, which may have a fairlylong "Coulomb tail" inversely proportional to the aim distance. In this case, one must consider a more realistic model where probability $P(\rho)$ is not zero, when the electron flies by the atom without touching it, i.e. at aim distances ρ greater than a. So, it is necessary to consider the long "tail" of $P(\rho)$ distribution, which falls inversely proportionally to the aim distance (see Fig. 1). Thus, the total ionization cross section will depend on density and have an additional term, inversely proportional to the cubic root of media density n:

$$\sigma_{tot} = \int_0^{2\pi} d\varphi \int_0^{a} \rho d\rho + \int_0^{2\pi} d\varphi \int_a^{l} \frac{a}{\rho} \rho d\rho = \pi a^2 + 2\pi a(l-a) = -\pi a^2 + 2\pi a l = -\sigma_i + 2(\pi\sigma_i)^{1/2} n^{-1/3}$$

The probability of ionization per one atom will be: $P(n) = \sigma_{tot} n^{2/3} = -\sigma_i n^{2/3} + 2(\pi\sigma_i)^{1/2} n^{1/3}$. It is evident that in extremely rarified media where $\sigma_i n^{2/3}$ is significantly below 1, the second member of this formula leads and significantly exceeds the first. Thus, probability of ionization of one atom becomes inversely proportional to the cubic root of density, i.e. depends on density in a very smooth way. This, in turn, leads to a gradual reducing of the ion background dependency on density and this background cannot be ignored even in highly rarified media. For example, a fall in pressure within the experimental setup of two orders of magnitude leads to a fall in the ionic background equal to the cubic root of pressure, i.e. 4–5 times. Our experiment observed exactly this behavior of ionic background and, as we'll show later in this report, such smooth dependency on density is experimentally demonstrated when measuring spectra of double coincidences obtained by our and emiT groups.

Analysis and comparison of double coincidences spectra

Here let's pause to analyze the spectra of double coincidences between beta-electron and recoil proton, and compare our spectrum with the results obtained by other authors. We have published the diagram of our experimental equipment in the past [5, 6, 8]. Here we will simply note that in its sizes our equipment is comparable to the equipment used by the two other groups and the distance between the observed decay zone and the proton detector in our equipment is about 0.5 m. The accelerating potential of the electric field is also approximately the same in all three equipment sets, so all three experiments should lead to similarly forms of double and triple coincidences spectra.

Fig. 2 demonstrates the summary statistics on double e-p coincidences (coincidences of electron with delayed proton). Fig. 2 clearly shows two major peaks: one peak with a maximum in channels 99–100, which is the peak of zero or prompt coincidences [6, 8]. The position of this peak marks the zero time count, namely the time when the electron detector registered the electron. This peak is not physics-related in its nature. Instead, it is a reaction of the detectors and the electronic system to the registration of the beta electron. It is namely the pulse from the electron channel that opens the time windows on spectra Fig. 2 for 2.5 μs forward and backwards. The next peak visible on Fig. 2 has a maximum in channel 120 and is the peak of e-p coincidences of beta-electron with delayed proton.

An analogous situation was observed in experiments on the measurement of the correlation coefficients by two independent groups at ILL [10] and emiT group at NIST [11], and it was also mentioned at [12]. We would especially like to emphasize the correspondence of our spectrum of double coincidences with an analogous spectrum from the result obtained by the emiT group from NIST [11]. On Fig. 3 we present their spectrum and diagram for the registration of the beta electron and the recoil proton. A comparison of our results with the results of the emiT group shows their unquestionable similarity. Moreover, the position of the second proton peak in Fig. 3 (emiT group), like in Fig. 2 (our result), corresponds well to the simple estimate obtained by dividing the length of a proton trajectory by its average speed.

Here we will also note the presence of a significant homogenous ionic background in Fig. 2 and Fig. 3. However, in both cases this background allows to easily distinguish the neutron decay peak. As we will shortly demonstrate, this ionic background will play a

dominant role in the presence of a strong magnetic field and it will become impossible to distinguish events of ordinary neutron decay against it.

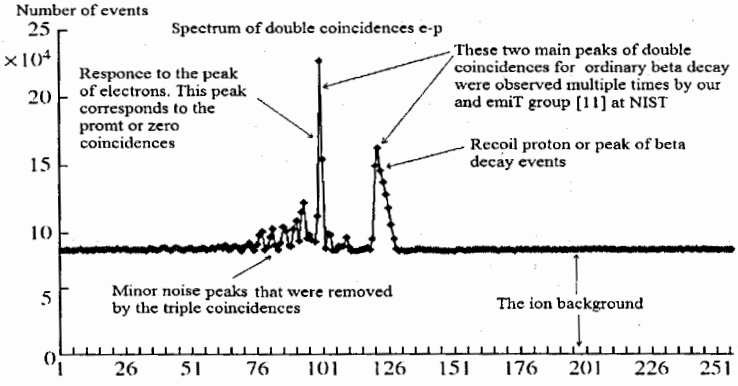

Fig. 2. Timing spectrum for e-p coincidences. Each channel corresponds to 25 ns. The peak at channel 99–100 corresponds to the prompt (or zero) coincidences. The coincidences between the decay electrons and delayed recoil protons (e-p coincidences) are contained in the large peak centered at channel 120.

Following Avogadro's law, even in the case of a very deep vacuum under pressure of $10^{-6} - 10^{-8}$ mbar air molecule concentration remains very high. In fact, it is sufficient for beta-electrons produced in neutron decay to create a significantly high ionic background. Here one must note that the probability of ion creation along the trajectory of beta-electron in inverse proportion to the average distance between neighboring ions, i.e. proportional not to the molecule concentration but to the cubic root of this value. From this observation it follows that the value of the ionic background does not significantly depend on the vacuum conditions inside the experimental chamber. In our case, pressure was two orders of magnitude greater than the pressure in the emiT experiment. However, we observed an ionic background of only 4–5 times their background. This estimate is confirmed when one compares the spectra on Fig. 2 and Fig. 3. Our spectrum, presented on Fig. 2, has a 1:1 ratio of the value of e-p coincidences peak and the value of the background. The emiT group (Fig. 3) spectrum has a ratio of 4:1 – 5:1, i.e. only 4–5 times our number, that is equal to the cubic root of pressure ratio in both teams' work (see Introduction).

Fig. 2 shows that the total number of events in e-p coincidences peak in our experiment equals $N_D = 3.75 \cdot 10^5$. This value exceeds the value we obtained in our previous experiment conducted on beam PF1 at ILL by two orders of magnitude. It was precisely because of the low statistics volume that we could not identify the events of radiative neutron decay in that experiment and instead defined only the upper B.R. limit [5]. It is very important to note that the peak of double coincidences between electron and the delayed proton is observed against a non-homogenous background (see Fig. 2 and Fig. 3): besides the homogenous ionic background, which has a value comparable to the value of the e-p coincidences peak, there is an obvious peak in channels 99–100. In essence, this peak is a response peak to the time spectrum of electron registration, which contains just one peak in

channels 99–100, signifying the time when the electron detector registered the electron. We will shortly see that the radiative peak of triple coincidences appears against a non-homogenous background with not one, but two response peaks.

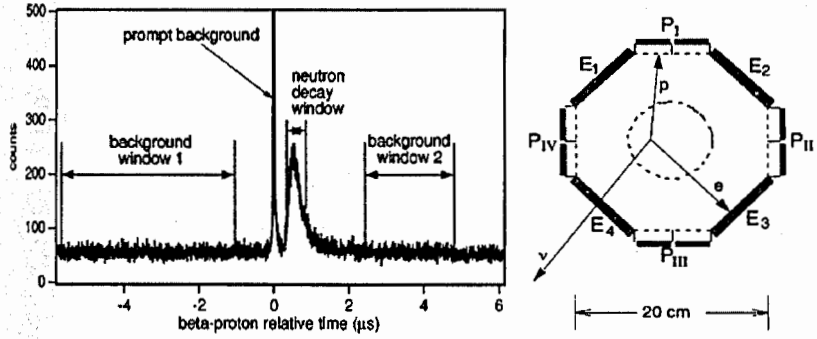

Fig. 3. Spectrum of double electron-proton coincidences obtained by emiT Group [11] with two peaks and ion background value comparable to the neutron decay peak; emiT group scheme for registering beta electron and recoil proton.

The remaining peaks on Fig. 2 are small, with just seven peaks distinct from the statistical fluctuations. These occurred because of the noise in the electric circuits of the FRMII neutron guide hall. There are no other physics-related reasons for their occurrence. These peaks appeared and disappeared depending on the time of day, reaching their maxima during the work day and disappearing over the weekends. Such behavior was observed throughout the experiment as we collected statistics. Since the nature of these seven small peaks is in no way related to radiative and ordinary decay, we did not emphasize them in our article.

The comparison conducted demonstrates that the spectra of double coincidences obtained in our experiment completely correspond with the results obtained by the emiT group. Now we will compare these two spectra with the spectrum of double coincidences obtained by the third group. Unfortunately, the authors did not publish the spectrum of double coincidences in their original article [7] instead it was only published this year in paper [13]. Fig. 4 displays the spectrum of double coincidences and the diagram of their experimental equipment.

The significant deviation obtained is explained by the fact that the peak in the NIST experiment consists not of beta-decay protons, but rather of ions. The density of gas molecules inside the equipment is proportional to pressure and according to the Avogadro's Law is at the order of 10^7 mol/cm^3 even at the pressure of 10^{-8}–10^{-9} mbar. This is a very significant number, which quite enough for creation the large ionic background in the presence of ionizing radiation. The energy of beta-electrons significantly exceeds the energy of ionization. Besides, the probability of ion creation by electrons is inverse proportional not to volume taken up by one molecule but to the average distance between molecules. It is precisely due to this reason that the ionic background falls proportionally to the cubic root of the pressure and not proportionally to pressure. In the emiT group experiment the pressure was the same as in the NIST experiment, so the ionic background should be the same too. The

light ions, together with the beta protons, should have a delay time comparable to 1 μs. The pulses from these particles are simply not visible in the spectrum due to the NIST group's use of combined electron-proton detector (see Fig. 5 with the shape of electron and ion pulses). The maximum of the "proton" peak in the NIST experiment, according to the delay times estimations (delay time is proportional to square root of ion mass), falls exactly to the air ions 4–6 μs.

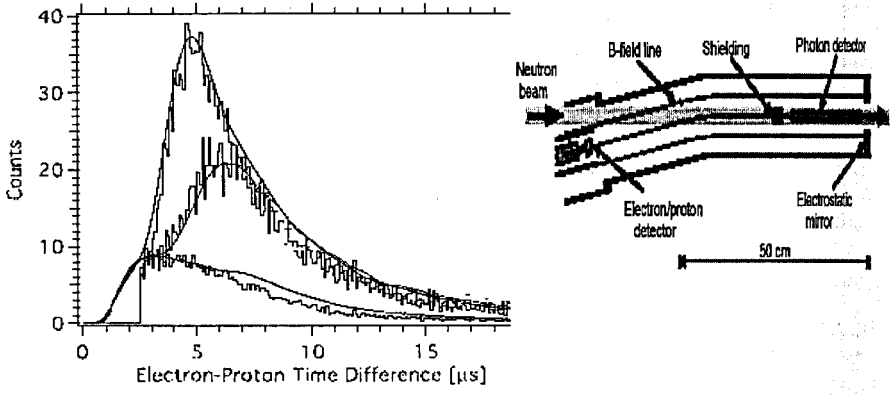

Fig. 4. Equipment diagram and the single peak of "electron-proton" coincidences, published in [13]. The lower curve corresponds to 0 volts, the middle curve corresponds to 300 volts and the highest curve corresponds to 500 volts in an electrostatic mirror. The location of the peak's maximum and its significant width differ from our and the emiT results subsequently by one and two orders of magnitude. The location and the width of the peak also deviate by one and two orders of magnitude from the elementary estimates of delay times (see below).

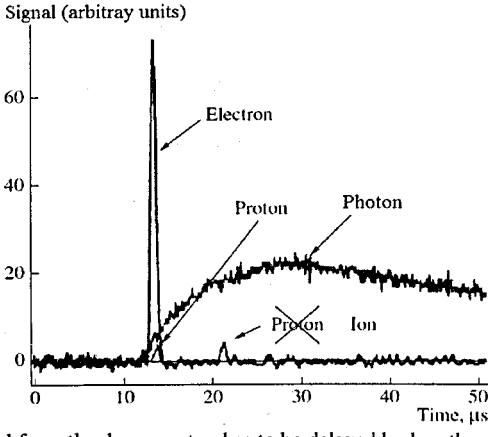

Fig. 5. The signal from the decay proton has to be delayed by less than one microsecond, which is why it is located at the base of the electron pulse (see line number 2) and so cannot be registered by the combined electron-proton detector. The pulses that are delayed by longer than 1 microsecond are pulses not from decay protons, as it was indicated in ref. [7], but rather from ions, formed in the decay zone. The line number 1 shows the shape of pulses from the gamma detector.

Fig. 5 presents the pulse forms on the electron-proton detector. As was pointed out above, the significantly delayed pulses of low amplitude correspond to ion pulses, and the pulses from protons are simply invisible due to a presence of a wide electron pulse of high amplitude. Namely this fact explains the dead zone around zero on the spectrum of electron-ion coincidences on Fig. 4.

Analysis and comparison of triple coincidences spectra

In paper [11] the emiT group researched only the ordinary decay mode, thus this comparison is limited to our spectrum of triple coincidences, presented in Fig.5, and the only peak published by the NIST authors in Nature [7], presented on Fig.7. Analysing the double coincidences spectra obtained by our and the emiT groups (both of which present two main peaks) shows that in the spectrum of triple coincidences we should observe not two but three peaks. Namely, along with the sought after radiative peak, the triple e-p-gamma coincidences spectrum should show two (not one!) response peaks to the registration of beta-electrons and the registration of protons. Fig.5 of triple coincidences clearly shows three peaks, and the leftmost peak with the maximum in channel 103 is connected to the peak of the radiative gamma-quanta in question, as this gamma-quantum is registered by the gamma detectors in our equipment before the electron.

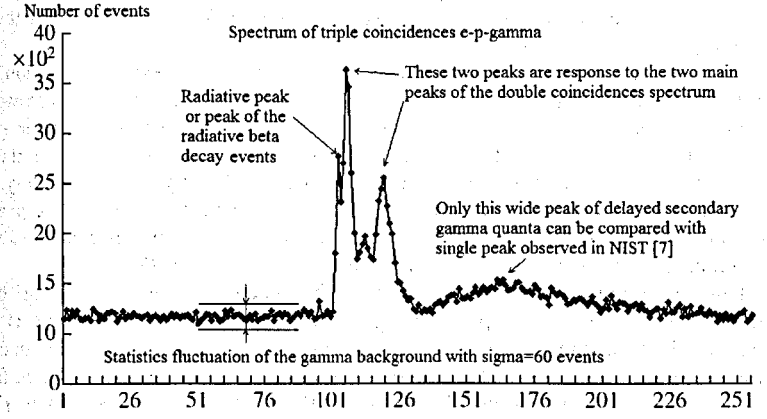

Fig. 6. Timing spectrum for triple e-p-g coincidences. Each channel corresponds to 25 ns. In this spectrum, three main peaks in channels 103, 106 and 120 can be distinguished. The left most peak in 103 channel among these three main peaks is connected with the peak of radiative decay events.

It is also important to note that while both teams' double coincidences spectra show the peaks at a distance from each other and easily distinguishable, in the spectrum of the triple coincidences the radiative peak is on the left slope of the response peak to electron registration. This means that we observe the peak of radioactive neutron decay events against a heterogeneous background. At the same time, both response peaks on the spectrum of triple coincidences are significantly wider and located closer to each other than in the original

spectrum of double coincidences. As we demonstrate below, one must take into account such spectrum behavior (related to the presence of a response in the electron detector system of data collection) by introducing the non-local response function. Using this well known method it is possible to distinguish N_T the number of triple coincidences from the heterogeneous background, arriving at the experimental BR value.

Comparing Figs. 2 and 6, it becomes clear that if we ignore the first leftmost peak with the maximum in channel 103 in Fig. 6, the spectrum of double e-p coincidences will resemble the spectrum of triple e-p-γ coincidences on Fig. 2. The peak with the maximum in channel 106 on Fig. 6 is connected to the left peak of false coincidences on Fig. 2, and the peak with the maximum in channel 120 on Fig. 6 is connected to the right peak of e-p coincidences on Fig. 2. The emerging picture becomes obvious when one uses a standard procedure, introducing a response function for gamma channel $R_\gamma(t,t')$ [6], which is also necessary for calculating the number of triple radiative coincidences N_T in radiative peak:

$$S_{out}(t)=\int S_{in}(t')R_\gamma(t,t')dt'$$

Using the method of response function, one can confidently define our double-humped background: the narrow peak with the maximum in channel 106 on Fig. 6 is the response to the narrow peak of zero coincidences (by other words this peak is response to beta-electron registration) in channels 99–100 on Fig. 2, and the second peak in this double-humped background on Fig. 5 is the response to the peak in channels 117–127 on Fig. 2 (or this peak is response to proton registration).

It must be noted that in our case we have to use the non-local response function, as the peaks on the original spectrum $S_{in}(t)$ of double coincidences are significantly narrower than those in the spectrum $S_{out}(t)$ of triple coincidences and also are shifted in their relative positions. In this case we use "functional" multiplication, however if we use the local response function, the triple coincidences spectrum is arrived at by simple multiplying the double coincidences spectrum by a number, in which case neither the width of the peaks nor their position change. It is also evident that the local response function approach leads to an erroneous number of triple coincidences N_T and, therefore, the wrong BR value.

When discussing the similarities between the spectra on Fig. 2 and Fig. 6, it is important to note that the response peak on Fig. 6 with a maximum in channel 106 is shifted to the right or delayed in comparison to the peak responding to electron registration in channel 100 on Fig. 1. This is due to the fact that in our electron diagram we used a constant fraction discriminator (CFD). CFD has its own delay line and the location of the time-pickoff signal it generates is determined by the method of comparing the fraction of the original signal to the delayed (CFD method [14]). Thus, there is a shift in the first response peak with a maximum in channel 106 on Fig. 6 versus the first peak on Fig. 2 with the maximum in channel 100. The value of this delay is equal to the front duration of the gamma quantum signal and is on average 150 ns. The CFD method obviously also shifts the radiative peak, but it should be located to the left of the response peak, as is observed on Fig. 6.

As for the wide, almost indistinguishable peak in channel 165 on Fig. 6, its influence on the radiative peak in channel 103 is negligible. Its nature is in no way related to the researched phenomenon, so we do not discuss it in our article. This peak is created by the radioactive gamma quanta delayed on average by 1.25 μs and emitted by the radioactive medium within our experimental equipment. The medium is activated by registered beta-electrons. This event of artificial, induced radioactivity has been known for over 100 years

and does not have anything in common with the new event of radiative neutron decay which is the subject of current research. As we will demonstrate below, only this 1 microsecond peak and delayed from the registration time by about the same time can be compared to the peak observed by the authors of paper [7] at NIST (see Fig. 7). Thus, the authors of this experiment observed not the events of radiative decay but rather the event of artificial radioactivity, already well known in the time of Joliot-Curie.

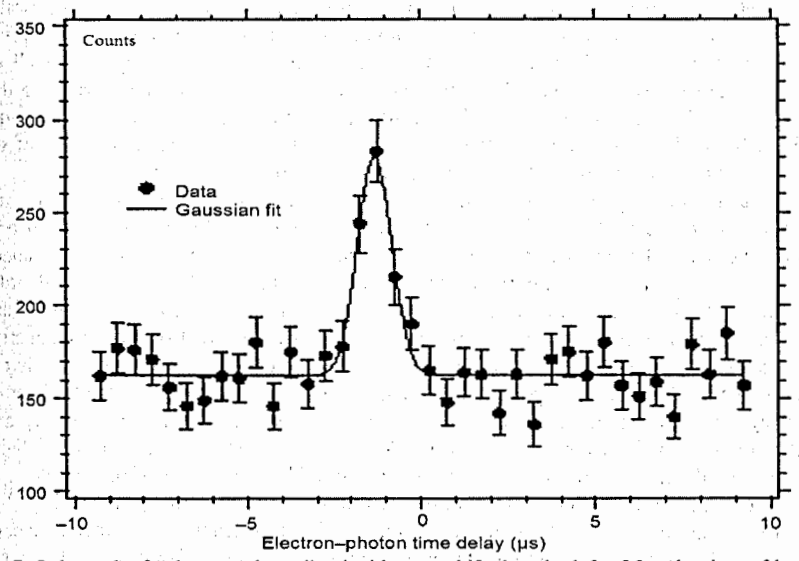

Fig. 7. Only peak of "electron-photon" coincidences, shifted to the left of 0 – the time of beta-electron registration – by 1.25 microseconds, published in [7, 11].

After analyzing the spectra with the help of the non-local response function $R_\gamma(t,t')$ we finalize the average value for the number of radiative neutron decays $N_T = 360$ with a statistics fluctuation of 60 events. B.R. can be expressed as a ratio of N_T to N_D as BR = $k(N_T/N_D)$, where coefficient k = 3.3 is the geometrical factor that we can calculate by using anisotropic emission of radiative gamma-quanta [4]. With the number of observed double e-p coincidences $N_D = 3.75 \cdot 10^5$ and triple e-p-γ coincidences $N_T = 360$, one can deduce the value for radiative decay branching ratio of $(3.2 \pm 1.6) \cdot 10^{-3}$ (99.7 % C.L.) with the threshold gamma energy $\omega = 35$ keV. The average B.R. value we obtained deviates from the standard model, but because of the presence of a significant error (50%) we cannot make any definite conclusions. The measurements must be made with greater precision. According to our estimates, in the future experiment we will be able to make more definite conclusions about deviation from the standard electroweak theory with experimental error less than 10%.

The difference between the NIST experiment and our experiment becomes immediately apparent. First and foremost, it is the time scale: in our spectra, the scale is measured in nanoseconds, while in the other experiment the scale is in microseconds. Besides, we used three types of detectors, each of which registered its own particle: one detector for the electrons, one for the protons, and six identical detectors for the radiative gamma-quanta (see [6]). The duration of the front pulse from the electron and proton detectors is 10

nanoseconds in our experiment and 100 times greater than that in the NIST experiment, in the order of 1 μs. The rise time of gamma signal from our gamma-detectors is on average 150 ns, and from avalanche diode on the NIST equipment greater than 10 μs, besides that the diode pulse arrives with significant noise, which makes the thickness of the front pulse line equal to more than 0.5 μs (see the photon line on Fig. 7 from [7]). All of this leads to our factual time resolution being two orders of magnitude better than the resolution achieved in the NIST experiment. However, as the two experiments used equipment which was practically the same in size and smaller than 1 meter, the choice of the time scale is a matter of principle. Given this geometry, it is impossible to get microsecond signal delays from all of the registered charged particles, i.e. electrons and protons. In this light, it is surprising that the peak identified by the authors of the NIST report [7] as the peak of radiative gamma-quanta, is shifted by 1.25 microseconds to the left. The expectation that magnetic fields of several tesla in magnitude delay all electrons and protons, are absolutely ungrounded.

Indeed, the magnetic field cannot change the speed of charged particles. It can only twist a line trajectory into a spiral. The length l of this spiral depends on angle θ between particle velocity and magnetic field direction. In beta decay, electrons can fly out under any angle θ, therefore the magnetic field can increase the time of delay by several orders of magnitude only for a negligible portion of the charged particles. Even this negligible number of particles that flew out at an almost 90 degree angle to the direction of the magnetic field that coincides with the direction of the narrow neutron guide (see Fig. 4) will most likely end up on the walls of the neutron guide rather than reach and hit the detector due to the presence of the strong electrostatic field.Because the distance between the point of decay and the detector is about 0.5 meter and electron velocity is comparable with speed of light, the electron time of delay should be less than a microsecond by two orders of magnitude.

Thus, both the 1 microsecond shift and the width of the only peak on Fig. 7 in the experiment conducted at NIST, is in sharp contradiction to elementary estimates. We, on the other hand, did not observe any wide peaks before electron registration and our gamma background is very even in this part of the spectrum (see Fig. 6). However, when we assume that the NIST experiment authors observed the wide peak, shifted by 1 microsecond, not before, but after the registration of beta-electrons. In that case, the wide peak on our spectrum in Fig. 6 completely corresponds to the wide peak on Fig.7. However, as noted above, density of gas molecules remains high even with the pressure of $10^{-8} - 10^{-9}$ mbar and this residual gasis activated by beta-electrons. The wide peak in our spectrum is formed by the delayed gamma quanta from this induced artificial radioactivity.

Conclusions

The main result of our experiment is the discovery of the radiative peak namely in the location and of the width that we expected. The location and the width of the radiative peak correspond to both estimates and the detailed Monte Carlo simulation of the experiment. Thus, we can identify the events of radiative neutron decay and measure its relative intensity, which was found to be equal B.R. = $(3.2 \pm 1.6)\cdot 10^{-3}$ (with C.L.= 99.7% and gamma quanta energy over 35 keV).

At the same time, the average experimental B.R. value exceeds the theoretical value by 1.5 times. However, due to a significant error we cannot use this result to assert that we observe a deviation from the standard model. Therefore, our most immediate goal is to increase experiment precision, which we can improve by several percents according to estimates.

For last two years we were preparing this new experiment and conducted number of tests for our new electronics. We constructed multi channel generator what can generate the pulses with the same forms as our electron, proton and gamma detectors. During these tests we got the same responses as during our last experiment on real neutron beams at FRMII. It means that all additional peaks on our spectra have no any physics reasons and It proves once more that we were absolute correct when applied the response function method for explaining these peaks as response ones and for developing our experimental spectra.

We created and tested our new electronic system for obtaining experimental spectra. By using this new programmable electronics we can significantly reduce the influence of response peaks on peak with radiative decay events. Now we can get this peak almost isolated from responses. On our estimations all these allow us to reach accuracy for our new experiment about 1%. So, on the base of our new electronics we can confirm or refuse the deviation of our average experimental value of BR from the standard model one.

As concerning the comparison of our experimental results with others we can make the following two main conclusions. The main parameters of our spectrum of double electron-proton coincidences identifying the events of ordinary neutron decay fully coincide with an analogous spectrum published by emiT group in [11].

Unfortunately we cannot say same for another experiment measuring the radiative neutron decay published in [7]. Particularly vexing is the authors' unsubstantiated assertion that they observe their only wide peak of gamma quanta before the registration of beta-electrons. Both the position and the width of this peak are located in sharp contradiction to both the elementary estimates, and the results of our experiment. In the course of our entire experiment we did not observe such a wide peak in the triple coincidences spectrum, located before the arrival of electrons at a huge distance of 1.25 μs. However, it is possible to reconcile our spectra of triple coincidences with the one isolated peak observed at NIST if we assume that at NIST, the gamma-quanta were registered after the beta electrons. Only in this case does the NIST peak almost completely coincide with the peak we observed in the spectra of triple coincidences with the maximum in channel 165, both in terms of the huge delay of 1.25 μs and in terms of its huge width. This peak is created by the delayed secondary radioactive gamma-quanta, arising from the activation by beta electrons of the media inside experimental chamber, which was the real object of the NIST experimentalists' observation.

Despite the recent disagreements [15], which we consider to be subjective in nature [16], we acknowledge the contribution of our Western colleagues Profs. N. Severijns, O. Zimmer and Drs. H.-F. Wirth, D. Rich to our experiment conducted in 2005. Here it is important to note that the authors of the article published in Nature [7] consciously misled first our Western colleagues and then the physics community at large by insisting that their only wide peak is removed by 1.25 microseconds to the left from the time of electron registration, when in reality this peak was formed by delayed gamma-quanta, emitted by the activated medium inside the experimental equipment, and corresponds to our wide peak with the maximum in channel 165 (refer to Fig. 6) [15, 16]. The authors would like to thank Profs. D. Dubbers and Drs. T. Soldner, G. Petzoldt and S. Mironov for valuable remarks and discussions. We are also grateful to the administration of the FRMII, especially Profs. K. Schreckenbach and W. Petry for organizing our work. We would especially like to thank RRC President Academician E.P. Velikhov and Prof. V.P. Martem'yanov for their support, without which we would not have been able to conduct this experiment.Financial support for this work was obtained from RFBR (Project N 014-02-00174).

References

[1] GaponovYu.V., Khafizov R.U. Phys. Lett. B**379** (1996) 7–12.

[2] Radiative neutron beta-decay and experimental neutron anomaly problem. By Yu.V. Gaponov, R.U. Khafizov. Weak and electromagnetic interactions in nuclei (WEIN '95): proceedings. Edited by H. Ejiri, T. Kishimoto, T. Sato. River Edge, NJ, World Scientific, 1995. 745p.

[3] About the possibility of conducting an experiment on radiative neutron beta decay R.U. Khafizov, N. Severijns Proceedings of VIII International Seminar on Interaction of Neutrons with Nuclei (ISINN-8) Dubna, May 17–20, 2000 (E3-2000-192), 185–195.

[4] Khafizov R.U. Physics of Particles and Nuclei, Letters **108** (2001) 45–53.

[5] M. Beck, J. Byrne, R.U. Khafizov, et al., JETP Letters **76**, 2002, p. 332.

[6] R.U. Khafizov, N. Severijns, O. Zimmer et al. JETP Letters **83** (2006) p. 5.

[7] J.S. Nico, et al. Nature, v. **444** (2006), p.1059–1062.

[8] Discovery of the neutron radiative decay R.U. Khafizov, N. Severijns et al. Proceedings of XIV International Seminar on Interaction of Neutrons with Nuclei (ISINN-14) Dubna, May 24–25, 2006.

[9] B.G. Yerozolimsky, Yu.A. Mostovoi, V.P. Fedunin, et al., Yad. Fiz. **28**, (1978) 98 [Sov. J. Nucl. Phys. **28**, 48 (1978) 48].

[10] I.A. Kuznetsov, A.P. Serebrov, I.V. Stepanenko, et al., Phys.Rev.Lett., **75** (1995) 794.

[11] L.J. Lising, S.R. Hwang, J.M. Adams, et al., Phys. Rev. C. v.**6**, 2000, p. 055501.

[12] J.Byrne, R.U. Khafizov, Yu.A. Mostovoi, et al., J. Res. Natl. Inst. Stand. Technol. 110, p.415, (2005).

[13] R.L. Cooper, T.E. Chupp, M.S. Dewey, et al, Phys. Rev. C **81**, (2010) 035503.

[14] T.J. Paulus, IEEE Transactions on Nuclear Science, v.NS-32, no.3, June, p.1242, 1985.

[15] N. Severijns, et al., e-print arXiv:nucl-ex/0607023; J. Nico, private communication.

[16] R.U. Khafizov, V.A. Solovei, e-print arXiv:nucl-ex/0608038.

Isomers Production of Sn Nucleus in Nuclear Reactions Induced by Photons and Fast Protons

C. Oprea, A.I. Oprea

Frank Laboratory of Neutron Physics (FLNP), Joint Institute for Nuclear Researches (JINR), 141980 Dubna, Moscow Region, Russian Federation

Abstract. The isotopes of Sn can be obtained in the nuclear reactions of type (p,n) on Indium nucleus and in photoneutron processes on Sn nucleus. The cross sections of (p,n) and (γ, xn) processes were evaluated and compared with experimental data. For each reaction was evaluated the contribution of compound, direct and pre – equilibrium processes. Further, the parameters of nuclear potentials and other data were extracted. It was obtained a quite good agreement between existing experimental data and present evaluations and therefore we have calculated the isomer ratios using different models of incident gamma and protons sources. It is a new proposal for corresponding experiments at FLNP JINR Dubna basic facilities.

INTRODUCTION

Nuclear reactions, induced by fast protons and gamma particles with neutrons emission, are of interest for fundamental and applied researches. These reactions provide for fundamental studies, data in the investigation of reactions mechanism and nuclear structure and represent a source of new isotopes for applications in medicine, electronics and other industry domains and human activities.

Indium is a chemical element with order number Z = 49 (protons number) which has two natural isotopes, ^{113}In, ^{115}In with abundances 4.29% and 95.71%, respectively. Stannum is a nucleus with magical number of protons (Z = 50) and therefore it has many natural isotopes which are the followings (atomic mass A– abundance %): 112– 0.96% 114– 0.66%, 115– 0.35%, 116– 14.30%, 117– 7.61%, 118– 24.03%, 119– 8.58%, 120– 32.85%, 122– 4.72%, 124– 5.94%). The Sn isotopes can be obtained in the (p,n) reactions with fast protons on In or in photons induced reactions (γ,xn) (x= 1,2,...) with energy higher than neutrons threshold on Sn isotopes[1,2].

The ^{113}In(p,n)^{113m,g}Sn (Q= –1.82 MeV) and ^{114}Sn(γ,n)^{113m,g}Sn (Q= –10.302 MeV) reactions are analyzed. In these nuclear reactions it is obtained the same Sn isotope in the ground (g) and isomer (metastable, m) states. The spin, parity and time of life of the isomer state ^{113m}Sn are $J^{\Pi} = (7/2)^+$ and τ = 21.4 m. For the ground state of ^{113g}Sn these values are: $J^{\Pi} = (1/2)^+$ and τ = 115.09 d [3]. For both reactions the production cross sections of ^{113m,g}Sn isotopes starting from neutron threshold and up to 25–35 MeV were evaluated. Theoretical evaluations were compared with experimental values from literature. Further the isomer ratios using different model of incident particle sources and nuclear data were extracted.

THEORETICAL BACKGROUND

Cross sections for ^{113}In(p,n)^{113m,g}Sn and ^{114}Sn(γ,n)^{113m,g}Sn reactions were evaluated with Talys computer code, a free software, working under Linux, dedicated to nuclear reactions and atomic nuclei structure calculations [4].

With the help of Talys it is possible to calculate inclusive and exclusive cross sections. In the case of a binary reaction of type A(a,b)B, inclusive processes are defined those

reactions in which in the final stage are considered emergent b particles coming from other open channels with participation of particle b. If the final stage is well defined and the emergent particle b is considered only from the channel b+B then the cross section in this case is defined as exclusive. These notions, inclusive and exclusive cross sections are very useful in the processing of experimental data [4].

In the cross sections evaluations, the compound, direct and pre-equilibrium nuclear reaction mechanisms were considered for incident energies starting from the neutron threshold up to 25–35 MeV. Compound processes, including the multiple emission, are described by Hauser–Feshbach formalism [5], direct processes by Distorted Wave Born Approximation (DWBA) [6] and pre-equilibrium by two-component exciton model [7]. In the evaluations, discrete and continuum states of the residual nuclei were considered using corresponding nuclear states density based on Fermi gas model [8].

Isomer ratios measured in the experiment give us new data on cross section, nuclear structure like, states density, nuclear density parameters, deformations and other. Using the cross section obtained with Talys, the isomer ratios can be calculated according with the expression [9]:

$$R = \frac{Y_m}{Y_g} = \frac{\int_{E_{thr}}^{E_{max}} N_0 \Phi_{inc}(E_{inc}) \sigma_m(E_{inc}) dE_{inc}}{\int_{E_{thr}}^{E_{max}} N_0 \Phi_{inc}(E_{inc}) \sigma_g(E_{inc}) dE_{inc}} \quad (1)$$

Here $Y_{m,g}$ is yields of isomer and ground state; E_{thr} is neutron threshold energy; E_{max} is maximal energy of incident particles given by the source; E_{inc} is energy of incident particles; N_0 is number of particles in the target; Φ_{inc} is flux of incident particles; $\sigma_{m,g}$ is production cross section of isomer and ground states, respectively.

Relations (1) will be used in the both (p,n) and (γ,n) reaction considering different type of source of incident particles. In the case of photoneutron reaction a flux of incident photons close to real case, has a form according to Kramer expression [10,11]:

$$\Phi(E_\gamma) \sim I_\gamma = i_b Z (E_0 - E_\gamma) E_\gamma^{-1} \quad (2)$$

Here I_γ is intensity of gamma quanta; Z is a charge of stopping element; i_b is electron beam current; E_0 is energy of accelerated electrons; E_γ is energy of gamma quanta.

For cross sections evaluations the nuclear potentials, in the incident and emergent channels are necessary. Potentials are of Woods–Saxon type, including volume, surface, spin - orbit and other contributions. A large data base, of local optical potentials, extracted mainly from experimental data for many nuclei in different channels, are implemented in Talys. There is also a possibility to introduce the optical parameters considered by user. For those nuclei for which the potentials are not defined it is possible to enable the, so-called, global optical parameters defined by Konig and Delaroche [4,12].

RESULTS AND DISCUSSION

In the Figure 1 the inclusive cross sections (CS) for ^{113}In(p,n) reaction with the contribution of different nuclear reaction mechanisms and type of residual nucleus states are shown.

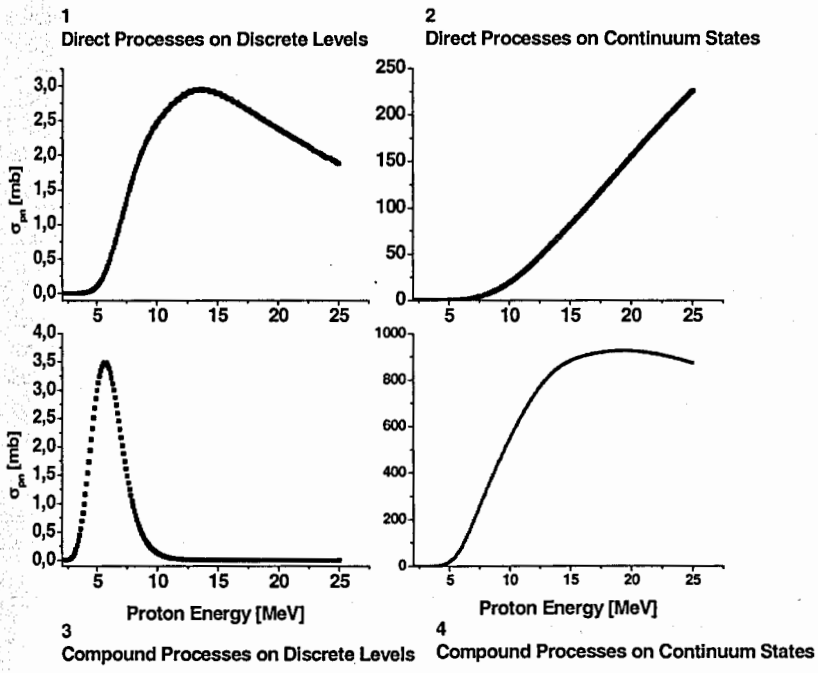

Figure 1. Inclusive CS in ^{113}In(p,n) process.

From Figure 1 results that the compound processes on continuum states of residual nucleus are dominant followed by direct processes. Compound and direct processes on discrete states can be neglected and for ^{113}In(p,n) reaction can be explained by the presence of Coulomb barrier. With the increasing of the protons energy, the origin of compound and direct processes are due to pre-equilibrium ones.

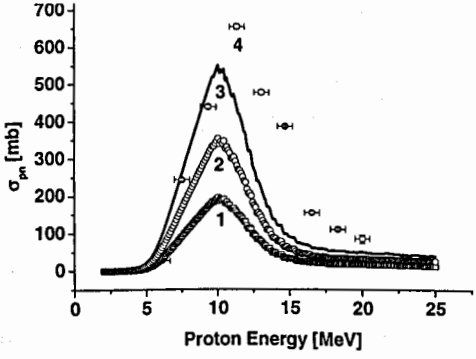

Figure 2. Exclusive CS in ^{113}In(p,n)^{113m,g}Sn. 1. – ground; 2 – isomer ; 3 – total (m+g); 4 – experimental data.

In the Figure 2 the exclusive cross sections in the $^{113}In(p,n)^{113m,g}Sn$ reaction are represented. Because for exclusive processes the final states are well defined, the production of ^{113}Sn isotope in the ground (Fig. 2 curve 1) and isomer states (Fig. 2 curve 2) respectively can be evaluated. The curve 3 from Fig. 2 is the total production of ^{113}Sn isotope which is compared after with experimental data (Fig. 2 curve 4). The contribution of other levels of ^{113}Sn can be neglected. In the low energy part the experimental data are very well described. After the maximum, the shape of the dependences is maintained but some differences appear. The differences can be explained by the fact that after 10 MeV are opened other channels including neutrons which could not be separated from those neutrons coming from "n+^{113}Sn" channel of interest. Experimental data are taken from [13].

The results are obtained with standard Talys input parameters and therefore the agreement between theory and experiment can be considered as good. Further, using relations (1) with different model of protons flux, the isomer ratios can be evaluated. In the more simple case, for proton flux equal with unity (Φ_{inc}= 1), starting from the neutron threshold E_p= 1.83 MeV, up to E_{max}= 25 MeV, the isomer ratio R is:

$$R = 1.82 \pm 0.26 \quad (3)$$

The absolute error in the result from relation (3) comes from the transformation of integrals from relations (1) in sums due to numerical calculations. The proton energy step in relation (3) was equal to 0.1 MeV.

The isotope ^{113}Sn can be obtained in $^{114}Sn(\gamma,n)$ photoneutron reaction also. The main cross sections results are shown in Figure 3.

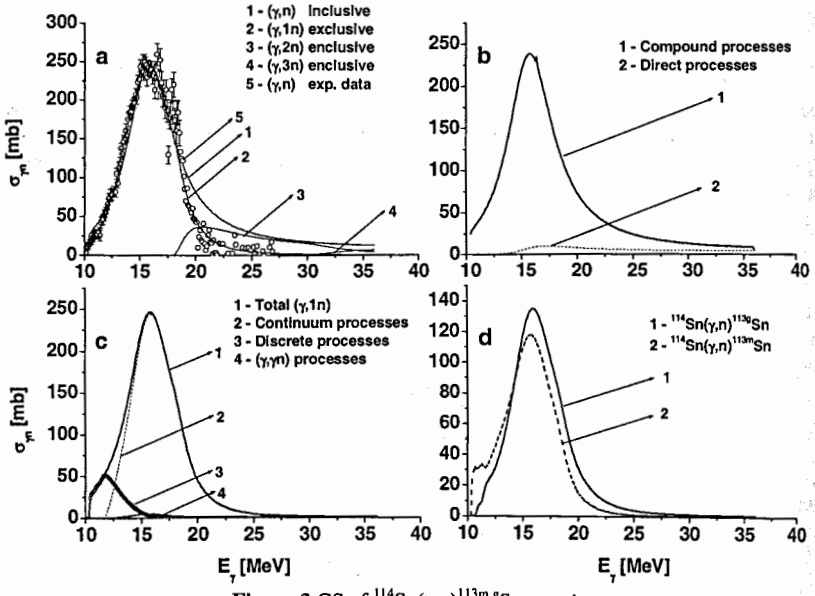

Figure 3.CS of $^{114}Sn(\gamma,n)^{113m,g}Sn$ reaction.

In the Figure 3.a are represented the exclusive (γ,xn) (x,1,2,3,...) reactions. The inclusive (γ,n) reaction, as is possible to observe, is a superposition of the other exclusive processes. Experimental data from literature [13] are very well described by the (γ,1n) process. In the Figure 3.b, the contribution of compound and direct processes, to the cross sections were obtained. By far, compound processes are dominant. Further, in Figure 3.c, the (γ,1n) reaction is separated in continuum and discrete processes. In Figure 3.d, the production cross section of ^{113}Sn isotope in isomer and ground states are represented. These results are necessary for the isomer ratio calculations. It is easy to observe that the sum of the isomer and ground states contribution, coincides practically with the (γ,1n) cross section. The contributions of other levels and channels including neutrons are small in comparison with (γ,1n) cross section and therefore were neglected.

The isomer ratios (IR) were evaluated, considering relation (1), energy of incident photons from neutron threshold up to 25–35 MeV (E_{max}) with flux (Φ_{inc}) equal with unity in one case, and in according with Kramers law from relation (2) in the other case. In the Table 1 are given the results for ^{114}Sn(γ,n)^{113m,g}Sn reaction (with bold), including also other photoneutron reactions on Sn isotopes analyzed by the authors.

	Reaction	(Case 1) R_1	(Case 2) R_2	(Case 3) R_3
1	**^{114}Sn(γ,n)^{113m,g}Sn**	**1.142±0.203**	**1.121±0.173**	**0.995±0.159**
2	^{118}Sn(γ,n)^{117m,g}Sn	0.081±0.015	0.077±0.012	0.062±0.010
3	^{120}Sn(γ,n)^{119m,g}Sn	0.131±0.025	0.126±0.022	0.104±0.018
4	^{122}Sn(γ,n)^{121m,g}Sn	0.258±0.052	0.243±0.045	0.170±0.030
5	^{124}Sn(γ,n)^{123m,g}Sn	4.075±0.532	4.187±0.785	5.078±0.954

Table 1. IR. 1) Φ_{inc}=1; E_{max}=35 MeV; 2) Φ_{inc}=1; E_{max}=25 MeV; Φ_{inc}=from (1); E_{max}=35 MeV; E_0=30 MeV.

In reactions 2,3,4,5 from Tabel 1, isomer ratios in photoneutrons reactions are also obtained. For all five reactions Talys evaluations show that compound processes are dominant, in comparison with others nuclear reactions mechanisms. The isomer ratios become constants with the increasing of maximal energy (E_{max}), but are more sensitive to the energetic dependence of incident flux (Φ_{inc}).

CONCLUSIONS

The protons and gamma induced reactions with neutrons emission for obtaining isotopes and isomer of Sn were analyzed. For both type of reactions, (p,n) and (γ,n), the inclusive and exclusive cross sections were evaluated. The dominant nuclear reaction mechanisms was determined with a separation between the contributions of discrete and continuum states. Obtained cross section results are compared with existing experimental data and in both cases the agreement between theory and experiment can be considered as good. Further the isomer ratios, in a few cases were calculated, using different maximal energy and different model of incident particle fluxes.

Cross sections evaluations were done with Talys computer code. It was demonstrated that Talys software represents and efficient tool for experimental data analysis.

As it is possible to observe, experimental data on cross sections exist for some energy regions, but for isomer ratios we have not found yet. In conclusions, for both processes would

be of interest, cross sections and isomer rations experimental measurements which in principle are possible to run at the LNF JINR Dubna basic facilities.

Acknowledgement. The work was supported by Cooperation Program between JINR Dubna and Romanian Research Institutes coordinated by JINR Dubna Romanian Plenipotentiary Representative on 2016 – 2017 years and FLNP Thematic Plan.

REFERENCES

[1] G. Audi, A.H. Wapstra, Nucl. Phys. A, **565,** p. 1–65 (1993).
[2] G. Audi, A.H. Wapstra, Nucl. Phys. A, **595**, p. 408–490 (1993).
[3] R.B. Firestone, V.S. Shirley, S.Y.F. Chu, C.M. Baglin, J. Zipkin, Tables of Isotopes. CD ROM Edition, Wiley-Interscience (1996).
[4] A.J. Koning, S. Hilaire and M.C. Duijvestijn, .TALYS-1.0., Proceedings of the International Conference on Nuclear Data for Science and Technology, April 22–27, 2007, Nice, France, editors O.BERSILLON, F.GUNSING, E.BAUGE, R.JACQMIN, S.LERAY, EDP Sciences, p. 211 (2008).
[5] W. Hauser, H. Feshbach, Phys. Rev., **87**, 2, p. 366 (1952).
[6] G.R. Satchler, Direct Nuclear Reactions, Oxford University Press, New York (1983).
[7] A.J. Koning and M.C. Duijvestijn, Nucl. Phys. A, **744,** p. 15 (2004).
[8] G.A. Miller, Nucl. Phys. B (Proc. Suppl.), **112**, p. 223–225 (2002).
[9] B.S. ISHKHANOV, V.V. VARLAMOV, PHYSICS OF ATOMIC NUCLEI, **67**, 9, P. 1664 (2004).
[10] H.A. Kramers, The London, Edinburgh and Dublin Philosophical Magazine and Journal of Science, 46:275, p. 836–871 (1923).
[11] G.G. Poludniovsky, Medical Physics, **34** (6), p. 2175–2186 (2007).
[12] S. Hilaire, S. Goriely, A.J. Koning, M. Sin, R. Capote, Phys. Rev. C **79**, 024612 (2009).
[13] Experimental data EXFOR – http://www-nds.iaea.org.

THE DETAILED RESPONSE FUNCTION INVESTIGATION OF THE FAST NEUTRONS SPECTROMETER BASED ON THE STILBENE CRYSTAL

P.S. Prusachenko, V.A. Khryachkov, V.V. Ketlerov

Institute for Physics and Power Engineering (IPPE), Obninsk, Russia

1. Introduction

Organic scintillators are widely used for fast neutron detection [1-3]. However, there are a few problems which give some limitations to used its. One of them relates to low energy region, it is a problem in n/γ separation for low energies. There is a problem for high energy neutrons, it comes from poorly known role of (n,α) reaction on carbon nuclei, the inelastic scattering on the structural materials of the detector and the influence PMT on response for fast neutrons. All this processes can influence on detector efficiency, and, as a result, on accuracy of neutron spectra measurement. The purpose of our work was to study the influence of the above-mentioned processes on the response of the detector with the stilbene crystal.

2. Experimental setup

The measurements were carried out using the time-of-flight method at the Tandetron accelerator in IPPE. The accelerator operated in a pulsed mode. The average pulse width was 1.4 ns. We used $^{7}Li(d,n)^{8}Be$ reaction as a fast neutron source. The result of interaction deuteron with infinity thick target was continuous neutron spectrum with a maximum energy up to 22 MeV.

The length of flight path in the experiment was 3 m. The detector was stilbene crystal with size of 40x40 mm. Both signals, and the signal from the detector, and the signal from the accelerator interrupt system were digitized. The waveform digitizer has the sampling rate of 500 MS/s and ADC resolution of 14 bits.

Also, the detector was placed in a specialized neutron shielding. It consists from lead layer with thickness of 10 cm and mixture of paraffin and lithium carbonate with a thickness of 50 cm. The scheme of experimental setup is shown in fig. 1.

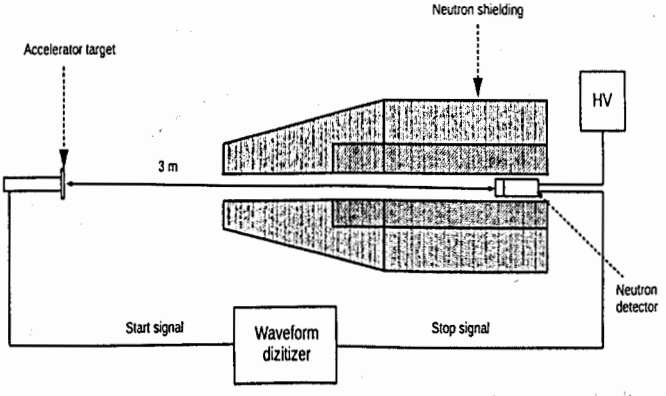

Fig. 1. The scheme of experimental setup.

3. Signal processing

The correlation analysiswas used for digital signal processing. The correlation analysis allows simply and very accurate determine the start time of the signals, to obtain the signal area and to estimate their shape. The maximum of correlation function is the evaluation of particle type, and its position – the start time of the signal. The methods of signal analysis was described in detail in [1,4]. One of the method's advantages is an opportunity to analyze the signals separated by a small time gap (fig. 2).

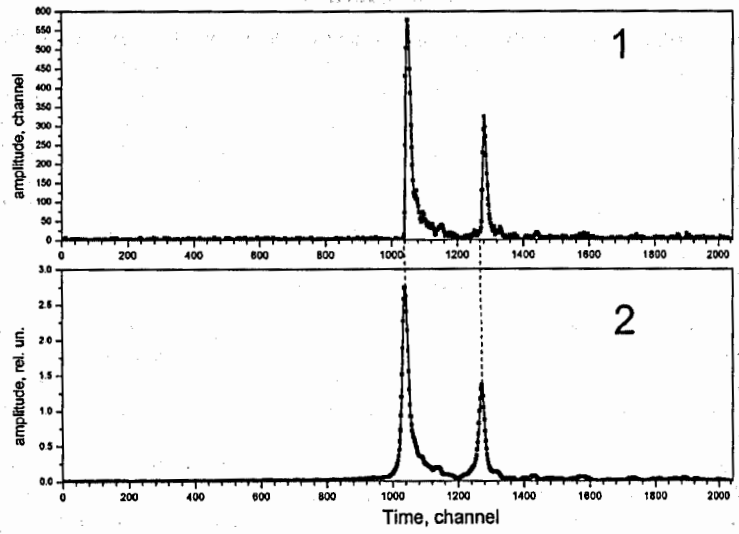

Fig. 2. The pile-up signal and correlation function for them.

As the first results of the work, it is possible to demonstrate time-of-flight spectra (fig. 3). In this figure, red points – the array of all signals, blue points – the ToF spectrum after n/γ suppression.

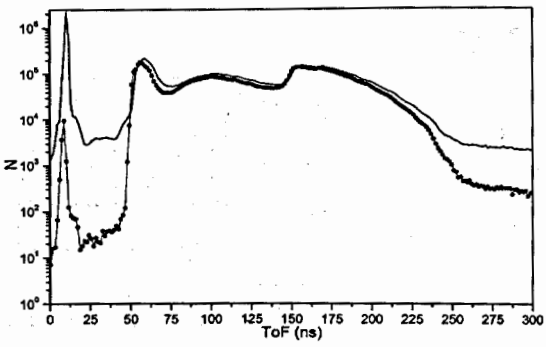

Fig. 3. The time-of-flight spectra. Solid line – integral ToF spectrum, points – neutron ToF spectrum after gamma-background suppression.

4. Results and discussion

4.1. The detector response for the different particle types

The some results of signal processing are shown in fig. 4, a. It is the two-dimensional spectrum, signal's area vs. separation parameter Robtained from correlation analysis (parameter R). We can see threeclear separated event's groups and one additional group. We selected the signals fromthese groups and built the average signal for each of them. This averaged signals are shown in fig. 4, b. We interpreted these groups. Here, there are signals, due to the interaction of gamma rays with the detector material (points in fig. 4, b) and recoil protons (solid line in fig. 4, b). It is also possible to observe a poorly separated from the proton events group of particles, corresponding to alpha-particle from (n,α) reaction on carbon nuclei (dashed line in fig. 4, b).

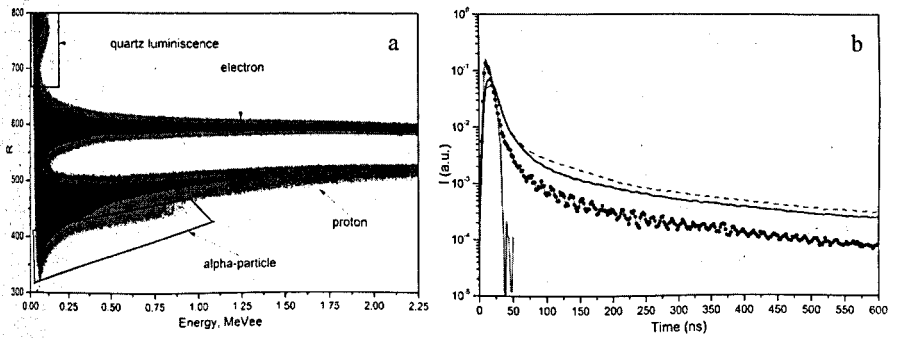

Fig. 4. a – signal's area vs. separation parameter; b – response signal for different particle type.

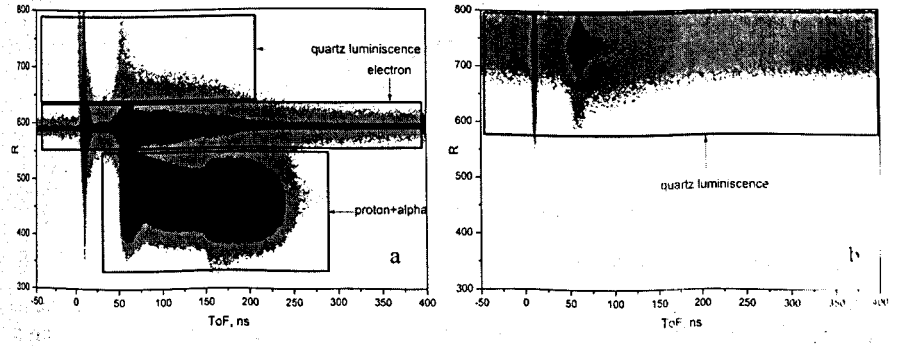

Fig. 5. Time-of-flight vs. separation parameter R. a – experiment with stilbene, b – experiment without stilbene.

The some special case is the group of events that is located above the electrons in fig. 4, a. This events corresponds very short averaged signal without tail (grey line in fig. 4, b). To understand the nature of these signals, the special experiment was done.

In this experiment, we irradiated the detector twice. First time – it was the detector with the

stilbene crystal. Second time – we removed the stilbene crystal from the detector. All other conditions were identical to the first irradiation. The results are shown in fig. 5. In fig. 5 (b), which corresponds with the experiment without stilbene, the events from electron and proton disappeared. But, the group of short events remained on place. We interpreted these events as intrinsic luminescence of quartz input window of PMT. As can be seen from the fig. 4, such events are in the low-energy region. Therefore, for measurements with a low detection threshold, it is important to have a good separation in order to confidently cut off such background events.

4.2. Gamma quanta timing distribution

On the next step of our investigation we tried to understand the shape of gamma-quanta time distribution (fig. 6). In the beginning of the distribution narrow peak corresponding the prompt gamma-ray emission is located. On right side of this peak the many events which appears after the neutron pulse is observed. These events have a clear timing structure. Their timing distribution has a maximum corresponding to small time-of-flight region (the neutrons with high energy). With increasing time-of-flight (and, correspondingly, neutron energy), the number of such gamma quanta decreases. We believe that this gamma-quanta are resulted the inelastic scattering of fast neutron on detector materials. The main element on which the inelastic scattering occurs in the detector is carbon. The inelastic scattering cross-section for carbon contained in stilbene begins to increase sharply after the neutron energy 4.5 MeV. Also in structural materials of the detector is a large number of Al. Inelastic scattering by these two elements will basically determine the time-correlated gamma background for the fast neutron region.

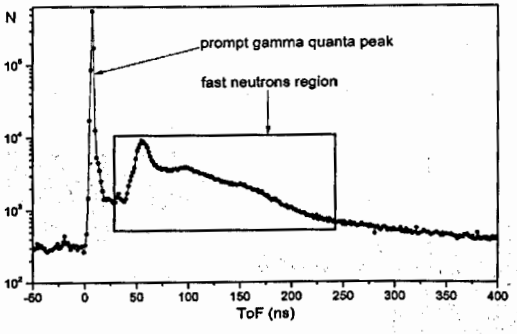

Fig. 6. Time-of-flight spectrum for gamma-quanta.

4.3. Light output for alpha-particles and protons

It's well known, that light output in organic scintillators are depended on the ionizing capacity of the particles [5]. The biggest light output corresponds electrons. For protons it is much less. The light output of alpha-particles is poorly studied.

Ionizing capacity for heavy charged particles will be different depending on their energy [3-6]. Therefore, for them, the nonlineardependence of light output on energy will be observed. For electrons, the ionizing capacity is independent of energy. Therefore, the light output for them will depend linearly on the energy of the particles.

Our setup allows to make a direct measurements of light output energy dependence. The two-dimensional spectrum, time-of-flight vs. light output in MeVee, is shown in fig. 7, a. We

selected narrow ranges of time-of-flight separating the neutrons with certain energy. Next, the amplitude distribution for them was built (fig. 7, b). The most right edge of the distribution corresponds the protons obtaining the all energy of incident neutron. Knowing the energy of the incident neutron, we know the energy of the recoil proton and can compare it with the light output of electrons.

The situation for alpha particles is similar to the situation for recoil protons. At the preliminary stage, it is necessary to select events, which according to the separation parameter correspond to alpha particles. The residual nucleus makes practically no contribution to the light output. Therefore, the distribution of amplitudes for reaction products will be due only to alpha particles and will depend on their angular distribution. The right edge of this distribution will correspond to the alpha particles emitted at an angle of 0 degrees. It will have maximum energy. Knowing the neutron energy can easily calculate the energy of the alpha particle emitted at 0 degrees.

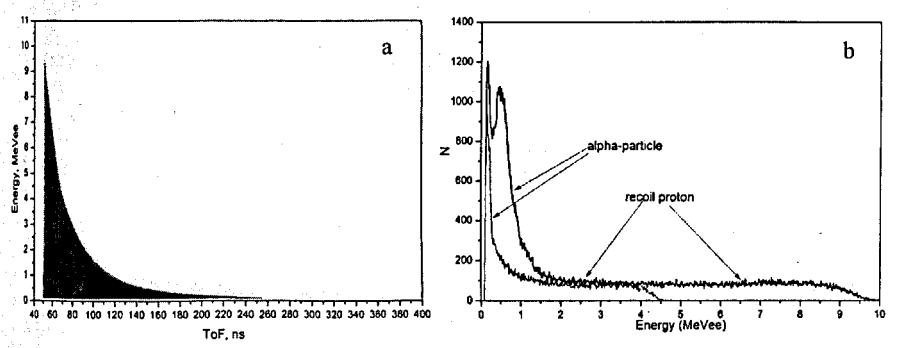

Fig. 7. a - time-of-flight vs. light output in MeVee; b - Amplitude distribution of signal for different neutron energy (9 and 18 MeV).

The results are shown in fig. 8. Round points corresponds to recoil protons, square points corresponds to alpha particles. A solid line is the light output for electrons.

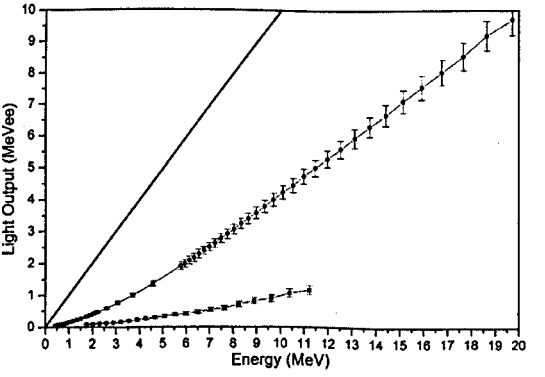

Fig. 8. The energy dependence of light output for different particle types. Solid line – electrons, round points – recoil protons, square points – alpha particles.

5. Conclusion

Digital spectrometer for fast neutron detection was developed. The response of the spectrometer to the excitation by different particle types was investigated.Influence of quartz window of PMT was studied. It was shown that for low energy region it can be significant. Response signal for this effect was obtained. The role of inelastic scattering of fast neutrons on the carbon nuclei is noted. This leads to a significant increase in the gamma background. The energy dependence of the light output for alpha particles and protons in a wide energy range is obtained. Obtained results allow to better understandingprocess, which take place during registration process.

Refenences

[1] N.V. Kornilov, V.A. Khriatchkov, M. Dunaev, et al., Nuclear Instruments and Methods in Physics Research Section A **497** (2003) 467.

[2] A. Sardet, C. Varignon, B. Laurent, T. Granier, A. Oberstedt,Nuclear Instruments and Methods in Physics Research Section A **792** (2015) 74.

[3] N.V. Kornilov, I. Fabry, S. Oberstedt, F.-J. Hambsch,Nuclear Instruments and Methods in Physics Research Section A **599** (2009) 226.

[4] Prusachenko P.S., Bondarenko I.P., Ketlerov V.V., Khryachkov V.A., Poryvaev V.J., EPG Web of Conferences 146 (2017).

[5] J. Iwanowska, L. Swiderski, T. Krakowski,Nuclear Instruments and Methods in Physics Research Section A **781** (2015) 44.

[6] R. A. Cecil, B. D. Anderson, R. Madey, Nuclear Instruments and Methods **161** (1979) 439.

THE ABSOLUTE NEUTRON FLUX MEASURMENT AT THE VAN DE GRAAFF ACCELERATOR OF THE FRANK LABORATORY OF NEUTRON PHYSICS

E. Sansarbayar[1,2], A. Assylova[1,3], M.V. Sedysheva[1],
I.A. Chuprakov[1,4], and A.Oprea[1]

[1]*Frank Laboratory of Neutron Physics, JINR, Dubna, Russia;*
[2]*Nuclear Research Center, National University of Mongolia, Ulaanbaatar, Mongolia;*
[3]*L.N.Gumilyov Eurasian National University, Astana, Kazakhstan;*
[4]*The Institute of Nuclear Physics, Almaty, Kazakhstan.*

Abstract

We have measured the flux of fast neutrons at 4.6 MeV. The twin gridded ionization chamber and two ^{238}U samples in back-to-back geometry have been employed. Experiments were performed at the Van de Graaff accelerator of the Frank Laboratory of Neutron Physics, Joint Institute for Nuclear Research, Dubna, Russia. Fast neutrons were produced through the $D(d,n)^3He$ reaction by using a deuterium gas. Cross section at E_n= 4.6 MeV of the $^{238}U(n,f)$ reaction was used as the standard for the absolute neutron flux determination. The abundance of the ^{238}U isotope in the sample is 99.999%. The working gas of the ionization chamber was $Ar+3\%CO_2$.

1. Introduction

Monoenergetic neutron beams of known flux are needed in studies of nuclear structure and reaction mechanisms. In addition, this kind of neutron beam is in continuous demand for development of the technology of fission and fusion reactors, health physics and nuclear astrophysics. The $D(d, n)^3He$ reaction is extensively used as a neutron source. We are using the standard cross section method for the determination of the absolute neutron flux.

2. Details of measurements

Experiments were performed at the Van de Graaff accelerator of FLNP, JINR. The experimental setup consists of three main parts: a double-section gridded ionization chamber (GIC) with a common cathode, neutron source, and neutron flux detectors. A deuterium gas target was used to produce the monoenergetic neutron through the $^2H(d,n)^3He$ reaction.

The diameter and the length of the cylindrical gas cell were 9 and 20 mm, respectively. The deuterium gas cell was separated from the beam-line vacuum tube by a molybdenum foil 6.0 μm in thickness. The deuterium gas pressure was 2 atm during the experiment.

In the present work, enriched ^{238}U foil samples were prepared. Data of the samples are listed in Table 1.

Table 1. Description of the samples. ([a] Forward sample, [b]Backward sample)

Samples	Material	Isotopic abundance (%)	Thickness (mg/cm^2)	Diameter (mm)
$^{238}U^a$	$^{238}U_3O_8$	99.999	0.57	44.0
$^{238}U^b$	$^{238}U_3O_8$	99.999	0.54	44.0

The working gas of the ionization chamber was Ar + 3% CO_2 flowed through the volume at the pressure 1.0 atm. A sample changer was set in the common cathode of the ionization chamber with five sample positions and two back-to-back samples can be placed at each of them. A ^{238}U sample was placed in the GIC at the forward direction on the different positions of the sample changer to determine the absolute neutron flux by measuring the fission fragments.

The neutron flux monitor is a ^{3}He counter. The axis of the ^{3}He counter and the normal line of the electrodes of the ionization chamber were at 0° to the neutron beam line. Two-dimensional spectra of the cathode-anode coincidence signals for forward and backward directions were recorded separately, from which the number of fission-events from the measured (n,f) reactions can be obtained. The data-acquisition system (DAqS) can be found in Ref [1].

The experimental process in turn is as follows: 1) α source measurement for energy calibration of the DAqS, 2) foreground measurement for fission events, 3) background measurement with tantalum sheets.

We have measured neutron flux at $E_n = 4.6$ MeV, the $^{238}U(n,f)$ reaction were used as the standard to perform the measurement, the neutron flux can be calculated by the following equation:

$$\Phi_n = \frac{N_f}{N_{samp} * t * \sigma} \quad (1)$$

The σ is the standard $^{238}U(n,f)$ cross sections taken from ENDF/B-VIII library [2]. The N_f is the detected counts above the energy threshold from the $^{238}U(n,f)$ reaction (after background subtraction). The t is the time of our experiment. The N_{samp} is the numbers of ^{238}U nuclei in the samples.

3. Data processing, results

The number of nuclei in the sample determined by the alpha decay of ^{238}U.

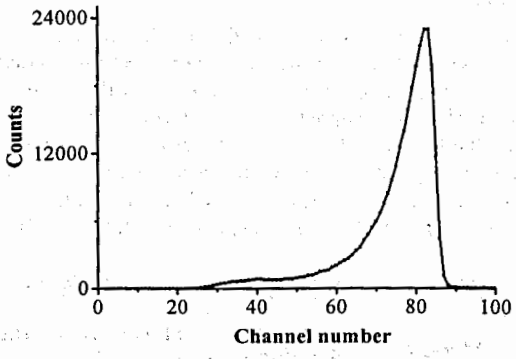

Fig. 1. Anode spectrum of the alpha decay of ^{238}U.

Fig. 1 shows the anode spectrum of α-events. The α counts above the threshold can be obtained from the anode spectrum. As it is shown in Fig. 1, the α counts above threshold, there are also α events below the threshold which cannot be detected. Therefore, threshold and

self-absorption corrections are needed. The determination of the detection efficiency of α-particle, the anode spectra were simulated as shown in Figs. 2 and 4 with the red curves. First of all, we determined the detection efficiency of α-particle used the equation [3]:

$$\varepsilon = \frac{1}{2}\left[1 - \frac{\tau}{2(R_{\max} - R_{\text{threshold}})}\right] \quad (2)$$

The SRIM code [4] was used to get the stopping power of α-particles in the samples. The $R_{\max}$ is the maximum range at 4.6 MeV energy. The $R_{\text{threshold}}$ is the initial range at 1 MeV (we get the alpha spectra).

The detection efficiency for alpha-particle is about 97% for our twin grid ionization chamber. We also have done fitting calculations on the front part of the alpha and fission fragment spectrum using the program OriginPro8. It helps to calculate the number of alpha decay cut by the threshold and the number of fission events.

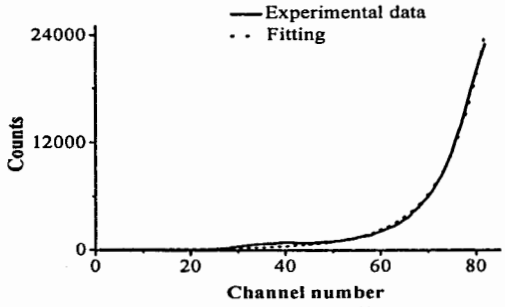

Fig. 2. Anode spectrum of the alpha decay of ^{238}U (fitted by Origin Pro8).

The events of fission fragments can be obtained from the anode spectrum of the fission fragments from the $^{238}U(n, f)$ reaction. The anode spectrum at E_n= 4.6 MeV is shown in Fig. 3. The correction of fission fragments' counts were made by Origin Pro8. Two-dimensional spectrum of the ^{238}U fission fragments is given in Fig.4.

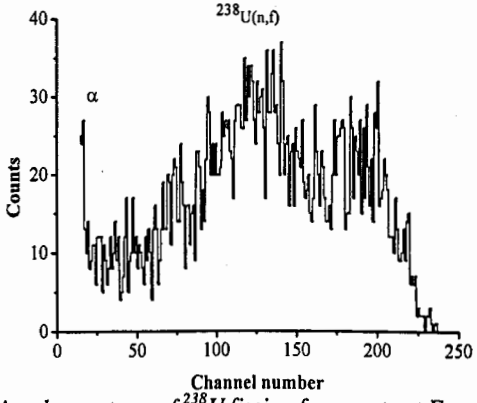

Fig. 3. Anode spectrum of ^{238}U fission fragments at E_n = 4.6 MeV.

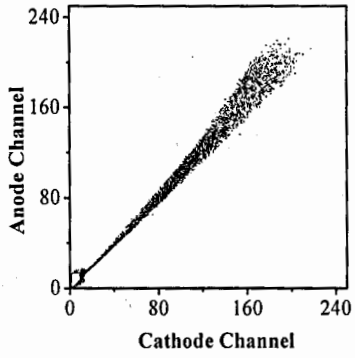

Fig. 4. Two-dimensional spectrum of the ^{238}U fission fragments.

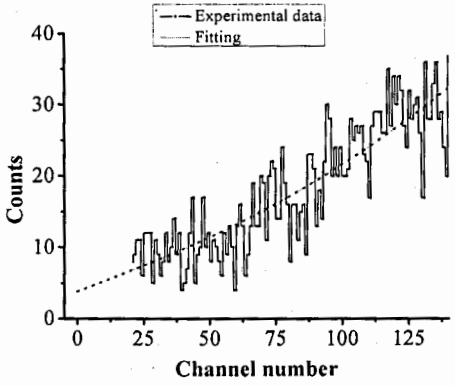

Fig. 5. Simulated anode spectrum of the ^{238}U fission fragments at E_n = 4.6 MeV.

The dotted curve in Fig. 5 shows the simulated result for the fission fragments with low energy.

Table 2. Thicknesses and neutron flux of the samples

Sample	Thickness(mg/cm^2)	Neutron flux(10^5 n/cm^2*sec)		
		Formula (1)	OriginPro	Energy Set Pro
$^{238}U^a$	0.57	1.13±0.05	1.15±0.06	1.72±0.23
$^{238}U^b$	0.54	1.1±0.04	1.13±0.05	1.72±0.23

4. Conclusion

In the present work, the ionization chamber with five pairs of exchangeable samples was used as a detector. The neutron flux measured for neutron energy E_n = 4.6 MeV. Our results are generally in agreement with simulation data. The neutron flux determined by the standard ^{238}U(n,f) cross sections and the Energy Set ver 3.1 [5].

5. References

[1] Yu.M. Gledenov, L. Krupa, E. Sansarbayar, I.A. Chuprakov, "Spectrometer of Charged Particles on the EG-5 FLNP,JINR" Proceedings of international seminar on interaction of neutron with nuclei, Dubna, Russia, May 25-29, 2015.

[2] ENDF: Evaluated Nuclear Data File, database version of September 02, 2014, https://www-nds.iaea.org/exfor/endf.htm.

[3] Bruno B. Rossi, Hans H. Saub. Ionization Chambers and Counters. Experimental techniques. McGRAW-HILL book company, inc, 1949.

[4] J.F. Ziegler, SRIM-2013, http://www.srim.org/#SRIM.

[5] EC-JRC-IRMM, EnergySet ver.3.1.

A Sequential Coded Apertures Imaging System

D. Wang[1,3], E. V. Lychagin[2], H. Hu[1], Yu. N. Kopatch[2], and I. N. Ruskov[2,4]

[1]*School of Energy and Power Engineering, Xi'an Jiaotong University, 710049Xi'an, China*
[2]*Frank Laboratory of Neutron Physics, Joint Institute for Nuclear Research, 141980 Dubna, Moscow region, Russian Federation*
[3]*Northwest Institute of Nuclear Technology, 710024Xi'an, China*
[4]*Institute for Nuclear Research and Nuclear Energy of Bulgarian Academy of Sciences, 1784 Sofia, Bulgaria*

ABSTRACT

To measure the intensity distribution of the n/g radiation emitted from the target of the Intense Resonance Neutron Source (IREN), a new n/g imaging system is proposed. The spatial resolution of an imaging system is usually limited by that of the position n/g-sensitive detector. In this work, we present a new imaging method, which takes advantages of a sequence of coded apertures. With this method, the number of pixels in the position-sensitive detector we needed can be significantly reduced. The simulations for thermal neutrons show that, when the number of detecting pixels is limited, these sequential coded apertures lead to a higher signal-to-noise ratio (SNR), than the widely used modified uniformly redundant array (MURA).

1. INTRODUCTION

At the moment the IREN facility is in stage of testing and modification. The current intensity of the neutron radiation from the neutron producing target (NPT) is ~10^{11} n/s. To control the n/g- production process, we are going to visualize the NPT using n/g imaging system. Because the neutron yield is not very high, the coded aperture imaging technique may be suitable for this task.

The coded aperture imaging [1] consists of two steps: encoding process and image reconstruction. In the first step, a coded aperture is placed between the neutron source and a position-sensitive detector. The coded aperture could be a pinhole array, penumbral aperture, ring aperture, and so forth. In the second step, the source's n/g-radiation distribution is reconstructed from the coded image with the knowledge of the aperture used. If a suitable aperture and reconstruction method are employed, it is possible to recover the source's n/g-radiation distribution with a high resolution and an improved statistical quality.

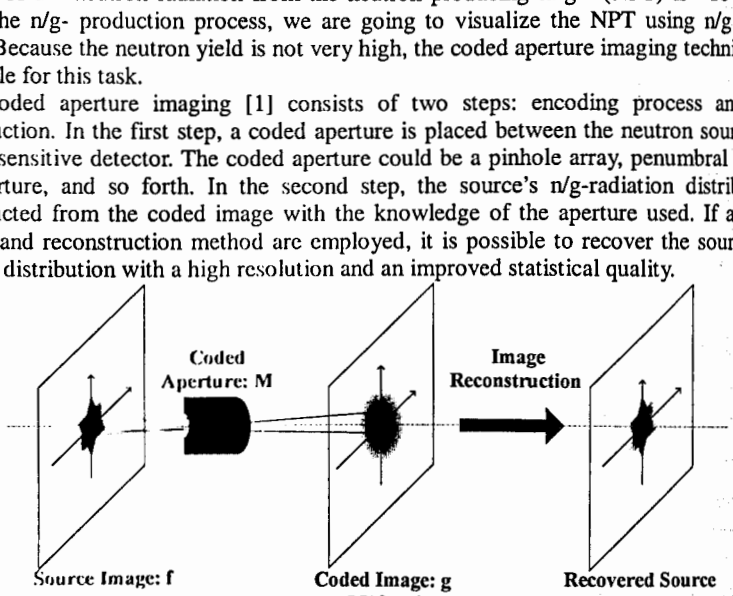

Fig. 1. Two steps of the coded aperture imaging.

2. THE IMAGING SYSTEM

We are going to use an 8×8 Si-stripe pad as a position-sensitive thermal neutron (n_{th}) detector. The number of the "effective pixels" of this detector is 64, and each pixel's size is 1.5 x 1.5 cm. To detect the thermal neutrons, a n_{th}-converter is needed. Two materials are considered: ^{6}LiF and B_4C. The Boron consists of 80% ^{10}B and 20% ^{11}B. Monte Carlo simulations (Geant4) shows that the detection efficiency of ^{6}LiF (optimal thickness = 25 mm) is much larger than that of B_4C (optimal thickness = 1 mm). Thus, a ^{6}LiF converter is adopted in the following analysis.

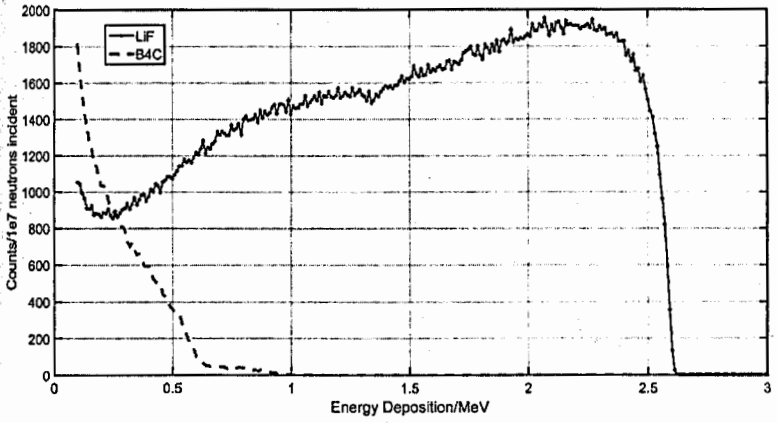

Fig. 2. Energy depositions in silicon.

Because the number of Si-pixels is rather small, two schemes are designed to overcome this problem. In scheme I (Fig. 3), the Si-detector is removable. After a measurement is finished, the detector is moved to another position for the next measurement. In this way, we can record 64x64 pixel coded images.

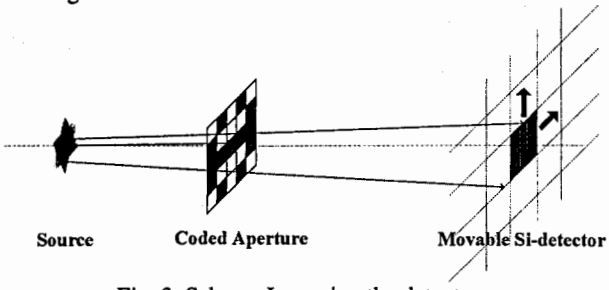

Fig. 3. Scheme I: moving the detector.

In scheme II (Fig. 4), the detector is fixed, but the pattern of the coded aperture is different in each measurement. The coded aperture consists of two groups of orthogonal strips, similar to the Pseudo-Noise Product (PNP) coded aperture array [2], except that the pattern is not invariable during imaging. Before each measurement, the strips are randomly rearranged - insert or pull out some strips. This idea comes from the single pixel camera [3] in *compressed sensing*. In this way, the source image is sampled in a compressed form, thus the number of detecting pixels required can be significantly reduced.

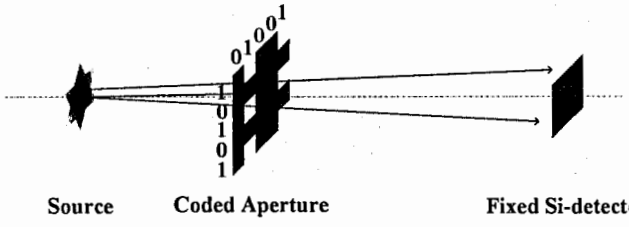

Fig. 4. Scheme II: changing the aperture's pattern.

3. SIMULATION RESULTS AND DISCUSSION

To compare these two schemes, we have carried out some simulation calculations for thermal neutrons. The coded aperture used in scheme I is a 61 × 61 MURA coded pinhole array [4] (basic patterns: 31 × 31), the size of each element is 7.5 × 7.5 mm. In scheme II there are 24 strips in horizontal and 24 in vertical positions. The material of aperture is cadmium (Cd) with a thickness of 0.5 mm. The other parameters are: total thermal neutron yield (in 4π) = 10^{12}, field-of-view in the source's plane FOV = 20 × 20 cm^2; source-to-aperture distance = 1.5 m; source-to-detector distance = 6.0 m. The image recover method used in this work is a L1-minimization algorithm [5].

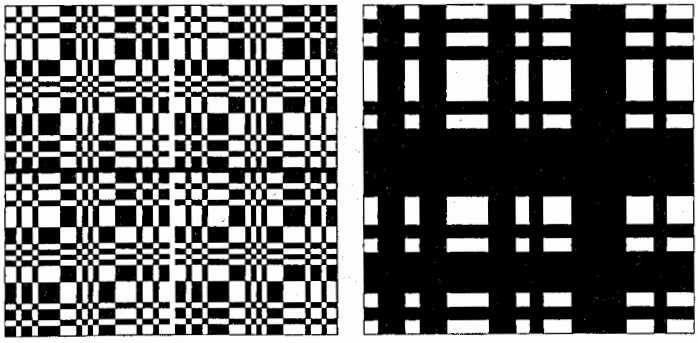

Fig. 5. Coded apertures used in this work.
Left: the MURA. Right: one of the sequential coded apertures.

Note that in scheme I we should take 64 measurements to record the whole coded image. Thus, in scheme II we also take 64 measurements to make a fair comparison. The neutron yield in each measurement is $10^{12}/64$. With the same neutron yield and number of measurements, the scheme II could lead to a higher SNR (with source image as the reference) and sharper edges, as shown below in Fig. 6.

To study the relationship between the SNR of the recovered source and the number of measurements, we adjusted the latter in scheme II. The neutron yield is each measurement is $10^{12}/64$. The results are shown in Fig. 7. At first, the SNR of the recovered image increases fast with increasing the number of measurements. With more than 20 measurements the SNR of this scheme will exceed that of scheme I with 64 measurements.

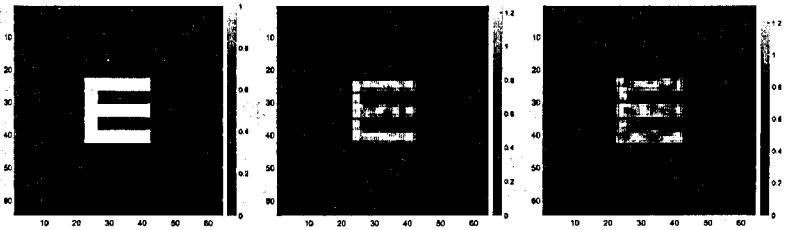

Fig. 6. Simulated reconstruction images. Left: the source image. Middle: by Scheme I, SNR=11.9 dB. Right: by Scheme II, SNR=15.1dB.

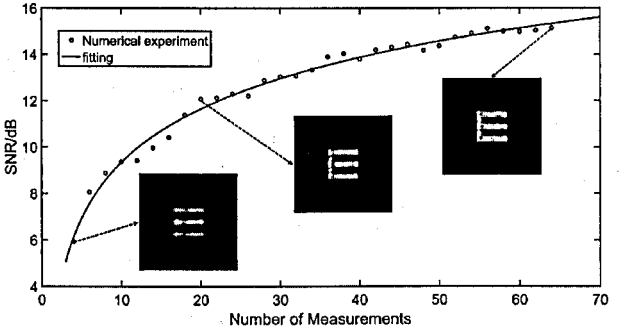

Fig. 7. The SNR of recovered source vs. number of the measurements.

4. CONCLUSIONS

In this work we present a sequential coded apertures imaging system for a radiation source that can be measured repeatedly. The simulated thermal neutron image reconstruction shows that, with a limited number of detecting elements (sensor pixels), this method could also lead to high fidelity source distribution within dozens of measurements. This method can also be used in gamma imaging. In that case, the position resolution and energy resolution can be achieved simultaneously.

ACKNOWLEDGMENTS

One of us (W. D.) would like to thank the Director of FLNP, Sc.D. V. N. Shvetsov, for his interest in this work and helpful discussions on IREN facility.

REFERENCES

[1] Barrett H.H., Swindell W., Radiological imaging: the theory of image formation, detection, and processing. Academic Press, 1996.

[2] Gottesman S.R., Schneid E.J., PNP - a new class of coded aperture arrays, IEEE Transactions on Nuclear Science, 1986, **33**(1): 745-749.

[3] Duarte M.F., Davenport M.A., Takbar D., *et al.*, Single-pixel imaging via compressive sampling, IEEE signal processing magazine, 2008, **25**(2): 83-91.

[4] Gottesman S.R., Fenimore E.E., New family of binary arrays for coded aperture imaging, Applied optics, 1989, **28**(20): 4344-4352.

[5] Chambolle A., Pock T., A first-order primal-dual algorithm for convex problems with applications to imaging, Journal of Mathematical Imaging and Vision, 2011, **40**(1): 120-145.

Position Sensitive Twin Ionization Chamber for Nuclear Fission Investigations

Zeynalov Sh.[1], Sedyshev P.[1], Sidorova O.[1], Shvetsov V.[1], Svetov L.[2]

[1]*Frank Laboratory of Neutron Physics, Joint Institute for Nuclear Research, Dubna, Russia*
[2]*Dubna International University of Nature, Society and Man, Dubna, Russia*

Abstract. In this work we report the recent achievements in design of twin back-to-back ionization chamber (TIC) for fission fragment (FF) mass, kinetic energy and FF orientation. Correlated FF kinetic energies, their masses and the angle of the fission axes in 3D Cartesian coordinates can be determined from analysis of the heights and shapes of the pulses induced by the fission fragments on the anodes of TIC. Anodes of TIC were designed as consisting of isolated Δ-shaped strips connected to nodes of the chain filter, made of serially connected two-port networks. Double charge division method was implemented by digitizing four waveforms at the endpoints of the chain filters. It was shown how the fission fragments emission point on the target plane may be determined using the measured data. Position sensitive neutron induced fission detector for neutron imaging applications with both thermal and low energy neutrons was found as another possible implementation of the designed TIC. Preliminary measurements with the thermal neutron induced fission were done with RC chain filters and the results were demonstrated.

Keywords: ionization chambers, fission; thermal neutrons.

1. Introduction

Nuclear fission model and prompt fission neutron emission (PFN) was first developed by N. Bohr and J. Wheeler, where nuclei considered as a drop of charged liquid, which surface constantly distorted in competition between attractive nuclear and repulsive Coulomb forces. Rarely large distortion brought the nuclear into the configuration, where repulsion could not be compensated by nuclear force and the system split, sometimes after neutron emission. In this case the neutrons, called scission neutrons in order to distinguish them from the PFN, which are emitted from the fully accelerated fission fragments. The configuration of nuclear shape just before split can be monitored experimentally by measurement of fission fragment (FF) kinetic energy release along with PFN velocity and the angle between fission axis and PFN measured in single fission event. In new experimental approach developed in ref. [1] authors investigated PFN emission in spontaneous fission of ^{252}Cf using twin Frisch-grid ionization chamber (TIC) for FF kinetic energies and PFN emission angle along with PFN velocity measurement with help of liquid scintillator (NE213 or equivalent liquid) based neutron detector (ND). The authors demonstrated a power and high capacity of the new approach, which was further elaborated by replacing the traditional analog electronics by modern digital pulse processing (DPP) described in ref. [2]. The PFN detection efficiency of the method was limited by use only two fast neutron detectors, allocated along the TIC axis, because of the FF angle in TIC could be measured in respect to the certain axis. If the PFN detector allocated along this axis, then the measured angle was the same as between FF and PFN emission. Therefore the next modification of the method was intended to measure correlated FFs angles in respect to three axes of 3D Cartesian coordinate frame in the event by event basis. If the PFN detectors allocation in the same Cartesian frame was fixed and well known, then the angle between FF and PFN emission could be evaluated for each fission

event. It should be noticed that two correlated FF was emitted along the straight line called fission axis for the considered fission event. That means that for each fission event the coordinates of two points on the fission axis could be measured refs [2, 3]. This gives the possibility to evaluate the 2D coordinates of the crossing point of the fission target plane with fission axis - neutron capture location. The modification was expected to improve the quality of experiments with targets like ^{239}Pu, ^{235}U, ^{237}Np in resonance neutron induced fission. In addition the slight modification of the developed 2D coordinate readout principle expected became very competitive solution for the neutron imaging, tomography and similar applications.

2. Ramo-Shokley Theorem and Charge Division

Using the Ramo-Shokley theorem (see ref. [4]) calculation of so called weighting potential in 3D Cartesian coordinate system was done. According to the theorem condition the weighting potential in the TIC volume was calculated for one Δ-electrode potential raised to 1, leaving other electrodes grounded. If the strips operated at positive potential relative to the cathode surface, then ionization electrons would be attracted along the real field lines (calculated for homogeneous electric field between anode-cathode). From the calculated weighting potential *F(x, y, z)* the slices *F(x, y=const, z)* were derived and plotted in Fig. 2 to demonstrate the charge division along the Y-coordinate of the anode plain.

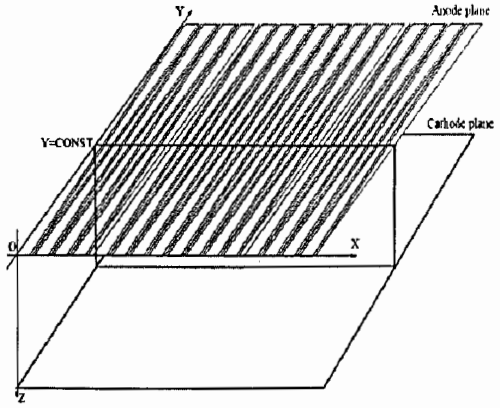

Fig. 1. The allocation of the electrodes for one of the TIC.

Full scale of X, Y, Z - coordinates was 400, 300, 300 units respectively. It should be noticed that weighting potential almost has zero values everywhere except the close vicinity of the anode plane. If the cathode-anode distance was chosen large to keep the FFs stopping far enough from the anode plane, then there was no need in Frisch-grid as screening electrode. From the Y-dependence of weighting potentials the linear behaviour of the charge division between complementary Δ-electrodes was concluded. This fact was utilized to evaluate the Y-coordinate value from the induced signals on the anode. The charge induced on the Δ-electrode was calculated according to Ramo-Shockley theorem as:

$$Q = q \cdot \Delta F , \qquad (1)$$

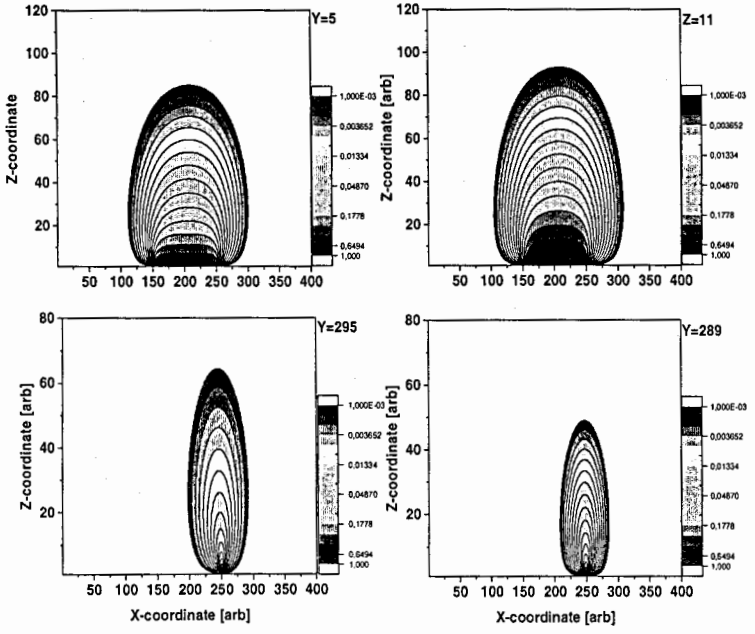

Fig. 2. Weighting potential $F(x, y=const, z)$ shown for Y= 5 and Y=11 along with Y=295 and Y=289 for complementary Δ-electrodes.

where ΔF is the difference of weighting potentials between the point of charged particle q origin and the point where the charged particle was collected at the anode surface and Q is the induced charge. The FFs create ionisation electrons along their deceleration path in the TIC working gas. In description of pulse formation in TIC the charge "centre of gravity" considered as a good measure of FF coordinate. Therefore in this paper all calculation of FF coordinates referred to that value, calculated according to the formula:

$$\overline{X} = \frac{1}{Q_f} \int_0^{\infty} \rho(x) \cdot x \cdot dx, \quad Q_f = \int_0^{\infty} \rho(x) dx, \tag{2}$$

where integration was done along the FF deceleration path, $\rho(x)$ is the density distribution of ionization electrons along the FF deceleration path and Q_f is the full charge of ionization electrons.

3. Charge Division on the Chain Filter

The position information along the X-coordinate was obtained by two methods: the charge attenuation and the pulse delay. Both methods based on the charge split at the node of chain filter. Chain filter was created by serially connected two-port networks created by resistor R, inductance L and capacitance C of Δ-electrode as shown in Fig. 3. Induced charge splits into

the respective inputs of pair of symmetric two-port networks. If the chain filter ends loaded with wave impedance, then the charge splits into two equal portions between two ends of chain filter. The operational calculus is conventional method to study of signal propagation along the serially connected two port networks (chain filter). Circuit diagram of the chain filter made of passive electrical components depicted in Fig. 3,

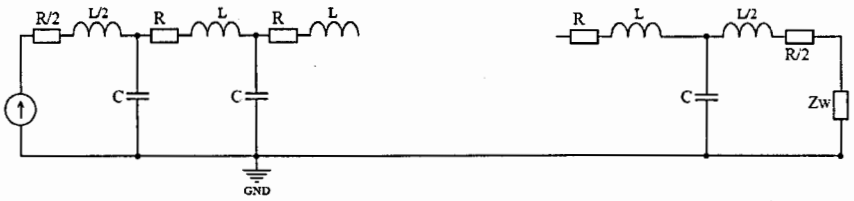

Fig. 3. Circuit diagram of the chain filter.

Chain filters terminated with the wave impedance Z_w at the end. If the resistance could be neglected, then Eq. 3 represents the Laplace transform of the unit step signal after passing the m two-port networks. The inverse

$$i_m(t) \supset \sqrt{\frac{C}{L}}\frac{1}{p}\frac{1}{\sqrt{\left(\frac{b}{p}\right)^2+1}\cdot\left[\frac{b}{p}+\sqrt{\left(\frac{b}{p}\right)^2+1}\right]^{2m}}, \qquad b=\frac{1}{2\sqrt{LC}}. \tag{3}$$

Laplace transform could be found using transform tables [5]:

$$i_m^{ind}(t)=\sqrt{\frac{C}{L}}\int_0^{\infty} J_0(2\sqrt{bt\tau})J_{2m}(\tau)d\tau \ . \tag{4}$$

Eq. 4 describes propagation of the unit step signal over chain filter made of inductance and capacitance (resistance is very small). In case when the resistance could not be neglected, then the result is as follows:

$$i_m^{res}(t)=\sqrt{\frac{C}{L}}\int_0^{t}\exp(-\frac{R}{L}\cdot t)J_{2m}(\frac{2\cdot t}{\sqrt{LC}})d(\frac{2\cdot t}{\sqrt{LC}}) \ . \tag{5}$$

Eq. 5 describes propagation of the unit step signal over chain filter made of resistance and capacitance (inductance very small). The wave impedance and the speed of signal propagation given by the following formulas for both cases, considered above:

$$Z_w=\sqrt{\frac{(R+pl)^2}{4}+\frac{R+pL}{pC}}, \qquad \frac{m}{t}=\frac{1}{\sqrt{LC}} \ . \tag{6}$$

It should be noticed that in case of resistive chain filter the pulse height of the unit step attenuated exponentially, passing the chain filter.

4. Numerical Simulations

The dependence of output pulse height on the sequential numbers of two- port networks, composing the chain filter, consisting of 16 two-port networks plotted in Fig. 4. The calculation was done using digital RC-filter representing two-port network. The attenuation of the unit step signal height by factor exp(-m/T) on passing sequentially the m two-port networks was calculated and plotted on the left of Fig. 5 and T value was found by fitting.

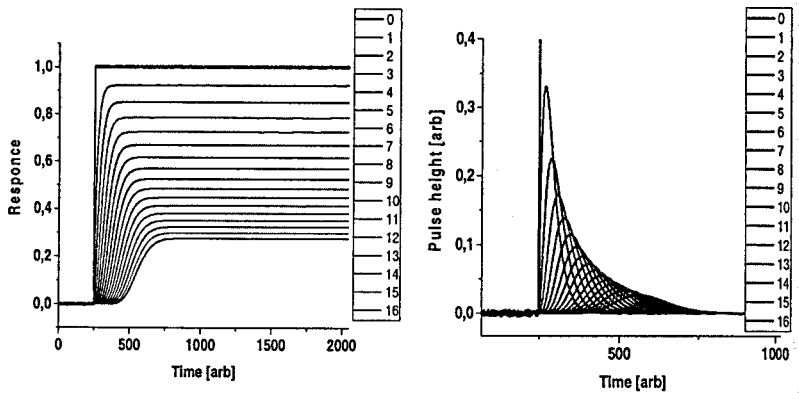

Fig. 4. Unit step signal attenuation after passing m times the two-port networks (on the left) and the pulses obtained after differentiating the unit step signals (on the right).

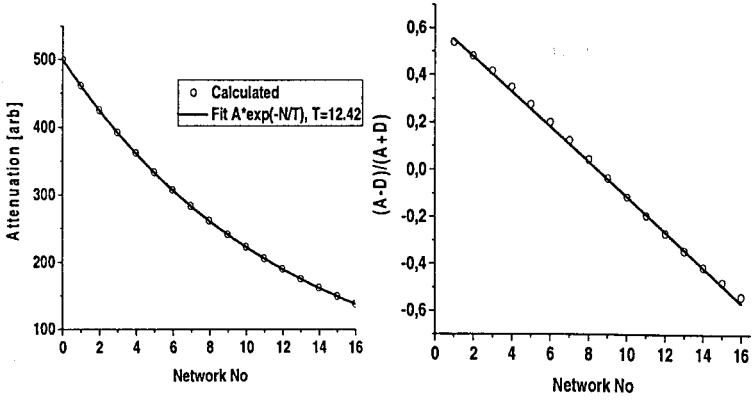

Fig. 5. Attenuation of unity sep signal height after passing number m of two-port networks (on the left) and position evaluated from simulated data (on the right).

The T parameter could be used to correct the attenuation of total charge induced on the strips. The coordinate m of the charge "centre of gravity" were evaluated from the simulated pulses using the following formula:

$$m = \frac{A - B}{A + B}, \tag{7}$$

where A and B were the pulse heights calculated for two-port network with sequential number m and 16-m respectively. Result demonstrated almost perfect linear dependence on the network number (left graph on Fig. 5). Another way to determine the coordinate m was connected to measurement of delay between unit step signal and its response at the ends of two port networks as demonstrated in the right plot of Fig. 4.

5. Experimental Measurements

Experiments were performed with ionization chamber with anode of rectangular shape made of 16 strips each consisted of 2 Δ-electrodes as shown in Fig. 6.

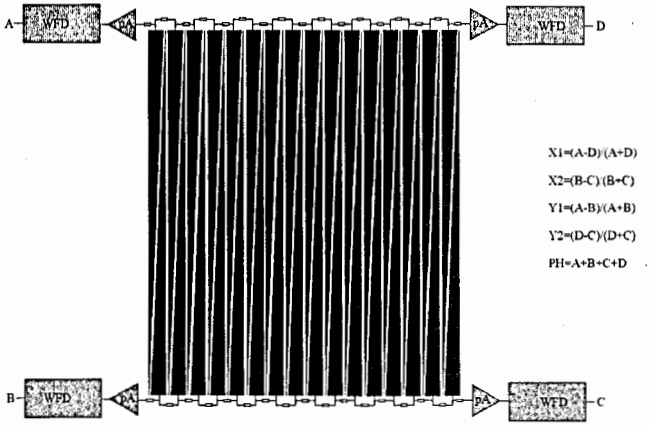

Fig. 6. Sketch of data readout system used in the experiment.

Each Δ-electrode connected to the nodes of the sequentially connected resistors. These resistors connected with Δ-electrode capacitance created two-port network. The ending resistors were connected to the input of charge-sensitive preamplifier. Output signals of preamplifiers were digitized by for synchronous waveform digitizers (WFD) with sampling frequency of 250 MHz and pulse height resolution of 8 bits. Target made of $^{235}UF_6$ deposited on the surface of thick Al foil. The target thickness was ~500 μG/cm^2, and it was mounted on the centre of circular cathode with diameter 180 mm. Distance between the cathode and the anode was ~45 mm. The working gas of ionization chamber was standard P10 mixture (90%Ar+10%CH_4). Chamber was operated at constant gas flow ~35 ml/min with pressure 1.07 bars. FFs were produced by thermal neutron flux ~10^4 neutrons/sec. The capture of thermal neutron by ^{235}U nuclei cause the fission, producing two FFs, one of which was decelerated in the working gas of ionization chamber. Ionization electrons created by FF drifted along the electric field lines toward the anode, inducing the signals on Δ-electrodes. After amplification the signals were recorded by four WFD and collected on PC memory for further off-line data analysis. There were four waveforms recorded for each fission event, which were used for FF charge "centre of gravity" evaluation. The organization of the measurement apparatus provided the possibility to made measurement of each coordinates in

two different independent ways. This was used to evaluate the precision of the coordinate measurement as demonstrated in the Fig. 7. For example coordinate X was measured as:

$$X_1 = \frac{A-D}{A+D} \quad \text{and} \quad X_2 = \frac{B-C}{B+C}, \tag{8}$$

where A, B, C, D were the pulse heights, obtained from the correlated waveforms, and recorded for the same fission event. These measured coordinates were used to made 2D plot $P(x, y)$ in coordinates x, y calculated for each fission event using formulas:

$$x = (X_1 + X_2)/2, \qquad y = (X_1 - X_2)/2. \tag{9}$$

The function $P(x, y)$ was plotted on the left of Fig. 7 and demonstrates scattering of the points due to random errors. The function $G(x, y)$ was constructed in the way similar to $P(x, y)$ using the following formulas:

$$Y_1 = \frac{A-B}{A+B} \quad \text{and} \quad Y_2 = \frac{D-C}{D+C}. \tag{10}$$

From the values of Y_1, Y_2 coordinates of 2D function $G(x, y)$ were constructed using the following formulas:

$$x = (Y_1 + Y_2)/2, \qquad y = (Y_1 - Y_2)/2. \tag{11}$$

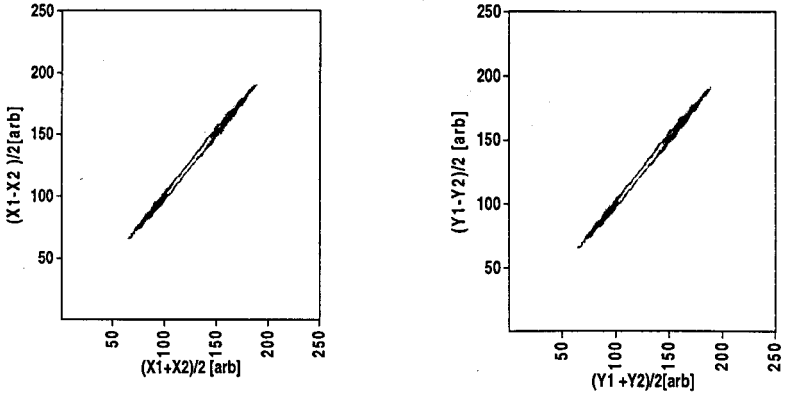

Fig. 7. Two dimensional plots demonstrating the scattering of measured data in respect to average values for X and Y coordinates in the anode plain.

Plot of $G(x, y)$ was presented on the right of Fig. 7. The measured functions $P(x, y)$ and $G(x, y)$ were used for precision evaluation of x, y-coordinate measurements. It was done integrating functions $P(x, y)$ and $G(x, y)$ over variable x. Results were presented in Fig. 8 on the left.

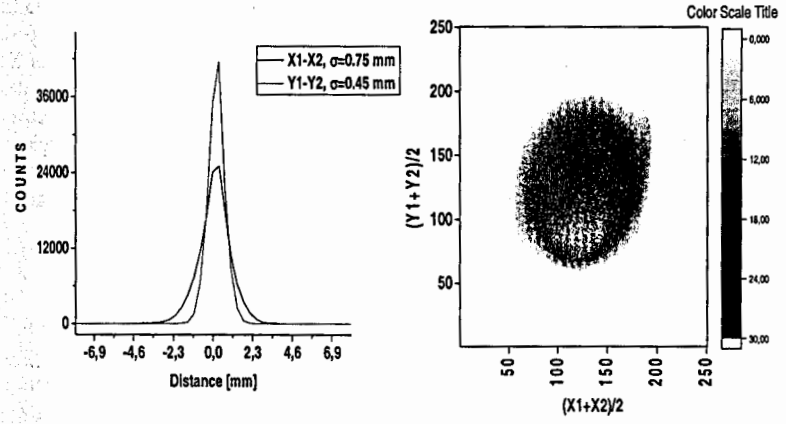

Fig. 8. One dimensional plot, demonstrating precision of position of charge "centre of gravity" measurement (on the left) and the image of the ^{235}U target.

On the right of Fig. 8 the image of the ^{235}U target measured in this experiment was presented. It should be noticed that measurements was done with one of the TIC chambers due to target backing was tick enough to absorb the complementary FF. That is why in performed experiment fissile nucleus position could not be measured directly. The kinetic energy release of FF was analyzed using all four waveforms, recorded in event by event basis. These waveforms first were corrected for attenuation in the chain filter as was described above. The corrected waveforms were unfolded to single one taking into account that sampling of the four signals actually was made sequentially with 1 GHz frequency. That means that first signal sampled at first rising edge of 1 GHz oscillator, second signal at the next edge and so on. The unfolded signal was used for evaluation of the Z-coordinate of FF charge "centre of gravity" and the angles between FF and Cartesian frame axes as it was described in refs. [2,3,7]. Using coordinates, kinetic energy, and the angle measured for one of the FF the coordinates, the similar parameters for correlated FFs were evaluated neglecting the target thickness. Correlated FF kinetic energy was calculated using total kinetic energy value for $^{235}U(n_{th},f)$ reaction known from the literature [6]. The location of the point on the target plane then was evaluated as the crossing point of straight line drawn between two "center of gravity" points of two correlated FF. The evaluated accuracy of the coordinates was found to be better than 0.2 mm.

6. Conclusions

Theoretical and experimental investigation of signal propagation trough the chain filter made of serially connected two-port networks was performed with objective of position sensitive ionization chamber design for PFN emission investigation with arbitrary allocated fast ND. Relations between 2D Cartesian coordinate (X,Y) information and response of chain filter was found and investigated by digital simulation. It was shown that coordinate information can be obtained by both the double charge division and time delay method. Implementing both methods provided better accuracy in coordinate measurement. Dependence of pulse height data on coordinate was investigated for resistive chain filter. The procedure of pulse

height data correction was developed. Measurement of neutron imaging with U-235 target was done to demonstrate the quality of the double charge division method for position sensitive ionization chamber. Good position resolution was demonstrated: 0.7 mm for X and 0.5 mm for Y coordinates. New design for He-3 imaging proportional chamber with double charge division method could utilize the double charge division method to improve the coordinate resolution in comparison with double delay line readout system. Digitization electronics was implemented for data acquisition system, and the data analysis software was developed and tested in experiments. The data analysis was done using DPP algorithms developed by authors in previous publications in Ref. [7] as the recursive procedures.

References

1. C. Budtz-Jorgensen, H.-H. Knitter, Ch. Straede, F.-J. Hambsch and R. Vogt, *Nucl. Instr. and Meth.* **A258** (1987) 209-220.
2. Sh. Zeynalov, O. Zeynalova, M.A. Nazarenko, F-J. Hambsch and S. Oberstedt, *Aip. Conf. Proc.* 1487, 405 (2012); doi: 10.1063/1.4758984.
3. A. Gook, W. Geerts, F.-J. Hambsch, S. Oberstedt, M. Vidali, Sh. Zeynalov, *Nucl. Instr. and Meth*, **A830** (2016) 366-374.
4. G.F. Knoll, *Radiation detection and measurements*, (Wiley, New York, 2000), p. 789.
5. G.A. Korn, T.M. Korn, *Mathematical Handbook for Scientists and Engineers.* (McGraw-Hill Book Company, New York, 1968 edition), p. 926.
6. C. Wagemans ed, *The Nuclear Fission Process*, (Boca Raton: Boca Raton, 1991), p. 323.
7. L. Svetov, O. Sidorova, Sh. Zeinalov. *In proc. of XXIV International Seminar on Interaction of Neutrons with Nuclei*, Dubna, May 24-27, 2016, JINR E3-2017-8, p. 430.

A Proton Imaging System for Magnetic Proton Recoil Neutron Spectrometer

Zhang Jianfu, Zhang Xianpeng, Ruan Jinlu, Yang Shaohua, Liu Jinliang, Chen Liang, Liu Linyue, Ma Jiming

State Key Laboratory of Intense Pulsed Radiation Simulation and Effect (Northwest Institute of Nuclear Technology), Xi'an, 710024, China

ABSTRACT

Magnetic proton recoil (MPR) neutron spectrometer is considered as a high-performance instrument to measure deuterium-tritium (DT) neutron energy spectrum in magnetic confinement fusion, inertial confinement fusion experiments and other fusion devices. A compact proton imaging system (PIS) has been developed for MPR neutron spectrometer. The PIS was used as focal plane detector (FPD) to detect and image the fluence distribution of recoil protons. The PIS consists of a thin plastic scintillator, fiber optic taper and image guide, electron-multiplying charge-coupled device (EMCCD) and data acquisition system. The key imaging properties, including resolution, response to proton and capability as a FPD for the MPR neutron spectrometer, were evaluated using proton beams at accelerators. The PIS with Gd_2O_2S:Tb scintillator screen has higher performance in resolution and light yield than that with 2 mm plastic scintillator. The Gd_2O_2S:Tb scintillator screen can be used as an ideal candidate for proton imaging. The imaging properties of the PIS shown in this paper have demonstrated that the PIS is suitable for the MPR spectrometer in DT neutron measurement.

Keywords: MPR neutron spectrometer, proton imaging system, Gd_2O_2S:Tb scintillator screen, thin plastic scintillator, light yield, spatial resolution

1. Introduction

Magnetic proton recoil (MPR) neutron spectrometer is considered as a high-performance instrument to measure deuterium-tritium (DT) neutron energy spectrum in magnetic confinement fusion (MCF), inertial confinement fusion (ICF) experiments and other fusion devices [1–5]. The method of MPR is based on n-p elastic scattering and magnetic dispersion. Neutrons are converted to protons through n-p elastic scattering in the polyethylene (CH_2) foil. In the magnetic field of the MPR neutron spectrometer, the recoil protons are spatially separated according to their momentum and then focused on the focal plane detector (FPD) which records the spatial position of each recoil proton. Thus, the recoil proton energies distribution can be converted into a position distribution. The FPD for the MPR neutron spectrometer has to meet the requirement of a good position resolution, proton response and signal to background. Currently, measurements of recoil proton distribution for the MPR neutron spectrometer are performed using CR-39 track detectors or scintillation detector array. CR-39 is a plastic which is sensitive to appropriate energy charge particle as a track detector. It has 100% detection efficiency for protons less than 8 MeV. This kind of detector has been widely used as FPD in many ICF experiments [4,6,7]. However, CR-39 detector is quite time

consuming and difficult to implement since it needs to be etched, photomicrographed and digitized. The scintillation detector array called hodoscope has been applied as FPD in many MCF experiments [8-10]. The hodoscope based on the phoswich technique is less sensitive to background by working in counting mode of high frequency. The hodoscope is composed of an array of 32 plastic scintillators each connected to one photomultiplier tube. It has been upgraded to get better signal to background by each plastic scintillator connected to two photomultiplier tubes.

In this work, a proton imaging system (PIS) was developed as FPD for the MPR neutron spectrometer. The PIS can be considered as a position sensitive proton detector based on proton imaging method. The PIS will work with light integrating mode in real time. This paper describes the PIS configuration and presents some imaging properties measured using proton beams. The Gadolinium Sulphate Oxide doped with Terbium (Gd_2O_2S:Tb) scintillator screen (typically used in X-ray image converters) for proton imaging application is discussed by comparing its performance to thin plastic scintillator in terms of spatial resolution and light yield.

2. PIS design

The main objective is to design PIS that can record the proton distribution by achieving two-dimensional proton imaging under the condition of the MPR neutron spectrometer. Figure 1 is a schematic of the PIS for the MPR neutron spectrometer. The PIS consists of a thin plastic scintillator, fiber optic taper and image guide, electron-multiplying charge-coupled device (EMCCD) camera and data acquisition system. The EMCCD is based on standard CCD with the addition of a gain register, which allows the signal electrons to be multiplied with lower noise. The EMCCD camera used in this design is based on a back-illuminated CCD201 from E2V technologies. In the PIS, the thin plastic scintillator is used to efficiently convert the protons to visible light. The light escapes from the surface of scintillator can be conveyed through the relay optical system to the EMCCD camera of high spatial resolution (1000×1000, 13μm square pixel) and further processed by image data acquisition system to form a digital image. The digital image can be used to determine the distribution of protons.

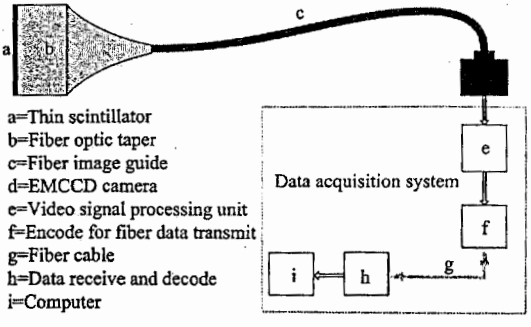

Fig. 1. Sketch of the PIS to be used for FPD on the MPR neutron spectrometer.

Plastic scintillators have been widely used for charged particle detection because of their fast time response, high light yield and favorable mechanical properties. It is easy to fabricate in large area and any shape. In the scintillator plate, the scintillation light is emitted in all directions. The light photon will be reflected back if its angle of incidence is larger than critical angle. The light spreading dimension depends on the reflection angle and the thickness of scintillator. The use of array of scintillating fibers can prevent resolution loss due to light spreading. In principle, the spatial resolution obtained with thin plastic scintillator is degraded because of the increased light spread distribution compared to array of scintillating fibers. Since 14 MeV protons will be completely stopped within plastic scintillator about 2 mm thickness, a simple thin plastic scintillator is reasonable for proton imaging instead of array of scintillating fibers for PIS.

In the PIS, the fiber optical system is composed of a fiber optic taper (tapering ratio3.3:1) and a fiber image guide (diameter of 1 cm) replacing a mirror and a lens. Fiber optical system coupling is usually more efficient than a lens. For this application, the EMCCD is equipped with a fiber optic window, which is used to directly couple to fiber image guide. The fiber optic taper is used to increase the effective detection area of the PIS. To avoid radiation damage to the EMCCD sensor, the EMCCD camera will be located far from the irradiation by using a long fiber image guide. Because of the distance and shielding, the EMCCD camera is able to obtain images with little background from irradiation.

An image data acquisition system (DAC) for protons imaging was developed [11]. In present work, the DAC based on fiber communication and the standard USB transfer is employed. EMCCD video signals are digitized and transmitted to long-distance acquisition hardware through fiber cables, and the raw digital images are stored on the memory installed in the computer. The terminal of DAC can be placed in the measurement room to control the EMCCD camera by fiber cables of several tens meters.

3. Experiment and results

3.1. Resolution measurement

The resolution measurement was performed with proton beams from the 2×6 MV tandem accelerator at Peking University. In the experiment, the proton beam was defocused at the end of the beam line with the beam intensity of several tens pA. During the measurement, the accelerator was operated in a continuous mode and the proton beam was delivered through a Ti film window of ϕ10 mm diameter and 5 μm thickness with a frequency of 50 Hz. The proton beam at the energy 10 MeV was selected. The line spread function (LSF) provides a detailed description of the spatial resolution. The tungsten (W) edge image is usually used to measure the LSF of imaging system. In the measurement, the W edge was placed between the Ti window and the scintillator with the edge aligned along the proton beam line. The digital W edge image was derived as the following. First, each image was smoothed with a 2-D median filtering to suppress little high frequency noise. The filtered image was then corrected by subtracting the average background of readout noise. The background image was measured without any protons (dark current image). Line profile perpendicular to the W edge image was averaged to get the edge spread function (ESF). The LSF was then obtained by differentiating the ESF.

Gd_2O_2S:Tb scintillator screens are typically used in X-ray image converters. It has excellent scintillation properties such as high light yield and good resolution. Gd_2O_2S:Tb scintillator screen used for the PIS consists of a reflecting layer and a phosphor layer of 0.2 mm thickness. To test its applicability for proton imaging, the spatial resolution of Gd_2O_2S:Tb scintillator screen (FWHM of LSF) was first evaluated by comparing to thin plastic scintillator. Figure 2 (a) and (b) show the background-subtracted W edge image recorded with the PIS, using the 2 mm plastic scintillator and Gd_2O_2S:Tb scintillator screen, respectively. Fig. 2(c) shows the comparison of the LSFs of the PIS. The two FWHMs calculated from the LSFs were estimated to be 0.95 mm and 0.72 mm, respectively for 2 mm plastic scintillator and Gd_2O_2S:Tb scintillator screen. The result presented here shows an improvement in spatial resolution with Gd_2O_2S:Tb scintillator screen.

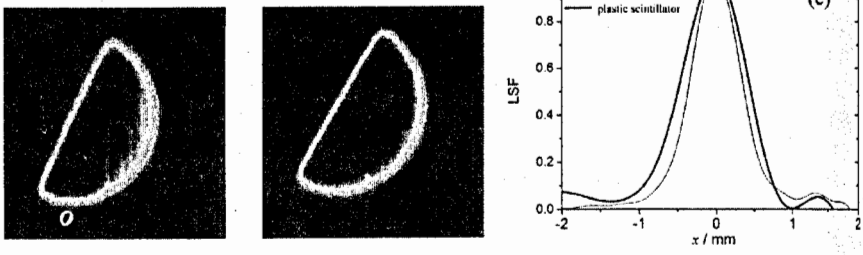

Fig. 2. The background-subtracted W edge image recorded with the PIS, (a) 2 mm plastic scintillator, (b) Gd_2O_2S:Tb scintillator screen; (c) Comparison of the LSFs of the PIS with 2 mm plastic scintillator Gd_2O_2S:Tb scintillator screen using the proton beam at 10 MeV.

3.2 Response to protons

Light yield of the scintillator detected by the PIS should be linear to proton intensity so that the proton fluence distributions can be measured. Response to protons of the PIS allows us to evaluate its applicability for determining the proton fluence. The response to protons was also performed with proton beams of 10 MeV at the 2×6 MV tandem accelerator. Response to protons of the PIS working in light integrating mode is defined by the average gray values (AGV) on each pixel per unit proton fluence. Response to protons was obtained by measuring the gray values of the image varying with the proton fluence. The AGV of image represents light yield of the scintillator detected by the PIS over the EMCCD integration time. The beam intensity was monitored by a Faraday cup detector of 3 cm^2 and the proton fluence was normalized by the integration time of the PIS. The typical integration time of the EMCCD in the measurement was 150 ms. The internal gain of the EMCCD camera was set to get the desired image according to the beam intensity.

Response to protons of the PIS with Gd_2O_2S:Tb scintillator screen and 2 mm plastic scintillator was measured at 10 MeV proton. The internal gain of the EMCCD with the Gd_2O_2S:Tb scintillator screen and 2 mm plastic scintillator was set to EM=1 and EM=80, respectively. This reduction of internal gain is due to the high light yield of the Gd_2O_2S:Tb

scintillator screen. The internal gain ratio of 69 (EM=80/EM=1) was measured to correct the gray values. Figure 3 presents AGV of the image (EM=1) as a function of proton fluence. Linear best fit the measured data, meaning that the outputs of AGV are proportional to the proton fluence. The response to protons of the PIS with the Gd_2O_2S:Tb scintillator screen and 2 mm plastic scintillator are 300 and 13 AGV/proton (EM=1), respectively. It can be adjusted by setting the EMCCD camera with different internal gain. Response to protons of the PIS with Gd_2O_2S:Tb scintillator screen is about 23 times higher than that with 2 mm plastic scintillator at 10 MeV protons.

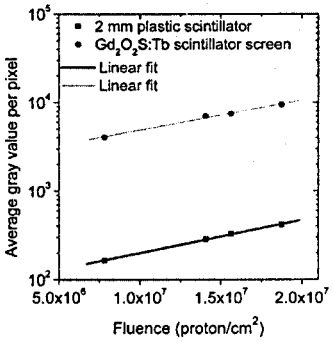

Fig. 3. Average gray value of the images (EM=1) as a function of proton fluence at 10 MeV.

3.3 Testing on MPR neutron spectrometer

In order to evaluate the performance of the PIS using for the MPR neutron spectrometer, a test using proton beam was carried out at the HI-13 tendon accelerator at China Institute of Atomic Energy (CIAE). In the test, the PIS acted as the FPD of the MPR neutron spectrometer. The protons was closely Gaussian in shape and had a FWHM of 90 keV energy spread at the energy of 14.3 MeV before entering into the proton collimator with width of 2 mm. Then the protons were allowed to enter into the magnetic part of the MPR spectrometer. The protons in the magnetic field were momentum analyzed and focused on the focal plane. The proton distribution was finally recorded by the PIS with 2 mm plastic scintillator and Gd_2O_2S:Tb scintillator screen, respectively. The effective detection area of the PIS was increased to cover a lager proton energy range by using a fiber optic taper of 7:1.1 cm. The protons exit of vacuum chamber was made of a thin Ti window of 100μm thickness and 80 mm in diameter, which allows the PIS to obtain precise position determination of the protons outside the vacuum chamber.

Figure 4 (a) and (b) show the raw digital images of the proton distribution detected by the PIS, from which the FWHMs can be obtained. Figure 4(c) compares the profiles of the image (a) and (b), normalized to peak height. The FWHMs of the position resolution are estimated to be 4.4 mm and 4.3 mm respectively for plastic scintillator and Gd_2O_2S:Tb scintillator screen. The dispersion on the focal plane of the MPR neutron spectrometer is ~40 keV/ mm. The energy resolutions, including the proton energy spread and magnetic field

spread, result in the FWHMs of 176 keV and 172 keV, respectively. Moreover, the MPR neutron spectrometer typically works with energy resolution larger than 2% (~280 keV FWHM) for measuring DT neutrons. Thus, the resolution of the PIS has little effect on the resolution of the MPR neutron spectrometer. The PIS with Gd_2O_2S:Tb scintillator screen allows better quality of proton imaging to be achieved.

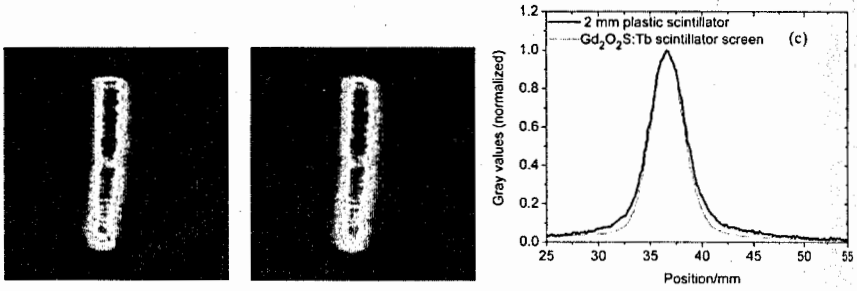

Fig. 4. The raw digital images of the proton distribution detected by the PIS, (a) Gd_2O_2S:Tb scintillator screen, (b) 2 mm plastic scintillator; (c) comparison of the horizontal line profiles of the images with 2 mm plastic scintillator and Gd_2O_2S:Tb scintillator screen.

4. Discussions

We have preliminarily tested some performances of the PIS with 2 mm plastic scintillator and Gd_2O_2S:Tb scintillator screen. Since it is used to detect the proton distribution under the condition of the MPR neutron spectrometer, the PIS will suffer irradiation from the background (e.g. scattering neutrons and gamma rays) and generate background image. Thin plastic scintillator has low sensitivity to background because of the low detection efficiency. If the range of particles produced by background is larger than the thickness of scintillator, the energy deposited in the thin scintillator will be less than the full energy of neutrons. In addition, the resolution of the PIS becomes degraded due to the spread of the light generated in the thicker scintillator. To obtain better resolution and suppress more background, the thickness of scintillator should be as thin as possible. However, for 14 MeV recoil protons, if the scintillator thickness is less than 2 mm, they will also not deposit their entire energy to achieve the best signals. So there exists an optimum thickness of the thin plastic scintillator according to practical application.

The Gd_2O_2S:Tb scintillator screen has the capability to convert the protons to visible light with maximum quantum efficiency around 545 nm, matching the peak in the quantum efficiency of the EMCCD. Thus, the use of Gd_2O_2S:Tb scintillator screen can improve quantum efficiency. Due to its effective thickness of 0.2 mm, the Gd_2O_2S:Tb scintillator screen can also provide higher resolution for proton imaging applications. Obviously, The Gd_2O_2S:Tb scintillator screen is more suitable for the PIS in spatial resolution and light yield comparing to 2 mm plastic scintillator. The PIS used in this paper can meet the requirement of the MPR neutron spectrometer in resolution and proton response. For higher resolution applications, array of scintillating fibers might be better choice. However, the economic and technical factors of large area structured crystals should be concerned.

5. Conclusion

In this paper, a PIS has been developed to detect recoil proton distribution for the MPR neutron spectrometer. Thin plastic scintillator and Gd2O2S:Tb scintillator screen were used for proton imaging instead of array of scintillating fibers. The use of thin scintillator and fiber optical coupling system makes the PIS a compact, simple in structure and more efficient FPD. The main imaging properties of the PIS were evaluated using proton beam and the PIS used as a FPD for the MPR neutron spectrometer was tested. Due to its high performances in spatial resolution and light yield, Gd_2O_2S:Tb scintillator screen can be used as an ideal candidate for proton imaging. The imaging properties of the PIS shown in this paper have demonstrated that the PIS is suitable for the MPR spectrometer in DT neutron measurement. Further improvements will be focused at allowing the PIS to work in photon-counting mode.

Acknowledgements

This work is supported by the National Natural Science Foundation of China (Grant No. 11175141 and 11275153). We would like to thank the staffs in the HI-13 tandem accelerator laboratory at CIAE and the staffs in the 2×6 MV tandem accelerator at Peking University. The authors are also grateful to Dan Su, Xichao Ruan and Long Hou at CIAE.

References

[1] J. Källne and H. Enge, Magnetic proton recoil spectrometer for fusion plasma neutrons, Nucl. Instr. and Meth. **A 311**(1992)595.

[2] Göran Ericsson, L. Ballabio, S. Conroy et al., Neutron emission spectroscopy at JET—Results from the magnetic proton recoil spectrometer, Rev. of Sci. Instrum., **72**(2001)759.

[3] J.A. Frenje, K.M. Green, D.G. Hicks et al., A neutron spectrometer for precise measurements of DT neutrons from 10 to 18 MeV at OMEGA and the National Ignition Facility, Rev. of Sci. Instrum, **72**(2001)854.

[4] J.A. Frenje, D.T. Casey, C.K. Li et al., First measurements of the absolute neutron spectrum using the magnetic recoil spectrometer at OMEGA, Rev. of Sci. Instrum., **79**, (2008)10E502.

[5] QI Jian-Min, ZHOU Lin and JIANG Shi-Lun, Design and performance analysis of a compact magnetic proton recoil spectrometer for DT neutrons, Chinese Physics C, 2011, 35(4): 374–380.

[6] D. T. Casey J. A. Frenje, M. Gatu Johnson et al., The magnetic recoil spectrometer for measurements of the absolute neutron spectrum at OMEGA and the NIF, Review of Scientific Instruments, **84**(2013)043506.

[7] M. Gatu Johnson, J.A. Frenje, C.K. Li et al., Measurements of fuel and ablator ρR in Symmetry-Capsule implosions with the Magnetic Recoil neutron Spectrometer (MRS) on the National Ignition Facility, Rev. of Sci. Instrum., **85**(2014)11E104.

[8] E.A. Sundén, H. Sjöstranda, S. Conroy et al., The thin-foil magnetic proton recoil neutron spectrometer MPRu at JET, Nucl. Instr. and Meth. **A 610**(2009)682.

[9] M. Tardocchi, S. Conroy, G. Ericsson et al., The monitoring system of a high performance fusion neutron spectrometer, Nucl. Instr. and Meth. **A 485**(2002)624.
[10] H. Sjöstrand, E. A. Sundén, S. Conroy et al., Gain stabilization control system of the upgraded magnetic proton recoil neutron spectrometer at JET, Rev. of Sci. Instrum., **80**, (2009)063505.
[11] Shao-hua Yang, Bin-kang Li, Ming-an Guo et al., Design of 1000 Frame Per-Second High Sensitivity EMCCD Video Processing, International Conference of China Communication and Technology, 2010: 214–217 (in Chinese).
[12] F.J. Beekman and G.A. de Vree, Photon-counting versus an integrating CCD-based gamma camera: important consequences for spatial resolution, Phys. Med. Biol. **50**(2005) N109–N119.

Fission

ANISOTROPY IN THE FRAGMENTS EMISSION FROM FISSION INDUCED BY INTERMEDIATE ENERGY NEUTRONS (1–200 MeV) IN ^{nat}Pb AND ^{239}Pu

A.M. Gagarski[1], A.S. Vorobyev[1], O.A. Shcherbakov[1], L.A. Vaishnene[1], A.L. Barabanov[2,3]

[1]*NRC "Kurchatov Institute", B.P. Konstantinov Petersburg Nuclear Physics Institute, 188300, Gatchina, Leningrad district, Russia*

[2]*NRC "Kurchatov Institute", 123182, Moscow, Russia*

[3]*Moscow Institute of Physics and Technology, 141700, Dolgoprudny, Moscow Region, Russia*

Abstract

New results of the neutron-induced fission experiments carried out at the neutron time-of-flight spectrometer GNEIS of the PNPI are given. Angular distributions of fission fragments from the neutron-induced fission of ^{239}Pu and ^{nat}Pb nuclei have been measured in the energy range 1-200 MeV using position sensitive multiwire proportional counters as fission fragment detector. The preliminary data on anisotropy of fission fragments deduced from the measured angular distributions are presented in comparison with the experimental data of other authors.

1. Introduction

Angular distributions of fission fragments arise due to two factors. First, an ensemble of spins of fissioning nuclei is to be aligned and, second, distribution of transitional states over the projection K of nuclear spin on the fission axis should be nonuniform. The first factor is determined by the processes which precede to fission, while the latter one is given by the mechanism of fission. At the energies much exceeding the fission barrier, the fission is preceded by the multi-step particle emission. A relative contribution of equilibrium and nonequilibrium processes into the dynamics of highly excited nuclei is not clear up to now. The angular distribution of fragments from neutron-induced fission at the energies up to 200 MeV may shed some light on these questions. Besides, the data on nuclear fission in this intermediate energy range are of prime importance for the advanced nuclear technologies such as Accelerator-Driven Systems (for nuclear power generation and nuclear transmutation).

We present here the results of recent measurements which continue the neutron-induced fission experiments at the neutron time-of-flight (TOF) spectrometer GNEIS [1] of the PNPI. In the previous papers [2-4] we have reported the data on angular anisotropy of fragments from neutron-induced fission of the target nuclei ^{233}U, ^{235}U, ^{238}U, ^{232}Th and ^{209}Bi in the intermediate energy range 1-200 MeV. The similar measurements recently were made at the n_TOF [5-7] for ^{235}U, ^{238}U and ^{232}Th nuclei, and at the LANSCE [8, 9] for ^{235}U nucleus.

The data for ^{239}Pu are of special interest due to its significance as fuel element. Up to now there were no experimental data for ^{239}Pu on the fragment's angular anisotropy for incident neutrons above 16 MeV (this is the upper limit of the rather old measurements [10-16]). In this paper the results of our study of the angular distribution of fragments from fission of ^{239}Pu nuclei by neutrons with the energies 1-200 MeV are presented.

Lead and ^{209}Bi are of interest due to their role in current and future nuclear power technologies. Lead-bismuth eutectic (alloy) is one of the primary coolant candidates for advanced nuclear reactors and Accelerator-Driven System. In addition to, this alloy is proposed as a target material for high power spallation neutron sources of new generation. Bismuth is also considered as a possible candidate to be used as a secondary standard for the

cross section of neutron-induced fission because it is a mono-isotope with a high fission threshold about 40 MeV. Up to now, only one measurement of fragment angular anisotropy for ^{209}Bi has been performed with the use of quasi-monoenergetic neutrons of 75 MeV at The Svedberg Laboratory (TSL, Uppsala, Sweden) by Eismont et al. [17]. Our recent measurement was the first successful attempt to study the energy dependence of the fragment's angular anisotropy for ^{209}Bi in the neutron energy range from threshold up to 200 MeV [3, 4].

In a case of neutron-induced fission of lead there are no experimental data on fission fragment angular distributions and anisotropy at all. That is why the results of our measurements carried out for ^{nat}Pb in the neutron energy range up to 200 MeV are the data obtained for the first time.

2. General description of the experimental set-up

The measurements were carried out at the 36 m flight path of the neutron TOF-spectrometer GNEIS. A schematic view of the experimental set-up is shown in Figs. 1, 2. Detailed description of the set-up and delay line readout system created on the basis of waveform digitizers can be found in our previous publications [2, 3].

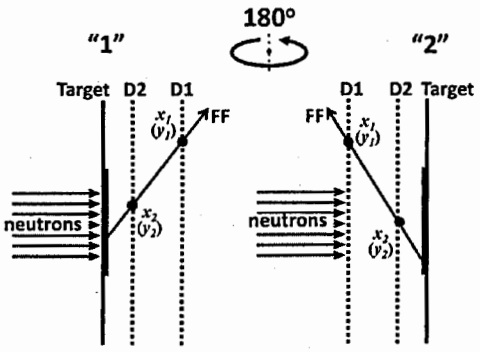

Fig. 1. Schematic view of the experimental set-up at two orientation relative to the neutron beam direction (downstream and upstream).

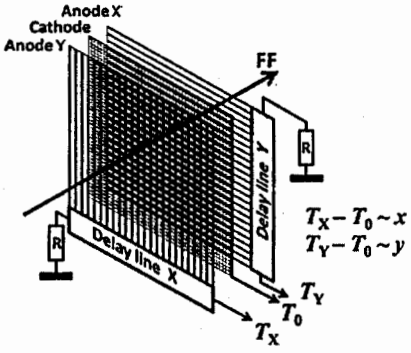

Fig. 2. Construction of the MWPC and principle of the coordinate determination.

The ^{239}Pu (99.76 % enrichment) target 80 mm of diameter was made by conventional painting technique with a PuO_2 deposit on a 100 μm thick Ø100 mm Al-metal foil. The target thickness was 325μg/cm^2. The metal ^{nat}Pb target 120×120 mm^2 of size and 150 μg/cm^2 was made by vacuum deposition of high purity ^{nat}Pb on a 2 μm thick Mylar foil.

The fission fragment registration was performed by two coordinates sensitive multiwire proportional counters D1 and D2 (MWPC) 140x140 mm^2 of size [18]. The fragment counters D1 and D2 were placed close to the target in the beam one after the other. The neutron beam axis came through the geometrical centers of the target and the MWPC's electrodes being perpendicular to them. In order to have a possibility to take into account for the linear momentum contribution into the measured angular distribution, the measurements with two set-up orientations relative to the beam direction (downstream and upstream) were performed.

A value of cos(θ), where θ is an angle between neutron beam axis and fission fragment momentum, can be derived easily from the coordinates of the fission fragment measured by two counters. Time and pulse-height analysis of the signal waveforms allowed to derive the neutron energy and the fission fragment coordinates on the MWPCs, and, hence, the angle information.

3. Data processing

The measured angular distributions for selected fission fragment events were corrected for the efficiency of fission fragment registration. This efficiency was calculated by means of the Monte-Carlo method taking into account following parameters: the electrode wire structure, distances between MWPCs and target, sizes of electrodes and distances between them, sizes of the target and neutron beam, the position (angular) resolution (~2 mm). Also, the additional corrections due to the differential nonlinearity of the delay line chips and the mutual influence (signal crosstalk) of the anodes of two adjacent MWPCs were taken into account [3].

An anisotropy $W(0^\circ)/W(90^\circ)$ of angular distributions of fission fragments in the center-of-mass system were deduced from the corrected cos(θ) angular distributions in the laboratory system for two set-up orientations relative to the neutron beam direction (cos(θ) bins were equal to 0.01) by fitting them in the range $0.24 < \cos(\theta) < 1.0$ by the sum of even Legendre polynomials up to the 4-th order. To account for the linear momentum contribution into the measured angular distributions, the measured anisotropies were averaged over two set-up orientations (downstream and upstream).

4. Results

The angular distributions of fission fragments in the centre of mass system for ^{239}Pu are presented in Fig. 3 for four neutron energy intervals, in comparison with experimental data of the other authors [10-13]. The results of the data fitting by the sum of even Legendre polynomials up to the 4-th order are also shown in Fig. 3.

As mentioned above, the results from EXFOR data base [19] on the fission fragment anisotropy for ^{239}Pu nuclei induced by neutrons with energies exceeding 1 MeV are not numerous. Apart from our data, the results of six former experiments are shown on Fig. 4. Only three data sets [11, 12, 15] deal with the data in the energy range 10-16 MeV.

At present the measurements with the ^{239}Pu target are continued. Therefore, status of the data presented in this report is PRELIMINARY. Nevertheless, some remarks and conclusions can be done right now. In the energy range below ~8 MeV our results agree within experimental uncertainties with the most complete data sets by Shpak [16] and Simmons [10]. In the energy range 10-16 MeV our data are between the "min" and "max" data points of Blumberg [11] and Androsenko [15], being in agreement with the data of Leachman [12]. Average value of the present uncertainties of our data is equal to 2÷3 % in the energy range 20 - 200 MeV.

An experimental data set on the energy dependence of ^{nat}Pb anisotropy in the neutron energy range 1-200 MeV has been obtained for the first time. As in a case of our data for ^{209}Bi, at the achieved accuracy level, it can be stated for ^{nat}Pb that at the energy of ~ 50-60 MeV there is a maximum of the anisotropy equal to 1.6±0.2 followed by a smooth descend with an increase of the neutron energy which resulted in a plateau about 1.15±0.05 of height. This behavior of the energy dependence of anisotropy qualitatively coincides with the result of theoretical calculations carried out by Eismont et al. [17].

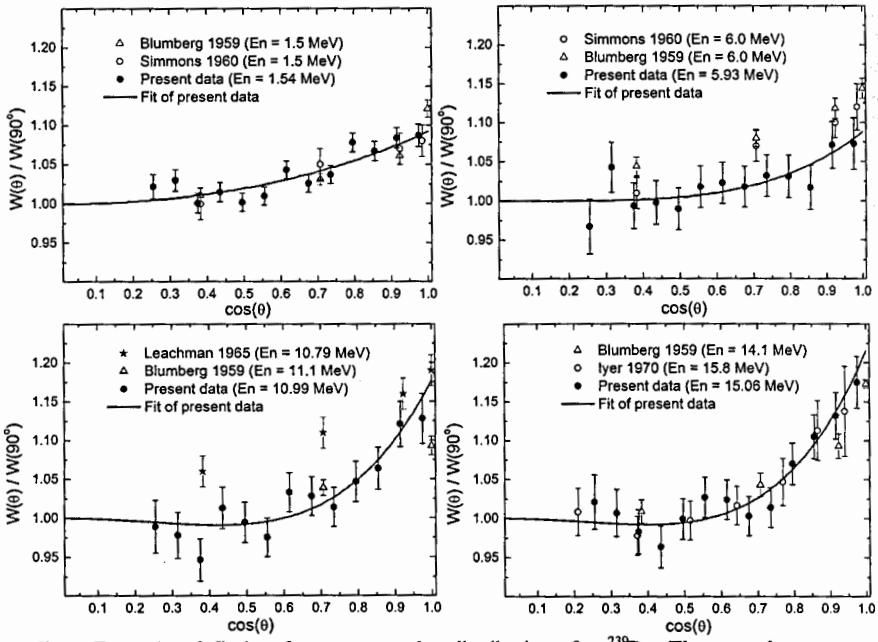

Fig. 3. Example of fission fragment angular distributions for ^{239}Pu. The error bars represent statistical uncertainties. Solid line is a result of the fitting by the sum of even Legendre polynomials up to the 4-th order.

The anisotropy W(0°)/W(90°) obtained from fitting of the fission fragment distributions measured in present work for ^{239}Pu and ^{nat}Pb in the neutron energy range 1-200 MeV are shown in Fig. 4.

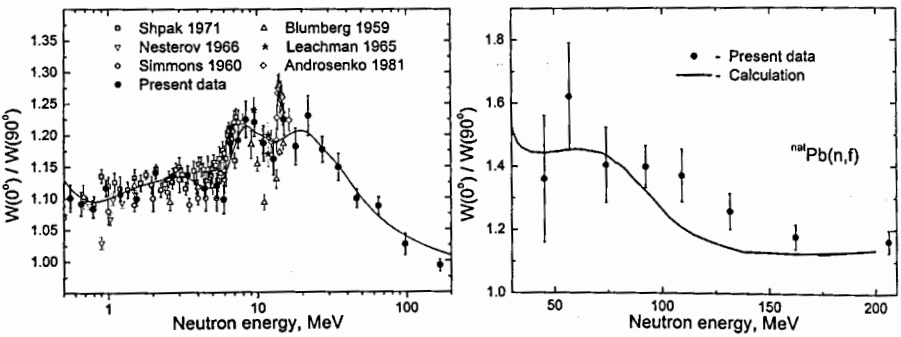

Fig. 4. Anisotropy of fission fragment of ^{239}Pu (left) and ^{nat}Pb (right) compared with the experimental data of other authors ([10-12, 14-16] for ^{239}Pu). The error bars represent statistical uncertainties. The solid curve for ^{239}Pu is only the eye guide to the experimental data while for ^{nat}Pb that is calculation from ref. [17].

5. Conclusion

New experimental data on the angular distributions of fragments from neutron-induced fission of the ^{239}Pu and ^{nat}Pb nuclei in the neutron energy range 1-200 MeV are presented. Apart from its significance for applications, these data are of great interest from theoretical point of view. Together with the other experimental results obtained in a course of present investigation, a vast amount of data for three different groups of nuclei, fissile (^{233}U, ^{235}U, ^{239}Pu), non-fissile (^{238}U, ^{232}Th) actinides and non-actinides (^{209}Bi, ^{nat}Pb) could provide valuable information to separate the contributions of equilibrium and pre-equilibrium processes to the evolution of nuclear spin alignment during the evaporation cascade. Thus the new directions to study nuclear dynamics at high excitation energies may be open.

Acknowledgments

The authors would like to thank the staff of the Accelerator Department of the NRC KI - PNPI for their permanent friendly assistance and smooth operation of the synchrocyclotron during the experiment.

References

[1] N.K. Abrosimov, G.Z. Borukhovich, A.B. Laptev, V.V. Marchenkov, G.A. Petrov, O.A. Shcherbakov, Yu.V. Tuboltsev, and V.I. Yurchenko, Nucl. Instrum. Methods Phys. Res. A **242**, 121 (1985).

[2] A.S. Vorobyev, A.M. Gagarski, O.A. Shcherbakov, L.A. Vaishnene, and A.L. Barabanov, JETP Letters **102(4)**, 203 (2015).

[3] A.S. Vorobyev, A.M. Gagarski, O.A. Shcherbakov, L.A. Vaishnene, and A.L. Barabanov, JETP Letters **104(6)**, 365 (2016).

[4] A.S. Vorobyev, A.M. Gagarski, O.A. Shcherbakov, L.A. Vaishnene, and A.L. Barabanov, Proc. of the Int. Conf. "Nuclear data for Science and Technology ND-2016", September 11-16, 2016, Bruges, Belgium. EPJ Web of Conferences **146**, 04011 (2017).

[5] L.S. Leong, PhD Thesis, Universite Paris Sud, CERN-Thesis-2013-254.

[6] L.S. Leong, L. Tassan-Got, D. Tarrio, *et al.* Proc. of the Int. Conf. "Nuclear data for Science and Technology ND-2013", March 4-8, 2013, New York, USA. EPJ Web of Conferences **62**, 08003 (2013).

[7] E. Leal-Cidoncha, I. Duran, C. Paradela, *et al.* Proc. of the Int. Conf. "Nuclear data for Science and Technology ND-2016", September 11-16, 2016, Bruges, Belgium. EPJ Web of Conferences **111**, 10002 (2016).

[8] V. Kleinrath, PhD Thesis, Technischen Universitat Wien, 2015.

[9] V. Geppert-Kleinrath, F. Tovesson, J. S. Barrett, et al., arXiv preprint: 1710.00973, 2017.

[10] J.E. Simmons and R.L. Henkel, Phys. Rev. **120**, 198 (1960).

[11] L. Blumberg, R.B. Leachman, Phys. Rev. **116**, 102 (1959).

[12] R.B. Leachman and L. Blumberg, Phys. Rev. **137**, B814 (1965).

[13] R. H. Iyer, M. L. Sagu, in Proceedings of the Nuclear Physics and Solid State Physics Symposium, December 27–30, 1970; Madurai, India: Nuclear Physics, Vol. 2, p.57 (1970).

[14] V.G. Nesterov, G.N. Smirenkin, and D.L. Shpak, Yadernaya Fizika **4(5)**, 993 (1966).

[15] Kh. D. Androsenko, G. G. Korolev, and D. L. Shpak, VANT, Ser.Yadernye Konstanty **46(2)**, 9 (1982).

[16] D.L. Shpak, Yu.B. Ostapenko, G.N. Smirenkin, Soviet Journal of Nuclear Physics **13**, 547 (1971).

[17] V.P. Eismont, N.P. Filatov, A.N. Smirnov, et al. Proc. Int. Conf. "Nuclear Data for Science and Technology", September 26 – October 1, 2004; Santa Fe, N.M., USA. AIP Conference Proceedings **769**, 633 (2005).

[18] G.F. Knoll, Radiation Detection and Measurements, NY: J. Wiley, 3rd ed., 2000, p. 190.

[19] N. Otuka, E. Dupont, V. Semkova, B. Pritychenko, A.I. Blokhin, et al., Nuclear Data Sheets **120**, 272 (2014).

STUDY OF PROMPT NEUTRON EMISSION IN ^{235}U(n,f) AT THE GELINA FACILITY

Alf Göök, Franz-Josef Hambsch, and Stephan Oberstedt
European Commission - Joint Research Centre
Directorate G - Unit G.2
Retieseweg 111
B-2440 Geel, Belgium

Abstract: Experimental activities at JRC-Geel on prompt fission neutron (PFN) emission in response to OECD/NEA nuclear data requests are presented in this contribution. Specifically, on-going investigations of PFN emission from the reaction ^{235}U(n,f) in the region of the resolved resonances, taking place at the GELINA facility, are presented. The focus of this contribution lies on studies of PFN correlations with fission fragment properties. The experiment employs a scintillation detector array for neutron detection, while fission fragment properties are determined via the double kinetic energy technique using a position sensitive twin ionization chamber. This setup allows us to study several correlations between properties of neutrons and fission fragments simultaneously.

I. INTRODUCTION

Improved knowledge on the properties of the prompt fission neutrons (PFN), their multiplicities, as well as their energy and angular distributions can shed light on the fission process near the scission point. These properties are related to the deformation of fission fragments at scission, the sharing of excitation energy between the fragments and the time scale of the process itself. Experimental investigations of prompt fission neutrons and fission fragment properties in resonance neutron induced fission on ^{235}U are taking place at the GELINA facility of the JRC-Geel. In recent years large efforts have been put into the modelling of PFN emission in fission, see for example Ref. [1] and references therein. The efforts are quite successful in both consistency between the different approaches and in reproducing available experimental data. However, in the case of ^{235}U(n,f) difficulties have been encountered, especially regarding the dependency of $\overline{\nu}$ on the total kinetic energy (TKE) of the fission fragments, see for example Ref [2]. Focusing on the high TKE range Kornilov, et al. has suggested that the experimental observation of $\overline{\nu}$ substantially larger than zero at the maximum available energy is a signature of scission-neutron emission [3]. It was argued that, because evaporation neutrons from the fragments are energetically not allowed at such high TKE the observed neutrons would have to originate from another source. The difference between experimental data and calculation of $\overline{\nu}$(TKE) based on neutrons evaporated from fragments was used to estimate the scission-neutron yield. Possible deficiencies in the experimental data were also pointed out [3]. In order to address these issues it is of interest to revisit PFN and fragment correlations in ^{235}U(n,f) experimentally. All results on correlations between fission fragment properties and PFN properties presented here are from the selected incident neutron energy range [0.3 eV, 45 keV]. The average energy of the neutrons inducing fission is 1.16 keV.

II. EXPERIMENTAL SETUP

The experiment has been performed at the GELINA facility of the JRC-Geel. The experimental setup, illustrated in Fig. 1, is located at a distance of about 9 m from the GELINA neutron source. Fission fragments are detected in a position sensitive twin ionization chamber (IC). This detector has been developed at JRC-Geel, and is described in detail in Ref. [4]. Essentially, it is a standard twin Frisch grid ionization chamber with the anode plates replaced by position sensitive readouts. It is capable of determining the fission axis orientation in space with a resolution of 7°, simultaneously with the fission fragment masses and energies.

Neutrons are detected in an array of proton recoil scintillators. The array consist of 19 NE213 equivalent BC-501 liquid scintillators, 3 paraterphenyl and 1 stilbene crystal scintillators. The detectors are placed in a quasi-spherical geometry around the center of the ^{235}U-target at distance of about 50 cm. The actual position of the detectors relative to the IC has been determined with high

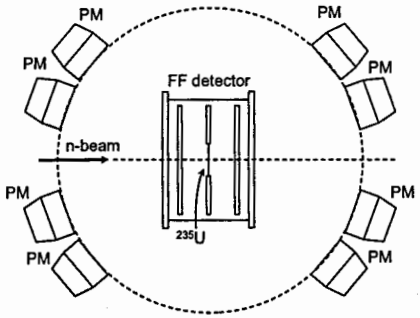

FIG. 1. Schematic representation of the experimental setup located at the GELINA facility. The ^{235}U-target is placed inside the twin ionization chamber (IC), 9 m away from the neutron producing target. The neutron detectors are placed in a quasi spherical geometry around the IC at a distance of about 50 cm from the center of the ^{235}U-target.

precision ($\pm$0.2 mm) using a ROMER arm [5] measuring device.

The data acquisition is based on wave-form digitizers, sampling the detector signals at 400 MSample/s with 14-bit resolution. A fission trigger derived from the charge induced on the central cathode of the IC, triggers the data acquisition. For every fission trigger digital wave-forms of all neutron detectors as well as the IC's electrodes are stored on disk, together with time-stamp information, for off-line analysis. The time stamp is reset by every beam pulse from the GELINA and used to determine the incident neutron time-of-flight (ToF).

III. DATA ANALYSIS

A. PFN data

Events in the scintillation detectors corresponding to neutrons are selected by means of pulse-shape discrimination (PSD). The PFN energy is measured by means of the ToF technique, with a resolution of $\sim$1 ns (FWHM). In addition to PFNs, fission is also accompanied by prompt fission γ-rays, which might be detected in the scintillation detectors as well. Most of the γ-emission takes place within a few ns after the instant of fission. Therefore, the range of high-energy neutrons is most sensitive to false events induced by γ-rays. The PSD is not able to give a clean discrimination between γ-rays and neutrons for pulse heights corresponding to small proton recoil energies. In order to reduce the background caused by the γ-emission a dynamic light-threshold [6] is applied.

Each detector in the SCINTIA array has been characterized using the PFNs from ^{252}Cf(sf), with experimental setup and procedures described in Ref. [7]. To correct for the energy dependent detection efficiency and multiple scattering of neutrons on the surrounding materials, the setup is modeled with GEANT4. The simulation uses experimentally determined proton light output functions, for other recoil-particle species literature data are used [8, 9]. The Monte-Carlo model has been validated against the standard PFN spectrum [10] from the spontaneous fission decay of ^{252}Cf.

In Fig. 2 the ^{235}U(n,f) PFN spectrum observed in this study, when selecting the incident neutron energy range [0.3 eV, 45 keV], is compared to the spectrum from cold neutron induced fission determined by Kornilov et al. [11]. The two spectra are in quite close agreement, although the spectrum observed in the resonance region is slightly softer. The systematic uncertainty of the data points in Fig. 2 was estimated by a χ^2-analysis of the variance of the results from individual detectors.

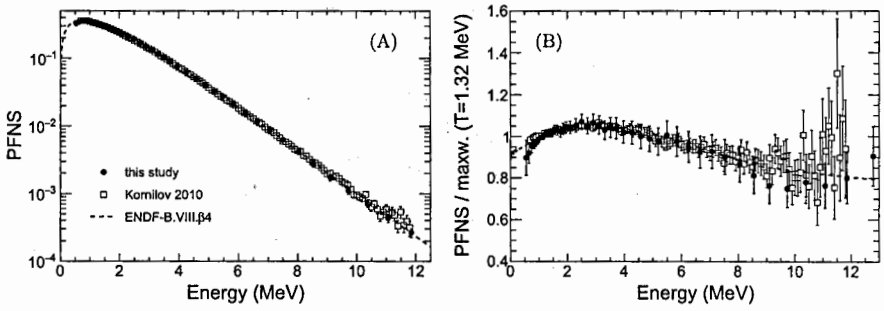

FIG. 2. (A) The prompt fission neutron spectrum in the laboratory frame compared to data from cold-neutron induced fission from Kornilov et al. [11]. (B) The prompt fission neutron spectrum represented as a ratio to a Maxellian with a temperature of 1.32 MeV.

B. Determination of fission fragment properties

The fission fragment mass and kinetic energy before neutron emission is obtained by means of the well-established double kinetic energy (2E) technique, which relates the masses $m^*_{1,2}$ and energies $E^*_{1,2}$ before neutron emission in a binary fission event according to

$$m^*_{1,2} = m_{cn} \cdot \frac{E^*_{2,1}}{E^*_1 + E^*_2}, \tag{1}$$

where m_{cn} is the mass of the compound nucleus undergoing fission. Under the assumption of isotropic neutron emission from fully accelerated fragments, the energies before neutron emission E^* are related to the energies after neutron emission E according to

$$E^* = E \cdot \frac{m^*}{m^* - \overline{\nu}(m^*, \mathrm{TKE})}, \tag{2}$$

where $\overline{\nu}$ is the number of neutrons emitted by the fragment. The dependence of $\overline{\nu}$ on mass and TKE can only be derived from the data once the 2E-analysis is completed. As initial assumption we have used the evaluated data on $\overline{\nu}(m^*)$ from Wahl [12] and the parameterization

$$\begin{aligned} \overline{\nu}(m^*, \mathrm{TKE}) &= \overline{\nu}(m^*) + \frac{\overline{\nu}(m^*)}{\overline{\nu}(m^*) + \overline{\nu}(m_{cn} - m^*)} \cdot \Delta_{\mathrm{TKE}}, \\ \Delta_{\mathrm{TKE}} &= \frac{\overline{\mathrm{TKE}}(m^*) - \mathrm{TKE}}{E_{\mathrm{sep}}}, \end{aligned} \tag{3}$$

where $E_{\mathrm{sep}} = 8.6$ MeV/n is the average energy necessary to emit a neutron [13]. The analysis was later repeated using the results on $\overline{\nu}(m^*)$ and $E_{\mathrm{sep}} = 8.51$ MeV/n derived from the data of the present experiment. No significant changes in the results were observed between the two analyses. In the 2E-technique the main contribution to the mass resolution is the neutron evaporation, since Eq. (2) only holds on average. In this work the mass resolution is 4-5 u (FWHM), determined by comparing the measured thermal mass yield to data from Ref. [14]. For events where neutrons and fission fragments are detected in coincidence, an additional correction [15] for the recoil energy imparted to the fragment is added to Eq. (2).

IV. EXPERIMENTAL RESULTS

A. Prompt fission neutron angular distributions

Most model calculations of the properties of PFNs are based on the assumption that the neutrons are emitted from the fragments after they have reached their terminal velocity. However, theoretical arguments have been raised asserting that at least a fraction of the neutrons are emitted during the scission process [16] and/or during the acceleration of the fragments [17, 18]. A large number of experiments have been devoted to investigate the source of prompt neutrons in detail. However, considering the variation of experimental results it is difficult to draw definitive conclusions. The experimental method used here, as well as in many earlier studies [19–21] of PFN emission in ^{235}U(n,f), assumes that the neutrons are emitted from fully accelerated fragments. Hence, it is of great importance to investigate to what extent the experimental data support this assumption. In order to do so, we follow a procedure similar to that of Vorobyev et al. [22]. The energy–angle distribution of neutrons emitted from moving fragments when observed in the laboratory frame is

$$N(E_n,\theta) = N_L(\eta_L,\vartheta_L)\sqrt{\frac{E_n}{\eta_L}} + N_H(\eta_H,\vartheta_H)\sqrt{\frac{E_n}{\eta_H}}, \tag{4}$$

where $N_{L,H}(\eta_{L,H},\vartheta_{L,H})$ are the center-of-mass (c.m.) energy–angle distributions of neutrons from the light and heavy fragments, respectively. The neutron energies in the c.m. frame $\eta_{L,H}$ can be derived from experimental observables in the laboratory frame; light (L) and heavy (H) fragment energies $E_{L,H}$ and masses $m_{L,H}$, neutron energy E_n and angle θ between the neutron's and the light fragment's directions of motion

$$\eta_L = E_n + E_L\frac{m}{m_L} - 2\sqrt{E_nE_L\frac{m}{m_L}}\cos\theta, \tag{5}$$

$$\eta_H = E_n + E_H\frac{m}{m_H} + 2\sqrt{E_nE_H\frac{m}{m_H}}\cos\theta, \tag{6}$$

where m is the mass of the neutron. For the purpose of the model a single fragmentation is used, with $E_L\frac{m}{m_L} = (1.02 \pm 0.01)$ MeV and $E_H\frac{m}{m_H} = (0.491 \pm 0.01)$ MeV taken as averages from the experimental data. Under the assumption of isotropic emission from the fully accelerated fragments, only the neutron spectra in the c.m. frame are unknown. They are determined from the experimental data by selecting small angles in the laboratory frame, where the contribution of neutrons from the complementary fragment is the smallest. Neutrons detected at angles smaller than 12° relative to the motion of the light and heavy fission fragments are selected. The observed laboratory spectra for these selections are transformed into the c.m. frame of the respective fragment and corrected for the small contribution of neutrons from the complementary fragment. Each of the spectra has been fitted with a linear superposition of a Maxwellian and a Watt spectrum shape. The fitted shapes are then used to calculate the spectrum as a function of the angle between the light fission fragment direction and the detected neutron, according to Eq. (4). In Fig. 3 the zeroth (A) and the first (B) moments of the calculated and experimentally observed spectra as a function of $\cos\theta$ are compared. The agreement is fair, although a clear underestimation of the experimental data is evident at large angles with the fission axis. The underestimation amounts to 2.5% of the total neutron yield. The description of the experimental data could be improved by assuming a small anisotropy in the c.m. frame [22]. However, we did not include an anisotropy term in the evaluation of the laboratory data as the angular distribution observed in the c.m. frame does not allow for this degree of freedom. Note that the uncertainties given in Fig. 3 are statistical only, evaluation of the associated systematic uncertainties are on-going.

The complete experimental determination of all relevant kinematic parameters allows the transformation from the laboratory frame of reference into the rest frame of the fully accelerated fission fragments. This transformation is, however, complicated by the fact that for each laboratory angle only the sum of contributions from the two fission fragments is observed. Thus, an unknown contribution must first be subtracted from any observed distribution. Fortunately, the contribution of neutrons emitted from the fragment flying away from the neutron detector is small [23]. Therefore, in

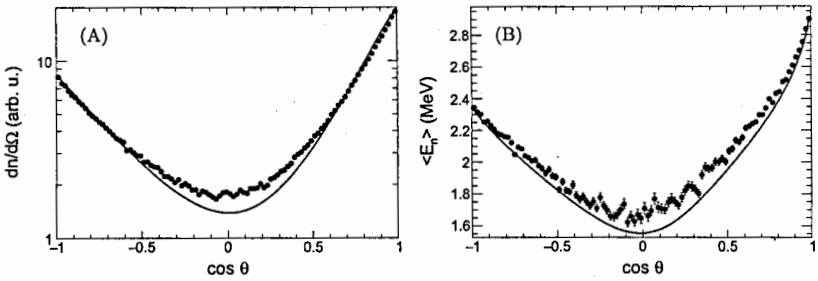

FIG. 3. (A) Angular distribution of prompt neutrons integrated over all neutron energies. (B) Average neutron energy as a function of $\cos\theta$. The full lines represent the result of the model calculation.

a first approximation it is assumed that all neutrons that are detected with a c.m. angle smaller than 90° originate from the fragment directed towards the neutron detector. The resulting distribution is then used to calculate the disturbing component from the complementary fragment. Using this procedures, the angular distribution of prompt neutrons in the rest frame of the fully accelerated fragments has been determined. Figure 4 shows the angular distribution integrated over all c.m. neutron energies and all fission configuration, i.e. no selection in mass or TKE has been made. The result has been fitted with a second order Legendre polynomial. Obviously, the result supports isotropic emission in the c.m.-frame. This does, however, not exclude neutron from emission sources other than fully accelerated fragments, due to the selection of events with $\theta_{c.m.} > 90°$. The selection implies that events with laboratory neutron energies smaller than the fragment energy per nucleon are not taken into account.

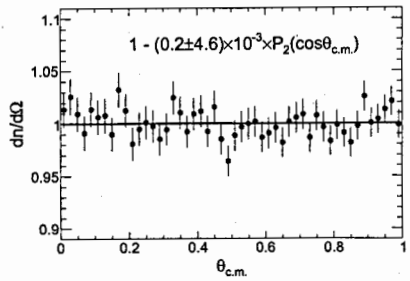

FIG. 4. The angular distribution of prompt neutrons in the c.m.-frame integrated over all neutron energies and fission configurations. The full line is the best fit of a second order Legendre polynomial.

B. Average neutron multiplicities

The average neutron multiplicity as a function of the fragment mass is shown in Fig. 5 (A). For comparison, experimental data from Refs. [19, 20] are also shown in the figure. The general shape is reproduced in this work, however the minima around mass number ~80 u for the light fragments and ~130 u for the heavy fragments appear more pronounced in the present data. The average neutron multiplicity per fission is shown as a function of the heavy fragment mass in Fig. 5 (B). A pronounced minimum close to heavy fragment mass A_H ~132 u observed.

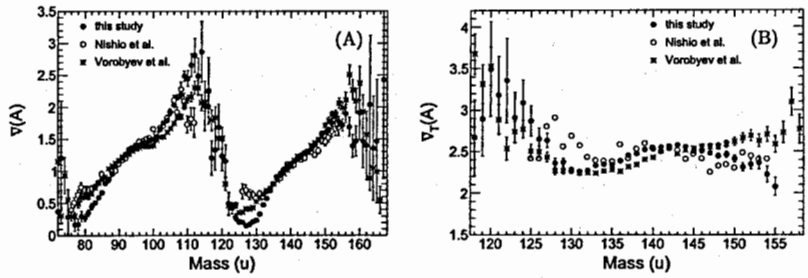

FIG. 5. (A) The average neutron multiplicity per fragment as a function of the fragment mass from this study compared to data from Refs. [19, 20]. (B) The average neutron multiplicity per fission as a function of the heavy fragment mass from this study compared to data from Refs. [19, 20].

In Fig. 6 the average neutron multiplicity per fission is plotted as a function of the fragment TKE. As expected, a close to linear dependence is observed, except for TKE$\lesssim$145 MeV. A least square fit results in $-\partial \mathrm{TKE}/\partial\overline{\nu} = 12.0$ MeV/n. This value is substantially lower than the values 16.7 – 18.5 MeV/n determined in earlier studies, performed at thermal incident neutron energy [19–21, 24]. Data from Refs. [19–21] are also included in Fig. 6(A). By studying the fission fragment TKE distributions from Refs. [19–21] it has been found that these studies suffer from substantial resolution broadening. The broadening also affects the correlation with detected neutrons, which explains the strong difference between the present data and the literature data. This conclusion was already drawn form a subset of the present data, and a more detailed discussion of this has been published in Ref. [25].

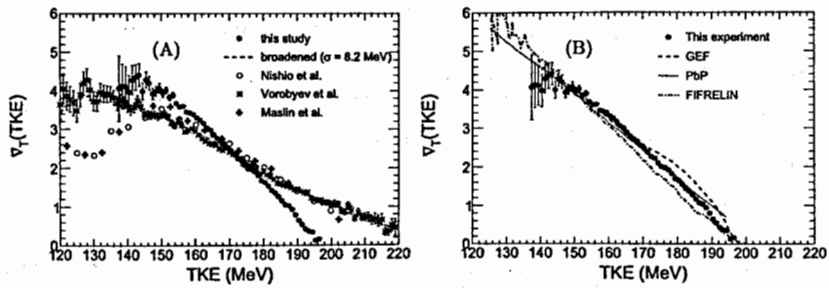

FIG. 6. The average neutron multiplicity per fission as a function of the TKE. (A) The result from this study is compared to experimental data from Refs.[19–21]. (B) The result from this study is compared to model calculations [1, 26]. The fission yield as a function of TKE determined in this study is also shown.

A comparison of the experimental result for average neutron multiplicity per fission $\overline{\nu}_T$(TKE) with different model calculations, taken from a recent review of available fission fragment deexcitation models [1, 26], is shown in Fig. 6(B). The different models presented in Ref. [1] agree well with each other. Therefore, not all of them are included in the figure. It is clear that the model calculations are in much better agreement with the present data set than with earlier experiments.

V. CONCLUSION

A multi-parameter experiment on correlations between the properties of fission fragments and PFNs in the reaction ^{235}U(n,f) for an incident neutron energy range [0.3 eV,45 keV], with a mean neutron

energy of 1.16 keV, has been presented. The laboratory angular distribution of prompt neutrons have been compared with a model calculation based on isotropic emission from fully accelerated fragments. The model agrees fairly well with the experimental data, however the model calculation does underestimate the neutron yield at large angles with the fission axis. The underestimation amounts to 2.5 % of the total neutron yield. Results on average neutron multiplicities in correlation with fission fragment mass and TKE show significant differences to earlier studies on this reaction, induced by thermal neutrons. The sawtooth shape of the average neutron multiplicity per fragment show more pronounced minima at $A \approx 130$ and $A \approx 80$. The TKE dependence of the neutron multiplicity per fission shows an inverse slope $\partial \mathrm{TKE}/\partial\overline{\nu}$ approximately 35% weaker than observed in earlier studies [19–21, 24]. The difference can be attributed to improved fission fragment TKE resolution in the present experiment. The present result for the average neutron multiplicity as a function of TKE is in good agreement with model calculations [1, 26].

[1] R. Capote, Y.-J. Chen, F.-J. Hambsch, N.V. Kornilov, J.P. Lestone, O. Litaize, B. Morillon, D. Neudecker, S. Oberstedt, T. Ohsawa, N. Otuka, V.G. Pronyaev, A. Saxena, O. Serot, O.A. Shcherbakov, N.-C. Shu, D.L. Smith, P. Talou, A. Trkov, A.C. Tudora, R. Vogt, A.S. Vorobyev, Nucl. Data Sheets **131**, 1 (2016)
[2] S. Lemaire, P. Talou, T. Kawano, M. Chadwick, D. Madland, Phys. Rev. C **72** (2005), cited By 71
[3] N.V. Kornilov, F.-J. Hambsch, A.S. Vorobyev, Nucl. Phys. A **789**, 55 (2007)
[4] A. Göök, W. Geerts, F.-J. Hambsch, S. Oberstedt, M. Vidali, S. Zeynalov, Nucl. Instr. and Meth. A **830**, 366 (2016)
[5] http://www.hexagonmi.com/products/portable-measuring-arms/romer-absolute-arm
[6] N.V. Kornilov, Tech. rep., IAEA, INDC(USA)-108 (2015)
[7] N.V. Kornilov, I. Fabry, S. Oberstedt, F.-J. Hambsch, Nucl. Instr. and Meth. A **599**, 226 (2009)
[8] V.V. Verbinski, W.R. Burrus, T.A. Love, W. Zobel, N.W. Hill, R. Textor, Nucl. Instr. and Meth. **65**, 8 (1968)
[9] M. Tajik, N. Ghal-Eh, G.R. Etaati, H. Afarideh, Nucl. Instr. and Meth. A **704**, 104 (2013)
[10] W. Mannhart, *IAEA-TECDOC-410* (Leningrad, 1986), p. 158
[11] N.V. Kornilov, F.-J. Hambsch, I. Fabry, S. Oberstedt, T. Belgya, Z. Kis, L. Szentmiklosi, S. Simakov., Nucl. Sci. and Eng. **165**, 117 (2010)
[12] C. Wahl, Atomic Data and Nuclear Data Tables **39**, 56 (1988)
[13] H. Nifenecker, C. Signarbieux, R. Babinet, J. Poitou, 3rd IAEA Symp. on the Physics and Chemistry of Fission **2**, 117 (1973)
[14] P. Geltenbort, F. Gönnenwein, A. Oed, Radiation Effects **93**, 57 (1986)
[15] A. Gavron, Nucl. Instr. and Meth. **115**, 99 (1974)
[16] M. Rizea, N. Carjan, Nucl. Phys. A **909**, 50 (2013)
[17] V.P. Eismont, Jour. Nucl. Energy A/B **20**, 875 (1965)
[18] V.P. Eismont, Atomnya Energiya **19**, 113 (1965)
[19] K. Nishio, Y. Nakagome, H. Yamamoto, I. Kimura, Nucl. Phys. A **632**, 540 (1998)
[20] A.S. Vorobyev, O. Shcherbakov, A. Gagarski, G. Val'ski, G. Petrov, EPJ Web of Conf. **8**, 03004 (2010)
[21] E.E. Maslin, A.L. Rodgers, W.G.F. Core, Phys. Rev. **164**, 1520 (1967)
[22] A.S. Vorobyev, O.A. Shcherbakov, Yu.S. Pleva, A.M Gagarski, G.V. Val'ski, G.A. Petrov, V.I. Petrova, T.A. Zavarukhina, Nucl. Instr. and Meth. A **598**, 795 (2009)
[23] C. Budtz-Jørgensen, H.-H. Knitter, Nucl. Phys. A490, 307 (1988)
[24] J.W. Boldeman, A.R. de L. Musgrove, R. L. Walsh, Aust. J. Phys. **24**, 821 (1971)
[25] A. Göök, F.-J. Hambsch, S. Oberstedt, EPJ Web of Conf. ND 2016 Int. Conf. on Nucl. Data for Sci. and Tech. (2016)
[26] K.H. Schmidt, B. Jurado, C. Amouroux, C. Schmitt, Nucl. Data Sheets **131**, 107 (2016)

Dependence of ROT-effect on light charged particle energy in ternary fission of ^{235}U induced by polarized neutrons

I. Guseva[1], A. Gagarski[1], F. Gönnenwein[2], Yu. Gusev[1]

[1]*Petersburg Nuclear Physics Institute of National Research Centre "Kurchatov Institute", 188300 Gatchina, Russia*
[2]*Physikalisches Institut, Universität Tübingen, D-72076 Tübingen, Germany*

Abstract

The shift of the light charged particles angular distribution arising in neutron induced fission of ^{235}U due to spin-flip of polarized neutron beam was obtained with the help of trajectory calculations for rotating nucleus. For the first time the influence of ^{3}H nuclei was considered. It was shown that the inclusion in the calculation of tritons besides of alpha-particles significantly improves the agreement of the experimental ROT-effect dependence on the light charged particle energy and the results of calculation.

In the process of ternary fission besides of two fragments with large masses also light charged particles are observed. There is a wide variety of such particles in neutron induced ternary fission of ^{235}U [1]. They can be separated by a charge, mass, energy and angular distributions. Light charged particles (LCPs) are also different in their outputs. In ternary fission of ^{235}U alpha-particles are emitted most often. In the Table 1 their yield is considered equal to 10000. The alpha-particles are followed by tritons. The yield of such particles is 7.2% of the alpha-particles yield.

Table 1

light charged particle	the most probable energy, MeV	full width at half maximum, MeV	extrapolated yield, relative units
^{2}H	8.6±0.15	7.1±0.2	50.0±2.0
^{3}H	8.2±0.1	6.5±0.2	720.0±30.0
^{4}He	15.9±0.1	9.8±0.1	10000
^{6}He	11.1±0.2	11.2±0.2	196.0±8.0
^{8}He	10.2±0.2	6.8±0.4	6.0±0.4
^{7}Li	14.8±0.9	13.0±1.0	4.4±0.6
^{8}Li	13.2±0.9	12.1±1.3	2.6±0.3
^{9}Be	18.0±1.3	13.0±1.8	3.2±0.5
^{10}Be	17.5±0.6	15.2±0.9	37.0±3.0

The nuclear fission is a very complex process and represents a big problem for its description. However, when the nucleus rupture has already happened and nuclear forces have stopped to influence, two fragments and ternary particle (TP) move only due to their mutual Coulomb interaction. Their motion can be reproduced using Monte Carlo simulations [2÷7]. The result of computer simulation for this final fission phase is a complex of calculated trajectories for all described objects, which can give information about angular and energy

distributions for ternary particles at the moment of their registration. The energy distributions for several light charge particles one can see as example in Fig.1. Points correspond to experimental data [1] and lines are calculated distributions. They are very close to the Gaussian shape.

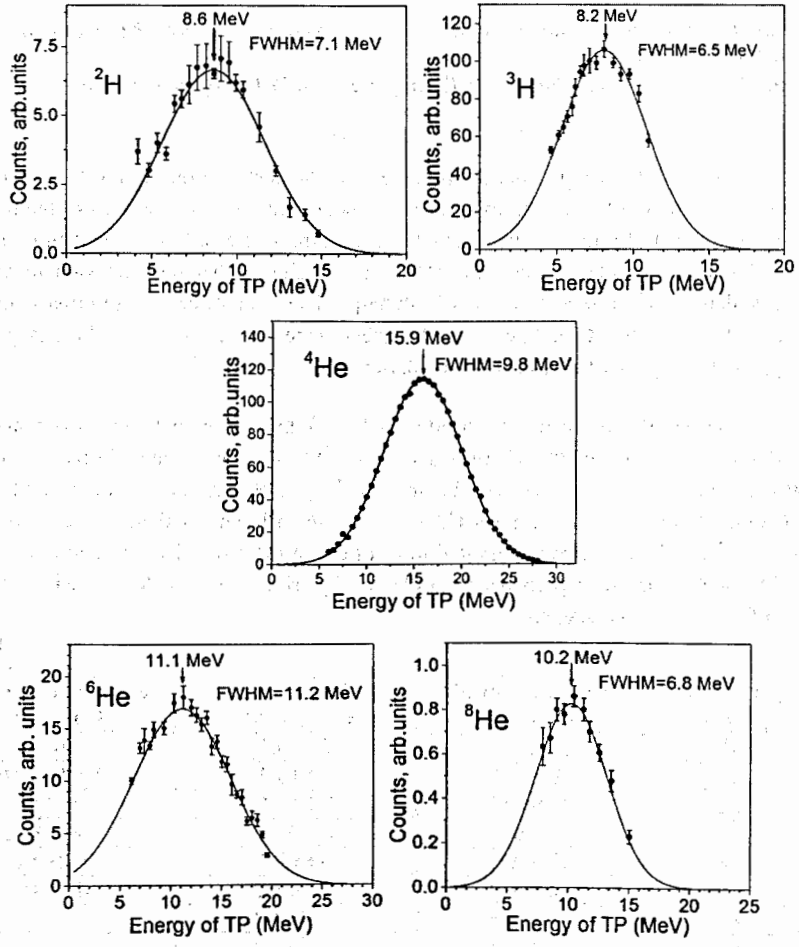

Fig.1. *The energy distributions for some ternary particles in neutron induced fission of ^{235}U. Points correspond to experimental data, lines are calculated distributions.*

All calculated distributions were fitted to experimental data using a variation of initial calculation parameters such as: a distance between fragments, initial velocities of fragments, starting position of ternary particle just after the moment of scission and their starting energy and angular distributions. This set of initial parameters allows us to find characteristics of fissile system acceptable soon after the rupture point.

The trajectory calculations cannot be performed in closed analytical form. It is necessary to replace the differential equations of motion

$$\frac{dX_{ij}}{dt} = V_{ij}, \qquad m_i \frac{dV_{ij}}{dt} = F_{ij} \tag{1}$$

by a set of difference equations

$$X_{ij}^{n+1} = X_{ij}^{n} + \tilde{V}_{ij}^{n}\Delta t, \qquad V_{ij}^{n+1} = \tilde{V}_{ij}^{n} + \frac{1}{2m_i} F_{ij}^{n}\Delta t. \tag{2}$$

Then iterative way is used to find step by step time dependence of coordinates for fission fragments (FFs) and TP. It is necessary to have small time intervals in the calculation process, what means that every partner has to move during each period approximately along the straight line with fixed velocity.

At the first steps of iterative process all partners are still close together and their directions of motion and velocities change rapidly. When described objects are already widely separated and their characteristics of motion change slowly we do not need the same small size of the time interval. To make calculations more quickly an exponential function of n for total time t_n after n time intervals is commonly used:

$$t_n = t_0(e^{na} - 1). \tag{3}$$

and hence the size of the n-th time interval is given by

$$\Delta t_n = t_n - t_{n-1} = t_{n-1}(e^{a} - 1). \tag{4}$$

The calculated individual trajectory patterns for FFs and α-particle are shown in Fig.2. As one can see the final direction of α-particle motion with respect to the light fragment is about 80° independently from initial angle of its emission. To get the angular and energy distributions of ternary particles several millions of similar trajectories were calculated.

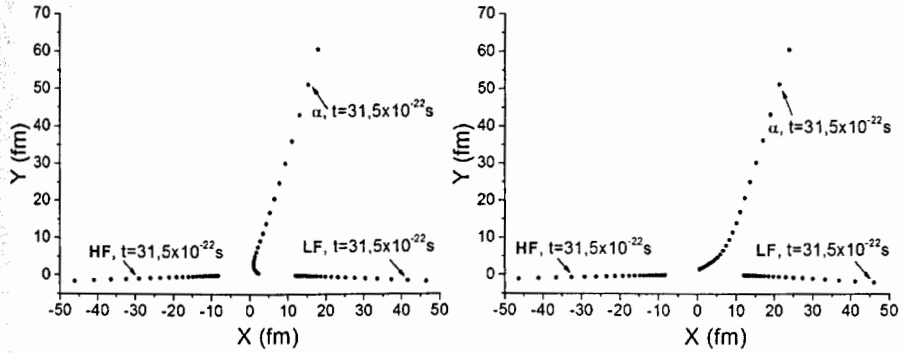

Fig.2. *The calculated trajectory patterns. The coordinates of the object centers are labelled by circles. Their positions are in iterative step order. The arrows point at the simultaneous object placements.*

It is necessary to mention that such standard trajectory calculations are commonly used to describe spontaneous ternary fission or ternary fission induced by unpolarized neutrons. The study of nuclear fission in (n,f) reactions with polarized neutrons as projectiles has revealed particular features of the process, that cannot be described by standard method.

Let us remind you about experiments related to ternary fission of some actinides induced by cold polarized neutrons [8]. In Fig.3 you can see the schema of experimental setup for such measurements. The polarized neutron beam was hitting the fissile targets mounted at the center of a reaction chamber. Detectors for fission fragments and ternary particles were installed in a plane perpendicular to the neutron beam.

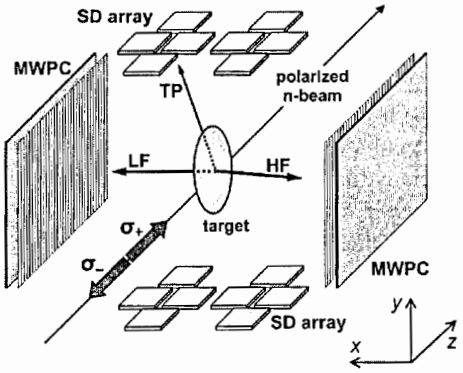

Fig.3. *Layout of the experimental setup: fissile target locating at the center; polarized neutron beam running horizontally; two MWPC detecting complementary fission fragments to the left and right of the target, two arrays of Si detectors on top and bottom of the target intercepting ternary particles. All centers of particle detector assemblies lie in a plane perpendicular to the beam.*

In the process of these experiments some modification of the light charged particles angular distribution was observed due to spin-flip of a polarized neutron beam. Such transformation (see Fig.4, a) of the angular distribution can be divided into two components: the relative change in the amount of recorded particles in the lower and upper hemispheres (Fig.4 b) and the shift of the angular distribution (Fig.4 c). These phenomena were named TRI and ROT-effects, respectively. Now it is shown that both effects are present simultaneously, but with different weights for the four studied actinides [8].

The asymmetry corresponding to TRI-effect is attributed to the Coriolis force present in the nucleus while it is rotating up to scission. The size of the asymmetry is typically 10^{-3}. This phenomenon should be described with the help of quantum mechanics. The ROT-effect, in contrast to this, mostly develops during the next time interval, namely after the nucleus rupture and when nuclear forces have already stopped to action. This phenomenon arises due to the motion of charged objects (two fragments and light particle) in the rotating field of Coulomb forces. To describe this effect we can apply classical estimation using trajectory calculations, but they must be modified taking into account rotation of fissile system.

The rotational structure should be expected in the spectrum of fission channels at energies not much higher than the fission threshold. After slow neutron capture by the target nucleus with the angular momentum I it is possible to obtain compound states with $J = I + 1/2$ and

$J = I - 1/2$. In this case the fission process comes through a few transitional states (fission channels) with fixed K values, where K is the projection of spin J on the symmetry axis. Any rotation of axial nucleus comes around a perpendicular to a line of nuclear symmetry and angular velocity ω can be obtained from this expression [9]:

$$\omega^2 \Im^2 = \hbar^2 (J(J+1) - K^2), \tag{5}$$

where $\Im$ is the moment of inertia of the fissile system.

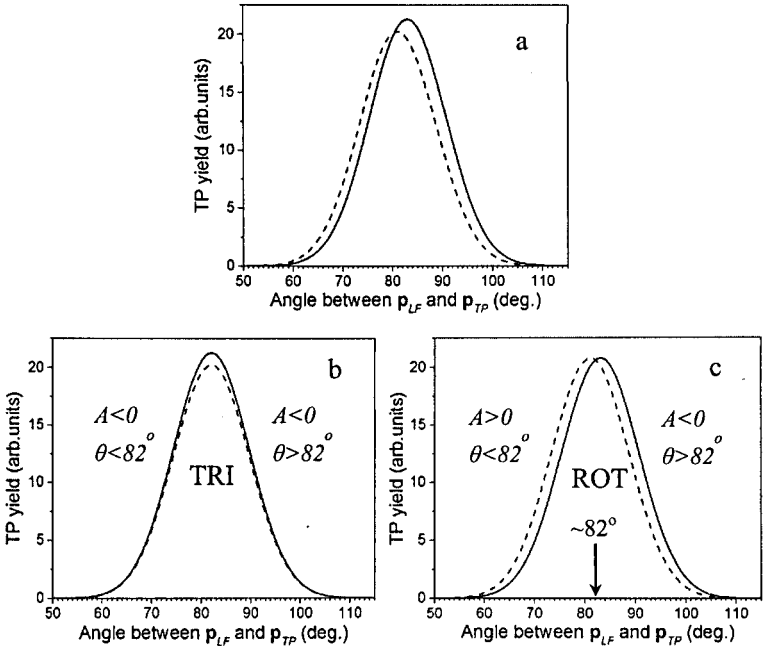

Fig.4. *a) The modification of the angular distribution for light charged particles, which was observed due to spin-flip of a polarized neutron beam; b) the relative change in the number of recorded particles in the lower and upper hemispheres (TRI-effect); c) the shift in the angular distribution (ROT-effect).*

Note that even with a fixed fission axis, we have many directions of fissile nucleus rotation. It is possible to say only about an alignment of rotational axis in a plane perpendicular to the fission axis. Randomly oriented rotation of compound nucleus does not form any regular shift of TP angular distribution, because averaged angular velocity for all nuclei equals zero. Such phenomenon can be observed in ternary fission experiments with unpolarized neutrons and targets. In contrast to this, in case of polarized neutrons it is possible to obtain a non-zero effective angular velocity for the fissile system rotation around the line of neutron beam polarization. The angular velocity for fixed J and K one can get using quantum-mechanical expression:

$$\omega(J,K) = < J_Z(K) > / \Im. \tag{6}$$

As it was shown by Kadmenski and Bunakov [10] this expression can be written in the form:

$$\omega_{+/-}(J,K) = \begin{cases} \dfrac{J(J+1)-K^2}{J} \cdot \dfrac{\hbar}{2\Im} \cdot p_n & for \quad J = I+1/2 \\ -\dfrac{J(J+1)-K^2}{(J+1)} \cdot \dfrac{\hbar}{2\Im} \cdot p_n & for \quad J = I-1/2 \end{cases} \tag{7}$$

The different signs of angular velocities for $J = I+1/2$ and $J = I-1/2$ in these expressions indicate the opposite directions of fissile system rotation.

If several transition states contribute to the fission, it is necessary to perform summation over all possible K values:

$$\omega(J) = \sum_K \left|a_K^J\right|^2 \omega(J,K), \tag{8}$$

where $\left|a_K^J\right|^2$ is the probability to find the component with corresponding value K in the resonance wave-function. To obtain the final effective angular velocity ω it is necessary to take into account the relative contribution of resonance components with different J to the total fission cross-sections:

$$\omega_{eff} = \frac{\omega_+(J)\cdot\sigma_{I+1/2} + \omega_-(J)\cdot\sigma_{I-1/2}}{\sigma_{I+1/2} + \sigma_{I-1/2}}. \tag{9}$$

Here $\sigma_{I+1/2}$ and $\sigma_{I-1/2}$ are the partial fission cross-sections for $J = I+1/2$ and $J = J-1/2$, respectively.

Using such effective angular velocity we can modify trajectory calculations. In case of nuclear system rotation this requires only a change of all initial velocities for described objects [11, 12], namely, additional tangential components for FFs and TP should be taken into account. They can be obtained as a product of the angular velocity on the object distance, on which this object is located soon after the nucleus rupture, from the rotational axis. For the angular velocity calculation it is necessary to find inertia moment of the fissile system, which mostly depends on the fragment masses ratio and on the initial distance between fragments.

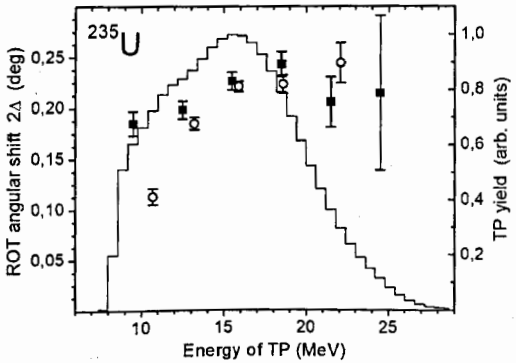

Fig.5. *Angular ROT shift as a function of TP energy for reaction $^{235}U(n,f)$. Experimental data (squares). Theoretical calculation with TPs assumed to be α-particles (open points). The experimental TP energy spectrum is given as histogram with scale to the right.*

The modified trajectory calculations give us the possibility to evaluate the ROT angular shift for light charge particles. Before now these calculations have been performed only with alphas as third particle, since they dominate in ternary fission. The evaluated angular shift averaged over the energy of α-particles was in good agreement with the experimental result, but the detailed distribution of the calculated ROT-effect values depending on the energy of α-particles deviated from the experimental data (see Fig.5). The experimental angular shift [8] was larger than the calculated result in the energy range (8÷13) MeV of the third particle.

It was assumed that this discrepancy can be explained by the presence of other light charged particles in addition to the alphas, because corresponding measurements in this experiment were performed without identification of light charged particles. It was therefore supposed, that taking into account the presence of tritium, which contributes about 7% to the ternary particles yield, it may be possible to bring closer together calculated and experimental results.

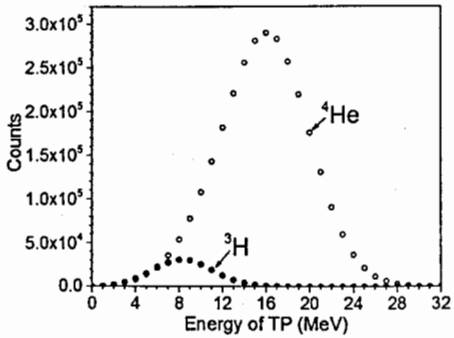

Fig.6 *Calculated energy distributions of light charge particles in neutron induced ternary fission of* ^{235}U.

Fig.6 shows the energy distributions of α-particles and tritons, which were obtained with the help of standard trajectory calculations. The initial calculation parameters for tritons were similar to those of α-particles. The most probable energies and widths of these distributions completely coincide with experimental data [1]. In addition, the calculated angular distributions of the LCPs and fragment's kinetic energies were also in a good agreement with experimental values. This confirms that initial parameters were well selected. The amounts of emitted particles were taken proportional to the corresponding particles yields in neutron induced ternary fission of ^{235}U. They were established in agreement with the experiment.

Using obtained by such a way initial parameters and calculated effective angular velocity (9) it was possible to get energy dependences of the angular shift for both α-particles and tritons with the help of the modified trajectory calculations (Fig.7 a). In order to get the final result, we need to sum two calculated ROT-effects with their weights.

In Fig.7 b one can see the result of ROT-effect estimation, where the influence of tritium was considered using the modified trajectory calculations. It is demonstrated that alphas and tritons taken together improve the agreement between calculated and experimental values of the ROT-effect depending on the energy of light charged particles.

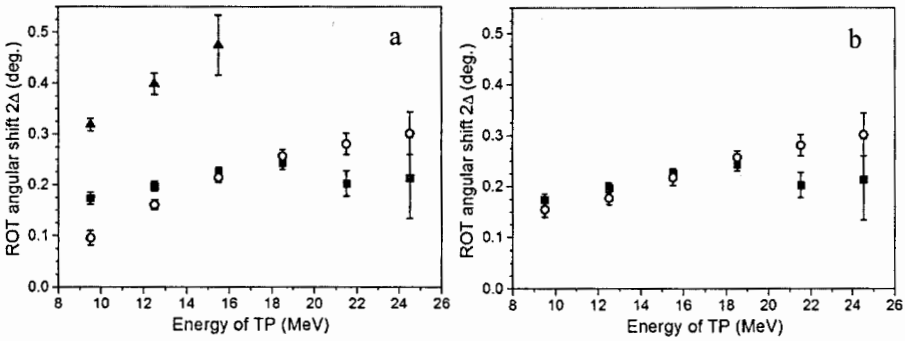

Fig.7. *Angular ROT shift 2Δ as a function of TP energy for the reaction $^{235}U(n,f)$: a) squares are experimental data, triangles – calculated result for tritons, open dots show the result of calculation for α-particles; b) squares are experimental data, open dots show the weighted sum of calculated results for tritons and α-particles.*

Conclusion

The ROT-effect dependence on light charged particle energy was calculated using modified trajectory calculations. The influence of ^{3}H nuclei is considered for the first time. It was shown that the inclusion in the calculation of tritons, in addition to α-particles, significantly improves the agreement between experimentally obtained data and calculation results.

References

1. D. M. Seliverstov, Ph.D. Thesis, Ioffe Physico-Technical Institute, Academy of Sciences of the USSR, "Investigation of ternary fission by thermal neutrons using magnetic-transit mass spectrometer", 1969.
2. Y. Boneh, Z. Fraenkel and I. Nebenzahl, *Phys. Rev.* **156**, 1305-1316 (1967).
3. Y. Gazit, A. Katase, G. Ben-David., R. Moreh, *Phys. Rev.* **C4**, 223-236 (1971).
4. G. Guet, C. Signarbieux, P. Perrin et al., *Nucl. Phys.* **A 314**, 1-26 (1979).
5. M. Borkovski, Yu. Gusev, Yu. Zalite, D. Seliverstov, Proceedings of the 18th International Symp. on Nucl. Physics, Physics and Chemistry of Fission, Gaussing, 1988, pp. 181-185.
6. W. Baum, "Teilchenbegleitete Spaltung von ^{235}U und ^{242}Am", Ph.D. Thesis, Institute für Kern-physik, TH Darmstadt, 1992.
7. A. Roshchin, V. Rubchenya and S. Yavshits, *Yad. Fiz.* **57**, 974-983 (1994) [*Phys. At. Nucl.* (Engl. Transl.) **57**, 914-923].
8. A. Gagarski, F. Gönnenwein, I. Guseva, "Particular features of ternary fission induced by polarized neutrons in the major actinides $^{233,235}U$ and $^{239,241}Pu$", Phys. Rev C **93**, 054619 (2016).
9. A. Bohr, B.R. Mottelson, *Nucl. Structure*, V.2, N. Y., Amsterdam, W. Benjamin, 1974.
10. V. Bunakov, S. Kadmensky, Proc. Int. Sem. ISINN-16, Dubna JINR, 2009, pp. 325-332.
11. I. S. Guseva and Yu. I. Gusev, "A Shift of the Angular Distribution of Light Charged Particles due to the Rotation of the Fissioning Nucleus", Bull. Russ. Acad. Sci., Phys. Ser.71, 367 (2007).
12. I. Guseva and Yu. Gusev, "The Rotation of Scissioning Nucleus Considered Trajectory Calculations for Ternary Fission Induced by Cold Polarized Neutrons", AIP Conf. Proc. 1175, 355 (2009).

Measurements of the Temporal Characteristics of Delayed Neutrons from Neutron Induced Fission of ^{241}Am in the Energy Range from 14.2 to 18 MeV

Gremyachkin D.E., Piksaikin V.M., Egorov A.S., Mitrofanov K.V.

State Scientific Center of Russian Federation
Institute of Physics and Power Engineering, 249033, Obninsk, Russia

Abstract

Analysis of existing database on the relative abundances of delayed neutrons and half-lives of their precursors measured for neutron induced fission of heavy nuclei in the energy range above 14 MeV shows that such data are not available for many nuclides which are important for nuclear fuel cycle. In the present work for the first time the time dependence of delayed neutron activity for the neutron-induced fission of ^{241}Am in the energy range from 14.2 to 18 MeV.

Introduction

In the recent years efforts to purification of nuclear physics database on delayed neutrons was substantially referred to analysis of delayed neutron characteristics for neutron induced fission of ^{235}U, ^{238}U, ^{239}Pu in energy range from thermal values to several MeV [1]. Nuclides and energy range used in this work have been determined first of all by needs of power engineering.

At the same time the energy range of primary neutrons exists for which physical characteristics of delayed neutrons are known significantly worse. First of all, it belongs to energy range above 14 MeV. This energy range is interesting for practical applications related to the development of nondestructive methods used for analysis of fissile materials which is based on delayed neutron registration.

The neutron source

The reaction T(d,n)^{4}He was used to generate neutrons in energy range from 14.2 to 18 MeV. Solid tritium target was irradiated by the beam of the accelerated deuterons from cascade generator CG-2.5 SSC RF-IPPE. Energy of accelerated deuterons was varied from 0.5 to 2 MeV. Interruption of the beam was made using a Faraday cup. Energy dependence of neutrons generated in the T(d,n)^{4}He reaction on incident deuteron energy is shown in Fig. 1.

Beams of neutrons emitted at the angle 0 and 90 degrees against the deuterons beam direction were used. This allowed us to study temporal characteristics of delayed neutrons in the energy range from 14.2 to 18 MeV.

Experimental method and preliminary analysis of the obtained data

The experimental method used in present experiments based on cyclic irradiation of the fissile sample in a well-known neutron flux and consequent measurement of the time dependence of delayed neutron activity. For that, the guide tube of pneumatic transport system with the sample under investigation was placed between two ionization fission chambers near the target of the electrostatic generator CG-2.5.

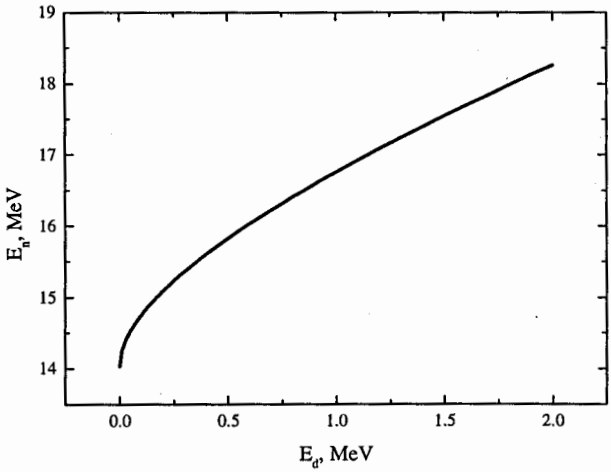

Fig. 1. Energy dependence of neutrons generated in the T(d,n)^{4}He reaction on the incident deuteron energy.

Experimental set-up used in the present work was placed on the beams of electrostatic accelerator CG-2.5 of SSC RF–IPPE. The basic components of the set-up are shown in Fig. 2.

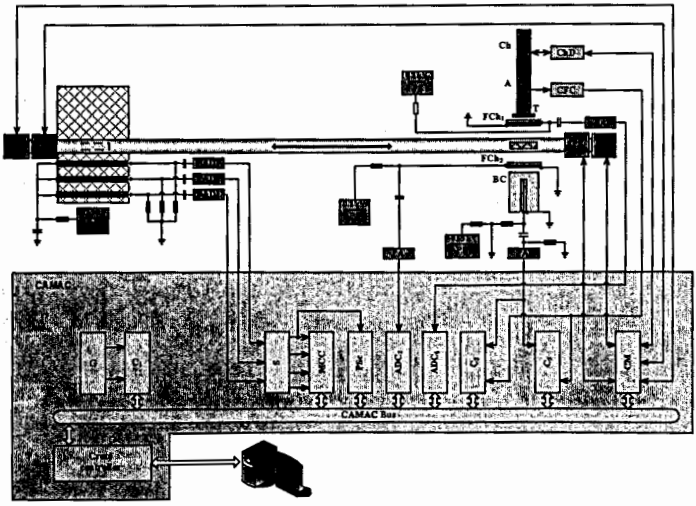

Fig. 2. Block diagram of the experimental setup: (PAD) preamplifier, amplifier, and discriminator; (S) summator; (PA) preamplifier and amplifier; (V) electromagnetic valve; (SPS) sample position sensor; (CM) controlled unit; (CFC) current-to-frequency converter; (ADC) analog-to-digital converter; (PSc) preset-scaler ; (MCC) multichannel counter; (G) quartz generator of pulses; (PS) power source; (Ch) chopper; (ChD) magnetic chopper drive; (A) ion guide aperture; (T) accelerator target; (FCh) fission chamber; (BC) boron counter of neutrons; (C1) counter with a preset exposure time; (C2) counter of total counts from the CFC and BC; and (C3) counter of the CFC and BC counts within preset time intervals.

Boron counters SNM-11 were chosen the main element of the registration of detector, because of their low sensitivity to γ-rays. Detector presents the assay of 30 counters,distributed in polyethylene moderator. It consists of three concentric circles, which have radiuses 53, 80 and 110 mm. Inner ring consists of 6 boron counters, medium and outer rings consist of 12 counters each. Outer diameter of moderator was equal to 400 mm, length – 300 mm. The counters were operating in proportional mode at bias voltage 650 V [2]. There was an opening ∅36 mm in the center of detector for seen for installation of investigated fissile sample. The detector was shielded with boron carbide, cadmium and borated polyethelene.

Short transportation time of the sample (~100-150 ms) from the irradiation position to the detector was accomplished by the fast pneumatic system. It enabled allowed us to measure delayed neutron yields of short-lived precursors. Sample transport tube was a thin-walled stainless steel tube with an outer diameter 10 and a wall thickness of 0.3 mm. Two electromagnetic valves controled the supply of compressed air into the guide tube. The position of the sample in the neutron detector was fixed with a plug with a hole in the center for controlling the discharge of excess pressure in front of a moving sample and mitigate the impact of the sample. Information on the status of the sample was obtained from the two photodiodes and light sources mounted on the guide tube on the irradiation position and neutron detector.

Preliminary processing of the experimental data consisted in the summation of delayed neutron decay curves obtained in the separate measurement cycles. The summed curves was analyzed using the iterative least squares method with the purpose to estimate the relative abundances of delayed neutrons a_i and half-lives of their precursorsT_i. The information on correlation coefficients of group parameters a_i,T_i under estimation, which was later used for averaging of group parameters sets corresponding to the definite energy of initial neutrons was obtained.

Experimental control and acquisition of experimental information was performed by the data acquisition and storage systembased on the CAMAC standard with a personal computer connected to the CAMAC crate using the controller FK-4410.

Experimental conditions and additional experiments

It should be noted that specific features of the T$(d,n)^4$He reaction, concerned with high intensity and high energy of generated neutrons beams essentially complicated the processing procedure of measured data, which is usually used for the work with neutron sources based on T$(p,n)^3$Heand D$(d,n)^3$He reactions. Additional experiments was made to estimate the magnitude of the effect, concerned with blocking of the neutron detector being in the intensive neutron flux and the effect of the concomitant source (D$(d,n)^3$He reaction), appearing as a result of deuteron implantation into the backing of the tritium target.

Processing of the experimental data

Thenumberofcounts of delayed neutron detector $N(t_k)$, registered in the k-channel of time analyzer t_k with duration Δt_k after the sample irradiation using the neutrons from T$(d,n)^4$He and D$(d,n)^3$He reactions can be represented as follows

$$N_l(t_k) = A_l \cdot \sum_{i=1}^{n} F_{li} \cdot \frac{a_{li}}{\lambda_{li}} \cdot \exp(-\lambda_{li} \cdot t_k) \cdot \left(1 - \exp(-\lambda_{li} \cdot \Delta t_k)\right) + B_l(t_k) \cdot \Delta t_k, l = (T, D), k = (1, ..., m), \quad (1)$$

Where T and D related to the measurements using T$(d,n)^4$He and D$(d,n)^3$He reactions correspondingly, a_{li} and λ_{li}– relative abundance and decay constant of ith delayed neutron group, $B_l(t_k)$ – intensity of neutrons background, A_l – saturation activity,

$$F_{li} = (1-\exp(-\lambda_{li} \cdot t_{ir})) \cdot \left(\frac{N}{1-\exp(-\lambda_{li} \cdot T)} - \exp(-\lambda_{li} \cdot T) \cdot \left(\frac{1-\exp(-n \cdot \lambda_{li} \cdot T)}{((1-\exp(-\lambda_{li} \cdot T))^2} \right) \right) \quad (2)$$

Presents the expression considering the irradiation history of the sample and registration of accumulated activity, which includes the following experimental parameters: N – the number of irradiation cycles, T – duration of the one measurement cycle, which consisted of irradiation time in one cycle t_{ir}, transportation time of the sample to the neutron detector and the count time of delayed neutron activity [3].

Results

Time dependences of neutron activity after neutron induced fission of ^{241}Am in the energy range from 14.2 to 18 MeV obtained in the present work considering the blocking effect and effect of concomitant source (filled squares, open squares, circles, triangles) are shown on figure 3.The discrepancy of the experimental data is a consequence of few statistics. Data obtained as result of estimation of delayed neutrons parameters represented by continuous curves. Estimation of the parameters A, B, a_i,λ_i (i = 1, ...,n) on the observed values of time dependence $N(t_k)$ (k=1,...,m) (eq. 1, 2) was made within the 6-group representation using the iteration least squares method.

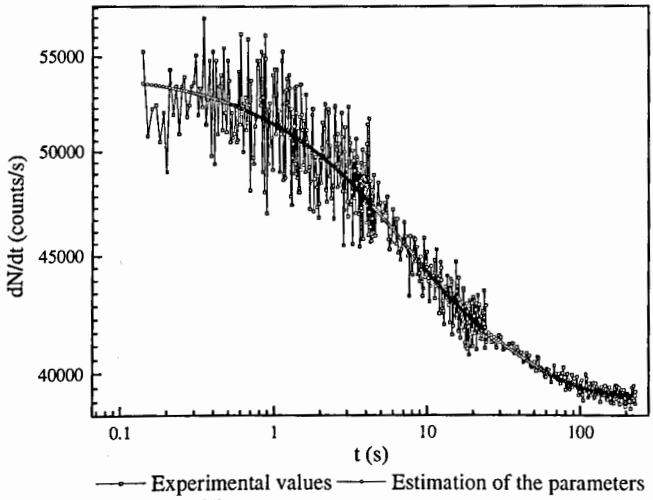

Fig. 3 – Time dependence of ^{241}Am sample activity. Irradiation time 180 s. Black squares – experimental data including the corrections on the blocking effect and effect of concomitant source; red circles curve – data obtained as result of estimation of delayed neutrons parameters.

The obtained results on energy dependence of relative abundances of the separate delayed neutron group a_i and half-lives of their precursors T_i for neutron induced fission of ^{241}Am in the energy range from 14.2 to 18 MeV are presented in the Table 1. Values of group parameters (a_i,T_i) shown in the Table 1 in a six-group representation was obtained by

averaging of these parameters of several series of the measurements, corresponding to the similar energy of the primary neutrons. The average half-life was calculated for each energy using the following formula

$$<T>=\frac{\sum_i a_i T_i}{\sum_i a_i}, \quad (3)$$

Where a_i – the relative abundances of the ith delayed neutron group; T_i – the half-life of the ith delayed neutron group.

Table 1. Relative abundances and half-lives for neutron induced fission of the ^{241}Am in the energy range from 14.2 to 18 MeV.

E_n, MeV	Group number							Average half-ife, s
	i	1	2	3	4	5	6	
14,23±0,20	a_i	0,0382 ±0,0008	0,224 ±0,005	0,461 ±0,010	0,195 ±0,004	0,063 ±0,001	0,019 ±0,004	9,20 ± 0,14
	T_i	56,0 ±1,2	12,1 ±0,2	7,47 ±0,14	4,46 ±0,09	0,44 ±0,01	0,174 ±0,004	
15,84±0,20	a_i	0,0420 ±0,0003	0,229 ±0,002	0,427 ±0,003	0,215 ±0,002	0,067 ±0,001	0,019 ±0,002	10,81 ± 0,08
	T_i	55,1 ±0,5	24,1 ±0,2	5,26 ±0,04	3,23 ±0,03	0,49 ±0,004	0,175 ±0,002	
16,20±0,20	a_i	0,0399 ±0,0008	0,258 ±0,005	0,388 ±0,008	0,221 ±0,005	0,073 ±0,002	0,020 ±0,004	11,47 ± 0,19
	T_i	55,6 ±1,2	24,4 ±0,4	5,76 ±0,11	3,12 ±0,07	0,47 ±0,01	0,177 ±0,004	
16,70±0,20	a_i	0,0394 ±0,0008	0,274 ±0,002	0,367 ±0,008	0,226 ±0,005	0,075 ±0,002	0,020 ±0,004	11,19± 0,20
	T_i	54,7 ±1,2	23,2 ±0,5	5,50 ±0,11	2,77 ±0,06	0,48 ±0,01	0,178 ±0,004	
17,98±0,20	a_i	0,0399 ±0,0007	0,257 ±0,004	0,372 ±0,006	0,234 ±0,004	0,077 ±0,001	0,020 ±0,003	10,74± 0,16
	T_i	54,4 ±0,9	23,5 ±0,4	4,99 ±0,08	2,69 ±0,05	0,49 ±0,008	0,178 ±0,003	

Figure 4 represents the energy dependence of the average half-life of delayed neutron precursors for neutron induced fission of the ^{241}Am in neutrons energy range from 14.2 to 18 MeV. Each energy point has been obtained by averaging of the <T> values from the separate series of the measurements. For each energy point the correlation matrix of the delayed neutron parameters has been obtained. Summation method was used to obtain the value of the average half-life using the following expression

$$<T_{1/2}>=\frac{\sum_i P_{ni} \cdot CY_i \cdot T_{1/2}^i}{\sum_i P_{ni} \cdot CY_i}, \quad (4)$$

where CY_i– the cumulative yield of *i*th precursor, P_{ni} and $T^i_{1/2}$ - the delayed neutron emission probability and the half-life of *i*th precursor, respectively. Summation was made over 368 precursors. The data on cumulative yields from *ENDF/B-VII.1* library was used for the present calculation [4]. The data on probabilities of delayed neutron emission and half-lives of delayed neutron precursors were used from *Abriola et al, 2013*[5].

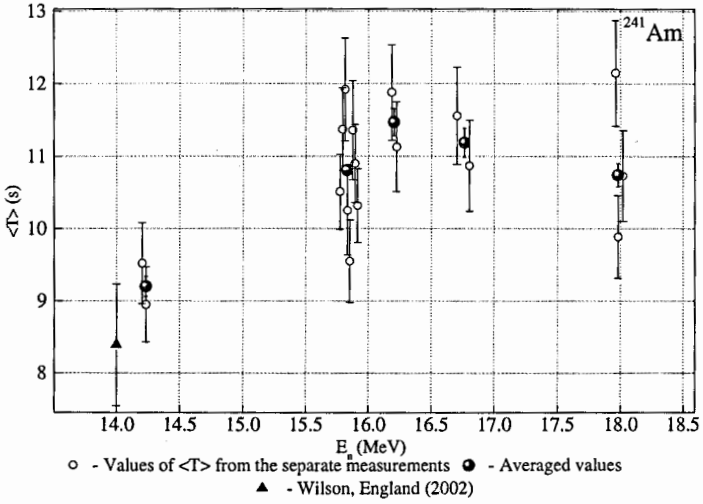

Fig. 4. Energy dependence of the average half-life of delayed neutron precursors for neutron induced fission of the ^{241}Am in the energy range from 14,2 to 18 МэВ. Open circles – the values of the average half-lifefrom the separate series of experiments; filled red circles – the values of the average half-life averaged from the experimental series, filled blue triangle – average half-life of delayed neutron precursors obtained using summation method.

Table2 – Correlation matrix of group parameters obtained for the case of neutron induced fission of ^{241}Am by neutrons with energy of 17.9 MeV

	a1	*T1*	*a2*	*T2*	*a3*	*T3*	*a4*	*T4*	*a5*	*T5*	*a6*	*T6*
a1	1											
T1	-0.32	1										
a2	0	0	1									
T2	0.06	-0.11	0	1								
a3	-0.2	-0.06	0	0.01	1							
T3	-0.03	-0.26	0	0	-0.11	1						
a4	0	0.09	0	-0.01	0.06	0.11	1					
T4	-0.35	0.05	0	0.02	-0.08	-0.01	0.02	1				
a5	0.09	0.05	0	0	0.05	0.07	-0.03	0.05	1			
T5	-0.19	0.04	0	0	-0.01	0.01	0	-0.09	0.01	1		
a6	0.1	0	0	0	0.01	0.01	0	0.02	0	0.01	1	
T6	-0.03	0	0	0	0	0	0	0.01	0	0	0	1

Correlation matrix of delayed neutron parameters was obtained for each energy of incident neutrons. Correlation matrix of estimated group parameters obtained for the case of neutron induced fission of ^{241}Am by neutrons with energy of 17.98 MeV represented in the Table 2.

Conclusion

Measurements of the temporal dependence of neutron activity for the case of neutron induced fission of the ^{241}Am in energy range from 14.2 to 18 MeV have been made for the first time. The obtained decay curves were processed with considering the effect of additional source and blocking effect, inevitably arising when T(d,n)^{4}He reaction is used as a neutron source. Values of the group parameters based on the processed decay curves have been obtained for each incident neutrons energy, which in turn have been used for calculation of the average half-lives of delayed neutron precursors. Data on energy dependence of relative abundances and half-lives of their precursors for neutron induced fission of the ^{241}Am in the energy range from 14.2 to 18 MeV are presented in numerical form.

Reference list

1. D'Angelo. An international cooperation to improve delayed neutron data. Progress in Nuclear Energy, Vol. **41**, No. 1–4, pp. 1–3, 2002.
2. http://www.ortec-online.com/download/428.pdf (16.05.16)
3. Piksaikin V.M., Kazakov L.E., Isaev S.G., Tarasko M.Z., Roshchenko V.A., Tertytchnyi R.G., Springs G.D., Campbell J.M. Energy dependence of relative abundances and periods of delayed neutrons from neutron-induced fission of ^{235}U, ^{238}U, ^{239}Pu in 6- and 8-group model representation. Prog. Nucl. Energy **41** (1–4), 203-222,2002a.
4. JANIS Database. URL: http://www.oecd-nea.org/janis/ (16.05.16).
5. Abriola D., Singh B., Dillmann I. Beta-delayed neutron emission evaluation. IAEA Report INDC(NDS)-0599/BN, G, ND. – IAEA, Vienna, Austria. – 2011.

THE ANGULAR AND SPIN DISTRIBUTIONS OF THE BINARY AND TERNARY LOW-ENERGY NUCLEAR FISSION PRODUCTS AND THE TRANSVERSE WRIGGLING- AND BENDING-VIBRATIONS OF THE COMPOUND FISSILE NUCLEI

S.G. Kadmensky

Voronezh State University, Voronezh, Russia
e-mail: kadmensky@phys.vsu.ru

Abstract

It has been demonstrated, that the angular and spin distributions of products of the binary and ternary low-energy nuclear fission can been successfully described with taking into account the influence of the zero-point transverse wriggling- and bending-vibrations of the compound fissile nucleus near it's scission point with the domination of the wriggling-vibrations.

1. INTRODUCTION

The normalized light fission fragments angular distribution $T^J_{MK}(\Omega)$ in the laboratory coordinate system (LCS) for the low-energy binary nuclear fission from the transition fission state (TFS) [1] *JMK* of compound fissile nucleus (CFN) can be represented [2-4] through the analogous distribution $T(\Omega')$ in the internal coordinate system (ICS):

$$T^J_{MK}(\Omega)=\frac{2J+1}{16\pi^2}\int d\omega\left[\left|D^J_{MK}(\omega)\right|^2+\left|D^J_{M-K}(\omega)\right|^2\right]T(\Omega'), \qquad (1)$$

where the solid angles Ω, Ω' are defined by the fragment emission angles φ, θ and φ', θ' in LCS and ICS correspondingly, $D^J_{MK}(\omega)$ is the generalized spherical function depending from Euler angles $\omega=(\alpha,\beta,\gamma)$, which define the orientation of the axial symmetrical fissile nucleus axes relatively to the axes LCS.

As a rule, the distribution $T(\Omega')$ is constructed with the usage of A. Bohr's hypothesis [1]: $T(\Omega')=T_0(\Omega')$, where the fission fragments distribution $T_0(\Omega')$ has a δ-function character [2-4]:

$$T_0(\Omega')=\frac{1}{2\pi}\left[\delta(\xi'-1)\right], \qquad (2)$$

where $\xi'=\cos\theta'$. Then the distribution $T^J_{MK}(\Omega)$ (1) is determined by the distribution $\left(T^J_{MK}\right)_0(\Omega)$:

$$\left(T^J_{MK}\right)_0(\Omega)=\frac{2J+1}{8\pi^2}\left[\left|D^J_{MK}(\omega)\right|^2+\left|D^J_{M-K}(\omega)\right|^2\right]_{\alpha=\varphi,\beta=\theta,\gamma=0}, \qquad (3)$$

coinciding with the probability of the orientations of ICS axes in LCS defined by Euler angles $\alpha=\varphi$, $\beta=\theta$, $\gamma=0$.

Because of the angular distribution (2) differs from zero for a fixed value of the angle $\theta'=0$, from the quantum-mechanical uncertainty relation [5-6] for ΔL and $\Delta\theta'$:

$$(\Delta L)^2(\Delta\theta')^2\geq h^2/4,$$

it follows that the distribution (2) corresponds to the case of complete uncertainty $\Delta L = \infty$ in the values of the relative orbital moment of fission fragments L. Therefore for real experimental situations it is necessary instead of distribution (2) to use [2-4] the physically close distribution $T(\Omega')$, which differs from zero in a small vicinity of the angle $\theta' = 0$ at $\Delta\theta' = 1$:

$$T(\Omega') = \left|A(\Omega')\right|^2 . \tag{4}$$

The amplitude $A(\Omega')$ of the named above distribution is represented by the formula:

$$A(\Omega') = \sum_L \psi_L Y_{L0}(\Omega') , \tag{5}$$

where the wave function ψ_L defines the L-distribution $W(L) = \left|\psi(L)\right|^2$ of fission fragments in the vicinity of the scission point of the CFN. Because of the approximate validity of formula (2) characteristic orbital moments L in the sum (5) will have large values in comparison with the value of the compound fissile nucleus spin J. Then from the law of compound nucleus total spin conservation $\mathbf{J} = (\mathbf{F} + \mathbf{L})$, where $\mathbf{F} = (\mathbf{J}_1 + \mathbf{J}_2)$ is the summary fission fragments spin, it follows $\mathbf{F} \approx -\mathbf{L}$ and for L ? J the summary spin F must have the large values F ? J.

The experimental multiplicities, energy and angular distributions of instantaneous neutrons and γ-quanta, evaporated from thermalized fragments of low-energy fission, isomeric ratios of yields of final fragments, as well as characteristics of delayed neutrons emitted during the β-decay of named above final fragments are consistent with the fact [7-15] of the appearance of large values of fission fragments spins $\mathbf{J}_1$, $\mathbf{J}_2$, which are oriented perpendicularly to the direction of CFN symmetry axis.

The question arises about mechanisms of appearance of the large values of the relative orbital moments L and spins J_1, J_2 fission fragments. Attempts of the explanation of these facts through the Coulomb interaction of strongly deformed primary fission fragments were unsatisfactory, since this interaction can change [8-9] the average values of spins and orbital moments of fission fragments only on small quantities $\Delta\bar{L}$, $\Delta\bar{J}_1$, $\Delta\bar{J}_2 \leq 2$. The answer to this question can be obtained on the base of the development the representations of the quantum theory fission [1-4] in papers [17-20], allowing simultaneously to take into account effects of transverse wriggling- and bending-vibrations of the compound fissile nucleus with the defining role of wriggling-vibrations.

2. CHARACTERISTICS OF THE LOW-ENERGY BINARY AND TERNARY NUCLEAR FISSION

In the description of the binary and ternary low-energy nuclear fission it is used the following predictions:

1) the conservation of the direction of the symmetry axis of the fissile nuclear system at all stages of it's evolution including the internal collective deformation motion of CFN [21] to scission point of this nucleus to the fission fragments;
2) the coldness [1] of fissile nucleus at all fission stages after passage of the first fission barrier up to it's scission point;
3) connected with named above coldness the conservation of the projection K of the spin J of fissile nucleus on the symmetry axis [1-4, 22-23];

A modern understanding of the nature of the appearance of large values of the relative orbital moments and spins of fission fragments is based [17-20] on the account of the two types of collective transverse vibrations of the CFN introduced in paper [16] in the vicinity of it's scission point, which must have the character of zero-point vibrations due to named above coldness of CFN.

The first type includes bending-vibrations associated with rotations of the symmetry axes of two strongly deformed fission fragments that touch their vertices in the neck region of a strongly deformed CFN and pass after the scission of named above neck into primary fission fragments. These rotations occur in opposite directions around axes perpendicular to the symmetry axis of CFN. Because of the law of conservation of the total spin of CFN the spins $\mathbf{J}_{b1}$ and $\mathbf{J}_{b2}$ of fission fragments connected with the bending-vibrations satisfy the condition $\mathbf{J}_{b1} = -\mathbf{J}_{b2}$.

The second type of transverse vibrations corresponds to the wriggling-vibrations of CFN, which are associated with rotations of the symmetry axes of the analogous fission fragments in the unit direction around axes perpendicular to the symmetry axis of CFN, which lead to the appearance of equally directed and large in magnitudes spins of the these fission fragments $\mathbf{J}_{w1}$ and $\mathbf{J}_{w2}$. In order to compensate for the nonzero total spin of these fragments $\mathbf{J}_w = \left(\mathbf{J}_{w1} + \mathbf{J}_{w2}\right)$, CFN rotates about the axis parallel to the axes of rotation of the fission fragments in the opposite direction, that leads to the appearance of relative orbital momenta of the named above fission fragments $\mathbf{L}$, which have values $\mathbf{L} = -\mathbf{J}_w$ because of the law of conservation of the total spin of CFN.

Both types of transverse vibrations contribute to the values of the spins J_1 and J_2 of the emitted fission fragments, the average values of which are larger than the usually observed values of the spin J of the CNF. But only wriggling-vibrations define the distribution of the orbital moments L of the fission fragments, which have characteristic values, as will be shown below, significantly exceeding the values of J.

The wave functions of zero-point wriggling- and bending-vibrations in the orbital momentum representation $\Psi_0(J_{w_x})$, $\Psi_0(J_{w_y})$ and $\Psi_0(J_{b_x})$, $\Psi_0(J_{b_y})$ depend from the spin projections for wriggling- and bending-vibrations J_{w_x}, J_{w_y} and J_{b_x}, J_{b_y} [16], which are related with projections of the spins $\mathbf{J}_1$ and $\mathbf{J}_2$ fission fragments on the axis X, Y perpendicular to the symmetry axis of CFN as

$$J_{w_x} = J_{1x} + J_{2x},\ J_{w_y} = J_{1y} + J_{2y};\ J_{b_x} = J_{1x} - J_{2x},\ J_{b_y} = J_{1y} - J_{2y};\ J_1^2 = J_{1x}^2 + J_{1y}^2,\ J_2^2 = J_{2x}^2 + J_{2y}^2. \quad (6)$$

As a result $\Psi_0(J_{w_x})$ and $\Psi_0(J_{b_x})$ can be represented in the forms [30]:

$$\Psi_0(J_{w_x}) = \left(\pi C_w\right)^{-1/4} \exp\left(-\frac{J_{w_x}^2}{4C_w}\right); \qquad \Psi_0(J_{b_x}) = \left(\pi C_b\right)^{-1/4} \exp\left(-\frac{J_{b_x}^2}{4C_b}\right), \quad (7)$$

where $C_w = M_w \hbar\omega_w$, $C_b = M_b \hbar\omega_b$ and frequencies ω_w and ω_b of both wriggling- and bending-vibrations are determined by the classical formulas $\omega_w = \sqrt{K_w / M_w}$ and $\omega_b = \sqrt{K_b / M_b}$, where K is the stiffness parameter, and M is the mass parameter. Expressing the spins distribution function $W\left(\mathbf{J}_1, \mathbf{J}_2\right)$ of the fission fragments as

$$W(\mathbf{J}_1,\mathbf{J}_2)=\left|\Psi_0(J_{w_x})\right|^2\left|\Psi_0(J_{w_y})\right|^2\left|\Psi_0(J_{b_x})\right|^2\left|\Psi_0(J_{b_y})\right|^2, \tag{8}$$

it can obtain [16]:

$$W(\mathbf{J}_1,\mathbf{J}_2)=\frac{4J_1J_2}{\pi C_bC_w}\exp\left[-\frac{1}{2}\left(\frac{1}{C_b}+\frac{1}{C_w}\right)\left(J_1^2+J_2^2\right)+\left(\frac{1}{C_b}-\frac{1}{C_w}\right)J_1J_2\cos\phi\right], \tag{9}$$

where $\phi(0\le\phi\le 2\pi)$ is the angle between the two-dimensional spin vectors of the fragments $\mathbf{J}_1$ and $\mathbf{J}_2$ lying in the plane *xy*. By integrating formula (9) with respect to the variables J_2 and ϕ, one can obtain [16] the spin distribution $W(J_1)$ of one from initial fission fragment:

$$W(J_1)=\frac{4J_1}{C_b+C_w}\exp\left[-\frac{2J_1^2}{C_b+C_w}\right]. \tag{10}$$

Then the average spin $\bar{J}_1$ of this fragment has the value:

$$\bar{J}_1=\int_0^{\infty}J_1W(J_1)dJ_1=\frac{1}{2}\sqrt{\frac{\pi}{2}}\left(C_b+C_w\right)^{1/2}. \tag{11}$$

From the estimates of [16] for fissile actinide-nuclei it can be obtained values: M_w = 1.6·10^6 MeV·Fm^2·s^2; M_b = 2.0·10^6 MeV·Fm^2·s^2; K_w = 295 MeV·rad^{-2}; K_b = 52 MeV·rad^{-2}; $\hbar\omega_w$ = 2.3 MeV; $\hbar\omega_b$ = 0.9 MeV; $C_w=132$ and $C_b=57$, from which it follows that the stiffness parameters, the quantum energies and the coefficients for the wriggling-vibrations turn out to be noticeably larger than the analogous values for the bending-vibrations . Then the quantity $(C_b+C_w)/2$ determining the character of the distribution (10) turns out to be ≈ 95, which leads to the average value (11) of the spin of the fission fragment $\bar{J}_1\approx 8.6$. At the same time, if the value $C_b=57$ is neglected in the comparison with value $C_w=132$ in the formula $(C_b+C_w)/2$, the average value of the spin of the fission fragment turns out to be equal to 6, which differs by a factor of 1.5 from the spin value obtained above, while taking into account the wriggling- and bending-vibrations. Hence, the conclusion is drawn that the wriggling-vibrations play a predominant role in comparison with bending-vibrations in the formation of the distribution of the spins of fission fragments.

The approach developed above to the description of the spin distribution of fission fragments based on the concept of the coldness of CFN at the scission point and taking into account the zero-point transverse vibrations of CFN is fundamentally different from the approach of [24, 8-11], in which the assumption of appreciable thermalization of fission fragments near scission point of the fissile nucleus, when the temperature T of the fission fragments exceeds 1 MeV. In this case, due to the significantly lower energy of the $\hbar\omega_b$ quantum of bending-vibrations compared to the analogous energy $\hbar\omega_w$ of the quantum of wriggling-vibrations (for example, for the nucleus), the main role in the temperature distribution of the fission fragments in terms of the number n_b and n_w quanta of bending- and wriggling- vibrations is played by the bending-vibrations. But, since the fissile nucleus remains in the cold state near it's scission point to fragments of fission, the representation of papers [24, 8-11] are not realized, and the formation of spin distributions of fission fragments is determined by zero wriggling- and bending- vibrations of CFN with the dominant role of wriggling-vibrations.

A modern understanding of the nature of the appearance of large values of the relative orbital moments and spins of fission fragments is based [17-20] on the account of the two types of collective transverse vibrations of the CFN introduced in paper [16] in the vicinity of it's scission point, which must have the character of zero-point vibrations due to named above coldness of CFN.

The first type includes bending-vibrations associated with rotations of the symmetry axes of two strongly deformed fission fragments that touch their vertices in the neck region of a strongly deformed CFN and pass after the scission of named above neck into primary fission fragments. These rotations occur in opposite directions around axes perpendicular to the symmetry axis of CFN. Because of the law of conservation of the total spin of CFN the spins $\mathbf{J}_{b1}$ and $\mathbf{J}_{b2}$ of fission fragments connected with the bending-vibrations satisfy the condition $\mathbf{J}_{b1} = -\mathbf{J}_{b2}$.

The second type of transverse vibrations corresponds to the wriggling-vibrations of CFN, which are associated with rotations of the symmetry axes of the analogous fission fragments in the unit direction around axes perpendicular to the symmetry axis of CFN, which lead to the appearance of equally directed and large in magnitudes spins of the these fission fragments $\mathbf{J}_{w1}$ and $\mathbf{J}_{w2}$. In order to compensate for the nonzero total spin of these fragments $\mathbf{J}_w = \left(\mathbf{J}_{w1} + \mathbf{J}_{w2}\right)$, CFN rotates about the axis parallel to the axes of rotation of the fission fragments in the opposite direction, that leads to the appearance of relative orbital momenta of the named above fission fragments $\mathbf{L}$, which have values $\mathbf{L} = -\mathbf{J}_w$ because of the law of conservation of the total spin of CFN.

Both types of transverse vibrations contribute to the values of the spins J_1 and J_2 of the emitted fission fragments, the average values of which are larger than the usually observed values of the spin J of the CNF. But only wriggling-vibrations define the distribution of the orbital moments L of the fission fragments, which have characteristic values, as will be shown below, significantly exceeding the values of J.

The wave functions of zero-point wriggling- and bending-vibrations in the orbital momentum representation $\Psi_0(J_{w_x})$, $\Psi_0(J_{w_y})$ and $\Psi_0(J_{b_x})$, $\Psi_0(J_{b_y})$ depend from the spin projections for wriggling- and bending-vibrations J_{w_x}, J_{w_y} and J_{b_x}, J_{b_y} [16], which are related with projections of the spins $\mathbf{J}_1$ and $\mathbf{J}_2$ fission fragments on the axis X, Y perpendicular to the symmetry axis of CFN as

$$J_{w_x} = J_{1x} + J_{2x},\ J_{w_y} = J_{1y} + J_{2y};\ J_{b_x} = J_{1x} - J_{2x},\ J_{b_y} = J_{1y} - J_{2y};\ J_1^2 = J_{1x}^2 + J_{1y}^2,\ J_2^2 = J_{2x}^2 + J_{2y}^2. \quad (6)$$

As a result $\Psi_0(J_{w_x})$ and $\Psi_0(J_{b_x})$ can be represented in the forms [30]:

$$\Psi_0(J_{w_x}) = (\pi C_w)^{-1/4} \exp\left(-\frac{J_{w_x}^2}{4C_w}\right); \qquad \Psi_0(J_{b_x}) = (\pi C_b)^{-1/4} \exp\left(-\frac{J_{b_x}^2}{4C_b}\right), \quad (7)$$

where $C_w = M_w \hbar\omega_w$, $C_b = M_b \hbar\omega_b$ and frequencies ω_w and ω_b of both wriggling- and bending-vibrations are determined by the classical formulas $\omega_w = \sqrt{K_w / M_w}$ and $\omega_b = \sqrt{K_b / M_b}$, where K is the stiffness parameter, and M is the mass parameter. Expressing the spins distribution function $W(\mathbf{J}_1, \mathbf{J}_2)$ of the fission fragments as

$$W(\mathbf{J}_1,\mathbf{J}_2)=\left|\Psi_0(J_{w_x})\right|^2\left|\Psi_0(J_{w_y})\right|^2\left|\Psi_0(J_{b_x})\right|^2\left|\Psi_0(J_{b_y})\right|^2, \tag{8}$$

it can obtain [16]:

$$W(\mathbf{J}_1,\mathbf{J}_2)=\frac{4J_1J_2}{\pi C_bC_w}\exp\left[-\frac{1}{2}\left(\frac{1}{C_b}+\frac{1}{C_w}\right)\left(J_1^2+J_2^2\right)+\left(\frac{1}{C_b}-\frac{1}{C_w}\right)J_1J_2\cos\phi\right], \tag{9}$$

where $\phi(0\le\phi\le 2\pi)$ is the angle between the two-dimensional spin vectors of the fragments $\mathbf{J}_1$ and $\mathbf{J}_2$ lying in the plane xy. By integrating formula (9) with respect to the variables J_2 and ϕ, one can obtain [16] the spin distribution $W(J_1)$ of one from initial fission fragment:

$$W(J_1)=\frac{4J_1}{C_b+C_w}\exp\left[-\frac{2J_1^2}{C_b+C_w}\right]. \tag{10}$$

Then the average spin $\overline{J}_1$ of this fragment has the value:

$$\overline{J}_1=\int_0^\infty J_1W(J_1)dJ_1=\frac{1}{2}\sqrt{\frac{\pi}{2}}\left(C_b+C_w\right)^{1/2}. \tag{11}$$

From the estimates of [16] for fissile actinide-nuclei it can be obtained values: M_w = 1.6·10^6 MeV·Fm^2·s^2; M_b = 2.0·10^6 MeV·Fm^2·s^2; K_w = 295 MeV·rad^{-2}; K_b = 52 MeV·rad^{-2}; $\hbar\omega_w$ = 2.3 MeV; $\hbar\omega_b$ = 0.9 MeV; C_w = 132 and C_b = 57, from which it follows that the stiffness parameters, the quantum energies and the coefficients for the wriggling-vibrations turn out to be noticeably larger than the analogous values for the bending-vibrations . Then the quantity $(C_b+C_w)/2$ determining the character of the distribution (10) turns out to be ≈ 95, which leads to the average value (11) of the spin of the fission fragment $\overline{J}_1$ ≈ 8.6. At the same time, if the value C_b = 57 is neglected in the comparison with value C_w = 132 in the formula $(C_b+C_w)/2$, the average value of the spin of the fission fragment turns out to be equal to 6, which differs by a factor of 1.5 from the spin value obtained above, while taking into account the wriggling- and bending-vibrations. Hence, the conclusion is drawn that the wriggling-vibrations play a predominant role in comparison with bending-vibrations in the formation of the distribution of the spins of fission fragments.

The approach developed above to the description of the spin distribution of fission fragments based on the concept of the coldness of CFN at the scission point and taking into account the zero-point transverse vibrations of CFN is fundamentally different from the approach of [24, 8-11], in which the assumption of appreciable thermalization of fission fragments near scission point of the fissile nucleus, when the temperature T of the fission fragments exceeds 1 MeV. In this case, due to the significantly lower energy of the $\hbar\omega_b$ quantum of bending-vibrations compared to the analogous energy $\hbar\omega_w$ of the quantum of wriggling-vibrations (for example, for the nucleus), the main role in the temperature distribution of the fission fragments in terms of the number n_b and n_w quanta of bending- and wriggling- vibrations is played by the bending-vibrations. But, since the fissile nucleus remains in the cold state near it's scission point to fragments of fission, the representation of papers [24, 8-11] are not realized, and the formation of spin distributions of fission fragments is determined by zero wriggling- and bending- vibrations of CFN with the dominant role of wriggling-vibrations.

For construction of the distribution $W(L)$ of the relative orbital moments of the fission fragments the spin distribution of the fission fragments (8) can be transformed to the form:

$$W(\mathbf{L},\mathbf{J}') = \frac{1}{\pi^2 C_w C_b} \exp\left[-\frac{\mathbf{L}^2}{2C_w} - \frac{\mathbf{J}'^2}{2C_b}\right], \tag{12}$$

where the relative orbital momentum $\mathbf{L}$ and the relative spin $\mathbf{J}'$ of the fission fragments can be represented as

$$\mathbf{L} = -(\mathbf{J}_1 + \mathbf{J}_2), \quad \mathbf{J}' = (\mathbf{J}_1 - \mathbf{J}_2)/2; \tag{13}$$

$$\mathbf{J}_1 = -\mathbf{L}/2 + \mathbf{J}', \quad \mathbf{J}_2 = -\mathbf{L}/2 - \mathbf{J}', \tag{14}$$

with the Jacobian of the change in the transition from the phase volume element $d\mathbf{J}_1 d\mathbf{J}_2$ to the element $d\mathbf{L}d\mathbf{J}'$ is equal to 1. Taking into account that the elements of the phase volume $d\mathbf{L}$, $d\mathbf{J}'$ for two-dimensional vectors $\mathbf{L}, \mathbf{J}'$ can be represented in the cylindrical coordinate system as

$$d\mathbf{L} = LdLd\varphi_L, \quad d\mathbf{J}' = J'dJ'd\varphi_{J'} \tag{15}$$

and integrating the distribution (12) with respect to $dJ', d\varphi_{J'}, d\varphi_L$ can obtain the distribution normalized by integration with respect to unity:

$$W(L) = \frac{L}{C_w} \exp\left[-\frac{L^2}{2C_w}\right]. \tag{16}$$

As expected, the obtained distribution $W(L)$ is determined only by a constant C_w for wriggling-vibrations. Then the average value $\bar{L}$ of the relative orbital momentum L of the fission fragments is defined as

$$\bar{L} = \int_0^\infty L|\psi(L)|^2 dL = \frac{1}{C_w}\int_0^\infty L^2 \exp\left(-\frac{L^2}{2C_w}\right) dL = \sqrt{\frac{\pi}{2}}(C_w)^{1/2}. \tag{17}$$

With usage of the found above value $C_w = 132$ for the nucleus ^{236}U the value $\bar{L}$ is equal 14.4 and significantly exceeds the values of the spin J of CFN.

3. THE DESCRIPTION OF SPIN DISTRIBUTIONS OF FISSION FRAGMENTS

After the scission point of CFN initially cold i-th fission fragment (i = 1, 2) in a short time (of the order of 10^{-21}s) go over to equilibrium state, for which the distribution of excitation energy E_i^* and spin J_i in [1] is built as Gibb's distribution $\rho_i(E_i^*, J_i)$:

$$\rho_i(E_i^*, J_i) = \rho_i(E_i^*)\rho_i(J_i), \tag{18}$$

where the energy $\rho_i(E_i^*)$ and spin $\rho_i(J_i)$ distributions with the temperature T_i and the fission fragment moment of inertia $\Im_i$ have forms:

$$\rho_i(E_i^*): \ \exp(-E_i^*/kT_i), \tag{19}$$

$$\rho_i(J_i): \ (2J_i+1)\exp[-\hbar^2 J_i(J_i+1)/\Im_i kT_i]. \tag{20}$$

In later papers [8, 12-13] it was used the representation according to which the statistical equilibrium in thermalized fission fragment arises only for their excitation energies, but the spin distribution $\rho_i(J_i)$ of fission fragment is nonequilibrium, since it forms at the scission point of the cold CFN and is not associated with the temperature of the fission fragment after it's thermalization. In this case $\rho_i(J_i)$ it is presented in the "standard" form [12]:

$$\rho_i(J_i):\ (2J_i+1)\exp[-J_i(J_i+1)/B^2], \tag{21}$$

where the value B^2 can differ markedly from the value $\Im_i kT_i/\hbar^2$ in formula (20). Based on the statistical model of nuclear reactions [27-28] and the cascade-evaporation model [29], using energy (19) and spin (21) distributions of thermalized fragments of spontaneous and low-energy fission of actinide nuclei, multiplicities, energy and angular distributions instantaneous neutrons [11] and gamma quanta [8, 13], evaporated from thermalized fragments, relative yields of the ground and isomeric states of the final fission fragments [8, 13], as well as the characteristics of the delayed neutrons emitted during the β-decay of these fragments. The parameter B^2 in formula (21) was assumed to be (80-120), which leads to the average values of the spins of the fission fragments $\bar{J}_i$ in the range (7-9), close to their experimental values.

The spin distribution of the fission fragments (21) coincides in form with the introduced above analogous distribution (10) caused by transverse wriggling- and bending-vibrations of CFN near its scission point, for which the constant B^2 has the form:

$$B^2=\frac{C_b+C_w}{2}. \tag{22}$$

The presented above values of constant $(C_b+C_w)/2 \approx 95$ and average spin of fission fragment $\bar{J}_i \approx 8.6$ from (10) are clearly correlated with the range of values (80-120) for B^2 and (7-9) for the average spin of the fission fragment $\bar{J}_i$ calculated in [12-13].

4. THE ANGLE DISTRIBUTIONS OF FRAGMENTS OF THE LOW-ENERGY PHOTOFISSION

The angular distribution $W(\Omega)$ of the fragments of the photofission reaction of even-even target nucleus can be represented with the usage of the formalism [1] as

$$W(\Omega)\equiv\frac{d\sigma_{\gamma f}(\theta)}{d\Omega}=\sum_J\sum_M\sigma(E_\gamma,JM)\sum_{K=0}^{J}\frac{\Gamma_f(JK)}{\Gamma(J)}T^J_{MK}(\Omega)\ . \tag{23}$$

where $\sigma(E_\gamma,JM)$ is the cross section for the formation of CFN with spin J ($J=1$ for electric dipole and $J=2$ for electric quadrupole photons) and it's projection M on the direction of the incident beam of photons with energy E_γ, $\Gamma_f(JK)$ and $\Gamma(J)$ are the fission and total widths of the transition fission state of CFN. Using the formulas (1, 4-5) coefficient $T^J_{MK}(\Omega)$ can be represented [20] by formula:

$$T^J_{MK}(\Omega)=\sum_l B_{JKMl}P_l(\cos\theta), \tag{24}$$

where

$$B_{JKMl}=\frac{2J+1}{4\pi}\sum_{LL'}\psi_L\psi_{L'}\sqrt{(2L+1)(2L'+1)}\sum_{jl}(-1)^{j+J+l}\frac{\sqrt{2l+1}}{\sqrt{2J+1}}C^{jK}_{JLK0}C^{jK}_{JL'K0}C^{l0}_{LL'00}C^{JM}_{JM0}\begin{Bmatrix}L & j & J\\ J & l & L'\end{Bmatrix}, \tag{25}$$

at that for $l=0$ value $B_{JKM0}=1/4\pi$.

Using the formulas (1, 4-5) and the wave function ψ_L associated with the distribution $W(L)$ (16) as $\psi_L=\sqrt{W(L)}$, it can be obtained [20] for the anisotropy of the angular distribution (23):

$$\frac{d\sigma_{yf}(\theta)/d\Omega}{d\sigma_{yf}(90^\circ)/d\Omega} = a + b\sin^2\theta + c\sin^2(2\theta), \qquad (26)$$

The coefficients a, b, c in formula (26) are defined in [20].

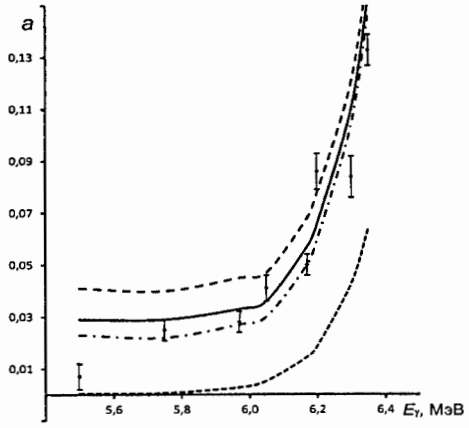

Fig. 1. Approximation of the energy dependence of the angular distribution coefficients of fragments of the subthreshold photofission ^{234}U for different values of the wriggling-vibrations parameter (- - - - $C_w = 70$; ——— $C_w = 110$; -.-.-.-.- $C_w = 140$; --------$C_w \to \infty$ (A. Bohr limit)).

From Fig. 1, where dependences from γ-quanta energy E_γ of the experimental and theoretical values of asymmetry coefficient a for different values of parameter C_w are represented, it is seen that values of the parameter C_w lie in the range $C_w = 130 \pm 40$ and are in good agreement with the estimate of the wriggling-vibrations parameter $C_w = 132$ for ^{234}U obtained in [16] and essentially different from A. Bohr limit $C_w \to \infty$. Similar values of the parameter C_w are optimal [20] for comparison of the theoretical and experimental values of the asymmetry coefficients a for the photofission of the ^{236}U and ^{238}U nuclei.

5. CONCLUSION

The successful description of the angular distributions fission fragments of low-energy nuclear, as well as the characteristics of the instantaneous neutrons and gamma quanta, evaporated from fission fragments after their thermalization, is based on the use of introduced above three basic representations. The first of these representation introduced at the first by A. Bohr is related to the coldness of the CFN at its scission point. The second representation is based on taking into account the transverse bending- and wriggling-vibrations of this CNF [16], which because of named above coldness of CFN have the zero-point character and lead to the appearance of large values of the spins and relative orbital momentum of the fission fragments oriented perpendicular to the symmetry axis of CFN at the moment of its rupture. And, finally, the third representation uses of the generalized cascade-evaporation model,

taking into account the nonequilibrium character of the distributions of spins and relative orbital moments of fission fragments due to considered above bending- and wriggling-vibrations with the domination role of wriggling-vibrations.

REFERENCES

1. Bohr, and B. Mottelson, *Nuclear Structure* (NY, Amsterdam, 1969, 1975) V. 1, 2
2. S.G. Kadmensky, Phys. At. Nucl. **65**, P. 1390 (2002);
3. S.G. Kadmensky, L.V. Rodionova, Phys. At. Nucl. **66**, 1219 (2003);
4. S.G. Kadmensky, L.V. Rodionova, Bull. Russ. Sci. Phys. **69**, 751 (2004)
5. S.G. Kadmensky, Phys. Atom. Nucl. **65**, 1390 (2002); **66**, 1785 (2002);
6. V.E. Bunakov, S.G. Kadmensky, Bull. Bull. Russ. Acad. Sci. Phys. **71**, 346 (2007)
7. K. Hoffman, Phys. Rev. B **133**, 714 (1964);
8. J. O. Rasmussen, W. Norenberg, H. J. Mang, Nucl. Phys. A **136**, 456 (1969);
9. J. B. Wilhelmy, *et al.*, Phys. Rev. C **5**, 2041 (1972);
10. M. Zielinska-Pfabe, K. Diethrich Phys. Let. B 49, 123, (1974);
11. T. M. Sheidman *et al*, Phys. Rev. C 65, 064302 (2002);
12. A. Gavron, Phys. Rev. C 13, 2562 (1976);
13. L. G. Moretto, G. F. Peaslee, G. J. Wozniak, Nucl. Phys. A 502, 453 (1989);
14. S. Musicu et al, Phys. Rev. C 60, 034613 (1999);
15. O. T. Grudzevich *et. al*, Phys. At. Nucl. 64, P. 1643 (2001)
16. J.R. Nix, W.J. Swiatecki, Nucl. Phys. A 71, 1(1965)
17. S. G. Kadmensky, D. E. Lyubashevsky, L. V. Titova, Bull. Russ. Acad. Sci.: Phys. 75, P. 989 (2011);
18. S. G. Kadmensky, D. E. Lyubashevsky, L. V. Titova, Bull. Russ. Acad. Sci.: Phys.79, P. 975 (2015);
19. S. G. Kadmensky, D. E. Lyubashevsky, V.E. Bunakov, Phys. At. Nucl., 77, P. 198 (2015)
20. S. G. Kadmensky, D. E. Lyubashevsky, L. V. Titova, Bull. Russ. Acad. Sci.: Phys. 81, P. 792 (2017);
21. M. Brack, *et al.*, Rev. Mod. Phys. 44, 320 (1972)
22. S.G. Kadmensky, Phys. At. Nucl. 68, 2030 (2005);
23. S. G. Kadmensky, L. V. Titova, Phys. At. Nucl., 72, 1738 (2009)
24. K. Skarsvag, *and* K. Bergheim, Nucl. Phys. 45, 721 (1963)
25. T. Ericson, *and* V. Strutinsky Nucl. Phys. 8, 284 (1958);
26. V. M. Strutinsky, JETP. 37, 613 (1960)
27. H. Hauser, *and* H. Feshbach, Phys. Rev. 87, 366 (1952);
28. P. A. Moldauer, Phys. Rev. B 135, 6421 (1964)
29. E. S. Troubetzkoy, Phys. Rev. 122, 212 (1961)

THE QUANTUM-MECHANICAL NATURE OF TRI- AND ROT-ASYMMETRIES IN THE REACTIONS OF THE TERNARY FISSION OF NONORIENTED TARGETS-NUCLEI BY THE COLD POLARIZED NEUTRONS

S.G. Kadmensky[1], V.E. Bunakov[2]

[1] *Voronezh State University, Voronezh, Russia*
[2] *Peterburg Nuclear Physics Institute of Natioanal Research Centre "Kurchatov Institute", Gatchina, Russia*
e-mail: kadmensky@phys.vsu.ru

ABSRACT

It has been analyzed the deficiencies of the approaches to the description of T-odd ROT-asymmetries in the differential cross sections of ternary fission reactions of nonoriented target-nuclei by cold polarized neutrons with the emission of prescission α-particles and evaporational γ-quanta and neutrons based on taking into account the influence of the compound fissile system rotation on fission products angular distributions with the usage of the classical trajectory calculations method, in which the interference of fission widths amplitudes for various neutron resonance states sJ_s and $s'J_{s'}$ formed in the first well of the compound fissile nucleus deformation potential are absent. It has been demonstrated that the method of construction of T-odd TRI-asymmetries for prescission α-particles, based on taking into account collective bending-vibrations of compound fissile nucleus at rupture of it's scission point, contradict to the traditional representations of the generalized model of nuclei and to methods of description of these collective vibrations.

Within framework of the quantum fission theory it has been proposed the unified mechanism for the description of T-odd TRI- and ROT-asymmetries characteristics of analyzed ternary fission reactions, based on taking into account the influence of the quantum rotation of the compound fissile system on angular distribution as fission fragments, as well third prescission and evaporated particles. It has been shown that taking into account the interference of amplitudes of fission widths for named above neutron resonance states allows to use the proposed approach for the description of differences in signs of T-odd ROT-asymmetry coefficients for emission of prescission α-particles and evaporational γ-quanta and neutrons.

1. INTRODUCTION

The T-odd P-even asymmetries in the differential cross sections $\frac{d\sigma_{n,f}}{d\Omega_3}$ of reactions of the ternary fission of the compound fissile nuclei (CFN) formed by the capture of cold longitudinally polarized neutrons by target-nuclei ^{233}U, ^{235}U, ^{239}Pu and ^{241}Pu with the flight of the prescission α-particle as third particle were experimentally investigated in papers [1-7]. The values $\frac{d\sigma_{n,f}}{d\Omega_3}$ were analyzed in laboratory coordinate system (LCS), where axes Z and Y were chosen along the directions of the asymptotic light fission fragment wave vector $\mathbf{k}_{LF}$ and of the polarization vector of the incident neutron $\mathbf{s}_n$ correspondently. The coefficients of investigated T-odd asymmetries $D(\Omega_3)$ were calculated by the formula:

$$D(\Omega_3)=\left(\frac{d\sigma^{(+)}_{n,f}}{d\Omega_3}-\frac{d\sigma^{(-)}_{n,f}}{d\Omega_3}\right)\Bigg/\left(\frac{d\sigma^{(+)}_{n,f}}{d\Omega_3}+\frac{d\sigma^{(-)}_{n,f}}{d\Omega_3}\right), \quad (1)$$

where the signs (+/–) correspond to the two opposite directions of the neutron polarization vector $\mathbf{s}_n$.

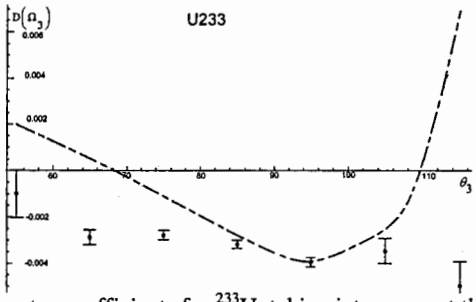

Fig. 1. T-odd asymmetry coefficients for ^{233}U, taking into account the error in the experimental determination of the emission angle of the light fission fragment.

As can be seen on Fig. 1, taken from [1, 7] for the target-nucleus ^{233}U, the coefficient $D(\Omega_3)$ does not change sign and is approximately constant in the wide range of angles θ_3. This asymmetry was called in [1] as T-odd TRI (Time Reversal Invariance)-asymmetry, because it was assumed that the named above asymmetry is connected with the representation about the violation of T-invariance in investigated nuclear reactions, which was not confined later. The mechanism of the investigated TRI-asymmetry appearance was related [6] with the influence on the formation kinematic characteristics of the emitted α-particle by classical catapult forces caused by decrease in the time of the collective rotation frequency of the fissile system after the scission of CFN, and later [7] with the influence on the these characteristics of the transverse bending-vibrations of CFN in the vicinity of it's scission point.

Later in the papers [3-7] it has been demonstrated that (see Fig. 2, 3, 4) the experimental coefficients $D(\Omega_3)$ for target-nuclei ^{235}U, ^{239}Pu and ^{241}Pu change sign in the vicinity of the angle $\theta_3 \approx 90°$ corresponding to the maximum angular distribution of α-particles emitted during fission of the same nuclei by cold nonpolarized neutrons [8].

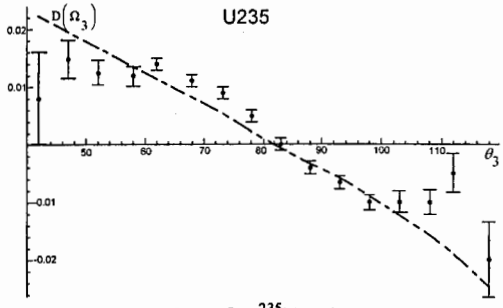

Fig. 2. T-odd asymmetry coefficients for ^{235}U, taking into account the error in the experimental determination of the emission angle of the light fission fragment.

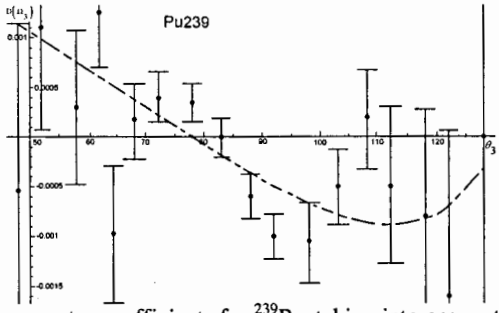

Fig. 3. T-odd asymmetry coefficients for ^{239}Pu, taking into account the error in the experimental determination of the emission angle of the light fission fragment.

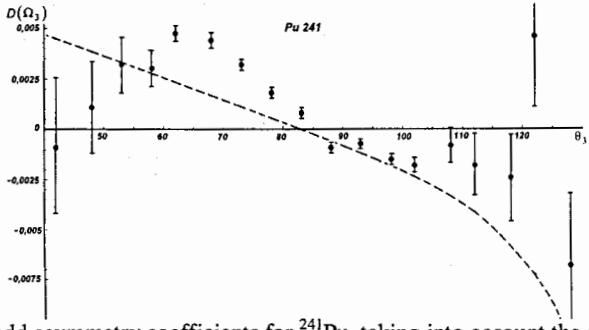

Fig. 4. T-odd asymmetry coefficients for ^{241}Pu, taking into account the error in the experimental determination of the emission angle of the light fission fragment.

Such an asymmetry in [3-7] was connected with the prevailing role of the new T-odd asymmetry, named by ROT (Rotation)-asymmetry, which was related with taking into account of the influence of the collective rotation of the polarized CFN on the angular distributions of the emitted fission fragments and α-particles on the base of the classical scheme of trajectory calculations [3, 5].

In the general case the T-odd asymmetry coefficients for the reactions of the ternary nuclear fission by cold polarized neutrons were presented [1-7] as

$$D(\Omega_3) = D_{ROT}(\Omega_3) + D_{TRI}(\Omega_3), \qquad (2)$$

where the coefficients $D_{ROT}(\Omega_3)$ and $D_{TRI}(\Omega_3)$ correspond to the T-odd ROT- and TRI-asymmetries correspondently and are constructed with taking into account named above mechanism of their appearance as

$$D_{ROT}(\Omega_3) = 2\Delta \frac{W'(\Omega_3)}{2W(\Omega_3)}, \; D_{TRI}(\Omega_3) = const, \qquad (3)$$

where Δ is the difference between the turn angles of the light fission fragment and the α-particle with taking into account the influence of CFN rotation, $W(\Omega_3)$ is the angular distribution of the α-particle for the ternary nuclear fission by nonpolarized cold neutrons.

Somewhat later in [9-12] in the differential cross sections $\frac{d\sigma_{n,f}}{d\Omega_3}$ of the fission reaction for target-nuclei ^{233}U, ^{235}U by cold polarized neutrons with evaporated by fission fragments instantaneous neutrons and γ-quanta as third particles the T-odd asymmetries were found, for which the coefficients $D(\Omega_3)$ correspond to the discussed above ROT-asymmetry (see Fig. 5 taken from [11] for evaporative γ-quanta).

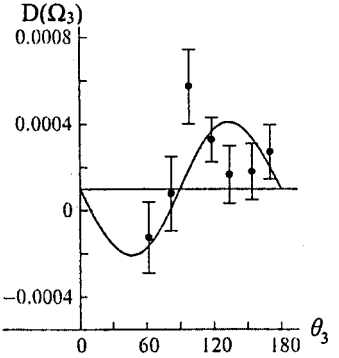

Fig. 5. T-odd asymmetry coefficients for ^{233}U taking into account the error in the experimental determination of the emission angle of evaporative γ-quanta.

At present time, the mechanisms of the appearance of observable T-odd asymmetries are actively searched. The problem consists in finding of the answer to the question - why the target-nuclei ^{233}U, ^{235}U, ^{239}Pu and ^{241}Pu having close masses, charges, angular and energy distributions of third particles $W(\Omega_3)$ for ternary fission by cold nonpolarized neutrons can have so much different forms (see Fig. 1-4) of the coefficients of the discussed T-odd asymmetries in the ternary fission of these nuclei by cold polarized neutrons.

The aim of this paper is to demonstrate that all the discussed T-odd asymmetries for ternary fission reactions of nonoriented target-nuclei by cold polarized neutrons can be explained in principle within the framework of quantum fission theory [13-24] taking into account the interference of the fission amplitudes of the neutron resonance states formed in compound fissile nucleus in the it's first potential well.

2. CHARACTERISTICS OF THE LOW-ENERGY BINARY AND TERNARY NUCLEAR FISSION

In this paper for the description of the binary and ternary low-energy nuclear fission it will be used the following representations reasonably well-founded within the framework of the quantum fission theory

1) the conservation of the axial symmetry at all stages of deformation motion of CFN [25] towards to it's scission point;

2) the coldness [26] of CFN at all fission stages after it's passage of the second fission barrier towards to it's scission point;

3) connected with named above coldness the conservation of the projection K of the spin J of CFN on the it's symmetry axis [26, 13, 16, 18, 20];

4) connected with named above coldness the necessary of taking into account only zero wriggling- and bending-vibrations [27] for the formation of angular and spin fission fragments distributions [23, 24];

5) the nonevoporational and nonadiabatical mechanism [28, 29] of the flight of prescission third particles;

6) for P-even T-odd asymmetries in angular distributions of prescission third particles for the ternary fission of nonoriented target-nuclei by cold polarized neutrons the spin density matrix of CFN must be constructed in the form, taking into account the interference of fission amplitudes of two different named above *s*-neutron resonances of the fissile compound nucleus with same and different spins J, J' and it's projections M, M' [15]:

$$\rho_{MM'}^{JJ'} = \frac{1}{2(2I+1)}\delta_{J,J'}\delta_{M,M'} + \frac{is_n}{2(2I+1)}A(J,J')\left[C_{J1M1}^{J'M'} + C_{J1M-1}^{J'M'}\right], \tag{4}$$

where $A(J,J')$ is defined as

$$A(J,J') = \delta_{J,J'}\left(\sqrt{\frac{J}{2(J+1)}}\delta_{J,J_<} - \sqrt{\frac{J+1}{2J}}\delta_{J,J_>}\right) - \sqrt{\frac{2J+1}{2J}}\delta_{J,J'+1} + \sqrt{\frac{2J+1}{2(J+1)}}\delta_{J,J'-1}. \tag{5}$$

7) the amplitude of nonperturbated by CFN rotation angular distribution of α-particle $W(\Omega_3)$ in the internal coordinate system (ICS) can be represented as

$$A(\theta') = \sum_l d_l Y_{l0}(\theta') = \sum_l \{d_l\} e^{i\delta_l} Y_{l0}(\theta'), \tag{6}$$

where θ' is angle between the direction of α-particle flight and CFN symmetry axis, $\{d_l\}$ and δ_l is the real main value and the phase of quantity d_l. Because the Coulomb parameter $\eta = \frac{2Ze^2}{h v_\alpha} >> l$, where quantity Z is connected with charges of light and heavy fission fragments, v_α is the α-particle relative velocity and l – the relative orbital moment of α-particle, it can be used the quasi-classical approximation, in which phase δ_l is independent from the α-particle orbital momentum l and has the form $\delta_l = \delta_0$. Then the amplitude $A(\theta')$ can be represented as

$$A(\theta') = e^{i\delta_0}\{A(\theta')\} = e^{i\delta_0}\sum_l \{d_l\} Y_{l0}(\theta'), \tag{7}$$

and the α-particle angular distribution $P(\theta')$ is defined as

$$P(\theta') = |A(\theta')|^2 = \{A(\theta')\}^2 \tag{8}$$

Then representing the amplitude $A(\theta')$ (7) as

$$A(\theta') = A^{ev}(\theta') + A^{odd}(\theta') \tag{9}$$

where the amplitude $A^{ev}(\theta')$ ($A^{odd}(\theta')$) is defined by the formula (7) with only even (odd) orbital moments. Since at the inversion of the α-particle wave vector $\mathbf{k}_3$ the distribution $P(\theta')$ transits to distribution $P(\pi-\theta')$, with the usage of formulae (8-9) it can be found:

$$\{A^{ev}(\theta')\} = \frac{1}{2}\left[\sqrt{P(\theta')} + \sqrt{P(\pi-\theta')}\right]; \quad \{A^{odd}(\theta')\} = \frac{1}{2}\left[\sqrt{P(\theta')} - \sqrt{P(\pi-\theta')}\right]$$
$$\{A(\theta')\} = \sqrt{P(\theta')}. \tag{10}$$

Using the normalized experimental angular distribution of α-particle $P(\theta')$ for ternary fission of target-nuclei ^{235}U by cold nonpolarized neutrons [8]:

$$P(\theta') = A\exp\left(-\frac{1}{2}\left(\frac{\theta'-\theta_0}{w}\right)^2\right), \tag{11}$$

where $\theta_0 = 81.65°$, $w = 11.57°$, it can be calculated amplitudes $\{A^{ev}(\theta')\}$ and $\{A^{odd}(\theta')\}$, which presented on the Fig. 6, where lines 1, 2 and 3 correspond to $\{A(\theta')\}$, $\{A^{ev}(\theta')\}$ and $\{A^{odd}(\theta')\}$.

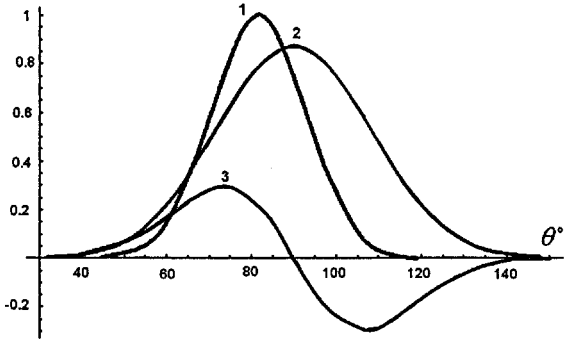

Fig. 6. Dependence of the amplitudes $A(\theta_\alpha)$ (line 1), $A_0^{ev}(\theta_\alpha)$ (line 2) и $A_0^{odd}(\theta_\alpha)$ (line 3) on the emission angle of the third particle.

From Fig. 6 it can be seen that the amplitude $|A^{ev}(\theta')|$ has the positive sign and it's maximal value prevailing the maximal value of quantity $|A^{odd}(\theta')|$ by factor 3.

3. T-ODD TRI- AND ROT-ASYMMETRIES FOR TERNARY FISSION AND CORIOLIS INTERACTION

The appearance of all types of T-odd asymmetries in the reactions of ternary fission of nonoriented nuclei-targets by cold polarized neutrons with emission of prescission α-particles can be connected [15, 19, 21-22] by the influence of the rotation CFN on the angular distributions of ternary fission products through the Hamiltonian H_{cor} of the Coriolis interaction consisting of two terms: the first term associated with the interaction of the total spin **J** of CFN with the relative orbital momentum **L** fission fragments and the second term associated with the interaction of the total spin **J** with the relative orbital momentum **l** of the third particle:

$$H_{cor} = -\frac{h^2}{2\Im_\perp}\left([J_+L_- + J_-L_+] + [J_+l_- + J_-l_+]\right), \tag{12}$$

where operators $J_\pm$, $L_\pm$ and $l_\pm$ are defined in ICS of CFN as

$$J_\pm = J_1 \pm iJ_2;\ L_\pm = L_1 \pm iL_2,\ l_\pm = l_1 \pm il_2 \tag{13}$$

and $\Im_\perp$ is the moment of inertia of the axial-symmetrical CFN for it's rotation around an axis perpendicular to CFN symmetry axis.

The action of the operators $J_{\pm}$, $L_{\pm}$ and $l_{\pm}$ on the functions $D^{J}_{MK}(\omega)$, $Y_{LK_L}(\Omega'_{LF})$ and $Y_{lK_l}(\Omega'_{\alpha})$ is defined as:

$$\begin{aligned} J_{\pm}D^{J_s}_{M_s,K_s}(\omega) &= \left[(J_s \pm K_s)(J_s \mp K_s + 1)\right]^{1/2} D^{J_s}_{M_s,(K_s \mp 1)}(\omega); \\ L_{\pm}Y_{LK_L}(\Omega'_{LF}) &= \left[(L \mp K_L)(L \pm K_L + 1)\right]^{1/2} Y_{L(K_L \pm 1)}(\Omega'_{LF}); \\ l_{\pm}Y_{lK_l}(\Omega'_{\alpha}) &= \left[(l \mp K_l)(l \pm K_l + 1)\right]^{1/2} Y_{l(K_l \pm 1)}(\Omega'_{\alpha}). \end{aligned} \tag{14}$$

Since the Coriolis interaction is small, it can be taken into account in the first order of perturbation theory.
Using the formula:

$$Y_{L0}(\theta'_{LF_0,k_\alpha}) = \sqrt{\frac{4\pi}{2L+1}} \sum_{K_L} Y_{LK_L}(\theta'_{LF_0}) Y^{*}_{LK_L}(\Omega'_{k_\alpha}) \tag{15}$$

and the adiabatic approximation associated with the slowness of the rotation motion of CFN in comparison with it's nucleons internal motion the wave functions $\Psi^{J_s M_s}_{K_s}$ of the transitional fission states of CFN can be represented as

$$\psi^{J_s M_s}_{K_s} = \sum_c \sqrt{\frac{2J_s+1}{16\pi^2}} \sqrt{\frac{\Gamma_{cK}}{h\upsilon_c}} \frac{e^{ik_c\rho}}{\rho^{5/2}} \left\{ D^{J_s}_{M_s,K_s}(\omega)\chi_{K_s} + (-1)^{J_s+K_s} D^{J_s}_{M_s,-K_s}(\omega)\chi_{\overline{K_s}} \right\} B^{(0)}(\Omega'_{LF}) A^{(0)}(\Omega'_3). \tag{16}$$

Because of the effect of the pumping of large values of fission fragments relative orbital moments associated with zero wriggling-vibrations of CFN the amplitude of the normalized fission fragments angular distribution in formula (16) coincides with the high degree of accuracy with the amplitude of the "spreaded" δ-function:

$$B^{(0)}(\Omega'_{LF}) = \frac{1}{\sqrt{2\pi}} \delta^{1/2}(\cos\theta'_{LF} - 1) = \sum_{L=0}^{L_m} b_l Y_{L0}(\Omega'_{LF}), \tag{17}$$

where

$$b_l = \left\{ \sum_{L=0}^{L_m} (2L+1) \right\}^{-1/2} \sqrt{2L+1}.$$

The influence of the polarized CFN rotation on the fission fragments angular distributions is defined by the term of the Hamiltonian of the Coriolis interaction H_{cor} (12), depending from orbital momentum L, and with the usage of formulae (15), (18) leads to the appearance of the amplitude $B^{(cor)}(\Omega'_{LF})$ of fission fragments angular distribution in the first order of perturbation theory for H_{cor} having the form:

$$\begin{aligned} B^{(cor)}(\Omega'_{LF}) &= b(L_m) \sum_L \sqrt{L(L+1)} \left[Y_{L(-1)}(\Omega'_{LF}) - Y_{L1}(\Omega'_{LF}) \right] \sqrt{(2L+1)/4\pi} = \\ &= -2\cos\varphi'_{LF} \frac{d\delta^{1/2}(\cos\theta'_{LF} - 1)}{d\theta'_{LF}} \end{aligned} \tag{18}$$

Taking into account the similar transformations for the amplitudes $A^{(0)}(\Omega'_3)$ of the third particle angular distribution it can be obtain:

$$A^{cor}(\Omega'_3) = \sum_{l \geq 1} b_l \sqrt{l(l+1)} \left[Y_{l(-1)}(\Omega'_3) - Y_{l1}(\Omega'_3) \right] = -2\cos\varphi'_3 \sum_{l \geq 1} b_l \frac{dY_{l0}(\theta'_3)}{d\theta'_3}. \tag{19}$$

Then the components of the asymmetry coefficient (2) can be represented [24] as

$$D_{ROT}(\theta,\varphi)=\alpha_{ROT}\frac{d\left\{A^{(0)ev}(\theta)\right\}}{d\theta}\frac{\cos\varphi}{\left\{A^{(0)}\right\}}\Delta\theta, \tag{20}$$

$$D_{TRI}(\theta,\varphi)=\alpha_{TRI}\frac{d\left\{A^{(0)odd}(\theta)\right\}}{d\theta}\frac{\cos\varphi}{\left\{A^{(0)}\right\}}\Delta\theta, \tag{21}$$

where

$$\alpha_{ROT}=\left(\sin(\delta_{sJ_ss'J_{s'}}+\overline{\delta}_{ev}-\delta^0)k^{ev}-\sin(\delta_{sJ_ss'J_{s'}})\right), \tag{22}$$

$$\alpha_{TRI}=\left(\sin(\delta_{sJ_ss'J_{s'}}+\overline{\delta}_{odd}-\delta^0)k^{odd}-\sin(\delta_{sJ_ss'J_{s'}})\right), \tag{23}$$

and the angle of turn out $\Delta\theta$ is represented as

$$\Delta\theta=-\omega(K_s,J_s,J_{s'})\tau. \tag{24}$$

The effective angular velocity of rotation $\omega(K_s,J_s,J_{s'})$ is determined by the relation of paper [24]:

$$\omega(K_s,J_s,J_{s'})=\frac{hp_n}{2\Im_0}g(K_s,J_s,J_{s'}), \tag{25}$$

where

$$g(K_s,J_s,J_{s'})=\begin{cases}\dfrac{J_s(J_s+1)-K_s^2}{J_s} & \text{для } J_s=I+1/2\equiv J_>\\[2ex] -\dfrac{J_s(J_s+1)-K_s^2}{J_s+1} & \text{для } J_s=I-1/2\equiv J_<\end{cases}$$

$$g(K_s,J_<,J_>)=g(K_s,J_>,J_<)=\frac{K_s\sqrt{J_s^2-K_s^2}}{J_>} \tag{26}$$

On the basis of χ^2-method the formulae (20) – (21) were used in [21] for analysis of the angular dependences of the coefficients $D^{\exp}(\Omega_\alpha)$ for ternary fission reactions for target-nuclei ^{233}U, ^{235}U, ^{239}Pu and ^{241}Pu by cold polarized neutrons [2-5] and to calculate the values of D_{ROT} and D_{TRI} in (2). As can be seen from Figs. 2, 3 and 4 the angular dependences of experimental and theoretical coefficients $D^{\exp}(\Omega_\alpha)$ and $D(\Omega_\alpha)$ at the angle θ_3 are in good agreement one with another for the target-nuclei ^{235}U, ^{239}Pu and ^{241}Pu.

At the same time the angular dependence of the theoretical coefficient $D(\Omega_\alpha)$ for the target nucleus ^{233}U (see Fig. 1) corresponds to the similar dependence of experimental coefficient $D^{\exp}(\Omega_\alpha)$ in the $60° < \theta_3 < 110°$ range of angles, where the value of undisturbed experimental amplitude $A^0(\theta_3)$ is significantly differ from zero. The noticeable discrepancy between these coefficients is observed at ranges of angles $\theta_3 < 60°$ and $\theta_3 > 110°$. It is not excluded that this discrepancy is associated, on the one hand, with the inaccuracy of the definition [21-22] of the theoretical amplitudes $\left\{A_{ev}^{cor}(\theta_3)\right\},\left\{A_{odd}^{cor}(\theta_3)\right\}$ though amplitudes

$\frac{d\{A^0_{ev}(\theta_3)\}}{d\theta_3}$, $\frac{d\{A^0_{odd}(\theta_3)\}}{d\theta_3}$ and on the other hand, with possible inaccuracy in the definition experimental values of $D^{exp}(\Omega_\alpha)$.

4. CONCLUSION

In the present paper the consideration of the T-odd asymmetries for prescission and evaporative third particles appearing in the ternary fission of the actinide nuclei by cold polarized neutrons has allowed to concretize the basic dynamic mechanisms for the binary and ternary nuclear fission, which determinate at the formation of these asymmetries. It has been shown that the considered T-odd asymmetries can be classified by taking into account the effects connected with interference of the fissile amplitudes of neutron resonances and the different influence in the common case of the appearance of the even and odd orbital moments of the third particles.

REFERENCES

1. P. Jessinger *et al.*, Nucl. Instrum. Methods A **440**, 618 (2000)
2. P. Jessinger *et al.*,, Nucl. At. Phys. **65**, 662 (2002)
3. A. M. Gagarski *et al.*, *Proceedings of the ISINN-14, Dubna, Russia,* 2006, 93 (JINR, Dubna, 2007)
4. F. Gonnenwein *et al.* Phys. Lett. B **652**, 13 (2007)
5. A. M. Gagarski *et al.*, *Proceedings of the ISINN-16, Dubna, Russia, 2008*, 356 (JINR, Dubna, 2009)
6. A. Gagarski *et. al.*, *Proceeding of 4-Internal Workshop*, 323 (Cadarache, France, 2012)
7. A. Gagarski *et. al.*, Phys. Rev. C **93**, 054619 (2016)
8. M. Mutterer, J.P. Theobald, *Nuclear Decay Modes* (Bristol: Inst Publ., 1996)
9. G. V. Danilyan, J. Klenke, V.A. Krakhotin, Phys. At. Nucl. **72**, 1872 (2009)
10. G. V. Danilyan, P. Granz, V.A. Krakhotin, Phys. Lett. B **679**, 25 (2009)
11. G. V. Danilyan, J. Klenke, V.A. Krakhotin, Phys. At. Nucl. **73**, 73 (2010)
12. G. V. Danilyan, J. Klenke, Yu. N. Kopach, Phys. At. Nucl. **77**, 715 (2014)
13. S.G. Kadmensky, Phys. At. Nucl. **65**, 1390 (2002)
14. S.G. Kadmensky, Phys. At. Nucl. **66**, 1846 (2003)
15. V. E. Bunakov, S. G. Kadmensky, Phys. At. Nucl. **66**, 1846 (2003)
16. S.G. Kadmensky, L.V. Rodionova, Phys. At. Nucl. **66**, 1219 (2003)
17. S.G. Kadmensky, L.V. Rodionova, Bull. Russ. Sci. Phys. **69**, 751 (2004)
18. S.G. Kadmensky, Phys. At. Nucl. **68**, 1968 (2005)
19. V. E.Bunakov, S. G. Kadmensky, S. S. Kadmensky, Phys. At. Nucl., **71**, 1887 (2008)
20. S. G. Kadmensky, L. V. Titova, Phys. At. Nucl. **72**, 1738 (2009)
21. D. E. Lyubashevsky, S. G. Kadmensky Bull. Russ. Acad. Sci.: Phys. **74**, 791 (2010)
22. S. G. Kadmensky, D. E. Lyubashevsky, L. V. Titova, Bull. Russ. Acad. Sci.: Phys. **75**, 989 (2011)
23. S. G. Kadmensky, D. E. Lyubashevsky, L. V. Titova, Bull. Russ. Acad. Sci.: Phys. **79**, 975 (2015)
24. S. G. Kadmensky, D. E. Lyubashevsky, V.E. Bunakov, Phys. At. Nucl., **77**, 198 (2015)
25. M. Brack, *et al.*, Rev. Mod. Phys. **44**, 320 (1972)
26. A. Bohr, and B. Mottelson, *Nuclear Structure* (NY, Amsterdam, 1969, 1975) V. 1, 2
27. J.R. Nix, W.J. Swiatecki, Nucl. Phys. A 71, 1(1965)
28. O. Tanimura, T. Fleshbach, Z. Phys. A **328**, 975 (1987)
29. S. G. Kadmensky, L. V. Titova, A. O. Bulychev, Phys. At. Nucl. **78**, 716 (2015).

COAXIAL FISSION FOR THREE COMPARABLE MASS FRAGMENTS AS A CONSEQUENCE OF THE COLLECTIVE MODEL OF NUCLEUS

F. F. Karpeshin

Mendeleev All-Russian Research Institute of Metrology
190005 Saint-Petersburg, Russia

Abstract

The trajectory calculations for the fragments of spontaneous true ternary fission of the ^{252}Cf nuclei are performed, aimed at studying the effect of the collective rotation of the fragments on their angular distribution. The rotation arises at the moment of scission due to formation of spins in the fragments, in spite of conservation of zero total angular momentum. The conclusion is that the collinear flight of all the fragments of the spontaneous true ternary fission of ^{252}Cf, which is in the model on the prescission stage, survives at the final stages of spreading of the fragments. The results prove the experimental data obtained.

Introduction

The question of fission into three comparable fragments has a long, challenging and fascinating story. As distinct from traditional ternary fission, where emission of two massive fragments is accompanied with a ternary light particle, like an α particle, sometimes it is called true ternary fission (TTF). Strutinsky *et al.* were the first who proposed search for this process [1]. Attempts of creating a theory of TTF were undertaken by many theorists. Proceeding from typical initial conditions on the top of usual fission barrier, within the framework of the liquid drop model, Nix [2] demonstrated formation of a third very light fragment which arose between two other massive fragments in the case of very heavy fissioning systems with $A \gtrsim 300$. Family of shapes leading to fission into three massive fragments was deduced in Ref. [3, 4]. Legendre-polynomial expansion up to tenth order and more was usually exploited. In some papers, though, the role of hexadecapole deformation was underlined. The idea of generic mechanism of TTF was expressed in Refs. [5, 6, 7], in contrast to the consecutive one. It is suggested that TTF develops along a special dynamical path to which the nucleus enters at the very beginning of fission. The predetermining role belongs to the hexadecapole deformation, as the quadrupole deformation plays the leading role in habitual binary fission.

First experimental studies were undertaken, searching for this mode in fission of actinide nuclei by thermal neutrons [8] and α particles [9], in heavy-ion collisions [10], or spontaneous fission of ^{252}Cf [11]. Only upper limits of the probability of the processes were established at the level of $10^{-4} - 10^{-8}$. It is worthy of noting that there was a tacit contradiction between theory and experimental search. From the theoretical point of view, linear form of a fissile nucleus is more favourable than a clover-leaf shape (*e. g.*

[5] and refs. cited therein). However, experimental efforts were mainly aimed at detecting fragments at approximately similar angles, i.e., $\sim 120°$. Based on general considerations, the experimenters likely believed that the mutual electrostatic repulsion could align the spreading angles. Solyakin et al. proposed the collinear mode of tripartition [12], when searching for TTF of ^{238}U by 1-GeV protons. This concept was most successfully realized in JINR experiments on FOBOS and mini-FOBOS setup [13, 14, 15]. Use of the missing-mass method in combination with net detectors led to conclusion that the collinear mode of TTF of ^{235}U and spontaneous fission of ^{252}Cf may be at the level of up to $10^{-4} - 10^{-5}$. At first sight, this mode is in contrast with ordinary ternary fission, where α particles or protons are emitted approximately perpendicularly to the fission axis. At the same time, there is a small fraction ~10 percent of polar alpha particles, emitted along the fission axis (e.g. [16] and refs. cited therein). In Ref. [17] the authors doubted a possibility of a "perfectly" collinear flight in the case of three massive fragments. It follows from this qualitative consideration that the question of angular distribution of the fragments is of primordial interest. As we will see, the collinear character of fragment flight off follows the same principles the collective model of nuclear motion is founded on. As a result, the description turns out to be completely different in the cases of usual ternary fission accompanied by emission of an alpha particle, and TTF. In the first case, the two nascent massive fragments form an axially-symmetric core, in the field of which the alpha particle is formed and emitted. In the latter case, all three nascent fragments form the core, which may be axially-symmetric, if all three fragments are moving coaxially before separation, or not to be. These two possibilities have drastic consequences, as, according to the first principles, the axially-symmetric shape replies to the projection of the core angular momentum on the fission axis $K = 0$. Then the nascent fragments move co-axially till scission. Broken axial symmetry is associated with $K > 0$. In order to realize this possibility, some energy is needed for collective rotation around the fission axis. This leads to an effective increase of the fission barrier and related suppression of the fission probability. Actually, this consideration is founded on the same ground as the known Bohr's hypothesis [18, 19] about the predominance of a certain channel in photofission of ^{238}U. In the case of spontaneous fission of spinless nuclei of ^{252}Cf, considered herein, the condition $K = 0$ undoubtedly holds up to the first scission. Therefore, the nascent fragments move strictly co-axially on the fission axis.

In principle, the equality $K = 0$ does not forbid rotation in the plane of symmetry. Arising rotation of the fission axis perpendicular to the fission direction brakes picture of the co-axial fragment flight after scission, as this is shown below. This kind of the collective rotation is also absent in our case of spontaneous fission of ^{252}Cf yet. However, also in this case, the co-axial symmetry is broken at scission [20]. In the case of binary fission of actinide nuclei, the mean value of the fragment spin is ~ 7 to 8 [21, 22]. Moreover, the arising rotational moment is likely directed perpendicularly to the fission axis [20]. Therefore, one may expect that the total angular momentum of the relative motion of all three fragments of TTF may achieve as much as $L \sim 10 - 20$ and more. Conserving after scission, such a rotation might brake the collinear scenario of fragment flight off.

A similar effect is known in fission of nuclei with spins different from zero. Then the angular momentum of such a collective rotation before scission goes over the transverse velocity of the fission fragments after scission. In the case of fission with polarized neutrons, this gives rise to the known ROT effect [23]. It manifests as correlation of

the direction of emission of alpha particle with the directions of heavy fragment and the spin of the fissile nucleus. The ROT effect is observed by the difference method in fission by polarized neutrons [23, 24]. As follows from the above consideration, the collective angular momentum arising at scission may be several times more that the spin of the fissile nucleus. However, it does not contribute to the ROT effect because of angular averaging: there is no correlation of the L direction with the spin of the fissile nucleus. But in TTF, where each event is detected independently of others, the presence of the collective moment L could easily prove itself in violation of the collinearity of the scattering of the fragments. We will proceed from a strongest assumption that the transverse spin of each fragment may be as high as 7 and even more, so that the total transverse collective spin after scission may reach values of $L \approx 20$. Such big conceivable values of the collective spin are compensated by the sum of the spins of each of the fragments, which is of the opposite sign. Of course, if the transverse collective spin is smaller, or even close to zero, all the more the trajectories of the fragments hold collinear. Let us consider the question in more detail.

Calculation formulas

Numerical simulation of trajectories of representative fragments is a classical method. Its applicability follows a known fact that wavelength is much smaller than the nuclear fragment size. Such calculations were found to work well for description of α data in ternary fission (e. g.[25]), specifically, of the ROT effect [26]. Representative trajectories are simulated in the next section by solving the Newton equations of motion with initial conditions of position and velocity for each fragment at scission. We consider the generic mechanism of the TTF, when the both scissions occure nearly simultaneously within a narrow zone comparable to R_0. For simplicity, it is assumed a spherical shape of the fragments. The choice of the initial conditions is presented in Fig. 1. Let the fission axis coincide with the quantization axis z at the moment of scission. Denote the extreme side fragments with indices 1 and 2, and the mean fragment as No. 3. In view of the axial symmetry of the problem, let x be the transverse direction axis. The atomic and mass numbers of the fragments are assumed to be Z_i and A_i, respectively, $i = 1$, 2 and 3, with the distances r_{12}, r_{23} and r_{13} between the fragments. The positions of the fragments must be selected, baring in mind their future total kinetic energy (TKE), which must not exceed reaction heat Q. For the parameterization purposes, the total Coulomb energy of the fragments is minimized, based on the position of the second fragment at fixed distance $D = r_{12}$ between the extreme fragments:

$$r_{23} = D\frac{\sqrt{Z_2}}{\sqrt{Z_1}+\sqrt{Z_2}}. \qquad (1)$$

Hence, the initial positions of all three fragments are fixed by the single parameter D defined by the TKE value T, $T \leq Q$:

$$T = (\frac{Z_1 Z_2}{r_{12}} + \frac{Z_1 Z_3}{r_{13}} + \frac{Z_2 Z_3}{r_{23}})e^2. \qquad (2)$$

Initial conditions for the trajectory simulations. V_1, V_2 and V_3 are the transverse velocities to the

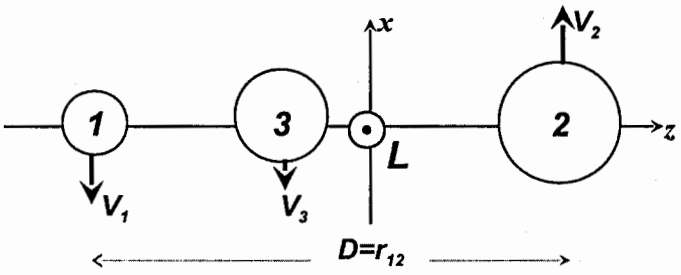

Figure 1: Initial conditions for the trajectory simulations. V_1, V_2 and V_3 are the transverse velocities to the fission axis of the fragments 1 – 3, which comprise the total relative angular momentum of the collective rotation of the fragments (directed towards us). D is the distance between extreme fragments.

fission axis of the fragments 1 – 3, which comprise the total relative angular momentum of the collective rotation of the fragments (directed towards us). D is the distance between extreme fragments. A small possible initial velocity of the fragments in the z direction is not important for the present purposes. In accordance with what is said in the Introduction, in order to calculate the initial velocity of the fragments in the transverse direction, we use the value of their assumed total angular momentum and the position of each fragment on the axis relative to their center of gravity. Let us designate the masses of the fragments and their positions along the axis of fission as M_1, z_1, M_2, z_2 and M_3, z_3, respectively. Center of gravity of the fragments, determined during fission, is set as

$$\zeta = (M_1 z_1 + M_2 z_2 + M_3 z_3)/M\,, \tag{3}$$

where $M = M_1 + M_2 + M_3$. Total angular momentum of the fragments is described by the equation

$$\omega\,[M_1(z_1 - \zeta)^2 + M_2(z_2 - \zeta)^2 + M_3(z_3 - \zeta)^2] = L\hbar\,, \tag{4}$$

and the initial transverse velocity of fragment i is

$$V_i = \omega(z_i - \zeta)\,. \tag{5}$$

The macroscopic—microscopic landscape of the potential deformation energy was calculated in Ref. [27] for the case of TTF of ^{252}Cf. It suggests the following mode as a likely candidate:

$$^{252}\mathrm{Cf} \to {}^{132}\mathrm{Sn} + {}^{48}\mathrm{Ca} + {}^{72}\mathrm{Ni}, \qquad Q = 251\,\mathrm{MeV}\,. \tag{6}$$

The Q value in fission (6) was calculated, using AME2012 atomic mass evaluation [28]. The presence of two magic or semimagic fragments in the final state provide a great released energy Q. The situation is like in three-partition of the atomic clusters of $_{27}Na^{+++} \to 3\ {}_9Na^+$ into three magic clusters of $_9Na^+$ [5]. The final TKE values of the fragments depend on the scission configuration: position of the fragments, thickness of the necks. Deformation of the fragments takes a part of the released energy, which is subtracted from the Q value. We will consider various representative TKE, and total angular momenta L. We will differ the extreme fragments as light and heavy ones, and the smallest fragment which we put in the middle we will call the ternary one.

Calculation results

In the landscape of the potential energy in Ref. [27], pronounced valleys favorable for ternary fission were found. One of they, which may be related with channel (6), lies after a saddle point at $R_{12} \approx 3R_0 = 22$ fm, where R_0 is the radius of the mother nucleus. At this distance, formation of the final fragment starts. This is close to the scission range in the case of binary fission, where the scission distance is approximately twice as large as the total radius of the both fragments. The valley presents a good opportunity for scission and separation of all three fragments somewhere at $r_{12} \gtrsim 30$ fm. Indeed, the TKE value $T = Q$ would be achieved if scission occurred at $r_{12} = 25.56$ fm. In practice, part of the released energy is stored in the deformation energy of the fragments, while scission occurs at a larger distance. Baring this in mind, we varied the parameter $D = r_{12}$ in the range up to 40 fm. Experimental results [15] confirm such an expectation. The results of the trajectory simulation are presented in Fig. 2 and Table 1. The calculated kinetic energies of each of the fragments, together with their TKE, are presented in Fig. 2 *versus* the distance between the extreme heavy and light fragments D at scission. All the energies smoothly decrease with increasing D, with TKE changing from $T = Q = 251$ MeV for $D = 25.6$ fm down to $T = 160$ MeV for $D = 40$ fm. As well as in ordinary binary fission, the heavy fragments are produced with lower kinetic energies. We note a characteristic feature of TTF displayed in Fig. 2: the ternary fragments, which are formed between the heavy and light ones, turn out to be very slow, with the kinetic energies of approximately 5 MeV. This is 15 – 20 times as small as the energies of the main fragments. This is in accordance with ref. [29].

The results concerning the angular distribution of the fragments are presented in Table 1. As a consequence of rotation of the fission axis, neither of the fragments continues to move along the z axis anymore, if $L \neq 0$. This is the same phenomenon which causes the ROT effect. For the configuration presented in Fig. 1, where the momentum L is directed towards the reader, the light Ni fragment goes below the z axis. In turn, the heavy Te fragment goes upwards. And the asymptotic rotation angle appears to be close to the value which can be expected, based on the value which is observed and reproduced by numerical simulations for the ROT effect. Thus, it comprises $\sim 2°$ for $L = 20$, that is about 0.1 degree per unit angular moment. The folding angle Θ between the fragments remains 180° in the case of binary fission. In our case of TTF, however, it changes, depending on the L value, diverging by 1 – 2 degrees from 180°.

The values of the angle Θ between the asymptotic directions of the two main fragments are presented in the Table for various L values. They are close to 180°. The ternary and the light fragments always fly in the same direction. The angle of divergence Φ between them is also presented against the value of the total transverse angular momentum L, which was varied in a wide range $0 \leq L \leq 20$. All three fragments remain in the same plane, wherein the projections of the velocities of the two fragments, the light and the ternary one, per axis perpendicular to the direction of emission of the heavy fragment have opposite signs. Flight off of the ternary fragment is equally probable into the upper and lower half-planes. From the presented results it follows that two fragments moving in the same direction diverge within one-two degrees at most, for all the considered L values. Such a divergence can be prettily neglected in the first approximation, at least in the conditions of the conducted experiments on FOBOS and

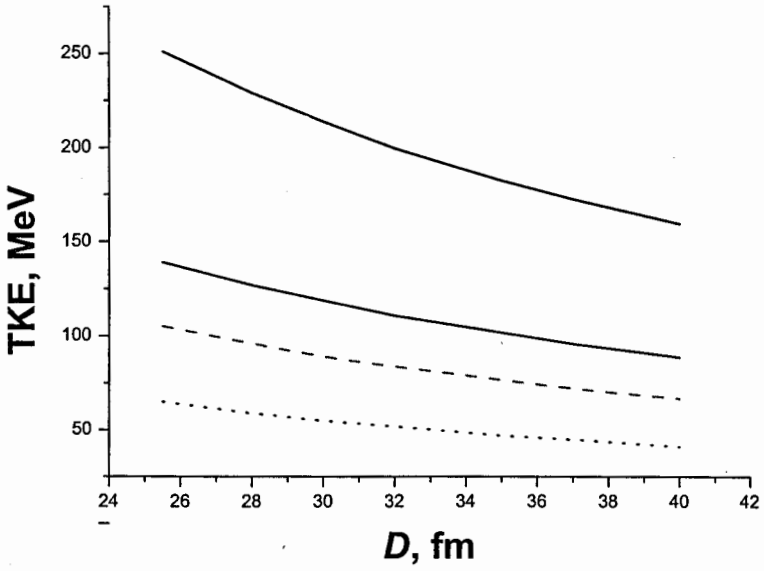

Figure 2: Kinetic energies of the fragments and their TKE values against the scission point D: fragments 1 and 2 — lower full and dashed lines, respectively, dotted line — the energy of the ternary fragment, scaled by a factor of 10, and full upper line — the total kinetic energy.

mini-FOBOS. This quite justifies the observed picture of collinear flight of the fragments in the TTF.

Conclusion

It follows from the considered model of scattering of the fragments of TTF that the approximately collinear picture of spreading of all the three fragments is most probable. In the case of $K = 0$, the reason is axially-symmetric shape of the fissile nucleus on its path towards fission. Because of the axial symmetry, there is a sole way of formation of the fragments, when they remain co-axial till scission. This is a remarkable illustration of the collective Bohr's model. Before, the Bohr's hypothesis marked application of the principles of symmetry in fission, which are laid in the base of the collective model. The hypothesis also works in the case of fission of ^{235}U by thermal neutrons, in which case the compound nucleus is characterized by full chaos over the K values: all the possible K values from 0 to 4 become equally probable due to the Coriolis mixing [30]. Also in this case, most probable channels with a certain K turn out to be those which reply to minimal energy over the fission barrier. The barrier works as the filter [30]. However, the angular distribution becomes more complicated because of the chaos on the stage

Table 1: Calculated angular distributions of the fragments of true ternary fission of ^{252}Cf (6) *versus* the scission point D and the relative angular momentum L in the c. m. system. Θ is the folding angle between the directions of the heavy and light fragments, Φ — the divergence angle between the light ^{72}Ni and ternary ^{48}Ca fragments

D, fm	L	$\Theta°$	$\Phi°$
25.6	5	179.9	0.7
	10	179.8	1.4
	15	179.7	2.1
	20	179.6	2.8
30	5	179.9	0.6
	15	179.7	1.9
35	5	179.9	0.6
	15	179.7	1.8
	20	179.6	2.4

of compound nucleus. In view of the results obtained above, the true ternary fission presents a bright example where the principles of symmetry comprising the foundation of the collective model, and specifically the Bohr's hypothesis concerning fission, manifest themselves in full shine.

The author is grateful to L. F. Vitushkin, Yu. I. Gusev, and I. S. Guseva for their helpful advice, as well as to S. G. Kadmensky and V. I. Furman for fruitful comments. He also thanks D. V. Kamanin and Yu. V. Pyatkov for discussions of the experimental data.

References

[1] V. M. Strutinsky, L. Ya. Lyashenko, and N. A. Popov, Zh. Exp. Teor. Fiz. **43**, 584 (1962) [Sov. Phys. — JETP, **16**, 418 (1963)].

[2] J. R. Nix, Nucl. Phys. **A130**, 241 (1969).

[3] S. Trentalange, S. E. Koonin ans A. J. Sierk, Phys. Rev. C **22**, 1159 (1980).

[4] Nicolae Carjan, Arnold J. Sierk and J. Rayford Nix, Nucl. Phys. **A452**, 38 (1986)1.

[5] F. F. Karpeshin, A. Vieira, C. Fiolhais, and J. da Providencia Jr., Europhys. Lett. **42**, 149 (1998).

[6] F. F. Karpeshin, Yad. Fiz. **78**, 591 (2015). [Phys. At. Nucl., **78**, 548 (2015)].

[7] F. F. Karpeshin, *4th South Africa — JINR Symposium "Few to Many Body Systems: Models, Methods and Applications", September 21–25, 2015, Dubna, Moscow region*, Proceedings, Ed. F. Šimkovich (Dubna, JINR, 2016), p. 119.

[8] M. L. Muga, Phys. Rev. Lett. **11**, 129 (1963).

[9] R. H. Iyer and J. W. Cobble, Phys. Rev. **172**, 1186 (1968).

[10] V. P. Perelygin, N. H. Shadieva, S. P. Tretiakova, A. H. Boos, and R. Brandt, Nucl. Phys. A **122**, 577 (1969).

[11] M. Mutterer *et al.*, *Proceedings of the International Conference on 50th Anniversary of Nuclear Fission*, Leningrad, 1989, p. 32; P. Schall, P. Heeg, M. Mutterer, and J. P. Theobald, Phys. Lett. B **191**, 339 (1987).

[12] A. V. Kravtsov, G. E. Solyakin, Pis'ma Zh. Eksp. Teor. Fiz. **53**, 385 (1991) [JETP Lett., **53**, 403 (1991)].

[13] D. V. Kamanin and Yu. V. Pyatkov, Lect. Notes in Phys. **3**, 183 (2013).

[14] Yu. V. Pyatkov, D. V. Kamanin, von Örtzen W. *et al.*, Eur. Phys. J. A **48**, 94 (2012).

[15] Yu.V. Pyatkov, D. V. Kamanin, A. A. Alexandrov, I. A. Alexandrova, Z.I.Goryainova, V.Malaza, N. Mkaza, E. A. Kuznetsova, A.O.Strekalovsky, O. V. Strekalovsky, and V.E.Zhuchko, Phys. Rev. C **96**, 064606 (2017).

[16] S. S. Kapoor, D. M. Nadkarni, Pramana — J. Phys. **24**, 155 (1985).

[17] P. Holmvall, U. Köster, A. Heinz, and T. Nilsson, Phys. Rev. C **95**, 014602 (2017).

[18] A. Bohr, B. Mottelson. *Nuclear Structure*, V. 2. (W. A. Benjamin, Inc. New York, Amsterdam, 1974).

[19] A. Bohr, in Proc. UN Int. Conf. on Peaceful Uses of Atomic Energy (Geneva, 1955), New York: United Nations, 1956, vol. 2, p. 151.

[20] F. F. Karpeshin, Eur. Phys. J. **A45**, 251 (2010).

[21] J. O. Rasmussen, W. Nörenberg, and H. J. Mang, Nucl. Phys. A **136**, 465 (1969).

[22] R. Vandenbosch and J.R. Huizenga, *Nuclear Fission* (London, Academic Press, 1973).

[23] A. Gagarski, F. Gönnenwein, I. Guseva, P. Jesinger, Yu. Kopatch, T. Kuzmina, E. Leli'evre-Berna, M. Mutterer, V. Nesvizhevsky, G. Petrov, T. Soldner, G. Tiourine, W. H. Trzaska, and T. Zavarukhina, Phys. Rev. C **93**, 054619 (2016).

[24] G. V. Danilyan, P. Granz, V. A. Krakhotin, F. Mezei, V. V. Novitsky, V. S. Pavlov, M. Russina, P. B. Shatalov, and T. Wilpert, Phys. Lett. B **679**, 25 (2009).

[25] E. Piasecki, M. Dakowski, T. Krogulski, J. Tys, and J. Chwaszczewska, Phys. Lett. B **33**, 568 (1970).

[26] I. S. Guseva, Yu. I. Gusev, Bull. RAS: Physics, **71**, 367 (2007).

[27] A. V. Karpov, Phys. Rev. C **94**, 064615 (2016).

[28] Meng Wang, G. Audi, F.G. Kondev, W. J. Huang, S. Naimi, and Xing Xu, Chinese Physics C **41**, 030003 (2017).

[29] K.R. Vijiayaraghavan, W. von Oertzen and M. Balasubramaniam, Eur. Phys. J. A **48**, 27 (2012).

[30] N. A. Gundorin, Sh. S. Zeinalov, Yu. N. Kopatch, A. B. Popov, and V. I. Furman, Physics of Particles and Nuclei, **47**, 681 (2016).

MEASUREMENT OF T-ODD EFFECTS IN THE NEUTRON INDUCED FISSION OF ^{235}U AT A HOT SOURCE OF POLARIZED RESONANCE NEUTRONS

Yu.N. Kopatch[1], *V.V. Novitsky*[1,2], *G.S. Ahmadov*[1,6], *A.M. Gagarsky*[3], *D.B. Berikov*[1,7], *K.Sh. Zhumadilov*[7], *G.V. Danilyan*[1,2], *V. Hutanu*[4], *J. Klenke*[5], *S. Masalovich*[5]

[1]Joint Institute for Nuclear Research, 141980 Dubna, Russia
[2]Institute for Theoretical and Experimental Physics of National Research Centre "Kurchatov Institute", 117218 Moscow, Russia
[3]Petersburg Nuclear Physics Institute of National Research Centre "Kurchatov Institute", 188300 Gatchina, Russia
[4]Institut für Kristallographie, RWTH Aachen and Jülich Centre for Neutron Science at Heinz Maier-Leibnitz Zentrum (MLZ), Lichtenbergstr. 1, 85748 Garching, Germany
[5]Forschungs-Neutronenquelle Heinz Maier-Leibnitz, D-85747 Garching, Germany
[6]National Nuclear Research Centre, Baku, Azerbaijan
[7]L.N.Gumilyov Eurasian National University, 010000 Astana, Kazakhstan

Abstract. The TRI and ROT asymmetries in fission of heavy nuclei have been extensively studied during more than a decade. The effects were first discovered in the ternary fission in a series of experiments performed at the ILL reactor (Grenoble) by a collaboration of Russian and European institutes, and were carefully measured for a number of fissioning nuclei. Later on, the ROT effect has been observed in the emission of prompt gamma rays and neutrons in fission of ^{235}U and ^{233}U, although its value was an order of magnitude smaller than in the α-particle emission from ternary fission. All experiments performed so far are done with cold polarized neutrons, what assumes a mixture of several spin states, the weights of these states being not well known. The present paper describes the first attempt to get "clean" data by performing the measurement of gamma and neutron asymmetries in an isolated resonance of ^{235}U at the POLI instrument of the FRM2 reactor in Garching.

1. Introduction

The T-odd effects in fission of heavy nuclei have been known since more than a decade. The first effect of this type, the so called TRI-effect was discovered at the ILL reactor (Grenoble) by a collaboration of Russian and European institutes [1,2] in an experiment aimed at the search for violation of time reversal invariance (TRI) following the idea, proposed in [3]. It was found that the probability of emission of an alpha-particle in ternary fission in the direction perpendicular to the plane formed by the neutron spin and the fragment momentum shows a pronounced anisotropy. The magnitude of the effect turned out to be surprisingly large, and the current explanation doesn't imply the existence of such a violation, but is based on the final state interaction of the reaction products. In other words, the effect is not connected with the violation of the time reversal invariance, but with the mechanism of the fission process. Nevertheless, the effect is still called the "TRI-effect" in literature.

Furthermore, it was noticed that when reversing the direction of polarization of the neutron beam, the angular distribution of α- particles is shifted by a small angle relative to the axis of fragment emission, the offset direction being determined by the direction of polarization of the neutron beam. The authors called this effect the ROT - effect [4]. Both, TRI and ROT effects are formally T-odd, but have no direct connection with the violation of the time reversal invariance.

From the semiclassical description of the ROT effect, which assumes the rotation of a polarized nucleus before it splits into two (or three) fragments it follows that a similar phenomenon can also be discovered in the angular distribution of some other particles accompanying the fission of a nucleus into two fragments. The effect can be observed only if this distribution is anisotropic with respect to the deformation axis of the fissioning nucleus at the moment of scission, and the asymmetry with respect to the initial direction of the deformation axis is fully or partly conserved after the escape of the fragments to infinity. Indeed, a similar effect has been observed in the emission of prompt gamma rays and neutrons in fission of ^{235}U and ^{233}U, although its value was an order of magnitude smaller than in the α-particle emission from ternary fission [5-7].

At present, there are several theoretical models which can describe both effects [8-13]. According to the model, proposed in [13], both effects depend on the quantum numbers J and K (the total angular momentum and its projection on the deformation axis), which characterize the fission channel. For the thermal (or cold) neutron induced fission (where all previous data are obtained), there is a mixture of several spin states, and the weights of these states are not known. The only way to get "clean" data is to perform measurements in isolated resonances. Such an experiment was performed at the POLI instrument of the FRM2 reactor in Garching, which provides the necessary polarized neutron beam with an energy of 0.27 eV, corresponding to the lowest resonance of ^{235}U. Preliminary results of this experiment are presented in this paper.

2. Experiment

We used the polarized hot neutron beam provided by the POLI instrument [14] at the FRM-II reactor in Garching. The schematic view of the experimental setup is shown in Fig. 1.

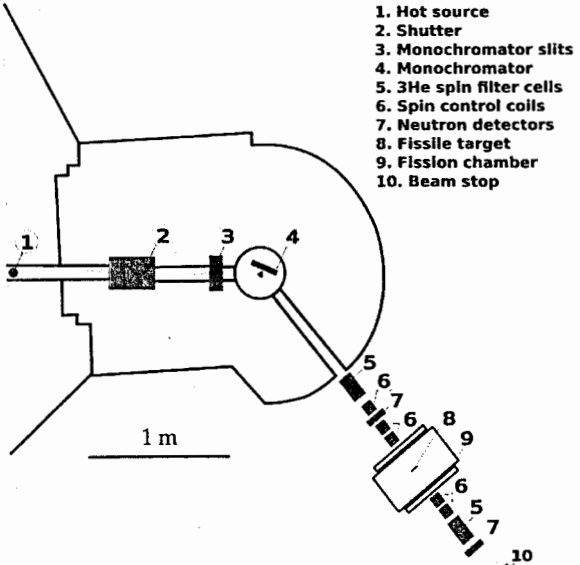

Fig. 1. Schematic view of the experimental setup at the POLI facility of FRM-II.

A monochromator made of a mosaic of Cu crystals was used to select a narrow neutron beam with the mean energy of 270 meV (λ=0.55 Å). This energy exactly coincides with the position of the lowest resonance of ^{235}U [15]. The monochromator also allows simultaneous focusing of the neutron beam on the target position providing the maximum intensity of unpolarized neutrons of about $4 \cdot 10^6$ n/cm^2/sec.

The neutrons were polarized using specially designed ^{3}He gas cells [16]. The same type of cell was also used as analyzer for measuring beam polarization. Since polarized nuclei of ^{3}He possess very high spin-dependent neutron absorption efficiency over a wide range of energies, the ^{3}He cell can be used as a broadband neutron polariser or analyser, with the possibility to optimise its efficiency for nearly all neutron wavelengths. In our experiment, the size of the cells was Ø60×130 mm and the gas pressure 2.5 bar (0.25 MPa), which provided the maximal neutron polarization of about 70%. The polarizer and analyzer cells were polarized in an external lab and placed into a special magnetic housing with highly homogeneous constant magnetic field. The polarization of ^{3}He in the cell exponentially decreased with the time constant of about 40 hours, therefore both cells were replaced every 24 hours.

Both, polarizer and analyzer provided vertical polarization of the neutron beam while the searched effect requires horizontal (longitudinal) polarization. For changing the polarization direction from vertical to horizontal, a specially designed spin control system was used, consisting of several μ-metal shielded magnetic coils, which allowed also flipping the spin at the target position by 180 degrees every 1.3 seconds.

The schematic view of the fission chamber surrounded by a set of gamma-ray detectors is shown in Fig. 2.

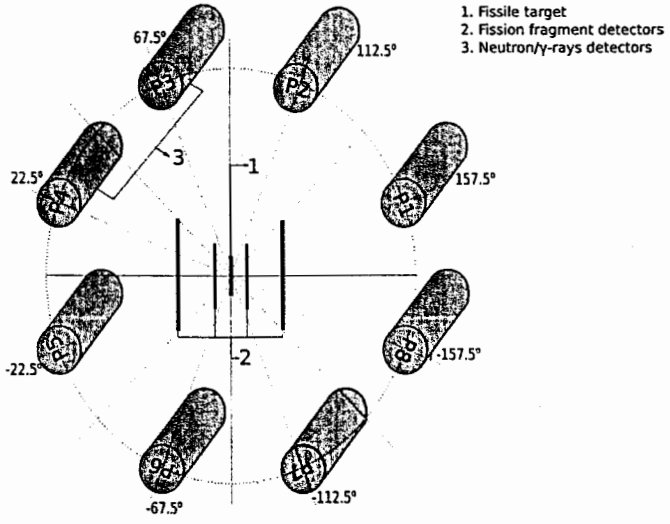

Fig. 2. Layout of the experimental facility. View from the beam direction.

The chamber was filled with CF_4 gas at a pressure of about 10 mbar. A uranium target containing about 82 mg of ^{235}U (99.99%) oxide-protoxide deposited on the two sides of a thick 40×100 mm^2 aluminium backing was arranged along the chamber axis. Thin low-pressure multiwire proportional counters (MWPC) were used as fission fragment detectors, being placed on two sides of the target at a distance of ~3 cm (start detector) and ~11 cm (stop detector). Start and stop detectors are supposed to be used for measuring the fragment velocities (momenta). Eight cylindrical plastic scintillators were inserted in a rotatable holder at a distance of about 30 cm from the target center that ensures subsequent measurements of coincidences of prompt fission gamma rays and neutrons with fission fragments at angles of ±22.5, ±67.5, ±112.5 and ±157.5 degrees with respect to the mean axis of the detection of fragments. The detectors of gamma rays and fission fragments were arranged in the plane orthogonal to the neutron beam direction, which also coincides with the axis of the polarization of ^{236}U nuclei.

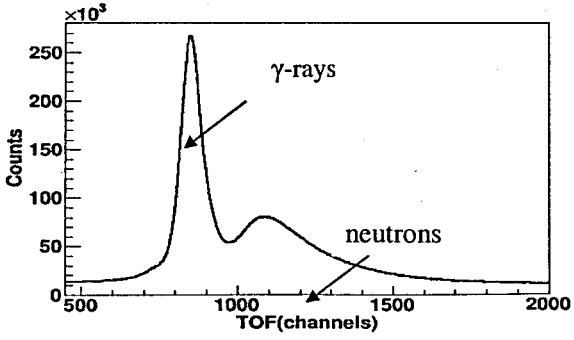

Fig. 3. Time-of-flight spectrum from one of the plastic detectors.

Prompt neutrons could be rather well separated from the prompt gamma-rays using the time-of-flight method (see Fig.3). Every event matching coincidence of the signals from the gamma/neutron and fragment detectors is digitized by a multichannel TDC CAEN V775N and stored together with the information about the direction of polarization of the neutron beam. A reversal of the polarization occurs at a frequency of 1.3 Hz, the input of the TDC being inhibited by the time of the neutron spin flip. At the same time, for the on-line control of the installation, the coincidence count rates of neutrons/γ-rays and the fission fragments were recorded by counters, which were read out every 5 min for each detector. The values of the asymmetries, calculated by the formula:

$$R = \frac{(N^+ - N^-)}{(N^+ + N^-)}, \qquad (1)$$

were constantly monitored. Here N^+ and N^- are the coincidence count rates for opposite directions of the neutron polarization. Simultaneously, the asymmetry of the fragment count rates was measured and controlled.

The total time allocated for the experiment at the POLI facility was 11 days. Four days were spent for the installation of the setup, calibration of the detectors, alignment of the spin control system etc. The statistic was accumulated during 7 days. Because of the rather short measurement time, to increase the coincidence rate only "start" fission fragment detectors were used in the analysis, which made the determination of the fragment mass (separation of light and heavy fragment groups) impossible and increased the angular spread of the fission fragments. For the ROT-effect the light-heavy fragment separation is not necessary, as the effect is mass-symmetric. The use of only the "start" detector increased the solid angle of the fission fragment detection which could lead to a decrease of the potentially observed effect,

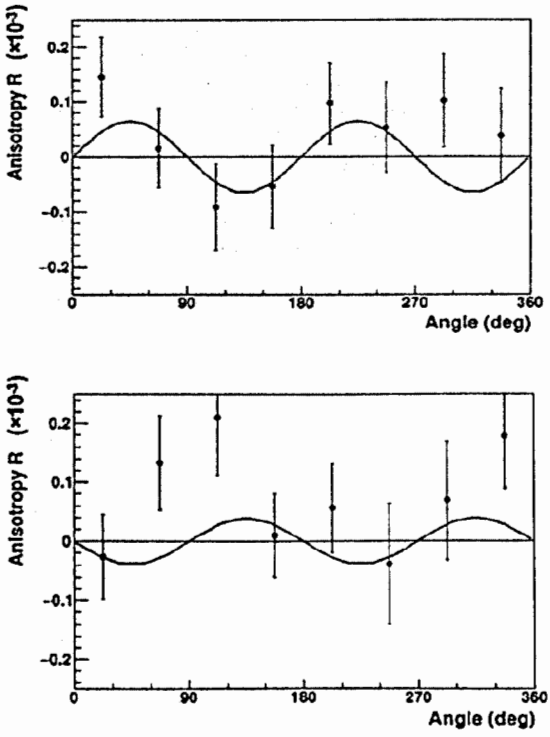

Fig. 4. Anisotropy ratio R as a function of angle for the gamma-rays (top) and neutrons (bottom).

but significantly increased the accumulated statistics, which was more important considering that the main aim of this pioneering experiment was to observe the effect, but not to measure its absolute value.

3. Results and discussion

Figure 4 shows the anisotropy ratio R determined from the experimental data according to formula (1), for prompt gamma-rays (top) and neutrons (bottom), detected in

coincidence with one of the fission fragments. Each point corresponds to the angular detector position with respect to the average direction of emission of the detected fission fragments. The angular dependence at first approximation can be fitted by the function $F = A \cdot sin(2\theta)$, which is shown on the plots. The anisotropy parameter A could be determined from the fit and equals to $A_\gamma = (-6.5\pm3.9)\times10^{-5}$ for the gamma-rays and $A_n = (+3.8\pm4.1)\times10^{-5}$ for the neutrons, χ^2/N being 0.98 and 1.70, respectively. These results can be compared to the corresponding values for ^{235}U, obtained with cold neutrons: $A_\gamma = (-16.6\pm1.6)\times10^{-5}$ (at 45 degrees) and $A_n = (-21.2\pm2.5)\times10^{-5}$ (at 22.5 degrees). Although the statistical accuracy is not sufficient to claim that the ROT effect has been observed in the lowest resonance of ^{235}U, one can conclude that the effect is definitely smaller than that in the cold neutron induced fission.

It should be mentioned that the authors of [13], who developed one of the most comprehensive models of the TRI- and ROT-effects, predicted such a decrease of the anisotropy coefficient for the 0.27 eV resonance of ^{235}U, based on the known contributions of the J=3 and J=4 partial cross sections for this nucleus and on the value of the most probable K-channel for these spins, derived from their work. Thus, the results of our experiment are in agreement with the most modern theoretical model prediction.

We believe that it is important to continue this type of experiments in order to gain better statistical accuracy for the 0.27 eV resonance and extend the measurements to higher energies, e.g. to the 1.14 eV resonance where the effect should be larger than for cold neutrons and where practically only the J=4 spin state is present.

This work has been supported by the Russian Ministry for Science and Education, German Ministry for Education and Research BMBF through the project 05K13PA3. The instrument POLI is operated by RWTH Aachen in cooperation with JCNS FZ Jülich (Jülich Aachen Research Alliance JARA). We're grateful to A. Sazonov, W. Luberstetter, and P. Stein for their help in setting up and conducting the experiment.

References

1. P. Jesinger, G.V. Danilyan, A.M. Gagarski, et al., Phys. At. Nucl. **62**, 1608 (1999).
2. P. Jesinger, A. Kotzle, A. Gagarski et al, Nucl. Instrum. Methods Phys. Res. A **440**, 618 (2000).
3. K. Schreckenbach, J. van Klinken, and J. Last, *Proceedings of the 2nd International Workshop on Time Reversal Invariance and Parity Violation in Neutron Reactions*, Dubna, Russia, May 4–7, 1993, (World Scientific Publishing Company, Singapore, 1994), p. 187.
4. F. Gönnenwein, M. Mutterer, A. Gagarski et al, Phys. Lett. B **652**, 13 (2007).
5. G.V. Danilyan, J. Klenke, V.A. Krakhotin, et al., Phys. At. Nucl. **72**, 1812 (2009).
6. G.V. Danilyan, J. Klenke, V.A. Krakhotin, et al., Phys. At. Nucl. **74**, 671 (2011).
7. G.V. Danilyan, J. Klenke, Yu.N. Kopach et al, Phys. At. Nucl. **77**, 677 (2014).
8. V.E. Bunakov and S.G. Kadmensky, Phys. At. Nucl. **66**, 1846 (2003).
9. V.E. Bunakov, S.G. Kadmensky, and S.S. Kadmensky, Phys. At. Nucl. **71**, 1887 (2008).
10. V.E. Bunakov and S.G. Kadmensky, Phys. At. Nucl. **74**, 1655 (2011).
11. A.L. Barabanov, in *Proceedings of the IX International Seminar on Interaction of Neutrons with Nuclei*, Dubna, May 23–26, 2001 (Dubna, Russia, 2001), p. 93.
12. A.L. Barabanov, Phys. Part. Nucl. Lett. **10**, 336 (2013).
13. A. Gagarski F. Gönnenwein, I.Guseva et al., Phys. Rev. C **93**, 054619 (2016).
14. V. Hutanu, J. Large-Scale Res. Facil. 1, A**16** (2015).
15. L.C. Leal, G. de Saussure & R.B. Perez, Nuclear Science and Engineering Vol. **109**, Iss. 1,1991.
16. V. Hutanu, M. Meven, S. Masalovich, G. Heger, and G. Roth, J. Phys.: Conf. Ser. 294, 012012 (2011).

Features of the Time Dependence of the Intensity of Delayed Neutrons in the Range of 0.02 s in the ^{235}U Fission by Thermal and Fast Neutrons

Mitrofanov K.V., Piksaikin V.M., Egorov A.S., Mitrofanov V.F., Gremyachkin D.E., Samylin B.F.

Joint Stock Company "State Scientific Centre of the Russian Federation – Institute for Physics and Power Engineering named after A. I. Leypunsky" (JSC "SSC RF – IPPE"), Obninsk, Russia

Abstract. In the present work the set-up created on the basis of the accelerator Tandetron (IPPE) for the experimental studies of the time dependence of delayed neutron activity from neutron induced fission of ^{235}U is described. Measurements were carried out with neutron beam generated by the $^{7}Li(p,n)$ reaction. The lower limit of the investigated time range was governed by the proton beam switching system that was 20 ms. The neutron detector is an assembly of three SNM-18 counters (working gas: a mixture of 97% He-3 + 3% Ar, pressure of 405 kPa) mounted in the polyethylene box. It was shown that the temporary characteristics of delayed neutrons from the fission of ^{235}U by epithermal neutrons are consistent with the time dependence which at present is recommended as a standard. In case of the fast neutron induced fission of ^{235}U the measured decay curve of delayed neutrons shows excess of counting rate in the time interval 0.01-0.2 s as compared with the decay curve corresponding to the recommended data. The microscopic approach using the data on the probability of emission of delayed neutrons and cumulative yields of fission products for 368 nuclei precursors also indicates the existence of short-lived component ($T_{1/2}$ <0.2 s) in the decay curve of activity of delayed neutrons emitted in the fission of ^{235}U.

1. The experimental setup

Experiment was carried out at the accelerator Tandetron (IPPE). Block diagram of the experimental setup is shown in Figure 1. The neutron detector is an assembly of three counters SNM-18 (Working gas: a mixture of 97% He-3 + 3% Ar. The pressure of 405 kPa) mounted in a polyethylene box. Signals from the counters SNM-18 received consistently to preamplifiers, amplifiers and conditioners. At the output of the last were formed TTL signals received on the adder, combined into a single digital stream of information transmitted by electronic analysis system and accumulation.

Electronic system of data collection, processing and visual process control during a session of experimental data acquisition is based on National Instruments (NI). The system includes a PXI-8104 controller and a timer-counter PXI-6602. All modules are installed in the chassis-rack PXI-1042 equipped with a bus PXI/PCI allowing to integrate the controller processor and the individual modules into a single platform. This system allows you to record the pulses spaced 12.5 ns. Therefore, the resolution time of countable channel is mainly determined by the neutron detector dead time (2.3 ms). In these measurements, the width of the channel in the time spectrum is 0.0001 seconds. Registration the number of pulses was carried out continuously including the irradiation time of the sample and the time of counting activity of the delayed neutron after an interruption of the proton beam.

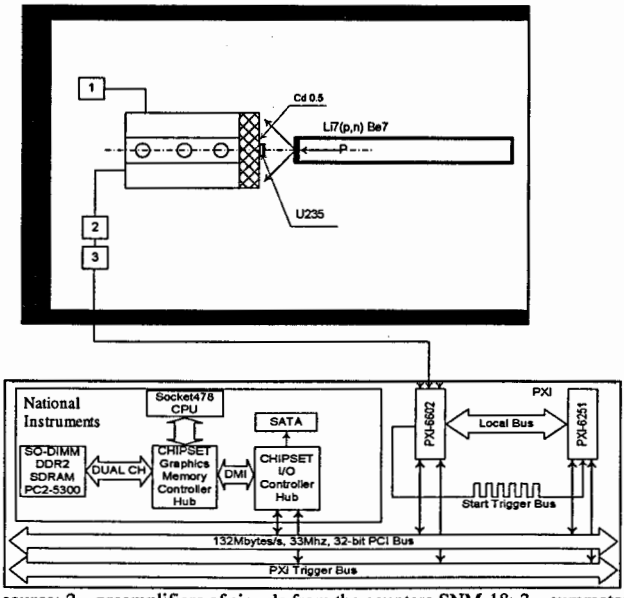

1 – high voltage source; 2 – preamplifiers of signals from the counters SNM-18; 3 – summator of signals from the preamplifier of detector counters.

FIG. 1. Block diagram of the experimental setup is performed on the basis of the system of accumulation of National Instruments.

2. The energy dependence of the neutron yield from neutron target

In this work, the neutron detector was set up, in which the effect of the distortion of the counting characteristics at the initial time after irradiation session was absent. In addition, the counting characteristics of the detector is not distorted even during irradiation intense beam of neutrons generated in the lithium target under the action of protons. The neutron source was a lithium target irradiated by a proton beam. The current in the experiment was 10 μA. The proton energy was 2.6 MeV. Figure 2 shows the energy dependence of the neutron yield from neutron target.

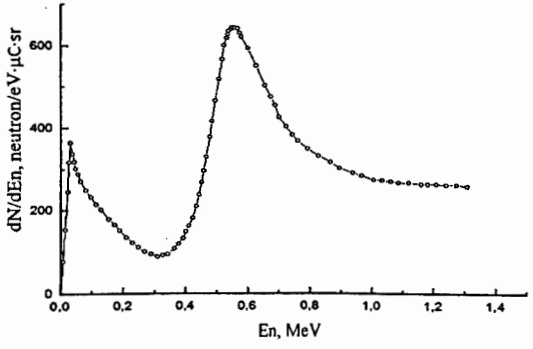

FIG.2. The energy dependence of the neutron yield from neutron target.

3. Two types of experiments

There were two types of experiments. In the first experiment, the irradiated sample was placed on a side surface of a neutron detector (FIG. 3). In a second experiment, a ^{235}U sample was placed in cadmium cover and a lead shield was placed between the detector and the sample (FIG. 4). Obviously, in the first experiment, the neutron spectrum is significantly softer than the case of experiment №2, because the direct beam of the neutrons from the target is added the neutrons scattered by the material of the neutron detector. In the second experiment, a sample of ^{235}U is at a distance of 5 cm from the detector, and the scattered neutron at the detector are intensity absorbed by cadmium filter. Lead filter is designed to protect the detector from the possible detection of delayed gamma rays from the sample ^{235}U. A sample of ^{235}U is a metal disk of 3 mm thickness and 41 mm in diameter, located in a metal shell. Measurements in the experiments were carried out for two different irradiation times – 180 s and 15 s. The experimental method used in this experiment based on the cyclic irradiation of fissile samples in a neutron flux of Li(p,n) reaction and the measurement of the time dependence of the intensity decrease of the delayed neutron [2].

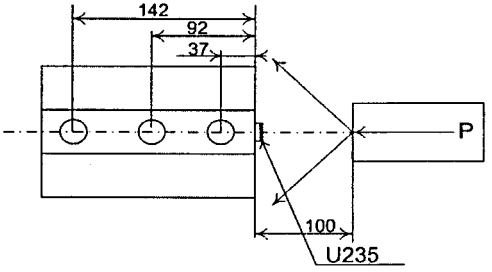

FIG.3. The first experimental scheme.

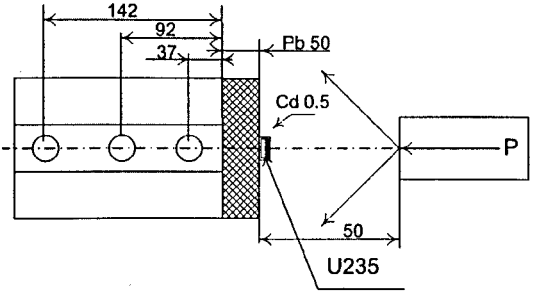

FIG.4. The first experimental scheme.

To verify the correct operation of all the experimental equipment (neutron detector with a registration tract, the electronic data storage system), the obtained data were processed to evaluate the time parameters of the delayed neutron. The estimation of parameters of the delayed neutron is performed by an iterative least-squares method [3]. The evaluation was carried out as part a 6-group model of time parameters of the delayed neutron. The obtained data are presented in Table 1. The table shows the analogous data from Kipin work [5]. The

value of the average half-life obtained in the present work is the same as the corresponding recommended data [4].

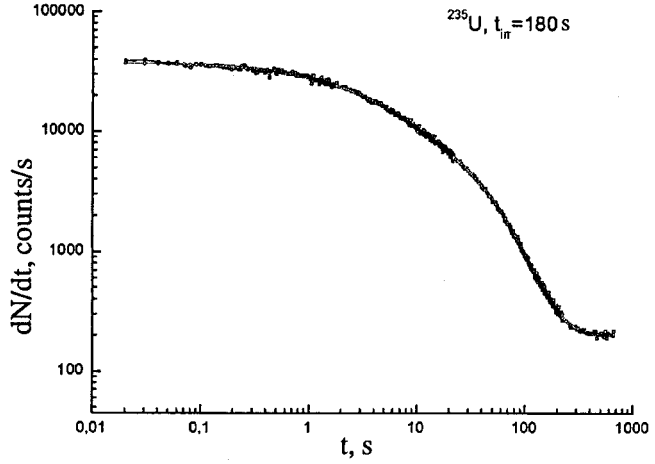

FIG. 5. Time dependence of the activity of the ^{235}U sample obtained in experiments №1 with irradiation time of the sample tirr = 180 s, presented as a count rate.

TABLE 1: Relative yields and periods of delayed neutrons in the fission of 235U by neutrons from the reaction 7Li (p, n).

№		1	2	3	4	5	6	$T_{1/2}$ ср
^{235}U (present work, hard spectrum)	a_i	0.03950 ± 0.00131	0.20823 ± 0.00692	0.19670 ± 0.00881	0.38126 ± 0.01501	0.14655 ± 0.00692	0.02776 ± 0.00139	8.90932 ± 0.48652
	T_i	54.12201 ± 1.01994	22.38173 ± 0.29337	6.09608 ± 0.22313	2.2432 ± 0.05674	0.45424 ± 0.02208	0.17896 ± 0.00894	
^{235}U Kipin (fast)	a_i	0.038	0.213	0.188	0.407	0.128	0.026	8.83
	T_i	54.51	21.84	6.0	2.23	0.496	0.179	

The Figures 5 and 6 show that in this configuration the experimental data for the time of irradiation tirr = 15 do not show a significant excess of delayed neutron intensity at the lower boundary of the investigated time range (0.01-0.5 s), as in the case of long irradiation (tirr = 180).

Similar results were obtained in experiments with a configuration corresponding to a fast spectrum of primary neutrons for the irradiation time of the sample tirr = 15 s. These data are presented as the count rate of pulses from a neutron detector in Figure 8. It is seen that there is an increase the count rate of delayed neutrons in the times region up to 0.12 s compared with the data obtained on the basis of the recommended data. Recommended data were measured in the time range starting from 0.1.

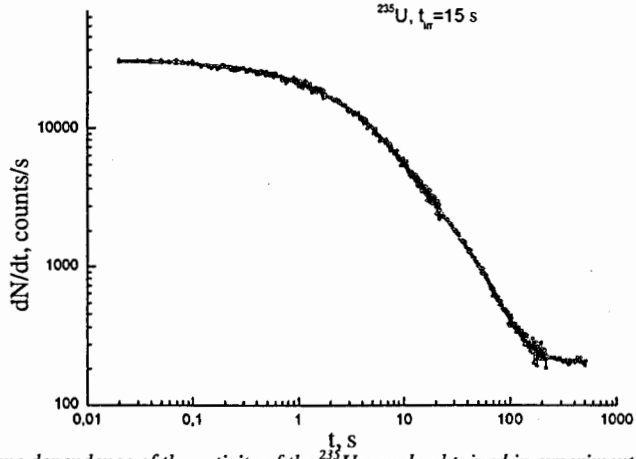

FIG. 6. Time dependence of the activity of the ^{235}U sample obtained in experiments №1 with irradiation time of the sample tirr = 15 s, presented as a count rate.

Figure 7 shows that data of experiment №2 indicate the excess of numbers of counts in the low times in relation to the recommended data [4].

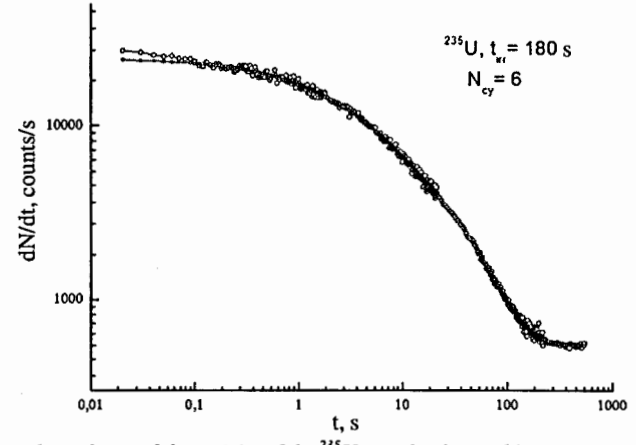

FIG. 7. Time dependence of the activity of the ^{235}U sample obtained in experiments №2 with irradiation time of the sample tirr = 180 s, presented as a count rate.

Thus, it was shown in the experiment that the measured dependence of delayed neutron activity of soft spectrum of primary neutrons coincides with the recommended. On the fast spectrum of primary neutrons on decay curve of activity of delayed neutrons in the time range of 0.01 - 0.2 s is observed the excess of numbers of count compared to the decay curve corresponding to the recommended data.

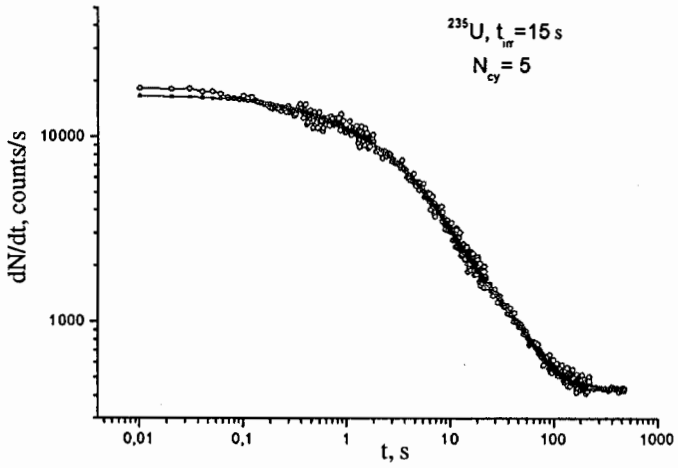

FIG. 8. Time dependence of the activity of the ^{235}U sample obtained in experiments №2 with irradiation time of the sample tirr = 15 s, presented as a count rate.

4. Conclusion

In this work, the set-up was created on the basis of the Tandetron (IPPE) allowing to measure the activity curves of delayed neutrons of fission of heavy nuclei by neutrons in the time range, which the lower limit is determined by the speed of the charged particle beam interruption. It was shown in the experiments that the measured dependence of activity curves of delayed neutrons in the fission of ^{235}U on the soft spectrum of primary neutrons coincides with the recommended. On the fast spectrum of primary neutrons the activity curves of delayed neutrons in the time range of 0.01 - 0.2 s is observed with the excess of numbers of count compared to the decay curve corresponding to the recommended data.

The microscopic approach using the data on the probability of emission of delayed neutrons and cumulative yields of fission products for 368 nuclei precursors also indicates the existence of short-lived component ($T_{1/2}$ <0.2 s) in the decay curve of activity of delayed neutrons emitted in the fission of ^{235}U.

References

1. http://www.ni.com/pdf/products/us/4daqsc386-393_386-387.pdf
2. PIKSAIKIN, V.M., SEMENOVA, N.N., "A method and setup for studying the energy dependence of delayed neutron characteristics in nuclear fission induced by neutrons from the T(p, n), D(d, n), and T(d, n) reactions", Nuclear experimental technique, Vol. **49**, pp. 765-777, 2006.
3. PIKSAIKIN, V.M., KAZAKOV, L.E., "Energy dependence of relative abundances and periods of delayed neutrons from neutron-induced fission of ^{235}U, ^{238}U, ^{239}Pu in 6- and 8-group model representation", Progress in nuclear energy, Vol. **41**, pp. 203-222, 2002.
4. SPRIGGS, G., CAMPBEL, J., PIKSAIKIN, V., "An 8-group delayed neutron model based on a consistent set of half-lives", Progress in nuclear energy. Vol. **41**, pp. 223-251, 2002.
5. KIPIN, G.R., "Physical basis of the kinetics of nuclear reactors", Atomizdat, 1967.

TO THE QUESTION OF VERIFICATION OF COLLINEAR CLUSTER TRI-PARTITION (CCT)

Yu.V. Pyatkov[1,2], D.V. Kamanin[2], A.A. Alexandrov[2], I.A. Alexandrova[2], Z.I. Goryainova[2], V. Malaza[3], E.A. Kuznetsova[2], A.O. Strekalovsky[2], O.V. Strekalovsky[2], V.E. Zhuchko[2]

[1]*National Nuclear Research University MEPhI (Moscow Engineering Physics Institute), Moscow, Russia*
[2]*Joint Institute for Nuclear Research, Dubna, Russia*
[3]*University of Stellenbosch, Faculty of Military Science, Military Academy, Saldanha 7395, South Africa*

INTRODUCTION

In recent publications [1–3], we have presented experimental indications of existence of a new at least ternary decay channel of low excited heavy nuclei known as collinear cluster tri-partition (CCT). A fragment mass M is calculated by the energy E and the velocity V. Mainly a scattering of fragments at the entrance of an E-detector gives background events simulating ternary decay. Selection of the "true" events was provided by applying the gates on the fragments momenta, velocities, experimental neutron multiplicity, and the parameters sensitive to the fragment nuclear charge. Observation of the specific linear structures in the M_1–M_2 distributions (mass correlation plots) served as a criterion for a sufficient suppression of the background. The structures were reproduced at the spectrometers of two types. Earlier experiments were performed using gas filled detectors (modules of the FOBOS setup [4]). Later we switched to solid-state detectors, namely timing detectors, on the microchannel plates and the mosaics of PIN diodes (COMETA setup [2] and the similar ones [3]). Even though mass reconstruction procedures for these two types of spectrometers strongly differ, the obtained results are in good agreement.

Estimation of the expected parameters of the CCT products was performed in the recent theoretical works [5–7]. The results obtained were taken into account in our model of the most populated CCT mode known as "Ni-bump".

EXPERIMENTS AND RESULTS

Figure 1(a) shows the region of the mass distribution measured at the COMETA setup [2] in the experiment Ex1 for the fission fragments (FFs) from ^{252}Cf (sf) around the Ni-bump (M_1 = 68–80 amu, M_2 = 128–150 amu). The structures are seen in the spectrometer arm facing the source backing only. No additional selection of the fission events was applied in this case, which resulted in the experiment having almost no background. A rectangular-like structure below the locus of binary fission is bound by magic nuclei (their masses are marked by the numbered arrows), namely ^{128}Sn (1), ^{68}Ni (2), and ^{72}Ni (3). In Figure 1(b), we demonstrate the projection of the linear structure seen at the masses of 68 and 72 amu.

Similar structures were revealed as well in the experiment Ex2 performed at the COMETA-F spectrometer which differs substantially from this used in Ex1 by the data acquisition system based on the fast flash-ADC (CAEN DT5742) and data processing [8].

Due to the background conditions only events with the velocities $V_2 < 0.8$ cm/ns are presented in Figure 1(c, d). Such selection conditions the difference in the structures below the line M_2=68 amu in the Figure 1(c) comparing Figure 1(a).

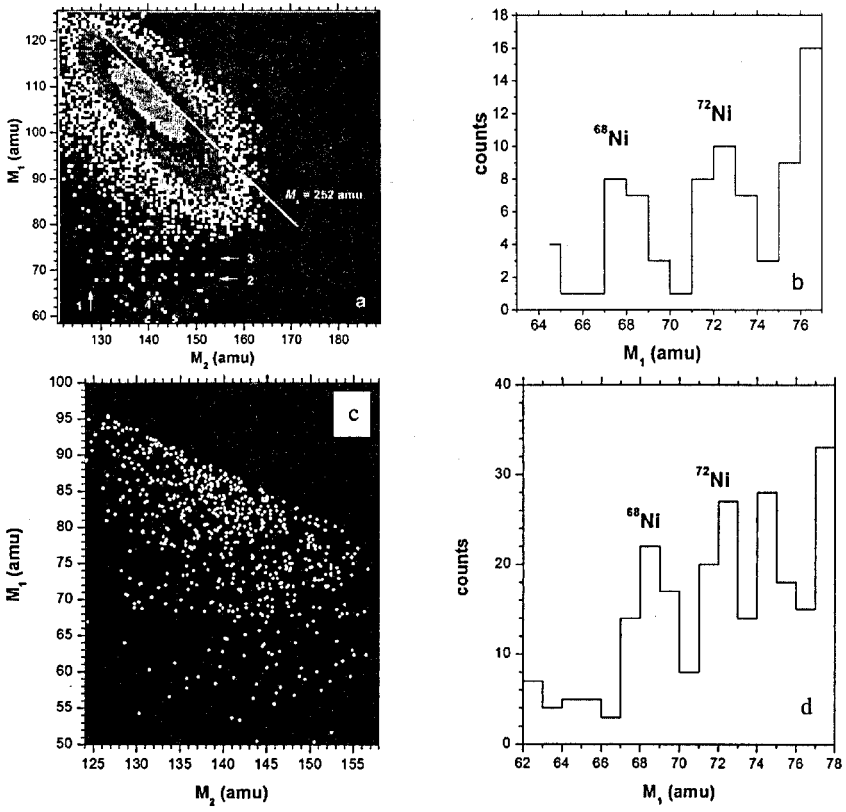

FIGURE 1. Region of the mass–mass distribution for the FFs from ^{252}Cf (sf) around the Ni-bump a) – in Ex1, c) – in Ex2). Projection of the lines 1, 2 onto M_1 axis in Ex1 (b) and in Ex2 (d). It should be indicated that Figures 1(a), (b) were published in Ref. [2].

In fact, only two fragments were detected in each decay event. The mass and velocity of the "missed" fragment could be calculated based on the laws of mass and momentum conservation. In each event showing the missing mass (ternary event), we mark the masses of the fragments in order of their decreasing masses M_H, M_L and M_T (Ternary particle) respectively. Figure 2(a) demonstrates a correlation between the velocities of two lighter partners of the ternary decay. Only the events for which M_L= (67–75) amu (Ni-peaks in Figure 1(b)) are under analysis. Their total yield does not exceed 2.5×10^{-4} per binary fission. Three different groups of events are vividly seen in the Figure 1. They are marked by the signs *w*1–*w*3 respectively. Each of the loci consists of two subgroups as can be inferred from the plot E_L–E_H (Figure 2(d)).

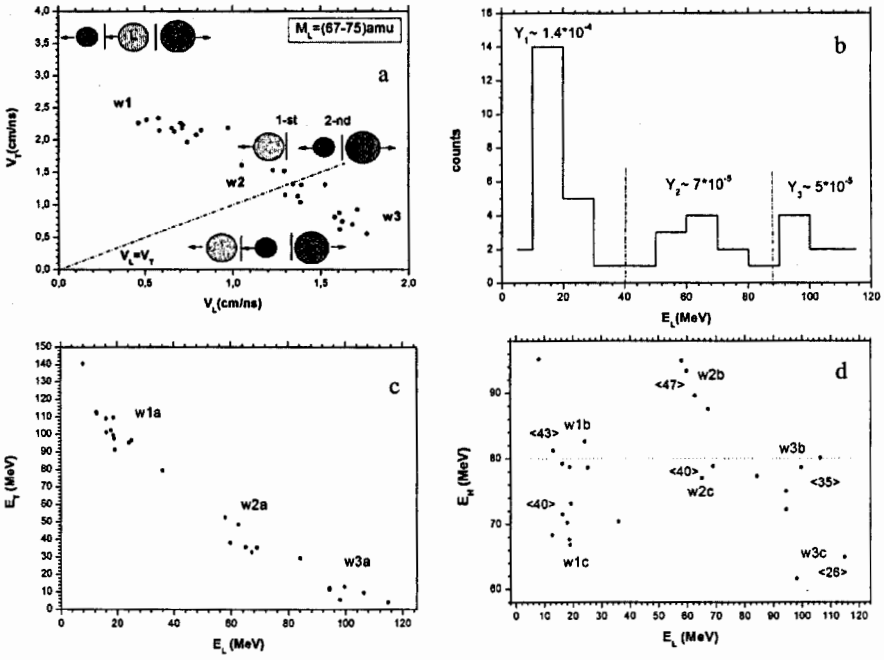

FIGURE 2. Ex1: velocities V and energies E for the ternary events with M_L = (67–75) amu (Ni-peaks in Figure 1 (b)). Correlation between the velocities of two lighter partners of the ternary decay – (a), energy spectrum of the detected Ni nuclei (the yields per binary fission are marked above each peak) – (b), energy correlations E_L–E_T and E_L–E_H– (c) and (d) respectively. The sketches in the panels illustrate the decay scenario to be discussed below. See the text for details.

SCISSION POINT CALCULATIONS

Among all the theoretical articles initiated by the results of the experiments, article [6] deserves special attention. Under the three-center shell model the potential energy surfaces for few ternary combinations in a fission channel were calculated for the ^{252}Cf nucleus. The fission barrier for the ^{132}Sn + ^{48}Ca + ^{72}Ni ternary splitting is shown in Figure 3(a). According to the Figure 3, the exit point corresponds to R ~ 22.4 fm, i.e. elongation of the system exceeds the length of the configuration of three touching spheroids. If just a Ca nucleus took upon itself all extra elongation, the axis ratio of the corresponding spheroid would be approximately 1:1.6.

Calculations [9] performed in ten dimensional deformation space demonstrate the shapes of a decaying Cf nucleus at large deformations (Figure 3(b)) in the potential valleys 3 and 4. The distance between the centers of the side constituents (R_{12}) are equal to approximately 18 fm and 23 fm. After the rupture at the narrowest section of the neck, almost all deformation energy concentrates in the light (panel c) or heavy fragment (panel d).

Typical shapes of fissioning nucleus at large deformations are confirmed independently by the neutron data from [10]. For the ^{248}Cm, such asymmetry in number of emitted neutrons from the light (ν_L) and heavy (ν_H) FFs was traced up to the ν_L/ν_H= 9/0. Just for a sense of the

scale of yields of highly deformed scission configurations, one can cite to the relative total yield Y_R of the fission events at $\nu_{tot} = 6$ and $\nu_L/\nu_H = 6/0$. Y_R was estimated to be 2.19 % and 0.72 % for ^{248}Cm and ^{252}Cf respectively [11].

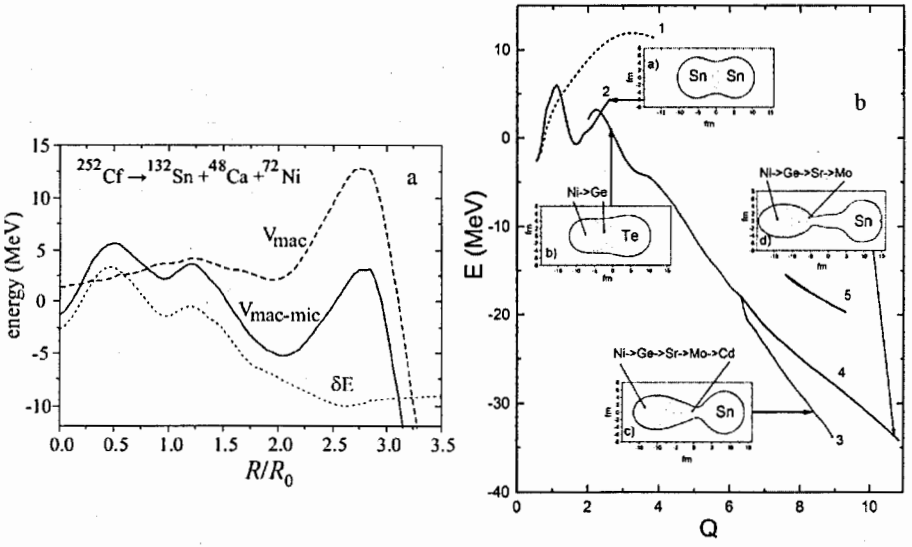

FIGURE 3. a) – macroscopic potential energy (dashed line), shell correction (dotted line), and total macro-microscopic potential energy (solid line) of the ^{252}Cf nucleus corresponding to the ^{132}Sn + ^{48}Ca + ^{72}Ni ternary splitting [6]. Here R is an approximate distance between the mass centers of the side fragments, $R_0 = 1.16\ A^{1/3}$ is a radius of a mother nucleus; b) – potential energy of a fissioning ^{252}Cf nucleus, corresponding to the bottoms of the potential valleys, as a function of Q, proportional to its quadrupole moment. The valleys found are marked by numbers 1 to 5. The panels depict the shapes of the system at the points marked by arrows [9].

The following scenario of the CCT process can be proposed based on our experimental findings and theoretical calculations. According to Ref. [6], the exit point from under the barrier in the potential valley leading to the ^{132}Sn + ^{48}Ca + ^{72}Ni ternary splitting (Figure 3(a)) corresponds to a much more elongated configuration in comparison with the chain of three touching spherical nuclei. The distance R_{12} between the centers of the side clusters was estimated to be above ~23 fm. Likely, the central fragment (Ca) takes upon itself almost all extra elongation. After a rupture occurs, for instance on the boundary of Ca and Sn clusters, the Ni cluster very quickly (in comparison to full acceleration time) attracts the Ca "neck". Part of the released deformation energy is spent on emission of neutrons flying apart isotropically. Thus, the formed pear-shaped Ni-Ca dinuclear system can rotate around the center of its gravity by 180^0.Such orientation is the most energetically favorable. Octupole vibrations could be another reason for the change in the orientation of the "tip". Formation of the Ca-Sn system with similar features is less probable [5]. The formed dinuclear system can evolve towards fusion or rupture. In the first case, we deal with a binary fission of a mother nucleus, and in the second instance with a ternary fission.

Presumable decay scenarios for all subgroups are presented in Table I. A precission configuration of the system is demonstrated in the third column of the table. For all the cases fission fragment FF_1 is supposed to be ^{70}Ni, the mass of the FF_2 corresponds to the mean mass

of the lightest cluster (shown in brackets in Figure 3(d)), and the mass of the heavy cluster is calculated using the law of mass conservation. The FFs charges are calculated according to the hypothesis of unchanged charge density. Configurations of the system after the first and the second ruptures are shown respectively in the fourth and the fifth columns of the table.

In the frame of the proposed scenario we have succeeded to reproduce the experimental energies of all three partners of ternary decay (Figure 2). More details results are presented in [12].

TABLE I. Pictograms illustrate scenarios of different CCT modes observed in the experiment. See the text for details.

row №	Label of the locus in Fig. 3(d)	Prescission configuration of the system	System configuration after the first rupture	System configuration at the moment of the second rupture
1	*w1b* *w1c*	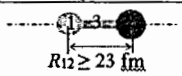	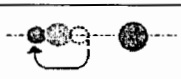	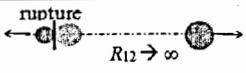
2	*w2b* *w2c*	"		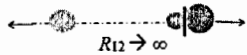
3	*w3b* *w3c*	"	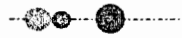	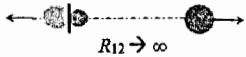
4	binary fission	"		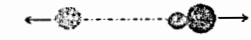

CONCLUSIONS

We assume that in contrast to conventional ternary fission the CCT occurs as a two-step decay of an extremely deformed prescission nuclear configuration in the valley of true ternary fission [6] or states associated with cold deformed fission in the binary channel [9]. According to the neutron data, the population of such CCT door-states reaches several percent.

As was mentioned above the "Ni-bump" is one of the most populated CCT modes observed and just low energy peak for Ni fragments from the bump (Figure 2(b)) has the greatest yield. Scission point calculations sheds light to the origin of this peak. Summing up, we would recommend registration of the Ni isotopes with the energy lower than 25 MeV at the mass-separator Lohengrin as the primary experiment for independent verification of the CCT.

ACKNOWLEDGMENTS

This work was supported, in part, by the Russian Science Foundation and fulfilled in the framework of MEPhI Academic Excellence Project (contract 02.a03.21.0005, 27.08.2013) by the Department of Science and Technology of the Republic of South Africa (RSA).

REFERENCES

1. Yu.V. Pyatkov et al., Eur. Phys. J. A**45**, 29 (2010).
2. Yu.V. Pyatkov et al., Eur. Phys. J. A**48**, 94 (2012).

3. D.V. Kamanin, Yu.V. Pyatkov, Clusters in Nuclei Lecture Notes in Physics 875 vol. **3** ed. C. Beck, Springer, 2013, p. 183.
4. H.-G. Ortlepp et al.,Nucl. Inst. Meth A**403**, 65 (1998).
5. A.K. Nasirov, R.B. Tashkhodjaev and W. von Oertzen, Eur. Phys. J. A**52**, 135 (2016).
6. A.B. Karpov,Phys. Rev. C**94**, 064615 (2016).
7. P. Holmvall, U. Köster, A. Heinz, and T. Nilsson, Phys. Rev. C**95**, 014602 (2017).
8. Yu.V. Pyatkov et al., J. Phys.: Conf. Series 675, 042018 (2016).
9. Yu.V. Pyatkov et al.,Nucl. Phys. A**624**, 140 (1997).
10. V.A. Kalinin et al. in Proc. of the "Seminar on Fission Pont D'Oye V", Belgium, 2003. World Scientific, Singapore, 2004. p. 73.
11. A.S. Vorobiev, Ph.D. thesis, B. P. Konstantinov Petersburg Institute of Nuclear Physics, 2004 (in Russian, http://www.gigabaza.ru/doc/2737-all.html).
12. Yu.V. Pyatkov et al., Phys. Rev. C (2017) (in press).

ANGULAR AND ENERGY DISTRIBUTIONS OF THE PROMPT FISSION NEUTRONS FROM THERMAL NEUTRON-INDUCED FISSION OF ^{239}Pu

A.S. Vorobyev[1], O.A. Shcherbakov, A.M. Gagarski, G.V. Val'ski, G.A. Petrov

B.P. Konstantinov Petersburg Nuclear Physics Institute of National Research Centre "Kurchatov Institute", Gatchina, Leningrad district, 188300, Russia

Abstract

The measurements of angular and energy distributions of the prompt fission neutrons from thermal neutron-induced fission of ^{239}Pu were carried out at the WWR-M research reactor in Gatchina, Russia. Some peculiarities were found in the angular distribution of the prompt fission neutrons. It is possible to explain them by assuming that in the centre of mass system of fission fragment the neutrons are more likely emitted along fission direction than in the perpendicular to one. The value of anisotropy of neutrons emission in the center of mass system of fission fragment was obtained and was equal to ~6%. Also the yield of "scission" neutrons and their spectrum have been estimated.

Introduction

Up to now many theoretical and experimental works were performed to investigate the low energy nuclear fission. A special attention was given to the details of the prompt fission neutron (PFN) emission: spectra and multiplicities, their dependence on fission fragment (FF) characteristics and all possible correlations between reaction products. These data are used widely for the construction of nuclear reactors and applied for the development of non-destructive methods of nuclear safety and for the control of non-proliferation of nuclear materials.

In spite of a notable advance achieved in theoretical description of the prompt fission neutron properties, still there are some problems (for example, [1, 2]). The difference observed between measured and calculated data is probably due to both an inadequacy of theoretical model used for this description and a deficit of experimental data. Because the properties of neutrons emitted before fragments have been accelerated (emission before and during the rupture of fissioning nucleus or at the initial stage of acceleration of the fragments in the Coulomb field – so called "scission" neutrons) are not established experimentally, in theoretical calculations it is usually assumed that the main part of prompt fission neutrons are emitted from accelerated fission fragments. Experimental studies dedicated to ascertain the mechanism of the prompt neutron emission are limited to spontaneous fission of ^{252}Cf and thermal neutron-induced fission of ^{235}U. For ^{239}Pu these investigations are limited to works shown in Table 1. Also, it ought to mention that up to now the energy spectra of the prompt fission neutrons are calculated using the semi-empirical systematics where an absence of information about the mechanism of emission of additional neutrons is compensated by the artificial variation of the nuclear model parameters. This circumstance significantly complicates production of the evaluated data files for the nuclei and energy ranges where experimental data are absent. That is why a new experimental investigation of the mechanism of fission neutrons emission will provide a good basis for future evaluations and enable to increase their accuracy and reliability.

Therefore, to clear up how well the model calculation can describe or predict the prompt fission neutron properties it is necessary to improve the quality of data obtained by

differential as well as integral experiments. A series of such experiments have been carried out in PNPI of NRC KI (Gatchina, Russia) [3-7]. In this paper some results of this investigation are presented.

Table 1. Main results of previous investigations of neutron emission mechanism for ^{239}Pu(n,f).

Author, References Experimental Set-up	Yield of "scission" neutrons	Average energy of "scission" neutrons	Anisotropy of PFN emission in c.m.s of FF, A
Investigation of (n,f)-angular correlation			
J.S. Fraser *et.al.* [8] (1965). Two plastic scint. for FFs spectroscopy (TOF with the base of 125cm and 99cm). Four neutron detectors (plastic scint.) were used, TOF (106cm). The neutron spectra measurements have been done simultaneously at 10°, 25°, 45° and 80° relative to FFs direction.	30%	~ 2 MeV	"... all results are consistent with A = 0."
Yu.S. Zamyatnin *et.al.* [9] (1979). IC with collimator used for FFs spectroscopy. One neutron detector (plastic scint.) was placed interchangeably at 0° and 90° relative to FFs direction, TOF (40cm).	20 ± 12%	---	Not investigated
Investigation of (n,n)-angular correlation			
I.S. Guseva *et.al.* [10] (2017). Two stilbene neutron detectors, n/γ pulse shape discrimination.	4.0 ± 1.5%	1.8 ± 0.2 MeV	Weakly sensitive

1. Experiment overview

The angular and energy distributions of prompt fission neutrons were measured in turn for neutron-induced fission of ^{239}Pu (beam on) and the spontaneous fission of ^{252}Cf (beam off) under identical experimental conditions. The measurements were carried out using the collimated neutron beam №1 of the research reactor WWR-M (Gatchina, Russia) with a flux of ~ 10^8 thermal neutrons/ cm^2 · sec. The ^{239}Pu target was deposited on 100 μm thick Al backing. The target thickness was 150 μg/cm^2 and made in the form of a circular spot 15 mm in diameter. A ^{252}Cf layer 10 mm in diameter was made on a 0.18 mm thick stainless steel foil. The fission fragments and prompt neutrons time-of-flights were measured simultaneously for 11 fixed angles, θ, between the axis of neutron detector and normal to the stop multi-wire proportional detectors (MWPDs) surface (coming through its center) in the range from 0° to 180° in 18° intervals. The schematic view of the experimental set-up is shown in Fig. 1.

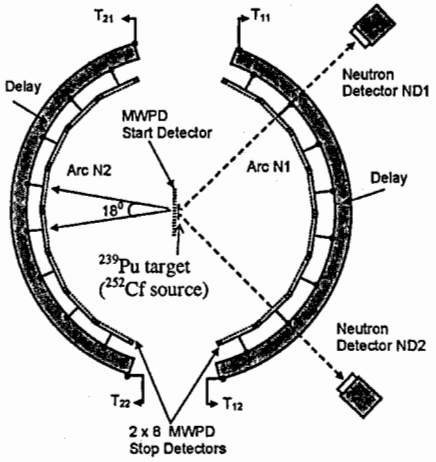

Fig.1. Schematic view of the experimental setup.

The neutron beam was coming along the chamber axis normally to the Fig.1 plane. It should be noted that realized scheme of the experimental set-up guarantees identity of conditions of the neutron spectra measurements at various angles relative to the fission axis, namely: the magnitude and composition of the background, the efficiency of the neutron detectors, and neutron re-scattering by the parts of experimental set-up. Also, the use of two neutron detectors with slightly different characteristics allows to estimate probable systematic errors of the data obtained.

The prompt neutrons were detected using two stilbene crystal detectors (Ø 50 mm x h 50 mm and Ø 40 mm x h 60 mm) positioned at a 90° angle between their respective axes at a distance of (47.2±0.2) cm and (49.2±0.2) cm, respectively, from the fissile target. The axes of neutron detectors ND1 and ND2 come through the centers of two stop MWPDs located on the Arc N1. Both neutron detectors were surrounded by a cylindrical shield made of 30 mm thick layer of lead and 40 mm thick layer of polyethylene (not shown in Fig. 1). The neutron registration threshold was 150 – 200 keV. To separate events corresponding to neutrons and γ-quanta, a double discrimination by the pulse shape and time-of-flight was applied. The full time uncertainties were defined from FWHM of the "fragment - γ-quantum" coincidence curve which was equal to 1.0÷1.2 ns.

The fission fragments were detected by MWPDs in conjunction with the TOF technique. The 8 rectangular MWPDs were located in the Arc N2 in the reaction chamber at the operating gas (isobutane) pressure of 4 ÷ 6 Torr.

As a result, for 11 fixed angles between neutron and light fragment directions the energy distributions of prompt neutrons emitted from fixed pair of fission fragments were obtained. During data processing, the following corrections were taken into account:

- for the fragment detector efficiency;
- for incomplete separation of light and heavy group of fission fragments;
- for angular and energy resolution of experimental setup;
- for neutron detector background and the neutron background due to accidental coincidence between fragment and neutron belonging to different fission events;
- the normalization correction arising from the fact that experimental angular histograms were used in the measurements instead of continuous distributions;
- for the neutron detector efficiency. The detector efficiency was determined for each neutron detector independently as the ratio of the obtained total prompt fission neutron spectrum (PFNS) of ^{252}Cf to a reference standard spectrum from ref. [11]. The total PFNS, were calculated by summing up the obtained angular-energy distributions over angle in the laboratory system.

In order to determine the PFNS from measured time-of-flight spectra, the relativistic equation was used. A description of the experimental method and the used data processing are omitted here since a full treatment is presented in ref. [3, 5, 6].

2. Model

In the model calculation it is used the assumption that PFN are emitted from fully accelerated fragments. In this case the angular and energy distributions of PFN in the laboratory system can be calculated using known spectra of PFN in the center-of-mass system of fragment. Since the fission fragments have a large angular momenta (~ 7ħ on average), which is usually considered to be normal to the fission axes (for example, Ref. [12]), the neutron emission anisotropy in the center-of-mass system of fragment should be included into the model calculation [13, 14]. The spectra of PFN in the center-of-mass system of fragment are calculated using experimental data for small angles (8.9°, 19.8° and 36.9°) relative to the fission direction. During this calculation it was assumed that prompt neutrons are emitted by two fragments with average mass and kinetic energy. The average energy per nucleon for light and heavy fragments were taken as $\langle E_L \rangle = 0.995 \pm 0.007$ MeV and $\langle E_H \rangle = 0.511 \pm 0.004$ MeV for ^{239}Pu(n_{th}, f). Further, the spectra obtained in the center-of-mass system are used for calculation of neutron angular and energy distributions in the laboratory system. These distributions are compared with the experimental distributions to estimate contribution and properties of "scission" neutrons.

It should be noted that the calculated spectra are free of any assumption about the prompt neutron spectra in the center-of-mass system (the number of neutrons emitted by heavy and light fragments, the neutron spectrum shapes, and so on). There is only one free parameter the anisotropy of PFN in the center-of-mass system of fragment, which is adjusted so as to describe in the best way all experimental data obtained in this investigation. The details could be found in ref. [3, 15].

The shape of the neutron spectrum and the number of neutrons obtained in the center-of-mass system both depend on the fragment velocities (or E_L and E_H for fission event). Therefore, strictly speaking, the analysis performed above is not valid, because it was assumed that the prompt neutrons are emitted only from two fragments (light and heavy) characterized by the average parameters. Fortunately, as it was demonstrated for total PFNS of ^{252}Cf in Ref. [15], a transition from the velocity distributions of fragments to the model of two fragments with average parameters has only a minor influence, and for angles near 90° the neutron yield changes within 4% [5].

At the same time, the existing calculation methods used in practice to describe angular and energy distributions of PFNS do not provide necessary accuracy. For example, the total PFNS of ^{235}U calculated by different commonly used codes [2] are presented in Fig. 2, where spectra calculated assuming that PFN are emitted from fully accelerated fragments and using the same input parameters are shown as a ratio to Maxwell distribution. It is seen that the existing calculation methods do not provide necessary accuracy to describe experimental data while the method realized in this work gives accuracy not worse than those of commonly used codes and does not require knowledge of a large number of input parameters.

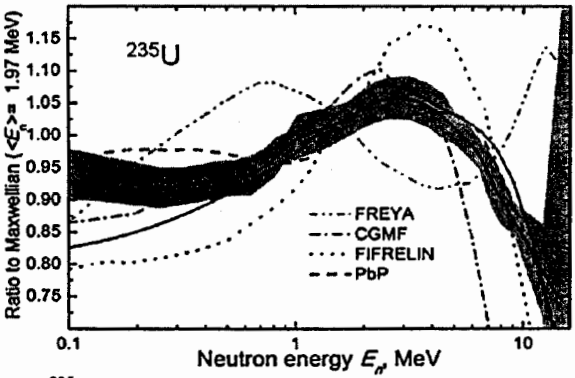

Fig. 2. Total PFNS of $^{235}U(n_{th},f)$: curve inside the shaded region – evaluation of experimental data within error corridor (GMA – generalized least square fit [2]); line – model calculation (two fragments approximation) [2]; **PbP** (Point by Point) - deterministic method developed at the University of Bucharest and JRC-IRRM team, which is an extended version of LAM (Los-Alamos or Madland-Nix model); **FREYA** (Fission Reaction Event Yield Algorithm) – Monte-Carlo fission model developed through a collaboration between LLNL and LBNL (USA); **CGMF** – Monte-Carlo code developed at LANL (USA); **FIFRELIN** (FIssion FRagment Evaporation Leading to an Investigation of Nuclear data) - Monte-Carlo code developed at CEA-Cadarache (France) with the aim of calculating the main fission observables.

3. Results and discussion

The PFNS for fixed angles in the laboratory system (obtained experimentally and calculated using an assumption that PFN are emitted from fully accelerated fragments with anisotropy parameters $A_2 \approx 0.04$ ($N(0°)/N(90°)=(1+A_2)/(1-A_2/2)$) are shown in Fig. 3. The yield and average energies of these PFNS are presented in Fig. 4.

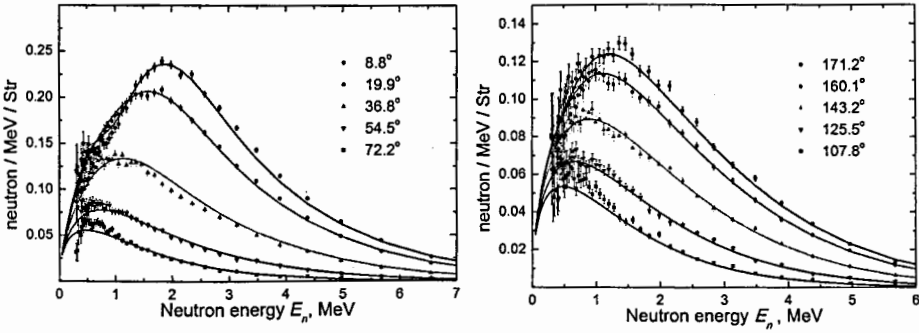

Fig. 3. The comparison of prompt fission neutron spectra measured for fixed angles relative to the direction of motion of the light fragment and calculated ones.

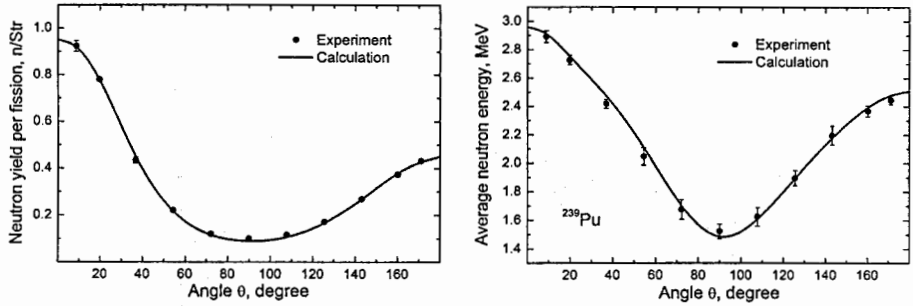

Fig. 4. Left – the prompt fission neutron yield as a function of the angle between neutron flight direction and the direction of motion of the light fragment. Right – the angular dependence of the average neutron emission energy in the laboratory system.

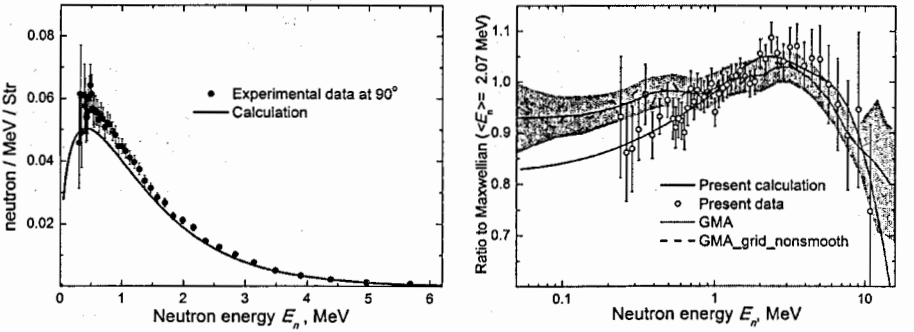

Fig. 5. Left – the PFNS measured for angle 90° relative to the fission fragment direction. Right – the total PFNS of ^{239}Pu(n,f) obtained by summing over angles θ are shown as a ratio to Maxwell distribution. GMA – generalized least square fit of prompt fission neutron spectra measured by different experimental groups (non-model evaluation) – taken from ref. [2].

The experimental and model neutron spectra have been compared in 0.2–10 MeV energy range. On the whole, the calculated model energy and angular distributions agree rather well with the experimentally obtained distributions. However, there is a minor distinction which is most clearly demonstrated at Fig. 5, where PFNS measured for angle 90° relative to fission fragment direction and the total PFNS obtained by summing over angles are compared with the corresponding calculated values. Note that the obtained total PFNS are in agreement with evaluated spectrum (GMA fit [2]) within experimental errors and, therefore, it can be said about the absence of any significant systematic measurement errors in our investigation. Then, the observed differences may be interpreted as a manifestation of "scission" neutrons and the average energy of these neutrons and their yield can be estimated.

The systematic difference of calculated total PFNS from total PFNS measured by different experimental groups (evaluated spectrum – GMA fit) is visible in the neutron energy range lower than 0.6 MeV. The "scission" neutron spectrum obtained as a difference between evaluated total PFNS (GMA fit) and model calculation is shown in Fig. 6 as a line with error corridor. To verify this statement, the PFNS measured for angles close to 90° relative to the direction of the light fragments' movement, were compared with calculated PFNS at the same angles. And the "scission" neutron spectrum was obtained with the use of the difference

spectra obtained as the difference between the measured and model spectra for angles of 72.2°, 90° and 107.8° with respect to the direction of motion of the light fragment. There is a good agreement within experimental uncertainties between spectra of "scission" neutrons obtained by two different ways (see Fig. 6). Further, the spectrum of scission neutrons found from partial data was approximated by the least squares method by two functions:

$$p_S(E) = \frac{p_0}{4\pi} \cdot \frac{E}{T_0^2} \cdot \exp\left(-\frac{E}{T_0}\right) \quad (1)$$

$$p_S(E) = \frac{p_0}{4\pi} \cdot \frac{E}{T_0^2} \cdot \exp\left(-\frac{E}{T_0}\right) + \frac{p_1}{4\pi} \cdot \frac{E}{T_1^2} \cdot \exp\left(-\frac{E}{T_1}\right) \quad (2)$$

The parameters p_0, T_0, p_1 and T_1 were varied. These two functions describe well the experimental data. The approximation Eq.(1) shown in Fig. 6 provides the following parameters of the spectrum of scission neutrons: the fraction of scission neutrons in the total number of prompt fission neutrons per fission event and the average energy of scission neutrons are equal to 3.6 ± 0.5 % and 0.9 ± 0.19 MeV, respectively. When Eq.2 is used, the corresponding values are 4.5 ± 0.9 % and 1.6 ± 0.2 MeV.

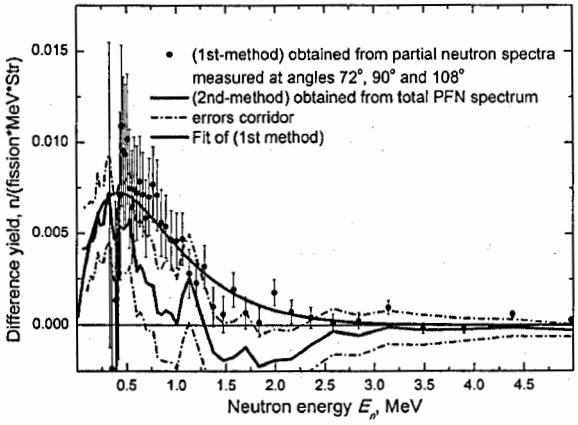

Fig. 6. Spectrum of "scission" neutrons for ^{239}Pu(n,f). Circles - the difference spectrum obtained using spectra measured at 72°, 90° and 108° relative to the direction of motion of the light fission fragment and the corresponding ones calculated under the assumption that all prompt neutrons are emitted from the accelerated fragments. Broken line - the difference between total PFNS obtained by experiment (estimated data and its errors) and calculated assuming that all prompt neutrons are evaporated from accelerated fragments. Solid line - fit of experimental data marked with circles by the equation (1).

It should be noted that these estimations of properties of "scission" neutrons were performed assuming isotropic emission of "scission" neutrons in the laboratory system. Probably, this assumption is very close to the real situation, because in the measurements of the angular dependency of the neutron-neutron coincidence curves (see table 1, ref. [10]), which are very sensitive to isotropic component in the laboratory system, the same values of "scission" neutron yield were obtained within experimental errors.

Conclusion

The angular and energy distribution of the prompt neutrons for ^{239}Pu have been measured.
A comparative analysis of the obtained angular and energy distributions of prompt neutrons from ^{239}Pu and calculated ones enabled to make the following conclusions:

- the angular anisotropy of the neutron emission in the fragment center-of–mass system should be taken into account;
- there are some surplus of measured neutron yield above calculated one in low energy range for the total prompt fission neutron spectrum as well as for neutron spectra at fixed angles near 90° (relative to fission fragments direction);
- the yield of this low energy component of "scission" neutrons is equal to 3.6 ± 0.5 % of total neutron yield per fission event;
- the maximum contribution of "scission" neutrons do not exceeds 5% of the total neutron yield.

Acknowledgements

We wish to thank L.S. Falev and V.E. Sokolov for help in adjustment of the equipment and conducting the experiments, T.E. Kuz'mina from Khlopin Radium Institute for producing the ^{239}Pu targets. The authors are very grateful to I.S. Guseva for helpful discussions.

References

[1] P. Talou, B. Becker, T. Kawano, M. B. Chadwick, and Y. Danon, Phys. Rev. C **83**, 064612 (2011).

[2] R. Capote, Y.-J. Chen, F.-J. Hambsch, N.V. Kornilov, J.P. Lestone, O. Litaize, B. Morillon, D. Neudecker, S. Oberstedt, T. Ohsawa, N. Otuka, V.G. Pronyaev, A. Saxena, O. Serot, O.A. Shcherbakov, N.-C. Shu, D.L. Smith, P. Talou, A. Trkov, A.C. Tudora, R. Vogt, A.S. Vorobyev, Nuclear Data Sheets, **131**, 1 (2016).

[3] A.S. Vorobyev, O.A. Shcherbakov, Yu.S. Pleva, A.M. Gagarski, G.V. Val'ski, G.A. Petrov, V.I. Petrova, T.A. Zavarukhina, *et. al., Nucl. Instr. and Meth.* **A598**, 795 (2009).

[4] A.S. Vorobyev, O.A. Shcherbakov, A.M. Gagarski, G.V. Val'ski, G.A. Petrov, EPJ Web of Conference **8**, 03004 (2010).

[5] A.S. Vorobyev, O.A. Shcherbakov, Yu.S. Pleva, A.M. Gagarski, G.V. Val'ski, G.A. Petrov, V.I. Petrova, T.A. Zavarukhina, Proc. of the XVII-th International Seminar on Interaction of Neutrons with Nuclei "Neutron Spectroscopy, Nuclear Structure, Related Topics", ISINN-17, Dubna, May 27-29, 2009, ed. A.M. Sukhovoj, JINR, Dubna, E3-2010-36, 2010, p. 60.

[6] A.S. Vorobyev, O.A. Shcherbakov, VANT, Ser. Nuclear Constants, Issue 1-2, 37 (2011-2012) [report INDC(CCP)-0455, IAEA, Vienna, 2014].

[7] A.S. Vorobyev, O.A. Shcherbakov, VANT, Ser. Nuclear Constants, Issue 2, 52 (2016).

[8] J.S. Fraser and J.C.D Milton, Ann. Rev. Nucl. Sci. **16**, 379 (1966).

[9] Yu. S. Zamyatnin, D. K. Ryazanov, B. G. Basova, A.D. Rabinovich, V.A. ,Korostylev Sov. J. Nucl. Phys. **29**, 306 (1979)

[10] I.S. Guseva, A.M. Gagarski, V.E. Sokolov, G.A. Petrov, T.A. Zavarukhina, Proc. of the XVIII-th International Seminar on Interaction of Neutrons with Nuclei "Fundamental Interaction & Neutrons, Nuclear Structure, Ultracold Neutrons, Related Topics", ISINN-24, Dubna, May 24-27, 2016, ed. A.M. Sukhovoj, JINR, Dubna, E3-2017-8, 2017, p. 387.

[11] W. Mannhart, in *Proceedings of the IAEA Consulting Meeting*, INDC (NDS)-220 (Vienna, 1989), p. 305.

[12] J.B. Wilhelmy, E. Cheifetz, R.C. Jared, *et. al.*, Phys. Rev. **C5**, 2041 (1972).

[13] T. Ericson and V. M. Strutinski, Nucl. Phys. **8**, 284 (1958).

[14] V. E. Bunakov, I. S. Guseva, S. G. Kadmenskii, and G. A. Petrov, Izv. Akad. Nauk, Ser. Fiz. **70**, 1618 (2006).

[15] A.S. Vorobyev, O.A. Shcherbakov, A.M. Gagarski, G.A. Petrov, G.V. Val'ski, JETP **125**(4), 619 (2017).

Научное издание

FUNDAMENTAL INTERACTIONS & NEUTRONS, NUCLEAR STRUCTURE, ULTRACOLD NEUTRONS, RELATED TOPICS

XXV International Seminar on Interaction of Neutrons with Nuclei

Proceedings of the Seminar

ФУНДАМЕНТАЛЬНЫЕ ВЗАИМОДЕЙСТВИЯ И НЕЙТРОНЫ, СТРУКТУРА ЯДРА, УЛЬТРАХОЛОДНЫЕ НЕЙТРОНЫ, СВЯЗАННЫЕ ТЕМЫ

XXV Международный семинар по взаимодействию нейтронов с ядрами

Труды семинара

Ответственная за подготовку сборника к печати *Л. В. Мицына.*

Сборник отпечатан методом прямого репродуцирования с оригиналов, предоставленных оргкомитетом.

E3-2018-12

Подписано в печать 05.04.2018
Формат 60×90/16. Бумага офсетная. Печать офсетная
Усл. печ. л. 26,5. Уч.-изд. л. 40,96. Тираж 80 экз. Заказ № 59356

Издательский отдел Объединенного института ядерных исследований
141980, г. Дубна, Московская обл., ул. Жолио-Кюри, 6.
E-mail: publish@jinr.ru
www.jinr.ru/publish/